International Association of Geodesy Symposia
148

Georgios S. Vergos
Roland Pail
Riccardo Barzaghi *Editors*

International Symposium on Gravity, Geoid and Height Systems 2016

Proceedings Organized by IAG Commission 2 and the International Gravity Field Service, Thessaloniki, Greece, September 19-23, 2016

Springer

International Association of Geodesy Symposia

Jeffrey T. Freymueller, Series Editor
Laura Sánchez, Series Assistant Editor

International Association of Geodesy Symposia

Jeffrey T. Freymueller, Series Editor
Laura Sánchez, Series Assistant Editor

More information about this series at http://www.springer.com/series/1345

International Symposium on Gravity, Geoid and Height Systems 2016

Proceedings Organized by IAG Commission 2 and the International Gravity Field Service, Thessaloniki, Greece, September 19–23, 2016

Edited by

Georgios S. Vergos, Roland Pail, Riccardo Barzaghi

Springer

Volume Editors

Georgios S. Vergos
Laboratory of Gravity Field Research
and Applications (GravLab)
Department of Geodesy and Surveying
Aristotle University of Thessaloniki
Thessaloniki
Greece

Roland Pail
Vice-Dean of Faculty of Civil, Geo and
Environmental Engineering
Institute of Astronomical and Physical Geodesy
Technische Universität München
Munich
Germany

Riccardo Barzaghi
DICA-Politecnico di Milano
Milano
Italy

Series Editor

Jeffrey T. Freymueller
Geophysical Institute and Department of Geology
and Geophysics
University of Alaska Fairbanks
Fairbanks
United States of America

Assistant Editor

Laura Sánchez
Deutsches Geodätisches Forschungsinstitut
Technische Universität München
Munich
Germany

ISSN 0939-9585
International Association of Geodesy Symposia
ISBN 978-3-319-95317-5
https://doi.org/10.1007/978-3-319-95318-2

ISSN 2197-9359 (electronic)

ISBN 978-3-319-95318-2 (eBook)

Library of Congress Control Number: 2018953055

This Springer imprint is published by the registered company Springer Nature Switzerland AG
The registered company address is: Gewerbestrasse 11, 6330 Cham, Switzerland

Preface

These proceedings include a selection of 27 papers presented at the International Association of Geodesy (IAG) symposium "Gravity, Geoid and Height Systems 2016" (GGHS2016). GGHS2016 was the first joint international symposium organized by IAG Commission 2 "Gravity Field", the International Gravity Field Service (IGFS) and the GGOS Focus Area "Unified Height System". It took place in Thessaloniki, Greece, in September 19–23, 2016, at the premises of the Aristotle University of Thessaloniki. The symposium was organized by the Department of Geodesy and Surveying of the Aristotle University of Thessaloniki, which presently hosts the IGFS Central Bureau. The focus of the symposium was on methods for observing, estimating and interpreting the Earth's gravity field as well as its applications.

GGHS2016 continued the long history of IAG's Commission 2 Symposia, GGG2000 (Banff, Canada), GG2002 (Thessaloniki, Greece), GGSM2004 (Porto, Portugal), GGEO2008 (Chania, Greece), GGHS2012 (Venice, Italy), with those of IGFS, 1st IGFS Meeting 2006 (Istanbul Turkey), 2nd IGFS Meeting 2010 (Fairbanks, Alaska, USA), and 3rd IGFS Meeting 2014 (Shanghai, China) under a unified umbrella, the latter being decided during the XXVI IUGG General Assembly in Prague.

For GGHS2016, 211 abstracts were received, out of which 94 were scheduled as oral presentations and 117 as posters. A total of 204 attendants from 36 countries participated in the conference. It should be particularly emphasized that this symposium was able to attract the younger generation of scientists, since 35% of the total number of participants were either MSc students or PhD candidates. All material and abstracts relevant to GGHS2016 can be accessed through the dedicated website at http://gghs2016.com/.

The scientific programme of GGHS2016 was of outstanding quality and showed significant scientific advancements in several fields of gravity field research, being structured in the following six sessions:

- Session 1: Current and future satellite gravity missions
  Chairs: Thomas Gruber and David Wiese
- Session 2: Global gravity field modelling
  Chairs: Nikolaos Pavlis and Shuanggen Jin
- Session 3: Local/regional geoid determination methods and models
  Chairs: Urs Marti and Hussein Abd-Elmotaal
- Session 4: Absolute and relative gravity: observations and methods
  Chairs: Leonid Vituskin and Jakob Flury
- Session 5: Height systems and vertical datum unification
  Chairs: Michael Sideris and Laura Sánchez
- Session 6: Satellite altimetry and climate-relevant processes
  Chairs: Ole Andersen and Annette Eicker

Many thanks go to all the session chairs, who devoted a lot of time in the compilation of the programme of the symposium and helped to make it successful. Sincere thanks go as well to Jeff Freymueller, the editor-in-chief of the IAG Symposia series, and to Laura Sánchez, assistant series editor, who both advanced and kept on track the publication of these

proceedings. Meanwhile, we would like to thank all reviewers, who are listed in this volume as an appreciation of their dedication.

The Local Organizing Committee was led by Georgios S. Vergos and consisted of Ilias N. Tziavos, Vassilios N. Grigoriadis, Dimitrios A. Natsiopoulos, Christopher Kotsakis and Dimitrios Tsoulis. Lastly, sincere thanks go out to all the participating scientists and graduate students who made the GGHS2016 symposium and these proceedings a success.

This volume contains selected papers from these sessions. All published papers were peer-reviewed. We warmly recognize the contributions and support of the associate editors and reviewers.

Photo of the GGHS2016 participants in the Aristotle University of Thessaloniki Main Ceremony Hall

Director Central Bureau of the International Gravity Field Service (IGFS)
Thessaloniki, Greece — Georgios S. Vergos

President IAG Commission 2 - Gravity Field
Munich, Germany — Roland Pail

Chair International Gravity Field Service (IGFS)
Milano, Italy — Riccardo Barzaghi

Contents

Rigorous Evaluation of Gravity Field Functionals from Satellite-Only Gravitational Models Within Topography

Michael B. Sheng, Petr Vaníček, Robert Kingdon, and Ismael Foroughi

Abstract

Currently, extensive work is being done in the field of geodesy on producing better gravitational models using purely space-based techniques. With the large datasets spanning a long timeframe, thanks to the GOCE and GRACE missions, it is now possible to compute high quality global gravitational models and publish them in a convenient form: spherical harmonics. For regional geoid modeling, this is advantageous as these models provide a useful reference which can be improved with terrestrial observations. In order for these global models to be usable below the topographical surface, certain considerations are required; topographical masses cause the function that describes the gravity potential to be non-harmonic in the space between the topographical surface and the geoid. This violates the mathematical assumptions behind solid spherical harmonics.

This paper aims to look at the error caused by evaluating solid spherical harmonics when topography is present. It thus provides a more rigorous methodology than the commonly used approach of computing the quasigeoid and then applying an approximate correction term for the geoid-quasigeoid separation. It is therefore well-suited for the Stokes-Helmert approach to high-precision regional geoid computation. Comparisons between the more rigorous methodology and the generally used algorithm are made in order to study the error that is committed. With a range of 23.6 cm and a standard deviation of 0.8 cm, this is a non-trivial error if the ultimate goal is to compute a regional geoid with an accuracy of better than 1 cm.

Keywords

Geoid • Gravitational model • Harmonic synthesis • Stokes-Helmert

1 Introduction

This paper describes a methodology for rigorously evaluating functionals from global gravitational models over land while accounting for topographical density and is designed specifically for use in the well documented SHGeo high-precision regional geoid computational scheme and associated software package (Vaníček and Martinec 1994). This paper also investigates the error that is committed by neglecting the requirement of harmonicity of the gravity potential within topography when one wishes to work with the global model below the topographic surface, or in our case, on the geoid. A similar methodology is presented in Wang et al. (2012) although the numerical results are not rigorously evaluated as they opt for an alternative approach more tailored for use with ultra-high degree reference geopotential models.

Initially, several satellite-only global models were considered in the computations: DIR-R5, GGM05S, and GOCO05S. These models were considered due to the

M.B. Sheng (✉) • P. Vaníček • R. Kingdon • I. Foroughi
Department of Geodesy and Geomatics Engineering, University of New Brunswick, Fredericton, Canada
e-mail: michaelsheng1@gmail.com

G. S. Vergos et al. (eds.), *International Symposium on Gravity, Geoid and Height Systems 2016*, International Association of Geodesy Symposia 148, https://doi.org/10.1007/1345_2017_26

differing data sources used in their formulation but only the results from DIR-R5 will be discussed in this paper as the results confirmed that the error committed by assuming that a non-harmonic function will behave as if it were harmonic depends on topography and is independent of the potential model. Due to the limited useful spectral content of the satellite-only models, the studied model is limited to degree and order 160 which is sufficient for providing a satellite-only reference field for computing regional high-precision geoids (Abdalla et al. 2012; Foroughi et al. 2016).

The model spherical harmonic coefficients are generally referred to the sphere with radius equal to the major-semi axis of the geocentric ellipsoid of revolution (a), such as the GRS80 reference ellipsoid. For various applications, we need to know the potential field described by the series on the geoid (i.e. inside of topography) and not on this sphere. This complicates matters as the field cannot be continued downward to the geoid because it does not behave in a harmonic manner within the topographical masses located between the Brillouin sphere and the geoid (Heiskanan and Moritz 1967). In practice, various functionals of the gravity field are often evaluated within the topography directly from the harmonic coefficients (Barthelmes 2009) which violates the fundamental assumptions of harmonic series (that the field they represent is harmonic in the space where the field is considered).

2 Methodology

The first fact to be considered is that topography protrudes in places above the sphere of radius a thus making the gravity potential in the space above the sphere inherently non-harmonic. In order to work around this problem, the spectral coefficients should be scaled to the Brillouin sphere of somewhat larger radius R_B. Then, by making use of Helmert's second condensation method, it is possible to more or less rigorously (the topographical density is known only to a certain degree) account for the effects of topographical masses and make the gravity potential everywhere above the geoid more or less harmonic (Helmert 1884; Vaníček and Martinec 1994). It should be noted that there are an infinite number of ways to compensate for the topographic masses (Helmert's condensations, Pratt-Hayford, Airy-Heiskanen, etc. (Heiskanen and Moritz 1967)), and that Helmert's second condensation was chosen here due to the direct applicability to the SHGeo computational scheme. The difference between the topographical and the condensed topographical potentials – the so-called direct topographical effect (DTE, δV) – is expressed in spectral form derived by Vaníček et al. (1995). Its subtraction transforms the gravity potential from the real space to the Helmert space in which the gravity potential behaves (more or less) harmonically everywhere above the geoid. We have:

$$\forall n \geq 0, m = 0, 1, \ldots, n : {W^H}_{nm} = W_{nm} - \delta V_{nm} \quad (1)$$

$$\forall n \geq 0, m = 0, 1, \ldots, n : \delta V_{nm} \cong 2\pi G\rho_0 \frac{n}{2n+1}\left(H^2\right)_{nm} \quad (2)$$

where G is the gravitational constant, ρ_0 is the global mean topographic density of 2,670 kg m^{-3}, and $(H^2)_{nm}$ are the coefficients of topographical height squared. The astute reader will notice the differences between Eq. (2) presented above and Eq. (20) from Vaníček et al. (1995); the difference comes from the choice to conserve the total mass of the Earth as opposed to conserving the centroid when transforming to Helmert's space (Wichiencharoen 1982; Martinec 1993). Once we have obtained Helmert's gravity potential W^H, the normal potential (U) generated by the GRS80 ellipsoid of revolution is subtracted from it to arrive at Helmert's disturbing potential:

$$\forall n \geq 0, m = 0, 1, \ldots, n : {T^H}_{nm} = {W^H}_{nm} - U_{n0}, \quad (3)$$

where U_{n0} has only even zonal harmonics different from 0.

Because the space through which the potential is to be "downward continued" has been made as free of mass as we know how, the gravitational potential behaves more or less harmonically and it is now possible to express Helmert's disturbing potential on the Helmert co-geoid by evaluating the harmonic coefficients of T^H for $r = r_g$:

$$T^H(r, \varphi, \lambda) = \frac{GM}{r}\sum_{n=0}^{n_{max}}\left(\frac{R}{r}\right)^n \sum_{m=0}^{n} \times \left({C^H}_{nm}\cos m\lambda + {S^H}_{nm}\sin m\lambda\right) P_{nm}(\sin\varphi) \quad (4)$$

where (φ, λ) are the geocentric latitude and longitude, C^H and S^H are the harmonic coefficients of Helmert's disturbing potential (${T^H}_{nm}$) in the geodetic norm (Varshalovich et al. 1988), P_{nm} are the associated Legendre polynomials, R is the radius to which the coefficients are referred (in our case the radius of the Brillouin sphere), and r is the radius of the surface where the disturbing potential T^H is synthesized (in our case, the radius of the geoid, r_g, approximated by r_e with a resulting error of less than 1 cm) (Barthelmes 2009; Vaníček et al. 1995). Let us note that the same expression in spectral form can be used in any space where the gravitational potential behaves harmonically above the surface r defined in Eq. (4) and Helmert's space was chosen for this study simply due to the ease of implementation with the SHGeo software package.

We note that a "Helmertisation" of a global field had already been attempted by Vaníček et al. (1995). In their derivations, Vaníček et al. assumed, incorrectly as it turns out, that the global field would be known at the reference ellipsoid level and be valid at the geoid. As this cannot be the case, their results are not quite correct.

Once "downward continued", Helmert's disturbing potential is transformed to give us the Helmert co-geoid (the geoid in Helmert's space) using Bruns's formula. If needed, the Helmert co-geoid is transformed to the real space by accounting, once again, for the residual topographical potential of the difference between topography and the condensation layer, also known as the primary indirect topographical effect on the geoid (PITE) or $\frac{\delta V}{\gamma_0}$. Thus, geoidal undulation (N) in the real space is obtained as:

$$N\left(\varphi,\lambda\right)=\frac{T^{H}\left(r_{g},\varphi,\lambda\right)}{\gamma_{0}\left(\varphi\right)}+\frac{\delta V\left(r_{g},\varphi,\lambda\right)}{\gamma_{0}\left(\varphi\right)} \tag{5}$$

where:

$$\delta V\left(r_{g},\varphi,\lambda\right)=\frac{GM}{r_{g}}\sum_{n=0}^{n_{max}}\left(\frac{R}{r_{g}}\right)^{n}\sum_{m=0}^{n}\times\left(C^{\delta V}{}_{nm}\cos m\lambda+S^{\delta V}{}_{nm}\sin m\lambda\right)P_{nm}\left(\sin\varphi\right) \tag{6}$$

3 Numerical Example

In this section several comparisons are made between the methodology described in the previous section and the not so rigorous methodology that directly estimates geoidal undulation without converting topography into a space in which the gravity potential is harmonic. This is done approximately by applying Eq. (116) from Barthelmes (2009) presented as:

$$N\left(\varphi,\lambda\right)\cong\frac{GM}{r_{e}\gamma\left(r_{e},\varphi\right)}\sum_{n=0}^{n_{max}}\left(\frac{R}{r_{e}}\right)^{n}\sum_{m=0}^{n}\times\left(C^{T}{}_{nm}\cos m\lambda+S^{T}{}_{nm}\sin m\lambda\right)P_{nm}\left(\sin\varphi\right)-\frac{2\pi G\rho_{0}}{\gamma\left(r_{e},\varphi\right)}\times\left[R\sum_{n=0}^{n_{max}}\sum_{m=0}^{n}\left(C^{H}{}_{nm}\cos m\lambda+S^{H}{}_{nm}\sin m\lambda\right)P_{nm}\left(\sin\varphi\right)\right]^{2} \tag{7}$$

where $C^{H}{}_{nm}$ and $S^{H}{}_{nm}$ are the spectral coefficients of topographical heights scaled by R and $C^{T}{}_{nm}$ and $S^{T}{}_{nm}$ are the spectral coefficients of disturbing potential after applying Eq. (3) in the real space. The first term of this equation is supposed to give the quasigeoid and the second term adds an approximation of the geoid-quasigeoid separation. Apart from the fact that the quasigeoid cannot be properly expressed either by a harmonic series, nor any other series, there are several mathematical and physical problems with this approach. Firstly, the quasigeoid is a folded surface; therefore, the quasigeoidal height cannot be described as a function of horizontal position. Secondly it seems peculiar to use an approximate formula for the geoid-quasigeoid separation in the computation of an accurate geoid model.

For the comparisons, DIR-R5 was used up to degree and order 160 using the two differing methodologies. This comparison will give us the error committed by overlooking the laws of physics and mathematics. The following assumptions were made for the purpose of these numerical tests:

1. Topographical surface of the Earth (being a discontinuous function) can be represented by an infinite summation of continuous functions in the mean sense.
2. Real density variations within topography can be approximated by mean topographic density; the effect of topo-density inhomogeneity should also be considered if this methodology is to be applied properly but was not available when computations were done for this paper.
3. The radius of the geoid (r_g) can be approximated by the geocentric radius of the reference ellipsoid (r_e) with a sufficient accuracy (Vaníček et al. 1995).

Height squared coefficients from DTM2006.0 (Pavlis et al. 2007) were used in Eq. (2). The differences quoted here are those between the geoidal undulations computed by applying Eqs. (1)–(5) and the geoidal undulations computed by applying Eq. (7) in the real space. Figure 1 shows the differences between the non-rigorous process and our more rigorous process; the statistical summary of the differences between the two approaches are presented in Table 1.

For this numerical example, geoidal undulation was chosen as the functional of the gravity potential that must naturally be computed within topography. It should be noted that similar errors will arise when attempting to evaluate any other functional of the gravity potential within topography.

4 Discussion and Conclusions

One problem people may perceive with the aforementioned methodology is that nominally, the interior gravity potential series (meaning interior to the Brillouin sphere) is divergent because the radial functions *R/r* are everywhere larger than 1 and the sequence of radial functions $(R/r)^{n}$ grows beyond all limits with growing *n*. Here we make the following reasonable assumption: that the series does in fact converge for all *r* between the Brillouin sphere and the geoid because the Helmert disturbing potential coefficient sequence converges to 0 faster than the sequence $(R/r)^{n}$ diverges. It is intuitively clear that this condition is always satisfied as gravity in the space between the geoid and the Brillouin sphere has been always observed to be well within finite limits. For

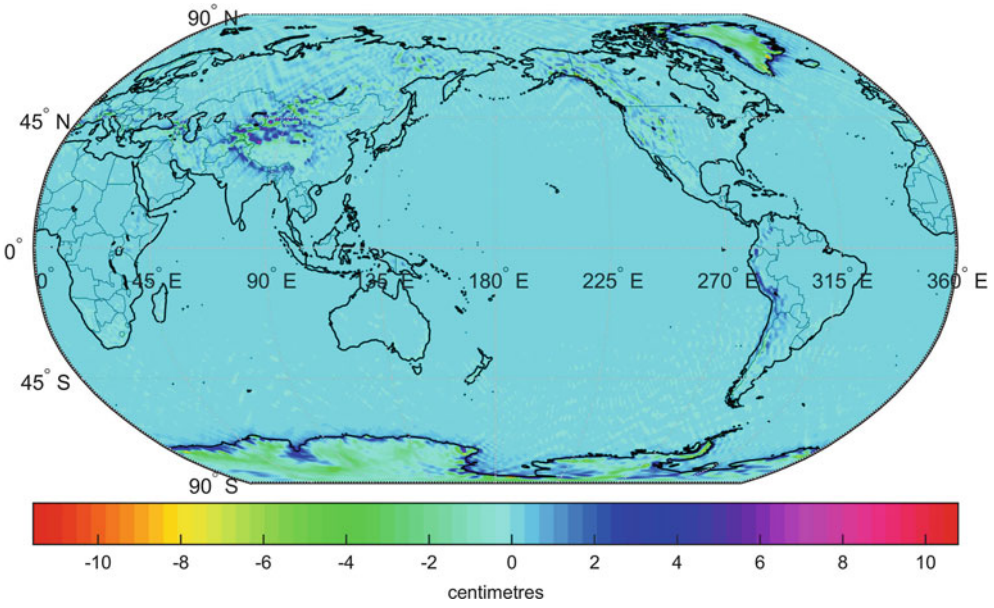

Fig. 1 Differences between approaches – DIR-R5

Table 1 Statistics of the differences between non-rigorous and rigorous methodologies

	Maximum	Minimum	Mean	Standard deviation
DIR-R5	11.3 cm	−12.3 cm	0.00 cm	0.8 cm

the purpose of this project, it is also clear that the series cannot numerically diverge as we truncate the series at a finite degree and order and therefore even the sequence $(R/r)^n$ cannot diverge to infinity.

As can be seen from the values shown in Table 1, the differences in the two methodologies are significant. From Fig. 1 we can see that the differences are directly correlated to topographical heights as should be expected from Eq. (2). The large differences in Antarctica and Greenland are likely due to the assumption that the mean topographical density represents real density. If a topo-density inhomogeneity model were used, as it should have been, the differences between the rigorous and more commonly-used methodologies would have been smaller in these regions but possibly larger in others.

Numerically, it would appear that the error committed by neglecting the requirement of harmonicity of the gravitational potential is not negligible if one aims to compute a regional geoid model with accuracy of 1 cm; errors present in the global model will have a direct effect on the resulting regional model. The range of the differences is 23.6 cm with a mean that tends to zero and a standard deviation of 0.8 cm. It seems only logical that one should prefer to use a methodology that strictly adheres to physical and mathematical principles rather than one which does not.

The next step in testing would be to incorporate the effect of lateral density variations to better capture the effects of real topography. The continuation of this work should also include the assessment of the geoidal undulations over a sample of GPS/levelling benchmarks globally; this would allow us to gain a better sense of the geometrical fit and it would also make the assessment more trustworthy by virtue of using independent data. Finally, the effect on regional geoid modeling of neglecting the requirements of harmonicity of global models should be investigated. Global models are implemented in various stages of the regional formulations; therefore, the propagation of errors might be more complex than initially assumed.

References

Abdalla A, Fashir H, Ali A, Fairhead D (2012) Validation of recent GOCE/GRACE geopotential models over Khartoum state – Sudan. J Geodetic Sci 2(2):88–97

Barthelmes F (2009) Definition of functionals of the geopotential and their calculation from spherical harmonic models. Scientific Technical Report STR09/02, Potsdam

Foroughi I, Vaníček P, Novák P, Kingdon R, Sheng M, Santos M (2016) Optimal combination of satellite and terrestrial gravity data for regional geoid determination using Stokes-Helmert method. Paper presented at the IAG Commission 2 meeting, 22 September 2016, Thessaloniki

Heiskanan WH, Moritz H (1967) Physical geodesy. W.H. Freeman and Co., San Francisco

Helmert FR (1884) Die mathernatischen und physikalischen Theorieen der hoheren Geodasie, vol 2. B.G. Teubner, Leipzig. (Reprinted in 1962 by Minerva GMBH, Frankfurt/Main)

Martinec Z (1993) Effect of lateral density variations of topographical masses in view of improving geoid model accuracy over Canada.

DSS contract 23244-2-4356/01-SS, Geodetic Survey of Canada, Ottawa

Pavlis NK, Factor JK, Holmes SA (2007) Terrain-related gravimetric quantities computed for the next EGM. In: Proceedings of the 1st international symposium of the international gravity field service, vol 18, Harita Dergisi, pp 318–323

Vaníček P, Martinec Z (1994) The Stokes-Helmert scheme for the evaluation of a precise geoid. Manuscr Geodaet 19:119–128

Vaníček P, Najafi M, Martinec Z, Harrie L, Sjöberg LE (1995) Higher-degree reference field in the generalized Stokes-Helmert scheme for geoid computation. J Geod 70:176–182

Varshalovich DA, Moskalev AN, Khersonskii VK (1988) Quantum theory of angular momentum. World Scientific Publishing Co., Singapore

Wang YM et al (2012) The US Gravimetric Geoid of 2009 (USGG2009): model development and evaluation. J Geod 86:165–180

Wichiencharoen C (1982) The indirect effects on the computation of geoid undulations. Science Report 336, Department of Geodesy, Ohio State University, Columbus

Application of the Recursive Least-Squares Adaptive Filter on Simulated Satellite Gravity Gradiometry Data

Dimitrios Piretzidis and Michael G. Sideris

Abstract

This study investigates the applicability of the recursive least-squares (RLS) adaptive filter for gravity field modelling applications. Simulated satellite gravity gradients are used to assess the performance of the algorithm. The synthetic data follow the behavior of the Gravity Field and Steady-State Ocean Circulation Explorer (GOCE) mission observations. An analysis is carried out, where the convergence speed, computational efficiency and optimal impulse response of the adaptive filter are examined. The behavior of the filtered gravity gradients in the time and spectral domain is also studied. The algorithm is capable of converging to a mean-square error (MSE) of 0.013 Eötvös, which is very close to the level of Gaussian noise (0.011 Eötvös) added to the synthetic observations. Although the RLS algorithm shows a fast convergence speed, a strong disadvantage that should be considered before its implementation is its reduced time efficiency.

Keywords

Adaptive signal processing • Filtering • GOCE satellite mission • Recursive Least-Squares • Satellite gravity gradients

1 Introduction

A global dataset of gravity gradients of the Earth's gravitational field is available from the European Space Agency's GOCE mission, along with precise positions of the satellite orbit (Floberghagen et al. 2011). Deriving suitable filtering algorithms for processing GOCE observations is still considered a challenging area of research due to the noise characteristics of the satellite gradiometer and due to the final stage of the mission, where the spacecraft was orbiting in a lower altitude collecting observations with different properties.

So far, many signal processing techniques have been tested on real GOCE data, leading to more sophisticated filtering algorithms and processing schemes. Among them, the space-wise approach (Reguzzoni and Tselfes 2008) is a particularly interesting and complex method for the evaluation of spherical harmonic coefficients and the determination of combined global geopotential models. The iterative scheme of the space-wise approach uses a time-wise Wiener filter and a complementary Whitening filter (Gatti et al. 2014) to take into account the loss of localized signal information. Other techniques of constructing geopotential models from GOCE data are the direct approach and the time-wise approach. In the direct approach of evaluating global geopotential models, autoregressive moving average (ARMA) filters and cascaded high-pass and low-pass filters with various cut-off frequencies are used to filter GOCE gravity gradients (Pail et al. 2011). Data-adaptive ARMA filters are used by the time-wise approach to de-correlate GOCE observations (Krasbutter et al. 2014).

In general, conventional signal processing algorithms are implemented in all gravity field modelling techniques. The motivation of this study mainly comes from the recent work of Piretzidis and Sideris (2017), where adaptive filtering algorithms, and particularly the least-mean-square (LMS)

D. Piretzidis (✉) • M.G. Sideris
Department of Geomatics Engineering, University of Calgary,
2500 University Dr. NW, Calgary, AB, T2N 1N4 Canada
e-mail: dimitrios.piretzidis@ucalgary.ca

G. S. Vergos et al. (eds.), *International Symposium on Gravity, Geoid and Height Systems 2016*,
International Association of Geodesy Symposia 148, DOI 10.1007/1345_2017_24

algorithm, are introduced and tested on filtering real GOCE data. In the same study, a comprehensive discussion on the possible implementation of this technique in the space-wise approach is also provided. Until now, only a small number of geodetic applications of these adaptive algorithms, and primarily of the LMS algorithm, can be found. For example, a simple LMS and a variable length LMS (VLLMS) adaptive filter is used in the work of Liu et al. (2009) and Ge et al. (2000), respectively, to filter out multipath errors from GPS pseudo-range and carrier-phase measurements. In geophysical applications, adaptive algorithms have been used for the deconvolution of geophysical data, e.g., in the work of Wang (1977), where an adaptive Wiener prediction filter is implemented in seismic data. The present study focuses on the adaptive RLS algorithm to filter simulated satellite gravity gradient data that resemble the properties of GOCE satellite observations. The selection of the adaptive RLS filter is made due to the fact that no previous studies have been performed with this algorithm on GOCE data processing applications, and in order to test and potentially apply this algorithm on real GOCE data.

The most important results of this work are presented with respect to the algorithm performance and the filtering of the synthetic observations and an assessment of the advantages and disadvantages of the RLS algorithm is made.

2 Recursive Least-Squares Algorithm

The development of all adaptive signal processing algorithms is based on three fundamental signals, defined for a specific time epoch n. The first one is the observed or input signal, which is denoted as $u(n)$. In general, the observed signal is corrupted by noise which needs to be filtered out. The second one is the estimated or output signal, which is denoted as $y(n)$. The estimated signal is the result of the input signal passing through the adaptive filter. The third one is the desired signal, which is denoted as $d(n)$. The desired signal represents the theoretical value that the input signal $u(n)$ should have if the noise is completely removed. The estimated signal is compared with the desired signal, and their difference forms the error signal $e(n)$. In adaptive filtering algorithms, the error signal is used in the next iteration of the algorithm to adjust the parameters (i.e., filter weights) of the adaptive filter. The adaptive filter at epoch n, denoted as $\boldsymbol{w}(n)$, is formed by the filter weights as follows:

$$\boldsymbol{w}(n) = [w_0(n) \;\; w_1(n) \;\; w_2(n) \;\; \cdots \;\; w_{M-1}(n)]^T \tag{1}$$

where M is the number of filter weights. The estimated signal $y(n)$ will then be given by the convolution of the input signal with the filter weights. If a linear relation exists between the observed and the desired signal, the weights of the adaptive filter will converge to an optimal solution after several iterations (Sesay 2014). When convergence is achieved, the iterative (or training) procedure stops and the estimated filter weights can be used to filter the remaining input signal.

In the work of Piretzidis and Sideris (2017), the LMS algorithm was tested, which corresponds to an adaptive Wiener filter based on the technique of stochastic gradient descent. The minimization of the mean-square error (MSE) $J(\boldsymbol{w})$ with respect to the filter weights $\boldsymbol{w}$ was used as an optimization condition of the LMS algorithm, i.e.,

$$\min_{\boldsymbol{w}} J(\boldsymbol{w}) = \min_{\boldsymbol{w}} E\left[e^2(n)\right] \tag{2}$$

where $E[\bullet]$ denotes expectation; hence $J(\boldsymbol{w})$ is a statistical parameter and LMS is a stochastic filtering technique. Contrary to that, the RLS algorithm that is implemented and tested in this study is an adaptive technique of deterministic nature based on least-squares filtering (Young 2011). The optimization condition of the adaptive RLS algorithm is the minimization of the sum of weighted squared-errors, denoted as $\mathcal{E}(\boldsymbol{w})$, with respect to the filter weights $\boldsymbol{w}$, as follows:

$$\min_{\boldsymbol{w}} \mathcal{E}(\boldsymbol{w}) = \min_{\boldsymbol{w}} \sum_{i=1}^{n} \lambda^{n-i} e^2(i) \tag{3}$$

with $0 < \lambda \leq 1$. For stationary environments, λ should be very close or equal to one. The parameter $\lambda^{n-\mathrm{i}}$ is called forgetting factor and comprises the weights of the squared-errors (not to be confused with the filter weights $\boldsymbol{w}$) in the form of an exponential windowing function. The formulation of parameter λ in Eq. (3) allows the RLS algorithm to weigh observations close to the current epoch n more than observations far away from epoch n, as in the former case λ^{n-i} would result in a weight close to 1 and in the latter case a weight close to 0. The adaptive RLS algorithm is an iterative process, where at every time epoch n, the estimation of the optimal filter weights is done in the following order of computations (Haykin 2014, Table 10.1):

$$\boldsymbol{k}(n) = \frac{\boldsymbol{P}(n-1)\,\boldsymbol{u}(n)}{\lambda + \boldsymbol{u}^T(n)\,\boldsymbol{P}(n-1)\,\boldsymbol{u}(n)} \tag{4}$$

$$\xi(n) = d(n) - \boldsymbol{u}^T(n)\widehat{\boldsymbol{w}}(n-1) \tag{5}$$

$$\widehat{\boldsymbol{w}}(n) = \widehat{\boldsymbol{w}}(n-1) + \boldsymbol{k}(n)\xi(n) \tag{6}$$

$$\boldsymbol{P}(n) = \lambda^{-1}\left[\boldsymbol{P}(n-1) - \boldsymbol{k}(n)\boldsymbol{u}^T(n)\,\boldsymbol{P}(n-1)\right] \tag{7}$$

where $\boldsymbol{k}(n)$ is the Kalman gain vector, $\xi(n)$ is the a-priori estimation error and $\boldsymbol{P}(n)$ is the inverse correlation matrix. The initialization of the matrix $\boldsymbol{P}(n)$ and the vector $\boldsymbol{w}(n)$ is done as follows:

$$\boldsymbol{w}(0) = \boldsymbol{0} \tag{8}$$

$$\boldsymbol{P}(0) = \delta^{-1}\boldsymbol{I} \tag{9}$$

The regularization parameter δ in Eq. (9) is a positive constant used only for the initialization of matrix $\boldsymbol{P}(n)$. The magnitude of δ can be specified as follows (Moustakides 1997; Haykin 2014, pp. 440):

$$\delta = \sigma_u^2(1-\lambda)^a \tag{10}$$

where σ_u is the standard deviation of observed signal $u(n)$ and a is a parameter depending on the signal-to-noise ratio (SNR). For the purposes of this simulation, a noise with a standard deviation of 0.011 Eötvös is used (see also Sect. 3), and the SNR is close to 28 dB. For a high SNR of the order of 30 dB, the value of a should be greater than zero and close to one (Haykin 2014, pp. 441). Choosing $\lambda = 0.999$, a reasonable value for δ would be in the interval:

$$0 < \delta \leq 0.075 \tag{11}$$

A complementary sensitivity analysis with respect to δ and λ revealed that choosing a regularization parameter δ within the interval of Eq. (11) practically results in the same optimal filter weights, with differences of the order of 10^{-15} among different solutions. A value of $\delta = 0.01$ was eventually selected for this study. Also the results of the same analysis indicate that a value of λ less than 0.99 will result optimal filter weights with high fluctuations, and a value less than 0.94 will result in rapid divergence of the RLS algorithm. Therefore, the choice of $\lambda = 0.999$ can be considered fairly rational.

3 Simulation Study

The main objective of the simulation study presented here is to demonstrate the ability of the RLS adaptive filtering algorithm to identify the relation between a given observed and a desired signal by training the adaptive filter and estimating optimal filter weights that would later be used for the filtering of the observed signal. The strategy used to generate the synthetic observed signal $u(n)$ and the synthetic desired signal $d(n)$ is solely based on the spectral properties of real GOCE gravity gradients of the disturbing potential and their comparison to gravity gradients derived from a geopotential model. GOCE Level 2b measurements, provided by Prof. I.N. Tziavos within the context of GOCESeaComb research project (Tziavos et al. 2015), are processed according to the methodology provided in the work of Piretzidis and Sideris (2017). Only the second radial component T_{zz} is studied here. The synthetic observed signal is simulated in two stages. In the first stage, synthetic observations T_{zz}^{obs-1} are generated using the amplitude spectrum of real GOCE observations. GOCE observations are influenced by colored noise due to the satellite gradiometer performance. The relation between the synthetic observed signal T_{zz}^{obs-1} and the synthetic desired signal T_{zz}^{des} is as follows:

$$T_{zz}^{obs-1} = T_{zz}^{des} + v_{zz}^{c} \tag{12}$$

where v_{zz}^{c} is the colored noise of GOCE observations. For a realistic simulation, v_{zz}^{c} should also be synthesized from the spectral structure of the GOCE gradiometer errors. This can be done by calculating and examining either the trace of the GOCE gravity gradient tensor (Ince and Pagiatakis 2016; Piretzidis and Sideris 2017), or the differences between GOCE observations and gravity gradients derived from a geopotential model, assuming that the latter are free of colored noise. For the purposes of this study, a different, more simplistic approach is used. It is assumed that the error v_{zz}^{c} corresponds to the high-frequency differences between gradients from GOCE observations and from the geopotential model EGM2008 (Pavlis et al. 2012). It is noted that, in reality, the differences between GOCE observations and gravity gradients derived from a geopotential model show a more complicated behavior. The power spectral density (PSD) of the GOCE and EGM2008 T_{zz} component is provided in Fig. 1a. It is seen that the two sets of data have a different behavior after 0.04 Hz, which corresponds to a spatial resolution of approximately 185 km. This frequency is marked in Fig. 1a with a bold, black line. The PSDs of the differences between the GOCE and EGM2008 T_{zz} component, and the trace of GOCE gravity gradient tensor are also provided in Fig. 1a to examine the spectral structure of GOCE errors. For frequencies greater than 0.04 Hz, the two error PSDs show the same behavior. Using the aforementioned assumption for v_{zz}^{c}, the synthetic desired signal and colored noise can be estimated by low-pass filtering the synthetic observations and deriving the differences between the synthetic observed and synthetic desired signal, respectively:

$$T_{zz}^{des} = \boldsymbol{w}_{zz} * T_{zz}^{obs-1} \tag{13}$$

$$v_{zz}^{c} = T_{zz}^{obs-1} - T_{zz}^{des} = T_{zz}^{obs-1} - \boldsymbol{w}_{zz} * T_{zz}^{obs-1} \tag{14}$$

where the vector $\boldsymbol{w}_{zz}$ corresponds to the filter weights (impulse response) and the operator $*$ denotes convolution. A finite impulse response (FIR) low-pass filter with 501 filter weights and a cut-off frequency of 0.04 Hz is used to filter

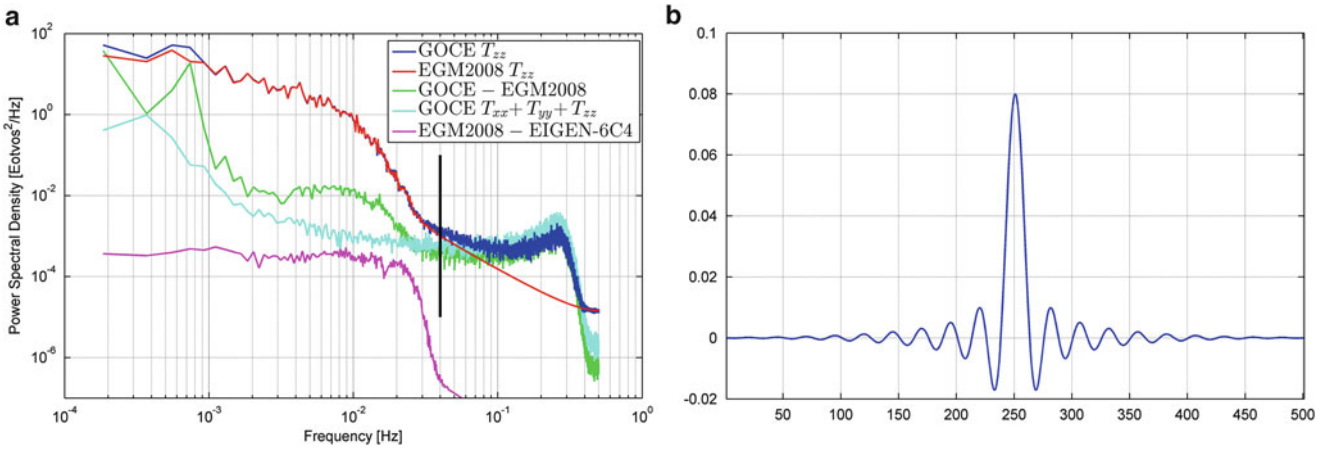

Fig. 1 (**a**) PSD of GOCE and EGM2008 T_{zz} component and (**b**) impulse response of low-pass FIR filter

T_{zz}^{obs-1} and derive the synthetic desired signal. The impulse response of the filter used is given in Fig. 1b. Simulating the desired signal in this way ensures that a linear relation between the observed and desired signal exists, as presented in Eq. (13). At this point, using T_{zz}^{obs-1} and T_{zz}^{des} signals in the RLS algorithm described in Sect. 2 will result in optimal filter weights and a filtered signal by definition exactly equal to $\boldsymbol{w}_{zz}$ and T_{zz}^{des}, respectively, making a performance analysis of the algorithm with regards to convergence speed and accuracy of the estimated signal unrealistic. For this reason, the signal T_{zz}^{obs-1} is further corrupted by white noise v_{zz}^{w} before passing through the adaptive algorithm, resulting the observed signal T_{zz}^{obs-2}:

$$T_{zz}^{obs-2} = T_{zz}^{obs-1} + v_{zz}^{w} = T_{zz}^{des} + v_{zz}^{c} + v_{zz}^{w} \qquad (15)$$

A standard deviation of 0.011 Eötvös is chosen for v_{zz}^{w}, which corresponds to the nominal accuracy of GOCE gradiometer within the bandwidth of 0.005–0.1 Hz (Wolf and Müller 2008). It is clarified that the synthetic desired signal T_{zz}^{des} is still simulated from T_{zz}^{obs-1} using Eq. (13) and not from T_{zz}^{obs-2}. A total number of 365 independent experiments are performed using 1 week of simulated data.

Two important remarks need to be made regarding the approach followed for this simulation. The first remark is related to the geopotential model selection. In theory, a GOCE-based geopotential model should be used for the simulation of the desired signal or the simulation of the error v_{zz}^{c}. A GOCE-based model would also ensure that the same geographic areas covered by GOCE observations are also covered by the data used for the construction of the selected geopotential model. EGM2008 is known to provide low accuracy in certain areas, such as South America, Africa and China, due to lack of available gravity data (Yi and Rummel 2014) and would not be the optimal choice. A more appealing choice would be the combined geopotential model EIGEN-6C4 (Förste et al. 2014), which includes both GOCE and terrestrial gravity data. In practice, the differences between EGM2008 and EIGEN-6C4 T_{zz} components have a standard deviation of 2.6 mEötvös, and their PSD is below the error PSDs given in Fig. 1a. The choice of geopotential model is of secondary importance only if the differences between the desired and estimated signals are greater than 2.6 mEötvös.

The second remark is related to the choice of directly simulating the observed signal, rather than constructing it by simulating and summing the desired signal and colored noise, independently. While the second case would result in a more realistic simulation, the performance analysis of the RLS algorithm would be limited to only a comparison between the desired and the estimated signal. The relation between the observed and the desired signal would not be completely known (although it can be estimated using, e.g., a Wiener filter, but the estimation would still contain an uncertainty) and the comparison between the estimated and the theoretical filter would be impossible. Simulating the observed signal, and later filtering it using known filter weights to derive the desired signal, might lead to a desired signal with different deterministic properties that depend on the simulation of the observations, but it would still guarantee that a theoretical relation between the desired and observed signal exists and is the same for all simulated samples.

4 Results

After running independent experiments using the synthetic data, the MSE is calculated for each iteration. A Gaussian noise of 0.011 Eötvös is added to the simulated data and, in theory, the minimum MSE cannot be below the level of

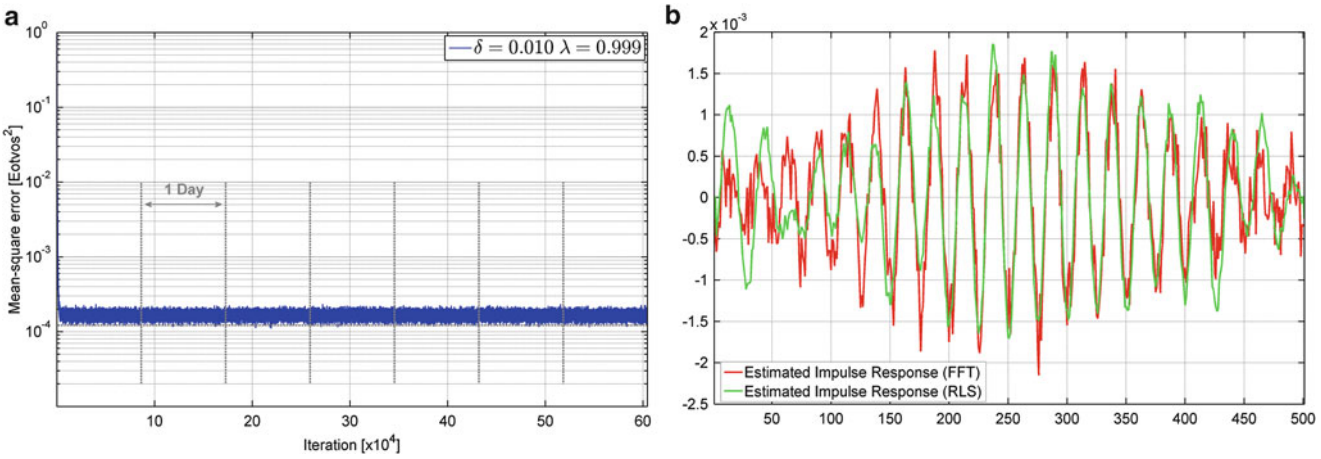

Fig. 2 (**a**) MSE convergence of RLS algorithm and (**b**) examples of differences between the optimal impulse response and the one estimated by the RLS algorithm (green line) and the Wiener filter (red line)

1.21×10^{-4} Eötvös^2. The MSE convergence of the RLS adaptive algorithm is given in Fig. 2a, where the theoretical level of the squared error is indicated with a grey dashed line. The adaptive RLS algorithm provides fast convergence speed, where the derivation of optimal filter weights is achieved within the first 5,000 iterations, corresponding to observations of approximately one full revolution of the satellite (5,400 s). The converged minimum MSE, using $\delta = 0.01$ and $\lambda = 0.999$, is 1.61×10^{-4} Eötvös^2. The differences between the estimated and theoretical optimal impulse response, after convergence is achieved, is presented in Fig. 2b. In red color is the difference between the estimated impulse response derived using conventional Wiener filter in the spectral domain (Bendat and Piersol 1993) and the true impulse response. The impulse response differences of both the RLS algorithm and the Wiener filter are not smooth. Also, the RLS algorithm produces an impulse response with higher differences for the filter weights at the edges. The execution time of the RLS algorithm for one independent experiment (7 days of observations) is approximately 1 h, making this algorithm highly time-consuming.

After the termination of the training procedure, the estimated optimal filter weights are used to filter the remaining observations and derive the estimated signal. In Fig. 3a, b, the results of the filtering are given in the time and spectral domain, respectively, for one experiment. Figure 3 also shows the relation between the synthetic observed and synthetic desired signal, where the high frequencies of the latter are suppressed. The estimated signal shows a good agreement with the desired signal, with a standard deviation of their differences equal to 3.4 mEötvös. In this case, and as discussed in Sect. 3, choosing between EGM2008 and EIGEN-6C4 would practically lead to the same estimated signal.

5 Summary and Conclusions

The use of suitable filtering algorithms is always a crucial component for the analysis and interpretation of geodetic signals. In this study, the adaptive RLS algorithm is used to filter simulated satellite gravity gradiometry data that resemble real GOCE satellite observations. The study is primarily focused on the performance of the adaptive algorithm in terms of convergence speed, estimated impulse response and computational efficiency. The properties of the estimated signal after the implementation of the RLS algorithm are also examined.

The RLS filter appears to be a very effective algorithm in terms of convergence speed but it is computationally intensive. The time inefficiency of the RLS algorithm is related to the complexity of the filter (e.g., number of filter weights) and the evaluation of the Kalman gain vector $\boldsymbol{k}(n)$, where computations with the correlation matrix $\boldsymbol{P}(n)$ of dimensions $M \times M$ are necessary, where M is the number of filter weights. Choosing a filter with lower number of weights could improve the execution speed of the algorithm. In the presence of white noise, measurements obtained during only one full revolution of the satellite, which correspond to less than 1 day of data, are needed for the convergence of the RLS algorithm, although this statement can be considered as unrealistically optimistic. For a more accurate simulation, the level and type of noise should also be taken into account, e.g., white noise, colored noise. For an added white noise of 0.011 Eötvös, the RLS filter converges to a MSE of 0.013 Eötvös, which is very close to the theoretical noise level and the resulting filtered gravity gradients show averaged differences of the order of 3 mEötvös compared to the desired gravity gradients. The RLS algorithm produces an estimated impulse response which is comparable to the

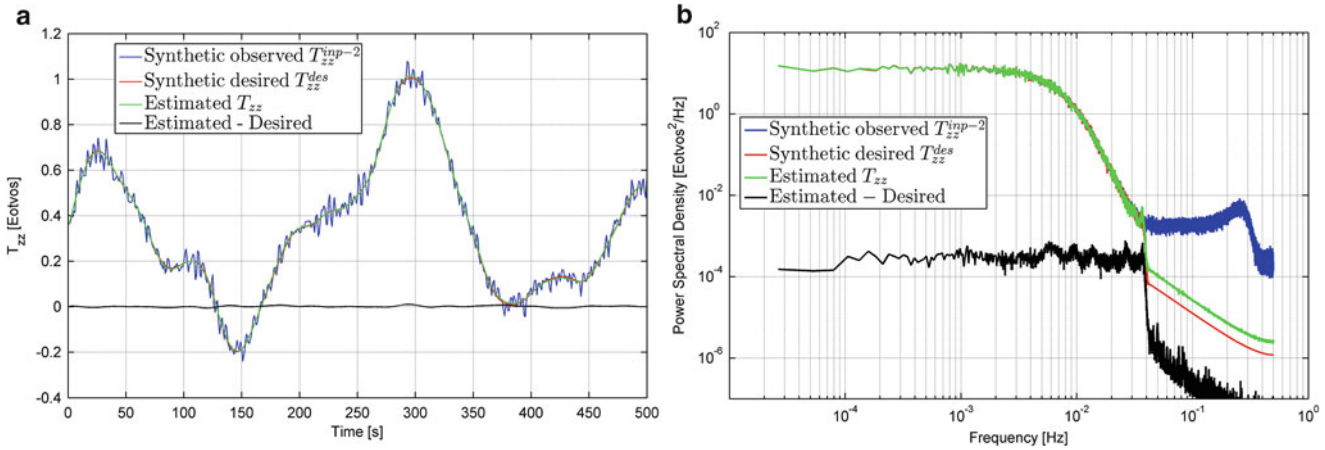

Fig. 3 Performance of filtered gravity gradients in (**a**) time domain and (**b**) frequency domain

one derived using a Wiener filter in the spectral domain. A comparison analysis between the LMS, RLS and, potentially, other adaptive filtering algorithms will be a subject of subsequent studies to further assess the capabilities of adaptive signal processing techniques in geodetic applications.

Acknowledgments This work is financially aided by a grant from Canada's Natural Sciences and Engineering Research Council (NSERC) to the second author. The GOCE Level 2b data were provided by Prof. I.N. Tziavos of the Aristotle University of Thessaloniki within the GOCESeaComb project. The two anonymous reviewers are thanked for their comments and suggestions for the improvement of this paper.

References

Bendat JS, Piersol AG (1993) Engineering applications of correlation and spectral analysis, 2nd edn. Wiley, New York

Floberghagen R, Fehringer M, Lamarre D et al (2011) Mission design, operation and exploitation of the gravity field and steady-state ocean circulation explorer mission. J Geod 85:749–758. https://doi.org/10.1007/s00190-011-0498-3

Förste C, Bruinsma SL, Abrikosov O et al (2014) EIGEN-6C4 The latest combined global gravity field model including GOCE data up to degree and order 2190 of GFZ Potsdam and GRGS Toulouse. In: EGU General Assembly 2014, Vienna, 27 April–2 May 2014. https://doi.org/10.5880/icgem.2015.1

Gatti A, Reguzzoni M, Migliaccio F, Sansò F (2014) Space-wise grids of gravity gradients from GOCE data at nominal satellite altitude. In: 5th international GOCE user workshop, Paris, 25–28 November 2014

Ge L, Chen H-Y, Han S, Rizos C (2000) Adaptive filtering of continuous GPS results. J Geod 74:572–580. https://doi.org/10.1007/s001900000120

Haykin SS (2014) Adaptive filter theory, 5th edn. Pearson, Upper Saddle River

Ince ES, Pagiatakis SD (2016) Effects of space weather on GOCE electrostatic gravity gradiometer measurements. J Geod 90(12):1389–1403. https://doi.org/10.1007/s00190-016-0931-8

Krasbutter I, Brockmann JM, Kargoll B, Schuh W-D (2014) Adjustment of digital filters for decorrelation of GOCE SGG data. In: Flechtner F, Sneeuw N, Schuh W-D (eds) Observation of the system earth from space - CHAMP, GRACE, GOCE and future missions. Springer, Berlin, Heidelberg, pp 109–114

Liu H, Li X, Ge L et al (2009) Variable length LMS adaptive filter for pseudorange multipath mitigation based on SydNET stations. J Appl Geod 3:35–46. https://doi.org/10.1515/JAG.2009.004

Moustakides GV (1997) Study of the transient phase of the forgetting factor RLS. IEEE Trans Signal Process 45:2468–2476. https://doi.org/10.1109/78.640712

Pail R, Bruinsma S, Migliaccio F et al (2011) First GOCE gravity field models derived by three different approaches. J Geod 85:819–843. https://doi.org/10.1007/s00190-011-0467-x

Pavlis NK, Holmes SA, Kenyon SC, Factor JK (2012) The development and evaluation of the earth gravitational model 2008 (EGM2008). J Geophys Res Solid Earth 117:B04406. https://doi.org/10.1029/2011JB008916

Piretzidis D, Sideris MG (2017) Adaptive filtering of GOCE-derived gravity gradients of the disturbing potential in the context of the space-wise approach. J Geod 91(9):1069–1086. https://doi.org/10.1007/s00190-017-1010-5

Reguzzoni M, Tselfes N (2008) Optimal multi-step collocation: application to the space-wise approach for GOCE data analysis. J Geod 83:13–29. https://doi.org/10.1007/s00190-008-0225-x

Sesay A (2014) Lecture notes on adaptive signal processing. The University of Calgary, Calgary

Tziavos IN, Vergos GS, Grigoriadis VN et al (2015) Validation of GOCE/GRACE satellite only and combined global Geopotential models over Greece in the frame of the GOCESeaComb project. Springer, Berlin, Heidelberg

Wang RJ (1977) Adaptive predictive deconvolution of seismic data. Geophys Prospect 25:342–381. https://doi.org/10.1111/j.1365-2478.1977.tb01174.x

Wolf K, Müller J (2008) Accuracy analysis of external reference data for GOCE evaluation in space and frequency domain. In: Sideris MG (ed) Observing our changing earth. Springer, Berlin, Heidelberg, pp 345–352

Yi W, Rummel R (2014) A comparison of GOCE gravitational models with EGM2008. J Geodyn 73:14–22. https://doi.org/10.1016/j.jog.2013.10.004

Young PPC (2011) Recursive least squares estimation. In: Recursive estimation and time-series analysis. Springer, Berlin, Heidelberg, pp 29–46

Accuracy of Regional Geoid Modelling with GOCE

Christian Gerlach and Vegard Ophaug

Abstract

Regional geoid models are based on the combination of satellite-only gravity field information and terrestrial data. Satellite information is conveniently provided in terms of spherical harmonic global potential models. Terrestrial information is mostly provided in terms of point or block mean values of gravity in the region of interest. Combination of the two sources of information in the overlapping spectral band is either based on deterministic or on stochastic considerations. We have tested different schemas for weighting satellite and terrestrial information and compared the results to GNSS-levelling data in Norway. The results provide implications for the quality of terrestrial data in the study area and for regional geoid modeling based on GOCE satellite models in general.

In order to minimize the computational burden, we avoid field transformation (from gravity anomalies to geoid heights) by employing an already existing regional geoid model to represent the terrestrial information. Combination is then performed by filtering geoid grids in the spatial domain.

Keywords

GNSS-levelling • GOCE • Regional geoid • Spectral combination

1 Introduction

High resolution gravity field and geoid models are of interest for geodetic and geophysical applications. A high resolution geoid model may, e.g., be used to define the vertical datum of a certain region with a focus on efficient determination of physical heights by means of GNSS-levelling (Rummel 2012) or to solve the height datum problem, i.e., to unify several mutually vertically shifted datum zones (Gruber et al. 2012; Gatti et al. 2013; Gilardoni et al. 2014).

A state-of-the-art high resolution geoid is based on (1) data from satellite gravity missions for modelling its large scale features and (2) terrestrial (including airborne and shipborne) data for those smaller scales which are not observable from space. Today, combined GRACE/GOCE models allow reconstructing the global gravity field down to resolutions of about 100 km with accuracies at the centimeter-level (Bruinsma et al. 2014). In our study, we use the global potential models (GPM) DIR5 (Bruinsma et al. 2014) and GOCO05s (Mayer-Gürr et al. 2015), both of which are based on GRACE and release-5 GOCE data.

In order to fully exploit the high quality of these GPMs, optimal combination with the terrestrial data available in the specific area of investigation is required. The selection of spectral weights for satellite and terrestrial data in the overlapping spectral band depends on the geographic location

C. Gerlach (✉)
Commission for Geodesy and Glaciology, Bavarian Academy of Sciences and Humanities, Alfons-Goppel-Str. 11, 80539 Munich, Germany

Faculty of Science and Technology, Norwegian University of Life Sciences, Drøbakveien 31, 1433 Ås, Norway
e-mail: gerlach@keg.badw.de

V. Ophaug
Faculty of Science and Technology, Norwegian University of Life Sciences, Drøbakveien 31, 1433 Ås, Norway
e-mail: vegard.ophaug@nmbu.no

G. S. Vergos et al. (eds.), *International Symposium on Gravity, Geoid and Height Systems 2016*,
International Association of Geodesy Symposia 148, DOI 10.1007/1345_2017_6

(due to slight inhomogeneities in the quality of satellite-only GPMs, see Fig. 1) and on quality and distribution of terrestrial observations. For example, in a region with sparse and/or less accurate gravity data, satellites may still provide valuable information for scales well below 100 km resolution (maybe down to 70 km), i.e. satellite information dominates the overlapping spectral band. However, in regions with dense and high quality terrestrial data (like the USA or central Europe) terrestrial information may outperform satellite data even for scales well above 100 km (say, up to 150 km, or so). Then terrestrial data dominates the common band. In the latter case the total error budget may end up at the level of some few centimeters in terms of geoid heights (see, e.g., Rülke et al. 2012; Denker 2016).

Optimal combination of satellite and terrestrial data requires selecting a weighting schema based on some optimization criterion. There exist deterministic and stochastic schemas, see, e.g., Sjöberg (2003) or Featherstone (2013).

Here we specifically test the stochastically optimal spectral combination method proposed by Wenzel (1981, 1982). Thereby, the error degree variances of the satellite-only global potential model, σ_l^{GPM}, and those of the terrestrial data, $\sigma_l^{\Delta g}$ are combined in a Wiener-type filtering schema according to

$$w_l = \frac{\left(\sigma_l^{\mathrm{GPM}}\right)^2}{\left(\sigma_l^{\mathrm{GPM}}\right)^2 + \left(\sigma_l^{\Delta g}\right)^2}. \quad (1)$$

For each spherical harmonic (SH) degree l, the w_l are spectral weights for the satellite information and $(1-w_l)$ represent the complementary weights for the terrestrial data. The approach assumes, (1) that the errors are isotropic and homogenous (thus they can be represented by error degree variances) and (2) that errors in satellite and terrestrial data are uncorrelated. Both aspects need to be considered in the construction of the error degree variances (see Sect. 2) and when interpreting the results (see Sect. 4).

Regarding the term *optimal combination*, we have to acknowledge the fact that employing error degree variances for description of satellite and terrestrial data allows only to investigate the average error behaviour. Taking into account spatial variability of the error characteristics would require to employ fully occupied error variance-covariance matrices for satellite and terrestrial data. In addition, the average error behaviour represented by error degree variances, in theory, is valid globally. However, as we scale the degree variances to fit the error amplitude expected (or tested) in our study area, the results represent exclusively the average error behaviour in our study area and cannot be transferred to other areas without adaption.

The aim of our study is to investigate different combination schemas for a test region in the Nordic countries. The focus is on data weighting in the spectral transition zone from satellite-only to terrestrial-only information. Because the quality description of the terrestrial data is difficult to judge, we derive Wenzel-weights w_l under different assumptions for $\sigma^{\Delta g}$, namely {0.2, 1.0, 2.0} mGal, and we compare the results to independent GNSS-levelling data in Norway. In addition to the stochastic approach, we test deterministic approaches, like the classical Wong & Gore kernel modification (Wong and Gore 1969) and simple data blending based on a Gaussian filter kernel as implemented, e.g., in Rülke et al. (2012). The Wong & Gore filter is chosen, because it is traditionally applied in the computation of Norwegian geoid models. Here we use the 2014-version regional geoid model NMA2014, provided by the Norwegian Mapping Authority (Ove Omang, personal communication). The model is a combination of terrestrial data and the release-4 GOCE model DIR4 (Bruinsma et al. 2013) employing a Wong & Gore type modification. The latter does not cut the kernel at one specific degree, but employs a linear transition of the weights (from 1 to 0) over the narrow spectral band between SH-degrees 130 and 140 (see the spectral weights in Fig. 2). The Gaussian filter is chosen, because it was used in Ophaug et al. (2015) for the generation of a simplified update of NMA2014. Thereby NMA2014 was combined with DIR5 using a Gaussian filter (correlation length 80 km), thus effectively "replacing" DIR4 by DIR5. This update decreased the standard deviation of the residuals with respect to GNSS-levelling from 3.5 to 3.0 cm.

As the focus of this study is on data weighting, we do not go into specific methods for geoid computation, like Stokes integration, least-squares collocation or other alternatives. Actually we avoid field transformation from gravity anomalies to geoid heights, but represent the terrestrial data by a high-pass filtered version of the regional geoid model. Geoid heights generated on the same geographic grid from the coefficients of a GPM are smoothed with the complementary low-pass filter and the two grids are added to form the combined geoid solution.

Section 2 presents the error degree variances used for construction of the spectral weights w_l. The latter are treated in Sect. 3. Based on the error degree variances and the spectral weights, formal errors are derived for the combined geoid solutions. The actual geoid models are compared to GNSS-levelling data, thus providing empirical error estimates. Formal and empirical errors are discussed in Sect. 4 and the results are summarized in Sect. 5.

We may also have to mention that, strictly speaking, the quantities we work with are height anomalies and normal heights. However, since our focus is on data weighting and the results should be independent from the technical

differences between geoid and quasigeoid computation, we will consistently use the term geoid throughout the text, even though this may seem a bit loose in some places.

2 Error Degree Variances

2.1 Error Degree Variance of Terrestrial Gravity Data

Regional geoid computation is based on point gravity data or corresponding area averages. Thereby the following error contributions are of relevance: (1) errors of original gravity observations, (2) errors of the point coordinates when computing anomalies, (3) any computational errors that arise in the process of forming area averages, or in applying data reductions and (4) last but not least, the representation error, i.e., the ability of a point value to represent the gravity field in its neighbourhood. In general, all of the above effects will lead to error characteristics which are neither homogenous nor isotropic, thus implying a fully occupied error variance-covariance matrix.

In many cases, information to fully account for all of the above errors is not readily available. In our case, we do not even go back to the original gravity data, but start with the regional geoid model derived from it. Trying to help out, we acknowledge that NMA2014 is based on a set of terrestrial gravity values which was in large parts provided for the computation of the European gravimetric geoid model EGG2008 (Denker 2013). Therefore, we approximate the error behaviour of NMA2014 by the error description of EGG2008 as published in Denker (2013). There it is provided in the form of the error covariance function of geoid heights which, according to Hofmann-Wellenhof and Moritz (2005), can be written in spectral representation as

$$C^{N,\mathrm{EGG2008}}(\psi) \;=\; R^2 \sum_{l=2} \sigma_l^{\mathrm{EGG2008}}\, P_l(\cos\psi), \qquad (2)$$

where $\sigma_l^{\mathrm{EGG2008}}$ are dimensionless error degree variances of EGG2008, R is the radius of the Earth (and provides a scaling from dimensionless degree variances to degree variances of geoid heights), $P_l(\cos\psi)$ are Legendre polynomials and ψ is spherical distance. We have used the spatial function published in Denker (2013) to derive error degree variances $\sigma_l^{\mathrm{EGG2008}}$ by spectral analysis of Eq. (2) as follows (see again Denker 2013)

$$R^2\,\sigma_l^{\mathrm{EGG2008}} \;=\; \frac{2l+1}{2} \int_{\psi=0}^{\pi} C^{N,\mathrm{EGG2008}}(\psi)\, P_l(\cos\psi)\, \sin\psi\; \mathrm{d}\psi \qquad (3)$$

The error description of EGG2008 is based on a 1 mGal correlated noise model (for the terrestrial part) and on error degree variances of the GPM EIGEN-5S (Förste et al. 2008); thus the satellite part is effectively represented by error degree variances from GRACE (see the error degree variances in Fig. 3). The spectral transition from pure GRACE to pure terrestrial information happens in the band between SH-degree 60 and 120. Thus the error model is exclusively based on terrestrial information only above degree 120. This does not exactly correspond to NMA2014, where terrestrial data starts being used only above degree 130 (degrees above 140 are exclusively based on terrestrial data). As will be shown later, optimal combination employs GOCE data even above degree 140. In essence, the error degree variances adopted for NMA2014 are free from satellite information above degree 120 and the combination with GOCE anyway relies on GOCE data for degrees below 140. Thus, we may with good reason set

$$\sigma_l^{\Delta g} \;\approx\; \sigma_l^{\mathrm{NMA2014}} \;\approx\; \sigma_l^{\mathrm{EGG2008}}. \qquad (4)$$

For the spectral band above degree $l = 140$ this seems to be a reasonable approximation for the error of the terrestrial data. For degrees below 140, however, where EGG2008 is to a large extent based on satellite data, the approximation is worse and it also violates the basic requirement for the Wenzel-approach in Eq. (1), namely that errors in satellite and terrestrial information should be uncorrelated. Still we accept this theoretical flaw, because in the spectral band in which the requirement is violated (i.e. degrees below 140) the combined solution will be dominated by GOCE anyway, such that NMA2014 hardly contributes. Consequently our computations are not hampered by the fact that in the spectral band below degree 140 $\sigma_l^{\Delta g}$, i.e. the error model for terrestrial data, largely represents error characteristics derived from satellite data.

2.2 Error Degree Variances from Satellite-Only Gravity Models

The error description of DIR5 and GOCO05s is provided in the form of the full error variance-covariance matrix (VCM). However, Eq. (1) requires rather condensed information in terms of error degree variances. The full VCM does not represent a globally homogenous and isotropic error behaviour as implied by using error degree variances. Here we use a two-step procedure to construct a degree variance model that allows approximating the full VCM in the study area.

In the first step, we approximate the full VCM by the diagonal blocks of constant SH-order m, hereafter termed as the m-block or mbm-approach. The m-blocks contain the most significant correlations of the full VCM and describe

about 99% of the geoid error, see Gerlach and Fecher (2012). The corresponding formal geoid error standard deviation is perfectly latitude-dependent but not homogenous, as shown in Fig. 1. It differs significantly from the formal geoid error derived from error degree variances only. This latter approach neglects not only all error correlations of the original VCM (it takes only error variances into account), but additionally assumes homogenous and isotropic error behaviour. The geoid error computed from this degree variance or c_n-approach is constant all over the globe (if evaluated on a sphere of constant radius).

The second step provides a local approximation of the mbm-approach by rescaling the error degree variances. Practically, the error covariance function is derived from the c_n-approach, but its amplitude is scaled to fit its error variance (gray curve in Fig. 1) to the error variance from the mbm-approach (black curve in Fig. 1). The scaling factor is a function of latitude. Because the factor changes only smoothly with latitude, we may use an average scaling factor to generate a sufficient approximation of the mbm-based geoid error for local to regional applications. For our test area in Norway we have used the scaling factor for the average latitude of 65° and applied it to the whole study area (which stretches from about 55° to 75° latitude). The corresponding latitude band is marked with gray in Fig. 1.

Considering Fig. 1, it is also worth mentioning that the dashed lines are valid on a sphere of constant radius $R = 6{,}378{,}137$ m, while the solid lines are valid on the surface of the ellipsoid, i.e., they involve downward continuation. Due to a slight orbit eccentricity of the GOCE satellite, the error is not symmetric with respect to the equator. This asymmetry is amplified through downward continuation, because the orbit height is larger over the southern hemisphere and smaller over the northern hemisphere. Thus the error is significantly larger in southern latitudes than in the corresponding northern latitudes.

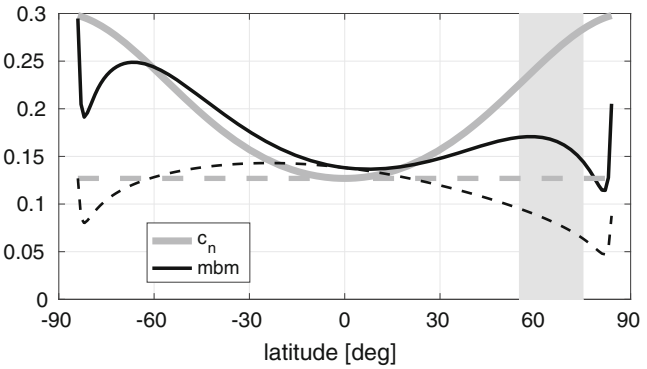

Fig. 1 Geoid height formal errors from GOCO05s (full resolution) as a function of latitude in units of [m]. Error propagation is based on either the c_n-approach (*gray curves*) or the mbm-approach (*black curves*). *Solid lines* include downward continuation to the surface of the ellipsoid, while *dashed lines* refer to a sphere of radius $R = 6378$ km. The *gray area* marks the latitude range of our test region (Norway)

3 Spectral Weights and Filter Functions

Figure 2 shows the spectral weights for some of the combination schemas. Comparing the three GOCO05s curves (each with different error assumption for the terrestrial data), it is obvious that the worse the terrestrial data is assumed to be, the higher the weights for GOCE data are. Comparison of DIR5 and GOCO05s (employing the same assumption on $\sigma_l^{\Delta g}$) shows that the DIR5-combination puts more weight on the satellite information. This is because the formal errors of DIR5 are smaller than the GOCO05s errors.

As satellite-only GPMs should provide the best information for the long wavelength, the weights should be equal to 1 for the lower part of the spectrum. This holds exactly true for the Wong&Gore-type modification which solely relies on GOCE information for the degree band below 130. It also holds almost perfectly for those Wenzel-type combinations which are based on the assumption, that $\sigma_l^{\Delta g} = 1.0$ mGal or worse. It does not hold, if the error degree variances for the terrestrial data are scaled to provide the smaller 0.2 mGal error amplitude. This is due to our specific definition of the error degree variances for the terrestrial data. As mentioned in Sect. 2.1, the terrestrial data errors $\sigma_l^{\Delta g}$ are taken from EGG2008. Thus the lower SH-degrees correspond to the errors of the GRACE-based model EIGEN-5S. Downscaling

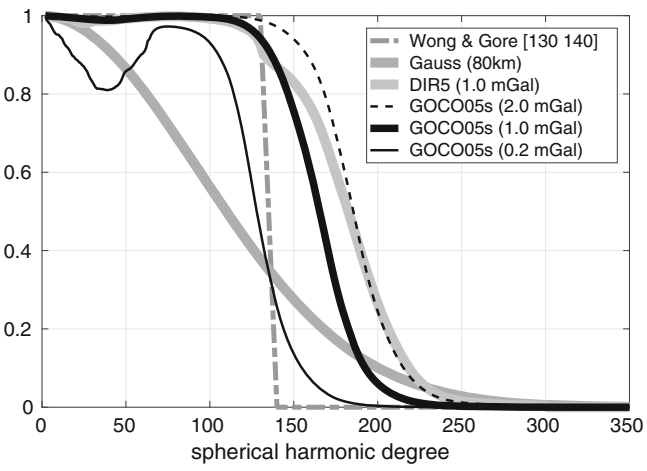

Fig. 2 Spectral filter weights w_l using different filtering schemas for combination. The Wong&Gore as well as the Gaussian weights are deterministic schemas. All other *curves* represent stochastic schemas according to Wenzel, employing scaled error degree variances for either DIR5 or GOCO05s along with different assumptions on the error amplitude of terrestrial gravity data

of the error degree variances for the 0.2 mGal scenario makes the low degree spectral band of $\sigma_l^{\Delta g}$ competitive to GOCE errors which therefore do not get full weight. This rather crude method of defining and rescaling the lower spectral band of $\sigma_l^{\Delta g}$ generates the artificial behaviour of the spectral weights (thin, black line in Fig. 2). However, we accepted this for our purpose as it hardly affects the overall cumulative error budget (effectively GOCO05s is partly replaced by the GRACE model EIGEN-5S, which also provides good information for the longer wavelengths).

Concerning the Gaussian weights, one may try to represent different quality of the terrestrial data by choosing a different filter length; if terrestrial data is assumed to be of good quality, the filter length will be larger. However, for various realistic error assumptions, the weights for the satellite data will always start decaying even for the longest wavelengths. Therefore, this approach can only provide good results, if both, terrestrial and satellite data are of good quality for long wavelengths. This is the case for our combination of NMA2014 and release 5 GOCE models. It may not be the case, when combining GOCE and an old regional geoid model, which is not already based on GRACE or GOCE data.

The isotropic spatial filter functions are constructed according to

$$W(\psi) = \sum_{l=2}^{\infty} w_l \, P_l(\cos\psi) \tag{5}$$

where $P_l(\cos\psi)$ are the conventional Legendre polynomials and ψ is the spherical distance between computation and integration point. In practise the summation is carried out to a high SH-degree (e.g. $l = 10{,}000$) and the integration is limited to a certain spherical cap around the computation point. Here we have taken care that the filter function smoothly tends to zero, by applying a Meissl-type modification (Meissl 1971). The effective integration cap for the different functions is around 2°. In addition, all functions are normalized (integral of the filter function over the spherical integration cap is equal to 1).

4 Results

Figures 3 and 4 show error degree variances resp. cumulative geoid errors of some selected geoid solutions. These numbers reflect the expected formal error of the geoid models. Table 1 shows the statistics of the comparison to GNSS-Levelling for several more scenarios. In contrast to the formal errors shown in the figures, these numbers represent empirical errors which also contain contributions from GNSS and levelling.

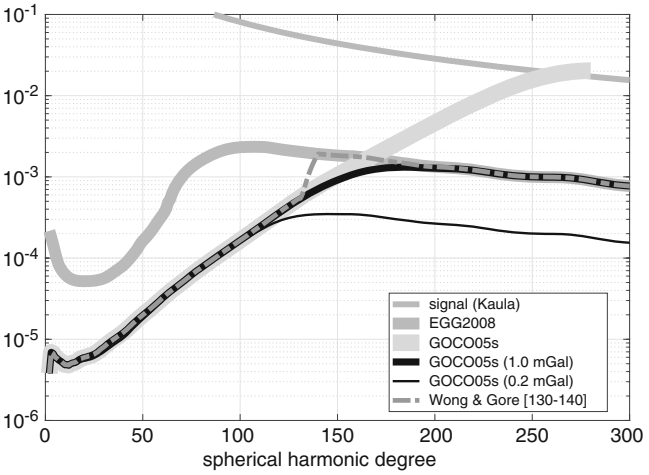

Fig. 3 Geoid height error degree variances for different geoid solutions in units of [m]

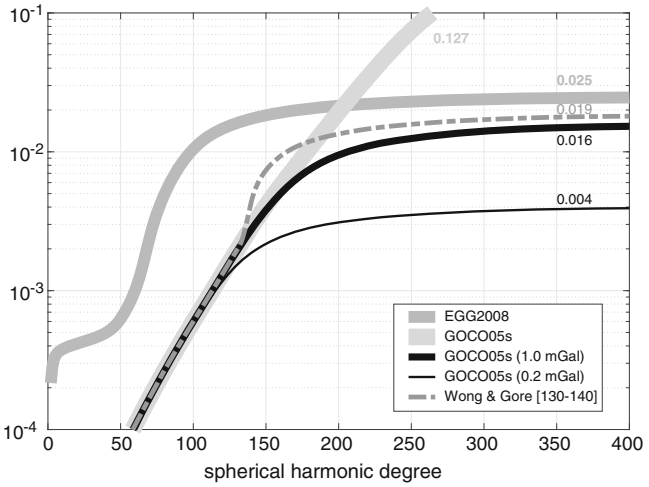

Fig. 4 Cumulative geoid height errors for different geoid solutions in units of [m]

Table 1 also contains results for some older nordic geoid models, namely NKG96 (Forsberg et al. 1999) and NKG2004 (Forsberg et al. 2004). The results nicely reflect the improvement brought by GRACE and GOCE during the last 10–15 years (part of the improvement is also due to improvements in the terrestrial databases). NKG96 (pre-GRACE era) gives an overall standard deviation of around 8 cm. This value is reduced to 6 cm for NKG2004 (which includes GRACE) and to around 3 cm for the latest, GOCE-based models.

The formal errors show the importance of optimal combination and of good knowledge of the quality of terrestrial data. The formal error of EGG2008 is estimated to be 2.5 cm. Including GOCE data, even based on the quite crude Wong&Gore combination, allows to reduce the error to below 2 cm. Using different error assumptions for the

Table 1 Statistics of the residuals of different geoid solutions with respect to GNSS-levelling data in Norway (mean subtracted)

Geoid model	Type of modification	min	max	std
NKG96	–	−35.99	19.47	8.48
NKG2004	–	−23.84	16.52	5.91
NMA2014	–	−14.94	12.23	3.41
EGG2015	–	−13.88	8.75	3.43
DIR5	Gauss (80 km)	−13.26	12.45	2.98
DIR5	mbm (2.0 mGal)	−13.25	12.31	2.93
DIR5	mbm (1.0 mGal)	−13.66	12.86	2.94
DIR5	mbm (0.2 mGal)	−13.88	13.10	3.10
DIR5	Wong & Gore	−13.79	13.13	3.11
GOCO05s	Gauss (80 km)	−12.66	12.19	3.00
GOCO05s	mbm (2.0 mGal)	−12.96	12.70	2.94
GOCO05s	mbm (1.0 mGal)	−13.30	12.97	3.01
GOCO05s	mbm (0.2 mGal)	−13.61	12.97	3.12

All modified solutions are combinations of either GOCO05s or DIR5 with NMA2014. Units are [cm]

terrestrial data allows to further reduce the error of the combined geoid model. Assuming an error level of 1 mGal, the geoid error goes further down to 1.6 cm; assuming 0.2 mGal yields an even smaller error of 0.4 cm.

Such a strong variation (from 2.5 to 0.4 cm) is not reflected by the empirical errors (see the statistics in Table 1) which also contain error contributions from GNSS and levelling data. Here all geoid models yield about a 3 cm fit to GNSS-levelling. This value fits well to the error budget of the Norwegian height reference surface HREF as derived by Mysen (2014). Therefore, we assume that the empirical error budget is dominated by errors in GNSS and levelling data, such that improving the geoid quality would not significantly change the overall empirical error.

There is only a slight tendency indicating that the Wong&Gore combination as well as the Wenzel-type combinations assuming high quality of terrestrial data (0.2 mGal) do obviously not take enough GOCE data into account. It also seems that the Gauss kernel proves better than the Wong&Gore combination, however, it can further be improved by the Wenzel-modifications which take more GOCE data into account in the medium wavelength. Besides this, the statistics show that DIR5 gives slightly better results than GOCO05s (when comparing solutions with identical error assumptions for $\sigma^{\Delta g}$).

5 Conclusions

We have generated several regional geoid models for our study area in Norway by applying different types of kernel modifications for optimal combination of GOCE and terrestrial data. The stochastically optimal Wenzel-modification was tested against deterministic modifications that have been used earlier for the study area, namely the Wong&Gore modifications and the Gaussian kernel. Empirical errors were derived from comparison to GNSS-levelling.

In general, the errors show that GRACE and GOCE have strongly improved the regional geoid over the last decade. The fit to GNSS-levelling drops from 8.5 cm (before the GRACE era) down to about 3 cm (with GOCE data).

The empirical errors vary only slightly around 3 cm. However, in tendency they confirm that those combinations are best, which put more weight on GOCE. This is also reflected by the formal errors. Therefore, the Wong&Gore filter used for NMA2014 does not seem to be optimal.

The formal errors are lower and show larger discrepancies between the different combination schemas. This could be an indication that the empirical error is dominated by the quality of GNSS-levelling data. Further inspection of these data sets will be valuable for future improvements of the regional geoid model and for deriving a realistic formal error budget. A realistic error budget should also take into account spatial variability in the error characteristics, such that fully occupied error variance-covariance matrices should be used.

Geoid modelling on the centimeter to sub-centimeter level is not an easy task. Our formal error budget shows significant differences depending on the quality of terrestrial data in the area of interest. The latest version of the European Gravimetric Geoid model, EGG2015, is optimized with respect to some other validation data sets and obviously not the optimal solution for Norway. It assumes $\sigma^{\Delta g} = 0.2$ mGal, which seems too optimistic for the Norwegian data set—an error of around 2.0 mGal seems more realistic. Thereby it is important to stress that not only the magnitude of the error is of relevance, but also the error correlations (in our study represented by the adopted error degree variance model) must be considered. Neglecting error correlations would degrade the quality of the combination, because any of the data sources would be penalized too much, leading, e.g., to over-smoothing the solution (see Gilardoni et al. 2014).

As the quality of terrestrial data is not necessarily constant for the area of interest, one may also pose the question, if further improvement of regional geoids can be achieved with the classical Stokes approach, where one chooses one single weighting schema for the whole area, i.e. one and the same modified Stokes function. This necessarily requires a compromise between subareas with highest and lowest quality (respectively density) of terrestrial data. Alternative approaches like least-squares collocation or spherical radial basis functions, which allow taking spatial variations in data quality into account, may prove to provide better results. This, however, was out of the scope of this study and will be subject to future research.

Acknowledgements Ove Omang (Norwegian Mapping Authority), Heiner Denker (University Hannover) and Torsten Mayer-Gürr (TU Graz) are gratefully acknowledged for providing data for this research. The study is part of the GOCODYN project, funded by the Norwegian Research Council under project number 231017.

References

Bruinsma SL, Förste C, Abrikosov O, Marty JC, Rio MH, Mulet S, Bonvalot S (2013) The new ESA satellite-only gravity field model via the direct approach. Geophys Res Lett 40:3607–3612. doi:10.1002/grl.50716

Bruinsma SL, Förste C, Abrikosov O, Lemoine JM, Marty JC, Mulet S, Rio MH, Bonvalot S (2014) ESA's satellite-only gravity field model via the direct approach based on all GOCE data. Geophys Res Lett 41(21):2014GL062,045. doi:10.1002/2014GL062045

Denker H (2013) Regional gravity field modeling: theory and practical results. In: Xu G (ed) Sciences of geodesy - II. Springer, Berlin/Heidelberg, pp 185–291

Denker H (2016) A new European gravimetric (Quasi)Geoid EGG2015. Paper presented at the IAG symposium on gravity, geoid and height systems 2016 (GGHS2016), Thessaloniki, Greece, 19–23 Sept 2016

Featherstone WE (2013) Deterministic, stochastic, hybrid and band-limited modifications of Hotine's integral. J Geod 1–14. doi:10.1007/s00190-013-0612-9

Forsberg R, Kaminskis J, Solheim D (1999) The NKG-96 Geoid. In: Proceedings of the 13th general meeting of the nordic geodetic commission, Gävle, Sweden, 25–29 May 1998, pp 255–262

Forsberg R, Strykowski G, Solheim D (2004) NKG-2004 geoid of the Nordic and Baltic area. Paper presented at the IAG symposium on gravity, geoid and space missions (GGSM2004), Porto, Portugal, Aug 30–Sept 3, 2004

Förste C, Flechtner F, Schmidt R, Stubenvoll R, Rothacher M, Kusche J, Neumayer KH, Biancale R, Lemoine JM, Barthelmes F, Bruinsma J, König R, Meyer U (2008) EIGEN-GL05C - a new global combined high-resolution GRACE-based gravity field model of the GFZ-GRGS cooperation. In: Geophysical research abstracts, vol 10, Abstract No. EGU2008-A-06944

Gatti A, Reguzzoni M, Venuti G (2013) The height datum problem and the role of satellite gravity models. J Geod 87(1):15–22. doi:10.1007/s00190-012-0574-3

Gerlach C, Fecher T (2012) Approximations of the GOCE error variance-covariance matrix for least-squares estimation of height datum offsets. J Geod Sci 2(4):247–256. doi:10.2478/v10156-011-0049-0

Gilardoni M, Reguzzoni M, Sampietro D (2014) Using GOCE to straighten and sew European local geoids: preliminary study and first results. In: Marti U (ed) Gravity, geoid and height systems. IAG symposia, vol 141. Springer, Berlin, pp 229–234. doi:10.1007/978-3-319-10837-7-29

Gruber T, Gerlach C, Haagmans R (2012) Intercontinental height datum connection with GOCE and GPS-levelling data. J Geod Sci 2(4):270–280. doi:10.2478/v10156-012-0001-y

Hofmann-Wellenhof B, Moritz H (2005) Physical geodesy. Springer, Wien/New York

Mayer-Gürr T, Kvas A, Klinger B, Rieser D, Zehentner N, Pail R, Gruber T, Fecher T, Rexer M, Schuh W, Kusche J, Brockmann J, Loth I, Müller S, Eicker A, Schall J, Baur O, Höck E, Krauss S, Jäggi A, Meyer U, Prange L, Maier A (2015) The new combined satellite only model GOCO05s. In: Geophysical research abstracts, vol 17, EGU2015-12364. doi:10.13140/RG.2.1.4688.6807

Meissl P (1971) Preparations for the numerical evaluation of second order Molodensky-type formulas. Report Nr. 163, Department of Geodetic Science, The Ohio State University, Columbus

Mysen E (2014) On the computation of reliable formal uncertainties in the densification of GPS-levelling networks by least-squares collocation. J Geod 88(10):917–926. doi:10.1007/s00190-014-0732-x

Ophaug V, Breili K, Gerlach C (2015) A comparative assessment of coastal mean dynamic topography in Norway by geodetic and ocean approaches. J Geophys Res Oceans 120:7807–7826. doi:10.1002/2015JC011145

Rülke A, Liebsch G, Sacher M (2012) Unification of European height system realizations. J Geod Sci 2(4):343–354

Rummel R (2012) Height unification using GOCE. J Geod Sci 2(4):355–362

Sjöberg L (2003) A general model for modifying Stokes' formula and its least-squares solution. J Geod 77(7):459–464. doi:10.1007/s00190-003-0346-1

Wenzel HG (1981) Zur Geoidbestimmung durch Kombination von Schweredaten und einem Kugelfunktionsmodell mit Hilfe von Integralformeln. Z Vermess 106:102–111

Wenzel HG (1982) Geoid computation by least squares spectral combination using integral formulas. In: Proceedings IAG general meeting, Tokyo, 7–15 May 1982, pp 438–453

Wong L, Gore R (1969) Accuracy of geoid heights from modified Stokes kernels. Geophys J R Astro Soc 18:81–91

The Effect of Noise on Geoid Height in Stokes-Helmert Method

Yosra Afrasteh, Abdolreza Safari, Michael Sheng, Robert William Kingdon, and Ismael Foroughi

Abstract

Noises are an inevitable part of gravity observations and they can affect the accuracy of the height datum if they are not treated properly in geoid determination. To provide data for geodetic boundary value problems, surface gravity observations must be transferred harmonically down to the geoid, which is called Downward Continuation (DC). Fredholm integral of the first kind is one of the physically meaningful ways of DC, where the Poisson kernel is used to evaluate the data on the geoid. DC behaves inherently as a high pass filter so it magnifies existing noise in Helmert gravity anomalies on geoid (free air anomalies after applying the Helmert's second condensation method); although the results on the geoid will be later smoothed by evaluating the Stokes's integral so the noise is less pronounced in the final geoid heights. The effect of noise in Stokes-Helmert geoid determination approach is numerically investigated in this study. The territory of Iran, limited to 44–62° longitude and 24–40° latitude, is considered as the area of interest in this study. The global gravity model EGM2008, up to degree/order 2160, is used to synthesize the free air gravity anomalies on a regular grid on topography and are then transferred to Helmert space using available Digital Elevation Models (DEMs). Different levels of noise are added to the data and the effects of noise are investigated using the SHGeo software package, developed at the University of New Brunswick (UNB). Results show that if the downward continuation of 5*5 arc-min surface points is required, the standard deviation of differences between *"noisy*" and *"clean"* data on the geoid will increase by *15%* with respect to the corresponding standard deviation on topography. These differences will increase for denser grid resolutions. For example, the noise of $\triangle g$ on geoid will increase up to *100%* if 1*1 arc-min points are used. The results of evaluating the Stokes integral show smoother results in terms of noise in the data. For example, 2 mGal noise in the gravity anomalies on a 5*5 arc-min grid can cause 1.5 cm of error in the geoid heights. This value is smaller when denser grids are used. Despite increasing noise in downward continuation steps, the results show smaller error in geoid heights if gravity anomalies are located on a denser grid.

Keywords

Downward continuation • Geoid • Observation noises • Stokes-Helmert

Y. Afrasteh (✉) • A. Safari
School of Surveying and Geospatial Engineering,
University of Tehran, Tehran, Iran
e-mail: yosra_afrashteh@yahoo.com

M. Sheng • R.W. Kingdon • I. Foroughi
Department of Geodesy and Geomatics Engineering,
University of New Brunswick, Fredericton, NB, Canada

G. S. Vergos et al. (eds.), *International Symposium on Gravity, Geoid and Height Systems 2016*,
International Association of Geodesy Symposia 148, https://doi.org/10.1007/1345_2017_25

1 Introduction

Geoid determination using Stokes formula requires data on a boundary (here geoid) where there is no mass above it. Masses above the geoid can be removed by computing the Direct Topographical Effect (DTE), Secondary Indirect Topographical Effect (SITE), and Direct Atmospheric Effect (DAE). To satisfy the first condition, the observations have to be reduced from the Earth's surface down to the geoid. This can be done by transferring surface gravity observations harmonically down to the geoid, so called harmonic downward continuation (DC).

To obtain Helmert gravity anomalies on the topographical surface Helmert's second condensation method is used. All topographic masses outside the geoid can be replaced by an infinitesimal condensation layer on the geoid (Lambert 1930; Heck 1993; Martinec et al. 1993). By evaluating the topographic and atmospheric direct and indirect effects (DTE, SITE, DAE), we can transform free-air gravity anomalies into Helmert gravity anomalies which are ready to be continued to the geoid.

DC is evaluated by the Poisson integral equation; this integration has to be done numerically. In the SHGeo scheme (Tenzer et al. 2003) this is done by discretizing the integration area over specific cells (say 1*1 arc-deg blocks) and applying an iterative solution for inverting the transformation matrix (B matrix). Because of the existence of noise, evaluating the exact solution (direct inverse) might cause big jumps of $\triangle g$ on the geoid (Kingdon and Vaníček 2011). The UNB approach uses the modified Stokes function along with global gravity models for the low-frequency part of the field. This scheme will treat the topographic effects in its spherical form instead of planar approximation (Ellmann and Vaníček 2007). The UNB approach has been used for computing local geoids in many areas and is considered a high accuracy method. The theory of the Stokes-Helmert method is reviewed in Tenzer et al. (2003) and the approach was used in Huang and Véronneau (2005), Ellmann and Vaníček (2007), and Vaníček et al. (2017) . It is worth studying the effect of noise on different grid sizes. In this paper five different level of white noises (2, 1, 0.5, 0.1, 0.01 mGal) were added to the data with five different resolutions (1, 2, 3, 4, 5 arc-min). To get an estimation of the noise in DC and Stokes integration steps, two datasets were considered in the process, "noisy" and "clean". The whole process of DC and Stokes integration was repeated for each resolution and noise level and the results were compared for these two datasets.

2 Transferring to Helmert Space

The disturbing potential T at the surface of the earth is defined as (Heiskanen and Moritz 1967):

$$T = W - U, \tag{1}$$

Where W and U represent the Earth's gravity potential and the normal gravity potential of the reference ellipsoid which equals to the gravity potential on the geoid, respectively. In Helmert's second condensation method, T is transformed to the Helmert disturbing potential by the following equation:

$$T^H = T - \delta V_t, \tag{2}$$

where δV_t is the difference between the potential of the topography and the potential of the condensed layer (Vaníček and Martinec 1994). The fundamental equation of physical geodesy for the Earth by spherical approximation can be expressed as:

$$\Delta g^{fa} = -\frac{\partial T}{\partial r} - \frac{2}{R}T, \tag{3}$$

where $\triangle g^{fa}$ is the free-air gravity anomaly at the Earth's surface. In the same way, it can be expressed in Helmert space:

$$\Delta g^H = -\frac{\partial T^H}{\partial r} - \frac{2}{R}T^H. \tag{4}$$

According to Eq. (2), the left hand side of Eq. (4) can be written also as:

$$\Delta g^H = \Delta \mathrm{g}^{fa} + \frac{\partial \delta V_t}{\partial r} + \frac{2}{R}\delta V_t, \tag{5}$$

where the second term on the right hand side is the DTE on gravity at the Earth surface and the third term is called the SITE on gravity at the Earth surface. Equation (5) provides values which are able to be used in the harmonic DC of the disturbing potential.

3 Downward Continuation of Gravity Anomalies

Since the topographical and atmospheric masses are condensed on the geoid, the Helmert space above the geoid is harmonic, so the Helmert gravity anomalies can be properly

continued down to the geoid. The Poisson integral equation has been used at UNB to apply DC to Helmert gravity anomalies. In mathematics, this type of equation is called a Fredholm integral equation of the first kind.

The Poisson integral for DC reads (Kellogg 1929):

$$\Delta g_t^H = \frac{R}{4\pi r}\int_{\Omega'} \Delta g_g^H K\,(r,\psi,\mathrm{R})\,\mathrm{d}\Omega', \tag{6}$$

where subscript "t" and "g" here means the values on topographic and geoid surface respectively and K is the spherical Poisson integral kernel (Heiskanen and Moritz 1967):

$$K\,(r,\psi,R) = \sum_{n=2}^{\infty}(2n+1)\left(\frac{R}{r}\right)^{n+1} P_n\,(cos\psi) = R\frac{r^2-R^2}{l^3}, \tag{7}$$

where ψ is the angular distance between geocentric directions Ω and Ω' and l is the spatial distance between (r,Ω) and (R,Ω'). DC is an inverse problem to the original Poisson integral. This integral equation can be solved iteratively according to Jacobi's iterative approach (Kingdon and Vaníček 2011). Equation (6) can be written as a system of linear algebraic equations (Martinec 1996; Huang 2002):

$$\Delta g_t^H = K\,[r,\psi,R]\,\Delta g_g^H, \tag{8}$$

where Δg_t^H is the Helmert gravity anomalies on the Earth surface, Δg_g^H is the Helmert gravity anomalies on the geoid and $K[r,\psi,R]$ is the transformation matrix consisting of the values of the Poisson integral kernel multiplied by the factor $\frac{R}{4\pi r_t}$. This equation is the discrete form of Eq. (6).

4 Stokes Integration

Due to limited availability of gravity anomalies over the entire Earth for evaluation of the original Stokes formula, the idea of splitting the integration zone to far-zone and near-zone was introduced by Molodenskii (1962). The integration area is limited to a domain (Ω_{ψ_0}) containing terrestrial gravity anomalies over computation points which is called the near-zone contribution. This will impose a truncation error (far-zone contribution) to the result which can be treated by modifying Stokes formula $S^M(\psi_0,\psi(\Omega,\Omega'))$ (Molodenskii 1962). In the UNB application this problem is treated by removing the reference field in Helmert space using EGMs up to degree M as the low-frequency part of gravity anomalies. The residual Helmert gravity anomalies then are evaluated to compute the residual Helmert geoidal heights using Stokes's integral. The reference spheroid of geoidal heights is added to residual values and they can be transferred to the real space by restoring topographic and atmospheric effects (PITE, PIAE). The Stokes's integral reads (Ellmann and Vaníček 2007):

$$\begin{aligned} N\,(\Omega) = {} & \frac{R}{4\pi\gamma_{0(\phi)}}\iint_{\Omega_{\psi_0}} S^M\left(\psi_0,\psi\,(\Omega,\Omega')\right. \\ & \times\left(\Delta g^H\,(r_g,\Omega) - \sum_{n=2}^{M}\Delta g_n^H\,(r_g,\Omega)\right) d\,\Omega' \\ & + \frac{R}{2\gamma_{0(\phi)}}\sum_{n=2}^{M}\frac{2}{n-1}\Delta g_n^H\,(r_g,\Omega) + \frac{\delta V^t\,(r_g,\Omega)}{\gamma_{0(\phi)}} \end{aligned} \tag{9}$$

Where $\gamma_{0(\phi)}$ is the normal gravity on the reference ellipsoid, r_g is the geocentric radius of the geoid surface, and ψ_0 is the spherical integration cap size.

5 Numerical Results

The selected area for the numerical investigation is Iran, limited by $44° < \lambda < 62°$ and $24° < \phi < 40°$. An extra 30 arc-min border strip on each side is needed to include sufficient far zone data in DC (Foroughi et al. 2016). The topography over the west and northern part of area goes up to 4,800 m (see Fig. 1).

Foroughi et al. (2017) investigated the accuracy of different global models in Iran and stated that EGM2008 has the best accuracy comparing with terrestrial gravity information of Iran. This model was used up to degree/order 2160 to compute the free air gravity anomalies on a regular grid on

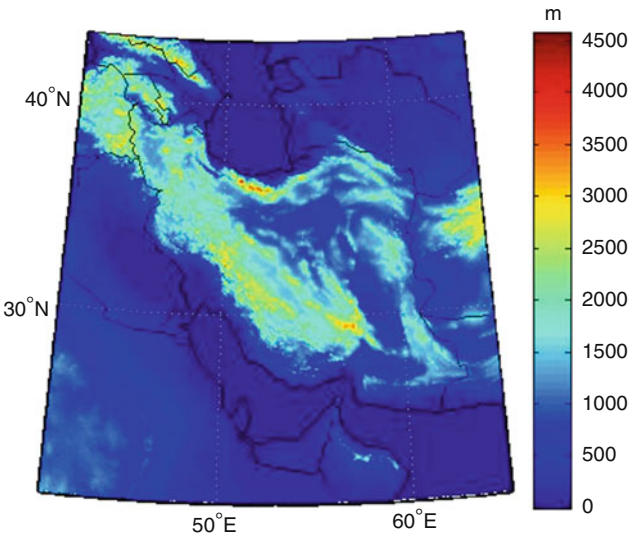

Fig. 1 Topography over Iran

topography and transferred to Helmert space by removing the DTE, SITE, and DAE using 3*3 arc-sec height information from the Shuttle Radar Topography Mission (SRTM) ver 4. The mean free air gravity anomalies were produced in 5 different resolutions: 5*5, 4*4, 3*3, 2*2 and 1*1 arc-min cell-centered grids. Two datasets, "noisy" and "clean", were considered for this process. The effect of five different level of white noises, 2, 1, 0.5, 0.1, 0.01 mGal were considered in this study.

The STD of differences between noisy and clean data on two surfaces, topography and geoid, were compared (Fig. 2). This figure clearly shows the increase of STD of differences between clear and noisy data in higher resolutions on geoid.

Figure 2 shows that for noise less than 10 μGal, the STD of noise on geoid remains the same for any resolution. Although new relative gravimeters claim accuracies of sub-μGal, due to observation conditions the average accuracy of input gravity data is larger than this. The increase in the STD of the any level of noises on the geoid when 5*5, 4*4 and 3*3 arc-min grid points are used is less pronounced. This can be because of the stability of DC with these resolutions which was shown mathematically by (Martinec 1996). He showed that the DC, using Poisson integral, is numerically stable if a grid resolution larger than 3*3 arc-min is used.

Reasonable results can be expected on geoid if maximum level of noise is less than 0.5 mGal for the 2*2 arc-min grid resolutions. However, this number is smaller (0.1 mGal) if data are in 1*1 arc-min grids. Results of this study can help to choose the proper grid resolution depending on the noise (or accuracy of input data). We should mention that the level of noise is not the only parameter to control the accuracy of DC on geoid, the scarcity of scattered points before gridding on the Earth's surface, gridding method, iterative algorithm to solve the DC and the topography of the area of interest can change the accuracy of DC too. We choose Iran as our area of interest because it has low and high topography at the same time and therefore we can get an average estimation of effect of noises on geoid. The synthetic gravity anomalies on grid points were used here which caused the gridding error to be neglected. The Jacobi iteration was chosen here to estimate the inverse of the B matrix (Eq. 8) as this method was already used in the SHGeo package and behaves well for DC. The number of iterations in the DC procedure was different for every resolution. In the 1*1 arc-min resolution, on average four iterations were needed while for 5*5 arc-min resolution data, an average of two iterations were required.

Now gravity anomalies can be integrated by the Stokes function to compute the residual geoid heights in Helmert space. The choice of integration cap size is corresponded to both the degree of reference field and Stokes's modification degree that is removed from the Helmert gravity anomalies on the geoid. The optimal degree of reference field and integration cap size was chosen in this study according to method introduced by (Foroughi et al. 2016). According to their method, the optimal pair of integration cap size and degree of reference field is chosen according to the quality of the terrestrial data and performance of EGMs in the area of interest; in this case, $M = 90$ and $\psi_0 = 2^o$ was chosen. The results of Stokes integration is illustrated in Fig. 3 and Table 1 presents the statistical results.

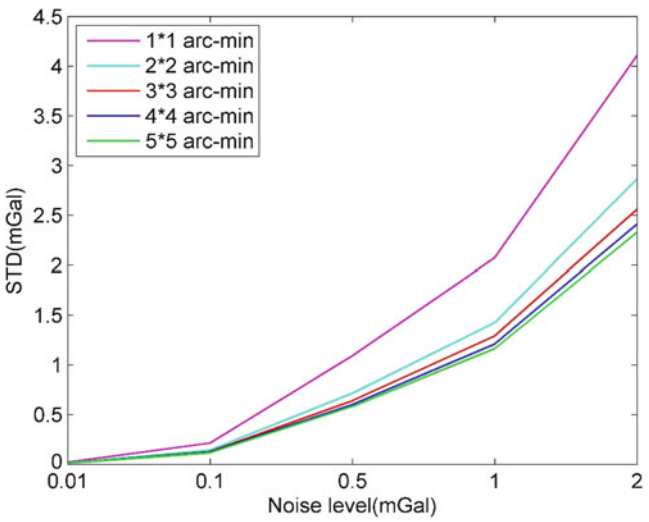

Fig. 2 Differences between std. of clean and noisy Δg data before and after DC

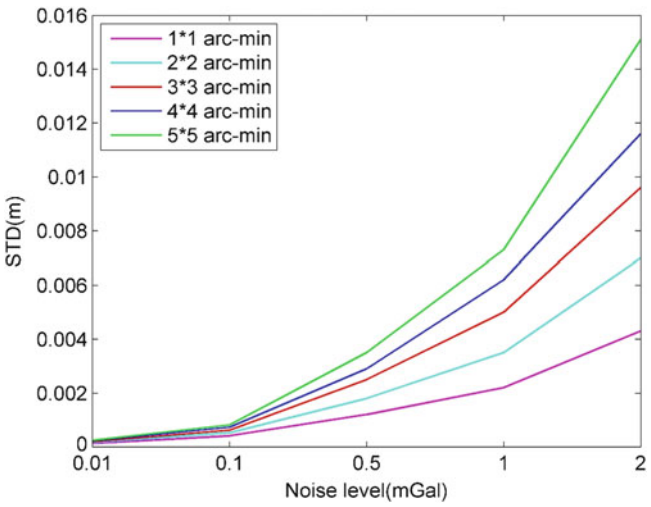

Fig. 3 STD of difference between clean and noisy geoidal height data after evaluation of Stokes integral

Table 1 STD of differences between clean and noisy geoidal height data after evaluation of Stokes integral

Noise (mGal)	STD (m)				
	1*1	2*2	3*3	4*4	5*5
$\sigma = 2$	0.0043	0.0070	0.0096	0.0116	0.0151
$\sigma = 1$	0.0022	0.0035	0.0050	0.0062	0.0073
$\sigma = 0.5$	0.0012	0.0018	0.0025	0.0029	0.0035
$\sigma = 0.1$	4.1104e-004	5.2611e-004	6.2102e-004	7.3221e-004	8.1419e-004
$\sigma = 0.01$	1.2666e-004	1.6204e-004	1.9647e-004	2.2208e-004	2.4503e-004

6 Conclusion

The effect of noise and distribution of gravity anomalies on geoid height was investigated using Stokes-Helmert technique. To investigate this, five grid resolutions and five different levels of noise were added to synthesized gravity anomalies in the area of Iran. The results showed that to get gravity anomalies on geoid with an error less than 2.5 mGal the data on the surface should be a maximum resolution of 3*3 arc-min. In case of denser data, the noise in gravity anomalies should be less than 1 mGal to get an accuracy of 2 mGal for the downward continued values. For the geoid height, to get a result with accuracy of 1 cm, the input data should be of 3*3 arc-min resolution or denser. Although in the DC step data with higher resolution had the worst results, after evaluation the Stokes function denser grids show more accurate results which shows the necessity of a dense gravity data set for local geoid determination. As it can be seen from Figs. 2 and 3, despite the DC steps, after Stokes integration 1*1 arc-min resolution data is less affected by the noise.

References

Ellmann A, Vaníček P (2007) UNB application of stokes–Helmert's approach to geoid computation. J Geodyn 43(2):200–213

Foroughi I et al (2017) Local evaluation of earth gravitational models, case study: Iran. Geod Cartography 43(1):1–13

Foroughi I, Vaníček P, Novák P, Kingdom R, Goli M, Sheng M, Santos M (2016) Harmonic downward continuation of scattered point gravity anomalies to mean anomalies on a mesh on the geoid. Presented at "Canadian Geophysical Union", Canada

Heck B (1993) A revision of Helmert's second method of condensation in geoid and quasigeoid determination. In: Geodesy and physics of the earth. Springer, Berlin, pp 246–251

Heiskanen WA, Moritz H (1967) Physical geodesy. Bull Géod (1946–1975) 86(1):491–492

Huang J (2002) Computational methods for the discrete downward continuation of the Earth gravity and effects of lateral topographical mass density variation on gravity and the geoid

Huang J, Véronneau M (2005) Applications of downward-continuation in gravimetric geoid modeling: case studies in western Canada. J Geod 79(1–3):135–145

Kellogg OD (1929) Foundations of potential theory, vol 31. Springer Science & Business Media, Berlin

Kingdon R, Vaníček P (2011) Poisson downward continuation solution by the Jacobi method. J Geod Sci 1(1):74–81

Lambert WO (1930) The reduction of observed values of gravity to sea level. Bull Géod (1922–1941) 26(1):107–181

Martinec Z (1996) Stability investigations of a discrete downward continuation problem for geoid determination in the Canadian Rocky Mountains. J Geod 70(11):805–828

Martinec Z et al (1993) On Helmert's 2nd condensation method. Manuscr Geodaet 18:417–417

Molodenskii MS (1962) Methods for study of the external gravitational field and figure of the Earth. Jerusalem, Israel Program for Scientific Translations, 1962;[available from the Office of Technical Services, US Dept. of Commerce, Washington]

Tenzer R et al (2003) A review of the UNB approach for precise geoid determination based on the stokes–Helmert method. Honour Acad Life Petr Vanicek Rep 218:132–178

Vaníček P, Martinec Z (1994) The stokes-Helmert scheme for the evaluation of a precise geoid. Manuscr Geod 19:119–128

Vaníček P et al (2017) Does Poisson's downward continuation give physically meaningful results? Stud Geophys Geod 61(3):412–428

Approximation of Local Quasi-Geoid Using Point Mass Method Based on Bjerhammar Theory

Dongming Zhao, Huan Bao, Shanshan Li, and Qingbin Wang

Abstract

Based on the solution for the Bjerhammar Boundary Value Problem (BVP) in physical geodesy, an approximation method of local quasi-geoid using point masses was proposed in the paper, and a multi-layer point mass model of the local quasi-geoid was constructed for some area within China. In the development of the method, the relation between ground gravity anomalies and disturbing potential was derived, which results in the point mass model of the disturbing potential, and then the formula for the derivation of height anomaly was obtained. Through analysis of the requirements on ground gravity anomaly, a multi-layer point mass model for the calculation of height anomaly was constructed. In the numerical test of the method, the Remove-Compute-Restore (RCR) method was also employed for comparisons of approximation results. Analyses of the results show that the proposed method can also be applied in the estimation of local quasi-geoid.

Keywords

Bjerhammar BVP • Height anomaly • Local quasi-geoid • Multi-layer point mass model • Point mass method

1 Introduction

The determination of the Earth's gravity field plays a more and more important role in geodesy, and it is commonly acknowledged that the contribution of the Earth's gravity field research is fundamental to a lot of applications, say, oceanography and geophysics. And the developing Global Navigation Satellite System (GNSS) and global height system is placing higher or even more strict demands on geodesy. The geoid or quasi-geoid serves as a height reference surface, so that the ellipsoidal heights provided by GNSS can be directly converted into gravity field related heights.

The past three decades have witnessed the accuracy improvement of the global gravity field by several dedicated gravity satellite missions, e.g., CHAMP, GRACE and GOCE, especially at long and medium wavelengths of the gravity field. The spherical harmonics that conventionally represents the global gravity field provides a global support, while the actual gravity field exhibits strong or even drastic signal variations in local area that is obvious in the higher-frequency parts of the gravity field, and thus a global solution cannot sufficiently take the regional detailed features into consideration. Therefore, regional gravity field modelling is drawing more and more attention.

To make use of the improvement on long-wavelength parts of the gravity field, the Remove-Compute-Restore (RCR) method (Forsberg and Tscherning 1981; Forsberg 1984; Sjoberg 1995) is frequently used in regional gravity field modelling. By removing the long-wavelength signal and reducing higher-frequency parts, say, terrain-induced potential effect, before gravity filed modelling, and finally restore the two parts to the computed residual field. There are a number of methods of anomalous gravity potential approximation. Tscherning (1981) made a review of the

D. Zhao (✉) • H. Bao • S. Li • Q. Wang
Zhengzhou Surveying and Mapping Institute, Zhengzhou, Henan Province, 450052 China
e-mail: zhaodongming@cntv.cn

G. S. Vergos et al. (eds.), *International Symposium on Gravity, Geoid and Height Systems 2016*,
International Association of Geodesy Symposia 148, DOI 10.1007/1345_2017_8

properties of various methods. Besides traditional Stokes's integral formulas and least-squares collocation (Heiskanen and Moritz 1967; Moritz 1980), recent years have emerged the methods of radial basis functions for the regional parameterization of the Earth's gravity field, in which the point mass kernel is extensively used (Needham 1970; Barthelmes 1989; Vermeer 1995; Antunes et al. 2003).

In the paper, the determination of geoid height using point mass method was discussed from a frequency perspective. In the test area two methods, the RCR method and the point mass method were used to approximate the local geoid. Results of approximation of each method were analyzed.

2 Geoidal Height Computation Using the RCR Method

As mentioned in Sect. 1, when the RCR is used in regional geoid modelling (Forsberg and Tscherning 1981), the residual gravity anomaly $\delta\Delta g$ was firstly obtained by subtracting the long wavelength part Δg_l and the short wavelength part Δg_s from the known gravity anomaly Δg.

$$\delta\Delta g = \Delta g - \Delta g_l - \Delta g_s \tag{1}$$

The long wavelength part Δg_l can be computed using a gravity potential model, and the short wavelength part is the effect of terrain on gravity which can be calculated using Digital Terrain Model (DTM). Therefore, the residual gravity anomaly is actually the medium wavelength part of gravity anomaly.

When the residual gravity anomaly is determined, then the medium wavelength part of the geoidal height can be calculated by

$$\begin{aligned} N_m &= \tfrac{R}{4\pi\gamma}\iint_{\sigma}\delta\Delta g S(\psi)\,d\sigma \\ &= \tfrac{R}{4\pi\gamma}\iint_{\sigma}(\Delta g - \Delta g_l - \Delta g_s) S(\psi)\,d\sigma \end{aligned} \tag{2}$$

And the complete geoidal height is

$$N = N_m + N_l + N_s \tag{3}$$

where N_l can be calculated using a gravity potential model, and N_s can be computed using some DTM.

3 Point Mass Based Frequency-Wise Representation of Geoid Height

The representation of the Earth's anomalous gravity field using the point mass model is particularly attractive because of its conceptual simplicity and the kernel's local support feature.

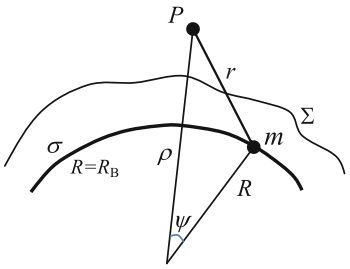

Fig. 1 Bjerhammar sphere

3.1 Representation of Geoid Height Using Point Masses

According to Bjerhammar (1963), the disturbing potential outside the Earth's surface can be approximated by virtual field sources (virtual gravity anomalies) on a sphere σ inside the Earth (Fig. 1). For the theory of Bjerhammar's boundary value problem both continuous and discrete solutions were proposed. The discrete solution was developed into the well-known point mass modelling method (Needham 1970; Sünkel 1981, 1983).

Assuming the point masses $\{m_i\}$ $(i = 1, 2, \ldots, n)$ on the Bjerhammar sphere σ have been solved for, then the disturbing potential T outside the Earth is represented by

$$T = \sum_{i=1}^{n} m_i r_i^{-1} \tag{4}$$

where r_i is the distance from the computation point P to the mass point on the sphere σ

$$r = \sqrt{\rho^2 + R^2 - 2\rho R\cos\psi} \tag{5}$$

in which ψ is the spherical angle between the radial vectors of the computation point P and the running mass point m.

From Eq. (4), the geoidal height N can be formulated as follows:

$$N = \frac{1}{\gamma}T = \frac{1}{\gamma}\sum_{i=1}^{n} r_i^{-1} m_i \tag{6}$$

3.2 Frequency-Wise Expression of Geoidal Height

According to the solution of the point masses, gravity anomalies are "mapped" onto the Bjerhammar sphere in the form of point masses. However, we can have a further insight into the gravity anomalies or point masses from the view of frequency, which means that the actual ground gravity

anomalies can be split into parts that belong to different frequency intervals.

As the gravity anomaly can be represented by an infinite series (Heiskanen and Moritz 1967)

$$\Delta g = \sum_{n=2}^{\infty} \Delta g_n = \frac{GM}{R^2} \sum_{n=2}^{\infty} (n-1) \times \sum_{m=0}^{n} \left(\overline{C}^*_{nm} \cos m\lambda + \overline{S}_{nm} \sin m\lambda \right) \overline{P}_{nm} (\sin \varphi) \tag{7}$$

where (φ, λ, ρ) are geocentric coordinates; f is the gravity constant; $\overline{C}^*_{nm}$ is the difference between the fully normalized geo-potential coefficient and the coefficient of the potential generated by a reference ellipsoid; $\overline{S}_{nm}$ denotes the fully normalized spherical harmonic coefficients; a is the equatorial radius of the Earth, and $\overline{P}_{nm} (\sin \varphi)$ is the fully normalized associated Legendre function.

$$\sum_{n=2}^{\infty} \Delta g_n = \delta\Delta g_1 + \delta\Delta g_2 + \delta\Delta g_3 + \cdots + \delta\Delta g_m + \delta\Delta g_M \tag{8}$$

in which

$$\Delta g_n = \gamma (n-1) \sum_{m=0}^{n} \left(\overline{C}^*_{nm} \cos m\lambda + \overline{S}_{nm} \sin m\lambda \right) \overline{P}_{nm} (\sin \varphi) \tag{9}$$

$\delta\Delta g_n \ (n = 1, 2 \ldots M)$ is called the step-wise residual, and $\delta\Delta g$ is the sum of Δg_n within some frequency interval, which can be written as follows

$$\begin{aligned} \delta\Delta g_1 &= \sum_{n=n_1+1}^{\infty} \Delta g_n \quad \rightarrow \textit{frequency} \text{ interval} : (n_1 + 1, \infty) \\ \delta\Delta g_2 &= \sum_{n=n_2+1}^{n_1} \Delta g_n \quad \rightarrow \textit{frequency} \text{ interval} : (n_2 + 1, n_1) \\ &\vdots \\ \delta\Delta g_m &= \sum_{n=M+1}^{n_{m-1}} \Delta g_n \quad \rightarrow \textit{frequency} \text{ interval} : (M + 1, n_{m-1}) \end{aligned} \tag{10}$$

$$\Delta g_M = \sum_{n=2}^{M} \Delta g_n = \gamma \sum_{n=2}^{M} (n-1) \sum_{m=0}^{n} \left(\overline{C}^*_{nm} \cos m\lambda + \overline{S}_{nm} \sin m\lambda \right) \overline{P}_{nm} (\sin \varphi) \tag{11}$$

which means that the gravity anomaly can be represented by the sum of $\delta\Delta g$ and the part expressed by a spherical harmonic series. Besides, the maximum degree of the gravity potential model truncated to degree and order N stands for its (frequency) resolution. By introducing the spatial resolution S° (or grid size) on a sphere, the relation between the two frequencies is

Table 1 Nodes of frequency-wise residual

Truncation degree	M	n_4	n_3	n_2	n_1
N	36	180	540	2,160	10,800
Resolution	5°	1°	20′	5′	1′

$$N = 180^\circ / S^\circ \tag{12}$$

which means that the spherical harmonic series truncated to degree and order N is equivalent to the integral over a S° spherical grid with respect to mean gravity anomalies. The relation between N and S is shown in Table 1.

For the point gravity anomaly and grid mean gravity anomaly, their corresponding frequency-wise residual can be expressed by Fig. 2.

In Fig. 2, $\overline{\Delta g}_i \ (i = 1, 2, \ldots M)$ stands for the $S_i^\circ \times S_i^\circ$ grid mean gravity anomaly. Obviously, the gravity anomalies contained in the frequency-wise residual are continuously linked, and their sum consists of the gravity anomaly for $n = 2 \rightarrow \infty$. Therefore, the frequency-wise gravity anomaly residuals can be calculated as follows

$$\begin{aligned} \delta\Delta g_1 &= \Delta g - \overline{\Delta g}_1 = \Delta g - \tfrac{1}{\Delta\sigma_1} \iint\limits_{\Delta\sigma_1} \Delta g \, d\sigma \\ \delta\Delta g_2 &= \overline{\Delta g}_1 - \overline{\Delta g}_2 = \overline{\Delta g}_1 - \tfrac{1}{\Delta\sigma_2} \iint\limits_{\Delta\sigma_2} \overline{\Delta g}_1 \, d\sigma \\ \delta\Delta g_3 &= \overline{\Delta g}_2 - \overline{\Delta g}_3 = \overline{\Delta g}_2 - \tfrac{1}{\Delta\sigma_3} \iint\limits_{\Delta\sigma_3} \overline{\Delta g}_2 \, d\sigma \\ &\vdots \\ \delta\Delta g_m &= \overline{\Delta g}_{m-1} - \overline{\Delta g}_M \end{aligned} \tag{13}$$

where

$$\overline{\Delta g}_M = \frac{1}{\sigma_M} \times \iint_{\sigma} \left[\gamma \sum_{n=2}^{M} (n-1) \sum_{m=0}^{n} \left(\overline{C}^*_{nm} \cos m\lambda + \overline{S}_{nm} \sin m\lambda \right) \overline{P}_{nm} (\sin \varphi) \right] d\sigma \tag{14}$$

or

$$\overline{\Delta g}_M = \gamma \sum_{n=2}^{M} (n-1) \left(\frac{a}{r} \right)^n \beta_n \times \sum_{m=0}^{n} \left(\overline{C}^*_{nm} \cos m\lambda + \overline{S}_{nm} \sin m\lambda \right) \overline{P}_{nm} (\sin \varphi) \tag{15}$$

in which β_n denotes the smoothing factor.

Following the relation between the spatial resolution and the truncation degree, a frequency-wise residual scheme can be determined, as shown by Table 1.

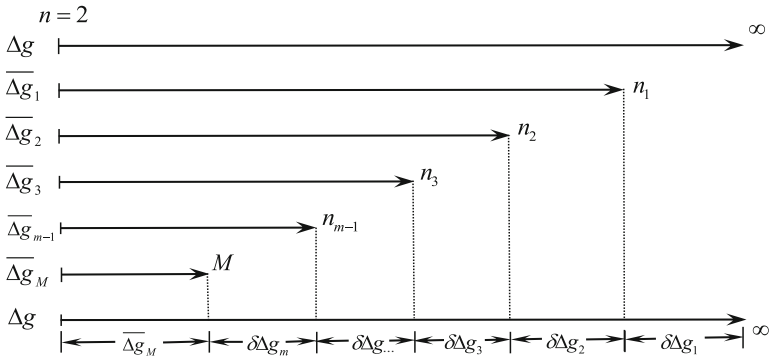

Fig. 2 Construction of frequency-wise residuals of gravity anomaly

And thus the residual is

$$\begin{aligned}\delta\Delta g_1 &= \Delta g_{1'\times 1'} - \overline{\Delta g}_{5'\times 5'}\\ \delta\Delta g_2 &= \overline{\Delta g}_{5'\times 5'} - \overline{\Delta g}_{20'\times 20'}\\ \delta\Delta g_3 &= \overline{\Delta g}_{20'\times 20'} - \overline{\Delta g}_{1^\circ\times 1^\circ}\\ \delta\Delta g_4 &= \overline{\Delta g}_{1^\circ\times 1^\circ} - \overline{\Delta g}_{5^\circ\times 5^\circ}\end{aligned} \tag{16}$$

Similarly, for the solution of point masses and calculation of geoidal height, the frequency-wise residuals are formed by the following process

$$\begin{aligned}\overline{\Delta g}^{e}_{1^\circ\times 1^\circ} &= \overline{\Delta g}_{1^\circ\times 1^\circ} - \overline{\Delta g}^{S}_{1^\circ\times 1^\circ} && \Rightarrow M_1 \Rightarrow \delta N_1\\ \overline{\Delta g}^{e}_{20'\times 20'} &= \overline{\Delta g}_{20'\times 20'} - \overline{\Delta g}^{S}_{20'\times 20'} - \overline{\Delta g}^{M_1}_{20'\times 20'} && \Rightarrow M_2 \Rightarrow \delta N_2\\ \overline{\Delta g}^{e}_{5'\times 5'} &= \overline{\Delta g}_{5'\times 5'} - \overline{\Delta g}^{S}_{5'\times 5'} - \overline{\Delta g}^{M_1}_{5'\times 5'} - \overline{\Delta g}^{M_2}_{5'\times 5'} && \Rightarrow M_3 \Rightarrow \delta N_3\\ \overline{\Delta g}^{e}_{1'\times 1'} &= \overline{\Delta g}_{1'\times 1'} - \overline{\Delta g}^{S}_{1'\times 1'} - \overline{\Delta g}^{M_1}_{1'\times 1'} - \overline{\Delta g}^{M_2}_{1'\times 1'} - \overline{\Delta g}^{M_3}_{1'\times 1'} && \Rightarrow M_4 \Rightarrow \delta N_4\end{aligned} \tag{17}$$

in the above expressions, the items with superscript S refers to the mean gravity anomaly calculated using a gravity potential model truncated to degree and order 36, and the symbol "⇒" means mapping the gravity anomaly residual into point masses. M_i (i = 1, 2, 3, 4) represents the point masses solved from each residual step respectively. The item with superscript M_i (i = 1, 2, 3, 4) stands for the grid mean gravity anomaly calculated using the ith group of point masses. Clearly, the frequency-wise residual of gravity anomaly is also equivalent to the frequency-wise point masses. When dealing with the depth selection of point masses, here we tend to use fixed-position point mass, due to the fact that there is already gravity observations in the test area.

4 Numerical Test

The test area has a coverage of 40′ × 60′, whose latitude interval is [38°20′, 39°], and longitude interval is [111°10′, 112°10′]. The heights and gravity anomalies of the test area are shown in Figs. 3 and 4. In Fig. 3, the white points are 25 known points with known GPS/Levelling observations.

Two methods were used to calculate the known height anomalies of the 25 points. The first method is the RCR method, which involved the Earth's gravity potential model EGM96 truncated to degree and order 36 which corresponding to a resolution of 5° × 5° and a local 1′ × 1′ digital terrain model, and the second method is the frequency-wise multi-layer point mass (PM) method. The latter consists of four layer point masses and the EGM96 truncated to degree and order 36. Each layer of point masses is resolved using a process similar to (Needham 1970). Details of the point mass model are summarized in Table 2.

In the selection of a gravity potential model with a better long wavelength part, some work indicates that when truncated to d/o 36, EGM96 and EGM2008 have almost the same performance. However, the bigger size of the EGM2008 coefficient file results in a longer time consumption in opening/reading file in computation, and hence the EGM96 file with a smaller size is preferable.

Results from both methods were compared with the known height anomalies, and the statistics of the differences with actual observations are listed in Table 3.

From Table 3, the RCR method performs better than PM method in the approximation of actual height anomalies. The RCR method takes into account of both the long wavelength part of the Earth's gravity field and the high frequency part of terrain effect. While in the construction of

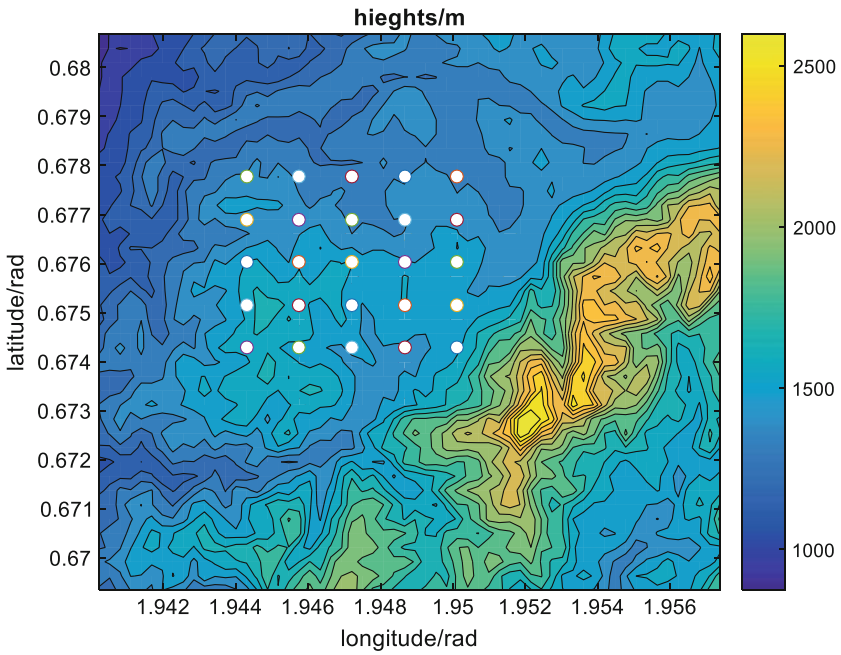

Fig. 3 Heights of the research area

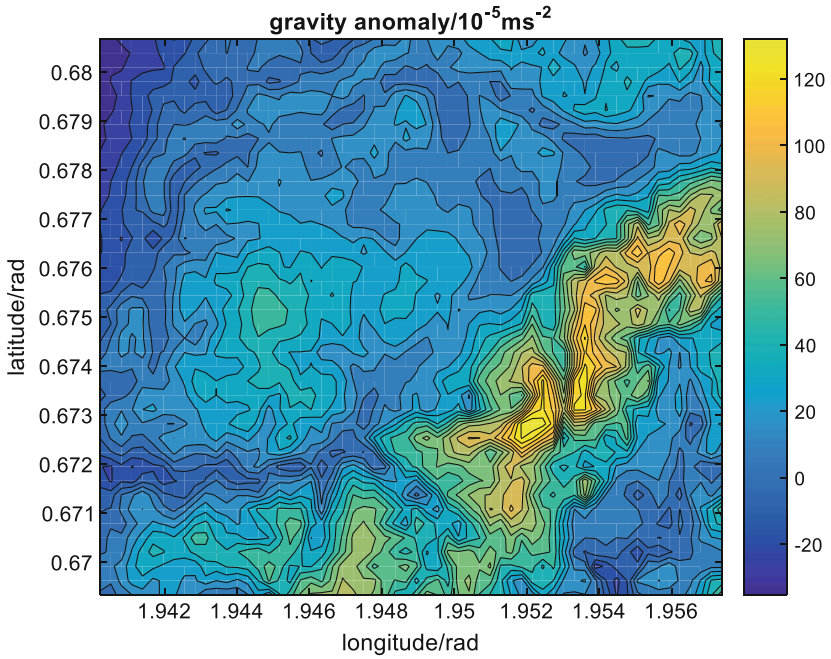

Fig. 4 Gravity anomaly of the research area

Table 2 Configuration of the point mass model

Point mass resolution	Coverage	Depth (km)
$1' \times 1'$	$80' \times 80'$	2
$5' \times 5'$	$4° \times 6°$	10
$20' \times 20'$	$8° \times 10°$	40
$1° \times 1°$	$60° \times 65°$	100

Table 3 Comparisons of results of the two methods with actual observations (unit: cm)

Method	Std	Mean	Min	Max
RCR	8.2	13.4	−7.9	26.4
PM	11.7	18.5	−9.6	35.1

multi-layer frequency-wise point masses, due to the depth of each layer point mass under the ground, the effect of local terrain was smoothed and has weak impact on the calculation of height anomaly on the ground. What's more, in the construction of the point mass model, the selection of point mass depth needs much attention while the result may not seem so good. Therefore, the comparison

of the results from the two methods has to be interpreted with care.

5 Summary

With the actual measurements of height anomalies in test area, two methods that approximate the height anomaly were proposed and tested. The two methods were Remove-Compute-Restore method and fixed-position multi-layer point mass method. Through calculations and comparisons with actual measurements, the results provided by the multi-layer point mass method are close to those of RCR method. Our future work is to explore the possible sources of difference and to improve the approximation accuracy of the point mass method, and the free-positioned point masses seem to be a better choice.

Acknowledgements The work in the paper is financially supported by the National Natural Science Foundation of China, No. 41574020.

References

Antunes C, Pail R, Catalao J (2003) Point mass method applied to the regional gravimetric determination of the geoid. Studia Geophysica et Geodaetica 47:495–509

Barthelmes F (1989) Local gravity field approximation by point masses with optimized positions. Report No. 102(2). Veroeffentlichungen des Zentralinstituts for Physik der Erde, Potsdam, Germany

Bjerhammar A (1963) A new theory of gravimetric geodesy. Royal Institute of Technology, Division of Geodesy, Stockholm

Forsberg R (1984) A study of terrain reductions, density anomalies and geophysical inversion methods in gravity field modeling: report 355. Department of Geodetic Science and Surveying, the Ohio State University, Columbus

Forsberg R, Tscherning CC (1981) The use of height data in gravity field approximation by collocation. J Geophys Res 86(B9):7843–7854

Heiskanen W, Moritz H (1967) Physical geodesy. W. H. Freeman and Co., San Francisco

Moritz H (1980) Advanced physical geodesy. Abacus Press, Tunbridge Wells Kent

Needham PE (1970) The formation and evaluation of detailed geopotential models based on point masses. Report 149. Department of Geodetic Science and Surveying, Ohio State University, Columbus, Ohio, USA

Sjoberg L (1995) On the quasigeoid to geoid separation. Manuscripta Geodetica 20:182–192

Sünkel H (1981) Feasibility studies for the prediction of the gravity disturbance vector in high altitudes. Report No. 311. Department of Geodetic Science, Ohio State University, Columbus, OH, USA

Sünkel H (1983) The generation of a point mass model from surface gravity data. Report No. 353. Department of Geodetic Science, Ohio State University, Columbus, OH, USA

Tscherning CC (1981) Comparison of some methods for the detailed representation of the Earth's gravity field. Rev Geophys 19:213–221

Vermeer M (1995) Mass point geopotential modeling using fast spectral techniques: historical overview, toolbox description, numerical experiments. Manuscrita Geodaetica 20:362–378

Optimal Combination of Satellite and Terrestrial Gravity Data for Regional Geoid Determination Using Stokes-Helmert's Method, the Auvergne Test Case

Ismael Foroughi, Petr Vaníček, Pavel Novák, Robert William Kingdon, Michael Sheng, and Marcelo C. Santos

Abstract

The precise regional geoid modelling requires combination of terrestrial gravity data with satellite-only Earth Gravitational Models (EGMs). In determining the geoid using the Stokes-Helmert approach, the relative contribution of terrestrial and satellite data to the computed geoid can be specified by the Stokes integration cap size defined by the spherical distance ψ_0 and the maximum degree l_0 of the EGM-based reference spheroid. Larger values of l_0 decrease the role of terrestrial gravity data and increase the contribution of satellite data and vice versa for larger values of ψ_0. The determination of the optimal combination of the parameters l_0 and ψ_0 is numerically investigated in this paper. A numerical procedure is proposed to find the best geoid solution by comparing derived gravimetric geoidal heights with those at GNSS/levelling points. The proposed method is tested over the Auvergne geoid computation area. The results show that despite the availability of recent satellite-only EGMs with the maximum degree/order 300, the combination of $l_0 = 160$ and $\psi_0 =$ 45 arc-min yields the best fitting geoid in terms of the standard deviation and the range of the differences between the estimated gravimetric and GNSS/levelling geoidal heights. Depending on the accuracy of available ground gravity data and reference geoidal heights at GNSS/levelling points, the optimal combination of these two parameters may be different in other regions.

Keywords

Geoid • Stokes integral • Satellite models • Terrestrial data

1 Introduction

Stokes's boundary-value problem requires gravity values to be known on the geoid. Moreover, gravity anomalies used as input data must be solid (Vaníček et al. 2004) in order to be continuable from ground down to the geoid. Helmert's gravity anomalies are solid above the geoid; thus, they can be downward continued. To derive Helmert's gravity anomalies on the Earth's surface, the direct topographical effect (DTE) as well as the direct atmospheric effect on gravity must be applied to free-air (FA) gravity anomalies. The latter effect is small and well known and will not be discussed. This gravity reduction, we call it "Helmertization" (see Fig. 1), is the first step in the geoid determination using Stokes-Helmert's method.

The geoidal heights in Helmert's space (N^h) can be evaluated by applying the Stokes integral to Helmert's gravity anomalies ($\triangle g^h$) on the geoid which should be available globally (Stokes 1849). Vaníček and Kleusberg (1987)

I. Foroughi (✉) • P. Vaníček • R.W. Kingdon • M. Sheng • M.C. Santos
Department of Geodesy and Geomatics Engineering,
University of New Brunswick, Fredericton, Canada
e-mail: i.foroughi@unb.ca

P. Novák
NTIS – New Technologies for the Information Society,
University of West Bohemia, Pilsen, Czech Republic

G. S. Vergos et al. (eds.), *International Symposium on Gravity, Geoid and Height Systems 2016*,
International Association of Geodesy Symposia 148, DOI 10.1007/1345_2017_22

Fig. 1 Three main computational steps of Stokes-Helmert's technique

introduced the idea of splitting the geoidal heights as well as Helmert's gravity anomalies to reference and residual parts:

$$\begin{aligned} N^h(\Omega) &= N^h_{ref}(\Omega) + N^h_{res}(\Omega), \\ \Delta g^h(\Omega) &= \Delta g^h_{ref}(\Omega) + \Delta g^h_{res}(\Omega) \end{aligned} \tag{1}$$

where Δg^h_{res} is the residual Helmert gravity anomaly and N^h_{res} is the residual geoidal height in Helmert's space. Δg^h_{ref} and N^h_{ref} represent the reference Helmert anomaly and the reference spheroid, respectively; they both can be synthesized from helmertized EGM as (Najafi-Alamadari 1996):

$$\begin{aligned} T^h_{ref}(R,\Omega) &= \tfrac{GM}{r}\sum_{l=2}^{l_0}\left(\tfrac{R}{r}\right)^l \sum_{m=-1}^{l} T^h_{l,m} Y_{l,m}\ (\lambda,\phi) \\ T^h_{l,m} &= \begin{cases} C^h_{lm} & m \geq 0 \\ S^h_{lm} & m < 0 \end{cases} \\ Y_{l,m} &= \begin{cases} P_{lm}\ (\cos\phi)\ \cos m\lambda & m \geq 0 \\ P_{lm}\ (\cos\phi)\ \sin|m|\,\lambda & m < 0 \end{cases} \end{aligned} \tag{2}$$

where R is the mean Earth's radius, r is the radius for which helmertized spherical harmonic coefficients (C^h_{lm}, S^h_{lm}) are evaluated; GM is the product of the Newtonian gravitational constant G and the Earth's mass M. The symbol $\Omega = (\phi, \lambda)$ represents the geocentric direction of the computation point and λ and ϕ are the geocentric spherical coordinates. The P_{lm} is the fully normalized associated Legendre function of the degree l and order m. The parameter l_0 is the maximum degree of the spherical harmonic expansion that defines the maximum contribution of satellite-only EGMs in a spectral way to the Helmert disturbing potential T^h_{ref}. This potential is defined as follows:

$$\begin{aligned} T^h_{ref}(R,\Omega) &= W^h_{ref}(R,\Omega) - U_0(\phi), \\ W^h_{ref}(r,\Omega) &= W_{ref}(r,\Omega) - \delta V^t_{ref}(r,\Omega) \end{aligned} \tag{3}$$

where U_0 is the latitude-dependent normal gravity potential and W_{ref} is the actual gravity potential. $\delta V^t_{ref}(r,\Omega)$ is the reference residual gravitational potential of the topographic masses (Novák 2000). By using Eq. (4) the Helmert reference gravity anomaly Δg^h_{ref} and the reference spheroid $N^h_{ref}(\Omega)$ can be computed using the fundamental equation of physical geodesy and spherical Bruns's formula, respectively (Heiskanen and Moritz 1967, Eqs. 2-148 and 2-144).

To evaluate the residual geoidal heights in Helmert's space, i.e., N^h_{res} in Eq. (3), the Stokes integration is employed. Its integration domain Ω_0 can be split into the near zone Ω_{ψ_0} and the far zone $\Omega_0 - \Omega_{\psi_0}$ (Vaníček and Kleusberg 1987). The size of the near zone dictates the contribution of terrestrial gravity data which reads:

$$\begin{aligned} N^h_{l>l_0,\Omega'_{\psi_0}}(\Omega) = &\frac{R}{4\pi\gamma_0(\phi)} \iint_{\Omega'\in\Omega_{\psi_0}} \Delta g^h_{res}(R,\Omega') \\ &\times S_{n>l_0}\left(\psi_0, \psi(\Omega,\Omega')\right)\, d\Omega' \end{aligned} \tag{4}$$

where $N^h_{l>l_0,\Omega'_{\psi_0}}$ is the residual geoid height in Helmert's space computed from the near-zone gravity data. The subscript $l > l_0, \Omega'_{\psi_0}$ indicates that the integration is performed over residual Helmert's gravity anomalies with frequencies higher than l_0 and limited to the cap size Ω'_{ψ_0}. The far-zone contribution $(N^h_{l>l_0,\Omega'_0-\Omega'_{\psi_0}})$ reads:

$$\begin{aligned} N^h_{l>l_0,\Omega'_0-\Omega'_{\psi_0}}(\Omega) = &\frac{R}{4\pi\gamma_0(\phi)} \iint_{\Omega'\in\Omega'_0-\Omega'_{\psi_0}} \Delta g^h_{res}(R,\Omega') \\ &\times S_{n>l_0}\left(\psi_0, \psi(\Omega,\Omega')\right)\, d\Omega' \end{aligned} \tag{5}$$

where Ω_0 stands for the geocentric solid angle $\left[\phi \in <-\frac{\pi}{2}, \frac{\pi}{2}>,\ \lambda \in <0, 2\pi>\right]$, Ω' represents the pair of the integration point coordinates and ψ is the spherical distance between the integration and computation points. The modified version of the spheroidal Stokes function $(S_{n>l_0})$ is used here; the modification minimizes the far-zone contribution in the least square sense. For more details, please refer to (Vaníček and Kleusberg 1987).

The contribution of satellite-only EGMs (in the spectral sense) is given by the maximum degree of the spherical harmonic expansion l_0 in Eq. (4) while terrestrial gravity data increasingly contributes to the geoidal height with the increasing size of the spherical integration cap ψ_0 in Eqs. (1) and (2).

The primary indirect topographical effect (PITE) is then added to the co-geoidal heights computed by Eq. (3) to convert them back to the real space; we call this step as "*de-helmertization*", see Fig. 1.

Featherstone and Olliver (1994) analyzed the coefficients of the geopotential model along with the terrestrial gravity data to find the optimal Stokes's integration cap size and the degree of reference field to compute the geoid in the British Isles. In the end they estimated as the maximum degree 257 and the radius of 1 arc-deg 57 arc-min. They did not use any higher degrees than 257 for computing the reference field because according to their analysis the standard errors of the gravity anomalies computed by then-available geopotential models started to exceed the coefficients themselves.

Vella and Featherstone (1999) set the degree of reference field to 360 and changed the Stokes integration cap size to find the optimal contribution of terrestrial gravity data to compute the geoid model of Tasmania. They compared the resulting geoid models with the geoid height from GPS/leveling points in their study area and found out that the cap radius of 18 arc-min gives the smallest STD.

These papers date back to the time when global fields did not have any gravity-dedicated satellite mission data included; thus, they were not as accurate in the low- and mid-wavelengths as they are now because of GRACE and GOCE satellite gravity data (Reigber et al. 2005; Pail et al. 2011).

The methodology proposed in the present study investigates all possible options to find the optimal degree of the reference field and the radius of the integration cap. The optimality is defined according to two criteria: minimum values of STD and range of the differences between the computed geoid model and geoidal heights at GNSS/levelling points described in Sect. 2. Numerical results of the proposed method summarized in Sects. 3 and 4 conclude the paper.

2 Proposed Method

Theoretically if EGMs represent the Earth's gravity field accurately (for l_0 going to infinity), the near-zone Stokes integration is not needed, i.e., the radius ψ_0 can be put equal to 0. If, on the other hand, EGMs were not good, we would have to disregard them and use terrestrial gravity data from the whole world, i.e., $\psi_0 = 180°$. As both EGMs and terrestrial gravity data are burdened with position-dependent noise, the optimal combination of l_0 and ψ_0 varies from place to place. The pair $l_0 = 90$ and $\psi_0 = 2^\circ$ has commonly been used in our previous geoid determinations (Ellmann and Vaníček 2007). To find the optimal pair for currently available EGMs in every region, the following algorithm is suggested:

1. Vary the degree of the reference field and spheroid and correspondingly the modification degree of Stokes's kernel function: $l_0 = 90 : 300$. Here we shall go only up to $l_0 = 300$ as this degree represents the maximum degree of current satellite-only EGMs.
2. Remove the helmertized reference field of the degree l_0 from Helmert's gravity anomaly on the geoid.
3. Vary the near-zone contribution by changing the integration radius $\psi_0 = 30' : 2^\circ$.
4. Compute the residual co-geoid by Stokes's integration as the sum of contributions from both near and far zones.
5. Add the reference spheroid of the degree l_0 to the residual co-geoid.
6. Compute the geoid in the real space by adding PITE to the co-geoid.
7. Evaluate geoidal heights at available GNSS/levelling points in the computation area.
8. Find the optimal geoid for the chosen l_0 in Step 1, the optimal choice can be based on the minimum norm of differences between the computed geoid and GNSS/levelling geoidal heights. The two most reasonable choices among all norms are $\|\|_2$ (L_2 norm), called also the standard deviation (STD) of the differences, and $\|\|_\infty$(L infinity norm) equal to the maximum absolute value of the differences. The latter is loosely connected to the range of the discrepancies.
9. Repeat Steps 1 to 8 for all degrees up to $l_0 < 300$.
10. Find the "global" optimal pair among the "local" ones which is then the optimal pair (l_0, ψ_0) for the computation area.

Depending on the step between degree/order of reference field and integration cap size, the computation of the proposed algorithm can be time demanding. The diagram in Fig. 2 describes how this algorithm works graphically:

3 Numerical Results

The proposed method was tested in Auvergne, the central area of France, which is limited by $(-1^\circ < \lambda < 7^\circ, 43^\circ < \phi < 49^\circ)$ (Duquenne 2006). The topography of this area

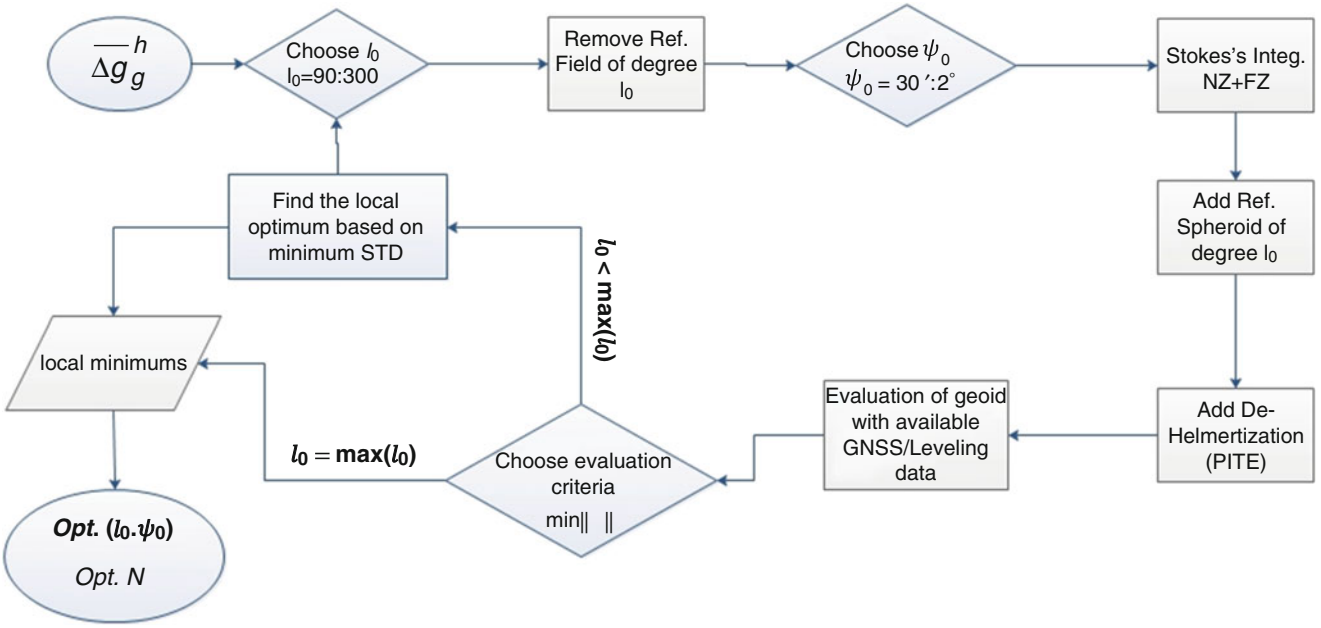

Fig. 2 Proposed method to estimate the optimal contributions of near-zone (NZ) and far-zone (FZ) in Stokes's integration

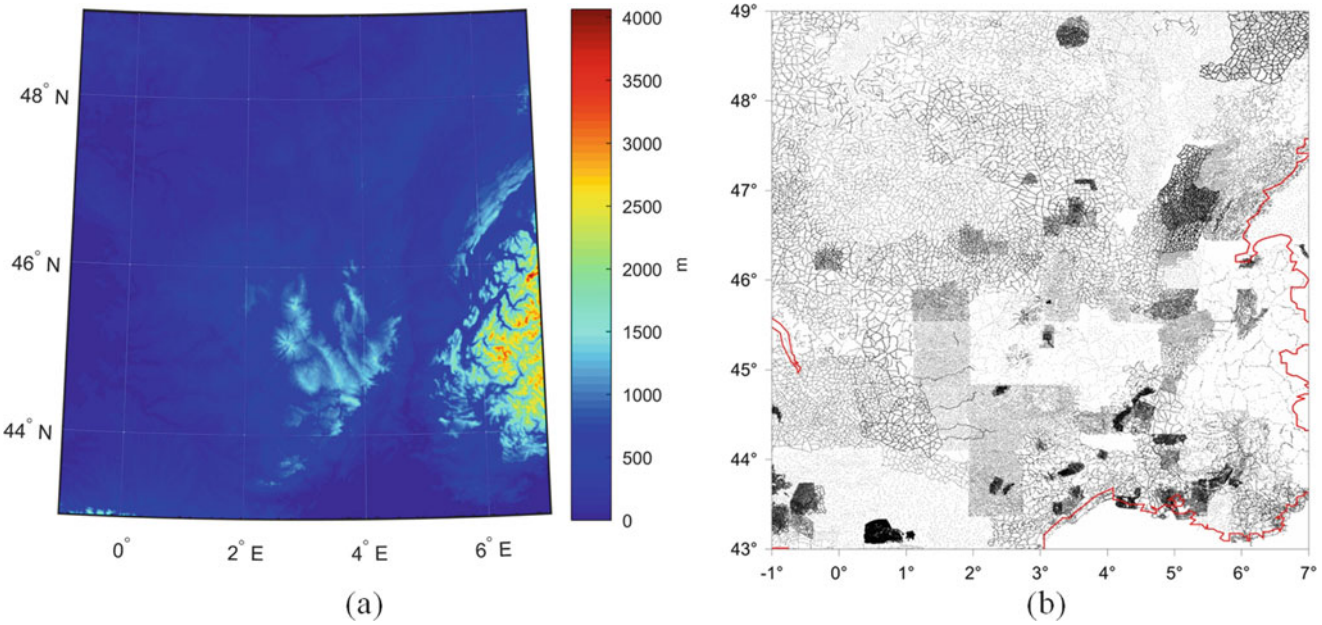

Fig. 3 Topography of the study area (**a**); distribution of terrestrial gravity data (**b**)

is shown in Fig. 3a. This area contains about 240,000 scattered free-air gravity points that have been extracted from the database of the Bureau Gravimetrique International (Fig. 3b). Seventy-five GNSS/levelling points are also available within the central square of the area of interest for the geoid computation ($1.5^\circ < \lambda < 4.5^\circ, 45^\circ < \phi < 47^\circ$). The data coverage area is larger than the geoid computation area to be able to test the different integration cap radii. Mean gravity anomalies of $1'$ resolution were computed from scattered observed gravity using complete spherical Bouguer anomalies, also known as NT anomalies, (they are known to be the smoothest) by means of inverse cubic distance interpolation. It was shown by Kassim (1980) that inverse cubic distance interpolation is superior for predicting gravity anomalies to other tested interpolation techniques. Mean Helmert's gravity anomalies on the Earth's surface were obtained by adding the DTE. The secondary indirect topographical effect (SITE), see Vaníček et al. (1999), was added to the predicted anomaly values to prepare them for the downward continuation.

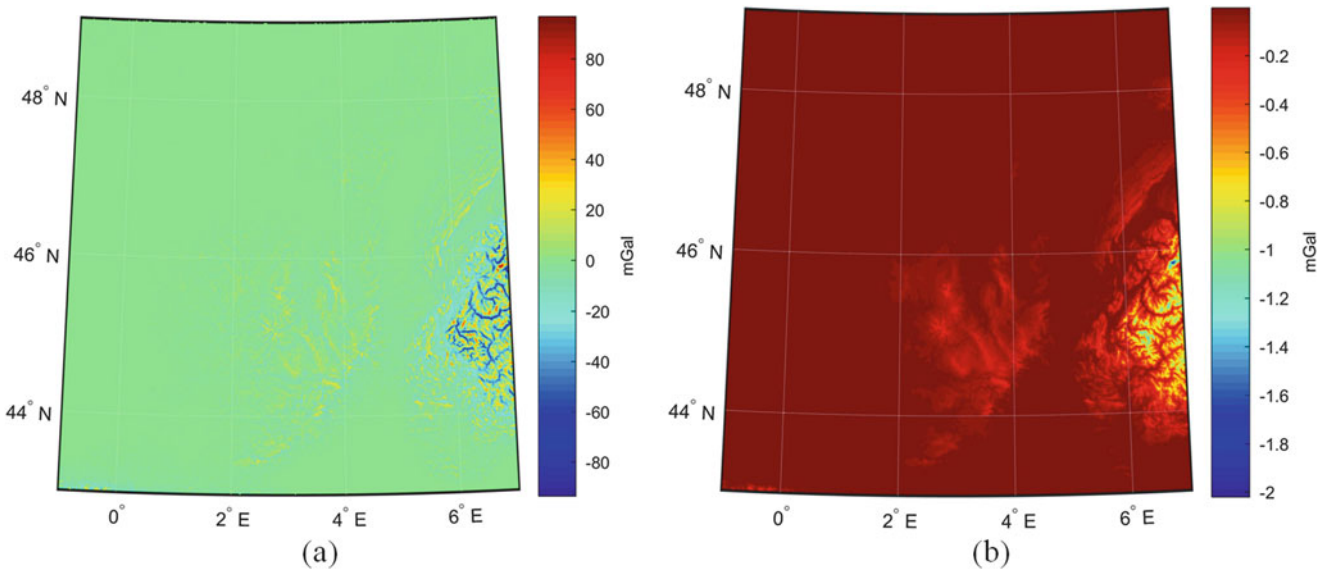

Fig. 4 Direct topographical effect (**a**); secondary indirect topographical effect on gravity anomalies (**b**)

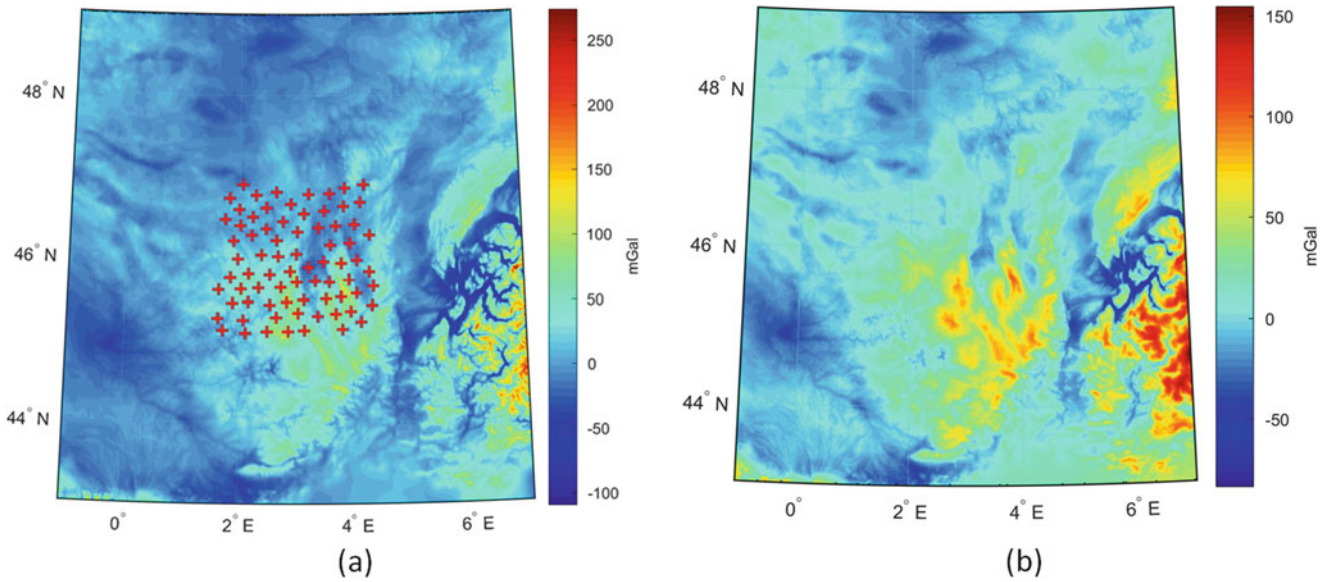

Fig. 5 Free-air gravity anomaly with red-cross signs showing GNSS/levelling points (**a**) and Helmert's gravity anomalies (**b**)

For computing the DTE at each gravity point, topographical heights over the entire Earth are needed. The integration is done separately in the inner, near and far zones. SITE was also computed for inner, near and far zones separately, but this effect for Helmert's space is much smaller than DTE. Values of DTE and SITE over the Auvergne area are shown in Fig. 4.

Applying DTE and SITE converts the free-air gravity anomalies to Helmert's gravity anomalies. Figure 5 shows the free-air and mean Helmert's gravity anomalies in the Auvergne area.

Mean Helmert's anomalies on the Earth's surface were then downward continued to mean Helmert's anomalies on the geoid. This was done using the Poisson integral equation solved by the iterative Jacobi process (Kingdon and Vaníček 2010). The downward continuation was done over 1 arc-deg squared cells augmented by a border strip 30 arc-min wide on all sides. Results from the individual cells were then fused together. On average, seven iterations were needed for the downward continuation in the individual squares. For the purpose of the fusion, an assessment of continuity of Helmert's gravity anomalies along the borders of two

adjacent arc-degree cells on the geoid was done by the technique described by Foroughi et al. (2015b). This assessment showed that discontinuities between the downward continued Helmert anomalies are random within the limits of $\pm 3\sigma$ (σ is the standard deviation of observed anomalies) which was assumed acceptable.

The next step is the evaluation of Stokes's integral which starts with removing long wavelengths from gravity anomalies using the reference field. In our case, the satellite-only DIR_R5 EGM (GOCE, GRACE and Lageos) was used for computation of the reference gravity field and the spheroid (Bruinsma et al. 2013). PITE was then computed for the locations of the 1 arc-min grid on the geoid, again separately for the inner, near and far zones (Fig. 6). This resulted in the geoid (in real space) for the pre-selected (l_0, ψ_0).

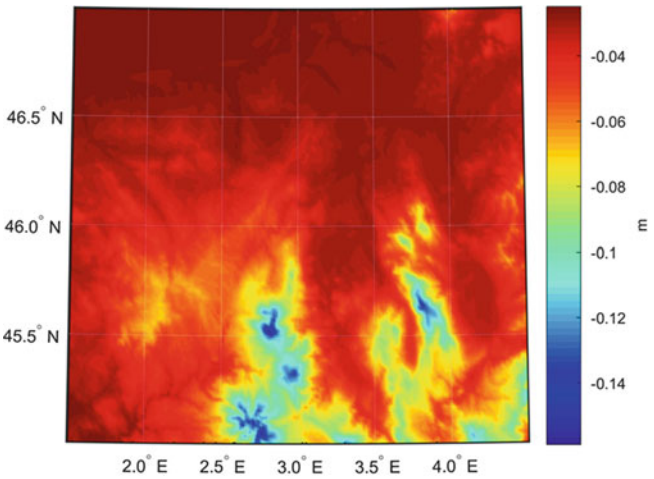

Fig. 6 Primary indirect topographical effect on geoidal heights in the Auvergne geoid test area

This geoid was then compared against the results from GNSS/levelling.

To find the optimal combination of the degree of the reference field l_0 and the radius of Stokes's integration ψ_0 the above proposed algorithm was repeatedly used. The first computation started with $l_0 = 90$ and $0^\circ < \psi_0 < 2^\circ$; the maximum integration cap size was chosen 2 arc-deg as commonly used by us with Stokes-Helmert's technique. This choice meant that we actually needed an extra 2 arc-deg data coverage in latitude direction and around 3 arc-deg in longitude direction outside the geoid computation area which was not covered by the original data. Foroughi et al. (2015a) solved this problem by padding the original data coverage by 3 arc-deg from each side, by using free-air gravity anomalies synthesized from EGM2008 up to the degree/order 2160. They showed this method was accurate enough for the purpose of covering a smaller gap in data coverage. This approach was used here wherever there were coverage gaps.

The proposed method tests all the possible choices of the parameter pair (l_0, ψ_0). The optimal geoid is chosen based on the agreement between the resulting gravimetric geoid and geoidal heights derived from GNSS/levelling. STD and ranges of the differences are chosen as tools for finding the optimal combination. Figure 7 shows 2D plots of the range and STD of the differences as functions of ψ_0 and l_0.

Figure 7 shows that for all considered degrees $l_0 = 140$ is the highest one should go to keep the range as small as possible. In combination with $\psi_0 = 0.75°$ it gives the smallest range of the differences, 16.3 cm in fact. We note that taking the larger integration cap does not improve the range, but larger ψ_0 will not make the range significantly

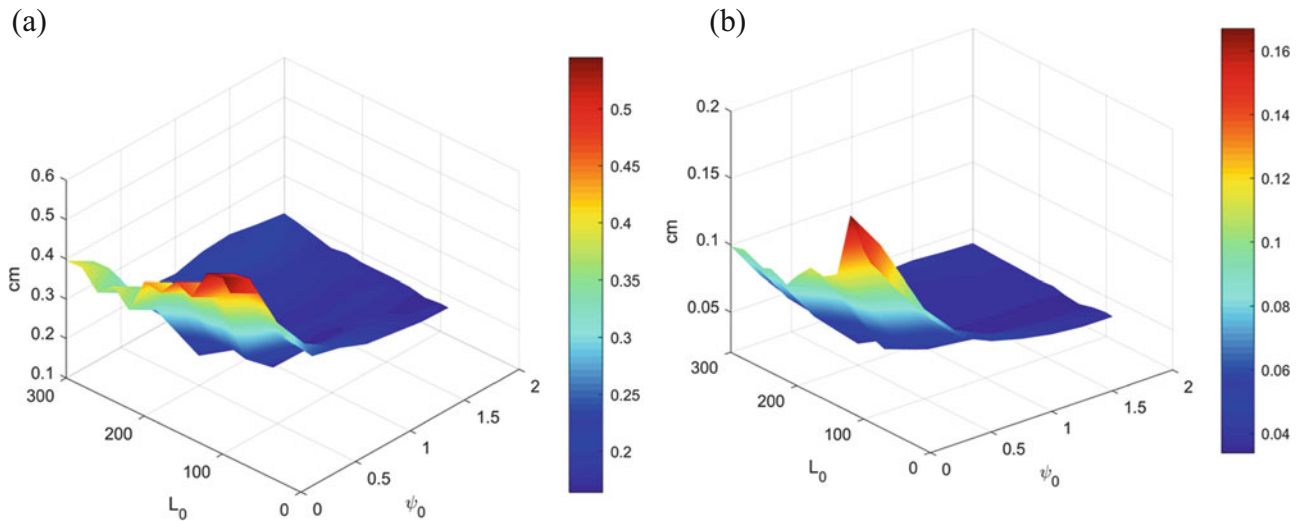

Fig. 7 Variation of STD and range of differences between resulting geoid and GNSS/levelling. (**a**) Variation of the range, minimum: $(l_0 = 140, \psi_0 = 0.75^\circ)$, (**b**) Variation of STD, minimum: $(l_0 = 160, \psi_0 = 0.75^\circ)$

larger either. Looking at STD values, it appears that a similar cut-off value should be used for l_0, i.e., about 160, while the choice of ψ_0 seems to be even less critical than for the range minimization criterion. The smallest STD = 3.3 cm is obtained for combination l_0= 160 and ψ_0 = 0.75°. Generally, it appears that taking l_0 larger than 160 and ψ_0 smaller than 0.75° should be avoided. The plots seem to indicate, however, that the deterioration of accuracy is much faster with the increasing degree of EGM than with the increasing radius of the integration cap.

4 Concluding Remarks

A numerical method was proposed to optimally combine terrestrial and satellite gravity data for computing the regional geoid using Stokes-Helmert's approach. The optimality of the results was measured by the differences between the derived gravimetric and GNSS/levelling geoidal heights in terms of their range and STD. This method was tested over the area of Auvergne and the optimal geoid was derived when the maximum contribution of the DIR-R5 EGM was set to $l_0 = 160$ and the near-zone Stokes integration cap size was set to $\psi_0 = 0.75^0$. The resulting optimal geoid of this study showed the 0.3 cm improvement in terms of STD and 2.4 cm improvement in the range with respect to the geoid computed by the standard choice of $l_0 = 90$ and $\psi_0 = 2^0$. Comparing the optimal geoid with the geoid computed using the maximum contribution from EGM, i.e., $l_0 = 300$ and $\psi_0 = 0.25^0$, showed the improvement of 4 cm in terms of STD and 19 cm in the range. The methodology proposed in this study would have to be tested in other regions as the present results were obtained in the Auvergne study area and might be different for other regions. The choice of the optimal integration cap size depends on the quality and spatial distribution of terrestrial gravity data. However, the estimated optimal degree of reference field (l0 = 160) could also be valid for other regions as Abdalla et al. (2012) found more or less the same number over the Khartoum state. They investigated the validation of all GOCE/GRACE geopotential models and concluded that the models do not show better results beyond degree 150. Due to inherent errors of satellite-only EGM higher-degree coefficients, they are not recommended to be used when reasonably good terrestrial gravity data are available.

Acknowledgments We wish to acknowledge that the leading authors Prof. Vaníček and Mr. Sheng were supported by an NSERC "Discovery grant". Pavel Novák was supported by the project 15-08045S of the Czech Science Foundation.

References

Abdalla A, Fashir H, Ali A, Fairhead D (2012) Validation of recent GOCE/GRACE geopotential models over Khartoum state – Sudan. J Geod Sci 2(2):88–97

Bruinsma S, Foerste C, Abrikosov O, Marty J-C, Rio M-H, Mulet S, Bonvalot S (2013) The new ESA satellite-only gravity field model via the direct approach. Geophys Res Lett 40:3607–3612

Duquenne H (2006) A data set to test geoid computation methods. In: Proceedings of the 1st international symposium of the international gravity field service. Harita Dergisi, Istanbul, pp 61–65

Ellmann A, Vaníček P (2007) UNB application of Stokes-Helmert's approach to geoid computation. J Geodyn 43:200–213

Featherstone WE, Olliver JG (1994) A new gravimetric determination of the geoid of the British Isles. Surv Rev 32(254):464–468

Foroughi I, Janák J, Kingdon R, Sheng M, Santos M, Vaníček P (2015a) Illustration of how satellite global field should be treated in regional precise geoid modelling (padding of terrestrial gravity data to improve Stokes-Helmert geoid computation). The EGU General Assembly, Vienna

Foroughi I, Vaníček P, Kingdon R, Sheng M, Santos M (2015b) Assessment of discontinuity of Helmert's gravity anomalies on the geoid. AGU-GAC-MAC-CGU Joint Assembly, Montreal

Heiskanen W, Moritz H (1967) Physical geodesy. W.H. Freeman and Co., San Francisco

Kassim F (1980) An evaluation of three techniques for the prediction of gravity anomalies in Canada. University of New Brunswick, Fredericton

Kingdon R, Vaníček P (2010) Poisson downward continuation solution by the Jacobi method. J Geod Sci 1:74–81

Najafi-Alamadari M (1996) Contributions towards the computation of a precise regional geoid. Doctoral thesis. University of New Brunswick, Fredericton

Novák P (2000) Evaluation of gravity data for Stokes-Helmert solution to the geodetic boundary-value problem. University of New Brunswick, Fredericton

Pail R, Bruinsma S, Migliaccio F, Förste C, Goiginger H, Schuh W-D, Höck E, Reguzzoni M, Brockmann JM, Abrikosov O, Veicherts M, Fecher T, Mayrhofer R, Krasbutter I, Sansò F, Tscherning CC (2011) First GOCE gravity field models derived by three different approaches. J Geod 85(11):819–843

Reigber C, Schmidt R, Flechtner F, Konig R, Meyer U, Neumayer KH, Schwintzer P, Zhu SY (2005) An Earth gravity field model complete to degree and order 150 from GRACE: EIGEN-GRACE02S. J Geodyn 39(1):1–10

Stokes G (1849) On the variation of gravity at the surface of the Earth. Cambridge University Press, Cambridge

Vaníček P, Kleusberg A (1987) The Canadian geoid-Stoksian approach. compilation of a precise regional geoid. Manuscripta Geodetica 12:86–98

Vaníček P, Huang J, Novák P, Véronneau M, Pagiatakis S, Martinec Z, Featherstone WE (1999) Determination of boundary values for the Stokes-Helmert problem. J Geod 73:180–192

Vaníček P, Tenzer R, Sjöberg LE, Martinec Z, Featherstone WE (2004) New views of the spherical Bouguer gravity anomaly. J Geophys Int 159(2):460–472

Vella JP, Featherstone WE (1999) A gravimetric geoid model of Tasmania, computed using the one-dimensional fast Fourier transform and a deterministically modified kernel. Geomat Res Aust 70:53–76

New Modifications of Stokes' Integral

Lars E. Sjöberg and Mehdi S. Shafiei Joud

Abstract

In the last decades several alternative methods of modifying Stokes' formula were developed. Here, a combination of two existing modifications from Meissl and Sjöberg is developed and presented. The latter applies a least squares method to minimize the truncation error (as well as the total error of the geoid determination), while the former forces the truncation coefficients to converge to zero more rapidly by using a continuous function. The question is whether the combined Least Squares-Meissl modification reduces the truncation and/or the total geoid determination error. To determine the modification parameters, a new system of equations satisfying simultaneously the faster convergence and minimizing the total error, are presented by using (a) Green's second identity, which is a conventional method, and (b) a set of smoothing averaging filters. The method (b) provides further flexibility when different smoothing filters can be utilized. The new modification reduces the contribution of the inner zone error by 1 mm of the estimated RMS error. The total error does not necessarily decrease, by using the new modification for cap sizes smaller than 3° versus the least squares modification of Sjöberg (Manusr Geod 16: 367–375, 1991).

Keywords

Kernel modification • Least squares modification • Meissl modification • Stokes' integral

1 Introduction

The main idea of modifying Stokes' formula was presented by Molodensky et al. (1962) to reduce the truncation error which is the error committed by limiting the integration to a spherical cap only near the computation point. A further consideration, developed theoretically by Meissl (1971a, b) was to confine the integration kernel to zero at the cap radius, i.e. the geocentric angle ψ_0. The method was further improved to an arbitrary cap radius by Heck and Grüninger (1987) by removing the value of the Stokes kernel $S(\psi_0)$ at the truncation border. By removing a low degree series of Legendre's polynomials from the Stokes kernel (see also Wong and Gore 1969) a further modification was obtained. These spectrally modified kernels (i.e. $S^L(\psi)$, up to degree L) have been applied for regional geoid determinations, e.g. by Vaníček and Kleusberg (1987), Vaníček and Sjöberg (1991) and Vaníček et al. (1995).

Another spectral modification of Stokes kernel by forcing the kernel to zero at each cap radius was presented in Featherstone et al. (1998). Jekeli (1981) already showed that conditioning the kernel to zero at the cap border results in a faster convergence (i.e. in lower degrees) of the series of the truncation error (see Evans and Featherstone 2000, and Šprlák 2010, for a detailed discussion on the rate of convergence), the question here is whether the Meissl-type (MT) modified kernel can reduce the truncation and/or the total error of the geoid determination. Featherstone et al. (1998) used a deterministic combination (the Vaníček-Kleusberg-Meissl modification) without discussing this question, while

L.E. Sjöberg • M.S. Shafiei Joud (✉)
Division of Geodesy and Satellite Positioning, Royal Institute of Technology (KTH), 10044 Stockholm, Sweden
e-mail: lars.sjoberg@abe.kth.se; smsj@kth.se

G. S. Vergos et al. (eds.), *International Symposium on Gravity, Geoid and Height Systems 2016*, International Association of Geodesy Symposia 148, DOI 10.1007/1345_2017_17

Jekeli (1980) already stated that despite the faster convergence to zero of the error series, the MT modification does not necessarily reduce the truncation error. Hence, the problem still needs more investigation (Evans and Featherstone 2000, and Šprlák 2010). Here, we use a similar combination as that of Featherstone et al. (1998) but we make use of a Least squares (LS) modification (Sjöberg 1991) with conditioning the kernel to zero at the cap border (i.e. MT). To represent the Least squares-Meissl modified Stokes kernel, two alternative methods will be investigated: (a) Based on the original derivation in Meissl (1971a, b, p. 43) using Green's second identity (see also Jekeli 1980, pp. 11–13; Featherstone et al. 1998; Evans and Featherstone 2000), and (b) Using smoothing kernels to average the gravity anomalies inside the cap. Both methods forces the modified kernel function to zero at the cap radius, but the shape of the kernel is different in each method. Then we estimate an RMS value of the error of the geoid model using the covariance model of the gravity anomaly signal. We will test the RMS errors for different variants of the modified kernel and compare them with that for the LS modified kernel of Sjöberg (1991).

Sjöberg (1984, 1986, 1991 and 2003) introduced the least squares modification to Stokes' integral. It means to optimize the modified kernel such that the effect of the terrestrial and Earth Gravitational Model (EGM) data errors, as well as the truncation error, are minimized in a least squares sense.

The truncation error was certainly the dominating source of error when Molodensky developed his method. However, in the era of high degree EGMs, the efforts of modifying Stokes' formula should be directed also to other sources of errors as mentioned above. In this paper, we consider whether the combination of MT and LS modifications could improve the geoid estimation and reduce the truncation and/or other sources of errors. In Sect. 2, we introduce the new modification and its two different types. In Sect. 3 the effect of the errors on the geoid is discussed. A least squares solution to minimize the total error will be developed in Sect. 4. Numerical results are given in Sect. 5, where we evaluate the error of the final estimation using the new modification. Sect. 6 concludes the paper.

2 Least Squares-Meissl Modified Stokes' Integral

Our intention is to use a combination of the unbiased LS (Sjöberg 1991) and MT (Meissl 1971b) kernel modifications of Stokes' integral. The LS modification minimizes the total error in a least squares sense while the MT causes the truncation coefficients converge to zero more rapidly by subtracting the value of the kernel at the cap border. The total error consists of the errors of the truncation, the EGM model, and the terrestrial gravity anomaly data.

Following Eq. 37 in Jekeli (1980) and Eq. 20 in Featherstone et al. (1998) the Stokes' integral can be extended such as:

$$N_P = \frac{c}{2\pi}\iint_{\sigma_0}\left(\mathrm{S}^L\left(\psi_{PQ}\right) - S^L_{\psi_0}\right)\Delta g_Q\, d\sigma_Q + \frac{c}{2\pi}\iint_{\sigma}\Delta K\left(\psi_{PQ}\right)\Delta g_Q\, d\sigma_Q + c\sum_{n=2}^{L} s_n \Delta g_n, \tag{1a}$$

where L is the maximum degree of modification,

$$\Delta K\left(\psi\right) = \begin{cases} S^L_{\psi_0} & 0 < \psi \le \psi_0 \\ \mathrm{S}^L\left(\psi\right) & \psi_0 < \psi \le \pi \end{cases}, \tag{1b}$$

N_P is the (quasi)geoid height at the computation point P, Δg_Q is the gravity anomaly at the dummy point Q, Δg_n is the degree n of the gravity anomaly signal, ψ_{PQ} is the spherical distance between points P and Q on the sphere, $d\sigma = \cos\psi\, d\psi\, d\alpha$ is the spherical surface element, α is the azimuth of the spherical distance, $S^L_{\psi_0} = S^L\left(\psi_0\right)$ is the value of the modified Stokes kernel at the cap border, c is a constant, σ denotes the sphere and σ_0 the spherical cap, and ΔK is the kernel of the truncation correction integral i.e. the second integral on the right hand side of Eq. (1a). The first integral on the right hand side runs over the cap area. $S^L(\psi)$ is the high-degree (i.e. higher than degree L) Stokes kernel (Sjöberg 1984):

$$\mathrm{S}^L\left(\psi\right) = \mathrm{S}\left(\psi\right) - \sum_{n=2}^{L}\frac{2n+1}{2}s_n P_n\left(\cos\psi\right), \tag{2}$$

where $S(\psi)$ is the (original) Stokes kernel and s_n is the modification coefficient of the modified Stokes kernel S^L and P_n are the fully normalized Legendre's polynomials of degree n.

A general estimator of the geoid height in Eq. (1a) is by using terrestrial data inside the cap (superscripted), and the EGM model (superscripted *EGM*) for the M Laplace' harmonics with degrees $n = 2, \ldots, L$:

$$\tilde{N}_P = \frac{c}{2\pi}\iint_{\sigma_0}\left(\mathrm{S}^L\left(\psi_{PQ}\right) - \mathrm{S}^L_{\psi_0}\right)\Delta g^T_Q\, d\sigma_Q + c\sum_{n=2}^{M} M^L_n \Delta g^{EGM}_n + c\sum_{n=2}^{L} s_n \Delta g^{EGM}_n, \tag{3}$$

where the truncation coefficient of degree n is (cf. Heiskanen and Moritz 1967, p. 260),

$$\begin{aligned} M_n^L &= \int_0^{\pi} \Delta K(\psi)\, P_n(\cos\psi) \sin\psi d\psi \\ &= \int_{\psi_0}^{\pi} \left(\mathrm{S}^L(\psi_{PQ}) - S_{\psi_0}^L\right) P_n(\cos\psi) \sin\psi d\psi. \end{aligned} \tag{4}$$

Equation (3) is the general form of a MT estimator. It is the Least Squares-Meissl (MS) modified estimator, if the parameters s_n are determined such that the expected global mean square error is a minimum.

3 Derivation of the Truncation Coefficients

To see if the truncation error series converges more rapidly to zero when using the MT condition, and if the answer is positive, whether it reduces the total and/or the truncation error, we need to compute the second term either in Eqs. (1a) or (3). The truncation correction can be obtained using the Legendre's transformation in Eq. (4), which can be rewritten such as:

$$M_n^L = Q_n^L - \mathrm{S}_{\psi_0}^L e_{n0}(\psi_0) \tag{5}$$

where $e_{n0}(\psi_0)$ is as in Appendix, and Q_n^L is the truncation coefficient of degree n for the spectrally modified kernel $S^L(\psi)$ (Sjöberg 1984):

$$Q_n^L = \int_{\psi=\psi_0}^{\pi} S^L(\psi)\, P_n(\cos\psi) \sin\psi d\psi, \tag{6}$$

To determine $e_{n0}(\psi_0)$ one can use the same formulation as in Meissl (1971a, b, p. 43) but for the modified kernel in Eq. (2) (see also Jekeli 1980, pp. 11–13, Featherstone et al. 1998). Alternatively using, Eqs. (4 and 5), one obtains for the truncation correction:

$$\begin{aligned} c\sum_{n=2}^{\infty} M_n^L \Delta g_n &= \frac{c}{2\pi} \iint_{\sigma-\sigma_0} \left(\mathrm{S}^L(\psi) - \mathrm{S}_{\psi_0}^L\right) \Delta g_Q d\sigma_Q \\ &= c\sum_{n=2}^{\infty} Q_n^L \Delta g_n + \frac{c}{2\pi} \mathrm{S}_{\psi_0}^L \iint_{\sigma_0} \Delta g_Q d\sigma_Q. \end{aligned} \tag{7}$$

The mean value of the gravity anomaly inside the cap can be determined using a weighting kernel or a smoothing operator (e.g. Sjöberg 1980; Jekeli 1981):

$$\frac{1}{\sigma_0} \iint_{\sigma_0} \Delta g_Q d\sigma_Q = \sum_{n=2}^{\infty} \beta_n^{\psi_0} \Delta g_n, \tag{8}$$

where $\beta_n^{\psi_0} = \beta_n(\cos\psi_0)$ is the smoothing filter of degree n. Inserting Eq. (8) into the last integral of Eq. (7) and realizing that $\sigma_0 = 2\pi(1-\cos\psi_0)$, one obtains:

$$M_n^L = Q_n^L + \mathrm{S}_{\psi_0}^L (1-\cos\psi_0)\, \beta_n^{\psi_0}. \tag{9}$$

The coefficient $e_{n0}(\psi_0)$ in Eq. (5) reads:

$$e_{n0}(\psi_0) = \begin{cases} \dfrac{P_{n-1}(\cos\psi_0) - \cos\psi_0 P_n(\cos\psi_0)}{n+1}, & \text{(10a)} \\ (1-\cos\psi_0)\, \beta_n^{\psi_0} & \text{(10b)} \end{cases}$$

where superscript ψ_0 shows that the coefficient is only dependent on the spherical radius of the cap. Equation (10a) has been recited after Meissl (1971a, b, p. 43) for the spectrally modified kernel (see also Jekeli 1980, pp. 11–13; Featherstone et al. 1998), while Eq. (10b) follows from Eq. (9).

4 Determination of Modification Parameters

The expected global mean square error is estimated by:

$$\overline{\delta N}_{total}^2 = E\left\{ \frac{1}{4\pi} \iint_{\sigma} \left(\tilde{N}_P - N_P\right)^2 d\sigma_P \right\}. \tag{11}$$

Assuming that the terrestrial and the EGM errors are uncorrelated one obtains (cf. Sjöberg 1991):

$$\begin{aligned} \overline{\delta N}_{total}^2 &= c^2 \sum_{n=2}^{\infty} \left(\frac{2}{n-1} - M_n^L - s_n\right)^2 \sigma_{n,T}^2 \\ &\quad + c^2 \sum_{n=2}^{\infty} \left(M_n^L + s_n\right)^2 \sigma_{n,EGM}^2 + \overline{\delta N}_{bias}^2, \end{aligned} \tag{12}$$

where

$$\overline{\delta N}_{bias}^2 = c^2 \sum_{n=M+1}^{\infty} \left(M_n^L + s_n\right)^2 c_n. \tag{13}$$

Here $\sigma_{n,T}^2$ and $\sigma_{n,EGM}^2$ are the terrestrial and the EGM data noise degree variances, respectively, and c_n is the n-th signal degree variance of the gravity anomaly. Applying the least squares condition $\overline{\delta N}_{total\, s_i, i=2,\cdots,L}^2 = \min$, we arrive at a set of $L-1$ linear equations (see Appendix):

$$\sum_{r=2}^{L} a_{kr} \hat{s}_r = h_k \quad ; k = 2, \cdots, L. \tag{14}$$

5 Numerical Results

The LS estimator of Eq. (3) is obtained by using the solution of Eq. (14) for the modification parameters. To solve the system of equations in (14) the signal and the noise degree variances need to be known beforehand. Some choices for the former can be found in Tscherning and Rapp (1974), Jekeli (1978) and more recently in Rexer and Hirt (2015, Eq. 29) using EGM from the dedicated satellite missions, terrestrial data and the topography-generated gravity field for a spatial resolution better than 10 km.

The error models used for the noise degree variances $\sigma^2_{n,T}$ is obtained taking into account the systematic errors and by assuming that the observation noise is correlated, which result in a more realistic error degree variance for different bandwidths (Ågren 2004, pp. 34–36; Ågren and Sjöberg 2012). We are not aiming to go into details about c_n and $\sigma^2_{n,T}$, because it has already been shown that the choice of the error and signal models, such as mentioned, play a minor role in the LS modification (e.g. Ellmann 2005; Ågren and Sjöberg 2012). In our case, the numerical results for the signal degree variances (c_n) are based on Tscherning and Rapp (1974), and the combined error degree variance error model is based on Ågren (2004, p. 36).

The coefficient matrix $[a_{kr}]$ in Eq. (14) is ill-conditioned, so we need to use a regularization method. We used the singular value decomposition (Anderson et al. 1999; Tikhonov 1963) and Total Least Squares (Huffel and Vandewalle 1991; see also Ellmann 2005) regularization methods. All the results in this section are based on the first method, while the results of the other above mentioned methods will not be reported here since the resulting MS kernels inside the cap and subsequently, the truncation coefficients do not change using aforementioned regularization methods.

The EIGEN-6S4v2 satellite only EGM (Förste et al. 2015) up to degree and order $n = 180$ is used here and its calibrated degree variances are used for computing $\sigma^2_{n,\mathrm{EGM}}$. In Sect. 5.1 we discuss the selection of different $e_{n0}(\psi_0)$ (Eq. 10). In Sect. 5.2 the MS modified kernels for various $e_{n0}(\psi_0)$ and cap sizes will be discussed. In Sect. 5.3 the errors using our modification method is compared with the unbiased LS modification of Sjöberg (1991).

5.1 Smoothing Filters and Conditioning the Equations

We use $e_{n0}(\psi_0)$ given by Eq. (10a) as in Meissl (1971a, b, p. 43), where the Green's second identity on the sphere was used so this type of $e_{n0}(\psi_0)$ will simply be referred as "Green". For $\beta_n^{\psi_0}$ in Eq. (10b) we use the Pellinen filter (PF) by applying the recursive formula of Sjöberg (1980), Eq. 7. We will also use the Gaussian type filter (GF) from Jekeli (1981), Eq. 56). Both types of filters average the gravity anomaly inside the cap. There are, of course, also other smoothing filters such as non-isotropic weighting kernels (e.g. Kusche et al. 2009). In other words, Eq. (10b) provides further flexibility in selecting the appropriate smoothing filter.

The GF of Jekeli (1981, Eq. 56) oscillates for some high degrees, which is a problem that limits its application for smoothing the gravity anomalies inside the cap. For example, for a half bandwidth radius of 450 km the filters are stable below $n = 180$, which may cause problems in computing the series in the first term on the right hand side of Eq. (12) and also the one in Eq. (13), which run to infinity (but set to $n_{max} = 21{,}600$, in our computations). One way to solve this problem is to ignore the oscillating terms by setting them to zero. However, in practice, this makes Eq. (14) even more unstable. This indicates that the solution of Eq. (14) is likely to be highly sensitive to the proper selection of $e_{n0}(\psi_0)$. On the contrary, the PF will be stable to very high degrees using the recursive equation in Sjöberg (1980).

Moreover, due to the ill-conditioning of the coefficient matrix, only some (around 10–15%) of the singular values (SVs) differ from zero in a floating number precision (10^{-15}), and the variation of the number of the used SVs for the final solution leads to different sets of estimates. Equation (14) conditions the modified kernel only for $\psi < \psi_0$, which means that the system has a null-space of solutions outside the cap (see also Ågren 2004, Chap. 3). Using singular value decomposition, the SVs are sorted from the λ_{max} to λ_{min}. By defining the condition number of the system as the ratio $\lambda_{max}/\lambda_{min}$ for $\psi_0 = 3^o$, the number becomes 10^{18}. So by neglecting all the SVs smaller than a limit which is slightly larger than the floating number precision, the solution is still numerically stable. It means to neglect all the eigen-vectors related to the SVs less than $\varepsilon^1 = 10^{-17} \times \lambda_{max}$. We can solve Eq. (14) using different sets of SVs starting from the corresponding floating number precision at ε^1 and keep those SVs that satisfy $\lambda_n \geq \varepsilon^i$; where $\varepsilon^i = 10^5 \times \varepsilon^{i-1}$, $i = 2, 3, 4$ in each step i. To see if the selection of the different sets of SVs affects the final solution we need to wait until the final modified kernels have been revealed (Sect. 5.2).

Summarizing, we investigate three types of the MS modification based on the various selection of $e_{n0}(\psi_0)$ namely those of Green, Pellinen and Gaussian types as well as the unbiased LS modification, which is identical to MS modification taking $e_{n0}(\psi_0) = 0$ (see Appendix).

5.2 Modified MS Kernels

Once the modification parameters have been determined we can use Eq. (2) to compute $S^L(\psi)$ and then subtract its value at the cap radius ψ_0 to obtain the MS modified kernels. Figure 1 shows the kernels for some example cap sizes ($\psi_0 = 1\,,3\,,5$ and 7 degrees), and the ordinary Stokes kernel is also depicted in magenta in all plots for a comparison. Clearly all MS kernels (Fig. 1b, c and d) confined to zero at the cap border. We also show the kernels for different saved numbers of the SVs. We start saving all SVs in the floating point precision (ε^1) and then reduce the number by the logarithmic step of 5. Using different numbers of SVs all the kernels are identical inside the cap except for the Gaussian type (Fig. 1d). This is the effect of the unstable smoothing GF mentioned before, which can be seen more clearly in the last plot of Fig. 1d (for $\psi_0 = 7^o$). Concluding that selecting a well-behaved smoothing filter the results are identical inside the cap regardless of the regularization method in use. Importantly, we need at least enough SVs for the determination of the parameters. Fig. 1 dotted black curves illustrates the conditioning by using only the SVs which are larger than $\varepsilon^4 = 10^{-2} \times \lambda_{max}$.

5.3 Error Reduction

The first term on the right hand side in Eq. (12) is the contribution of terrestrial data error $\overline{\delta N}^2_T$. The second term is the contribution of the EGM error $\overline{\delta N}^2_{EGM}$, and the bias term appears in Eq. (13). These bias terms are depicted in Fig. 2b for the three modification types namely, LS, Pellinen and Green. They show that the truncation error is not necessarily reduced using the new modification. Moreover, the two types of MS modifications have not resulted in exactly the same truncation errors. The total error (Fig. 2a), however, reduced by about 2 mm using MS modification for $\psi_0 > 3^o$. The reason is that the near zone error $\overline{\delta N}^2_T$ is generally reduced, and it reduces with increasing ψ_0, while for LS, the near zone error shows a constant value of 8.5 mm beyond $\psi_0 = 4^o$ (Fig. 2c). The constant value of the near zone RMS error of the LS solution in Fig. 2c, which continues up to degree $n = 20$, is in agreement with Sjöberg

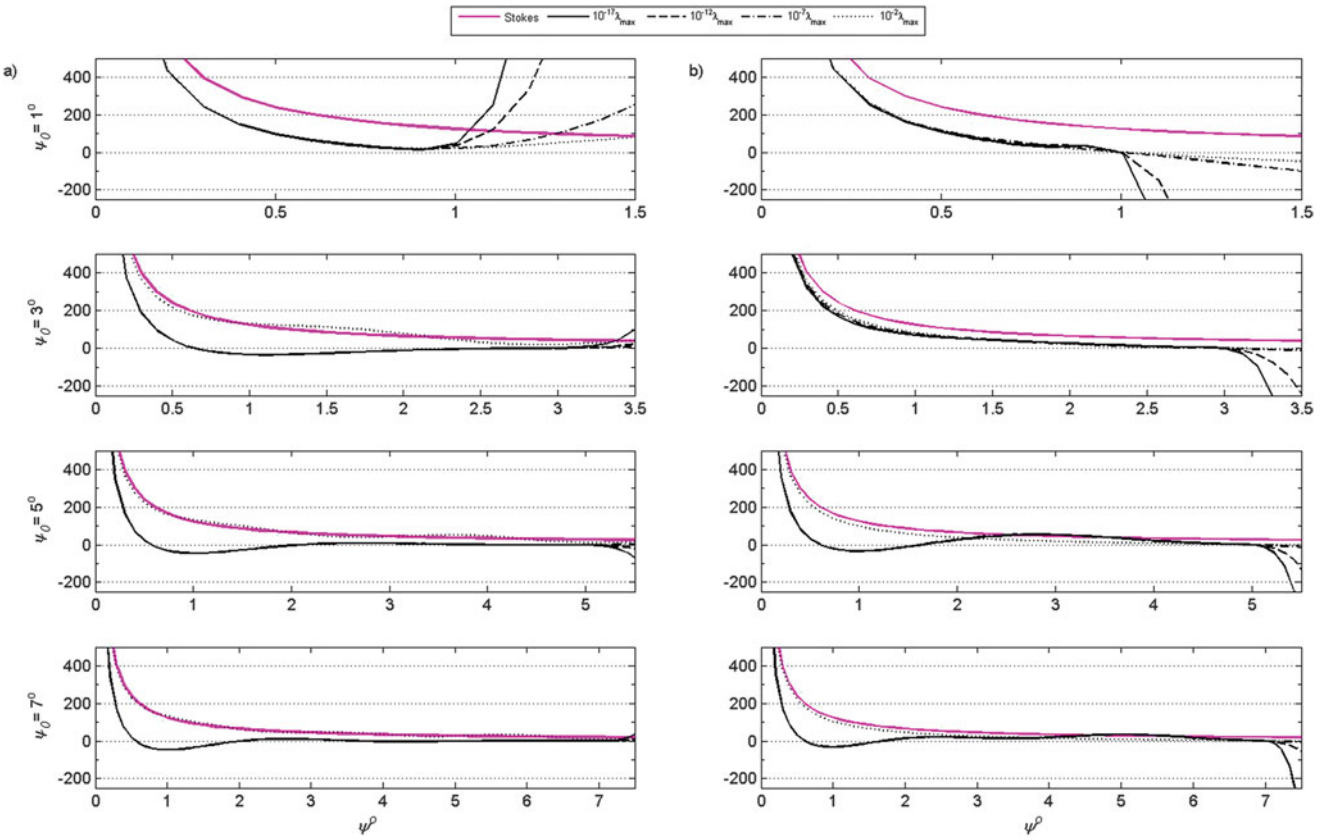

Fig. 1 The modified MS kernel for different types of $e_{n0}(\psi_0)$ (**a**) LS, (**b**) *Green*, (**c**) Pellinen and (**d**) Gaussian, and for various cap sizes from top to bottom $\psi_0 = 1\,,3\,,5$ and 7 degrees. The original Stokes kernel is also depicted in magenta for a comparison. The minimum limit of the singular values used for the computation of the kernel as a portion of the maximum singular value (λ_{max}) are in the legend

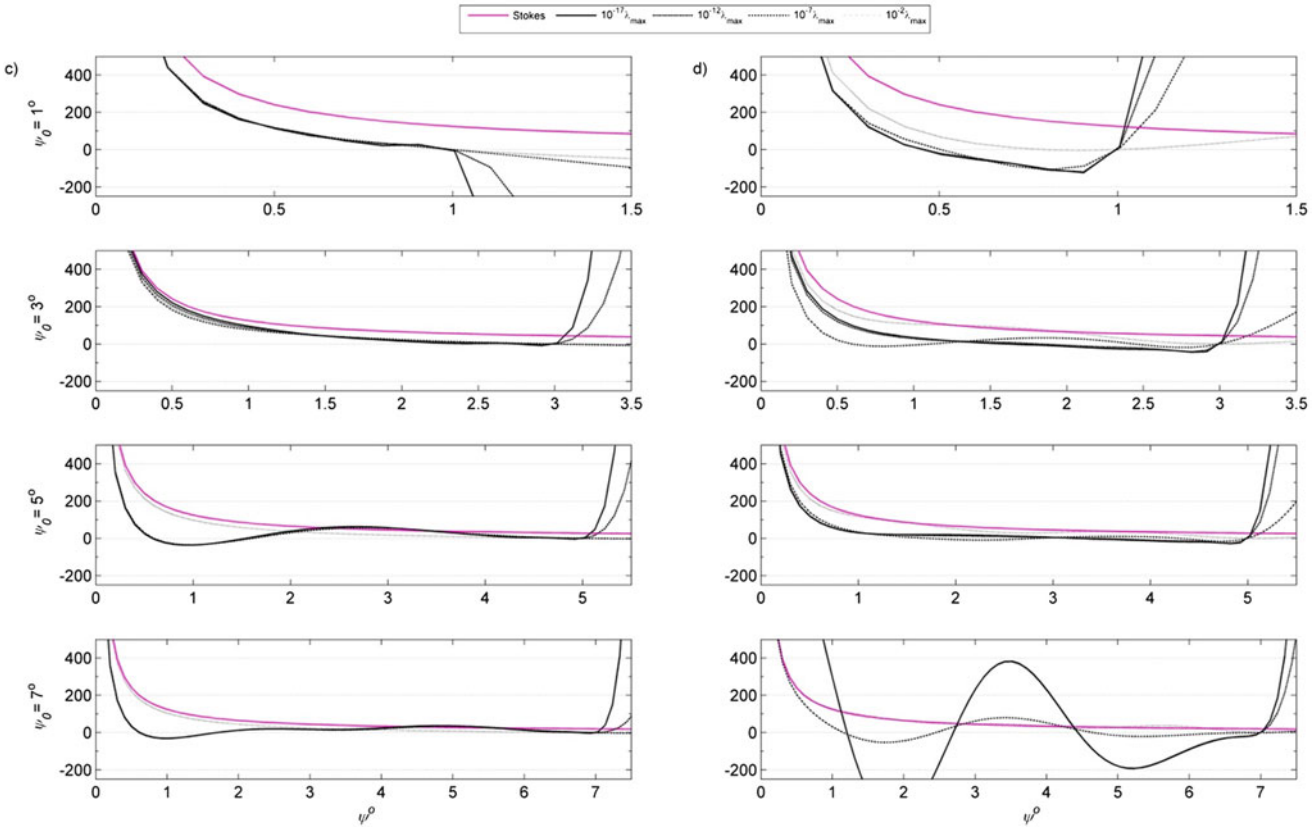

Fig. 1 (continued)

(1986). Figure 2c shows that even for very large cap sizes the LS solution may still have significant errors of about 9 mm. Using MS modification the total error is larger than for LS for $\psi_0 \leq 3^o$, but it decreases and becomes smaller immediately beyond $\psi_0 = 3^o$ and starts to decline monotonically (Fig. 2c).

It should be mentioned that in practical geoid applications of Stokes' integral the cap radius of the area of the integration is usually less than 3^o. Therefore the MS modification does not lead to reducing the total RMS error. However, the question whether using other smoothing filters may contribute to reducing the RMS error is still open and demands further studies. In addition the contribution of the terrestrial error is reduced by more than 1 mm in RMS (Fig. 2c) versus that for the unbiased LS modification. The contribution of the inner zone error on the geoid determination using unbiased LS modification is constant for all cap radii, while it is decreased using MS modification when the cap size increases. In other words, MS modification is likely a more favourable method when the near zone (terrestrial) data are poor. The dependence of the method to the accuracy of the terrestrial data decreases very slowly with increasing cap size (0.3 mm decrease from $\psi_0 = 3^o$–20^o).

6 Concluding Remarks

Stokes kernel has been modified such that it confines to zero at the cap border, and the expected mean square error of the geoid height estimator is minimized by least squares modification. The kernel is called MS modified kernel based on the main developers of the original methods. Two different approaches have been used for the derivation of the MS kernels and thus the truncation coefficients, which led to two different types of MS modifications, namely Green and Pellinen types. To determine the modification parameters we solved a highly ill-conditioned system of equations. Different regularized solutions led to identical kernels inside the integration cap. However, the kernels oscillate randomly outside the cap, which is out of interest for the geoid estimation. This feature was already noted for the LS kernel by Ågren (2004, Chap. 3). The so called unbiased least squares modification of Sjöberg (1991) can be seen as a special case of the MS modification; namely for $e_{n0}(\psi_0) = 0$. We compare the final total RMS errors of the geoid estimation via these methods with each other. The total error consists of the truncation error (the bias),

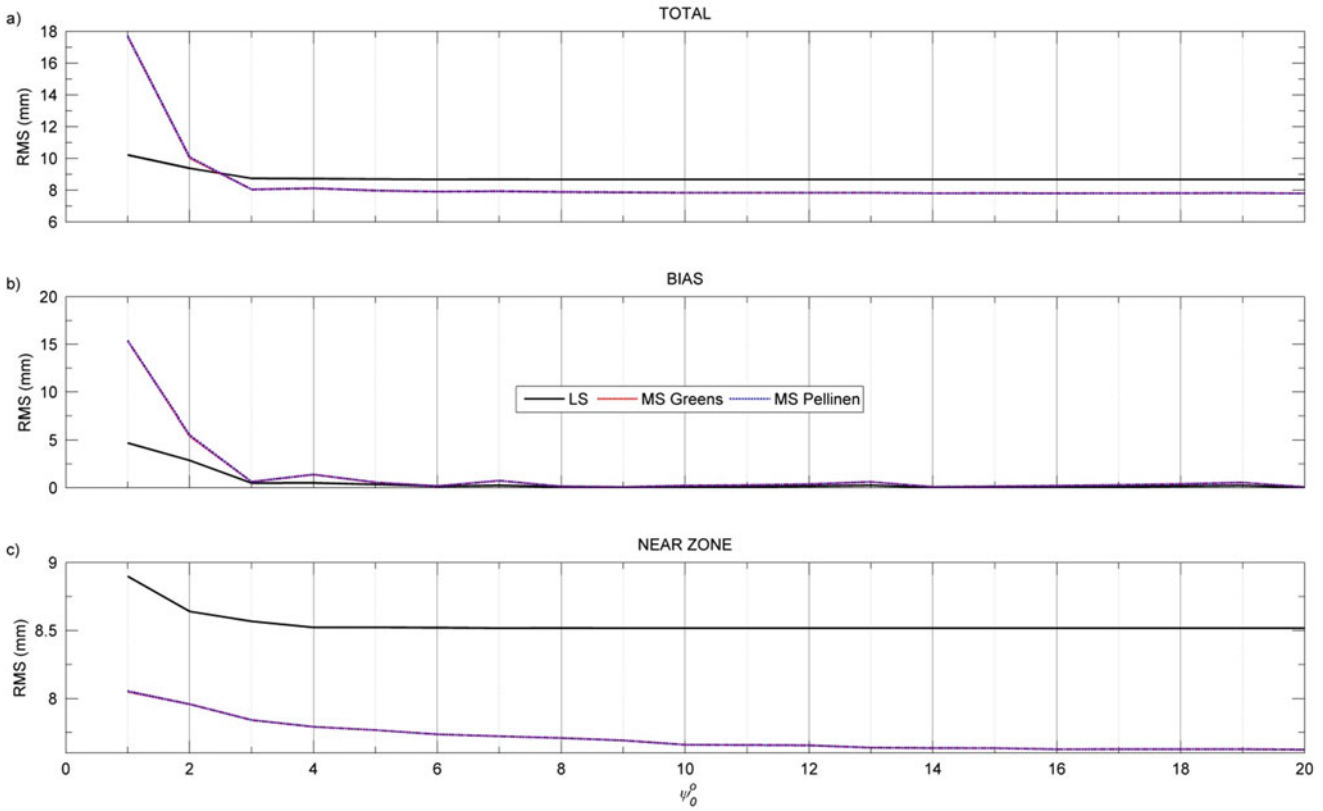

Fig. 2 The RMS error of the geoid estimation using LS (*black*), MS-Green's type (*red dashed*), and MS-Pellinen's type (*blue dash-dott*) for the truncation part, titled as BIAS see Eq. (13), for the integration inside the cap (NEAR ZONE) and the total RMS (TOTAL)

the terrestrial gravity anomaly error and the EIGEN-6S4v2 (Förste et al. 2015) EGM error. MS does not necessarily reduce the bias more than unbiased-LS, but its error for the near zone decreases relative to the LS modification, and it continues to decline when the cap size increases. This may favour the area with poor or less reliable terrestrial gravity data, also when a more precise EGM will be available. Considering ongoing developments of EGMs, the truncation bias will be reduced and more emphasize may be put on the near zone error.

For cap sizes smaller than 3 degrees the total error is smaller for the LS type than for the MS modification using either the Green's second identity or Pellinen smoothing filters. It has been shown that using the smoothing filters and the Green's second identity the RMS errors are slightly different. This suggests that using other filters may contribute to reducing the total error as well as the truncation bias. The MS modification can be carried out theoretically using any smoothing filter for averaging the gravity anomalies inside the cap, but the Gaussian filter with the common recursive equation is not stable for higher harmonic degrees needed for the determination of the modification parameters. In this case, the problem of determining the modification parameters becomes numerically singular (see Fig. 1d).

It should be stated that the solution space of the general MS modification, Eq. (3) differs from that of the ordinary Stokes' modified solutions (i.e. the same equation with $S^L(\psi_0) = s_0 = 0$). However, if the ordinary LS solution is extended to include a zero-degree modification parameter (s_0), its RMS error will be equal or smaller than that of the MS solution.

Appendix

Applying the least squares condition,

$$\overline{\delta N}^2_{total} = \min_{s_r, r=2,\cdots,L},$$

where $\overline{\delta N}^2_{total}$ is as in Eq. (12), to solve the system of equations in (14) yields for $k, r = 2, \cdots, L$,:

$$\begin{aligned} a_{kr} &= \delta_{rk} c_r^* - \frac{2k+1}{2} e_{rk}^{\#} c_r^* - \frac{2r+1}{2} e_{kr}^{\#} c_k^* \\ &+ \frac{2k+1}{2}\frac{2r+1}{2} \sum_{n=2}^{\infty} e_{nk}^{\#} e_{nr}^{\#} c_n^*, \end{aligned} \tag{15}$$

and the elements of the right hand side of Eq. (14) become:

$$\begin{aligned} h_k =& \frac{2}{k-1}\sigma_{k,T}^2 - \frac{2k+1}{2}\sum_{n=2}^{\infty}\frac{2}{n-1}e_{nk}^{\#}\sigma_{n,T}^2 \\ & - Q_k c_k^* + \frac{2k+1}{2}\sum_{n=2}^{\infty} Q_n e_{nk}^{\#} c_n^* \\ & - S_0 e_{n0} c_k^* + \frac{2k+1}{2} S_0 \sum_{n=2}^{\infty} e_{n0} e_{nk}^{\#} c_n^*, \end{aligned} \tag{16}$$

where

$$e_{nk}^{\#}(\psi_0) = e_{nk}(\psi_0) + e_{n0}(\psi_0)\, P_k(\cos\psi_0), \tag{17}$$

$$c_n^* = \begin{cases} \sigma_{n,T}^2 + \sigma_{n,M}^2 & , 2 \le n \le M \\ \sigma_{n,T}^2 + c_n & , M+1 \le n \end{cases}, \tag{18}$$

$$e_{nk}(\psi_0) = \int_{\psi=\psi_0}^{\pi} P_n(\cos\psi)\, P_k(\cos\psi) \sin\psi d\psi,$$

$$e_{n0}(\psi_0) = \int_{\psi=\psi_0}^{\pi} P_n(\cos\psi) \sin\psi d\psi,$$

If $e_{nk}(\psi_0) = 0$, the linear Equations (14) reduces to Eq. (2.7) in Sjöberg (1991) for the unbiased LS estimator. Hence, the MS modification is a generalization to the unbiased LS modification of Sjöberg (ibid).

References

Ågren J (2004) Regional geoid determination methods for the era of satellite gravimetry – numerical investigations using synthetic earth gravity models. Doctoral Dissertation in Geodesy, TRITA–INFRA 04-033, Royal Institute of Technology (KTH), Stockholm, p 246

Ågren J, Sjöberg LE (2012) Investigations of the requirements for a future 5 mm quasigeoid model over Sweden. In: IAG37, International Symposium on Gravity, Geoid and Height Systems GGHS 141:9–12

Anderson E, Bai Z, Bischof C, Blackford S, Dongarra J, Du Croz J, Greenbaum A, Hammarling S, McKenney A, Sorensen D (1999) LAPACK users' guide, vol 9. Siam

Ellmann A (2005) Computation of three stochastic modifications of Stokes's formula for regional geoid determination. Comput Geosci 31(6):742–755

Evans JD, Featherstone WE (2000) Improved convergence rates for the truncation error in gravimetric geoid determination. J Geod 74(2):239–248

Featherstone WE, Evans JD, Olliver JG (1998) A Meissl-modified Vaníček and Kleusberg kernel to reduce the truncation error in gravimetric geoid computations. J Geod 72(3):154–160

Förste C, Bruinsma S, Rudenko S, Abrikosov O, Lemoine JM, Marty JC, Neumayer H, Biancale R (2015) EIGEN-6S4: a time-variable satellite-only gravity field model to d/o 300 based on LAGEOS, GRACE and GOCE data from the collaboration of GFZ Potsdam and GRGS Toulouse. In: EGU General Assembly Conference Abstracts 17

Heck B, Grüninger W (1987) Modification of Stokes' integral formula by combining two classical approaches. In: Proceedings of the XIX General Assembly of the International Union of Geodesy and Geophysics, 2: 309–337

Heiskanen WA, Moritz H (1967) Physical geodesy. Bull Géodésique (1946–1975) 86(1):491–492

Jekeli C (1978) An investigation of two models for the degree variances of global covariance functions. Department of Geodesy Science Reports 275, Dept Geod Sci Surv, Ohio State University

Jekeli C (1980) Reducing the error in geoid undulation computations by modifying Stokes's function. OSU Rep 301, Department of Geodesy Science Surveying, Ohio State University, Columbus

Jekeli C (1981) Alternative methods to smooth the Earth's gravity field. Rep 327, Department of Geodesy Science Surveying, Ohio State University

Kusche J, Schmidt R, Petrovic S, Rietbroek R (2009) Decorrelated GRACE time-variable gravity solutions by GFZ, and their validation using a hydrological model. J Geod 83(10):903–913

Meissl P (1971a) On the linearization of the geodetic boundary value problem (No. DGS-152). Department of Geodesy Science Surveying, Ohio State University

Meissl P (1971b) Preparations for the numerical evaluation of second order Molodensky type formulas (No. DGS-163). Dept Geod Sci Surv, Ohio State University

Molodensky MS, Eremeev VF, Yurkina MI (1962) Methods for study of the external gravitational field and figure of the Earth. Transl. From Russian (1960), Israel Program for Scientific Translations, Jerusalem

Rexer M, Hirt C (2015) Spectral analysis of the Earth's topographic potential via 2D-DFT: a new data-based degree variance model to degree 90,000. J Geod 89(9):887–909

Sjöberg LE (1980) A recurrence relation for the βn-function. Bull Géodésique 54(1):69–72

Sjöberg LE (1984) Least-squares modification of Stokes's and Vening Meinesz's formula by accounting for truncation and potential coeffiecient errors. Manuscr Geod 9:209–229

Sjöberg LE (1986) Comparison of some methods of modifying Stokes's formula. Boll Geod Sci 45:229–248

Sjöberg LE (1991) Refined least-squares modification of Stokes's formula. Manusr Geod 16:367–375

Sjöberg LE (2003) A general model for modifying Stokes' formula and its least-squares solution. J Geod 77(7–8):459–464

Šprlák M (2010) Generalized geoidal estimators for deterministic modifications of spherical Stokes' function. Contrib Geophys Geod 40(1):45–64

Tikhonov A (1963) Solution of incorrectly formulated problems and the regularization method. Soviet Math. Dokl. 5:1035–1038

Tscherning CC, Rapp RH (1974) Closed covariance expressions for gravity anomalies, geoid undulations, and deflections of the vertical implied by anomaly degree variance models. Rep 355. Department of Geodetic Science, Ohio State University, Columbus

Van Huffel S, Vandewalle J (1991) The total least squares problem: computational aspects and analysis. Society for Industrial and Applied Mathematics SIAM, Philadelphia

Vaníček P, Kleusberg A (1987) The Canadian geoid- Stokesian approach. Manuscr Geod 12:86–98

Vaníček P, Kleusberg A, Martinec Z, Sun W, Ong P, Najafi M, Vajda P, Harrie L, Tomášek P, Horst B (1995) Compilation of a precise regional geoid. Final report on research done for the Geodetic Survey Division, Fredericton

Vaníček P, Sjöberg LE (1991) Reformulation of Stokes's theory for higher than second-degree reference field and modification of integration kernels. J Geophys Res 96(B4):6529–6539

Wong L, Gore R (1969) Accuracy of geoid heights from modified Stokes kernels. Geophys J R Astron Soc 18:81–91

Gravimetric Investigations at Vernagtferner

Christian Gerlach, Christian Ackermann, Reinhard Falk, Alexander Lothhammer, and Andreas Reinhold

Abstract

The globally observed melting of mountain glaciers is an indicator of local and regional effects of climate change. From the observational point of view, two research questions need to be answered for individual glaciers, namely how much mass is lost or gained from year to year and how much mass is there in total, i.e., how thick is the glacier. There exist various geophysical/glaciological methods for estimation of mass balance and thickness of mountain glaciers. Most of these methods are geometric in nature and not directly sensitive to mass. In contrast, gravimetry provides a direct measure for mass distribution and mass transport. Satellite gravimetry has proven to provide valuable information on regional to global scales. However, the limited spatial resolution does not allow to infer mass balance or ice thickness of individual mountain glaciers. Therefore, the Bavarian Academy of Sciences and Humanities has set up an observational program at Vernagtferner in the Austrian Alps, to test terrestrial gravimetry for small scale glaciological applications. The work reported in the present paper is conducted in collaboration with the Technical University Munich and the German Federal Agency for Cartography and Geodesy. The results are based on 5 years of repeated relative gravimetry and a first absolute gravity campaign conducted with an A10 instrument. We show, that gravimetric observations can be used to constrain glacier thickness as well as temporal mass variations along various profiles over the glacier. Thereby, reaching the target accuracy of 5–10 μGal seems to be feasible, at least what the internal accuracy of individual relative gravimetry sessions is concerned. The results also underline the importance of carefully checking instrumental parameters in order to reach such a demanding accuracy in absolute sense and to guarantee stability of long-term time series.

Keywords

Glacier mass variation • Glacier thickness • Terrestrial Gravimetry • Time variable gravity

C. Gerlach (✉)
Commission for Geodesy and Glaciology, Bavarian Academy of Sciences and Humanities, Alfons-Goppel-Str. 11, 80539 Munich, Germany
e-mail: gerlach@keg.badw.de

C. Ackermann
Chair of Astronomical and Physical Geodesy, Technical University Munich, Arcisstr. 21, 80333 Munich, Germany
e-mail: ackermann@bv.tum.de

R. Falk • A. Lothhammer
Federal Agency for Cartography and Geodesy, Richard-Strauss-Allee 11, 60598 Frankfurt/Main, Germany
e-mail: reinhard.falk@bkg.bund.de; alexander.lothhammer@bkg.bund.de

A. Reinhold
Federal Agency for Cartography and Geodesy, Karl-Rothe-Straße 10-14, 04105 Leipzig, Germany
e-mail: andreas.reinhold@bkg.bund.de

G. S. Vergos et al. (eds.), *International Symposium on Gravity, Geoid and Height Systems 2016*, International Association of Geodesy Symposia 148, DOI 10.1007/1345_2017_2

1 Introduction

Traditionally, mass variations of mountain glaciers are determined from the glaciological method (where yearly accumulation or wastage of snow and ice are read from stakes which are drilled into the ice surface, thus providing estimates of relative surface elevation change), the geodetic method (where absolute surface elevation changes are derived from a time series of topographic maps) or from the hydrological method (which is based on meteorological observations and modelling combined with runoff measurements at gauging stations), see Cuffey and Paterson (2010). The majority of observation techniques are not directly sensitive to mass, but are, e.g., of geometric nature (like surface elevation changes). Therefore, the gravimetric method can serve as a complementary method to constrain mass variations. On spatial scales larger than 100–200 km resolution, the satellite gravity mission GRACE (Tapley et al. 2004) has provided estimates of mass change over the polar ice caps, e.g., Velicogna and Wahr (2013) or Shepherd et al. (2012), but also over larger glaciated areas like in Alaska or high mountain Asia (Arendt et al. 2009; Farinotti et al. 2015; Jacob et al. 2012). The inherently limited spatial resolution of satellite gravimetry does not allow to infer estimates of mass variation of individual mountain glaciers. Here terrestrial gravimetry can serve as a valuable constraint for local mass variations. Being sensitive to local density anomalies, terrestrial gravimetry can also be used as constraint for glacier depth. Determination of ice thickness from terrestrial gravimetry was first studied by Klingelé and Kahle (1977) at Gorner glacier, Switzerland, and has also found application in airborne surveys of polar ice caps (Boghosian et al. 2015) and continental ice fields (Gourlet et al. 2016). Detailed investigations on the internal structure and ice content of rock glaciers from terrestrial gravimetry (respectively a combination of gravimetry and other geophysical measurement techniques) were carried out by Klingelé and Vonder Mühll (1993) and Hausmann et al. (2007, 2012). Gravimetric determination of local mass balance from repeated terrestrial gravimetry was tested, e.g., by Fukuda et al. (2007) for a study site in Antarcitca and at Hardangerjøkulen, Norway by Breili and Rolstad (2009), but is, in general, poorly studied.

The Bavarian Academy of Science and Humanities (BAdW) has a long tradition in applied geodesy and glaciology. One of its former members, the German mathematician Sebastian Finsterwalder (1862–1951), developed the method of terrestrial photogrammetry for mapping glaciers in the Austrian Ötztal valley, specifically Vernagtferner (location see Fig. 1) which was, since many centuries, known for its repeated rapid advances (Nicolussi 2013). He generated the first geodetic map of Vernagtferner as early as 1889 (Finsterwalder 1897), thereby laying the basis for the dedicated observational program carried out on a systematic basis by BAdW since the 1960s (Mayer et al. 2013a). Today, Vernagtferner is one of the best observed glaciers worldwide and, even though it is shrinking dramatically since the mid 1980s, it serves as test site for all different methods of glacier observation and modelling. Therefore Vernagtferner is well suited to validate gravimetric estimates of mass variations and ice thickness by comparison to various different data sets, e.g., yearly glaciological mass balance estimates, yearly surface elevation changes from GNSS, decadal surface elevation changes from areal photogrammetry or laserscanning and to ice thickness estimates from radar and seismics.

2 Observational Program and Instrumentation

Gravimetric investigations of Vernagtferner started in 2010, when BAdW's commissions of geodesy and of glaciology were joint to form a common research group. Since then, relative gravimetry campaigns were carried out every year, if possible at about the same epoch in summer season. For reasons of efficiency and redundancy, two or three instruments were jointly used in most of the campaigns. Until 2012 the vast amount of observations was performed with LaCoste & Romberg type G gravimeters available at BAdW (LCR-G87) or borrowed from ETH Zürich (LCR-G514) respectively TUM (LCR-G587). In addition, TUM carried out observations with a Scintrex-CG3 in 2010 and 2012. Since 2013, BAdW uses a newly acquired ZLS Burris gravimeter (ZLS-B78). The precision of the gravimeters can be expected to be below 10 μGal for CG3 (Hugill 1988), around 5 μGal for ZLS if only the electronic feedback system is used (Jentzsch 2008) and around 10–15 μGal for LCR-G instruments (Timmen 2010).

Figure 2 shows a shaded relief of Vernagtferner and the distribution of gravity sites occupied since 2010. The glacier covers an area of about 8 km^2 and an elevation range of 600 m, from about 2900 m to 3500 m. The elevation of the gravity sites ranges from about 2900 m (at GS01) to 3150 m (at PG01). As can be seen from Fig. 2, there are two groups of gravity sites, namely reference stations permanently marked with bolts on solid rock (triangles in Fig. 2) and sites on the ice surface (circles in Fig. 2). The latter are not marked, but set out in every campaign using global navigation satellite systems in real-time kinematic mode (GNSS-RTK).

Due to glacier melting, stations located on the ice are subject to temporal elevation changes. Time variable gravity therefore contains two components, (1) the gravitational effect of lost ice masses and (2) the gradient effect that comes into play when comparing values registered in different elevation. Because the gradient effect on gravity is about

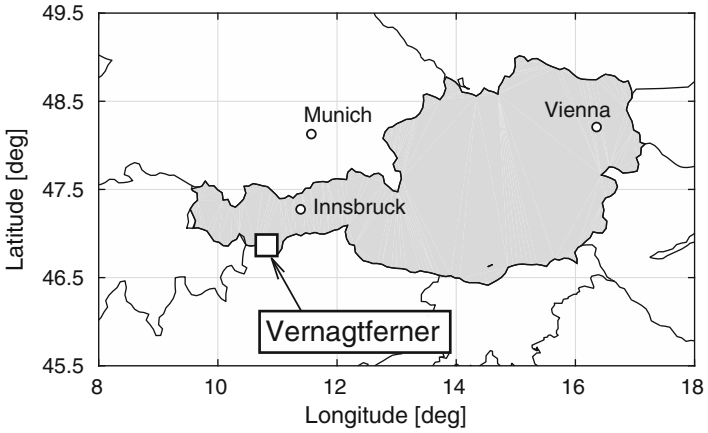

Fig. 1 Geographic location of Vernagtferner, Ötztal valley, Austria

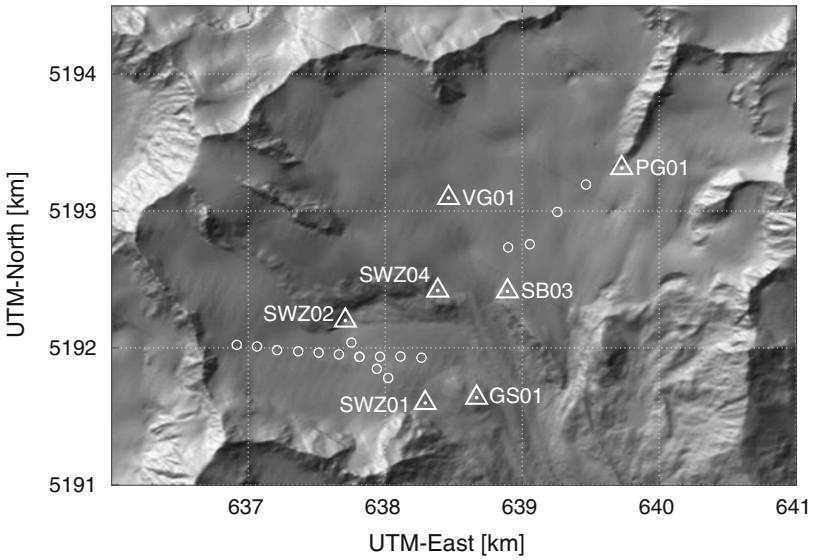

Fig. 2 Distribution of gravity sites at Verangtferner. *Triangles* indicate reference stations with permanent markers on solid rock. *Circles* indicate observation sites on ice

one order of magnitude larger than the mass effect, analysis of gravimetric time series requires precise knowledge of the vertical gravity gradient. In consequence, the vertical gravity gradient was observed on all stations located on ice. Preliminary results on local mass variations, observed along one of the gravity profiles across the glacier, are presented in Gerlach (2013).

Relative observations of all years are referred to station GS01, which is used as primary gravimetric reference site and also serves as base station for GNSS-RTK. GS01 is situated on solid rock and far enough from the glacier in order not to be affected by yearly ice mass variations. Due to the hydrogeological setting, mass variations other than glacier melting are expected to be insignificant, however, any unmodelled signal at GS01 is a limiting factor for building a long-term time series which is solely based on relative gravity campaigns and therefore relies on the stability of the gravity base station.

At stations on ice, another limiting factor is the positioning accuracy of the GNSS-RTK system. We tried to estimate the magnitude of the positioning error from repeated observations at the permanent markers. From 22 sets of coordinates, repeatedly determined at the different markers between 2010 and 2015, we find a mean deviation from nominal coordinates of 1.7 ± 0.9 cm in the horizontal and 1.9 ± 1.0 cm in the vertical direction. A vertical positioning error of 2–3 cm corresponds to a gravity uncertainty of 5–10 μGal, which also sets the target quality for our relative gravity values. Higher accuracies could not be exploited due to the contribution of the vertical positioning errors to the overall error budget. In addition, it does not actually seem realistic to achieve higher accuracies, considering field conditions with instrument transport in the backpack over rugged terrain. Relating the accuracy requirements for gravimetry to mass variations of the glacier, 10 μGal correspond to the mass effect of a layer of ice about 30 cm thick (using a Bouguer plate approximation). This corresponds to about the lower limit of what can be expected in terms of vertical positioning accuracy from repeated areal photogrammetric mappings of the area (Ch. Mayer, personal communication).

In order to validate the results provided by relative gravimetry, specifically to stabilize the intended long-term

time series, it was proposed to complement the relative observations with absolute gravimetry. In the ideal case, absolute gravity observations are carried out along with each and every relative campaign. However, since the logistic and financial efforts are difficult to realize on a yearly basis, and because the expected stability of the gravity value at GS01 lessens the necessity to do so, absolute gravity campaigns are planned to be repeated about every 5 years. The first absolute observations were conducted by the German Federal Agency for Cartography and Geodesy (BKG) in summer 2014 using Micro-g LaCoste Inc. field absolute gravimeter A10#33 on three of the permanently marked stations, namely GS01, SB03 and VG01. Transport of the instrumentation was performed by helicopter. GS01 was chosen, because it is the basic reference point for all relative campaigns and its long-term stability must be controlled. SB03 and especially VG01 are closer to the melting ice masses and therefore expected to experience significant temporal variations—here absolute observations validate the time variations determined from relative gravimetry. Thereby it is worth mentioning, that the expected precision of A10 gravimeters fits to the target accuracy of 5–10 μGal (Falk et al. 2012).

During our 2014 A10-campaign, the absolute gravimeter was set up twice during all site occupations (thereby being oriented towards North and South, respectively). In each of these two setups, measurements were performed in 6 sets, each consisting of 125 drops. So the final station gravity values are based on 1500 drops. The sets were repeated every 4 min, so observation time for one setup was about 25 min. Only in case of the glacier station SB03 there was time for only one setup left, so this value is based on 750 drops only. An electric power generator ensured a stable power supply in the field. Including helicopter transport, (un-)packing and setup of the instrument as well as the pure observation time, the three glacier stations could be determined within about 10 h. Two helicopter flights were necessary to transport all instrumentation and personnel from station to station.

In order to check the stability of the A10 instrument during the campaign, observations were performed before and after the helicopter flight on a newly installed validation site in the valley (RO01); an insignificant difference of 2 μGal was found between these observations. In addition, one observational session was carried out on the reference site of the Austrian gravity network in Obergurgl (which is about a 45 min drive from RO01 into another arm of the Ötztal back valley). The site in Obergurgl is repeatedly observed by the Austrian Mapping Authority since about 30 years with absolute gravimeters of type JILAg and FG5 (Arneitz et al. 2013).

In principle, absolute observations on more than one station allow for checking the scaling of the relative gravimeters in use. However, the gravity differences between the selected stations are not very large (about 30 mGal between GS01 and VG01) and do also not cover the whole signal range in the area. Therefore, instrument calibration is performed on other suitable calibration lines, like the one at Jungfraujoch, Switzerland. Calibration measurements with LCR-G87 and ZLS-B78 were carried out in the frame of the 2013 re-installation campaign of the Jungfraujoch calibration line (Marti et al. 2015).

3 Preliminary Results

3.1 Absolute Gravity and Instrument Calibration

Figure 3 shows A10#33 at reference station GS01. Table 1 lists the results of the absolute gravity campaign. The accuracy of the values is around 0.01 mGal. The gradients had been measured in an independent campaign some weeks earlier by relative gravimetry between ground level and about 70–80 cm above the ground marker. At the same time, relative connections between the three absolute stations were observed using ZLS-B78. Later, during the A10 campaign, the connection between RO01 and the reference site in Obergurgl was also observed with ZLS-B78. These two data sets (one on the glacier, one down in the valley) were used to calibrate the feedback scaling of ZLS-B78 with respect to the A10 absolute values, as described in the next paragraph.

The feedback range of ZLS Burris instruments is ±25 mGal and covers the observed gravity differences at the glacier and down in the valley, both of which are about 30 mGal. Therefore the measurement screw was kept fixed in both cases, such that mechanical errors do not show up.

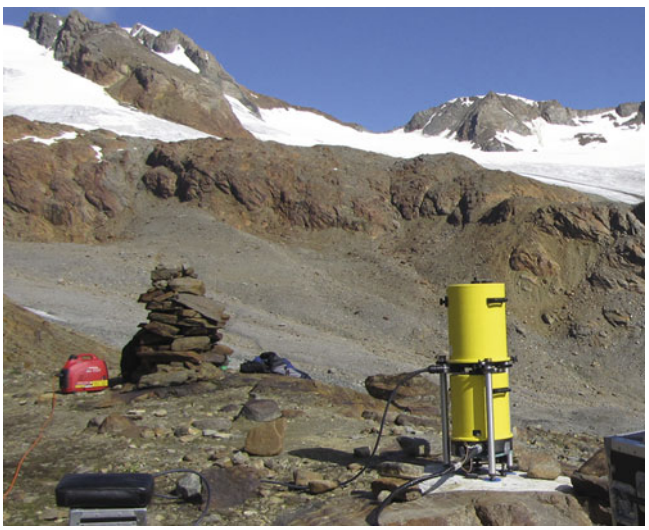

Fig. 3 A10#33 at reference site GS01 before the background of Vernagtferner (view in direction north-west towards SWZ04). During gravity measurement, a tent was placed around the instrument to shield it from wind

Table 1 Results of the absolute gravity observations performed on August 8, 2014, along with the vertical gravity gradients determined from relative gravimetry

Station	Absolute gravity [mGal]	Vertical gradient [mGal/m]
GS01	980 060.97	−0.38
SB03	980 049.84	−0.36
VG01	980 030.64	−0.37

However, the scaling coefficients determined in the two cases differ significantly. From adjustment of observations on the glacier a scaling coefficient of 1.0127±0.0007 was determined, while from the observations in the valley a coefficient of 1.0094±0.0005 was derived. We observe, that the feedback scaling set by the manufacturer deviates from the true value more than can usually be expected (about 1% error, which corresponds to about 500 μGal over the whole feedback range) and more importantly, it seems to vary considerably depending on the data set used. The observed differences of 0.33% translate into a gravity effect of about 100 μGal over the observed gravity differences of 30 mGal or to about 165 μGal over the whole feedback range. Both effects are much larger than the target accuracy of 5–10 μGal.

The observed variability of the scaling coefficient could later be verified in external comparisons with other relative and absolute instruments. Independent check of the doubtful data by the manufacturer confirmed an instrument defect and ZLS-B78 was sent back for repair during 2016. This defect is a possible explanation for the outlier reported in Marti et al. (2015). Despite the large variability of the instrument's scaling, it must be stated, that free network adjustment of ZLS-B78 observations gave estimated accuracies between 3 and 7 μGal in various campaigns, including those at Vernagtferner. This corresponds to the precision stated in the instrument data sheet, so there was no reason doubting the results. Only external comparisons to absolute values revealed, that ZLS-B78 has problems. In consequence, all relative campaigns will be reprocessed with a special focus on consistent scaling of the different instruments. Because this final data set is not yet available, only preliminary results from selected gravity data sets are shown in the following sections.

3.2 Temporal Gravity Variations at Selected Stations

The section in the western part of Vernagtferner is called the Schwarzwand glacier tongue. Its lower part is surrounded by the gravity stations GS01, SWZ01, SWZ02 and SWZ04. Figure 4 is a zoom-in version of the digital terrain model (DTM) shown in Fig. 2, overlayed by glacier elevation

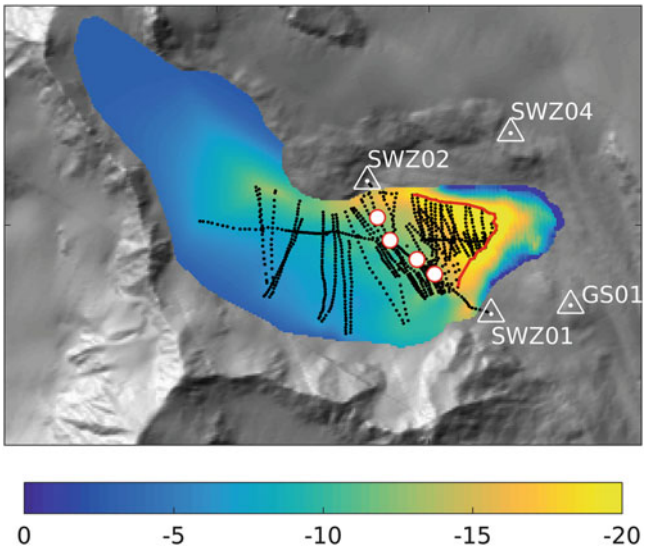

Fig. 4 Surface elevation changes at Schwarzwand glacier tongue during the time period 2006–2012 in units of [m]. *Black dots* indicate GNSS-RTK observations from 2012. The *red line* marks the glacier front in 2012. In addition, the stations of the gravity profile across the glacier tongue are marked (they are discussed in Sect. 3.3)

changes during the period 2006–2012. The elevation changes are derived from relating the 2012 GNSS observations to the 2006 DTM, the latter being based on airborne laserscanning. Elevation changes in the lower part of the glacier tongue are constrained by bedrock topography from ground penetrating radar (GPR) observations (Mayer et al. 2013b). The elevation changes are used to forward model gravity variations at the reference sites GS01, SWZ01, SWZ02 and SWZ04. Gravity variations at these sites have also been derived from gravimetric observations, where we show only those results not containing erroneous data from ZLS-B78. The comparison is thereby restricted to the period 2010–2012, where only LCR-G gravimeters and Scintrex-CG3 were used. Table 2 collects the results of forward modelling and gravity observations. The first of the three columns contains the absolute gravity effects from forward modelling the surface elevation changes of Schwarzwand glacier tongue. The mid column contains the same effects, but reduced to GS01. The right column contains observed time variations, also referring to GS01.

Based on the accuracy requirement of 5–10 μGal for relative gravity values, temporal variations between two epochs are a factor $\sqrt{2}$ worse, i.e., 7–14 μGal. Table 2 shows, that time variations at stations SWZ01 and SWZ04 roughly fulfill the requirements, while time variations at SWZ02 are worse. Further comparing observations and modelling results (thereby taking into account the different time spans), only station SWZ04 shows a good agreement, while stations SWZ01 and SWZ02 show large discrepancies. The reason may be, that SWZ01 and SWZ02 are much closer to the

Table 2 Gravity effects from forward modelling the surface elevation changes shown in Fig. 4 (first two columns) and observed time variations referring to GS01 (third column)

Station	Forward modelling (2006–2012) [μGal]		Observations [μGal]
GS01	8	0	0
SWZ01	37	29	55 ± 15 (2011–2012)
SWZ02	30	22	48 ± 24 (2010–2012)
SWZ04	−11	−19	−4 ± 12 (2010–2012)

ice masses. A closer look reveals, that they are quite close to the edge of the glacier, where GNSS observations are partly sparse (specifically around SWZ01) and gridding of GNSS heights may contain significant extrapolation errors. Deviations between observation and modelling may also be caused by the fact, that observations represent all mass variations in the area, while modelling takes only the surface elevation changes of Schwarzwand glacier tongue into account. Deviations may therefore be caused by additional mass variations, e.g. from north of the mountain ridge north of SWZ02, or from washing out large subsurface cavities which are completely neglected in the forward modelling. Actually the latter holds true for the section close to SWZ02. Despite of the deviations between modelling and observation at SWZ01 and SWZ02, we note, that at least the sign of the temporal evolution agrees. Without more detailed modelling (specifically on the evolution of subsurface cavities) we can only speculate on what actually causes the deviations.

3.3 Glacier Thickness

Employing a DTM with standard rock density for the computation of Bouguer anomalies at gravity profiles across the glacier, results in a relatively large anomalous signal caused by the unmodelled density contrast of about 1800 kg/m^3 between density of rock (2700 kg/m^3) and ice (900 kg/m^3). This can be used to constrain estimates of glacier thickness, see Klingelé and Kahle (1977). Alternatively, glacier thickness can be derived from seismics or radar techniques. Bedrock topography of Vernagtferner was determined in the late 1960s by explosive seismics (Miller 1972) and in 2007 by GPR (Mayer et al. 2013b). In some sections of the glacier, e.g. at Schwarzwand glacier tongue, the two datasets show deviations of several 10th of meters. Therefore, there was an interest in checking the agreement with the gravimetric observations.

We have chosen the gravity profile across the glacier tongue (profile stations are marked in Fig. 4) and forward modelled the gravity effect caused by the ice body. The results are shown in Fig. 5, where the circles indicate the observed (red) or modelled (green and blue) gravity effects and the solid lines show the elevation of the two bedrock estimates along the profile. Starting at SWZ02 and following the profile towards south, we observe that glacier thickness from both data sets increases to about 40 m after 200–300 m of profile length. After this, the radar bedrock flattens out (with a slight increase), while the seismic bedrock still decreases leading to an ice thickness of about 75 m, twice as much as the radar bedrock. The gravity signal modelled from the two bedrock datasets behaves accordingly, i.e. the one from seismics constantly decreases for about 5 mGal over the whole profile, while the one from radar flattens out after about 300 m and reaches only about half the magnitude. Observed gravity values behave similar to the one modelled from radar, which gives an indication, that the radar bedrock is more realistic than the one from seismics.

The same evidence can be drawn from comparing both bedrock estimates with GNSS observations of the bedrock, namely at the glacier front, as measured in 2012 (red line in Fig. 4). When the DTM from laserscanning was generated in 2006, the bedrock along the 2012 glacier front was still covered with about 20 m of ice. This can be see from Fig. 6 which shows the elevation of the laserscanning surface (DTM in 2006) and both of the bedrock topographies with respect to GNSS heights along the 2012 glacier front. Actually the radar bedrock hardly deviates from the GNSS heights (average difference is −1 ± 2 m), while the seismic bedrock shows deviations of up to about 50 m with an average difference of −27 ± 10 m.

4 Summary and Outlook

We have presented the setup of a terrestrial gravimetry project dedicated to the study of mass balance and thickness of small mountain glaciers. The observation site at Vernagtferner glacier in the Austrian Alps is chosen, because there exists a long-term glaciological observation program and the gravimetric results can be validated against several independent data sets. The majority of observations between 2010 and 2015 were carried out with relative gravimeters of type LaCoste & Romberg, Scintrex-CG3 and ZLS-Burris. Independent validation and control of the gravity observations are based on absolute gravimetry using A10 field instruments. The first absolute gravity campaign was carried out in August, 2014. Comparison of relative gravity differences between the absolute gravity sites revealed a systematic instrumental error of ZLS-B78, manifested in unrealistically large variations of its calibration factor. A thorough reprocessing and consistency check of all gravity data sets is necessary before going into more detailed analysis. For future activities, regular instrument checks are recommended for the relative instruments, specifically before and after field work, in order to support long-term quality and consistency of the results. Preliminary results show, that

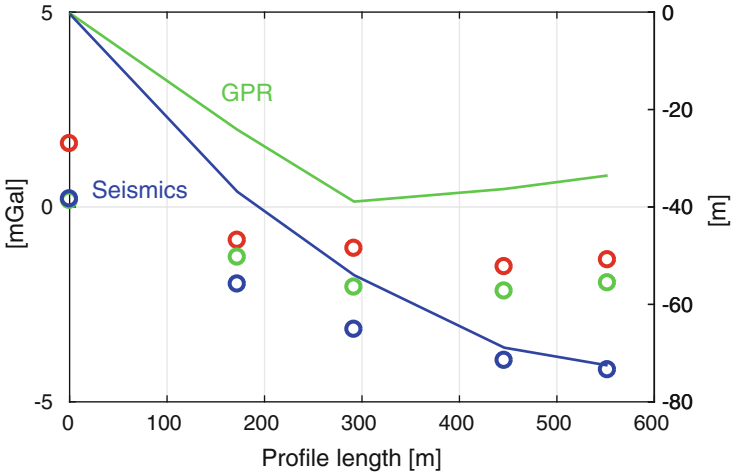

Fig. 5 Glacier thickness estimates and gravity effects along the gravity profile across Schwarzwandzunge; first station is SWZ02. Thickness estimates (*solid line*) from ground penetrating radar (GPR) and seismics, with thickness scale to the *right*. Gravity effects (*circles*) from observation (*red*) and from forward modelling based on GPR and seismics, respectively; gravity scale to the *left*

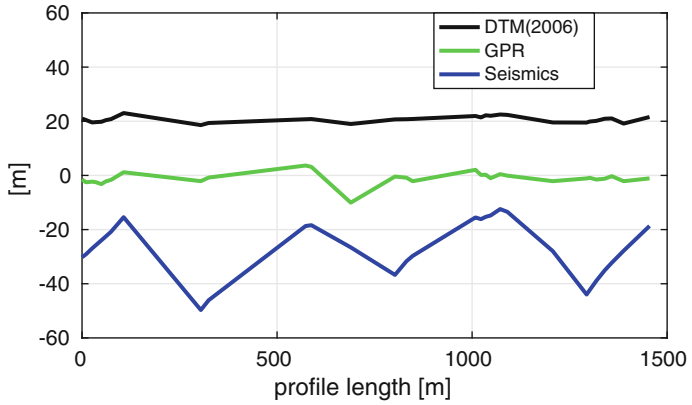

Fig. 6 Elevation differences along the 2012 glacier front (see *red line* in Fig. 4) between GNSS observations in 2012 and three other elevation data sets, namely a DTM of the glacier surface from laserscanning in 2006 (*black*) as well as bedrock topographies from ground penetrating radar (*green*) and seismics (*blue*)

the target accuracy of 5–10 μGal can be met in most of the campaigns. Comparison of observed gravity anomalies with those computed from seismic resp. radar-derived bedrock topographies, shows the potential of terrestrial gravimetry in constraining estimates of glacier thickness. The same holds for gravimetric estimates of glacier mass balance, which are a valuable complement to mass variations derived from other methods, e.g., from glaciologically determined glacier surface elevation changes. Future work will focus on optimization of the field work, on a consistent reprocessing of the available data sets and on modelling gravimetric signals from independent data sets.

Acknowledgements Werner Müller (BKG) is gratefully acknowledged for supporting the 2014 A10 field campaign.

References

Arendt AA, Luthcke SB, Hock R (2009) Glacier changes in Alaska: can mass-balance models explain GRACE mascon trends? Ann Glaciol 50(50):148–154. doi:10.3189/172756409787769753

Arneitz P, Meurers B, Ruess D, Ullrich Ch, Abermann J, Kuhn M (2013) Gravity effect of glacial ablation in the Eastern Alps – observation and modeling. TC 7:491–498

Boghosian A, Tinto K, Cochran JR, Porter D, Elieff S, Burton BL, Bell RE (2015) Resolving bathymetry from airborne gravity along Greenland fjords. J Geophys Res Solid Earth 2015JB012129 (2015). doi:10.1002/2015JB012129

Breili K, Rolstad C (2009) Ground-based gravimetry for measuring small spatial-scale mass changes on glaciers. Ann Glaciol 50(50):141–147. doi:10.3189/172756409787769717

Cuffey KM, Paterson WSB (2010) The physics of glaciers, 4th revised edition. Elsevier Ltd, Oxford/Burlington

Falk R, Müller J, Lux N, Wilmes H, Wziontek H (2012) Precise gravimetric surveys with the field absolute Gravimeter A-10. In: Kenyon S, Pacino MC, Marti U (eds) Geodesy for planet earth. International Association of Geodesy Symposia, vol 136. Springer, Berlin/Heidelberg, pp 273–279

Farinotti D, Longuevergne L, Moholdt G, Duethmann D, Mölg T, Bolch T, Vorogushyn S, Güntner A (2015) Substantial glacier mass loss in the Tien Shan over the past 50 years. Nat Geosci 8(9):716–722. doi:10.1038/ngeo2513

Finsterwalder S (1897) Der Vernagtferner, seine Geschichte und seine Vermessung in den Jahren 1888 und 1889. Technical Report 1, (1), Verlag des Deutschen und Österreichischen Alpenvereins, Graz

Fukuda Y, Hiraoka Y, Doi K (2007) An experiment of precise gravity measurements on ice sheet, Antarctica. In: Tregoning P, Rizos C, Sideris MG (eds) Dynamic planet. International Association of Geodesy Symposia, vol 130. Springer, Berlin/Heidelberg, pp 88–93

Gerlach C (2013) Gravimetrie und deren Potential für eine unabhängige Bestimmung der Massenbilanz des Vernagtferners. Z Gletscherk Glazialgeol 45/46:281–293

Gourlet P, Rignot E, Rivera A, Casassa G (2016) Ice thickness of the northern half of the Patagonia Icefields of South America from high-resolution airborne gravity surveys. Geophys Res Lett 2015GL066728 (2016) . doi:10.1002/2015GL066728

Hausmann H, Krainer K, Brückl E, Mostler W (2007) Internal structure and ice content of Reichenkar rock glacier (Stubai Alps, Austria) assessed by geophysical investigations. Permafr Periglac Process 18(4):351–367. doi:10.1002/ppp.601

Hausmann H, Krainer K, Brückel E, Ullrich Ch (2012) Internal structure, ice content and dynamics of Ölgrube and Kaiserberg rock glaciers (Ötztal Alps, Austria) determined from geophysical surveys. Aust J Earth Sci 105(2):12–31

Hugill AL (1988) The new Scintrex CG-3 Autograv gravity meter: description and test results. Paper presented at the ASEG/SEG Conference, February 1988, Adelaide, Australia

Jentzsch G (2008) The automated Burris Gravity Meter – a new instrument using an old principle. In: Peshekhonov VG (ed) Terrestrial gravimetry: static and mobile measurements (TG-SMM2007). Proceedings of the TG-SMM2007 International Symposium, Elektropribor, St. Petersburg, pp.21–28

Jacob T, Wahr J, Pfeffer WT, Swenson S (2012) Recent contributions of glaciers and ice caps to sea level rise. Nature 482(7386):514–518. doi:10.1038/nature10847

Klingelé E, Kahle HG (1977) Gravity profiling as a technique for determining the thickness of glacier ice. Pure Appl Geophys 115(4):989–998. doi:10.1007/BF00881221

Klingelé E, Vonder Mühll D (1993) Gravimetrische Untersuchungen im Permafrost des Blockgletschers Murtèl-Corvatsch (Oberengadin). Vermessung, Photogrammetrie, Kulturtechnik 91(10):575–580

Marti U, Baumann H, Bürki B, Gerlach C (2015) A first traceable gravimetric calibration line in the Swiss Alps. International Association of Geodesy Symposia. Springer, Berlin/Heidelberg, pp 1–9

Mayer C, Escher-Vetter H, Weber M (2013a) 46 Jahre glaziologische Massenbilanz des Vernagtferners. Z Gletscherk Glazialgeol 45/46:219–234

Mayer C, Lambrecht A, Blumenthaler U, Eisen O (2013b) Vermessung und Eisdynamik des Vernagtferners, Ötztaler Alpen. Z Gletscherk Glazialgeol 45/46:259–280

Miller H (1972) Ergebnisse von Messungen mit der Methode der Refraktions-Seismik auf dem Vernagt- und Guslarferner. Z Gletscherk Glazialgeol 8:27–42

Nicolussi K (2013) Die historischen Vorstöße und Hochstände des Vernagtferners 1600–1850 AD. Z Gletscherk Glazialgeol 45/46:9–23

Shepherd A et al (2012) A reconciled estimate of ice-sheet mass balance. Science 338(6111):1183–1189. doi:10.1126/science.1228102

Tapley BD, Bettadpur S, Watkins M, Reigber C (2004) The gravity recovery and climate experiment: Mission overview and early results. Geophys Res Lett 31(9):L09607. doi:10.1029/2004GL019920

Timmen L (2010) Absolute and relative gravimetry. In: Xu G (ed) Sciences of geodesy I. Springer, Berlin/Heidelberg, pp 1–48. doi:10.1007/978-3-642-11741-1_1

Velicogna I, Wahr J (2013) Time-variable gravity observations of ice sheet mass balance: precision and limitations of the GRACE satellite data. Geophys Res Lett 3055–3063. doi:10.1002/grl.50527

Analysis of the GRAV-D Airborne Gravity Data for Geoid Modelling

J. Huang, S.A. Holmes, D. Zhong, M. Véronneau, Y. Wang, J.W. Crowley, X. Li, and R. Forsberg

Abstract

In this study, airborne gravity data from the Gravity for the Redefinition of the American Vertical Datum (GRAV-D) project are compared with terrestrial gravity data in three survey blocks that cross the Canada-US border. One block (AN04) overlaps an area containing Alaska (USA) and the Yukon Territory (Canada) over a rough terrain while the other two blocks (EN05 and EN08) are within the Great Lakes-St-Lawrence River region with flat and moderate terrains. GRAV-D has an average flight altitude of about 6 km in the three blocks, in which each survey/cross line spans 240–700 km. The high flight altitude of GRAV-D puts forth a challenge for the comparisons. We have developed procedures to interpolate and continue the airborne and terrestrial gravity data to a mean flight height for each block. The remove-compute-restore Poisson method is used in the upward continuation of the terrestrial gravity data by removing and restoring the satellite-only geopotential model GOCO05S. The comparison between the datasets is done using Helmert gravity disturbances in order to satisfy the harmonic condition of the upward continuation. The comparisons show that differences between GRAV-D and terrestrial gravity data are 3.6 mGal for AN04, 1.8 mGal for EN05 and 2.3 mGal for EN08 in terms of Root Mean Square (RMS) at the mean flight height. The results can be improved for two blocks when applying a cross-over adjustment. The differences become 1.0 and 1.4 for EN05 and EN08, respectively.

Keywords

Direct topographical effect • GRAV-D airborne gravity • Helmert gravity disturbance • Upward continuation

D. Zhong was a casual employee in the Canadian Geodetic Survey in 2016.
S. A. Holmes passed away on May 26, 2017.

J. Huang (✉) • D. Zhong • M. Véronneau • J.W. Crowley
Canadian Geodetic Survey, Surveyor General Branch, Natural Resources Canada, Ottawa, ON, Canada
e-mail: jianliang.huang@canada.ca; marc.veronneau@canada.ca; john.crowley@canada.ca

S.A. Holmes
SGT, Inc., Greenbelt, MD, USA

Y. Wang
National Geodetic Survey, Silver Spring, MD, USA
e-mail: yan.wang@noaa.gov

X. Li
DST, Inc., Silver Spring, MD, USA
e-mail: xiaopeng.li@noaa.gov

R. Forsberg
DTU SPACE National Space Institute, Technical University of Denmark, Lyngby, Denmark
e-mail: rf@space.dtu.dk

G. S. Vergos et al. (eds.), *International Symposium on Gravity, Geoid and Height Systems 2016*, International Association of Geodesy Symposia 148, DOI 10.1007/1345_2017_23

1 Introduction

The Gravity for the Redefinition of the American Vertical Datum (GRAV-D) project aims to cover the US territory by airborne gravity measurements with an extension of about 100 km beyond the US border. As such, GRAV-D provides data blocks in the southern and north-western parts of Canada; in particular, GRAV-D has measured gravity over the Great Lakes region shared by the two countries for the development of the International Great Lakes Datum of 2020. These airborne gravity data provide important new gravity constraints on both US and Canadian geoid models over the Canada-US border regions to help unification of the North American vertical datums.

A few studies have used GRAV-D data to improve geoid models. By using the GRAV-D data over the Geoid Slope Validation Survey of 2011 (GSVS11) in the state of Texas, a relative geoid accuracy better than 1 cm was achieved for all baselines ranging from 0.4 to 325 km (Smith et al. 2013). In the Great Lakes region, the improvement of the geoid model by GRAV-D reaches decimetres over Lake Michigan where the legacy gravity data have significant errors (Li et al. 2016). A spectral combination method for satellite, airborne and terrestrial gravity data was also applied for GSVS11 demonstrating the contribution of GRAV-D for the middle wavelength components of the gravity field (Jiang and Wang 2016). In addition, the Least-Squares Collocation method was used to compare and combine the GRAV-D and terrestrial data over EN05 and EN08 (Zhong et al. 2016).

The objective of this study is to evaluate the discrepancies that the GRAV-D data have with respect to the existing terrestrial gravity data used for the development of the Canadian Geodetic Vertical Datum of 2013 (Véronneau and Huang 2016). We have selected GRAV-D data from three blocks that cross the Canada-US border and compare them with the upward continued terrestrial gravity data at flight heights. Block AN04 covers a section of Alaska, USA and the Yukon Territory, Canada over a rough terrain, block EN05 includes Lake Superior and block EN08 covers New-Hampshire, Vermont, upstate New York and south-west Quebec, a region with flat and moderate terrains.

The GRAV-D data cannot be compared directly with the terrestrial gravity data to evaluate the update due to the high altitude of the airborne data. One feasible solution is to downward continue the terrestrial gravity data to the geoid first and then to upward continue to the flight level. The downward continuation step requires removing and compensating for the topographical mass above the geoid to meet the harmonic condition. Helmert's second method of condensation can be applied for this topographical reduction (see e.g. Vaníček et al. 1999). By following this approach, the airborne Helmert gravity disturbances are first computed at the flight level while the terrestrial Helmert gravity disturbances are computed on the geoid. Second, the terrestrial Helmert disturbances are upward continued to the flight level. Finally, the GRAV-D-corrected data are evaluated at the flight level. The downward and upward continuation can be realized by using the analytical approach, the Poisson integral, or the Least-Squares Collocation (Heiskanen and Moritz 1967; Moritz 1980a; Tscherning et al. 1994). In this study, the Poisson integral is used for the upward continuation.

This paper consists of six sections. This section has introduced the background and objective of this study. Section 2 outlines the method of comparison. Section 3 describes the GRAV-D and terrestrial data in the three studied blocks. Section 4 estimates the upward continuation error by synthetic simulation. Section 5 deals with the computation and evaluation of the GRAV-D data against the terrestrial data. Section 6 summarizes this study.

2 Methods

The airborne Helmert gravity disturbance at the flight height (FH) above the reference ellipsoid is defined by

$$\delta g_H^{Air}(\Omega, h_{FH}) = \delta g^{Air}(\Omega, h_{FH}) - \delta g_{DTE}(\Omega, h_{FH}) \quad (1)$$

where the first term on the right-hand side of Eq. (1) is the gravity disturbance, and is defined by (Heiskanen and Moritz 1967)

$$\delta g^{Air}(\Omega, h_{FH}) = g^{Air}(\Omega, h_{FH}) - \gamma(\Omega, h_{FH}) \quad (2)$$

The first and second terms on the right-hand side of Eq. (2) are the gravity and normal gravity, respectively. The second term on the right-hand side of Eq. (1) is the direct topographical effect on the gravity disturbance, which is defined by

$$\delta g_{DTE}(\Omega, h_{FH}) = -\left.\frac{\partial \delta V_{DTE}(\Omega, h)}{\partial h}\right|_{h=h_{FH}} \quad (3)$$

The term δV_{DTE} is the difference between the potentials of the topographical masses and the condensation mass layer in terms of Helmert's second condensation method. In the spherical approximation, it can be represented by spherical harmonics (Eq. (28), Huang and Véronneau 2013). Consequently, Eq. (3) can be written as

$$\delta g_{DTE}(\Omega, h_{FH}) = 2\pi G\rho R \sum_{n=0}^{\infty} \frac{n+1}{2n+1}\left(\frac{R}{R+h_{FH}}\right)^{n+2} \times \sum_{m=-n}^{n} \overline{D}_{nm}\overline{Y}_{nm}(\Omega) \quad (4)$$

The spherical harmonic coefficients $\overline{D}_{nm}$ are given by Eq. (29) (Huang and Véronneau 2013). The Helmert gravity disturbance at the flight height can also be derived from the terrestrial Helmert disturbance by the Poisson's integral using the remove-compute-restore (RCR) technique:

$$\delta g_H^{Terr}(\Omega, h_{FH}) = \delta g_H^{Sat}(\Omega, h_{FH}) + \frac{R}{4\pi r}\int K(h,\psi) \times \left[\delta g_H^{Terr}(\Omega,0) - \delta g_H^{Sat}(\Omega,0)\right] d\sigma \quad (5)$$

The term $\delta g_{\mathrm{H}}^{Sat}$ in Eq. (5) is the Helmert gravity disturbance synthesized from a satellite Earth Gravity Model (EGM). K is the Poisson kernel and $\delta g_{\mathrm{H}}^{Terr}$ is the terrestrial Helmert gravity disturbance. The integral equation in Eq. (5) represents the Poisson upward continuation of the gravity disturbance residual, and can be computed accurately by a spherical approximation (Huang 2002).

The airborne gravity data can then be compared with the terrestrial data at the flight height level as

$$\varepsilon g(\Omega, h_{FH}) = \delta g_H^{Air}(\Omega, h_{FH}) - \delta g_H^{Terr}(\Omega, h_{FH}) \quad (6)$$

This study simply compares the upward continued terrestrial gravity disturbances to those obtained within the GRAV-D project, over 3 GRAV-D data collection blocks. Such comparisons are a necessary first step towards future possible combination of the two sources of gravity information.

3 Data

3.1 GRAV-D Airborne Gravity Data

The GRAV-D project uses the term "block" referring to a pre-defined geographic area with enough planned data lines and cross lines (GRAV-D Science Team 2013a). The nominal flight altitude of a block is about 6.3 km for the recovery of the mid-wavelength components of the gravity field with the minimum wavelength of 19.4 km approximately corresponding to the maximum spherical harmonic degree/order 1080. Each block consists of a series of flight lines and few cross lines that have length of 400–500 km. The cross lines were collected for the purpose of calculating the crossover errors at the intersections of the flight lines. The nominal distances between the flight lines and cross lines are about 10 km and 40–80 km, respectively. Airborne data are nominally sampled at the interval of 128.6 m along the flight and cross lines. Blocks are planned by taking into account factors such as gravity field signature and trend, terrain clearance, data sampling, and logistical requirements for field operations.

A Micro-g LaCoste Turn-key Airborne Gravimetry System (MGL TAGS) is used with either a NovAtel DL4+ or NovAtel DLV3 GPS unit integrated into its timing unit module. Nearly all flights have a second GPS on the aircraft that is integrated with an inertial measurement unit (IMU) into a positioning system. One or two GPS base stations are set up at temporary stations around the airport of operations as backups, in case GPS processing in differential mode is needed. A field-tested absolute gravimeter (MGL A10) is used to establish a base station on the airport tarmac. Finally, a gravity tie is measured between the base station and the TAGS sensor centre using a relative gravimeter.

The released GRAV-D data files contain: (1) a ReadMe file, (2) a gravity data file of the official products, (3) a supplementary data file (containing cross line data, transit line data, or other experimental data), (4) a .txt file containing xml metadata written according to Federal Geographic Data Committee (FGDC) standards, (5) a .kml file of the block extent, and (6) a .kml file of the line locations for that block. The gravity data file and supplementary data file are formatted into six columns: Block + Line Number, Time, Latitude, Longitude, Ellipsoid Height and Filtered Full Field Gravity.

For this study, three blocks are selected along the US-Canada border covering three types of landscapes. Figure 1 shows geographical areas of the three blocks: AN04, EN05 and EN08. AN04 is over a mountainous region that includes Alaska, USA and the Yukon Territory, Canada. Its data file contains 33 flight lines (no cross lines are publically available for AN04). The crossover error is listed as 1.31 mGal in RMS (GRAV-D Science Team 2013b). EN05 covers Lake Superior. Its data files contain 34 flight lines and eight cross lines. The crossover error is listed as 1.40 mGal in RMS (GRAV-D Science Team 2013c). Finally, EN08 overlaps the higher St. Lawrence River area with a mostly flat terrain and the moderate mountainous areas of New-Hampshire, Vermont and upstate New York. Its data files contain 43 flight lines and seven cross lines. The cross-error is listed as 1.78 mGal in RMS (GRAV-D Science Team 2014). Table 1 gives a statistical description of the gravity disturbances evaluated by Eq. (2) at flight heights. In addition, the table gives statistics on the topography of each block calculated using the Canadian Digital Elevation Data in the Yukon Territory, the National Elevation Data in Alaska and the Shuttle Radar Topography Mission for the states of New York, Vermont and New Hampshire. These DEMs are averaged into grids of $2'$ by $2'$ for the statistical information. Note that the atmospheric correction is applied according to the GRS80 convention (Moritz 1980b). The gravity disturbances are re-sampled by a three-point averaging along each flight line, increasing the nominal sampling interval from 128.6 to 385.8 m. Figures 2, 3 and 4 show the gravity disturbances at flight heights over the three blocks. One observation is that AN04 shows

Fig. 1 Locations of the AN04, EN05 and EN08 blocks. Flight lines and cross lines are displayed in white colour

Table 1 Statistics of the gravity disturbances, flight heights and the 2-arcmin DEM for AN04, EN05 and EN08

Block	Parameter	Min	Max	Mean	StdDev	RMS	# Pts
AN04	δg^{Air} (mGal)	−8.486	86.937	28.953	16.787	33.468	21,001
	h_{FH} (m)	6091.877	6379.777	6161.427	71.757	6161.845	21,001
	δg^{Terr} (mGal)	−52.917	141.981	21.975	35.165	41.467	1,638
	H (m)	182.900	2098.760	832.648	378.586	914.674	1,638
	DEM (m)	180.000	1906.000	759.114	310.558	853.612	15,456
EN05	δg^{Air} (mGal)	−70.282	81.476	−17.682	22.056	28.269	72,920
	h_{FH} (m)	5778.653	6964.582	6211.818	181.171	6214.460	72,920
	δg^{Terr} (mGal)	−96.426	117.617	0.330	33.686	33.688	24,620
	H (m)	175.560	633.900	362.209	108.129	378.004	24,620
	DEM (m)	154.000	628.000	311.420	124.302	335.318	24,753
EN08	δg^{Air} (mGal)	−57.211	42.713	−10.276	19.486	22.029	61,301
	h_{FH} (m)	5330.662	5600.316	5445.884	38.957	5446.023	61,301
	δg^{Terr} (mGal)	−77.465	78.511	−17.218	22.146	28.052	19,124
	H (m)	6.100	1205.800	224.065	158.063	274.206	19,124
	DEM (m)	0.000	1416.000	300.851	196.026	359.079	21,237

the smoothest field. Another observation is the lack of local details in these fields likely due to the high altitudes of the flight lines.

3.2 Terrestrial Gravity Data

The terrestrial gravity data for the areas of study are observed on land, lake surfaces and lake bottoms (EN05). The free-air gravity anomalies estimated from these data have generally a precision of 1–2 mGal. Most of the errors come from station elevations, which were either scaled from topographic maps or measured with barometric altimeters.

The gravity disturbances are calculated from the terrestrial gravity data and summarized statistically in Table 1. For the calculation, the ellipsoidal height of the terrestrial gravity data is determined using the sum of the published elevation at the point and the geoid height from CGG2013 (Véronneau and Huang 2016; Huang and Véronneau 2013). As expected, the terrestrial gravity disturbances have significantly more gravity signal than the corresponding airborne data as seen in Figs. 5 (AN04), 6 (EN05) and 7 (EN08). For AN04, the terrestrial data are very sparse on the western side of the Alaska-Yukon border. The GRAV-D data certainly improve the block coverage and could consequently benefit geoid determination over the area. For EN05 and EN08, the terrestrial gravity

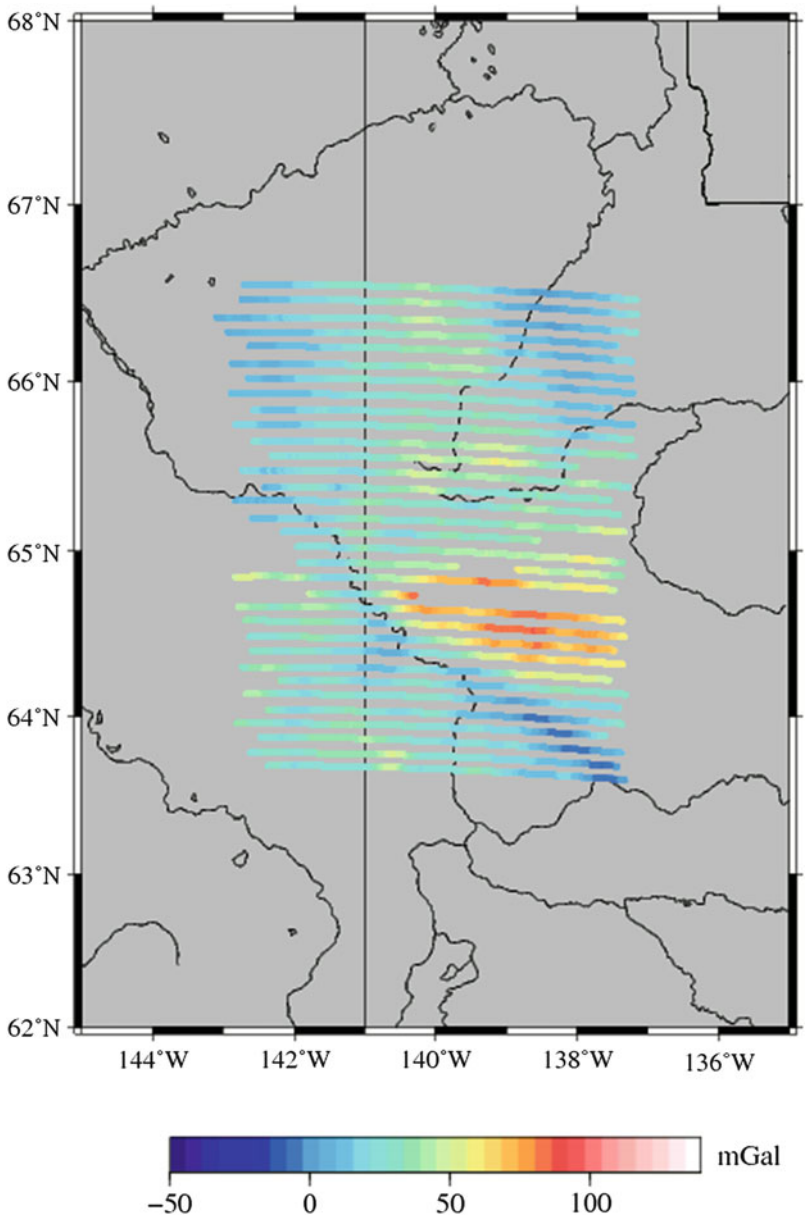

Fig. 2 The gravity disturbances at flight heights for AN04

data cover the two areas very well regardless of their uneven distribution. In these two blocks, the GRAV-D data may have less impact, but can certainly be used to confirm quality of the terrestrial gravity surveys or detect trends and biases between the two datasets. However, further independent analysis would be required to determine which dataset is of better quality. Table 1 also gives statistics on the heights above mean sea level at the gravity points. These statistics are representative of the terrain when compared with the statistics of the DEM.

The Helmert gravity anomaly grid on the geoid was produced for the development of CGG2013 over the areas of study. The procedure can be found in (Véronneau 2013). The Helmert gravity disturbance grid originates from the Helmert gravity anomaly grid by adding the normal gravity corrections to account for the Helmert co-geoid heights, which are computed as the differences between the CGG2013 geoid heights and the primary indirect effect grid for CGG2013 for each area.

4 Upward Continuation Simulation

The upward or downward continuation is an essential step to compare and combine airborne gravity data with terrestrial gravity data for geoid modelling. The comparison can be performed either at flight height or on the geoid. The former requires the upward continuation of the terrestrial gravity data while the latter involves the downward continuation, which is often considered an ill-posed problem in physical

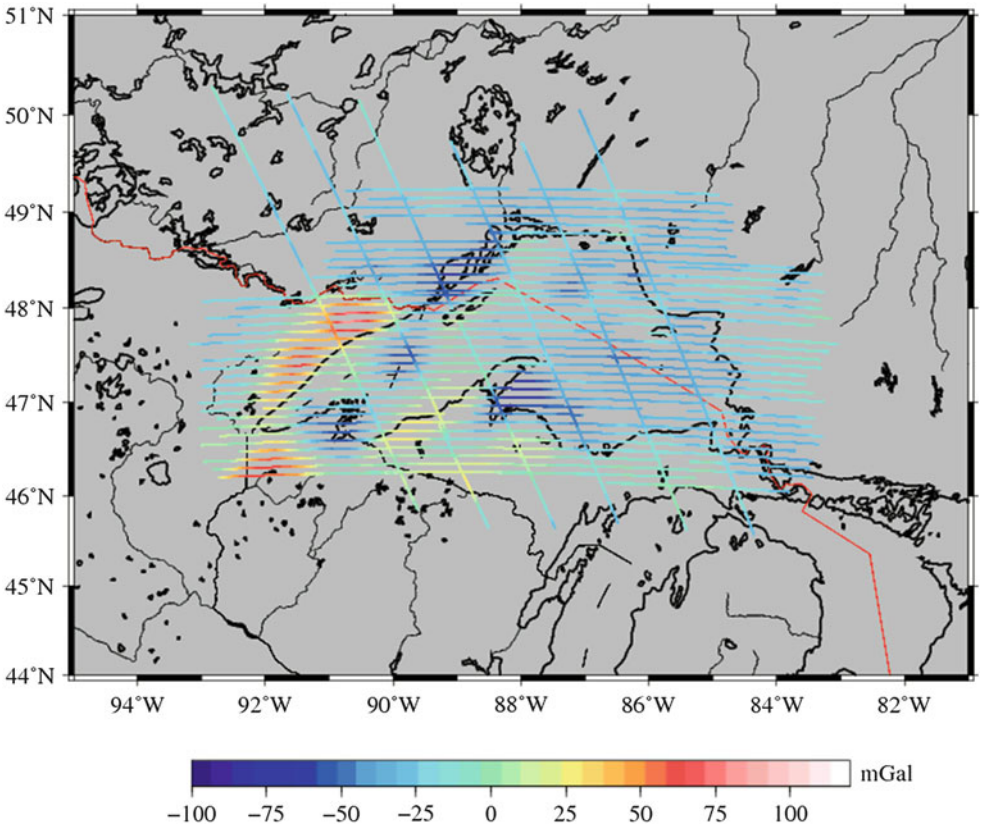

Fig. 3 The gravity disturbances at flight heights for EN05

geodesy. This paper focuses on the former leaving the latter for future studies. Errors in the upward continuation affect the comparison, and can be estimated by a synthetic simulation. EGM2008 includes terrestrial gravity data in the regions of study (Pavlis et al. 2012, 2013). It has a spatial resolution of 5 arc-minutes (10 km), which is close to the nominal line spacing of GRAV-D, making it suitable for this synthetic simulation. Figure 8 shows a flowchart for the simulation.

For the simulation, the gravity disturbances are synthesized using EGM2008 at two elevations: at a 6,000-m ellipsoidal height and on the reference ellipsoid. The latter is used as input while the former is the control to validate the output of the upward continuation. The difference between them indicates the error on the upward continuation.

Two aspects of the upward continuation are analysed through the simulation. First, it is to understand the numerical performance of the upward continuation method and software used for grid data, in particular with the remove-compute-restore (RCR) technique. Second, it is to understand the numerical performance for actual distribution of terrestrial gravity data over the three blocks. Note that this simulation does not consider input data errors. This is left for future studies.

Regarding the first aspect, two simulation cases have been evaluated for the EN05 block. On one hand (Case 1) the gravity disturbance is synthesized from spherical harmonic degree/order (d/o) 2 to 2,190 while on the other hand (Case 2) the disturbance extends from d/o 181 to 2,190. Case 2 and Case 1 correspond to with and without the RCR technique in the continuation process, respectively. The selection of d/o 181 as the lower limit is justified by recent GOCE satellite models that demonstrate accuracy of 1 mGal or better for d/o 180. The simulation area spans 10° in longitude and 5° in latitude (see Fig. 9). Input data are extended by 1° on the north and south boundaries and by 2° on the east and west boundaries at the zero height (or on the reference ellipsoid) to minimize the edge effect. The data spacing is 2′. The radius of the spherical cap for the Poisson's integral is 1° as in a previous study (Huang 2002).

The first and third rows in Table 2 give the statistics for the magnitude of the upward continuation, which is the difference of gravity disturbances between the flight height and reference ellipsoid. The results suggest that the RCR technique (Case 2) reduces the upward continuation error to less than 0.1 mGal in RMS. The error is about 1 mGal in Case 1. In addition, the offset of about 1 mGal in Case 1 becomes 0 mGal in Case 2. Figure 9 depicts the upward continuation errors for Case 2. The error features do not significantly correlate with the terrestrial gravity disturbances shown in Fig. 6, which have been used for the development of EGM2008. They characterize numerical errors for the Poisson upward continuation for the grid data with the RCR technique.

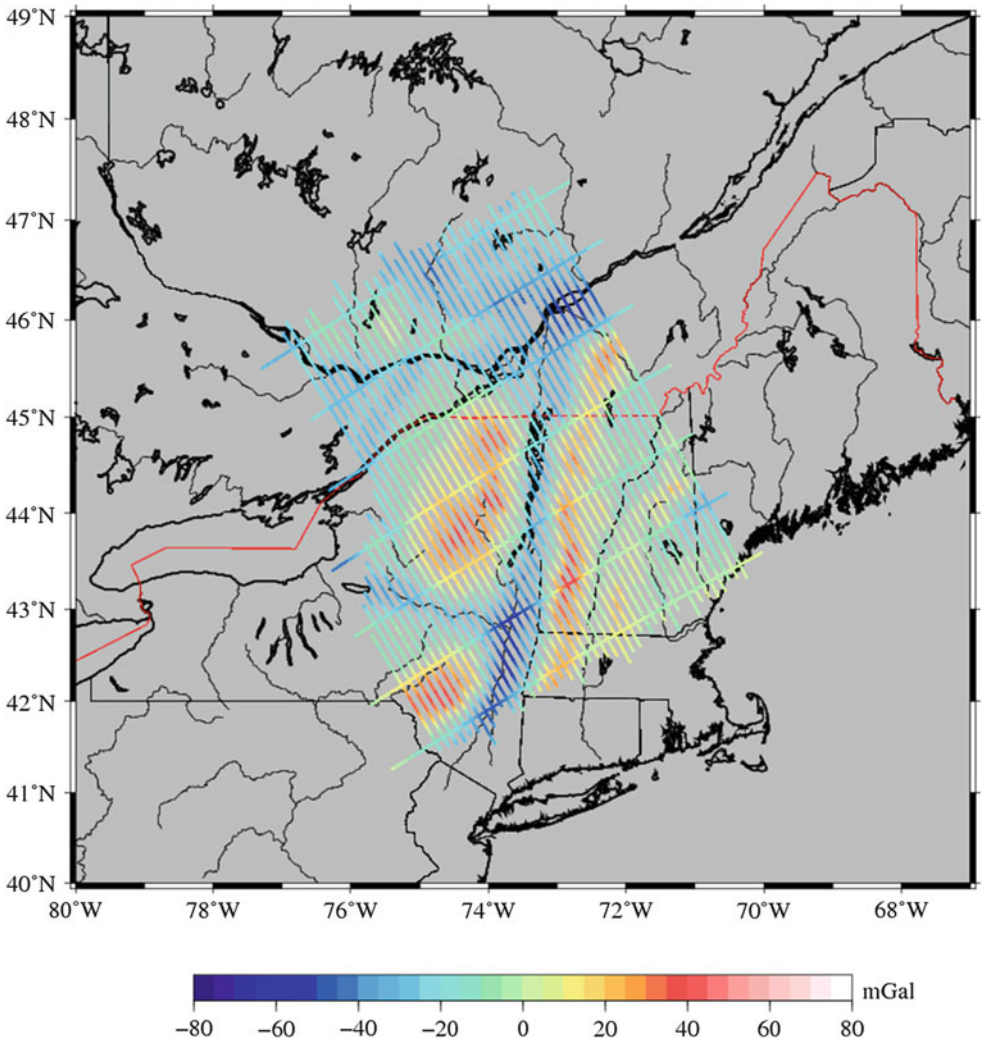

Fig. 4 The gravity disturbances at flight heights for EN08

Regarding the second aspect, input simulation data are created following this five-step process:

1. The gravity disturbances are synthesized from spherical harmonic d/o 2 to 2,190 on the reference ellipsoid at the same locations as the terrestrial gravity data shown in Figs. 5, 6 and 7.
2. These gravity disturbances are interpolated into a grid of 1′ by 1′ by Least-Squares Collocation (LSC) using the GEOCOL1 program, which is part of the GRAVSOFT package (Tscherning et al. 1994). The accuracy of the data is set at 2 mGal in order to be consistent with the upward continuation of the actual data in Sect. 5.
3. The 1′ by 1′ gravity disturbance grid is averaged into a 2′ by 2′ grid, and masks are applied to extract grid points only within each GRAV-D block.
4. The 2′ by 2′ gravity disturbances within each block are extended by 1° in latitude northwards and southwards, and 2–3° in longitude westwards and eastwards by gravity disturbance grids from d/o 2 to 2,190, respectively. This step is to prevent edge effect on the upward continuation.
5. The 2′ by 2′ gravity disturbances are synthesized from d/o 2 to 180 on the reference ellipsoid over the extended three blocks, and are removed from the grids created in the previous step.

The resulting data from this five-step process are used for the upward continuation analysis. Table 3 provides a statistical summary of the errors for the upward continuation when using gridded and randomly distributed dataset in a RCR technique (Case 2). The results suggest that the distribution of terrestrial gravity data is a significant factor in the interpolation and upward continuation comparisons. In the case of EN05 and EN08, the errors for the random distribution are one order of magnitude larger than those for the gridded data. As for AN04, the errors are two orders of magnitude larger than those for the gridded data and are highly correlated to the actual data distribution (see Figs. 5 and 10).

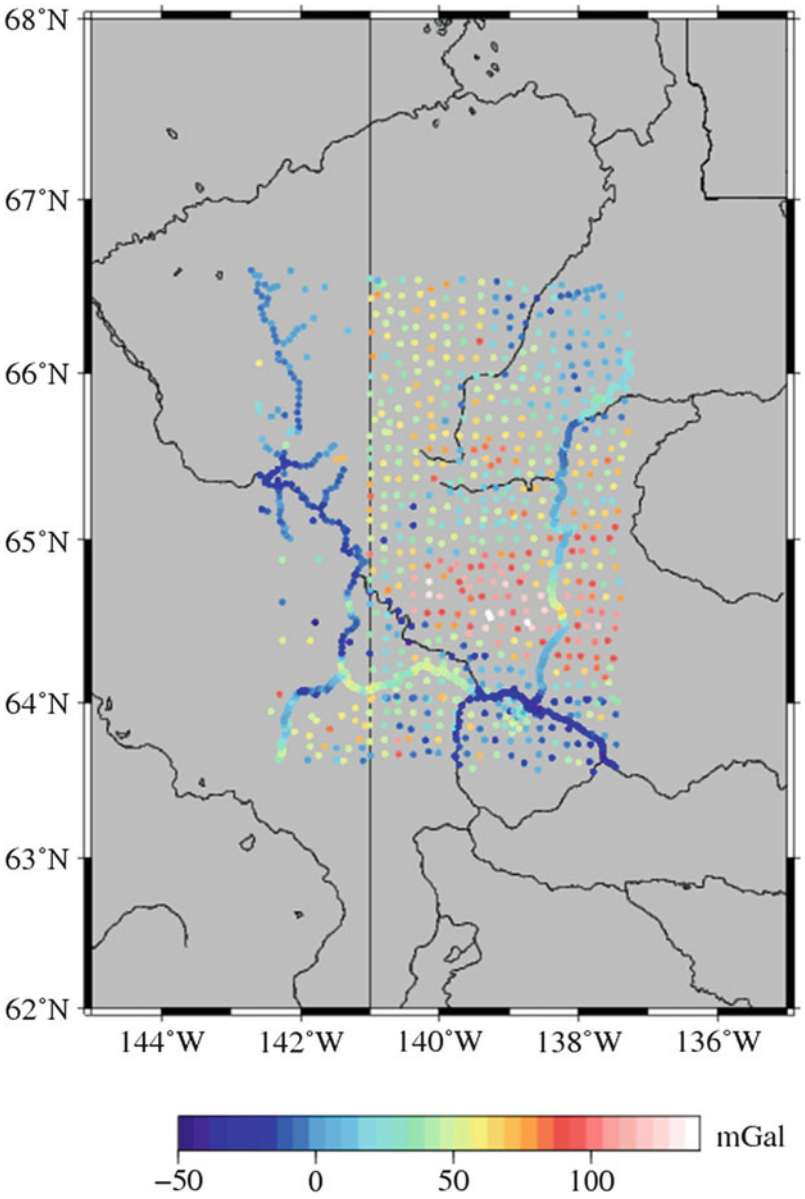

Fig. 5 The gravity disturbances at ground stations for AN04

5 Computations and Comparisons

5.1 Computation of Helmert Gravity Disturbances from GRAV-D Data

The Helmert gravity disturbances at the mean flight height (MFH) have been computed following these five steps:

1. Interpolate and reduce the gravity disturbances $\delta g^{\text{Air}}(\Omega, h_{\text{FH}})$ at flight level to a regular grid with a spacing of $1'$ at the mean flight height by LSC. The airborne gravity data are given an error of ± 2 mGal empirically.
2. Select grid points for which the standard deviations are smaller than 1 mGal. This is considered as an empirical requirement for geoid height with centimetre accuracy. The standard deviations are the error estimates of the predicted grid values by LSC. The covariance function of the signal used for the LSC was a fitted empirical covariance function through the actual observations (Tscherning et al. 1994).
3. Average the $1'$ grid from the previous step into a $2'$ grid to match the terrestrial grid spacing.
4. Synthesize the direct topographical effect at the mean flight height from spherical harmonic DEMs to the power of 3 complete to d/o 2700. The US National Geodetic Survey provided the spherical harmonic DEMs (Wang 2009).
5. Compute the Helmert gravity disturbances $\delta g_{\text{H}}^{Air}(\Omega, h_{\text{MFH}})$ at the mean flight height.

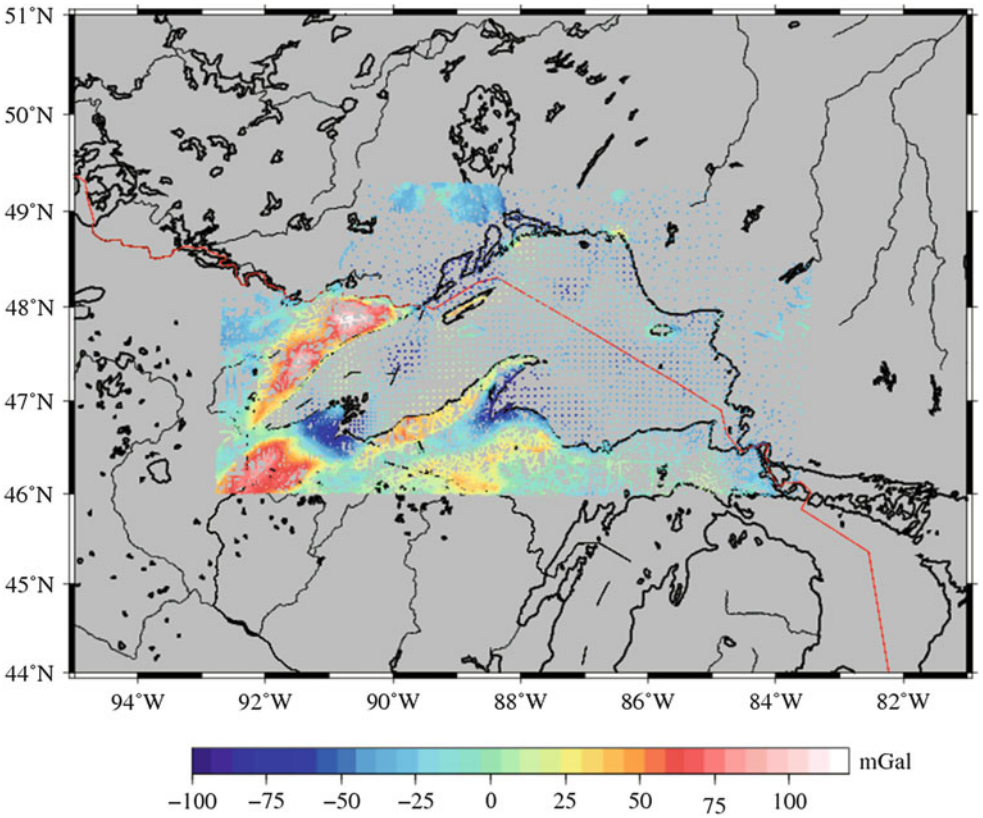

Fig. 6 The gravity disturbances at ground stations for EN05. Over Lake Superior, the data were evenly collected on both lake surface and bottom with gaps

The results are summarized in Table 4 for each block. The direct topographical effects at the mean flight heights are insignificant in comparison to the gravity disturbances due to the attenuation of the gravity pull with height. Among them, AN04 shows the strongest effect due to the rough terrain. Note that the direct topographical effects are computed by the spherical harmonic series complete to d/o 2,700. They represent a spatial resolution better than 5′, compatible with the nominal resolution of GRAV-D data. These effects can also be computed directly by Newton's integral. Further studies are required to analyse the effects in using high resolution DEM. The resulting Helmert gravity disturbances are also shown in Figs. 11, 12 and 13.

5.2 Comparisons of GRAV-D and the Upward Continued Terrestrial Gravity Data

The terrestrial Helmert gravity disturbances have been upward continued to the mean flight height for each block, and compared with the airborne Helmert disturbances. The results are shown in Table 4. The RMS differences are 3.6, 1.8 and 2.3 mGal for AN04, EN05 and EN08, respectively. They represent the combined errors from both the airborne and terrestrial data, as well as the interpolation error due to the distribution of terrestrial gravity data as the simulation analysis in Sect. 4 suggests. If we assume that both data sets have comparable accuracy, this leads to an error estimation of 2.5, 1.3 and 1.6 mGal for the respective blocks. Actual errors could be smaller or larger than these values for GRAV-D data.

Figures 14, 15 and 16 show the comparisons between the airborne and terrestrial gravity disturbances. In Fig. 14, large differences are found around the middle latitudes of the AN04 block. The differences on the Alaskan side are largely due to the sparse distribution of the terrestrial gravity data, as seen in Fig. 5, while the differences on the Yukon's side require further study to understand them. In Figs. 15 and 16, the larger differences are correlated with flight lines.

The cross-over adjustment has been used to reduce the line-correlated larger differences. To adjust the GRAV-D data, first EGM2008 reference values were removed from the raw airborne data, such that all crossover adjustment and data cleaning was applied to the obtained data residuals. For overlapping surveys, this crossover computation was performed as a single adjustment, allowing survey lines from many of the surveys to contribute to the adjustment of adjacent and overlapping surveys. In this way, all surveys from the Great Lakes (including EN05 and EN08), the Mid West and the East Coast were adjusted together. All surveys from Alaska (including AN04) were adjusted together. Additionally, this adjustment differed from standard practice in two ways. Firstly, the adjustment solved for line

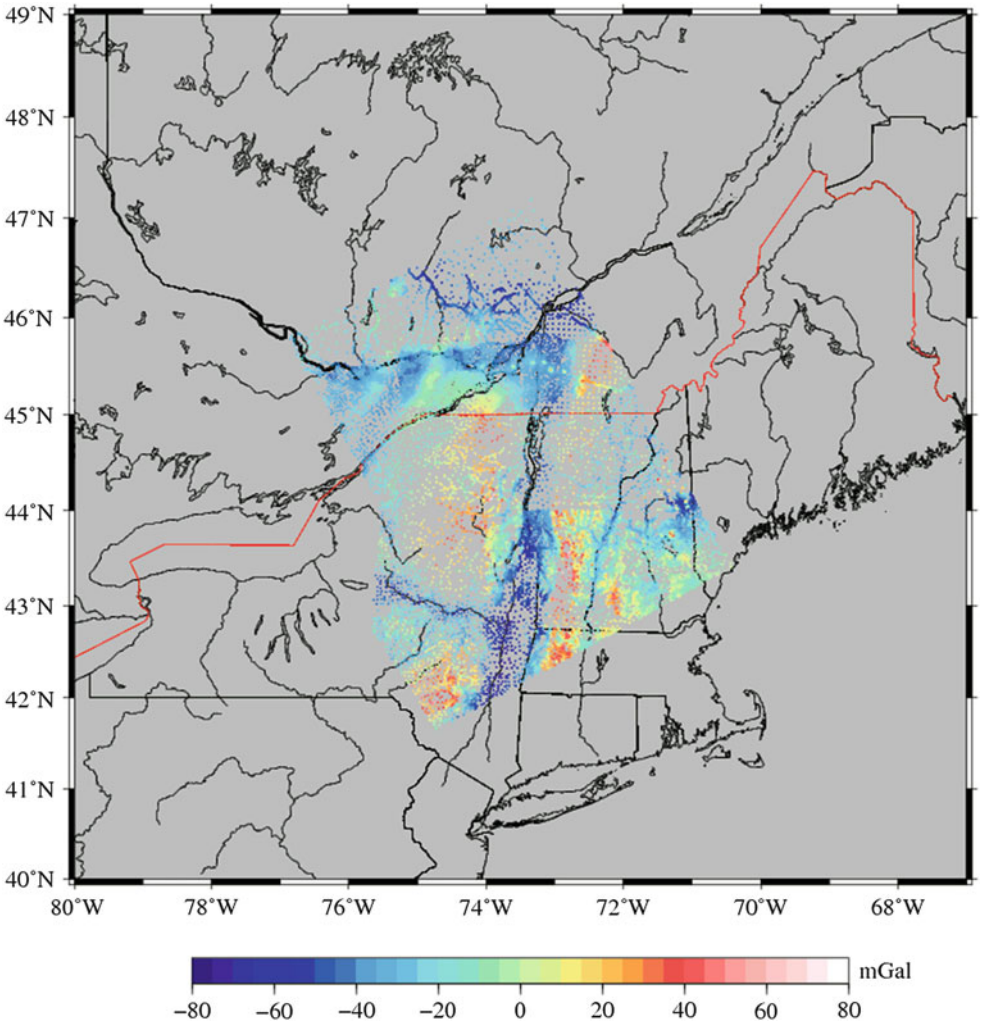

Fig. 7 The gravity disturbances at ground stations for EN08

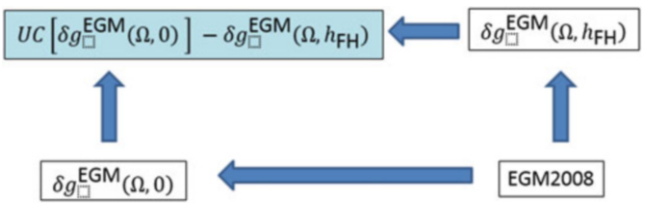

Fig. 8 Flowchart of the upward continuation simulation

biases only (not tilts). Secondly, in solving for the line biases, a rudimentary error model was applied to all adjustments. Here the 'sigma error' applied to each crossover value was computed by first adjusting each track-line to give a zero median residual with respect to EGM2008. The resulting crossover discrepancies were then adopted as the 'sigma error' value for each crossover point. The objective of these two modifications was to mitigate the extent to which large localized errors would be aliased into the solution for the biases, thereby dominating and corrupting the adjustment. For each survey, crossover adjusted residuals were compared against unadjusted residuals in terms of inter-line variability, and those few adjustments that were clear outliers were abandoned in favour of their unadjusted counterparts. The remaining residuals were cleaned by removing extreme outliers, and removing residuals corresponding to large prediction errors from least-squares gridding.

After the cross-over adjustment, the RMS differences are reduced to 1.0 and 1.4 mGal for EN05 and EN08, respectively. This implies that the GRAV-D data has an error estimation of 1.0 mGal or better after the cross-over adjustment. For AN04, the cross-over adjustment does not reduce the RMS difference significantly. This is most likely due to the sparse coverage of the terrestrial gravity data on the Alaskan side, which is not sufficient for the evaluation of the GRAV-D data.

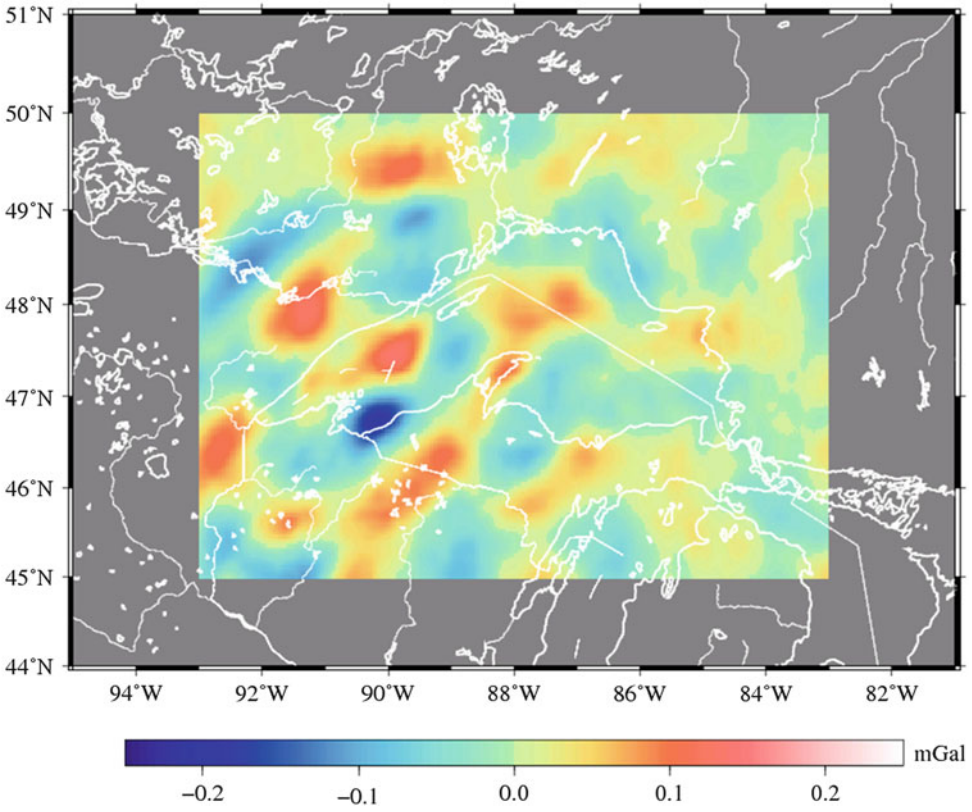

Fig. 9 Upward continuation errors for Case 2's simulation (or with the RCR technique)

6 Summary

The US GRAV-D data are compared with terrestrial gravity data at the mean flight heights over blocks AN04 (Alaska/Yukon), EN05 (Lake Superior) and EN08 (New Hampshire, Vermont upstate New York, and southwest Quebec). The comparisons are performed using Helmert gravity disturbances. The airborne Helmert gravity disturbances from GRAV-D data are calculated at the mean flight heights above the ellipsoid while the terrestrial Helmert gravity disturbances are upward continued to the same heights from the geoid by the remove-compute-restore method based on Poisson's integral. A simulation suggests that this upward continuation method, under ideal circumstances, has a numerical accuracy better than 0.1 mGal. However the accuracy degrades about ten times for EN05 and EN08, and about 100 times for AN04 when the simulation is performed at actual locations of the terrestrial gravity data.

Differences between the GRAV-D data and the terrestrial data are 3.6 mGal for AN04, 1.8 mGal for EN05 and 2.3 mGal for EN08 in terms of Root Mean Square (RMS). They represent combined errors from both airborne and terrestrial data, as well as the interpolation error due to irregular and sparse distribution of the terrestrial data. The differences show a significant correlation with some flight lines in blocks EN05 and EN08. In addition, the large differences found in block AN04 are largely due to the sparse distribution of the terrestrial gravity data on the Alaskan side. After a cross-over adjustment, the RMS's improve to 1.0 and 1.4 mGal for EN05 and EN08, respectively.

This is an ongoing study. Future steps will involve the downward continuation of the GRAV-D data to the geoid and its spectral combination with the terrestrial gravity data to further improve geoid models in the USA, its territories and overlap regions over Canada and Mexico.

Table 2 Upward continuation (UC) simulation errors for grid data without (Case 1) and with (Case 2) the RCR technique

Parameter	SH d/o range	Min	Max	Mean	StdDev	RMS
Case 1 UC	2–2,190	−27.327	39.643	−0.006	7.310	7.310
UC error		0.305	1.470	1.005	0.280	1.043
Case 2 UC	181–2,190	−26.691	37.652	−0.003	7.124	7.124
UC error		−0.204	0.138	0.000	0.041	0.041

Unit: mGal

Table 3 Errors for the upward continuation simulation using gridded and randomly located data in a RCR technique

Block	Data distribution	Parameter	Min	Max	Mean	StdDev	RMS	#Pts
AN04	Regular	UC	−63.225	38.375	0.193	11.884	11.886	14,054
	Regular	UC error	−0.179	0.136	0.001	0.054	0.054	14,054
	Random	UC error	−29.491	10.151	−1.441	4.049	4.298	14,054
EN05	Regular	UC	−37.652	26.691	−0.099	8.388	8.388	24,271
	Regular	UC error	−0.204	0.138	0.000	0.044	0.044	24,271
	Random	UC error	−5.102	3.797	−0.028	0.643	0.644	24,271
EN08	Regular	UC	−44.564	31.670	−0.075	8.054	8.054	17,435
	Regular	UC error	−0.114	0.144	0.001	0.040	0.040	17,435
	Random	UC error	−3.968	3.892	−0.092	0.412	0.422	17,435

Unit: mGal

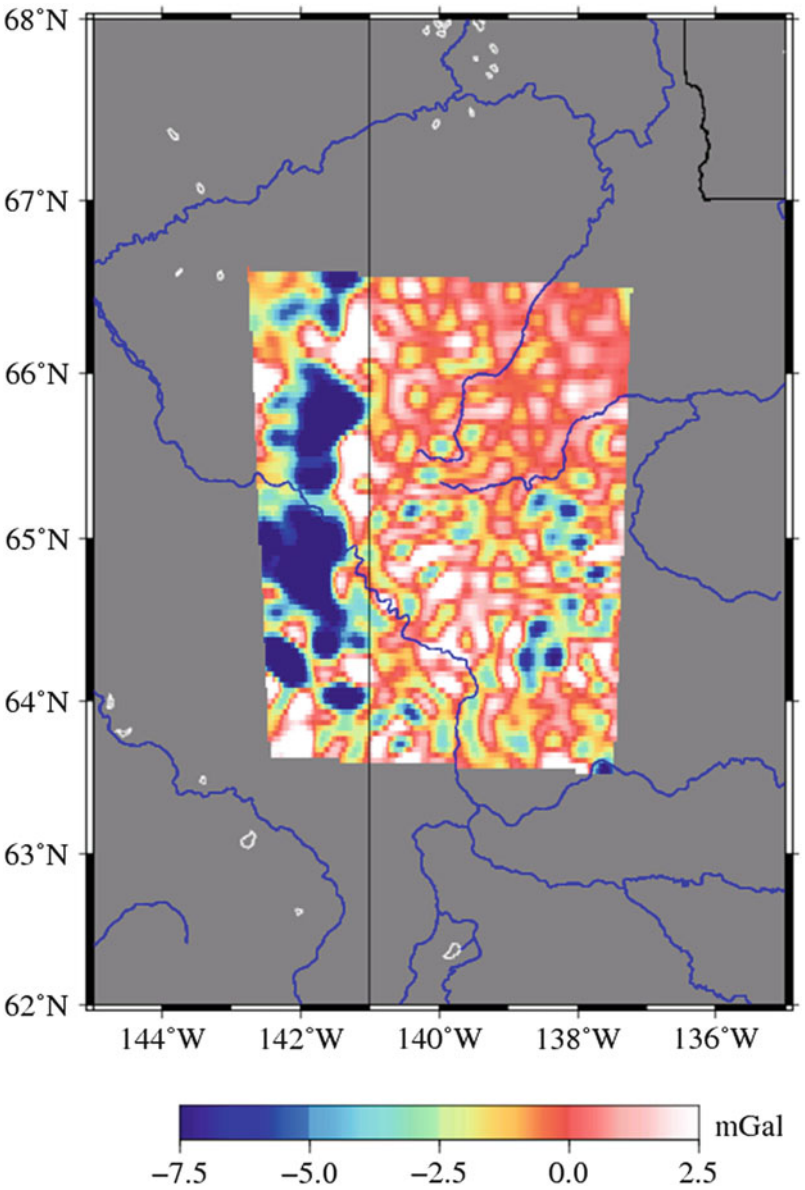

Fig. 10 Errors in the upward continuation for AN04 using synthetic data at the same locations as the terrestrial data. The errors represent the differences between the upward continued gravity disturbances and calculated synthetic gravity disturbances at the ellipsoidal height of 6,000 m

Table 4 Statistics of the airborne gravity disturbances, direct topographical effects, Helmert gravity disturbances, upward continued (UC) terrestrial Helmert gravity disturbances and the differences between the airborne and terrestrial Helmert gravity disturbances

Block	Parameter	Min	Max	Mean	StdDev	RMS	# Pts
AN04	$\delta g_{\mathrm{MFH}}^{Air}$	−7.514	84.909	29.678	17.231	34.317	15,456
	δg_{DTE}	−2.165	5.744	0.044	1.067	1.068	15,456
	$\delta g_{\mathrm{H}}^{Air}$	−6.029	82.273	29.634	16.564	33.949	15,456
	$\mathrm{UC}(\delta g_{\mathrm{H}}^{Terr})$	−10.213	84.409	27.650	16.787	32.347	15,456
	$\varepsilon g(\Omega, h_{\mathrm{MFH}})$	−10.170	20.711	2.028	2.937	3.569	15,456
EN05	$\delta g_{\mathrm{MFH}}^{Air}$	−70.385	80.125	−17.466	21.879	27.996	24,753
	δg_{DTE}	−0.375	0.547	−0.013	0.121	0.122	24,753
	$\delta g_{\mathrm{H}}^{Air}$	−70.263	79.755	−17.453	21.839	27.957	24,753
	$\mathrm{UC}(\delta g_{\mathrm{H}}^{Terr})$	−70.278	80.805	−16.969	21.942	27.738	24,753
	$\varepsilon g(\Omega, h_{\mathrm{MFH}})$	−10.225	8.523	−0.484	1.751	1.816	24,753
EN08	$\delta g_{\mathrm{MFH}}^{Air}$	−55.918	41.651	−10.561	19.463	22.143	21,237
	δg_{DTE}	−0.835	4.325	0.009	0.325	0.325	21,237
	$\delta g_{\mathrm{H}}^{Air}$	−55.593	40.797	−10.570	19.313	22.016	21,237
	$\mathrm{UC}(\delta g_{\mathrm{H}}^{Terr})$	−56.050	42.925	−11.550	19.381	22.562	21,237
	$\varepsilon g(\Omega, h_{\mathrm{MFH}})$	−16.930	12.804	0.981	2.051	2.273	21,237

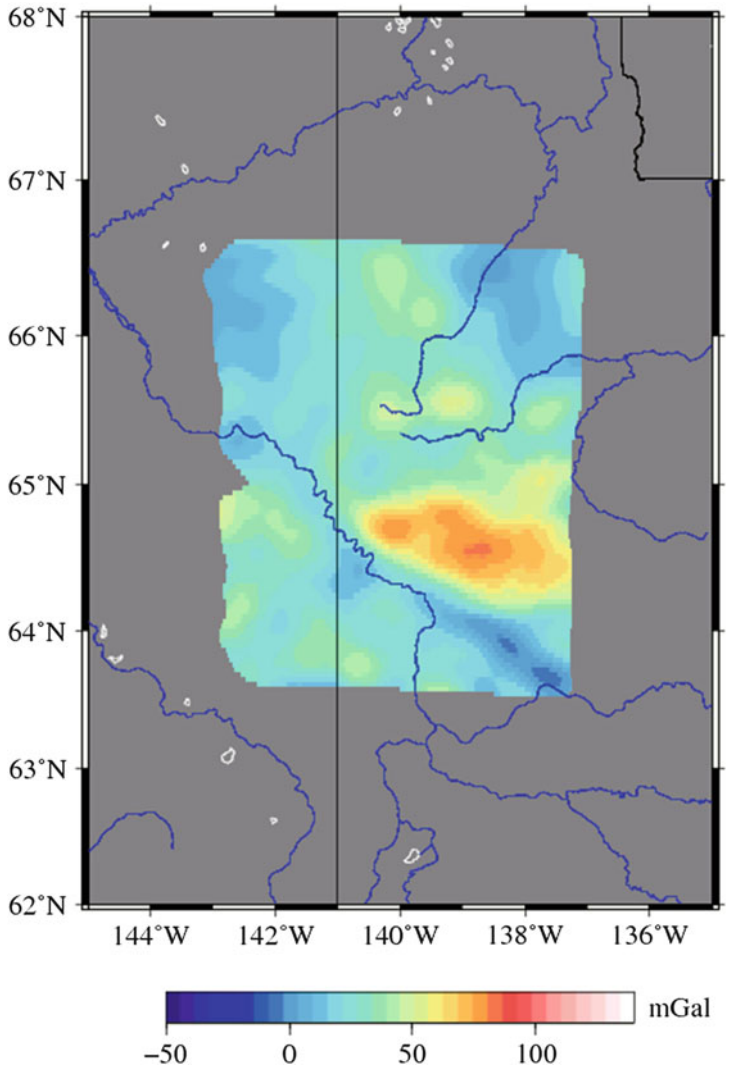

Fig. 11 The GRAV-D Helmert gravity disturbances at the height of 6161.427 m for AN04

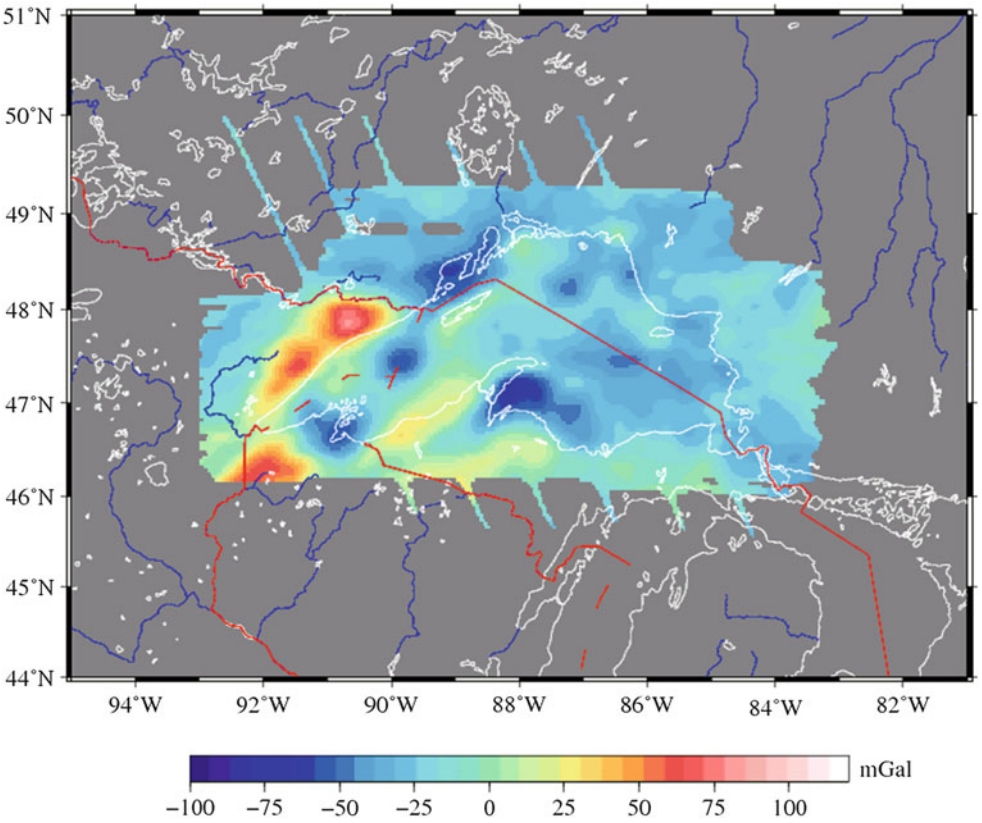

Fig. 12 The GRAV-D Helmert gravity disturbances at the height of 6211.818 m for EN05

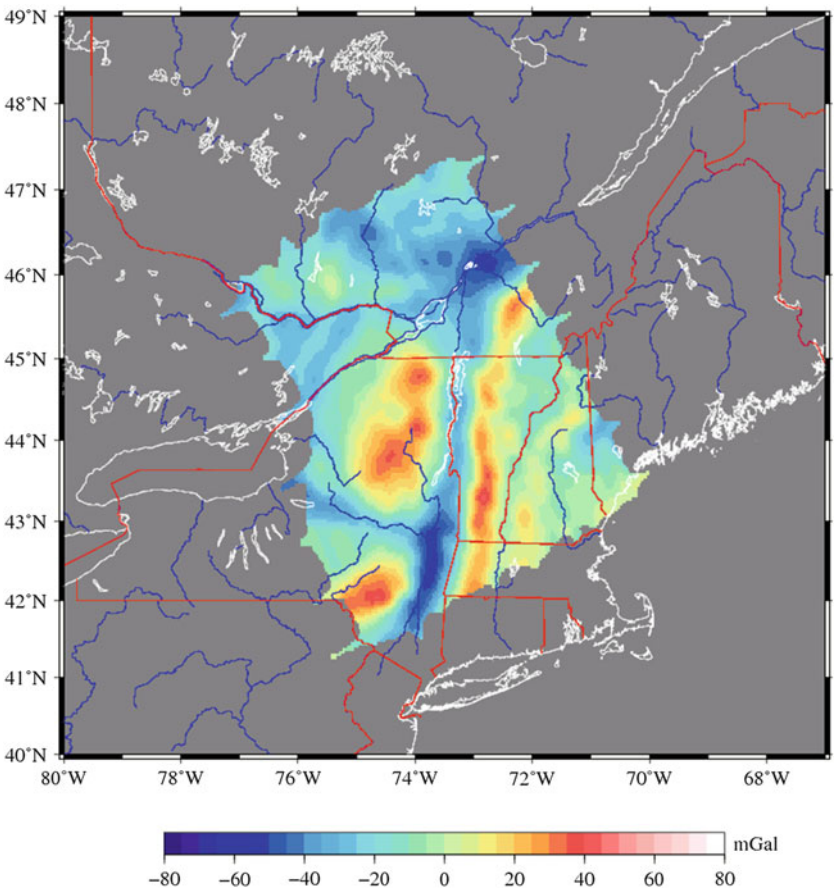

Fig. 13 The GRAV-D Helmert gravity disturbances at the height of 5445.884 m for EN08

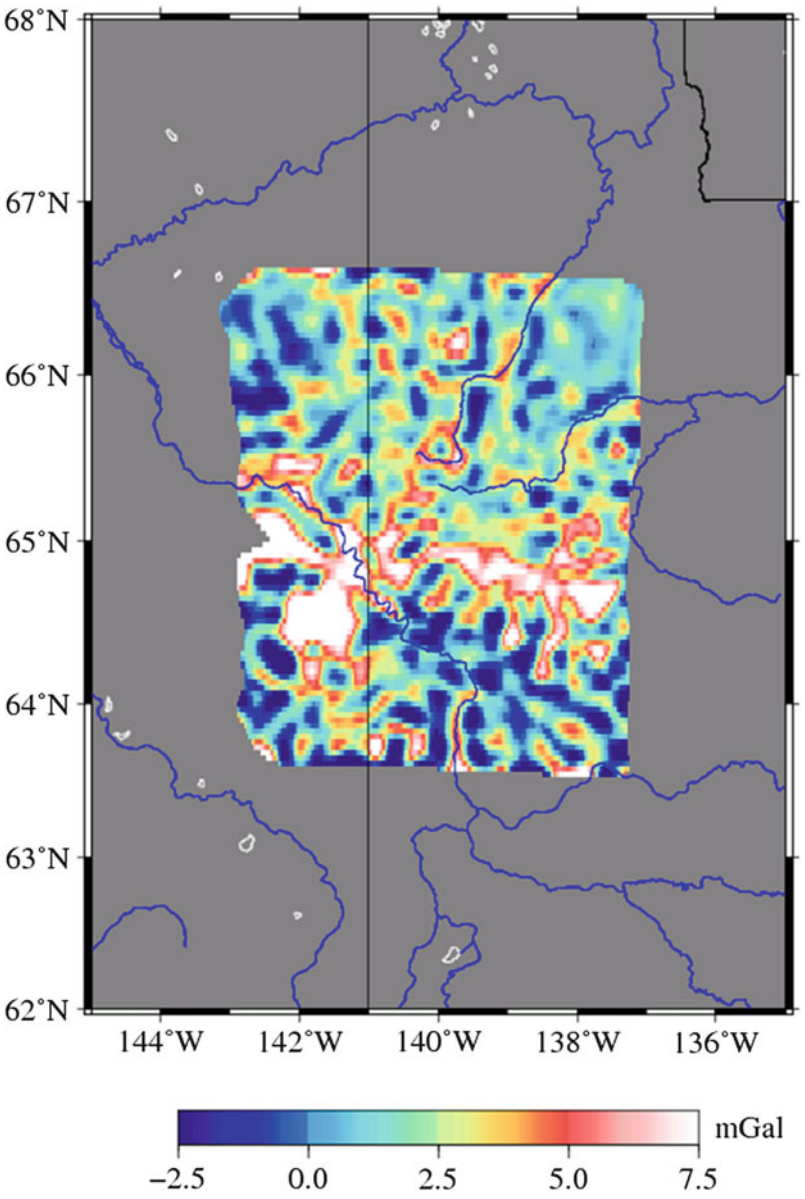

Fig. 14 Differences between the airborne and terrestrial Helmert gravity disturbances at the height of 6161.427 m for AN04

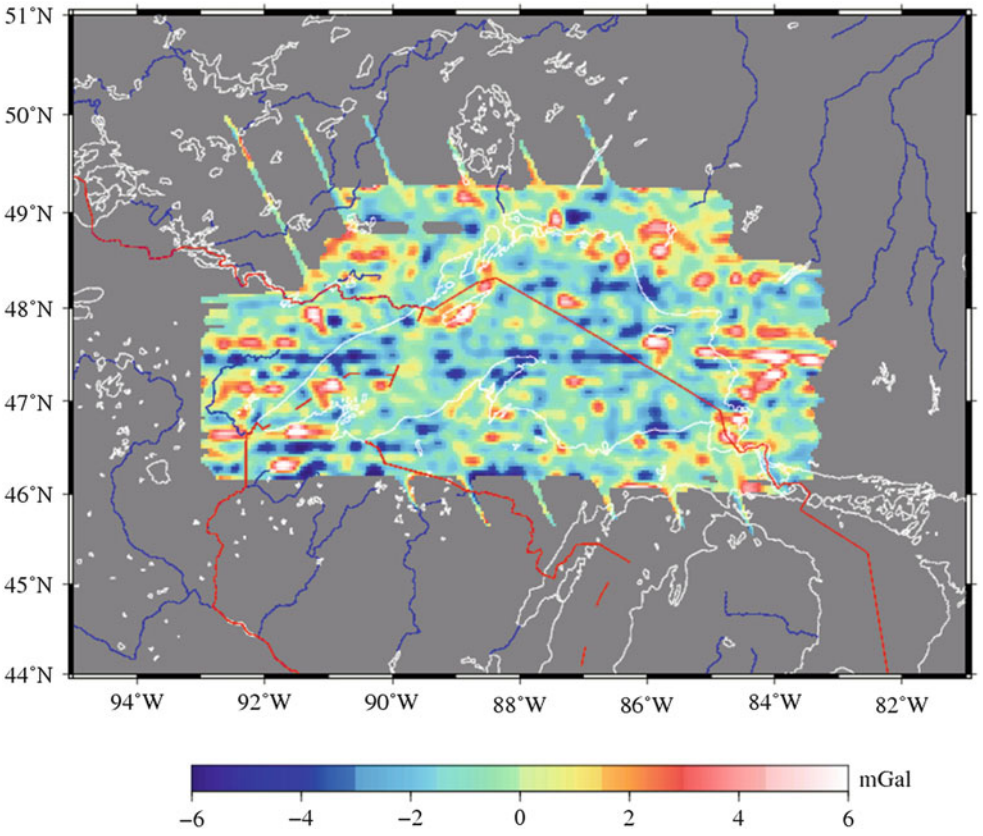

Fig. 15 Differences between the airborne and terrestrial Helmert gravity disturbances at the height of 6211.818 m for EN05

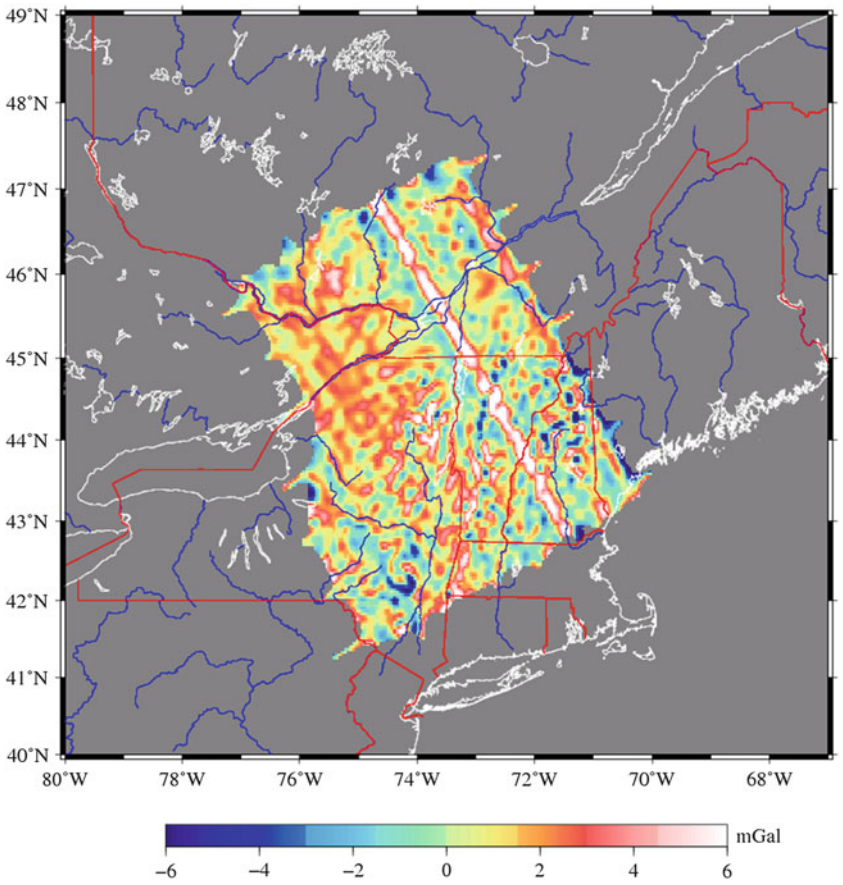

Fig. 16 Differences between the airborne and terrestrial Helmert gravity disturbances at the ellipsoid height of 5445.884 m for EN08

Acknowledgements We would like to thank two anonymous reviewers for their constructive comments and suggestions. NRCan Contribution number: 20170256.

References

GRAV-D Science Team (2013a) GRAV-D general airborne gravity data user manual. In: Damiani T, Youngman M (eds) Version 2. Available 2/2013. Online at: http://www.ngs.noaa.gov/GRAV-D/data_EN05.shtml

GRAV-D Science Team (2013b) Block AN04 (Alaska North 04); GRAV-D airborne gravity data user manual. In: Youngman M, Weil C (eds) Version BETA. Available 1/2013. Online at: http://www.ngs.noaa.gov/GRAV-D/data_AN04.shtml

GRAV-D Science Team (2013c) Block EN05 (Easter North 05); GRAV-D airborne gravity data user manual. In: Youngman M, Weil C (eds) Version BETA #2. Available 7/2013. Online at: http://www.ngs.noaa.gov/GRAV-D/data_EN05.shtml

GRAV-D Team (2014) Block EN08 (Eastern North 08); GRAV-D airborne gravity data user manual. In: Youngman M, Weil C (eds) Version BETA. Available 5/2014. Online at: http://www.ngs.noaa.gov/GRAV-D/data_EN08.shtml

Heiskanen WA, Moritz H (1967) Physical geodesy. W.H. Freeman, San Francisco

Huang J (2002) Computational methods for the discrete downward continuation of the Earth gravity and effects of lateral topographical mass density variation of gravity and geoid. GGE Technical report 216, Department of Geodesy and Geomatics Engineering, University of New Brunswick, Fredericton

Huang J, Véronneau M (2013) Canadian gravimetric geoid model 2010. J Geod 87:771–790. https://doi.org/10.1007/s00190-013-0645-0

Jiang T, Wang YM (2016) On the spectral combination of satellite gravity model, terrestrial and airborne gravity data for local gravimetric geoid computation. J Geod 90:1405–1418. https://doi.org/10.1007/s00190-016-0932-7

Li X, Crowley JW, Holmes SA, Wang YM (2016) The contribution of the GRAV-D airborne gravity to geoid determination in the Great Lakes region. Geophys Res Lett 43:4358–4365. https://doi.org/10.1002/2016GL068374

Moritz H (1980a) Advanced physical geodesy. Wichmann, Karlsruhe

Moritz H (1980b) Geodetic reference system 1980. Bull Geod 62(2):187–192

Pavlis NK, Holmes SA, Kenyon SC, Factor JK (2012) The development and evaluation of the earth gravitational model 2008 (EGM2008). J Geophys Res 117:B04406. https://doi.org/10.1029/2011JB008916

Pavlis NK, Holmes SA, Kenyon SC, Factor JK (2013) Correction to the development and evaluation of the earth gravitational model 2008 (EGM2008). J Geophys Res 118(5):2633. https://doi.org/10.1002/jgrb.50167

Smith DA, Holmes SA, Li X, Guillaume S, Wang YM, Bürki B, Roman DR, Damiani TM (2013) Confirming regional 1 cm differential geoid accuracy from airborne gravimetry: the geoid slope validation survey of 2011. J Geod 87(10–12):885–907

Tscherning CC, Forsberg R, Knudsen P (1994) GRAVSOFT – A system for geodetic gravity field modelling, http://cct.gfy.ku.dk/publ_cct/cct952.txt

Vaníček P, Huang J, Novák P, Pagiatakis SD, Véronneau M, Martinec Z, Featherstone WE (1999) Determination of the boundary values for the Stokes–Helmert problem. J Geod 73:180–192

Véronneau M (2013) The Helmert gravity grid used for CGG2010. Geodetic Survey Division, CCRS, Natural Resources Canada, Ottawa

Véronneau M, Huang J (2016) The Canadian geodetic vertical datum of 2013 (CGVD2013). Geomatica 70(1):9–19

Wang YM (2009) Investigation of the topographic effect by using high degree spherical harmonic expansion. IAG 2009 Scientific Assembly, Buenos Aires. August 31–September 4, 2009

Zhong D, Véronneau M, Huang J (2016) Proposals for evaluation and computation of the GRAV-D airborne gravity data with existing terrestrial gravity data. Technical Report, Canadian Geodetic Survey, Natural Resources Canada

The African 3″ × 3″ DTM and Its Validation

Hussein A. Abd-Elmotaal, Atef Makhloof, Mostafa Abd-Elbaky, and Mostafa Ashry

Abstract

This paper deals with creating a fine digital terrain model (DTM) for Africa and the surrounding region covering the window 42°S $\leq \phi \leq$ 44°N, 22°W $\leq \lambda \leq$ 62°E using the Advanced Spaceborne Thermal Emission and Reflection Radiometer (ASTER) Global Digital Elevation Model (GDEM) at a 3″ × 3″ resolution (which corresponds to roughly 90 m resolution on the earth's surface). The ASTER-GDEM model, which is available only on land, has been smoothed from its original 1″ × 1″ resolution to the used 3″ × 3″ resolution using the block average operator technique employing special characteristics at the coastal boarders. The 30″ × 30″ SRTM30+ has been used, after being interpolated to 3″ × 3″ grid size, to fill-in the missing sea regions of the ASTER-GDEM model. The created 3″ × 3″ DTM has been compared with the available point data both on land and on sea areas for a set of more than one million points. Residuals follow perfectly the Gaussian normal distribution.

Keywords

Africa • ASTER • DTM • SRTM-Plus

1 Introduction

In the framework of the IAG African Geoid Project, it is necessary to develop a detailed digital terrain model (DTM) for Africa to be used within the remove-restore technique for the geoid determination in Africa. The available DTM's for Africa suffer from their accuracy deficiency especially on land, therefore it is needed to develop a more precise DTM for Africa to be used in the geoid determination for Africa, among other geodetic purposes and applications.

This paper deals with creating a new digital terrain model for Africa and the surrounding region covering the window 42°S $\leq \phi \leq$ 44°N, 22°W $\leq \lambda \leq$ 62°E using the data available from the Advanced Spaceborne Thermal Emission and Reflection Radiometer (ASTER) (http://earthexplorer.usgs.gov/) at a 1″ × 1″ resolution, which is available only on land, and the global topography-bathymetry 30″ × 30″ SRTM30+ DTM (Becker et al. 2009).

The used data sets for the current investigation are described. The processing for creating the 3″ × 3″ DTM for Africa is described in detail. The created digital terrain model is then compared with reference-checking data on ocean and on land. Also, the created DTM has been compared with the African AFH13S30 DTM.

Several Digital Terrain Models have been developed for the African territory. A Digital Height Model for Egypt has been developed by Abd-Elmotaal (1999). Another set of digital height models for Egypt and the surrounding region, covering the window 19°N $\leq \phi \leq$ 35°N, 22°E $\leq \lambda \leq$ 40°E using the data available from Shuttle Radar Topography Mission (SRTM) at a 3″ × 3″ resolution, has been created by Abd-Elmotaal (2011). Fine digital height model (DHM) for Egypt and the surrounding region has been created using the Advanced Spaceborne Thermal Emis-

H.A. Abd-Elmotaal (✉) • A. Makhloof • M. Abd-Elbaky • M. Ashry
Civil Engineering Department, Faculty of Engineering,
Minia University, Minia, Egypt
e-mail: abdelmotaal@lycos.com

G. S. Vergos et al. (eds.), *International Symposium on Gravity, Geoid and Height Systems 2016*,
International Association of Geodesy Symposia 148, DOI 10.1007/1345_2017_19

sion and Reflection Radiometer (ASTER) Global Digital Elevation Model (GDEM) by Abd-Elmotaal et al. (2013). Abd-Elmotaal (2004) has developed a set of digital height models for Africa by merging the bathymetric model and the GTOPO30 model.

Other digital terrain models have been developed in different places of the world. An overview of the mission and the DEM production, as well as an evaluation of the DEM product quality, by spaceborne radar has been assessed by Rabus et al. (2003). Predicted sea floor topography, with the aid of the free air gravity anomalies derived from GEOSAT altimetry, has been estimated by Smith and Sandwell (1997). The accuracy of digital height models has been studied by Ackermann (1979). An accuracy analysis of the digital height models from SRTM C-band over large areas has been carried out by Passini and Jacobsen (2007). DEM's based on space images versus SRTM height models have been created by Jacobsen (2005). Digital height models based on Cartosat-1 images, SPOT-5 HRS and SRTM C-band have been established in a mountainous forest area in Turkey by Buyuksalih and Jacobsen (2008). DEM products created from SRTM data with respective products created from ASTER stereo-pairs was studied by Nikolakopoulos et al. (2006). Comparison of free high-resolution digital elevation data sets (ASTER GDEM2, SRTM v2.1/v4.1) and validation against accurate heights from the Australian National Gravity Database has been performed by Rexer and Hirt (2014).

It should be pointed out that the importance of the SRTM model for Africa is due to the fact that it is the best available model to date for the sea region of the African window.

2 Data Used

2.1 The 1″ × 1″ ASTER-GDEM Model

The Advanced Spaceborne Thermal Emission and Reflection Radiometer (ASTER) Global Digital Elevation Model (GDEM) was developed jointly by the U.S. National Aeronautics and Space Administration (NASA) and Japan's Ministry of Economy, Trade, and Industry (METI). Each ASTER-GDEM file covers an area of 1° × 1°. ASTER-GDEM files covering the window 42°S $\leq \phi \leq$ 44°N, 22°W $\leq \lambda \leq$ 62°E (land only) with a resolution of 1″ × 1″ are available for this investigation.

Figure 1 shows a combination of 10° × 10° sample files of the 1″ × 1″ ASTER-GDEM model. The black colour indicates no data and its value is set to zero.

It is worth mentioning that Fig. 1 clearly shows that the ASTER-GDEM doesn't have bathymetry values. Therefore, the SRTM30+ DTM model, after being interpolated to the 3″ × 3″ resolution, has been used to fill-in those areas *at sea regions only*. No filling in the land areas took place as the ASTER-GDEM doesn't have gaps on land.

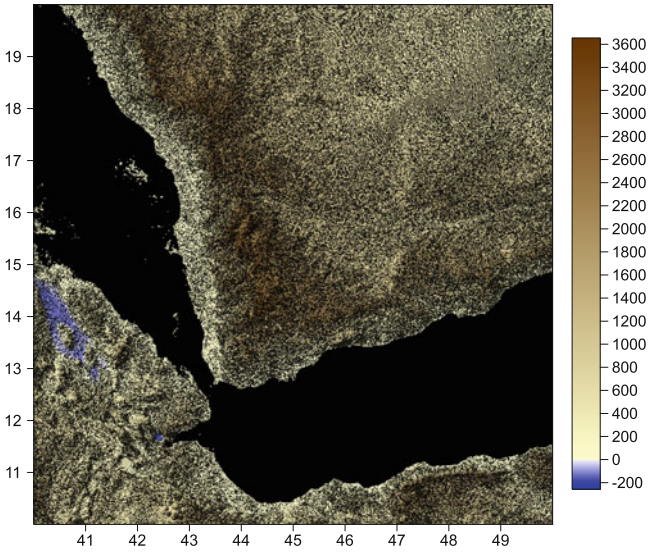

Fig. 1 Sample of the 1″ × 1″ ASTER-GDEM model. Units in [m]

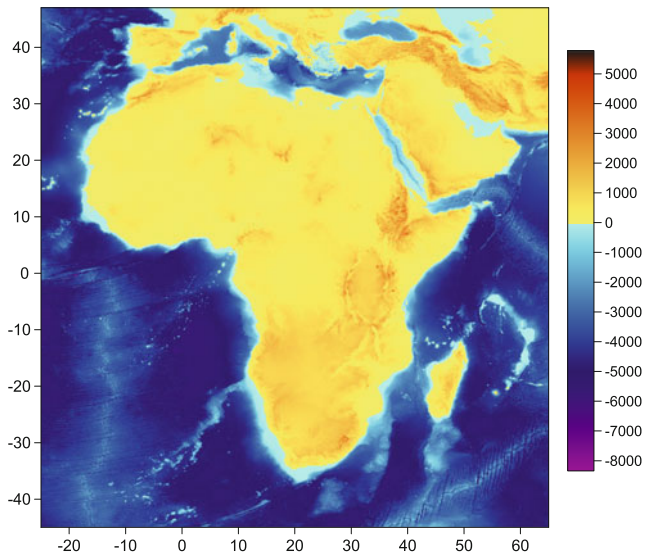

Fig. 2 The 30″ × 30″ SRTM30+ DTM for Africa covering the window of 45°S $\leq \phi \leq$ 47°N, 25°W $\leq \lambda \leq$ 65°E. Units in [m]

2.2 The SRTM30+ Model

The global 30″ × 30″ SRTM30+ DTM ver. 7.0 (Becker et al. 2009) is used as a basic data set for the current investigation. The 30″ × 30″ SRTM30+ DTM contains both topography and bathymetry. Figure 2 shows the SRTM30+ DTM with a resolution of 30″ × 30″ for Africa.

3 Creating the 3″ × 3″ DTM for Africa

3.1 Interpolating SRTM30+ DTM

As described above, the SRTM30+ DTM model, after being interpolated to the 3″ × 3″ resolution, has been used to fill-in the sea regions only of the ASTER-GDEM model. The Kriging interpolation technique with zero error variance (Stein 2012) has been used to grid the 30″ × 30″ SRTM30+ DTM on a 3″ × 3″ grid covering the African window 42°S ≤ ϕ ≤ 44°N, 22°W ≤ λ ≤ 62°E. In the sea region, we only have bathometric depths at the 30″ × 30″ grids of the SRTM30+ DTM. Accordingly, we used the Kriging interpolation technique with zero error variance because it is well-known that Kriging interpolation reproduces the data at the data points if their precision is set to zero (cf. e.g., Moritz 1980; Stein 2012). Figure 3 shows SRTM30+ before and after the interpolation into 3″ × 3″ resolution using the Kriging interpolation technique with zero error variance.

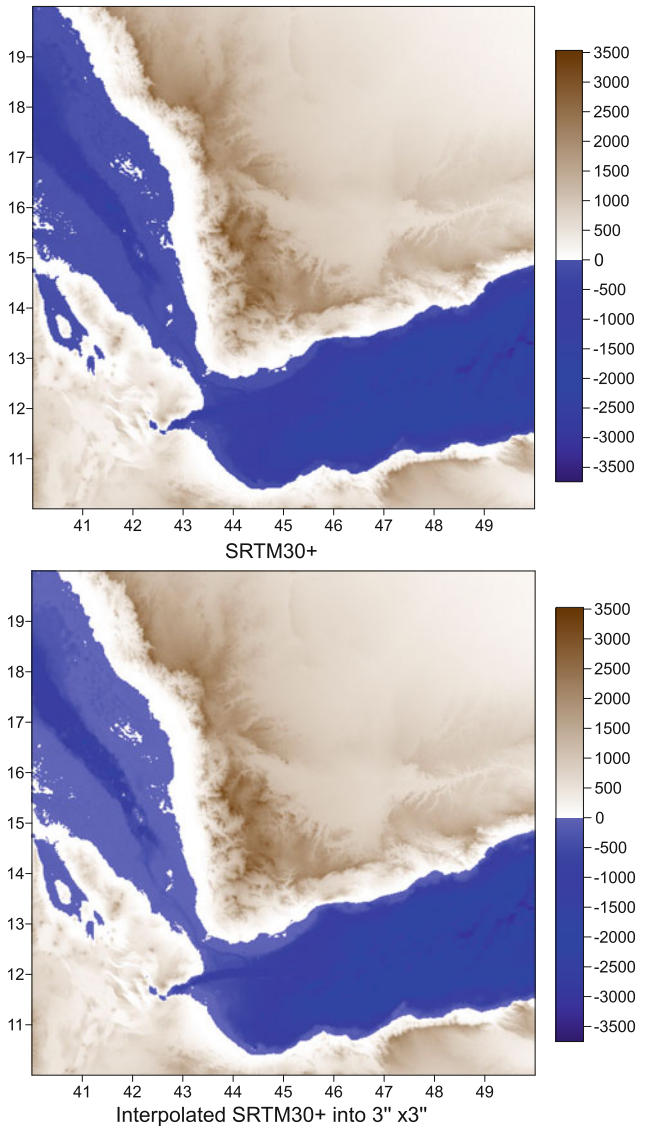

Fig. 3 SRTM30+ before and after the interpolation into 3″ × 3″ resolution using the Kriging interpolation technique with zero error variance. Units in [m]

3.2 Smoothing the 1″ × 1″ ASTER-GDEM DTM

A FORTRAN program has been written to smooth the land-only 1″ × 1″ ASTER-GDEM grid files into ASTER-GDEM grids with a resolution of 3″ × 3″ using the block average operator technique.

In case of a 3″ × 3″ coastal pixel, the program works as follows:

- If the number of the positive 1″ × 1″ ASTER-GDEM pixels is ≥5, the smoothed height is computed by averaging the remaining positive 1″ × 1″ pixels after removing the same number of the negative pixels having the largest positive elevations.
- If the number of the negative 1″ × 1″ ASTER-GDEM pixels is ≥5, the smoothed height is set to blanked pixel (i.e., no data).

On ocean regions, the smoothed height is always set to blanked pixel. The reason of assigning the blanked pixels is to fill these pixels from the interpolated SRTM30+ data on ocean regions.

Figure 4 shows the smoothed 3″ × 3″ ASTER-GDEM DTM, for the same region as of Fig. 3, after applying the developed FORTRAN program. Here the dark green colour means blanked data.

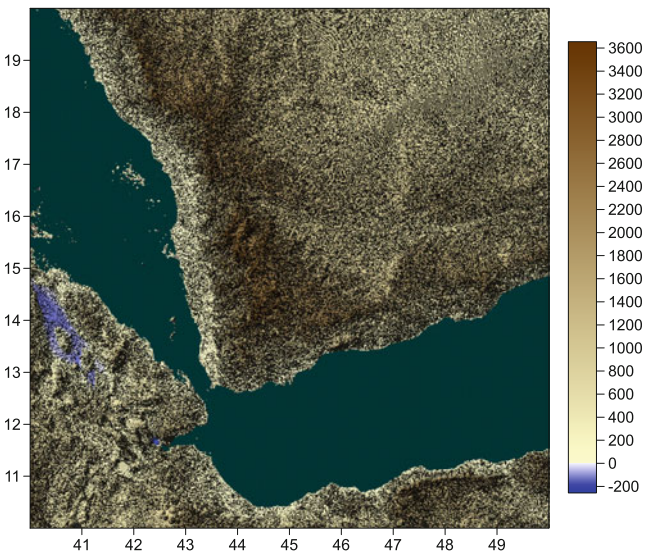

Fig. 4 The smoothed 3″ × 3″ ASTER-GDEM grid with blanked nodes for ocean pixels after correction. Units in [m]

3.3 Creating the 3″ × 3″ African DTM

The developed 3″ × 3″ DTM for Africa has been created by using the grid Mosaic utility of the Surfer software package, which replaces the blanked nodes of the smoothed 3″ × 3″ ASTER-GDEM DTM by the values of the corresponding pixels from the interpolated 3″ × 3″ SRTM30+ grid. Figure 5 shows the processing steps of creating the 3″ × 3″ DTM for Africa as described above.

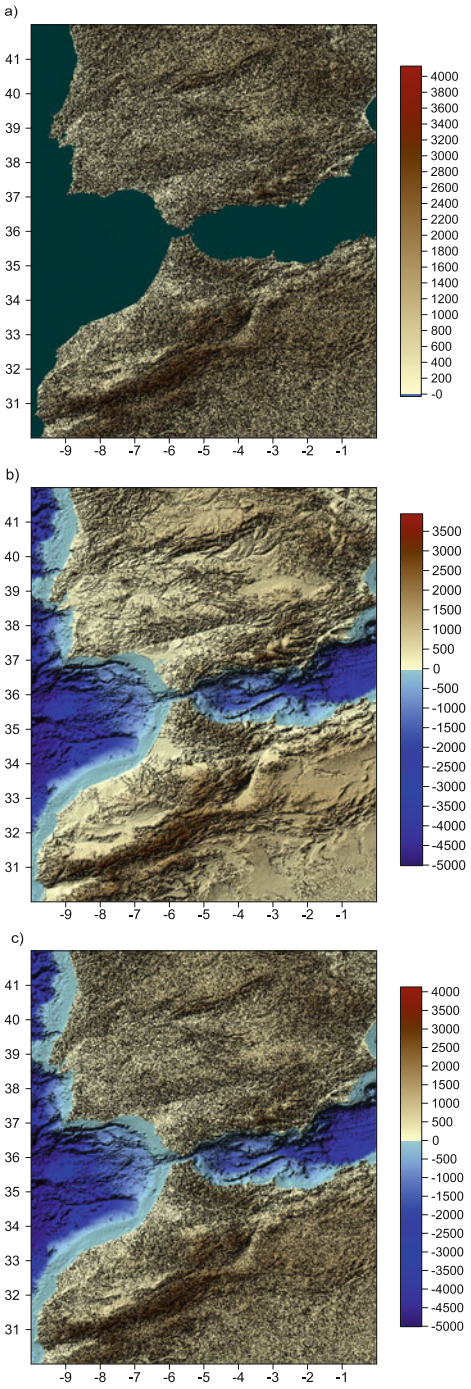

Fig. 5 Creating the 3″ × 3″ AFH16S03 DTM using the Surfer Mosaic utility of the 3″ × 3″ smoothed ASTER-GDEM DTM and the interpolated 3″ × 3″ SRTM30+ DTM. Units in [m]. (**a**) ASTER-GDEM (smoothed). (**b**) Interpolated SRTM30+ into 3″ × 3″. (**c**) Final DTM AFH16S03

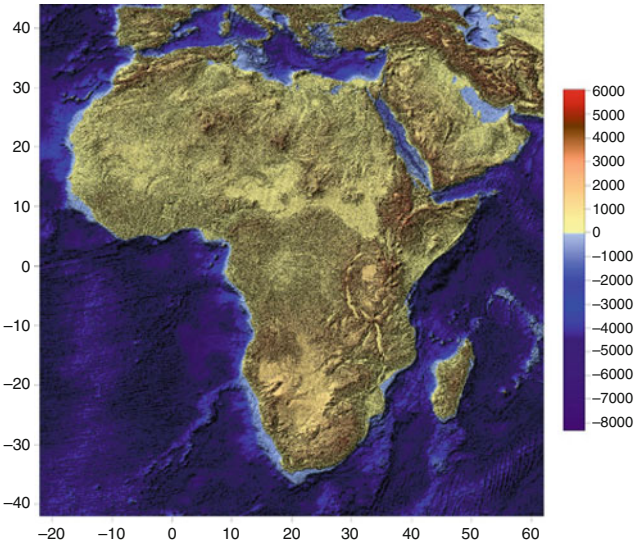

Fig. 6 The 3″ × 3″ AFH16S03 DTM for Africa. Units in [m]

Finally, Fig. 6 shows the outcome of the processing approach, the developed 3″×3″ DTM for Africa (AFH16S03 model).

4 Validation of the Developed African DTM

4.1 Comparison with AFH13S30

The developed 30″ × 30″ AFH16S30 DTM (created by employing the block average operator technique on the 3″ × 3″ AFH16S03 DTM) has been compared with the 30″ × 30″ AFH13S30 DTM (Abd-Elmotaal, 2013, personal communication). The 30″ × 30″ AFH13S30 DTM was created based on the 30″ × 30″ SRTM30+. Filling the gaps has been done using the old AFH04 DTM (Abd-Elmotaal 2004).

Figure 7 shows the differences between the 30″ × 30″ AFH13S30 DTM and 30″ × 30″ AFH16S30 30″ × 30″. No significant differences were found on ocean regions. This is due to the fact that both models on ocean regions depend on SRTM30+.

The stripes structure appearing in Fig. 7 is due to the used method by Becker et al. (2009) for filling the gaps on land of the SRTM DHM in generating the SRTM30+ DTM (which has been used to create AFH13 DTM). The SRTM model has exactly the same gap-strips structure appearing in Fig. 7 (see also, e.g., Abd-Elmotaal 2011, Fig. 3). This indicates

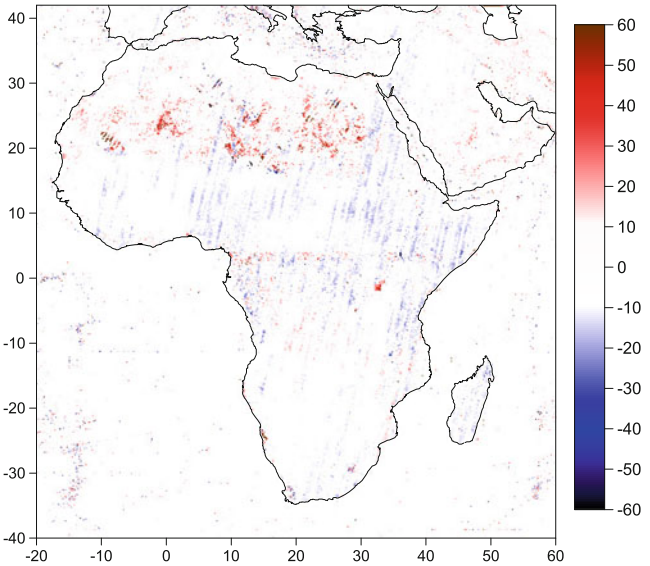

Fig. 7 Differences between the 30″ × 30″ AFH16S30 DTM and the 30″ × 30″ AFH13S30 DTM. Units in [m]

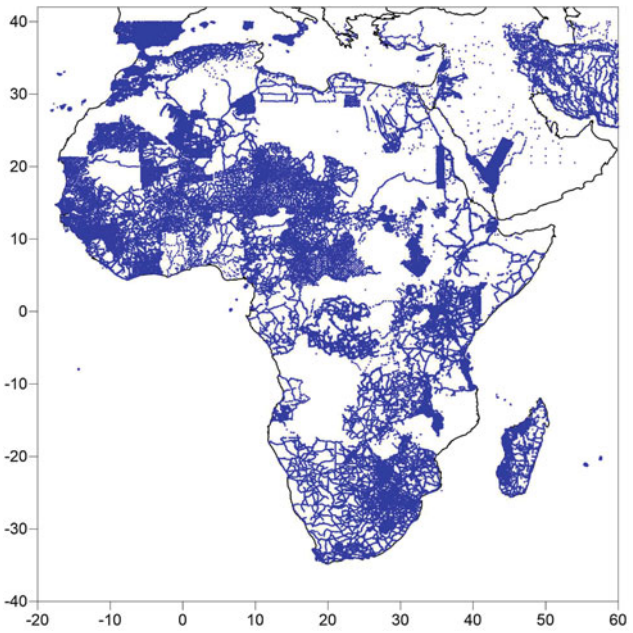

Fig. 8 Distribution of the used reference-checking data points on land (after Abd-Elmotaal et al. 2015)

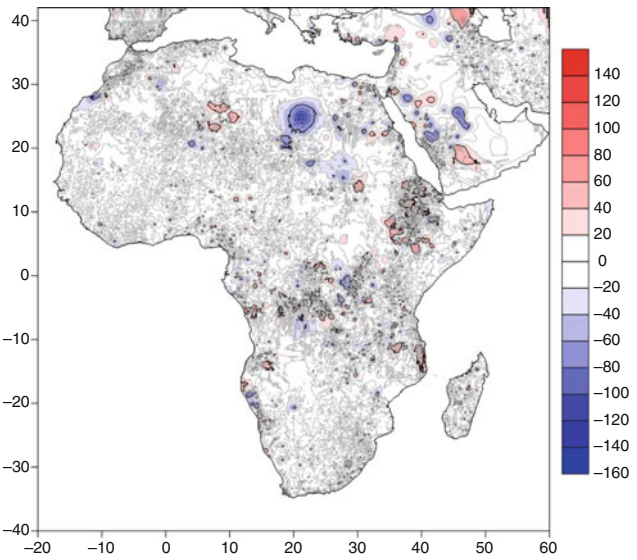

Fig. 9 Differences between reference-checking data and the 3″ × 3″ AFH16S03 DTM on land. Units in [m]

that the developed DTM has improved the situation on land (no stripes structure). This improvement is due to the usage of a finer resolution sources (the 1″ × 1″ ASTER-GDEM model) in establishing the developed DTM instead of using SRTM30+, which has a lower resolution.

4.2 Comparison with Reference-Checking Data on Land

The 3″ × 3″ AFH16S03 DTM has been validated using a set of about 200 thousands data points on land. Figure 8 shows the distribution of the used reference-checking data points on land. This reference-checking data set on land is the one used for establishing the gravity database for Africa. For details on this data set, the reader is invited to refer to Abd-Elmotaal et al. (2015).

Figure 9 illustrates the differences between the reference-checking data and the 3″ × 3″ AFH16S03 DTM on land. The differences between the reference-checking data and their corresponding values of the 3″ × 3″ AFH16S03 DTM on land range between −158.4 and 158.4 m with an average of about −0.4 m and a standard deviation of 25.2 m.

In order to get a deeper insight of the validation of AFH16S03 DTM, two critical areas have been chosen to illustrate. The first area is located at the Moroccan territory, for which the differences are ranging between −85 and 100 m (cf. Fig. 10). Most of the differences are below 20 m (the white pattern). Only few spots at the Atlas high Mountain have larger differences up to 100 m. The reason of such relatively large differences comes from comparing the point data in a rough topography with a mean value of 3″ × 3″ pixel. Accordingly, Fig. 10 shows good quality of the developed AFH16S03 DTM model.

The second chosen sub-area is located at the high lands of Ethiopia. Figure 11 shows the validation of the AFH16S03 DTM there. This area has very rough topography (cf. Fig. 6). The differences are ranging between −158.4 and 158.4 m. Figure 11 shows some patterns of differences which are due to the very rough topography of this area.

Figure 12 shows a histogram of comparing the 3″ × 3″ AFH16S03 with reference-checking data on land. Figure 12

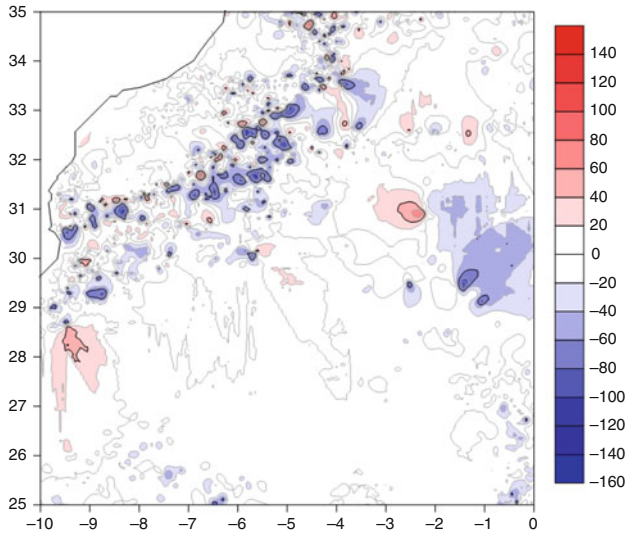

Fig. 10 Differences between reference-checking data and the 3″ × 3″ AFH16S03 DTM on land for Morocco. Units in [m]

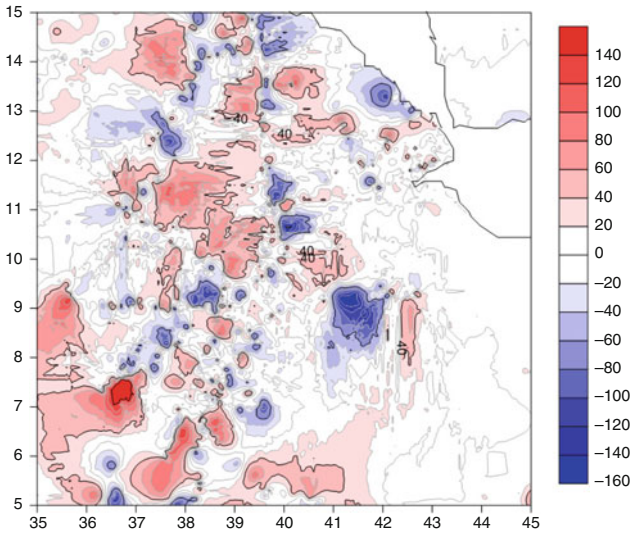

Fig. 11 Differences between reference-checking data and the 3″ × 3″ AFH16S03 DTM on land for the high lands of Ethiopia. Units in [m]

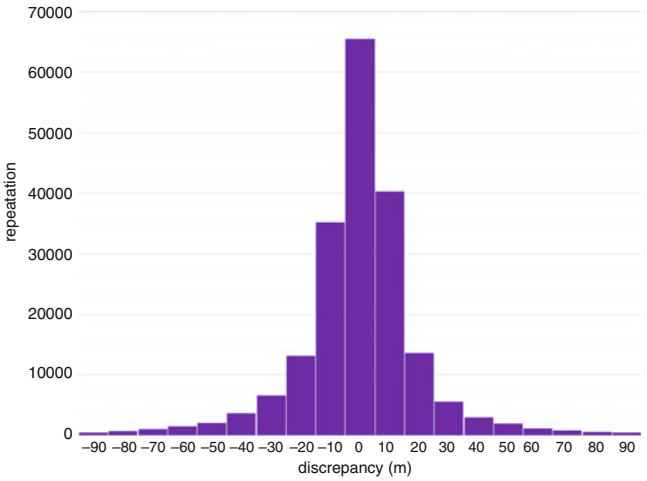

Fig. 12 Histogram of comparing the 3″ × 3″ AFH16S03 with reference-checking data on land

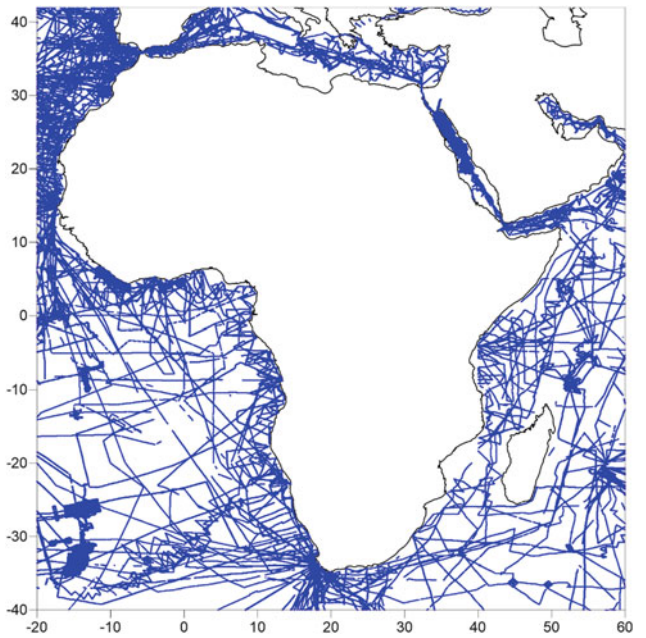

Fig. 13 Distribution of the used reference-checking data points on sea (after Abd-Elmotaal et al. 2015)

shows Gaussian normal distribution with high precision index.

4.3 Comparison with Reference-Checking Data on Ocean

The 3″ × 3″ AFH16S03 DTM has been validated using a set of more than one million data points on ocean. Figure 13 shows the distribution of the used checking data points on sea. This reference-checking data set on sea is the one used for establishing the gravity database for Africa. For details on this data set, the reader may refer to Abd-Elmotaal et al. (2015).

Figure 14 illustrates the differences between the reference-checking data and the 3″ × 3″ AFH16S03 DTM on ocean. The differences between the reference-checking data and their corresponding values of the 3″ × 3″ AFH16S03 DTM on ocean range between −138.5 and 133.1 m with an average of about zero and a standard deviation of 3.6 m. Most of the differences are below 2 m (the white pattern in Fig. 14).

Figure 15 shows a histogram of comparing the 3″ × 3″ AFH16S03 with the reference-checking data on ocean.

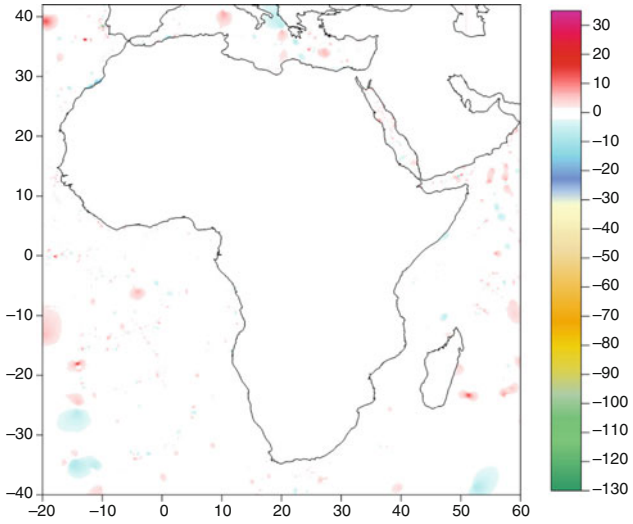

Fig. 14 Differences between reference-checking data and the 3″ × 3″ AFH16S03 DTM on ocean. Units in [m]

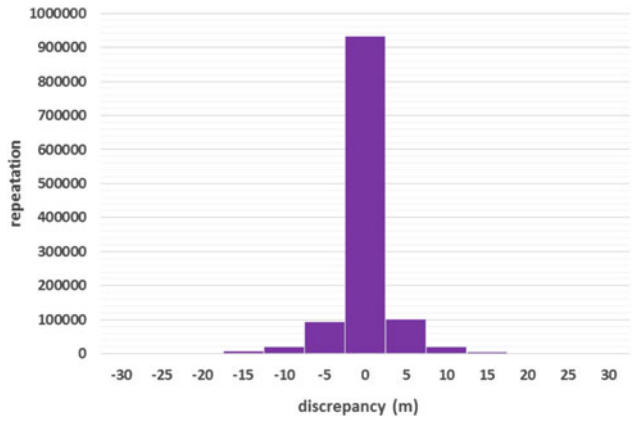

Fig. 15 Histogram of comparing the 3″ × 3″ AFH16S03 with reference-checking data on ocean

Figure 15 shows Gaussian normal distribution with very high precision index.

5 Conclusion

A 3″ × 3″ Digital Terrain Model for Africa and the surrounding marine region covering the window 42°S $\leq \phi \leq$ 44°N, 22°W $\leq \lambda \leq$ 62°E has been created within the current investigation. The process is very laborious and time consuming (handling more than 90 milliard pixels). However, the outputs (a set of DTMs with different resolutions) are very essential in the framework of the geoid determination process of the IAG African geoid project.

The developed DTM has been compared with the available point reference-checking data on both ocean and land. The created 3″ × 3″ DTM has been compared with the available point reference-checking data on land areas for a set of about 200 thousands points. Differences follow perfectly the Gaussian normal distribution. Most differences are below 20 m. The created 3″ × 3″ DTM has been compared with the available point reference-checking data on ocean areas for a set of more than one million points. Differences follow perfectly the Gaussian normal distribution. Most differences are below 2 m.

The created DTM has been tested with respect to the 30″ × 30″ AFH13S30. The new model shows enhancements mainly on land areas.

Acknowledgements This project was supported financially by the Science and Technology Fund (STDF), Egypt, Grant No. 7944. The support by the International Association of Geodesy (IAG) and the International Union of Geodesy and Geophysics (IUGG) is kindly acknowledged. The authors would like to thank the editor of the current paper and two anonymous reviewers for their useful comments.

References

Abd-Elmotaal HA (1999) The EGHA99 digital height models for Egypt. In: Proceedings of the 1st Minia international conference for advanced trends in engineering, Minia, 14–16 March 1999, vol 1, pp 205–211

Abd-Elmotaal HA (2004) The AFH04 digital height models for Africa. In: IAG international symposium on gravity, geoid and space missions "GGSM2004", Porto, 30 August–3 September 2004. www.minia.edu.eg/Geodesy/afrgeo/afdhm04.pdf

Abd-Elmotaal HA (2011) The new Egyptian height models EGH10. NRIAG J Geophys Special Issue:249–261

Abd-Elmotaal HA, Abd-Elbaky M, Ashry M (2013) 30 meters digital height model for Egypt. In: VIII Hotine-Marussi symposium, Rome, 17–22 June 2013

Abd-Elmotaal HA, Seitz K, Kühtreiber N, Heck B (2015) Establishment of the gravity database AFRGDB_V1.0 for the African Geoid. Int Assoc Geod Symp 144:131–141. doi:10.1007/1345_2015_51

Ackermann F (1979) The accuracy of digital height models. Photogramm Week 1979:133–144

Becker JJ, Sandwell DT, Smith WHF, Braud J, Binder B, Depner J, Fabre D, Factor J, Ingalls S, Kim SH, Ladner R, Marks K, Nelson S, Pharaoh A, Sharman G, Trimmer R, vonRosenburg J, Wallace G, Weatherall P (2009) Global bathymetry and elevation data at 30 Arc seconds resolution: SRTM30_PLUS. Mar Geod 32(4):355–371. doi:10.1080/01490410903297766

Buyuksalih G, Jacobsen K (2008) Digital height models in mountainous regions based on space information. In: EARSel workshop remote sensing-new challenges of high resolution, Bochum. www.ipi.uni-hannover.de/uploads/tx_tkpublikationen/DEM_Mountain_Bochum2008.pdf

Jacobsen K (2005) DEMs based on space images versus SRTM height models. In: ASPRS annual convention Baltimore. ftp://ftp.ecn.purdue.edu/jshan/proceedings/asprs2005/Files/0069.pdf

Moritz H (1980) Advanced physical geodesy. Herbert Wichmann, Karlsruhe

Nikolakopoulos KG, Kamaratakis EK, Chrysoulakis N (2006) SRTM vs ASTER elevation products. Comparison for two regions in Crete, Greece. Int J Remote Sens 27(21):4819–4838

Passini R, Jacobsen K (2007) Accuracy analysis of SRTM height models. In: Proceedings of 2007 American society for photogrammetry and remote sensing annual conference, Tampa, vol 711, pp 25–29

Rabus B, Eineder M, Roth A, Bamler R (2003) The shuttle radar topography mission – new class of digital elevation models acquired by spaceborne radar. ISPRS J Photogramm Remote Sens 57(4):241–262. doi:10.1016/S0924-2716(02)00124-7

Rexer M, Hirt C (2014) Comparison of free high resolution digital elevation data sets (ASTER GDEM2, SRTM v2. 1/v4. 1) and validation against accurate heights from the Australian national gravity database. Aust J Earth Sci 61(2):213–226

Smith WH, Sandwell DT (1997) Measured and estimated seafloor topography. In: National geophysical data center, NOAA. http://www.ngdc.noaa.gov/mgg/fliers/97mgg03.html

Stein ML (2012) Interpolation of spatial data: some theory for Kriging. Springer Science and Business Media, New York

Evaluation of the African Gravity Database AFRGDB_V1.0

Hussein A. Abd-Elmotaal, Kurt Seitz, Norbert Kühtreiber, and Bernhard Heck

Abstract

The AFRGDB_V1.0 gravity database has been generated in 2015 from a set of land, shipborne and altimetry-derived gravity anomalies. This gravity data set had significantly large gaps especially on land. Recently, a new gravity data set on land became available. Most of the points of the new data set are located on the large gaps of the data set used to establish the AFRGDB_V1.0 gravity database. This enables an external check of the AFRGDB_V1.0 gravity database at those new data points. An internal validation of the AFRGDB_V1.0 gravity database has been also carried out. The results show that the AFRGDB_V1.0 has an internal precision of about 9 mgal and external accuracy of about 16 mgal.

Keywords

Africa • Geoid determination • Gravity • Harmonic analysis • Tailored geopotential models

1 Introduction

The African gravity database AFRGDB_V1.0 (Abd-Elmotaal et al. 2015b) has been created from the available gravity data set in Africa in 2015. That gravity data set contained significantly large gaps. An underlying grid was used at these large gaps to minimize the free mobility of the solution. As the interpolation errors are inversely proportional to the degree of smoothness of the field, the used approach aimed to obtain a residual gravity field as smooth as possible. The used underlying grid was computed employing a tailored geopotential model for Africa developed in the process of establishing the gravity database. The developed tailored geopotential model for Africa has been suggested because the existing global models don't generally fit the African gravity field with reasonable accuracy (cf. Abd-Elmotaal 2015).

Recently, a new gravity data set on land has become available by the Bureau Gravimétrique International (BGI). This gravity set is located mainly at the very large data gaps of the previously available data set used to generate the AFRGDB_V1.0 gravity database. Accordingly, this new data set has been employed to externally validate the AFRGDB_V1.0 gravity database. Hence, the main objective of the current investigation is to evaluate the somewhat lengthy technique used to fill in the large data gaps in the old data set. The paper also provides the internal validation of the AFRGDB_V1.0 gravity database.

The data set used to generate the AFRGDB_V1.0 gravity database is illustrated. The approach employed to establish the AFRGDB_V1.0 gravity database is summarized. The

H.A. Abd-Elmotaal (✉)
Faculty of Engineering, Civil Engineering Department, Minia University, Minia, Egypt
e-mail: abdelmotaal@lycos.com

K. Seitz • B. Heck
Geodetic Institute, Karlsruhe Institute of Technology, Englerstrasse 7, 76128 Karlsruhe, Germany
e-mail: kurt.seitz@kit.edu, bernhard.heck@kit.edu

N. Kühtreiber
Institute of Geodesy, Graz University of Technology, Steyrergasse 30, A-8010 Graz, Austria
e-mail: norbert.kuehtreiber@tugraz.at

G. S. Vergos et al. (eds.), *International Symposium on Gravity, Geoid and Height Systems 2016*, International Association of Geodesy Symposia 148, DOI 10.1007/1345_2017_16

recent new data set is shown. The internal and external validation of the AFRGDB_V1.0 gravity database is carried out and discussed.

It should be noted that Merry et al. (2005) have carried out the first attempt to compute the African geoid model. For that geoid computation attempt, a $5' \times 5'$ gravity anomaly grid developed at Leeds University was used. Unfortunately, this data set is not available anymore.

2 Data Used to Generate the AFRGDB_V1.0 Gravity Database

The AFRGDB_V1.0 gravity database has been established based on point gravity data on land as well as shipborne and altimetry-derived gravity anomalies in sea regions. These data sets are described below.

2.1 Land Data

The available land gravity data set used for generating the AFRGDB_V1.0 gravity database consists of 96,472 gravity data points. Figure 1a shows the distribution of the land data set. It illustrates that the land data contain very large data gaps. A smart gross-error detection scheme has been carried out on the land data set (Abd-Elmotaal and Kühtreiber 2014). That gross-error detection scheme uses the least-squares prediction technique (Moritz 1980). The gross-error detection technique estimates first the gravity anomaly value at the computational point using the values of the surrounding stations excluding the computational point. Comparing the estimated and data values defines a possible gross-error. Accordingly, the effect of the computational point on the surrounding stations is examined. Data points which show a real gross-error behaviour are removed from the database. The free-air gravity anomalies on land range between −624.5 and 452.8 mgal with an average of about 1.9 mgal and a standard deviation of 60.7 mgal.

2.2 Shipborne Data

The available shipborne gravity data set used for generating the AFRGDB_V1.0 gravity database consists of 971,945 gravity data points. Figure 1b shows the distribution of the shipborne gravity data used for generating the AFRGDB_V1.0 gravity database. It illustrates a better distribution than that of the land data. The remaining gaps of the shipborne data are filled with the altimetry-derived gravity anomalies. A gross-error detection approach developed by Abd-Elmotaal and Makhloof (2013) has been carried out on the shipborne data set. This approach is based on the least-squares prediction technique (Moritz 1980). It estimates the gravity anomaly value at the computational point using the values of the surrounding stations excluding the computational point. Hence, a comparison between the estimated and data values is used to define a possible blunder. The gross-error technique works in an iterative scheme till the standard deviation of the discrepancy between the data and estimated values is less than 1.5 mgal. The shipborne free-air gravity anomalies range between −238.3 and 364.8 mgal with an average of about −6.5 mgal and a standard deviation of 40.4 mgal.

2.3 Altimetry Data

The available altimetry-derived gravity anomaly data set, which was constructed from the average of 44 repeated

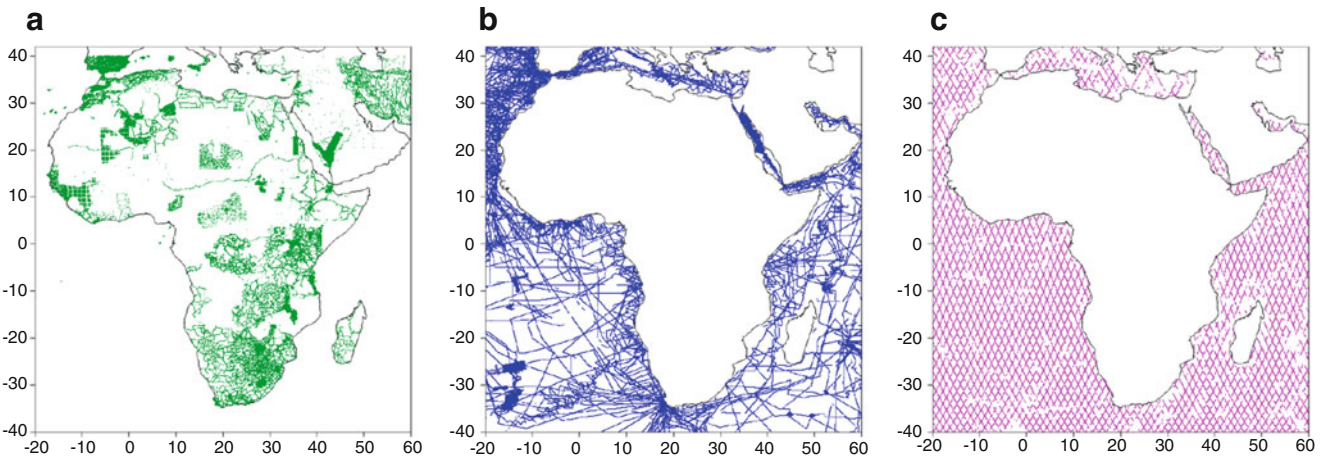

Fig. 1 Distribution of the (**a**) land, (**b**) shipborne and (**c**) altimetry African free-air gravity anomalies used to generate the AFRGDB_V1.0 gravity database

cycles of GEOSAT by the National Geophysical Data Center NGDC (www.ngdc.noaa.gov), used for generating the AFRGDB_V1.0 gravity database consists of 119,249 gravity data points. Figure 1c shows the distribution of the available altimetry data. It illustrates, more or less, a regular distribution. A similar gross-error detection technique to that applied on the shipborne data was carried out. As stated earlier, a combination between the shipborne and altimetry data took place (Abd-Elmotaal and Makhloof 2014). This combination causes some gaps along altimetry tracks when the altimetry data don't match with the shipborne data (cf. Fig. 1c). The altimetry free-air gravity anomalies range between −172.2 and 172.7 mgal with an average of 4.0 mgal and a standard deviation of 18.6 mgal.

3 The AFRGDB_V1.0 Gravity Database

This section gives a brief description on the methodology used to establish the AFRGDB_V1.0 gravity database. For more detailed information, one may refer to Abd-Elmotaal et al. (2015b).

The AFRGDB_V1.0 has been established employing a weighted least-squares prediction technique (Moritz 1980; Kraiger 1988). As the used data set suffers from very large gaps, especially on land (cf. Fig. 1), and in order not to let the solution be free on those gaps, an underlying grid has been used to fill in these gaps with a resolution of $30' \times 30'$. This underlying grid has been created using a high-degree tailored geopotential model for Africa. The high-degree tailored geopotential model has been created in the framework of the window remove-restore technique (Abd-Elmotaal and Kühtreiber 2003). Readers who are interested in computing tailored geopotential models, may refer, e.g., to Weber and Zomorrodian (1988), Wenzel (1998), Abd-Elmotaal (2007, 2014), Abd-Elmotaal et al. (2015a).

The tailored geopotential model for Africa is established within an iterative process. This iterative process works in such a way that in each iteration step the data gaps are filled with a $30' \times 30'$ grid computed by the tailored geopotential model generated at the previous iteration step. The weighted least-squares prediction technique is thus performed to estimate gridded gravity anomalies, which are used to compute a new tailored geopotential model. The estimation of the tailored model has been made and controlled using two harmonic analysis techniques; the FFT technique (Abd-Elmotaal 2004) and the least-squares technique (Heck and Seitz 1991). The iterative process is terminated when the solution stabilizes, i.e., when two successive tailored models give practically the same results. The latest tailored geopotential model has thus been used to generate the final underlying grid. Accordingly, a weighted least-squares prediction technique using all data types took place to establish the AFRGDB_V1.0 gravity database for Africa. The following standard deviations have been used: $\sigma_{land} = 1$ mgal, $\sigma_{shipborne} = 3$ mgal, $\sigma_{altimetry} = 5$ mgal, $\sigma_{underlying\ grid} = 10$ mgal.

4 The New Data Set on Land

Recently a new data set on land has been made available by the Bureau Gravimétrique International (BGI). BGI has collected data from different sources and different authors. Such detailed meta-data information is unfortunately not available for us. The new data set consists of 33,971 gravity data points. There is no overlap between the old and the new data sets on land. The free-air gravity anomalies for the new data set range between −148.4 and 453.6 mgal with an average of about 4.9 mgal and a standard deviation of 28.3 mgal. Figure 2 shows the distribution of the new gravity data set on land for Africa. The source of most of the old land data set as well as the new land data set is the BGI. Hence, the quality of the old and new land data is almost the same. Comparing Figs. 2 and 1a shows that most of the new data points are located in the very large data gaps (especially at West Africa) of the old data set used for generating the AFRGDB_V1.0 gravity database. This enables the comparison at those data points between the new data and the AFRGDB_V1.0 database, to measure the external accuracy of the AFRGDB_V1.0 gravity database.

The new data set doesn't, unfortunately, have further information on the age of the data, etc. A gross-error detection technique, similar to that implemented on the old land data set and described in Abd-Elmotaal and Kühtreiber (2014), has been carried out.

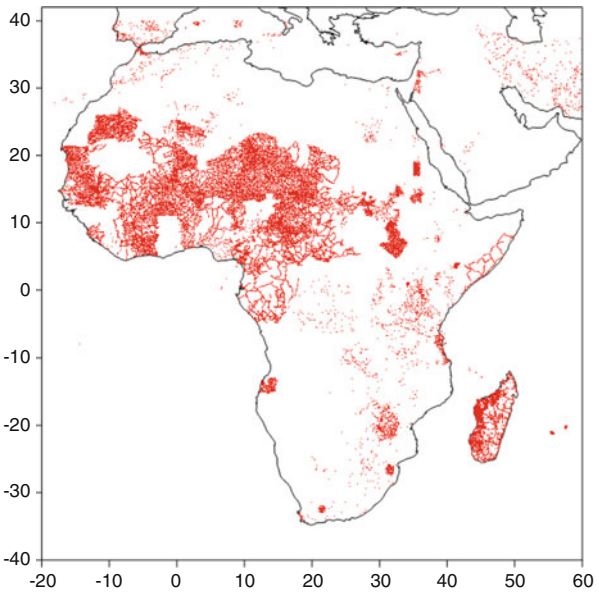

Fig. 2 The distribution of the new gravity data set on land for Africa

5 Validation of the AFRGDB_V1.0 Gravity Database

The validation of the AFRGDB_V1.0 gravity database, which is available on a $5' \times 5'$ grid, is made at two levels; at the new data points, which measures the external accuracy of the AFRGDB_V1.0 database (as described in Sect. 4), and at the old data points on land, which measures an internal accuracy of the AFRGDB_V1.0 database.

5.1 External Validation

Figure 3 illustrates the differences at the new data points on land between the new data and the AFRGDB_V1.0 gravity database values. The white pattern indicates differences below 10 mgal in magnitude. These differences range between −82.7 and 82.5 mgal with an average of about 3.2 mgal and a standard deviation of 16.3 mgal. This indicates that the external accuracy of the AFRGDB_V1.0 is about 16 mgal, which is rather a very good value compared to the very large gaps in the land gravity data set used to generate the AFRGDB_V1.0 gravity database.

In order to give a deeper look inside the external check, Fig. 4 is introduced. It illustrates again the differences at the new data points on land between the new data and the AFRGDB_V1.0 gravity database values, with the white pattern indicating differences below 40 mgal in magnitude. It shows that only 3.2% of the new data points have differences to the AFRGDB_V1.0 gravity database larger than 40 mgal in magnitude. Comparing Figs. 1a and 4 shows that most of these somewhat large differences occur at the large data gaps of the old land data set. Accordingly, Figs. 3 and 4 prove

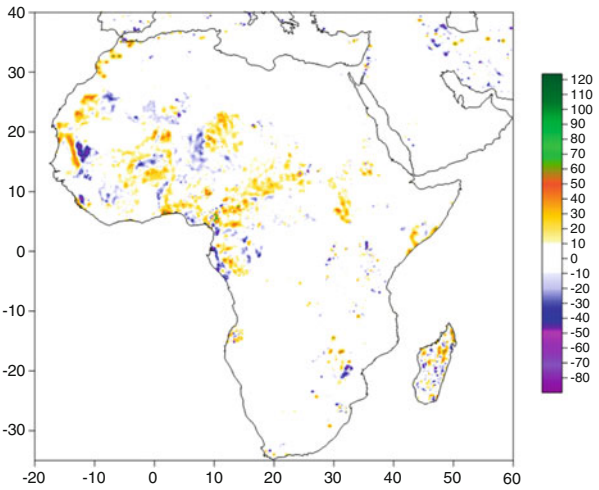

Fig. 3 External validation of the AFRGDB_V1.0 gravity data base. Contour interval: 10 mgal

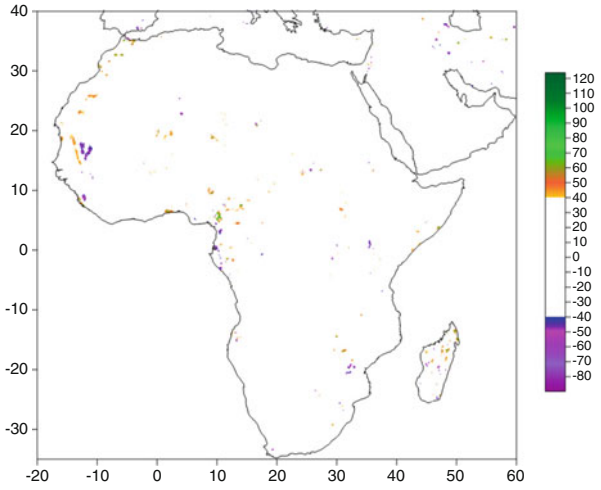

Fig. 4 External validation of the AFRGDB_V1.0 gravity data base. Contour interval: 40 mgal

that the procedure used to establish the AFRGDB_V1.0 is successful to a great extent.

It is interesting to compare the discrepancy between the old and new data sets at Madagascar. Figure 4 shows that the large discrepancies (nearly 50 mgal) occur at the northern part of Madagascar, where there are no data in the old land data set (cf. Fig. 1a). Also there are large discrepancies (attaining nearly the same level of 50 mgal) located at the middle part of Madagascar, where both new and old data exist (cf. Figs. 1a and 4). This indicates that both data sets for Madagascar may not match well. This conclusion may also be verified by comparing Figs. 4 and 6, where one sees also relatively large internal discrepancies at the middle part of Madagascar.

Figure 5 shows a histogram of the differences at the new data points on land between the new data and the AFRGDB_V1.0 gravity database values. Figure 5 shows Gaussian normal distribution with high precision index.

5.2 Internal Validation

Figure 6 illustrates the differences at the old data points on land (used to generate the AFRGDB_V1.0 database) between the data and the AFRGDB_V1.0 gravity database values. The white pattern indicates differences below 10 mgal in magnitude. These differences range between −52.8 and 52.5 mgal with an average of about −1.8 mgal and a standard deviation of 8.8 mgal (indicating the internal precision of the AFRGDB_V1.0 gravity database).

Figure 7 shows a histogram of the differences at the old data points on land (used to establish the AFRGDB _V1.0 database) between the data and the AFRGDB_V1.0 gravity database values. Figure 7 shows Gaussian normal

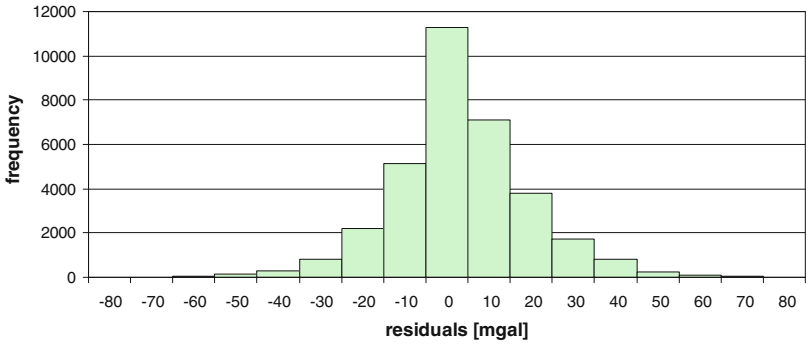

Fig. 5 Histogram of the external validation of the AFRGDB_V1.0 gravity data base on land

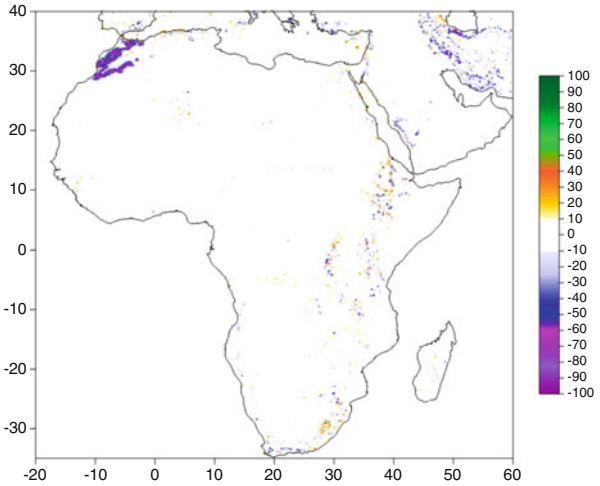

Fig. 6 Internal validation of the AFRGDB_V1.0 gravity data base. Contour interval: 10 mgal

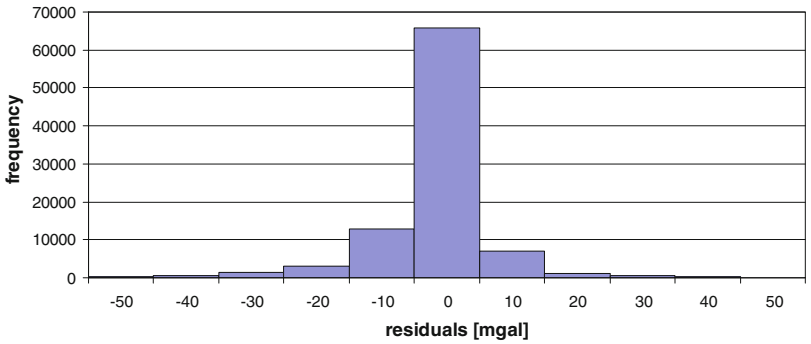

Fig. 7 Histogram of the internal validation of the AFRGDB_V1.0 gravity data base on land

distribution with higher precision index than that of the external accuracy histogram (compare Figs. 5 and 7).

6 Conclusion

The external validation of the AFRGDB_V1.0 database has been carried out in the current investigation. A value of about 16.3 mgal is found as an external accuracy of the AFRGDB_V1.0 at a new data set located mainly within the very large gaps of the data set used to generate the AFRGDB_V1.0 gravity database. This already proves that the approach used to generate the AFRGDB_V1.0 database was successful to a satisfactory extent, especially in view of the fact that the data set used to generate the AFRGDB_V1.0 had very large gaps on land.

A test of the internal precision of the AFRGDB_V1.0 gravity database on land has been performed. The results proved that the precision of the AFRGDB_V1.0 gravity database on land is about 8.8 mgal.

Acknowledgements This project was supported financially by the Science and Technology Fund (STDF), Egypt, Grant No. 7944. The authors would like to thank Dr. Sylvain Bonvalot, Director of the Bureau Gravimétrique International (BGI), for providing the new data set for Africa. The support by the International Association of Geodesy (IAG) and the International Union of Geodesy and Geophysics (IUGG) is kindly acknowledged. The authors would like to thank the editor of the current paper and two anonymous reviewers for their useful comments.

References

Abd-Elmotaal HA (2004) An efficient technique for harmonic analysis on a spheroid (ellipsoid and sphere). VGI 3(4):126–135

Abd-Elmotaal HA (2007) Reference geopotential models tailored to the Egyptian gravity field. Boll Geod Sci Affini 66(3):129–144

Abd-Elmotaal HA (2014) Egyptian geoid using ultra high-degree tailored geopotential model. In: Proceedings of the 25th International Federation of Surveyors FIG Congress, Kuala Lumpur, Malaysia, 16–21 June 2014. www.fig.net/pub/fig2014/papers/ts02a/TS02A_abd-elmotaal_6856.pdf

Abd-Elmotaal HA (2015) Validation of GOCE models in Africa. Newton's Bull 5:149–162

Abd-Elmotaal HA, Kühtreiber N (2003) Geoid determination using adapted reference field, seismic Moho depths and variable density contrast. J Geod 77(1–2):77–85

Abd-Elmotaal HA, Kühtreiber N (2014) Automated gross error detection technique applied to the gravity database of Africa. In: General Assembly of the European Geosciences Union, Vienna, Austria, 27 April–2 May 2014

Abd-Elmotaal HA, Makhloof A (2013) Gross-errors detection in the shipborne gravity data set for Africa. Geodetic Week, Essen, Germany, 8–10 October 2013. www.uni-stuttgart.de/gi/research/Geodaetische_Woche/2013/session02/Abd-Elmotaal-Makhloof.pdf

Abd-Elmotaal HA, Makhloof A (2014) Combination between altimetry and shipborne gravity data for Africa. In: 3rd International Gravity Field Service (IGFS) General Assembly, Shanghai, China, 30 June–6 July 2014

Abd-Elmotaal HA, Seitz K, Abd-Elbaky M, Heck B (2015a) Tailored reference geopotential model for Africa. International Association of Geodesy Symposia 143:383–390. doi:10.1007/1345_2015_84

Abd-Elmotaal HA, Seitz K, Kühtreiber N, Heck B (2015b) Establishment of the gravity database AFRGDB_V1.0 for the African geoid. In: International Association of Geodesy Symposia, vol. 144. doi:10.1007/1345_2015_51

Heck B, Seitz K (1991) Harmonische Analyse. Technical Report, Geodetic Institute, University of Karlsruhe

Kraiger G (1988) Influence of the curvature parameter on least-squares prediction. Manuscr Geodaet 13(3):164–171

Merry C, Blitzkow D, Abd-Elmotaal HA, Fashir H, John S, Podmore F, Fairhead J (2005) A preliminary geoid model for Africa. In: A Window on the Future of Geodesy. Springer, Berlin, pp 374–379

Moritz H (1980) Advanced physical geodesy. Wichmann, Karlsruhe

Weber G, Zomorrodian H (1988) Regional geopotential model improvement for the Iranian geoid determination. Bull Geod 62:125–141

Wenzel H (1998) Ultra high degree geopotential models GPM98A, B and C to degree 1800 tailored to Europe. Reports of the Finnish Geodetic Institute 98(4):71–80

New Absolute Gravity Measurements in New Zealand

Yoichi Fukuda, Hiroshi Takiguchi, Takahito Kazama, Jun Nishijima, Sergei Gulyaev, Tim Natusch, Matt Amos, Vaughan Stagpoole, and Christopher Pearson

Abstract

To enhance and extend the absolute gravity (AG) measurements in New Zealand, we conducted new measurements using a FG5 (#210 of Kyoto University) in January and March 2016. The measurements in the North Island were made at two existing points (the Warkworth Radio Astronomical Observatory and Wellington A) and at one newly established point at the Wairakei Research Centre, Taupo. The gravity measurements in the South Island were made at five existing AG points; Godley Head, Mt John, the University of Otago, Helipad and Bealey Hotel. At each point more than 4,000 drops were made and AG values were determined with measurement uncertainties better than 3 μGal (mostly better than 2 μGal) at 130 cm instrument height. The values are compared with those of the 2015 campaigns. Although the differences of about 10 μGal were observed at Wellington A and Godley Head, those at the other points were within 5 μGal. At points in the Southern Alps we combined AG with relative gravity measurements and achieved good agreement with the 2015 results. Definite values for long-term gravity trends at the points in Southern Alps and Christchurch could not be obtained from the survey, but the results are consistent with those of the previous studies. Further measurements are planned to accurately determine these gravity changes.

Keywords

Absolute gravity measurements • Gravity changes • Gravity network

1 Introduction

Precise gravity measurements play a basic role in providing information about the Earth's gravity field, i.e., mass distribution of the Earth. Absolute gravity (AG) measurements in particular can provide long-term stable references for monitoring the time variations of the gravity field because the AG measurements only depend on the basic physical standards of length and time (Faller and Marson 1988). From this point

Y. Fukuda (✉) • T. Kazama
Graduate School of Science, Kyoto University, Kyoto, Japan
e-mail: fukuda@kugi.kyoto-u.ac.jp

H. Takiguchi
Satellite Navigation Unit, Japan Aerospace Exploration Agency, Tsukuba, Japan

J. Nishijima
Department of Earth Resources Engineering, Kyushu University, Fukuoka, Japan

S. Gulyaev • T. Natusch
Institute for Radio Astronomy and Space Research, Auckland University of Technology, Auckland, New Zealand

M. Amos
Land Information New Zealand, Wellington, New Zealand

V. Stagpoole
Institute of Geological and Nuclear Science, Lower Hutt, New Zealand

C. Pearson
School of Surveying, University of Otago, Dunedin, New Zealand

G. S. Vergos et al. (eds.), *International Symposium on Gravity, Geoid and Height Systems 2016*, International Association of Geodesy Symposia 148, DOI 10.1007/1345_2017_18

of view, local or regional AG control have been desired, proposed and established in many countries or regions (e.g., Pujol 2005; Ayhan et al. 2015). Moreover, a portable absolute gravimeter (A10) has recently been employed to enhance and extend the AG control in several regions. For instance, Falk et al. (2012) conducted AG measurements in Germany using A10 at more than 200 field control points. Dykowski et al. (2014) also used A10 for establishing the gravity control in Poland.

In New Zealand (NZ), all the AG measurements made so far have been carried out using gravimeters from abroad in collaboration with foreign organizations. The first AG measurements in NZ were carried out in October 1995 at Godley Head, near Christchurch, using the FG5 #102 of the National Oceanic and Atmospheric Administration (NOAA), which was on the way to McMurdo Station in Antarctica (Sasagawa 1996). Since then AG measurements at Godley Head have been occasionally repeated by United States, Danish and French groups, usually en route to Antarctica. One notable campaign of AG measurements was conducted by a group from the University of Colorado and the University of Otago using the FG5 #111. They made a series of measurements across the NZ Southern Alps in 2000 and reoccupied the points in 2015 with the aim of studying the formation mechanism of the mountains (Bilham et al. 2000; Bilham et al. 2016, hereinafter referred to as BH2016). In February 2015, Institute of Geological and Nuclear Science (GNS) and Land Information New Zealand (LINZ), collaborating with Geoscience Australia, carried out AG measurements using the FG5 #237 from Australian National University at three existing AG points in South Island and five newly established points in North Island (Stagpoole et al. 2015, hereinafter referred to as SP2015). These were the first AG measurements in North Island, and contributed to establishing AG control in NZ.

To enhance and extend these measurements, we conducted new AG measurements using the FG5 #210 of Kyoto University in January and March, 2016. Since the main purpose of the measurements was to monitor the gravity changes, we have conducted the measurements at seven existing points from BH2016 and SP2015. In addition, to confirm the gravity changes obtained by BH2016 we also carried out relative measurements using a LaCoste and Romberg G-meter #680 (L&R G-680) in the Southern Alps. Furthermore, we established one new point at the Wairakei Research Centre, Taupo, mainly for future geothermal studies.

In this paper, we report the outline of the measurements, the values obtained and the results of comparisons with the previous studies.

2 Measurements

2.1 Gravity Points

For the AG measurements in the North Island, we selected two existing points from SP2015, namely Warkworth (WARG) and Wellington A (WELG). WARG is located at Warkworth Radio Astronomical Observatory of Auckland University of Technology (AUT), where VLBI (Very Long Baseline Interferometry) and GNSS (Global Navigation Satellite System) observations are being conducted. The presence of these collocated techniques is the main reason why WARG was recently established by LINZ in 2014. On the other hand, WELG is one of the International Gravity Standardization Net 1971 (IGSN71; Morelli et al. 1974) points, and has often been used as a gravity reference point. Therefore it has been selected as an AG control point by SP2015. In addition to these existing points, we established one additional new point we labeled Wairakei (WRKG) at the Wairakei Research Centre, Taupo. WRKG is located in an active geothermal field, and is expected to serve as a reference point for gravity monitoring in the area.

We conducted the AG measurements in the South Island at Godley Head (AAJB), Dunedin (OUGG), Mt John (MTJG), Helipad (HLPD) and Bealey Hotel (APBH). Among these points, AAJB, OUGG and MTJG were occupied by SP2015, and AAJB, MTJG, HLPD and APBH by BH2016. To supplement the AG measurements, we also made relative measurements between HLPD and Vexation and Leo Creek, and between APBH and Cass, Arthur's Pass and Jackson using L&R G-680. At these points, BH2016 gave the gravity changes for last 15 years. Although the accuracies of the relative measurements were inferior to the AG measurements, the values were independent from the previous results and can be used to confirm the results given by BH2016. The location of these points are depicted in Fig. 1a, b and summarized in Tables 1 and 2.

2.2 Measurements and Data Processing

Prior to the measurements, we exported the FG5 from Japan to NZ in December 2015. Having occasionally experienced instrumental troubles during transportation in the past we prepared for this by setting two periods for the campaign in 2016. The first period was from January 11 to 16 which we dedicated to adjusting the instrument and conducting test measurements in WARG. After the adjustments and tests had been satisfactorily completed the main campaign was

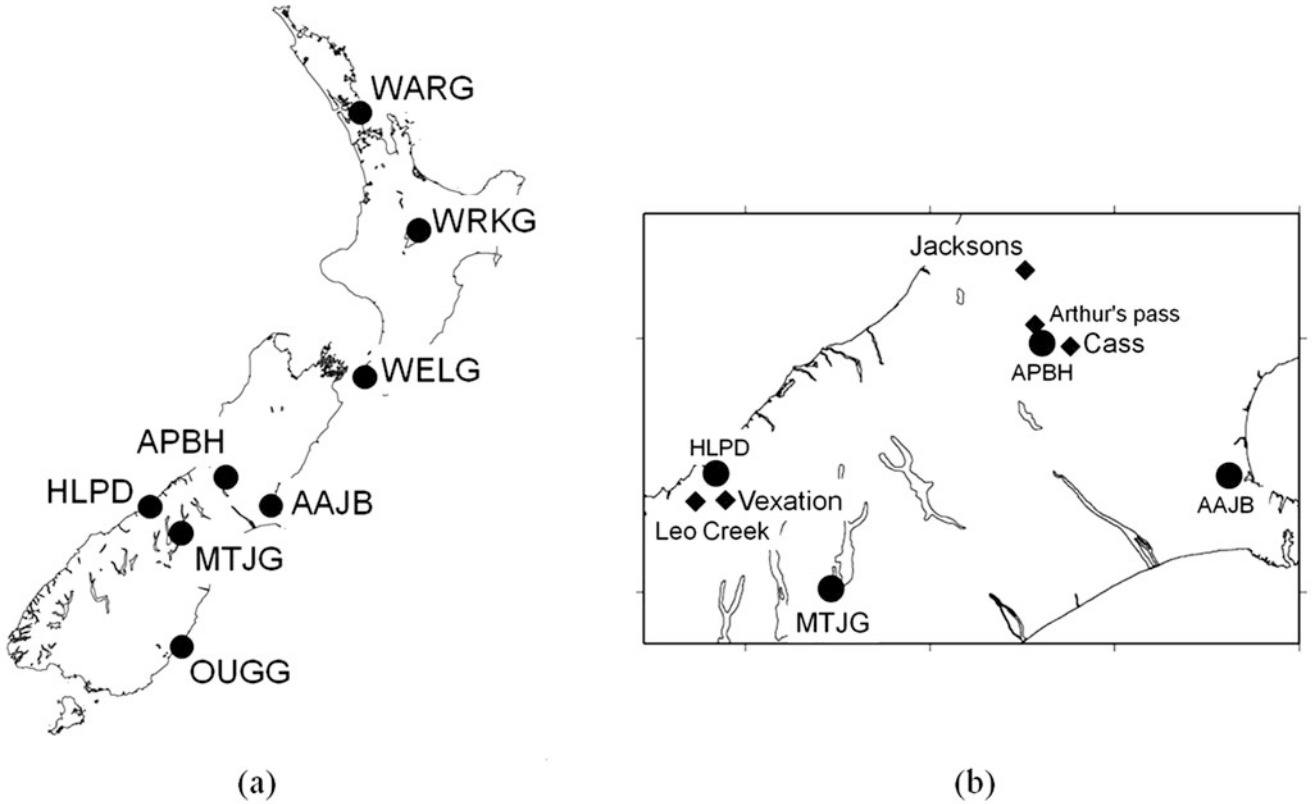

Fig. 1 Location map of the gravity points. (**a**) Absolute gravity points (*filled circles*), (**b**) Gravity points in South Island, where relative gravity measurements were made for points shown with *diamonds*

Table 1 Summary of the absolute gravity measurements

Station	Code	Lat (deg)	Lon (deg)	H (m)	Date (2016)	dg/dh (μGal/cm)	Gravity at 130 cm (μGal)	Total Unc. (μGal)	No. of set[a]
Warkworth[b]	WARG	−36.4345	174.6630	74	Jan 13–15	−3.348	979,885,818.8	1.94	33
					Mar 7	−3.348	979,885,816.2	1.91	26
Wairakei	WRKG	−38.6325	176.0936	375	9–10	−3.267	979,954,815.2	1.98	42
Wellington A[b]	WELG	−41.2842	174.7682	122	11	−2.922	980,250,613.0	1.89	49
Godley Head[b]	AAJB	−43.5882	172.8040	150	13–14	−3.504	980,489,031.4	2.73	59
Mt. John[b]	MTJG	−43.9855	170.4641	1, 025	16–17	−3.878	980,248,422.7	1.88	43
Dunedin[b]	OUGG	−45.8649	170.5152	10	18	−2.748	980,727,169.9	1.86	45
Helipad[c]	HLPD	−43.5340	169.8410	44	20	−2.92	980,439,461.5	1.96	44
Bealey hotel[c]	APBH	−43.0200	171.6100	631	22–23	−2.73	980,261,094.9	1.91	41

[a]One set consists of 100 drops of measurements
[b]Lat, Lon, H and dg/dh values were from SP2015
[c]Lat, Lon, H and dg/dh (3 digits are given) values were from BH2016

Table 2 Summary of the gravity values obtained by the relative measurements

Station	Lat (deg)	Lon (deg)	H (m)	Date (March, 2016)	dg/dh (μGal/cm)	Gravity at 0 cm (μGal)	Errors (μGal)
Vexation	−43.637	169.893	1, 475	20	−4.40	980,132,024	32
Leo Creek	−43.643	169.737	1, 630	20	−5.15	980,188,914	33
Cass	−43.035	171.759	589	22	−3.05	980,272,394	3
Authur's pass	−42.950	171.570	772	22	−2.33	980,229,212	4
Jacksons	−42.747	171.510	250	23	−2.79	980,336,320	9

The reference points are HLPD and APBH, and their AG values are given in Table 1. The locations (Lat, Lon, H) and the dg/dh values were from BH2016

conducted from March 7 to 26. We started from WARG and moved to the other points using a van-type vehicle. At each site, we spent up to 2 days obtaining more than 4,000 drop measurements.

For the AG data processing, we employed the "g9" software (Micro-g LaCoste 2012). The parameters for acquisition were typically 100 drops/set with a set interval of 30 min, and the instrumental corrections and the geophysical corrections (solid tides using Tamura's potential, ocean tides using Schewiderski model, atmospheric pressure with constant admittance of 0.30 μGal/hPa, polar motion using IERS Bulletin B final values) were applied to obtain gravity at 130 cm above the gravity marks. The final AG values were calculated as the weighted average of the set values.

Regarding the vertical gradient of gravity (dg/dh) values, we employed those of SP2015 if available, otherwise using those of Bilham et al. (2000) for HLPD and APBH. Bilham et al. (2000) includes the dg/dh values of −3.60 at AAJB and −3.91 at MGJG, while those of SP2015 are −3.504 and −3.878, respectively. The differences of the values may show a typical dispersion range of the dg/dh determinations. For the newly established point of WRKG, we determined the dg/dh value using the gravity differences at two points about 60 cm height difference measured by L&R G-680 and its estimated accuracies is 0.083 μGal/cm.

The set values at AAJB included large diurnal and semi-diurnal variations of about 30 μGal peak to peak amplitude due to insufficient ocean load corrections. The effect was removed by fitting diurnal and semi-diurnal curves. The difference between the value obtained by the curve fitting and the simple averaged one was 0.13 μGal.

Another note was that the built-in barometer did not work at MTJG, HLPD and APBH due to a bad connection to the PC. For these points, the data of an offline backup barometer were used to calculate the correction values. Fortunately, we obtained both the built-in and the offline barometers data at OUGG and calculated the difference of the correction values. It was less than 0.1 μGal, and thus we think the errors due to the different barometers were negligible.

Relative gravity measurements were conducted at Jacksons, Arthur's Pass and Cass relative to APBH and Vexation and Leo Creek relative to HLPD, as shown in Fig. 1b. Among these, Vexation and Leo Creek are located near the summits, and due to restricted time and weather condition, we only conducted a single loop measurement from and to HLPD using a helicopter. For the other three points the "star method" (Torge 1989) was employed, which repeated the tie measurements between each point and the reference point (APBH). After correcting for solid tide effects, the drift corrections were made by assuming a linear drift because the tie measurements were closed within 3–4 h at the longest. Then the gravity values were determined relative to the nearest AG points, i.e., HLPD or APBH. Because the instrument height of L&R G-meter (about 30 cm) is much lower than that of FG-5 (about 130 cm), the dg/dh values are very important for the comparison with the AG values measured by FG-5. In this study we employed the values of Bilham et al. (2000) for the consistency with the BH2016 values and calculated the gravity values at 0 cm above the marks.

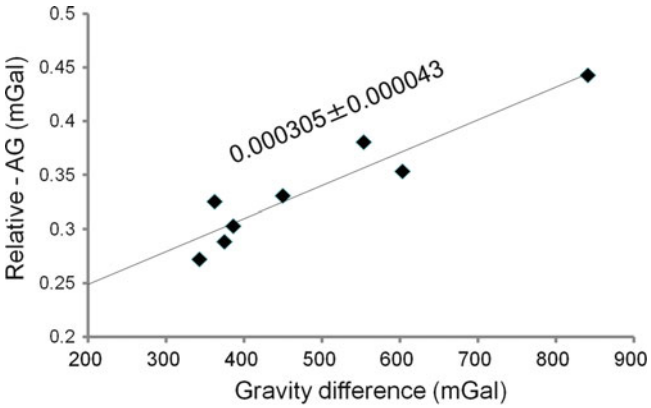

Fig. 2 Estimation of the correction factor for the scale factor table of L&R G-680

For the conversions of the gravity readings to gravity values, we primarily used the scale factor table provided by the manufacturer. It is well known that the scale factor table of L&R G-meters usually contains 10^{-3} to 10^{-4} order of the errors. Because the gravity difference between HLPD and Vexation, for instance, is about 300 mGal, the accuracy of the scale factor should be better than 2–3 × 10^{-5} to obtain 10 μGal accuracy. To estimate the correction factor for the scale factor table of L&R G-680, we made the gravity readings using L&R G-680 at all the AG points. Then we compared the AG gravity differences and the gravity differences calculated using the original scale factor table.

Figure 2 shows the relation between the AG differences (horizontal axis) and those of the relative gravity difference obtained by the original scale factor table minus the AG difference (vertical-axis). As shown in Fig. 2, they show a clear linear trend with the derivative 0.000305 ± 0.000043. Therefore, we estimate the correction factor of 1.000305 for the scale factor table of L&R G-680, and use this value for calculating the final gravity values in Table 2. We did not include the readings at points in Table 2 to determine the correction factor, therefore the values in Table 2 are independent from the previous observations and can be used for the comparisons with the results of BH2016.

3 Results and Discussions

3.1 Gravity Values

Table 1 summarizes the final AG values obtained. To reduce the effects of dg/dh uncertainties, gravity values were calculated at 130 cm above the marks. The "g9" software showed that the total uncertainties at 130 cm were less than 2 μGal at most points, while those at 0 cm were about 4–5 μGal due to the dg/dh uncertainties. The values of the set scatter were also about 2–4 μGal except AAJB where large uncorrected ocean tides caused the set scatter of about 10 μGal as described above. At WARG, we obtained gravity values in January and March. The difference of the two values was 2.6 μGals, which was almost same as the measurement uncertainties.

Table 2 summarizes the gravity values obtained by L&R G-680. Errors (the last column) in the table were the formal errors of least squares fitting assuming a linear drift. Due to the bad weather conditions and the restriction of the schedule, we only conducted a single tie measurement to Vexation and Leo Creek from HLPD. This is the main reason why the errors at these points were large. For other points, the instrumental drift was well controlled, hence the small formal errors. Considering other error sources (e.g., dg/dh), we expect the total uncertainties of these points were 10–20 μGal regardless of the small formal errors.

3.2 Comparisons of the Gravity Values

Tables 3 and 4 summarize the comparisons of this studies gravity values with those of SP2015 and BH2016, respectively. Since SP2015 gave the gravity values at 130 cm above the marks and we employed the same dg/dh values as theirs, the comparisons in Table 3 were straightforward. Although the differences at Wellington A and Godley Head were about 10 μGal, those at the others were less than 5 μGal. We could not find any systematic differences geographically or temporally for the Wellington A and Godley Head differences. Therefore the measurements were basically considered successful and the differences could be due to unidentified local effects, or merely unexpected measurement errors.

Since BH2016 gave the gravity values at 100 cm above the marks, we calculated the values at the same height using the same dg/dh values as theirs. Thus the comparisons of the AG values were almost free from the uncertainties of dg/dh values. Table 4 shows that the differences of the AG values were within ±2.5 μGal. They show the same tendency of the gravity changes observed by BH2016 except for Mt. John. The gravity differences were almost the same as the uncertainties of the measurements. Thus we can say that these differences were not statistically significant.

The lower half of the Table 4 (L&R G-680) shows the comparisons between the gravity values obtained by the relative measurement from the AG points of HLPD and

Table 3 Comparisons of the absolute gravity values from this study with those of SP2015

Station	dg/dh (μGal/cm)	This study (μGal) (FG-5#210)	SP2015 (μGal) (FG-5 #237)	Dif. (μGal)
Warkworth (January)	3.348	979,885,818.8	979,885,816.0	2.9
Warkworth (March)	3.348	979,885,816.2	979,885,816.0	0.2
Wellington A	2.922	980,250,613.0	980,250,624.5	−11.5
Godley Head	3.504	980,489,031.5	980,489,039.7	−8.1
Mt. John	3.878	980,248,422.7	980,248,427.0	−4.3
Dunedin	2.748	980,727,169.9	980,727,170.1	−0.2

The values were given at 130 cm above the marks

Table 4 Comparisons of the gravity values from this study with those of BH2016

Station	dg/dh (μGal/cm)	This study (μGal) (FG-5 #210)	BH2016 (μGal) (FG-5 #111)	Dif. (μGal)
Godley Head	−3.60	980,489,139.5	980,489,141.3	−1.8
Mt. John	−3.91	980,248,539.0	980,248,537.8	2.2
Helipad	−2.92	980,439,549.1	980,439,547.8	1.3
Bealey hotel	−2.73	980,261,176.8	980,261,179.3	−2.5
		(L&R G-680)		
Vexation	−4.40	980,131,584.2	980,131,588.3	−4.1
Leo Creek	−5.15	980,188,398.9	980,188,379.1	19.8
Cass	−3.05	980,272,088.8	980,272,100.3	−11.5
Authur's pass	−2.33	980,228,979.4	980,228,990.7	−11.3
Jacksons	−2.79	980,336,041.3	980,336,044.0	−2.7

The values were given at 100 cm above the marks

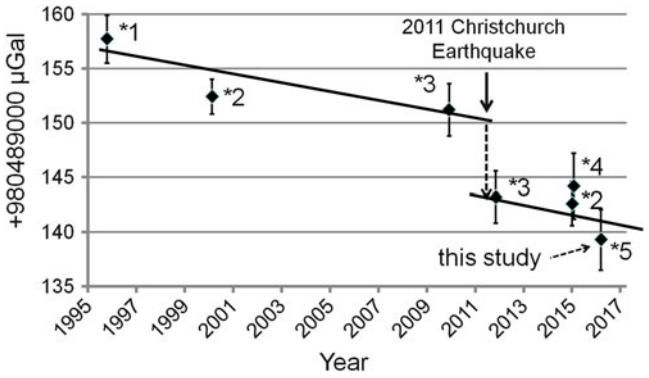

Fig. 3 Gravity changes at AAJB (Godley Head). FG5 employed for the measurements are *1: #102, *2:#111, *3:#206, *4:#237 and *5:#210

APBH with those of BH2016. Again the gravity values at 100 cm above the marks were calculated from the values in Table 2 with the dg/dh values shown in the Table 4.

The differences of the comparisons (the last column) show the gravity decreases except Leo Creek (19.8 μGal). BH2016 showed the gravity decreased at these points due to uplift, our results are basically consistent with that of BH2016, though the observed gravity changes are of the same order of magnitude as the uncertainties of the relative measurements.

3.3 Gravity Changes at Godley Head

Godley Head has the longest history of AG measurements in NZ but we note that the site was subject to the 2011 Christchurch Earthquake. BH2016 discussed the secular gravity trend and the gravity changes due to the earthquake. Figure 3 was reproduced from Fig. 4 and Table 3 of BH2016 including our newly observed value. Since the gravity values after the earthquake suggested no significant gravity trend, BH2016 argued that the gravity trend before 2010 was also small if the first value of 1995 was excluded. However, as shown in Fig. 3, inclusion of our value in 2016 suggested the same trend before and after the earthquake. Because the amount of gravity change was small, further measurements are required to confirm any secular trend.

4 Conclusions

We successfully conducted new AG measurements in NZ at eight points; five in the South Island, and three in the North Island including one newly established point. The AG values at the existing points were in good agreement with those of the 2015 measurements (SP2015; BH2016). This indicates that the new measurements have contributed to an improvement in the reliability of the AG control in NZ. Regarding the gravity changes in Southern Alps and at Godley Head, our values are in line with those observed by BH2016. We conclude, however, that more AG observations are required over a longer period to reveal the gravity trends with certainty.

Generally speaking, AG measurements are more accurate than measurements with relative meters. Thus AG measurements, even in a field environment, would be preferable for obtaining the most accurate measurements. Although BH2016 conducted AG measurements in Southern Alps successfully using a FG5 meter, these are logistically and technically difficult and can be much more time consuming than using a relative meter. An alternative is the use of an A10 gravity meter, as has been employed for various purposes (e.g., Nielson 2012; Fukuda et al. 2016), however an A10 was not available for the survey described here. Instead, we combined the AG and relative measurements. With careful determination of a correction factor for the relative meter and accurate dg/dh values, the gravity obtained is generally in good agreement with those of BH2016, although further improvements in the accuracies of measurements for the points located on the mountains could be obtained with more relative observations. Because combined the AG and relative measurements are much easier to conduct, this method can be used for the future measurements as well.

Acknowledgements This research was partially supported by JSPS KAKENHI Grant Number 15H05205. Prof. Roger Bilham of Colorado University provided us useful information about the gravity measurements in South Alps. The gravity measurements were supported by many colleagues and staffs of Canterbury University, University of Otago, GNS Science, Auckland University of Technology and other institutions. We thank all those who were involved in this research.

References

Ayhan ME, Al-Muslmani BSA, Kanney J, Al-Kherayef OAI (2015) Absolute gravity measurements by using FG5 and A10 absolute gravimeters in the Kingdom of Saudi Arabia. Arab J Geosci 8:6199. doi:10.1007/s12517-014-1593-6

Bilham R, Crawford R, Niebauer T (2000) Gravity measurements in South Island New Zealand February 2000. Report prepared for Land Information New Zealand

Bilham R, Niebauer T, Pearson C, Molnar P (2016) Changes in absolute gravity 2001–2015, South Island, New Zealand. N Z J Geol Geophys 59:176–186. doi:10.1080/00288306.2015.1108922

Dykowski P, Krynski J, Sekowski M (2014) Testing the suitability of the A10-020 absolute gravimeter for the establishment of new gravity control in Poland. IAG Symp 141:11–17. doi:10.1007/978-3-319-10837-7_2

Falk R, Ja M, Lux N, Wilmes H, Wziontek H (2012) Precise gravimetric surveys with the field absolute gravimeter A-10. IAG Symp 136:273–279. doi:10.1007/978-3-642-20338-1_33

Faller JE, Marson I (1988) Ballistic methods of measureing g – the direct free-fall and symmetrical rise-and-fall methods compared. Metrologia 25:49–55

Fukuda Y, Nishijima J, Sofyan Y, Taniguchi M, Yusuf M, Abidin HZ (2016) Application of A10 absolute gravimeter for monitoring land subsidence in Jakarta, Indonesia. IAG Symp 145:127. doi:10.1007/1345_2016_221

Micro-g LaCoste (2012) g9 user's manual. www.microglacoste.com

Morelli C, Gantar C, Honkasalo T, McConnell RK, Tanner JG, Szabo B, Uotila U, Whalen CT (1974) The International Gravity Standardization Net 1971 (I.G.S.N.71). Bull Géod 4:1–194

Nielson JE (2012) New Zealand A10 measurements 2011. Technical note prepared for Land Information New Zealand

Pujol E (2005) Absolute gravity network in Spain. Fís Tierra 17:147–163

Sasagawa G (1996) Absolute gravity observations at Godley Head, New Zealand. Report prepared for Land Information, New Zealand, 10 p

Stagpoole VM, Dando N, Caratori Tontini F, Black J, Amos M (2015) Absolute gravity observations at principal New Zealand stations 2015. GNS Science, Lower Hutt. GNS Science report 2015/46 iii, 48 p

Torge W (1989) Gravimetry. Walter De Gruyter, Berlin, 482 p

Strapdown Airborne Gravimetry Using a Combination of Commercial Software and Stable-Platform Gravity Estimates

Tim E. Jensen, J. Emil Nielsen, Arne V. Olesen, and Rene Forsberg

Abstract

For the past two decades, airborne gravimetry using a Strapdown Inertial Measurement Unit (SIMU) has been producing gravity estimates comparable to the traditional stable-platform single-axis gravimeters. The challenge has been to control the long term drift of the IMU sensors, propagating into the long-wavelengths of the gravity estimates. This has made the stable-platform approach the preferred method for geodetic applications. In the summer of 2016, during a large airborne survey in Malaysia, a SIMU system was flown alongside a traditional LaCoste&Romberg (LCR) gravimeter. The SIMU observations were combined with GNSS observations using the commercial software product "Inertial Explorer" from NovAtel's Waypoint software suite, and it is shown how gravity estimates can be derived from these results. A statistical analysis of the crossover differences yields an RMS error of 2.5 mGal, which is comparable to the results obtained from the LCR gravimeter. The properties of the SIMU and LCR systems are compared and a merging of the two is performed. A statistical analysis of the crossover differences of the merged product yields an RMS error of 1.3 mGal. These results indicate that the properties of the two units are complementary and that a combination of the two can result in improved gravity estimates.

Keywords

Airborne gravimetry • Inertial Explorer • Strapdown IMU

1 Introduction

Airborne gravimetry provides a fast and efficient way of covering large areas that are remote or otherwise inaccessible. Moreover, this technique is capable of providing seamless coverage in near-coastal areas, were shallow water makes it difficult for marine gravimetry and satellite altimetry derived models are generally not reliable (Andersen et al. 2015).

The advantages of airborne gravimetry were recognized early on (Thompson 1959). However, the technique did not become fully operational until the Global Positioning System (GPS) became available in the late eighties. The Geodynamics Department at the National Space Institute of Denmark (DTU Space) has carried out large airborne surveys since the early nineties (Brozena 1992), back then known as the Danish National Survey and Cadastre (KMS), using a LaCoste&Romberg (LCR) spring-type gravimeter (Valliant 1992). The concept was to mount a single-axis accelerometer on a stabilized platform, that to some extent isolates the movements of the gravimeter from the movements of the aircraft. This allows only for scalar gravimetry which, in contrast to vector gravimetry, estimates only the magnitude of the gravity acceleration.

The use of Inertial Measurement Units (IMUs) for airborne gravimetry has been attempted since the early nineties (Schwarz et al. 1992; Jekeli 1994; Wei and Schwarz 1998). The obvious advantages being smaller size, ease of operation and lower prize, compared to traditional air gravimeters.

T.E. Jensen (✉) • J.E. Nielsen • A.V. Olesen • R. Forsberg
Department of Geodynamics, DTU Space, Elektrovej 327, 2800 Kgs. Lyngby, Denmark
e-mail: timj@space.dtu.dk

G. S. Vergos et al. (eds.), *International Symposium on Gravity, Geoid and Height Systems 2016*, International Association of Geodesy Symposia 148, DOI 10.1007/1345_2017_9

Since the IMU contains three perpendicular accelerometers, it has the potential to do vector gravimetry and estimate the deflection of the vertical. Glennie et al. (2000) reported accuracies similar to the LCR system, with the IMU outperforming the LCR gravimeter in the short-wavelength components. The biggest challenge, when using the IMU for gravimetry, is the separation of gravity variation from long term drift in the sensors, leaking into the long-wavelengths of the gravity estimates (Glennie and Schwarz 1999; Jekeli and Kwon 1999; Glennie et al. 2000). However, the majority of the drift has been associated with temperature variation and temperature calibrations have been seen to significantly improve the results (Huang et al. 2012; Becker et al. 2015b; Becker 2016).

Since 2013, DTU Space has been flying an iMAR RQH IMU alongside the LCR system on a number of campaigns. This was done in collaboration with the Technical University of Darmstadt, who owns the unit. The IMU has been physically bolted to the floor of the aircraft, which is commonly known as strapdown mode. This approach will therefore be referred to as Strapdown IMU (SIMU) airborne gravimetry, or simply strapdown gravimetry. In April 2016, DTU Space purchased a similar iMAR RQH unit. The unit was flown alongside the LCR system on a large campaign in Malaysia during the summer of 2016.

Using the observations from this Malaysia campaign, this paper aims to show that gravity estimates can be produced using the commercial software product "Inertial Explorer", from NovAtel's Waypoint software suite. Although this method can be used to derive the full gravity vector, only the vertical component is considered here. It will also be shown that a combination with estimates from the LCR system yields results superior to the individual estimates.

2 Basic Principles

A gravimeter is basically an accelerometer, measuring specific force, $\mathbf{f}$. This is a combination of gravitational acceleration, $\mathbf{g}$, and kinematic acceleration, $\ddot{\mathbf{r}}$, where dots refer to time derivatives. In order to derive gravity from the observations, one must therefore separate the two effects as

$$\mathbf{g} = \ddot{\mathbf{r}} - \mathbf{f} \,, \tag{1}$$

where the kinematic component, $\ddot{\mathbf{r}}$, must be observed using some alternative sensor. Commonly, the Global Navigation Satellite System (GNSS) is used to estimate position, which is then double-differentiated in order to yield acceleration. This *direct approach* has been the most common method in airborne gravimetry (Jekeli 2001). However, one can also follow a more *indirect approach* by double-integrating the sensed accelerations as

$$\mathbf{r} = \iint (\mathbf{f} + \mathbf{g}) \, \mathrm{d}t \,, \tag{2}$$

and then derive gravity from a comparison of position estimates. This approach is commonly used in integrated IMU/GNSS navigation systems, where the entire theoretical framework is already well-developed. In this approach, one typically models the gravity variation as a stochastic process, which is based on the assumption of random variation with respect to spatial coordinates. Further assumptions such as stationarity, ergodicity and isotropy are typically also used, all of which can of course be questioned. Stochastic interpretations of the gravity field is however not unknown in the field of geodesy and is frequently used in e.g. least-squares collocation. See Jekeli (2001) for a more thorough discussion on the subject.

NovAtel's Inertial Explorer software uses the second approach for combining GNSS and IMU observations using a Kalman filter framework. The intended application is navigation, in which the two types of observations are often combined due to their complementary properties. The GNSS observations have a low short-term precision, compared to IMU observations, but a long term stability. The IMU observations are accurate on short time scales, but because errors are integrated, the long term stability is poor. In airborne gravimetry, however, this argument is no longer valid, since it is the difference between the two signals that is of interest.

In this framework, we therefore have to think of the IMU as a navigation system. The basic principle is that angular rates, measured by the gyroscopes, are integrated for attitude. The accelerations, measured by the accelerometers, are integrated once to yield velocity and twice to yield position. In this way, the IMU works as an Inertial Navigation System (INS), supplying estimates of attitude, velocity and position. These are then combined with GNSS estimates using a Kalman filter framework.

2.1 The Kalman Filter

The Kalman filter is a useful framework for combing estimates in a statistically optimal way. It is an *optimal recursive data processing algorithm*, rather than a filter (Maybeck 1979). Basically, the algorithm consists of two phases:

1. A measurement update phase
2. A system propagation phase

In order to get a more intuitive impression of how the algorithm works, consider the following one-dimensional example. In the **measurement update phase**, we have two observations, x and z, of the position, both associated with some standard deviation, σ_x and σ_z. The underlying assumption is that the associated probability density functions are

Gaussian. These two observations can be combined into one optimal estimate using the principle of least squares as

$$\begin{aligned}\mu &= \frac{\sigma_z^2}{\sigma_x^2+\sigma_z^2}x + \frac{\sigma_x^2}{\sigma_x^2+\sigma_z^2}z = x + \frac{\sigma_x^2}{\sigma_x^2+\sigma_z^2}(z-x) \\ &= x + K\delta z\end{aligned} \tag{3}$$

and

$$\sigma^2 = \frac{1}{1/\sigma_x^2 + 1/\sigma_z^2} = \sigma_x^2 + K\sigma_x^2 \,, \tag{4}$$

where $K = \sigma_x^2/\left(\sigma_x^2+\sigma_z^2\right)$ is known as the Kalman gain and $\delta z = z - x$ as the measurement innovation. With an assumption of Gaussian error distribution, this estimate is optimal according to any statistical measure (Maybeck 1979). The new estimate will therefore represent some linear combination of the two observations, with the weight distributed according to the confidence in each observation. The weighting factor is the Kalman gain.

In the **system propagation phase**, the current estimate, μ, is propagated forward in time by integrating the IMU observations. This is done until the next GNSS observation, at which point the two observations are again combined. The GNSS estimate comes with some associated uncertainty from the GNSS processing software used. The confidence in the IMU estimate is propagated forward in time from the previous estimate. In order to do this, one must define the following two properties:

- A *system model* consisting of a set of dynamics equations, basically describing the physics of the situation
- A *stochastic model* defining how gyroscope and accelerometer errors propagate onto the estimates. This model includes random noise, bias variation, scale factors etc., but also any vehicle dynamics not included in the system model as for example aircraft vibration

This one-dimensional example outlines the basic principles and recursive nature of the Kalman filter framework, on which the Inertial Explorer software is based. The system model is already included in the software and cannot be altered by the user. The user has the option to define her own stochastic model, corresponding to the error characteristics of her own IMU. The software does however have a number of pre-defined stochastic models, associated with both NovAtel's own products and a number of third party IMUs.

2.2 Inseparability of Accelerometer Bias and Gravity Variation

Extending the number of dimensions from one to three, there are nine basic navigation parameters to be estimated, along with a number of additional parameters determined by the user. In this case there are six additional parameters, giving a total of 15 parameters (five three-dimensional vectors) as

$$\mathbf{x} = \{\boldsymbol{\psi}, \mathbf{v}, \mathbf{p}, \mathbf{b}_\omega, \mathbf{b}_a\} \,, \tag{5}$$

where $\boldsymbol{\psi}$ denotes the attitude in terms of three Euler angles, $\mathbf{v}$ is the velocity and $\mathbf{p}$ the position. The two vectors, $\mathbf{b}_\omega$ and $\mathbf{b}_a$, represent estimates of gyroscope and accelerometer bias, respectively. The vector $\mathbf{x}$ is known as the state vector. The IMU provides estimates of attitude, velocity and position, while the GNSS system provides estimates of position and velocity. In order to obtain estimates of all 15 state parameters, the Kalman filter must exploit the covariance matrix which is built through the forward propagation phase, using the system dynamics equations defined within the Inertial Explorer software. In general, however, the observability and estimability, of the states depend on the type of observations and vehicle dynamics (Becker et al. 2015a).

Typically, to estimate gravity using this indirect Kalman filter approach, additional states are added to the state vector in order to model gravity as a stochastic process (Deurloo 2011; Becker 2016). This is not possible within the Inertial Explorer Software. However, when the aircraft manoeuvring is limited to horizontal non-accelerated flight, as is typically the case for long-range airborne gravity campaigns, the accelerometer bias variation and gravity variation become inseparable (Glennie and Schwarz 1999; Jekeli and Kwon 1999; Deurloo 2011; Becker 2016). In this static configuration, where both accelerometer bias and gravity varies with time, the system cannot separate the two sources of variability. Gravity will therefore be absorbed by the accelerometer bias estimates and consequently be a combination of actual bias variation and gravity variation.

This inseparability is usually the largest challenge in strapdown gravimetry. However, it can also be exploited to derive gravity estimates using a commercial software product, as will be shown in the following. Since Inertial Explorer already corrects for part of the gravitational signal using a model for the normal gravity field. The component of gravity that remains in the accelerometer bias estimates is the gravity disturbance.

3 Data

The dataset consists of 25 flights (129 h/27,257 km), flown in the South China Sea, Malaysia, during summer 2016. These flights were broken into 91 flight lines (68 h/21,288 km) as illustrated in Fig. 1. The entire survey was carried out using a BeechCraft King Air 200 aircraft.

The scientific instruments on board the flight were several GNSS receivers, linked to a GNSS antenna, along with

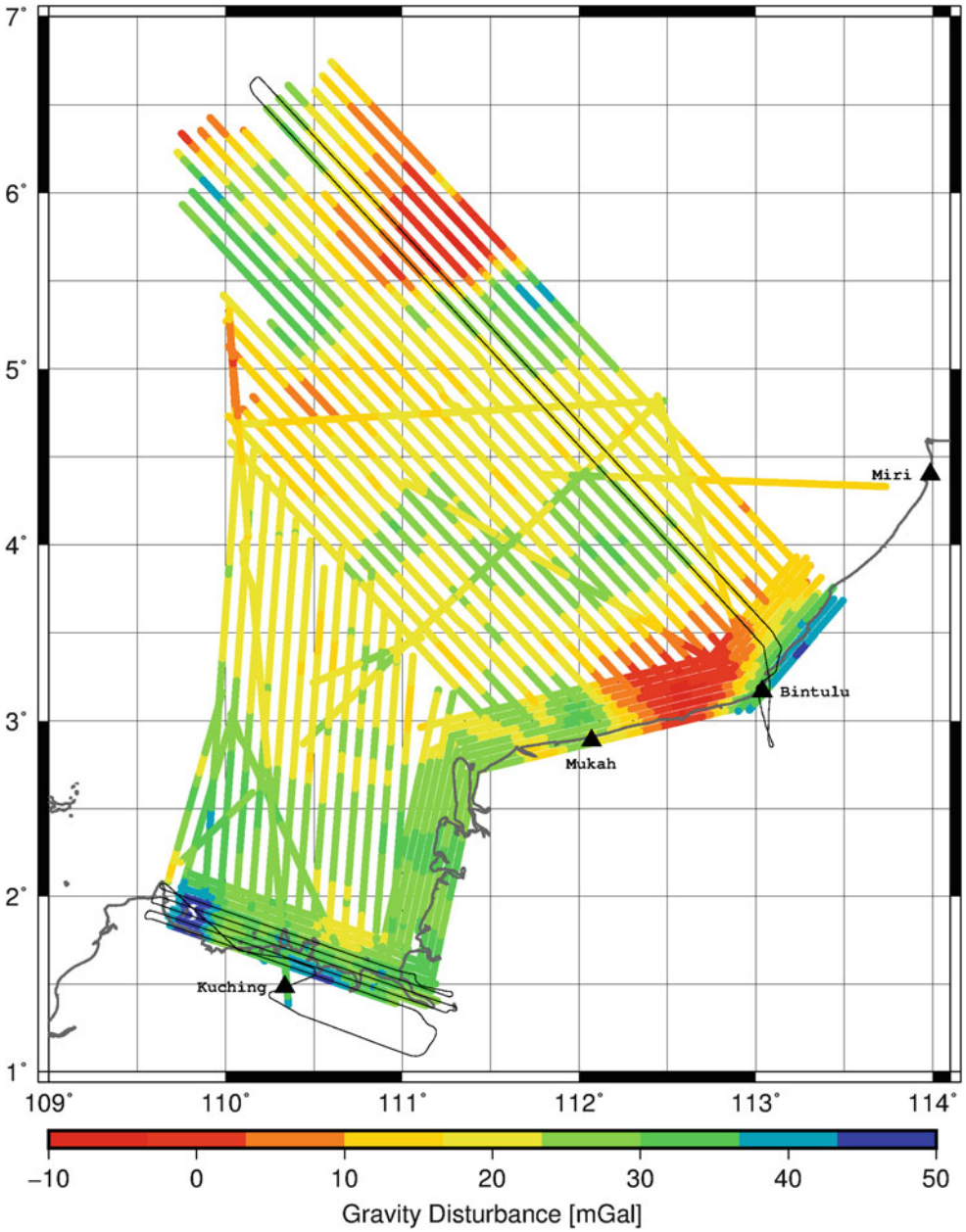

Fig. 1 Estimated gravity disturbance (combined IMU/LCR product) for the entire survey, consisting of 91 flight lines. The average speed was 88 m/s (std. dev. = 0.3, min. = 87, max. = 89) and the average altitude was 1966 m (std. dev. = 14, min. = 1885, max. = 1989), with only two low altitude outliers representing short line segment in the airport return phase. For two flights, the flight track is drawn in *black*. The results from these two flights are shown in Fig. 2

Table 1 Specification of the gyroscope and accelerometer components in the iMAR RQH unit owned by DTU Space

	Gyroscopes	Accelerometers
Bias instability[a]	$<0.002°/h$	$<10\,\mu g$
Random walk	$<0.0011°/\sqrt{h}$	$<8\,\mu g/Hz$
Scale factor	<5 ppm	<100 ppm

[a]Const. temperature

a LaCoste&Romberg single-axis gravimeter mounted on a stabilised platform (LCR system) and the iMAR RQH-unit mounted in strapdown mode (Table 1). For most of the flights, there was an on-ground reference GPS system at the airport.

4 Processing Methodology

The GNSS observations were processed using the Waypoint software. Where observations from a reference station were available, a differential solution was preferred. Otherwise a Precise Point Positioning (PPP) solution was produced. The processing was done using the final satellite ephemerid products.

Gravity disturbance was estimated from the LCR system according to the direct approach introduced earlier. In order to estimate the kinematic component, positions derived from GNSS were double-differenced and the Eötvös effect was accounted for. Besides removing the kinematic contribution,

the LCR accelerations were subjected to a platform tilt correction and a subsequent two-pass Butterworth filter of 150 s filter length (Olesen and Forsberg 2007). For a more thorough description of the LCR processing, see Olesen (2002).

The IMU logs the observed specific force and angular rates with an associated time stamp and temperature. The IMU unit contains an internal GNSS receiver, which synchronizes the observations with GPS time. The first step in the processing was to inspect the time stamps, since these were found to have some artefacts that needed to be corrected. The second step was to apply a simple warm-up temperature calibration to the vertical accelerometer only, which is observing the majority of the gravity signal (Becker et al. 2015b).

The IMU and GNSS data from all 25 flights were then processed in a loosely coupled mode using Inertial Explorer. Loosely coupled means that estimated GNSS observations are processed separately and introduced as positions and velocities (Groves 2013). The Inertial Explorer software has a pre-defined stochastic model associated with the error characteristics of the iMAR RQH unit. This model was used in the processing. The software will automatically process the data both forwards and backwards in time, apply a Rauch-Tung-Striebel (RTS) smoother (Brown and Hwang 2012) and combine the two results.

The products of further interest are the estimated attitudes and accelerometer biases. The accelerometer bias estimates are naturally along the three body-axes of the IMU, i.e. the front, starboard and down directions. The attitude solution allows us to transform any quantity between the body-frame and the local-level frame formed by the north, east and plumb-line directions, see e.g. Groves (2013).

4.1 Separating Gravity from Bias Variation

To arrive at gravity estimates, the gravity variation must be separated from the actual bias variation. In lack of better knowledge, it will be assumed that the bias variation is linear with respect to time. The gravity anomaly varies with position, which is constant in the beginning and end of the flight, since the aircraft is standing still.

At the beginning and end of the flight it is possible to separate the bias and gravity signals using tie values, i.e. external gravity measurements at these physical locations (Torge 1989). The measured tie value is along the local plumb-line direction and can be projected onto the three body-axes using the attitude solution.

Having projected the tie values onto each of the three body axes, a linear trend was estimated for each flight. Some statistics from these trends are presented in Table 2. These trends are assumed to represent accelerometer bias variation and are removed from the bias estimates in order to derive gravity. The gravity estimates are then transformed into the local-level frame and subjected to a two-pass Butterworth filter with a length of 150 s. The choice of filter length is based on a visual comparison with both LCR estimates, Earth Gravitational Model 2008 (EGM08) estimates, parallel flight tracks and cross-over points. For the further analysis, only the plumb-line component is considered.

Table 2 Statistics of the accelerometer bias drift estimates

Axis	Mean	Std	Min	Max	
x	15.2	74.0	−144.9	186.9	μGal/h
y	−6.6	213.2	−534.8	326.4	μGal/h
z	−3.8	14.3	−35.2	19.8	μGal/h

Finally, each flight was split into flight lines by manually discarding parts of the flight that contained a large degree of manoeuvring.

4.2 Merging IMU and LCR Estimates

A simple merging of the IMU and LCR estimates was performed. Since LCR estimates have proven themselves very reliable in the long-wavelength components (Valliant 1992), the objective was to prioritise the short-wavelength components from the IMU estimates and the long-wavelength components from the LCR estimates.

This simple merging was done based on a linear least squares fit of a straight line in the time domain. For each line produced by the IMU/Inertial Explorer processing, LCR estimates on that same line were identified based on time stamps. A straight line was then fitted to both time series, using only estimates with common time stamps. The linear model of the IMU estimates was then removed and replaced by the linear model estimated from the LCR estimates.

Three of the lines did not have any time stamps in common with the LCR estimates and were excluded in the analysis. For two of the lines, we found that not enough time stamps were in common for a linear fit. Instead a bias was estimated and used for the correction.

5 Results

Gravity disturbance estimates from both IMU and LCR systems were produced, together with a merged product. A statistical analysis, based on the line cross-over differences was performed and is summarized in Table 3. The merged IMU/LCR estimates are shown for all 91 flight lines in Fig. 1.

In Fig. 2, the IMU and LCR estimates are shown for two entire flights, together with gravity disturbance computed from EGM08. The top figure represents a flight over the

Table 3 Cross-over statistics from the gravity disturbance estimates

	iMAR	LCR	Merged	
No. of crossings	257	113	252	
Mean	0.59	−0.13	−0.08	mGal
Min	−10.28	−8.01	−4.38	mGal
Max	8.97	6.74	5.93	mGal
RMS	3.55	3.17	1.86	mGal
RMS error	2.51	2.24	1.32	mGal

No cross-over adjustment was applied

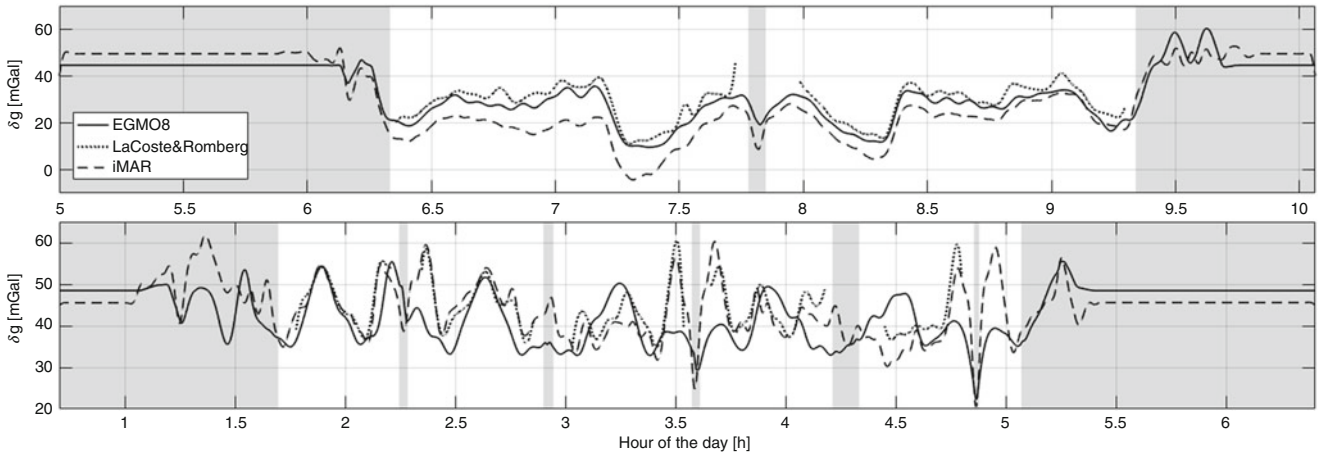

Fig. 2 Estimated gravity disturbances from both the IMU and LCR systems together with EGM08 up to degree 2190 and order 2159. The entire flight is shown above, but only the flight lines (*white areas*) are used in the statistical analysis. (*Top*) These two lines are mostly over the ocean and are shown in the north-eastern part of Fig. 1; (*Bottom*) These five lines were flown in the coastal area north of Kuching, see Fig. 1

ocean north of Bintulu and the bottom figure represents a flight in the coastal area north of Kuching, see Fig. 1.

6 Discussion

In Fig. 2, both IMU and LCR estimates are shown together with EGM08. The top figure represents a flight over the ocean north of Bintulu. Since satellite altimetry derived gravity is part of EGM08, we assume that EGM08 is quite reliable for this flight. The IMU estimates show both a bias and trend with respect to the LCR and EGM08 estimates, indicating that the long-wavelength components of the signal are not reliable. Except for this bias and trend, the variations in the three signals do seem to agree quite well, indicating that the short-wavelength components of the estimates are more reliable. In contrast, the LCR estimates appear to control the long-wavelength components well, while its high sensitivity to turbulence and manoeuvring become apparent at some occasions. This figure illustrates quite well the complementary properties of the IMU and LCR systems.

The bottom figure represents a flight in the coastal area north of Kuching. Here it is seen that the IMU and LCR estimates agree quite well, while EGM08 shows large deviations. This example represents a coastal area that altimetry-derived gravity, marine gravimetry and terrestrial methods can not cover and EGM08 therefore contains limited information. As mentioned in the introduction, airborne gravimetry is the only feasible method of covering these areas. Since most of the world's coastlines remain un-surveyed, although the majority of the population lives in coastal areas, this example clearly shows why airborne gravimetry is still needed in a time of satellite models.

Based on the statistical analysis in Table 3, the IMU and LCR gravity estimates are of similar quality. A comparison of the number of crossing points, on which the statistical analysis is based, indicates how large a portion of the LCR data that is usually discarded due to turbulence, manoeuvring and dynamic conditions in general.

These indications imply that the properties of the two systems are different. The IMU estimates appear to be more resilient to aircraft dynamics, resulting in more reliable results under such circumstances and more control over the short-wavelengths of the gravity estimates. On the other hand, the LCR gravimeter appears to have an excellent bias stability, making it superior in the long-wavelengths. These complementary properties motives a combined product, which leads to improved gravity estimates, based on the statistical analysis.

7 Conclusions

Using the commercial software product "Inertial Explorer", the IMU and GNSS observations were combined in order to form a navigation solution. This led to the gravity variation being absorbed by the accelerometer bias estimates. A simple approach was introduced to separate gravity from accelerometer bias. This separation was identified as the major challenge in strapdown gravimetry and was seen to influence the long-wavelength components of the gravity estimates.

A comparison of the IMU and LCR properties was performed. It was seen that the LCR system is very sensitive to dynamic conditions, which influence the short-wavelength components of the signal. The long-wavelength components are however very reliable. These features nicely complement the properties of the SIMU system, which can be exploited in order to arrive at improved gravity estimates.

Comparing the airborne estimates with EGM08, a good agreement was found in areas of open ocean. Large differences in the 10–20 mGal range was observed in coastal areas.

Acknowledgements The airborne survey in the South China Sea was done as part of the Marine Geodetic Infrastructure in Malaysian Waters (MAGIC) project on behalf of Info-Geomatik Sdn. Bhd. and the Department of Survey and Mapping Malaysia (JUPEM).

References

Andersen O, Knudsen P, Stenseng L (2015) The DTU13 MSS (mean sea surface) and MDT (mean dynamic topography) from 20 years of satellite altimetry. Springer, Berlin, Heidelberg, pp 1–10. doi:10.1007/1345_2015_182, http://dx.doi.org/10.1007/1345_2015_182

Becker D (2016) Advanced calibration methods for strapdown airborne gravimetry. PhD thesis, Technische Universität Darmstadt, Darmstadt. http://tuprints.ulb.tu-darmstadt.de/5691/

Becker D, Becker M, Leinen S, Zhao Y (2015a) Estimability in strapdown airborne vector gravimetry. Springer, Berlin, Heidelberg, pp 1–5. doi:10.1007/1345_2015_209, http://dx.doi.org/10.1007/1345_2015_209

Becker D, Nielsen JE, Ayres-Sampaio D, Forsberg R, Becker M, Bastos L (2015b) Drift reduction in strapdown airborne gravimetry using a simple thermal correction. J Geodesy 89(11):1133–1144. doi:10.1007/s00190-015-0839-8, http://dx.doi.org/10.1007/s00190-015-0839-8

Brown RG, Hwang PYC (2012) Introduction to random signals and applied Kalman filtering: with MATLAB exercises, 4th edn. Wiley, New York

Brozena JM (1992) The greenland aerogeophysics project: airborne gravity, topographic and magnetic mapping of an entire continent. Springer, New York, NY, pp 203–214. doi:10.1007/978-1-4613-9255-2_19, http://dx.doi.org/10.1007/978-1-4613-9255-2_19

Deurloo R (2011) Development of a Kalman filter integrated system and measurement models for a low-cost strapdown airborne gravimetry system. PhD thesis, Department of Geosciences, Environment and Planning, Faculty of Sciences, University of Porto

Glennie C, Schwarz KP (1999) A comparison and analysis of airborne gravimetry results from two strapdown inertial/dgps systems. J Geodesy 73(6):311–321. doi:10.1007/s001900050248, http://dx.doi.org/10.1007/s001900050248

Glennie CL, Schwarz KP, Bruton AM, Forsberg R, Olesen AV, Keller K (2000) A comparison of stable platform and strapdown airborne gravity. J Geodesy 74(5):383–389. doi:10.1007/s001900000082, http://dx.doi.org/10.1007/s001900000082

Groves PD (2013) Principles of GNSS, inertial, and multisensor integrated navigation systems, 2nd edn. Artech House Remote Sensing Library, Boston

Huang Y, Olesen AV, Wu M, Zhang K (2012) Sga-wz: a new strapdown airborne gravimeter. Sensors 12(7):9336–9348. doi:10.3390/s120709336, http://www.mdpi.com/1424-8220/12/7/9336

Jekeli C (1994) Airborne vector gravimetry using precise, position-aided inertial measurement units. Bull géodésique 69(1):1–11. doi:10.1007/BF00807986, http://dx.doi.org/10.1007/BF00807986

Jekeli C (2001) Inertial navigation systems with geodetic applications. Walter De Gruyter, Berlin

Jekeli C, Kwon JH (1999) Results of airborne vector (3-d) gravimetry. Geophys Res Lett 26(23):3533–3536. doi:10.1029/1999GL010830, http://dx.doi.org/10.1029/1999GL010830

Maybeck PS (1979) Stochastic models, estimation and control, vol 1. Academic, New York

Olesen AV (2002) Improved airborne scalar gravimetry for regional gravity field mapping and geoid determination. PhD thesis, Faculty of Science, University of Copenhagen

Olesen A, Forsberg R (2007) Airborne scalar gravimetry for regional gravity field mapping and geoid determination. In: Proceedings, Gravity Field of the Earth – 1st Meeting of the International Gravity Field Service, vol. 73, issue 18, 28th August–1st September, 2006. Harita Dergisi, Istanbul, pp 277–282.

Schwarz KP, Colombo O, Hein G, Knickmeyer ET (1992) Requirements for airborne vector gravimetry. Springer, New York, NY, pp 273–283. doi:10.1007/978-1-4613-9255-2_25, http://dx.doi.org/10.1007/978-1-4613-9255-2_25

Thompson LGD (1959) Airborne gravity meter test. J Geophys Res 64(4):488–488. doi:10.1029/JZ064i004p00488, http://dx.doi.org/10.1029/JZ064i004p00488

Torge W (1989) Gravimetry. De Gruyter, Berlin

Valliant HD (1992) The LaCoste and Romberg air/sea gravimeter: an overview. In: CRC handbook of geophysical exploration at sea. Hydrocarbons, 2nd edn. CRC Press, Boca Raton, FL, pp 141–176

Wei M, Schwarz KP (1998) Flight test results from a strapdown airborne gravity system. J Geodesy 72(6):323–332. http://dx.doi.org/10.1007/s001900050171

First Six Months of Superconducting Gravimetry in Argentina

Ezequiel D. Antokoletz, Hartmut Wziontek, and Claudia Tocho

Abstract

On December 16th, 2015, the superconducting gravimeter SG038 started to measure again after it was moved from the previous station in Concepcion, Chile to the Argentine-Germany Geodetic Observatory (AGGO) near the city of La Plata in Argentina.

The temporal gravity variations recorded with superconducting gravimeters (SG) enables research in several geodetic and geophysical studies that involve Earth's changes in the surface gravity field. In particular, it allows computing local models of earth tide parameters. The superconducting gravimeter SG038 at station AGGO was used to monitor gravity for the first 6 months after its installation.

The gravity time series was preprocessed after removing the principal constituents of the largest influences of the gravity signal that can be modeled sufficiently accurate like atmospheric effects, theoretical tides of the solid Earth, ocean loading effects and pole tides. In the remaining residual signal spikes were fixed, earthquake perturbations were reduced. Finally, the theoretical tides of the solid Earth and ocean loading effects previously removed were restored to obtain the corrected gravity signal.

The transfer function of the SG038 was determined by analyzing the step response of the whole system. Empirical amplitude and phase response functions are presented. The group delay at zero frequency was used in the tidal analysis.

By harmonic analysis of the preprocessed hourly data, amplitude factors and phases for tidal wave groups were estimated.

Keywords

Argentine-Germany Geodetic Observatory • Earth tide parameters • Superconducting gravimeter • Transfer function

1 Introduction

On 16th December 2015, the superconducting gravimeter SG038 was installed at the Argentine-German Geodetic

E.D. Antokoletz (✉)
Departamento de Gravimetría, Facultad de Ciencias Astronómicas y Geofísicas, Universidad Nacional de La Plata, Paseo del Bosque s/n B1900FWA, Buenos Aires, Argentina

Consejo Nacional de Investigaciones Científicas y Técnicas (CONICET), Buenos Aires, Argentina
e-mail: eantokoletz@fcaglp.unlp.edu.ar

H. Wziontek
Department G4, Gravity Metrology, Federal Agency for Cartography and Geodesy (BKG), Branch Office Leipzig, Karl-Rothe-Straße 10-14, 04105 Leipzig, Germany
e-mail: hartmut.wziontek@bkg.bund.de

C. Tocho
Departamento de Gravimetría, Facultad de Ciencias Astronómicas y Geofísicas, Universidad Nacional de La Plata, Paseo del Bosque s/n B1900FWA, Buenos Aires, Argentina

Comisión de Investigaciones Científicas de la Provincia de Buenos Aires (CIC), Calle 526 e/10 y 11, La Plata, Buenos Aires, Argentina
e-mail: ctocho@fcaglp.unlp.edu.ar

G. S. Vergos et al. (eds.), *International Symposium on Gravity, Geoid and Height Systems 2016*, International Association of Geodesy Symposia 148, DOI 10.1007/1345_2017_13

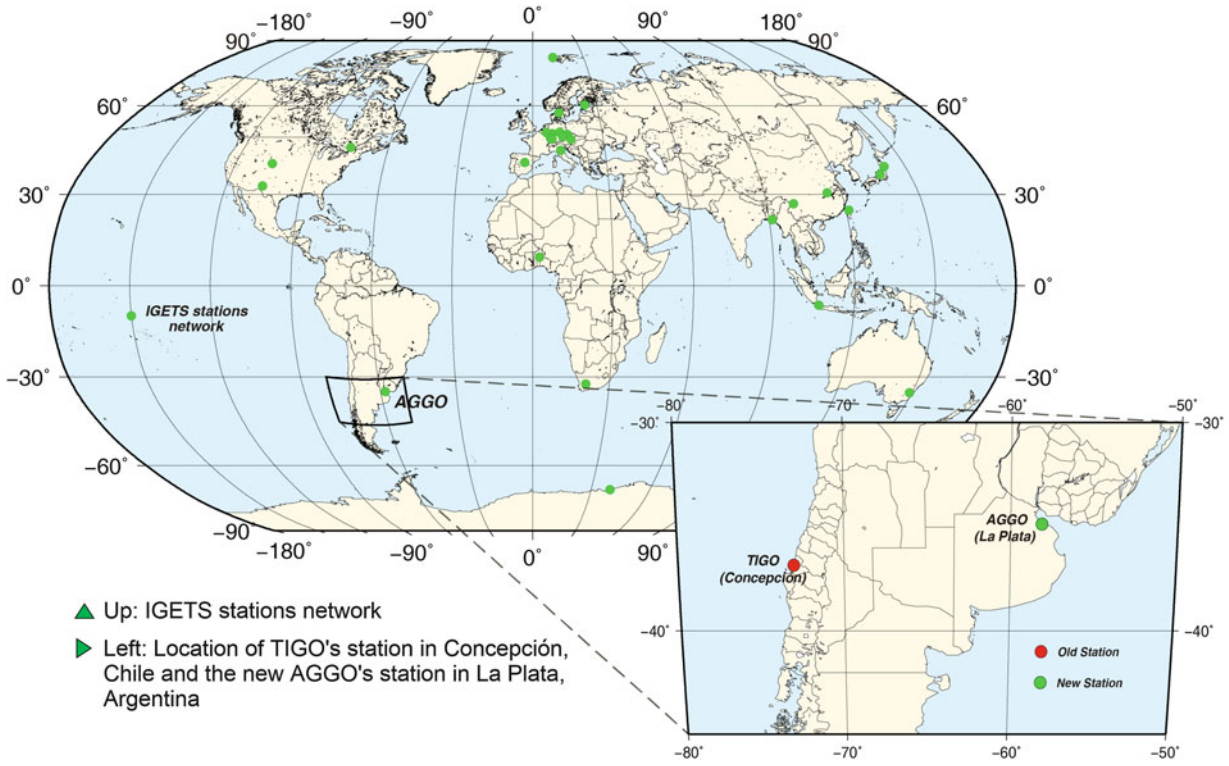

Fig. 1 Map of the global network of superconducting gravimeters grouped within the IGETS. Location of superconducting gravimeter SG038 at station AGGO

Observatory (AGGO) and it has been measuring continuously since then. AGGO is a fundamental geodetic observatory project of the Argentinean CONICET and the German Federal Agency for Cartography and Geodesy (Bundesamt für Kartographie und Geodäsie – BKG), located near the city of La Plata. This station is unique in South America and the Caribbean and one of five in the southern hemisphere (Fig. 1). AGGO contributes with the gravity time series to the International Geodynamics and Earth Tide Service (IGETS) of International Association of Geodesy (IAG), the worldwide network of superconducting gravimeters.

A superconducting gravimeter is a relative gravimeter with highest sensitivity and temporal stability. The measuring principle is based on a superconducting sphere levitated in the magnetic field generated by two superconducting coils. Observed is the voltage fed into a feedback coil in order to keep the sphere in its position (Hinderer et al. 2015). The changes in gravity are proportional to these voltage changes, which are low pass filtered with the analogue 'GGP1' filter by GWR and recorded with 1 s sample rate. The sensor of SG038 was the first where the magnetic gradient is fixed at the factory by carefully adjusting the turns-ratio of the upper and lower coils, which are connected in series. Therefore, only one current is used to levitate the sphere. Upon centering the sphere, the magnetic gradient is correctly adjusted. This is achieved by a separate small centering coil that operates independently from the series coil (Warburton et al. 2000). Due to this concept, only minor modifications of the magnetic field were necessary to re-levitate the sphere after more than 3,800 km overland transportation from Chile to Argentina.

The SG data enable research in several geodetic and geophysical studies that involve temporal changes in the Earth's surface gravity field. In particular, it allows to compute local models for the Earth's tides. In this study, the gravity signal recorded during the first 6 months after its installation was analyzed. As a precondition, the transfer function of SG038 has been experimentally determined.

2 The Station

AGGO is a fundamental geodetic observatory located in the east-central part of Argentina close to the city of La Plata. The transportable design of the observatory was chosen to allow for an operation at different locations to improve the global coverage and to stabilize the terrestrial reference frame. All main space geodetic techniques are established,

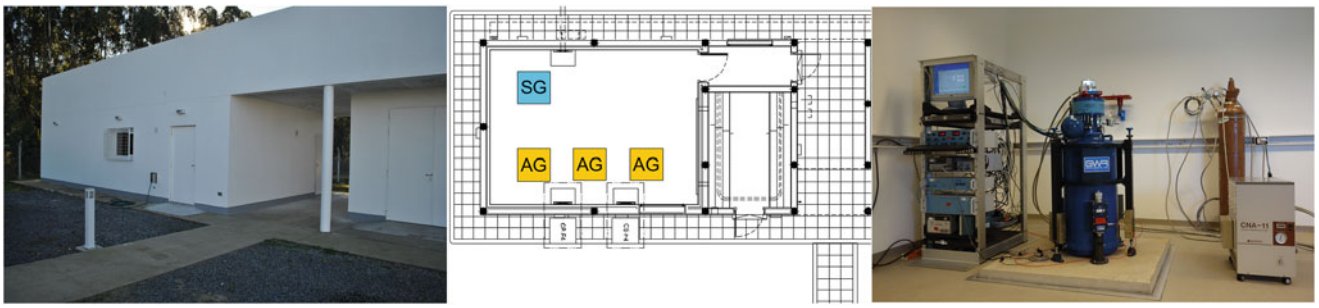

Fig. 2 Gravity laboratory (*left*), floor plan of the gravity laboratory (*middle*) and SG038 (*right*)

from very long baseline interferometry (VLBI), satellite laser ranging (SLR) to global navigation systems (GNSS). As a complementary technique, a superconducting gravimeter is part of the observatory. As precise time keeping is essential, different atomic clocks are operated, too.

In order to acquire environmental parameters, a weather station (precipitation, air temperature, air humidity, wind speed, wind direction, solar radiation, net radiation), soil moisture sensors (about 40 sensors in soil depths of 10–380 cm below surface) in two pits and two vertical profiles were installed in cooperation with the GFZ German Research Centre for Geosciences, Potsdam, Germany.

The complete instrumentation of the transportable integrated observatory (TIGO) was moved in April 2015 from the previous location close to the city of Concepcion, Chile, to the actual place. AGGO is the only station in South America and the Caribbean where all these different techniques are collocated.

The SG038 was the first instrument to start measuring on the 16th December 2015. The signal is recorded with 1 s sample rate by a digital voltmeter with 7 ½ digits resolution. The instrument can be accessed and controlled remotely via internet. It is installed in a dedicated gravity laboratory which has four stable monuments made of concrete, about 1 m^2 in size and founded 4 m deep, large enough to setup all types of FG5 absolute gravimeters. All monuments are separated from the floor of the building to minimize disturbances on the gravimeter. AGGO fulfils the requirements for a regional comparison site for absolute gravimeters and is a candidate for the future Global Absolute Gravity Reference System (Wilmes et al. 2016). Figure 2 shows the gravity lab, a floor plan and SG038.

3 Determination of the Frequency Transfer Function of SG038

Following the procedure of Van Camp et al. (2000), a step function with a pulse length of 10 min is added to the current of the feedback coil. The extra signal in the feedback loop induces an extra force, which causes the sphere to move out of its position. The displacement is detected immediately by the three plate capacitor surrounding the sphere, causing an additional signal at the input of the control loop. This signal, overlying the gravity signal, is transformed into an extra current in the feedback coil, forcing the sphere back to its center position. It is recorded and low pass filtered in the same way as the normal signal by the registration system.

With this experiment, the response of whole system can be identified, including (but not limiting to) the characteristics of the low pass filters. However, in normal operation, gravity changes do not cause the sphere to move, as the feedback loop is fast enough to compensate these forces. So this experiment characterizes the system under different conditions.

The experiment was performed at two times:

1. At the beginning of the operation at station TIGO/Concepcion (Chile) in December 2002,
2. After moving the SG to station AGGO/La Plata (Argentina) in May 2016.

First, tidal and atmospheric effects were removed by models. Then all valid response segments were cut to 3 min to avoid the impact of other signals. All segments were stacked and low pass filtered by a short finite impulse response (FIR) filter. Next it was transformed into the impulse response by numerical differentiation. In the frequency domain, the impulse response is identical to the transfer function of a linear time invariant system. To enhance the resolution at lower frequencies, the signal was transformed into the frequency domain using the chirp-z-transformation (Rabiner et al. 1969).

The characteristics of the frequency response is similar in both cases, the difference in the amplitude response is less than −20 dB (Fig. 3). A strong overshot is visible in the time domain (Fig. 4a), corresponding to an amplification of 2 dB (Fig. 4b, c), and a phase distortion in the range of 10 mHz (Fig. 4d, e). It is not clear, whether this represents a different characteristic of the system under the conditions of the experiment or if the system shows a non-

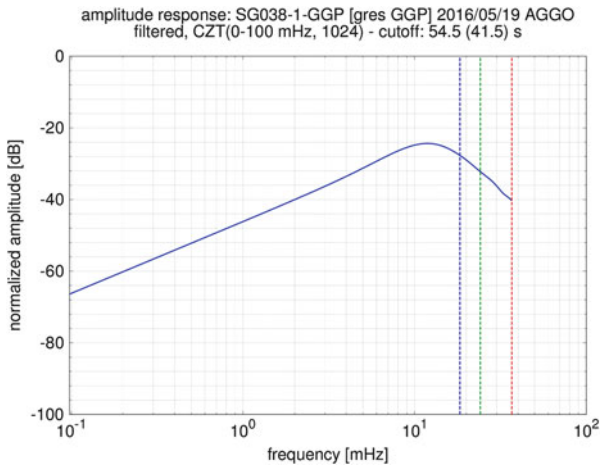

Fig. 3 Differences of amplitude responses between the two periods of time considered

linear behavior in a limited range. However, in the range of typical gravity signals below 1 mHz, the system is stable and responds linearly. The most important information for analysis of gravity time series is the time delay at zero frequency as can be seen in Fig. 4d, e It is assumed, that the delay below the lowest determined frequency at about 3 h remains constant and is representative for the whole tidal range, starting from zero frequency. The difference of 0.8 s between both experiments may be due to changes in the electronics during an upgrade of the SG038 in 2008 (Table 1).

4 First Tidal Analysis

For the first tidal analysis, 6 months of data from SG038 (from January to June 2016) were used. The TSOFT software (Van Camp and Vauterin 2005) was used for the following processing steps depicted in Fig. 5:

1. The registration in voltage was transformed to gravity units using the scale factor −736.5 nm/s^2/V as obtained from numerous parallel recordings mainly with the Absolute Gravimeter FG5-227 during the period 2006–2012 at station TIGO/Concepción.
2. To obtain preliminary residuals, the principal effects were modeled (atmosphere, theoretical tides, ocean loading and polar motion effect) and subtracted from the signal. Atmospheric effects were modeled with a simple air pressure admittance using a constant value of −3.0 nm/s^2/hPa (Torge 1989). Theoretical tides were computed using Tamura's catalogue of 1,200 waves (Tamura 1987) and synthetic Earth tide parameters (Dehant et al. 1999). The ocean loading effect on gravity was computed using the EOT11a model (Savcenko et al. 2012) with parameters provided by the ocean tide loading provider of M.S. Bos and H.-G. Scherneck (http://holt.oso.chalmers.se/loading/). The polar motion effect is based on the EOP C04 pole coordinate series of the International Earth Rotation and Reference Systems Service (IERS) using an amplitude factor of 1.16 (Wahr 1985).
3. Spikes were eliminated manually by linear interpolation in order to have a smooth signal without disturbances. No steps or gaps were recognized in the signal.
4. The signal was filtered with the purpose of eliminating the frequencies that do not contribute to the tidal model or generate noise. A low pass least squares filter was applied with a cut-off frequency of 50 cpd (cycles per day) and a window size of 200.
5. Finally, the theoretical Earth tide model and the ocean loading effect removed previously in step 2. were restored. In contrast, atmospheric and polar motion effects were not restored to the preprocessed residual signal. Then, the signal was decimated to 1 h sample rate.
6. The Earth tide parameters were then computed using the ETERNA 3.4 software package (Wenzel 1996) and tidal wave groups for 1 month. The time delay was taken into account. No air pressure admittance factor was estimated. The final results are included in Table 2.

Analyzing the standard deviation (Std. Dev.) of the results, the main diurnal and semidiurnal waves are well determined while this is not the case for longer period waves such as MM or SSA, which were omitted completely from the analysis, because the time series is not long enough to resolve these waves, due to the low amplitude at the latitude of the station (lower than 5 nm/s^2). As the time series of the SG grows, the longer period waves will be determined with better approximation.

After the tidal analysis, the spectrum of the final residuals (Fig. 6) shows a clear improvement over the residuals obtained from theoretical tides (WD model) and ocean tide loading (EOT11a model). Only small peaks at S1 and S2 remain as atmospheric tides could not be resolved independently due to the coarse wave grouping. Deviations in amplitude and phase at these particular frequencies from the elastic response of the solid Earth can currently not be modelled sufficiently well. A more efficient atmospheric correction, e.g. based on operational weather models, will certainly reduce the spectral energy further.

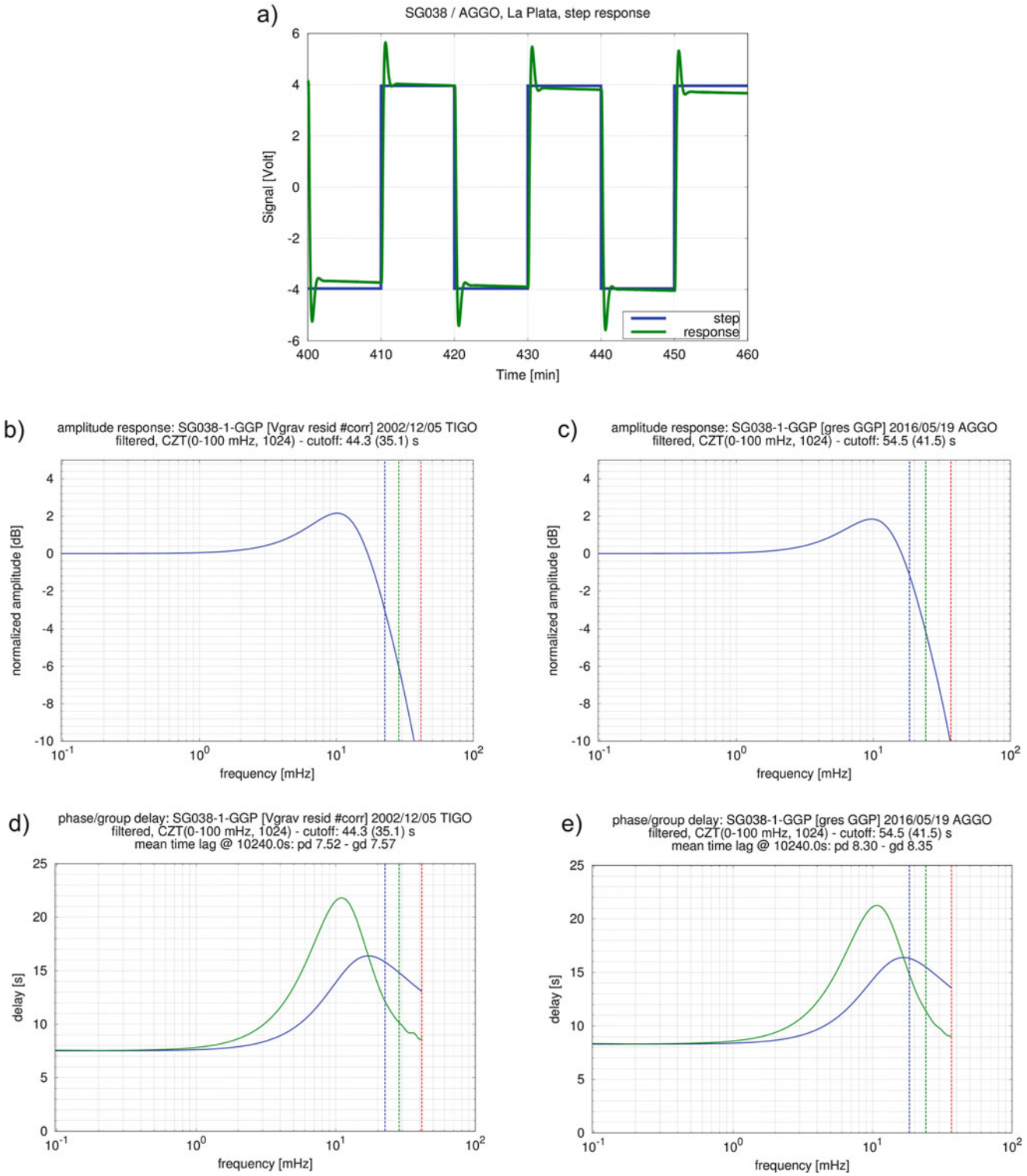

Fig. 4 Selected step response in time domain. The overshot after the step is clearly visible. The response is overlaid by tidal changes (**a**). (**b**, **c**) Shows the amplitude responses at stations TIGO and AGGO, respectively. (**d**, **e**) Shows the phase/group delay at stations TIGO and AGGO, respectively

Currently, no reliable estimate about the instrumental drift can be given as no absolute gravity measurements are available yet. This didn't affect the tidal analysis, as the signal was high pass filtered. An overall trend of approximately 250 nm/s^2/year provides a limit, overlaid by seasonal environmental effects. Estimates of local and global water storages changes are currently under investigation. As the instrument was moved cold and the currents were not purged in the coils, the sphere only needed to be centered. Therefore no major changes in the magnetic field occurred and only a small run-in effect of less than 40 nm/s^2 was observed during the first week. It is therefore assumed that the major characteristics of the sensor was preserved, which is partially demonstrated by the similar behavior of the transfer function. However, the overland transportation may have affected the instrumental drift, which was only about 60 nm/s^2/year at the previous location.

Table 1 Results of the transfer function for the two experiments (the first when the SG038 was at station TIGO and the second when it was moved to station AGGO)

Date	Phase delay (s) GGP1 low pass filter	Group delay (s) GGP1 low pass filter	Cutoff periods (s) (−3/−6/−12 dB)
1) December 2002	7.51	7.57	44.33/35.07/24.15
2) May 2016	8.30	8.35	54.47/41.46/27.16

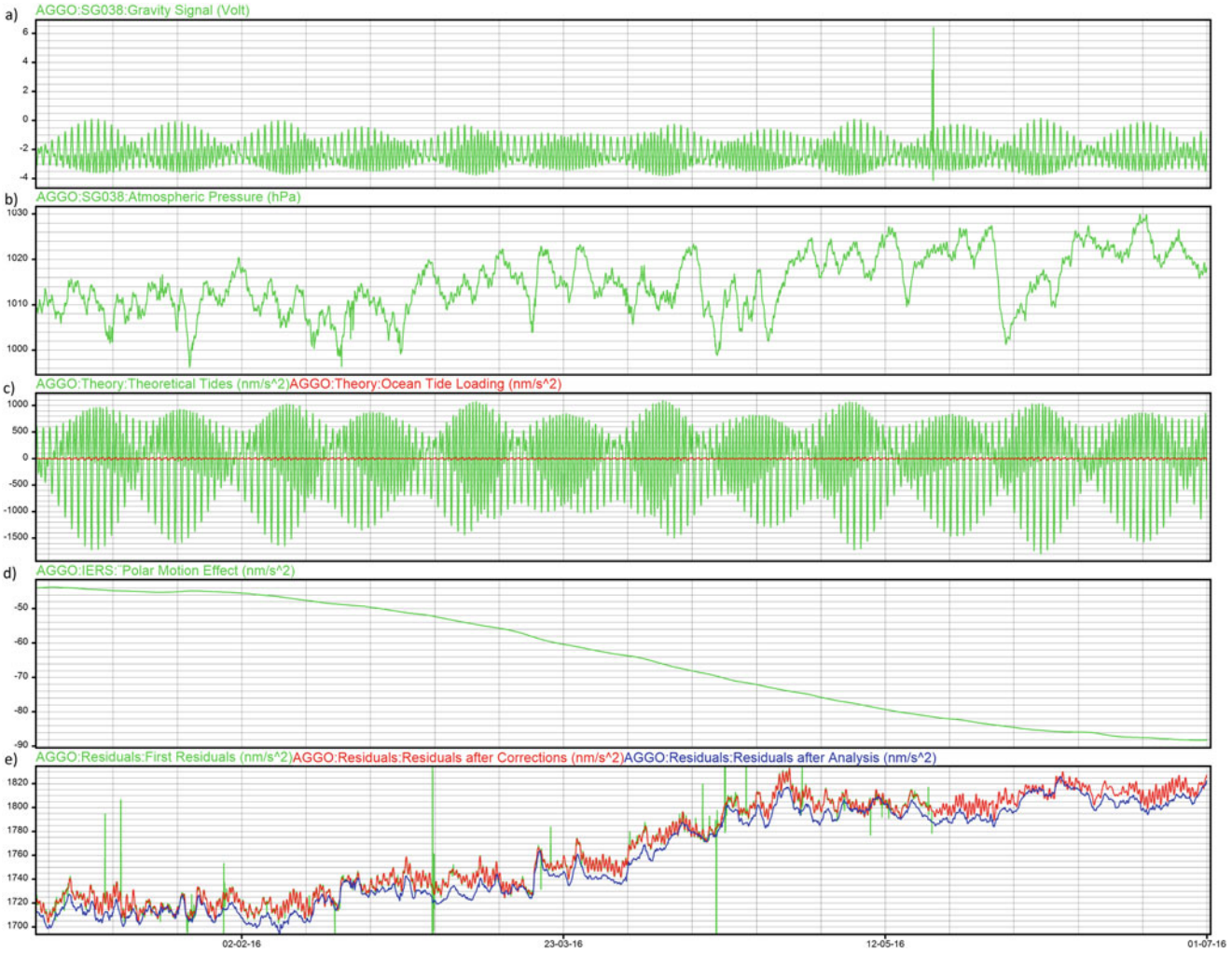

Fig. 5 (**a**) Gravity signal from the superconducting gravimeter SG038 at station AGGO from January to June, 2016; (**b**) Atmospheric pressure; (**c**) Tides based on theoretical elastic response and Tamura's potential catalogue (*green*); Ocean tide loading from model EOT11a (*red*); (**d**) Polar motion effect on gravity; (**e**) First residuals after removing the effects shown above (*green*); Residuals after removing spikes and disturbances and low pass filtering (*red*); Residuals after tidal analysis (*blue*)

Table 2 Earth tide parameters at station AGGO estimated using the 6 first months of observations taken with the SG038

Wave	Initial frequency (cpd)	Final frequency (cpd)	Observed amplitude factor (nm/s^2)	Std. dev. of amplitude factor (nm/s^2)	Observed phase (deg)	Std. dev. of phase (deg)
SGQ1	0.72	0.83	1.2810	0.0429	−0.2540	1.9224
SGM1	0.85	0.87	1.2068	0.0086	3.1025	0.4091
Q1	0.89	0.91	1.2029	0.0020	0.0753	0.0941
O1	0.92	0.94	1.1895	0.0004	−0.2227	0.0200
NO1	0.96	0.97	1.1828	0.0035	−0.0505	0.1672
PSK1	0.99	1.01	1.1563	0.0003	−0.3370	0.0147
J1	1.03	1.04	1.1819	0.0047	0.0227	0.2268
OO1	1.06	1.08	1.1761	0.0105	0.9708	0.5108
NU1	1.10	1.22	1.1485	0.0558	1.3217	2.7840
EPS2	1.72	1.84	1.1739	0.0074	1.8938	0.3603
2 N2	1.85	1.87	1.1931	0.0015	1.7293	0.0715
N2	1.89	1.91	1.1963	0.0003	0.9238	0.0165
M2	1.92	1.94	1.1825	0.0001	0.4918	0.0035
L2	1.96	1.98	1.1812	0.0021	0.2124	0.0999
S2 K2	1.99	2.01	1.1660	0.0002	0.0330	0.0077
ETA2	2.03	2.05	1.1864	0.0155	0.0195	0.7476
2 K2	2.07	2.18	1.1894	0.0487	−1.9669	2.3470
M3	2.75	3.08	1.0947	0.0027	0.7911	0.1433

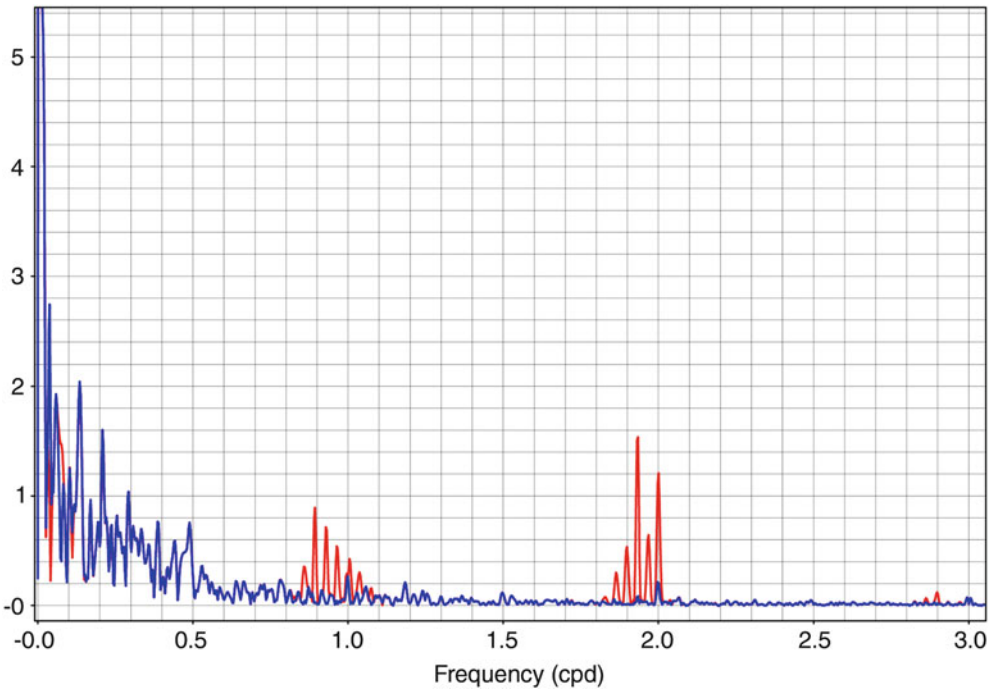

Fig. 6 Spectrum of the residuals, based on theoretical tides (WD) and ocean loading (EOT11a) (*red*) and after the tidal analysis (*blue*). Small peaks remain at S1/S2 as atmospheric tides could not be resolved independently

5 Conclusions

The first 6 months of data of the superconducting gravimeter SG038 were analyzed after setup at the new station AGGO. The time delay of the instrument was calculated from transfer functions for two periods of time. The difference in the time delay between both periods is probably caused by upgrades of the electronics of the instrument in 2008.

Parameters for the main diurnal and semidiurnal tidal waves were well determined. Longer period waves, e.g.

fortnightly waves could not be resolved due to the fact that the time series considered for the analysis was too short and the amplitude of these constituents is low at the latitude of the station. The wave group separation will be further enhanced when a longer time series becomes available.

A correlation between residuals from the tidal analysis and the atmospheric effect exists and will be studied in the future.

The influence of local water storage changes was not considered so far, but the extensive hydrological instrumentation will enable a detailed investigation in the future. As it can be seen from Fig. 5e, the residuals show a clear positive trend. This effect will partially contain seasonal variations of local, regional and global water storage changes. Furthermore, strong rain fall events as typical for the La Plata region will need to be separated from corresponding loading effects due to wind effects in the La Plata estuary.

Acknowledgements This work was possible thanks to the AGGO's scientific directors, Dr. Claudio Brunini and Dr. Hayo Hase, who ensured the access to the time series of the superconducting gravimeter SG038. We thank two anonymous reviewers for their constructive and careful comments which helped to improve the paper considerably.

References

Dehant V, Defraigne P, Wahr JM (1999) Tides for a convective Earth. J Geophys Res 104(B1):1035–1058. doi:10.1029/1998JB900051

Hinderer J, Crossley D, Warburton RJ (2015) Superconducting gravimetry. In: Treatise on geophysics, 2nd ed, vol 3. pp 59–115

Rabiner LR, Schafer RW, Rader CM (1969) The chirp z-transform algorithm and its application. Bell Syst Tech J 48:1249–1292. doi:10.1002/j.1538-7305.1969.tb04268.x

Savcenko R, Bosch W, Dettmering D, Seitz F (2012) EOT11a – Global Empirical Ocean Tide model from multi-mission satellite altimetry, with links to model results. doi:10.1594/PANGAEA.834232. Supplement to: Savcenko R, Bosch W (2012): EOT11a – Empirical Ocean Tide Model from Multi-Mission Satellite Altimetry. Deutsches Geodätisches Forschungsinstitut (DGFI), München, 89, 49 pp, hdl:10013/epic.43894.d001

Tamura Y (1987) A harmonic development of the tide-generating potential. Bull Inf Marées Terrestres 99:6813–6855

Torge W (1989) Gravimetry. Gruyter, Berlin

Van Camp M, Vauterin P (2005) TSOFT: graphical and interactive software for the analysis of time series and Earth tides. Comput Geosci 31(5):631–640. doi:10.1016/j.cageo.2004.11.015

Van Camp M, Wenzel HG, Schott P, Vauterin P, Francis O (2000) Accurate transfer function determination for superconducting gravimeters. Geophys Res Lett 27(1):37–40. doi:10.1029/1999GL010495

Wahr J (1985) Deformation induced by polar motion. J Geophys Res 90(B11):9363–9368

Warburton RJ, Brinton EW, Reineman R, Richter B (2000) Remote operation of superconducting gravimeters. In: Proceeding of the workshop: high-precision gravity measurements with application to geodynamics and second GGP workshop, Cahiers du Centre Européen de Géodynamique et de Séismologie, 17, Luxembourg, pp 125–136

Wenzel HG (1996) The nanogal software: Earth tide data processing package ETERNA 3.30. Bull Inf Mareés Terrestres 124:9425–9439

Wilmes H, Vitushkin L, Pálinkáš V, Falk R, Wziontek H, Bonvalot S (2016) Towards the definition and realization of a Global Absolute Gravity Reference System. In: International Association of Geodesy Symposia series. Springer, Heidelberg. doi:10.1007/1345_2016_245 (in press)

Tilt Susceptibility of the Scintrex CG-5 Autograv Gravity Meter Revisited

R. Klees, R.H.C. Reudink, and P.L.M. Flikweert

Abstract

In 2014 a team of researchers from five European universities reported on a high tilt susceptibility of the Scintrex CG-5 Autograv land gravity meter. In a series of experiments they demonstrated that the instrument provides incorrect readings after being tilted by angles of at least about 6° for a period of at least a few minutes. The readings may be offset by tens of μGal, and it may take hours before the first reliable readings can be taken. They recommend to keep the instrument in upright position within less than the critical angle of about 6° during transits, which may be unrealistic during field operations in hilly terrain, during car transportation or when walking with the instrument in a backpack. The instruments tested in 2014 were purchased between 2003 and 2011. Here, we report about the results of a series of experiments with the latest release of the Scintrex CG-5 purchased in 2015 using the same experimental set-up as in 2014. We show that the instrument is still susceptible to tilting though the initial offset has been reduced by about 50%. However, readings may still be offset by tens of μGal if the tilt exceeds about 6° and lasts for more than 1 min. Moreover, the time it takes the instrument to provide reliable readings in line with the specifications may still take several hours depending on the temporal duration of instrument tilting. From this we conclude that the problem of tilt susceptibility has not been solved yet.

Keywords

Accuracy degradation • Model 2015 • Scintrex CG-5 autograv • Susceptibility to tilt • Tilt

1 Introduction

The Scintrex CG-5 Autograv relative land gravity meter is one of the most widely used relative gravity meters today. It is frequently used in precise geodetic surveys, where high accuracies in line with the specifications of Scintrex Ltd. are required. In April 2012, a CG-5 (S/N 050300110) relative gravimeter was used to measure gravity differences between absolute gravity stations in the Netherlands. An analysis of the data revealed large systematic deviations between forward and backward measurements with a RMS difference of 72 μGal, and comparably large deviations from FG-5 data. Follow-up experiments pointed to a susceptibility of the Scintrex CG-5 relative gravity meter to tilting during transit between stations as the potential cause of the problems.

To investigate whether the susceptibility of the Scintrex CG-5 relative gravity meter is a design issue, a team from five European universities joined their effort and conducted a series of experiments with among others four CG-5 instruments, the results of which were published in Reudink et al. (2014). They found that when during transit the instrument is tilted for at least a few minutes and the tilt exceeds a critical value of about 6°, the initial readings taken at the site may be offset by ten to a few hundred μGal. Thereafter,

R. Klees (✉) • R.H.C. Reudink • P.L.M. Flikweert
Department of Geoscience and Remote Sensing, Delft University of Technology, 2600 GA Delft, The Netherlands
e-mail: r.klees@tudelft.nl; r.h.c.reudink@tudelft.nl

G. S. Vergos et al. (eds.), *International Symposium on Gravity, Geoid and Height Systems 2016*,
International Association of Geodesy Symposia 148, DOI 10.1007/1345_2017_4

the offset decays logarithmically as function of time. It may take several hours before the readings are accurate to within the specifications, depending on the temporal duration of instrument tilting. They also noted that reviewing the readings at the site for a typical session of 30 min (as suggested by Scintrex Ltd 2012) does not provide any evidence of an existing offset. Based on this, they recommend to keep the instrument in upright position to within 6° during transits. Moreover, they recommend to check, if possible, the "user sensor check voltage" permanently when in transit between sites. The voltage becomes close to zero when the critical angle of about 6° is exceeded. Voltages close to zero indicate offsets and long recovery times of several hours at the site. Voltages significantly above zero indicate unbiased readings of a quality which is in line with the specifications of Scintrex Ltd.

The four CG-5 instruments tested in Reudink et al. (2014) were purchased in the years 2003, 2005, 2006, and 2011, respectively. Nothing is known yet about the tilt susceptibility for instruments purchased after 2011. This applies in particular to instruments purchased after the publication of the paper (Reudink et al. 2014). Despite the fact that since recently Scintrex offers a new land gravity meter, the CG-6 Autograv, the CG-5 is still sold, and will remain the most widely used relative land gravity meter for precise geodetic applications for the next years. At the same time, the tilt susceptibility reported in Reudink et al. (2014) poses significant constraints to field operations with the CG-5. Therefore, finding answers to the following two questions may be of interest to the large community of present and future CG-5 users:

1. Has Scintrex Ltd. solved the tilt susceptibility problem with the latest release of the CG-5?
2. If not, to what extent is the CG-5 still susceptible to tilting?

TU Delft purchased a new CG-5 in 2016 (S/N 141041301). To answer the two questions, the experiments in Reudink et al. (2014) were repeated using this new instrument. To facilitate a direct comparison to the results in Reudink et al. (2014), one of the instruments investigated at that time, the CG-5 S/N 050300110, has also been used in the experiments to be reported.

2 Tests and Results

To answer the two questions of Sect. 1, the following experimental set-up has been chosen for the CG-5 S/N 050300110 (purchased in 2005) and the CG-5 S/N 141041301 (purchased in 2015): the instrument is levelled, turned on, and readings are recorded for 60 min. Then, the instrument is turned off, tilted by 8° and kept tilted for 1, 5, 10, 30, 60, and 90 min, respectively. Thereafter, the instrument is levelled, turned on, and readings are recorded for 24 h (except for a tilt duration of 1 min, where 1.5 h recording is sufficient). The recovery time is defined as the moment in time when the first 15-min mean value (after tilt of the instrument) is within $\pm 5\,\mu$Gal around the reference reading. The latter is the mean value of the 60-min record measured before the instrument was tilted. Here, "readings" refer to the values after the usual corrections for tides, loading etc have been applied.

Figure 1 shows the recorded readings for both instruments. It indicates that the CG-5 S/N 141041301 has a smaller initial offset, and the readings seem to stabilise faster compared to the CG-5 S/N 050300110. This is confirmed when depicting the offset and recovery time, respectively, as function of the duration of tilt as shown in Fig. 2. The corresponding numerical values are shown in Table 1 (initial offset) and Table 2 (recovery time). Figure 2 and Table 1 show that the initial offset of the CG-5 S/N 141041301 is about a factor of 2 smaller than that of the CG-5 S/N 050300110 for all durations of tilt investigated in this study. More relevant for field operations than the initial offset, is the recovery time (moment in time when the readings have stabilised, which is defined here as a band of $\pm 5\,\mu$Gal around the reference reading). Overall, the recovery time has improved for all investigated lengths of time in tilted state. However, the offsets and recovery times are still very critical for practical applications.

The recovery time of the CG-5 S/N 050300110 for a particular duration of tilt as shown in Table 2 differs from the values published in Reudink et al. (2014). There are several reasons for that. First of all, there is some uncertainty in the definition of the recovery time. Preferably, it is determined by the moment in time when the readings stabilised. However, readings never stabilise exactly, among others due to environmental noise, residual drift, and sensor resolution. Already a different choice of the band around the reference reading may alter the recovery time significantly. To illustrate this, Fig. 3 shows a graphical rendition of the recovery time as function of the duration of tilt when a band of $\pm 2\,\mu$Gal around the reference value is used instead of $\pm 5\,\mu$Gal. Table 3 shows the numerical values. Compared to Fig. 2 and Table 2, respectively, the recovery times have increased significantly, in particular for shorter lengths of time in tilting state.

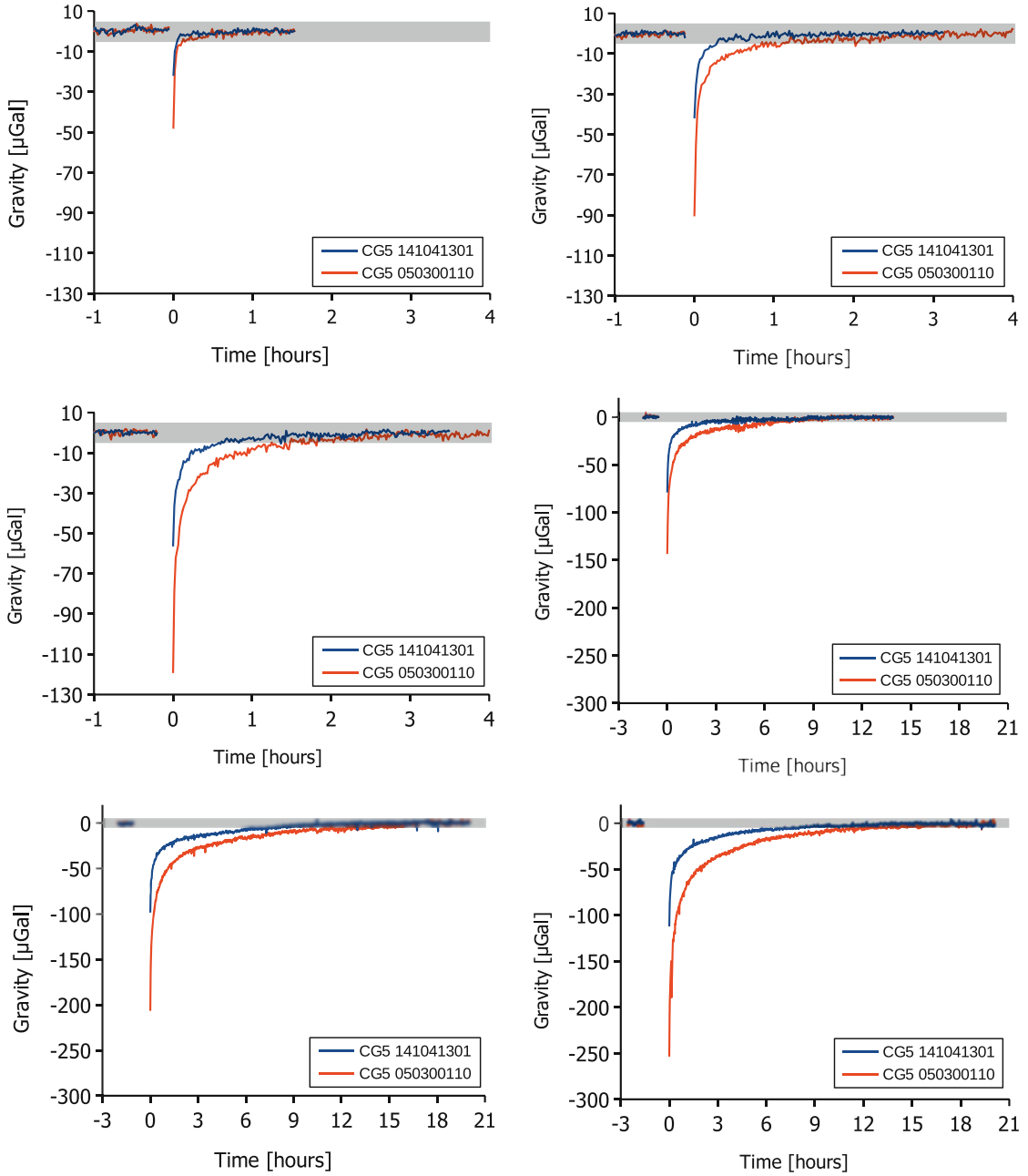

Fig. 1 Readings as function of time. The duration of tilt before readings are recorded is 1 min (*top left*), 5 min (*top right*), 10 min (*middle left*), 30 min (*middle right*), 60 min (*bottom left*), and 90 min (*bottom right*), respectively. CG-5 S/N 050300110 (purchased in 2005) versus CG-5 S/N 141041301 (purchased in 2015). The tilt angle is always 8°. The *grey bar* indicates the ±5 µGal band around the reference value

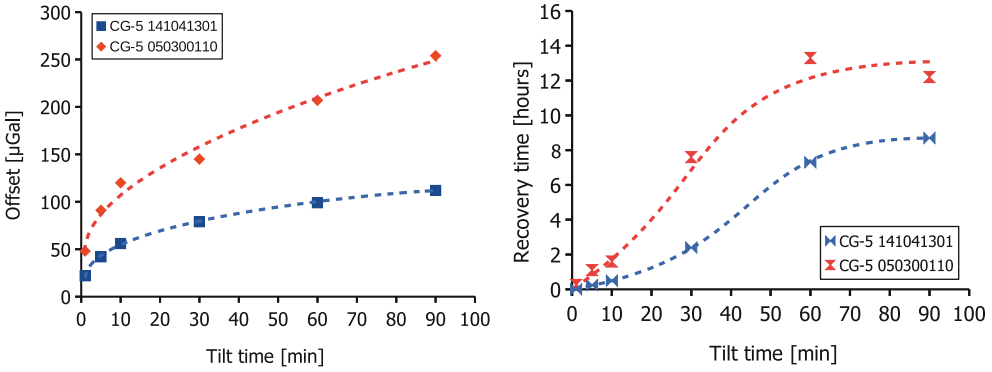

Fig. 2 Initial offset (*left*) and recovery time (*right*) as function of the duration of tilt. The recovery time is defined as the moment in time when the 15-min average readings have stabilised to within ±5 µGal around the reference value. CG-5 S/N 050300110 (purchased in 2005) versus CG-5 S/N 141041301 (purchased in 2015). Tilt is 8°

Table 1 Initial offset as function of the lengths of time in tilted state

Duration of tilt (min)	Initial offset (µGal)	
	CG-5 S/N 050300110	CG-5 S/N 141041301
1	−48	−22
5	−91	−42
10	−120	−56
30	−145	−79
60	−207	−99
90	−254	−112

CG-5 S/N 050300110 (purchased in 2005) versus CG-5 S/N 141041301 (purchased in 2015). In all experiments, the tilt is 8°

Table 2 Time till readings have stabilised (recovery time) as function of the lengths of time in tilted state

Duration of tilt (min)	Recovery time (hours)	
	CG-5 S/N 050300110	CG-5 S/N 141041301
1	0.25	0
5	1.1	0.25
10	1.6	0.5
30	7.6	2.4
60	13.3	7.3
90	12.2	8.7

The recovery time is defined as the moment in time when the 15-min average readings have stabilised to within ±5 µGal around the reference value. CG-5 S/N 050300110 (purchased in 2005) versus CG-5 S/N 141041301 (purchased in 2015). In all experiments, the tilt is 8°

Table 3 Time till readings have stabilised (recovery time) as function of the lengths of time in tilted state

Duration of tilt (min)	Recovery time (hours)	
	CG-5 S/N 050300110	CG-5 S/N 141041301
1	0.5	0.17
5	2.3	0.6
10	2.5	1.2
30	9.0	7.0
60	15.0	10.0
90	16.5	12.0

Compared to Table 2, the recovery time is now defined as the moment in time when the 15-min average readings have stabilised to within ±2 µGal around the reference value. CG-5 S/N 050300110 (purchased in 2005) versus CG-5 S/N 141041301 (purchased in 2015). In all experiments, the tilt is 8°

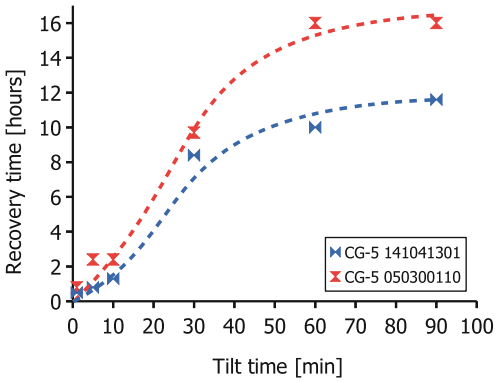

Fig. 3 Recovery time as function of the duration of tilt. Compared to Fig. 2, the recovery time is now defined as the moment in time when the readings have stabilized to within ±2 µGal around the reference value. CG-5 S/N 050300110 (from 2005) versus CG-5 S/N 141041301 (from 2015). Tilt is 8°

3 Summary and Recommendations

In this paper, we investigated the tilt susceptibility of a Scintrex CG-5 Autograv gravity meter purchased in 2015, and compared it to the results in Reudink et al. (2014) to answer the question whether Scintrex Ltd. has solved the tilt susceptibility problem with the latest release of the CG-5 Autograv gravity meter. The answer is "no". Though, initial offset and recovery time have improved significantly, the latter attains easily values of several hours if the tilt exceeds a critical value of about 6° that lasts for a minimum of a few minutes. As with the older CG-5 instruments investigated in Reudink et al. (2014), reviewing the readings at a site as suggested in the CG-5 manual (Scintrex Ltd 2012) does not give a clear indication that the readings may be far off the correct values. Therefore, we still advice users, who use the CG-5 for highly accurate surveys, to permanently watch the "Integrator Output Voltage" in the User Sensor Check when in transit between sites. According to Scintrex Ltd (2012), the displayed voltage should be between 0.5 and 2.7. If during transit the voltage is zero or close to zero (e.g., below 0.5) for at least 1 min, it is very likely that a significant offset and a long recovery time are to be expected at the site as documented in this study.

References

Reudink R, Klees R, Francis O, Kusche J, Schlesinger R, Shabanloui A, Sneeuw N, Timmen L (2014) High tilt susceptibility of the Scintrex CG-5 relative gravimeters. J Geod 88:617–622. doi:10.1007/s00190-014-0705-0

Scintrex Ltd (2012) CG-5 Scintrex autograv system operation manual, part 1 # 867700 revision 8. Scintrex Limited, Concord

Gravity Calibration Baseline Between Jeddah and Taif in the Kingdom of Saudi Arabia

Gokhan Arslan, Mehmet Emin Ayhan,
Bandar Saleh Abdulkareem Al-Muslmani, Meshal Ahmad Saad Al-Qulaity,
and Sultan Falah Alzulrah Al-Shahrani

Abstract

Relative gravimeters are calibrated for calibration factors relating observable units to gravity. The calibration correction factors with respect to the instrument calibration factors are estimated by measurements at gravity calibration baseline (GCB) stations. GCB is a gravity network where known gravity differences are compared to those measured by relative gravimeters. The GCB in the Kingdom of Saudi Arabia has endpoints in Jeddah and Taif. The endpoints were observed by FG5 (#111) and A10 (#029) absolute gravimeters in 2013–2014. Twelve new sites in between the endpoints were installed in the late 2014. There are two stations (center/inside and ex-center/outside) at each GCB sites, hence the GCB includes 28 stations. Absolute gravity (AG) at the GCB stations were observed simultaneously by two A10X (#021, #023) absolute gravimeters. The stations were also tied simultaneously by four CG5 relative gravimeters. Besides gravity gradient at each of the stations was measured by two CG5s. The gravity measurements were completed from December 2014 to January 2015. The total uncertainty of A10X is smaller than 6 μGal. The uncertainties of gravity gradient and tie measurements are smaller than 2 μGal/m and 5.4 μGal, respectively. Comparisons of ties observed by CG5 and A10X result in differences less than 9 μGal. The GCB network is adjusted by weighted constraint least squares. Estimated uncertainty of the gravity differences is 1–2 μGal. The gravity differences between the endpoints of the calibration line at Jeddah and Taif is 430.678 ± 0.002 mGal.

Keywords

A10X • Adjustment • Baseline • Calibration • CG5 • Gravity network • Micro-g LaCoste

1 Introduction

The response of gravimeters is not always linear and may also change with aging of the meters due to relaxation of its mechanic system and environmental effects. So relative gravimeters should be properly calibrated (scaled) before performing field work and regularly calibrated when utilized over long period. The most important calibration item is the mathematical model that relates observable units to gravity units. The model may consist of nonlinear calibration factors. The calibration correction factors with respect to the instrument calibration factors are obtained by performing calibration line measurements where large known differences in gravity are compared to those measured by the relative gravimeters.

Relative gravimeters available in the market have various measurement and mechanical systems. In order to combine measurements by different type of the gravimeters, the gravimeters are calibrated along a baseline installed in the field or in laboratory. The calibration line outside consists of absolute gravity at the high density points measured by absolute and/or relative gravimeters in order to investigate

G. Arslan (✉) • M.E. Ayhan • B.S.A. Al-Muslmani •
M.A.S. Al-Qulaity • S.F.A. Al-Shahrani
General Commission for Survey, Riyadh, Kingdom of Saudi Arabia
e-mail: a.gokhan@gcs.gov.sa

G. S. Vergos et al. (eds.), *International Symposium on Gravity, Geoid and Height Systems 2016*,
International Association of Geodesy Symposia 148, DOI 10.1007/1345_2017_5

nonlinearity in the calibration factor covering the worldwide range. It is also required spanning long gravity range, large height and latitude difference between the points, including high density points in fixed gravity and height intervals accessible in short driving distance as possible (Barlow 1967; Torge 1989).

United States Geologic Survey (USGS) installed 15 calibration lines in order to span two gals in the west of USA (Barnes et al. 1969). USGS also installed a gravity calibration line along road between Jeddah and Al-Hada/Taif by using four Lacoste & Romberg relative gravimeters in 1980. The line includes six stations at which gravity and height differences between the end stations are 503.873 mGal and 2007.5 m, respectively. The gravity interval between stations is about 100 mGal (Gettings 1985). However, presently, the calibration stations do not exist in the field. Therefore General Commission for Survey (GCS) installed a new gravity calibration baseline (GCB) which is described in Sect. 2. Pre-calibration of the gravimeters, absolute and relative gravity measurements at the calibration sites, reduction of the data are discussed in Sect. 3. Quality control of gravity measurements and comparison of absolute and relative ties are described in Sect. 4. In Sect. 5, adjustment of the GCB network is explained. Finally conclusions are given in Sect. 6.

2 Gravity Calibration Baseline (GCB): Site Selection and Monuments

Calibration line follows the road between Jeddah and Taif, and consists of fourteen (14) sites: two (2) existent AG sites at the endpoints and twelve (12) new sites (Fig. 1). At each site, an ex-center (outside) station within 20 m from the center (inside) station is located for the sake of the site is destroyed. The new sites are selected to be easily accessible all the times from existing roads in driving time as short as possible between the sites for observations preferable without being affected by local traffic. The sites are located over pre-Cambrian basement rocks (Gettings 1985) in environmentally quiet area providing long-term permanence. A concrete pad sized 80 cm × 80 cm and 50 cm depth, which is suitable for both relative and absolute gravity measurements, is installed at both center and ex-center stations. A marker is installed on the concrete pad (Fig. 2).

Jeddah and Taif absolute gravity sites were installed and observed by FG5 (#111) and A10 (#029) absolute gravimeters between December 2013 and February 2014 (Ayhan et al. 2015). The endpoints of the calibration line are almost at the same latitude so the main reason of the gravity span about 431 mGal is height difference (1,521 m). The

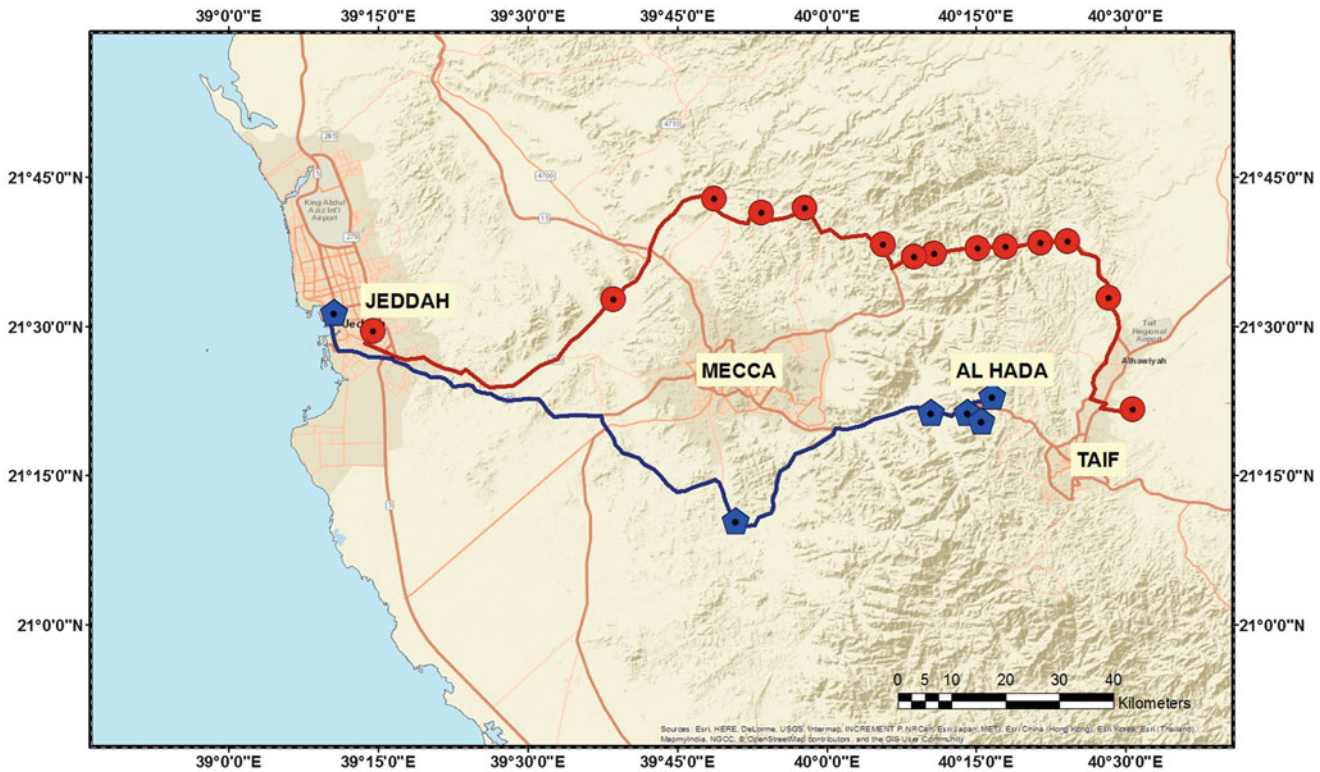

Fig. 1 GCB site locations. *Red circles* and *line* are the stations of GCS GCB and the road followed by GCS GCB and *blue pentagons* are the stations of USGS GCB and the road followed by USGS GCB, respectively

Fig. 2 Monument at calibration stations. (**a**) Cross section of concrete pillar (**b**) Pillar in *red* at center station (**c**) Pillar in *blue* at ex-center station

sites were installed from December 2014 to February 2015. Coordinates of all stations were measured in static mode by GNSS dual frequency receivers. A level line along the Jeddah-Taif road and connections to the calibration stations are also planned. In order to quantify stability of the stations repeat GNSS, leveling and absolute gravity measurements are required in future.

3 Measurements

GCB stations are measured by two A10X absolute gravimeters and four CG5 relative gravimeters, which were tested and calibrated before and after shipping. Micrograv and 'g9' software are used for processing and reducing CG5 and A10X measurements, respectively (Gettings 2009).

3.1 Calibration of Gravimeters

A10X portable absolute gravimeters which are improved version of A10 are used in absolute gravity measurements. Klopping (2015) reported that the precision and accuracy of the A10X are better than A10 uncertainties by 25% on ideal surfaces and by as much as 50% on soft surfaces, and repeatability of ± 3 μGal for A10X. A10Xs were checked in the Micro-g LaCoste Laboratory in Boulder, Colorado before shipping, which include: laser calibrations, rubidium oscillators, T2 Scope collimation, A10X beam verticality and A10X laser output. The A10X gravimeters have been read on a concrete pad at Micro-g LaCoste head office where many FG5 absolute gravity standard readings have been made. In order to verify gravimeter accuracy stability after shipping, before starting of absolute survey, two A10Xs (#021, #023) were checked in Jeddah absolute gravity station measured by FG5 in the early 2014 (Ayhan et al. 2015).

The repeatability of CG5 is declared as 5 μGal by the manufacturer (http://www.scintrexltd.com/). Before shipping, six CG5s (#40052, #40057, #40058, #41210, #41211, #126) were calibrated on the Rocky Mountain calibration line in Denver (Barnes et al. 1969). Before starting the relative gravity survey, calibration of the CG5s was checked between Riyadh and Kharj FG5 absolute gravity sites (Ayhan et al. 2015). After finishing the first calibration loops, all CG5s showed remarkable discrepancies, which suggest the need of the modifications of the used calibration factors. However, calibration factor modification utilized larger gravity difference than that of Riyadh and Kharj (33 mGal). Thus, it has been decided to re-calibrate the gravimeters between Jeddah and Taif points measured by A10X. Calibration measurements were processed using least squares software. Estimated drift and calibration factor for each CG5 are given in Table 1.

3.2 Absolute Measurements

The absolute gravity measurements at 28 GCB stations (14 center and 14 ex-center) were carried out by using Micro-g Lacoste (MGL) provided two A10Xs (#021 and #023) between December 2014 and January 2015.

The absolute gravity measurement is carried out at least ten evenly spaced sets each of which includes about 120 drops. All the sets take place 30 min. A10X repeatability for drops in one set is site dependent (50 μGal at quite site). Repeatability of sets is smaller than ± 3 μGal, and total uncertainty of observed absolute gravity is smaller than ± 6 μGal. Two (2) ten sets of 120 drops are obtained in row by two A10Xs at two different time over both the center and ex-center stations.

The real-time absolute gravity processing was performed in the field by 'g9' software package provided by MGL. 'g9'

Table 1 CG5 Calibration and drift factors estimated between Jeddah and Taif A10X stations

CG5 gravimeters	Calibration factor (mGal/CU)	Drift factor (mGal/day)
CG5 #40052	1.000124 ± 0.000004	0.141 ± 0.004
CG5 #40057	0.999859 ± 0.000002	0.030 ± 0.002
CG5 #40058	0.999844 ± 0.000001	0.022 ± 0.001
CG5 #126	0.999976 ± 0.000001	0.107 ± 0.001
CG5 #41210	0.999840 ± 0.000001	0.013 ± 0.001
CG5 #41211	0.999948 ± 0.000004	−0.007 ± 0.004

CU counter unit

processing incorporates the least- squared fit of the time-distance pairs for each drop with gravity gradient speed of light effects removed. Solid earth tide (Tamura), inelastic response to tides, ocean loading (FES2004), and ambient barometric and temperature corrections all counted for in real time processing. In post-processing, corrections of polar motion and height of instruments were applied (http://www.microglacoste.com/software.php). In correction of height of instrument, the absolute gravity values at each station were reduced from A10X reference mass height (82 cm) to reference heights (25 cm and on the marker). Because CG5 reference mass height from the marker was fixed at 25 cm by fixed tripod and aimed to compare absolute and relative gravity differences at the height.

Gravity gradient measurements at each station were carried out by multiple observations with up/down transfer by using two CG5 gravimeters and a tripod at three levels (25 cm, 75 cm, 125 cm) to parabolic (second order) estimation. The difference of gradient readings from mean at each level is obtained smaller than 2 μGal/m.

3.3 Relative Measurements

The relative gravity measurements between the GCB stations (ties) were carried out by using four CG5 relative gravimeters between January 2015 and Febraury2015. Each tie measurement between center—center or center—ex-center stations includes minimum three loop sequences (the difference sequence).

The gravimeters were set up one after another over the marker at one station and loop measurements were completed in 12 h in 1 day. In order to provide relaxation of the gravimeter, minimum 15 min time series and minimum ten acceptable readings at each station for one instrument were obtained. One acceptable reading period is at least 60 s. Standard deviation of acceptable readings from the mean is smaller than ±2 μGal. In order to correct and reduce gravity readings, ambient temperature, air pressure and the height of instrument (from bottom of the instrument to the top of the marker) are measured and stored. The instrument was oriented in the same way to the magnetic north by digital compass to avoid magnetic effect and the operator was at a distance of about 10 m from the gravimeters. A portable shutter was used to protect the instrument from wind, sunlight.

Pre-processing of CG5 measurements was carried by using both software embedded in CG5 and Micrograv (Gettings 2009). Reductions and corrections applied in pre-processing are calibration, ambient temperature, continuous tilt correction, auto rejection and seismic noise filter, earth tide correction, staircase drift correction, readout rejection and reference mass height correction. After pre-processing, we found tie uncertainty smaller than ±5.4 μGal.

4 Comparison of Absolute and Relative Gravity Measurements

Absolute gravities observed at the same station by the two A10Xs are compared, and the differences are shown in Fig. 3. The differences are expected to be smaller than 8.5 μGal which is satisfied almost at each station. The differences are mostly within 5 μGal, and scattered around the mean of 2.0 ± 2.2 μGal, which may be caused by the calibration difference of the two A10Xs.

Each of the ties between centre-centre and centre-excentre is observed independently by using four CG5s. The mean of the four measurements are computed for each ties. Then the difference of a tie by each CG5 from the mean is calculated and shown in Fig. 4. The differences are almost within 5 μGal. We found the mean of 0.1 ± 4.4 μGal, 0.4 ± 5.8 μGal and 1.6 ± 3.0 μGal for CG5 #40057, #41211 and CG5 #41210, respectively. However CG5s #40052, #40058 and #126 used replacing each other due to instability reveal the mean 2.7 ± 7.0 μGal. The RMS of the differences for all CG5s is ±5.4 μGal, which may indicate a measure of uncertainty for CG5. The large differences are likely outliers which would be detected in the adjustment.

Absolute gravity measurement at a station is an individual observation. In order to check absolute gravity measurement at one station, another absolute gravimeter can be used at the same point or pair of points at which absolute gravity observed can be tied by relative gravity measurements. For

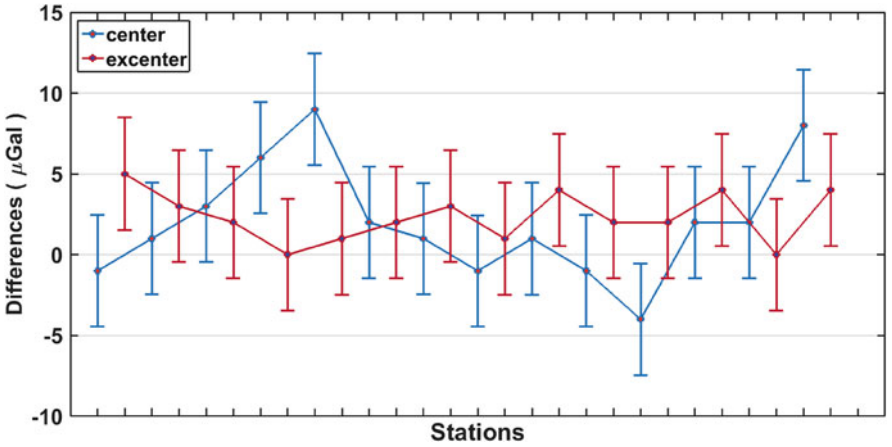

Fig. 3 Differences of absolute gravity by A10X #021 and A10X #023 at each station

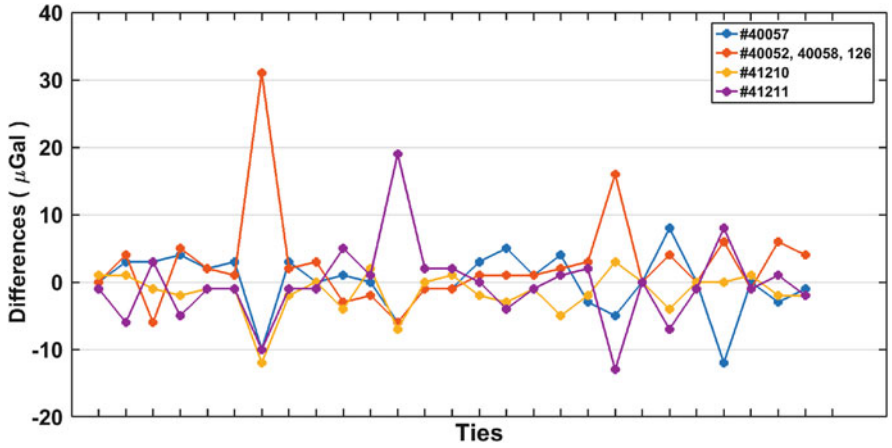

Fig. 4 Differences of four CG5s tie from the mean for each tie

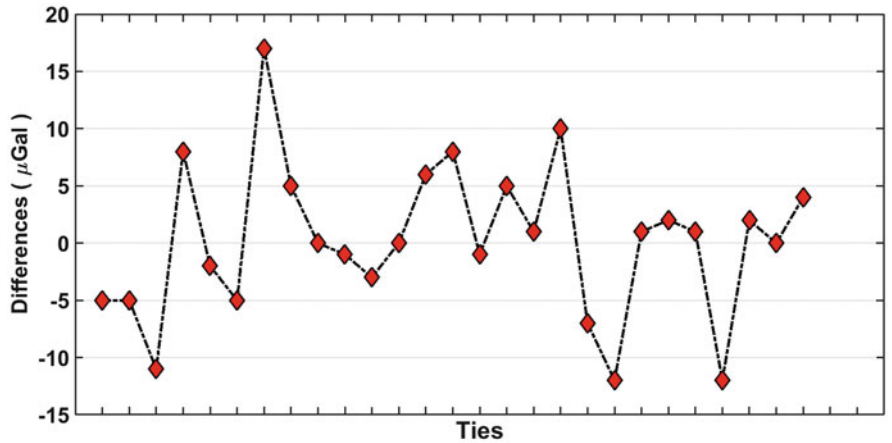

Fig. 5 The differences between the mean ties by four CG5s and by two A10Xs

the latter case the gravity differences between two points by absolute and relative gravity measurements are compared. This comparison provides quality check of the two types of measurements and coincidence of the gravimeter's calibration. For this aim we compared the mean ties obtained by both averaging the four CG5 tie measurements and the two A10X tie measurements. The differences shown in Fig. 5 are scattered around zero in the range of ±10 μGal, with RMS of ±6.6 μGal.

Absolute gravity at the endpoints of the calibration line (AG0050, AG0061) were observed by MGL FG5 (#111) in the early 2014 (Ayhan et al. 2015). Furthermore the endpoints are tied directly by using three CG5s. Cumulative sums of centre-centre gravity measurements by four CG5 and their mean are also calculated. Gravity differences (ties) between the endpoints measured by CG5, A10X and FG5 are listed in Table 2 for comparisons. Loop closures are calculated by subtracting the tie by FG5 from the ties by

Table 2 Tie between the endpoints (AG0050–AG0061) and loop closures

Gravimeters	CG5[a]	CG5[b]	A10X(#021)[c]	A10X(#023)[c]	FG5(# 111)[c]
Tie	430.671	430.6875	430.676	430.671	430.681
Loop closure	−0.010	0.0065	−0.005	−0.010	0.000

[a]Mean of cumulative sums by four CG5
[b]Mean of tie measurements by three CG5s
[c]Tie obtained by subtracting absolute gravity observed by A10X/FG5 at the endpoints Loop closures are calculated by subtracting tie by FG5(#111) from the ties by CG5[a], CG5[b], A10X(#021) & (# 023). (in mGal)

CG5s and A10Xs and are given in the last row of the Table. Loop closures for A10Xs are within 10 μGal which is in the uncertainty level of A10X and FG5 when we consider their total uncertainties (Ayhan et al. 2015). Loop closure of 6.5 μGal for CG5 tie is at the level of CG5 uncertainty whereas cumulative CG5 tie gives −10 μGal loop closure which is assumed to be caused by cumulative uncertainties along the calibration stations.

5 Adjustment

5.1 The Model

The observation equations of tie (gravity difference) and absolute gravity measurements are given below:

$$\Delta \boldsymbol{l}_{ij} + \boldsymbol{v}_{ij} = \boldsymbol{g}_j - \boldsymbol{g}_i + \Delta \boldsymbol{F}\left(\Delta z_{ij}\right) + \Delta \boldsymbol{D}\left(\Delta t_{ij}\right) \quad (1)$$

$$\boldsymbol{l}_i + \boldsymbol{v}_i = \boldsymbol{g}_i \quad (2)$$

where Δt_{ij} is time difference of measurements, Δz_{ij} is the gravimeter reading difference in counter unit (CU), Δl_{ij} is the corrected gravity difference between station i and j, $\boldsymbol{v_{ij}}$ is residual, g_i is unknown gravity at station i, ΔF is the polynomial calibration correction function and ΔD is the polynomial drift function of gravimeter, l_i is absolute gravity measurement at point i and $\boldsymbol{v_i}$ is its residual. Observation equations in matrix form are given below:

$$\boldsymbol{L}^b + \boldsymbol{V} = \boldsymbol{A}\boldsymbol{X} \quad (3)$$

$$\boldsymbol{L}_g + \boldsymbol{V}_g = \boldsymbol{A}_g \boldsymbol{X} \quad (4)$$

where; $\boldsymbol{L}$ is vector of measurements, $\boldsymbol{V}$ is vector of residuals, $\boldsymbol{A}$ is design matrix, $\boldsymbol{X}$ is vector of unknowns (gravity values g_i and gravimeter parameters (scale factor and drift constants)). Observations are assumed uncorrelated and weight of the observations is defined by $\boldsymbol{p}_{ij} = 1/\boldsymbol{\sigma}_{ij}^2$ and $\boldsymbol{p}_i = 1/\boldsymbol{\sigma}_i^2$ for gravity difference and absolute gravity, respectively. Matrix $\boldsymbol{A}$ has rank defect one in gravity networks so at least one fix point (constraint) is required. Absolute gravity observations in Eq. (4) are introduced as constraints and weighted constraint least squares solution of the network is obtained. After obtaining estimates of unknowns, residuals and their uncertainties, the global test and Pope's outlier test are applied in order to clean data set and verify the mathematical model (Hwang et al. 2002).

5.2 GCB Network Adjustment

GCB Network consists of 28 station, 112 tie measurements by CG5 and 56 absolute gravity measurements by MGL A10X. Network configuration is shown in Fig. 6. As it is seen in the figure we include tie measurements between the endpoints of the calibration line (AG050 and AG061) which are observed by three CG5s in 2015. So this network provides a long loop to control internally both the CG5 and A10X measurements.

The network adjustment was achieved by using in house software in matlab based on the theory explained in the previous section. We excluded 17 tie measurements by CG5 and six absolute gravity measurements as outliers. The gravity differences and their uncertainties are calculated based on the estimated absolute gravity at the stations between center-center and center-excenter stations, and given in Table 3.

6 Discussions

The standard deviation of CG5 relative measurements and total uncertainty of MGL A10X absolute gravity measurements are found smaller than ±5.4 μGal and about ±6 μGal, respectively. Estimated uncertainty for ties between the GCB stations is ±1–2 μGal which is remarkable improved.

The sites are not located at fix driving distance interval. Gravity interval between the sites is 60 mGal for four ties and between 3 and 40 mGal for the rest (Fig. 7a). Height differences between sites (center-center) vary from about 50 to 280 m (Fig. 7b). It was planned initially fix height difference about 100 m between the sites so that about 30 mGal gravity interval. However, this requirement was not be able to achieve in site selection. The gravity differences between center and ex-center stations vary between 0.043

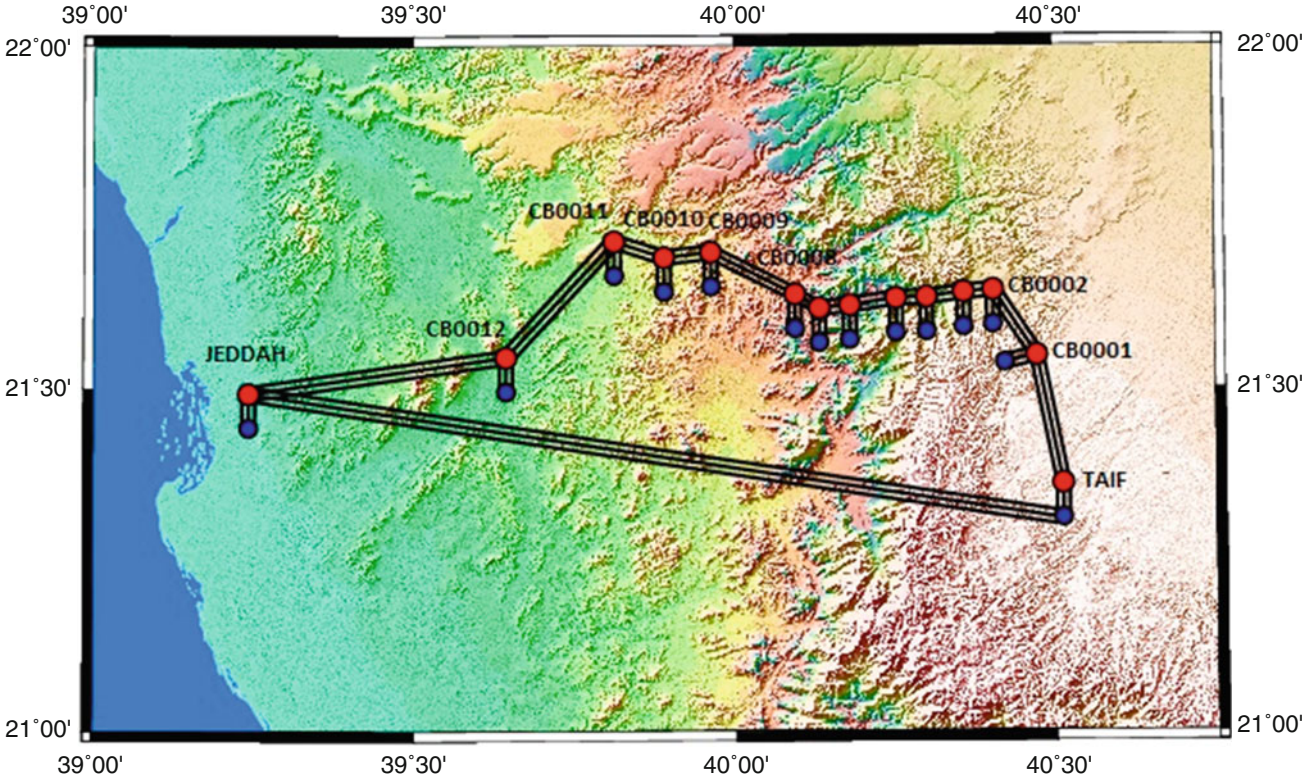

Fig. 6 GCB Network. *Red* and *blue solid cycles* are center and ex-center stations respectively. *Black line* is tie measurement

Table 3 The estimated ties (gravity differences) between center-center and center-excenter stations

Center-center	Tie estimates (mGal)(mGal)	Center-excenter	Tie estimates (mGal)(mGal)
AG050–CB120	63.279 ± 0.002	AG050–AG051	0.567 ± 0.002
CB120–CB110	21.813 ± 0.001	CB120–CB121	0.216 ± 0.001
CB110–CB100	19.366 ± 0.002	CB110–CB111	0.058 ± 0.001
CB100–CB090	14.599 ± 0.002	CB100–CB101	0.259 ± 0.003
CB090–CB080	58.531 ± 0.001	CB090–CB091	0.343 ± 0.001
CB080–CB070	18.143 ± 0.001	CB080–CB081	−0.043 ± 0.001
CB070–CB060	3.862 ± 0.001	CB070–CB071	0.151 ± 0.002
CB060–CB050	26.991 ± 0.001	CB060–CB061	0.024 ± 0.001
CB050–CB040	14.079 ± 0.001	CB050–CB051	0.027 ± 0.001
CB040–CB030	32.324 ± 0.001	CB040–CB041	0.086 ± 0.001
CB030–CB020	57.272 ± 0.001	CB030–CB031	−0.295 ± 0.001
CB020–CB010	62.030 ± 0.001	CB020–CB021	0.033 ± 0.001
CB010–AG060	38.498 ± 0.001	CB010–CB011	−0.179 ± 0.002
AG050–AG061	430.678 ± 0.002	AG060–AG061	−0.109 ± 0.001

and 0.567 mGal. Considering height and gravity difference between the endpoints, rate of gravity variation along the baseline is 0.284 mGal/m, which is close to free air gradient.

GCB stations were installed on the right side of the road in the direction from Jeddah to Taif. All the stations are located closed to the road which is separated in some segments by a barrier so that reaching some stations may be difficult.

7 Conclusions

The gravity differences between absolute measurements by using two A10X are found mostly smaller than 5 μGal. In general; the differences between observed gravity differences by each CG5 and the average of four gravity differences for

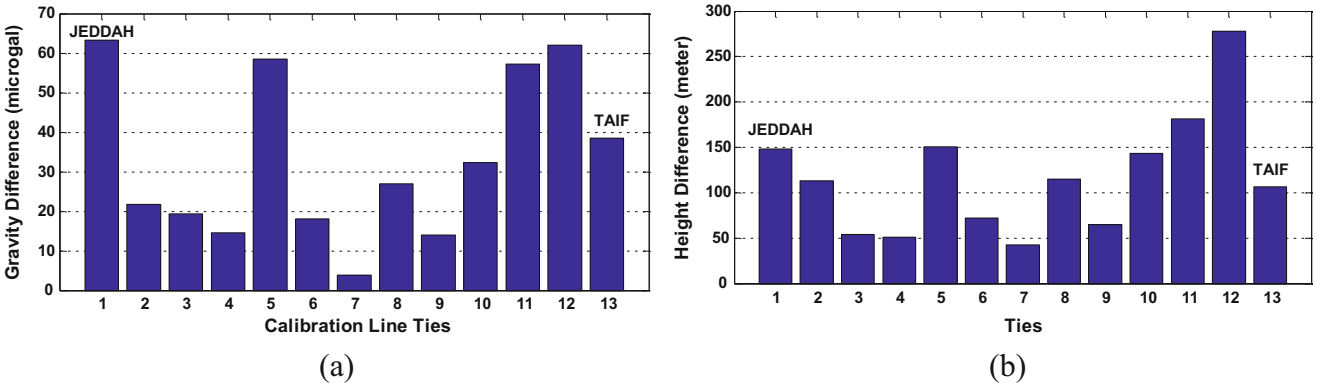

Fig. 7 (**a**) Gravity differences between sites. (**b**) Height differences between sites

each tie are within 5 μGal. The relative and absolute gravity differences between center-center stations are coincident within 10 μGal with RMS of ±6.6 μGal. Comparisons of the gravity differences between the endpoints of the baseline reveal that CG5 and A10X measurements are coincident with FG5 measurement within 10 μGal.

The estimated gravity differences vary between 3.861 and 63.280 mGal for the center-center stations and −0.295 and 0.567 mGal for the center-excenter stations. The GCB between Jeddah and Taif is appropriate for calibration of relative and absolute gravimeters, and satisfies a scale standard in gravity surveys by public institutes and private companies.

Acknowledgments We appreciate support of GCS for the project. Thanks to Jeff Kanney from MGL, Boulder, Colorado who did seriously A10X measurements. We also thank to field engineers and operators from Magee Geophysical Services, Reno, USA, for their precise field works of CG5 measurements.

References

Ayhan ME et al (2015) Absolute gravity measurements by using FG5 and A10 absolute gravimeters in the Kingdom of Saudi Arabia. Arab J Geosci 8:6199–6209

Barnes DF, Oliver HW, Robbins SL (1969) Standardization of gravimeter calibrations in the geological survey. EOS 50(10):526–527

Barlow BC (1967) Gravity meter calibration in Australia. Bureau of Mineral Resources, Geol. and Geophy., Rept. No.: 122. pp 48

Gettings ME (1985) Gravity base ties and gravimeter calibration in western Saudi Arabia. Open-File Report 85-26, Department of Interior, U.S. Geological Survey, USA

Gettings P (2009) High precision gravity measurements. Department of Geology & Geophysics, University of Utah, Salt Lake City

Hwang C, Wang CG, Lee LH (2002) Adjustment of relative gravity measurements using weighted and datum-free constraints. Comput Geosci 28:1005–1015

Klopping F (2015) A10X dropper development and applications. MGL in-house White Paper

Torge W (1989) Gravimetry. de Gruyter. Berlin. 465 pp

Investigation of Geoid Height Variations and Vertical Displacements of the Earth Surface in the Context of the Realization of a Modern Vertical Reference System: A Case Study for Poland

Walyeldeen Godah, Malgorzata Szelachowska, and Jan Krynski

Abstract

The GRACE (Gravity Recovery and Climate Experiment) mission launched in 2002 brought a unique opportunity for the determination of temporal mass variations within the Earth system. Their knowledge is essentially needed to achieve the best accuracy of a regional/local geoid model. They are also needed to investigate temporal displacements of the physical surface of the Earth. The aim of this contribution is to study temporal variations of geoid heights as well as to discuss the vertical displacements of the Earth surface in the perspective of the realization of the modern vertical reference system. The area of Poland has been chosen as a study area. Temporal geoid height variations have been determined over the area of Poland divided into four subareas. They have been analysed and modelled using the seasonal decomposition method. As an example, temporal vertical displacements induced from temporal water variations at the Borowa Gora Observatory (BGO) have been determined using GRACE mission data. The results obtained in a case study for Poland reveal that the combination of temporal geoid height variations and temporal vertical displacements of the physical surface of the Earth result in significant temporal variations of the vertical reference system for the area investigated.

Keywords

Geoid • GRACE • Vertical displacement • Vertical reference system

1 Introduction

The precise geoid model is essentially needed for the realization of a vertical reference system. In the recent two decades, a considerable progress has been achieved in the methods of the geoid modelling and in the acquisition of gravity data from terrestrial and airborne measurements as well as from satellite observations. Thus, the static geoid model of 1 cm accuracy has become achievable in global and regional/local scales (e.g. Tscherning et al. 2000; Krynski and Lyszkowicz 2006). Currently, the modelling of a regional geoid/quasigeoid with sub-centimetre accuracy is considered as one of the activities of the Commission 2 "Gravity Field" of the International Association of Geodesy (see Huang 2016). In the area of Poland, during the last two decades, an intensive research has been conducted for modelling the geoid/quasigeoid (for more details see Krynski 2007). The estimated fit of the recent static quasigeoid model developed over this area to GNSS (Global Navigation Satellite System)/levelling data is at the level of 1.4–2.2 cm in terms of standard deviation of differences (e.g. Szelachowska and Krynski 2014).

Temporal variations of geoid heights need to be considered for developing a regional/local geoid model of sub-centimetre accuracy as well as for the realization of the vertical reference system. During the past years, some investigations concerning temporal variations of geoid heights were conducted. For example, Rangelova (2007) combined

W. Godah (✉) • M. Szelachowska • J. Krynski
Centre of Geodesy and Geodynamics, Institute of Geodesy and Cartography, 27 Modzelewskiego Street, 02-679, Warsaw, Poland
e-mail: walyeldeen.godah@igik.edu.pl

G. S. Vergos et al. (eds.), *International Symposium on Gravity, Geoid and Height Systems 2016*, International Association of Geodesy Symposia 148, DOI 10.1007/1345_2017_15

GRACE data with GNSS, tide gauge/altimetry and absolute gravimetry data to develop a dynamic geoid model for Canada. Rangelova and Sideris (2008) estimated secular geoid changes in North America using GRACE and terrestrial geodetic data. Rangelova et al. (2010) conducted a feasibility study on implementing the resulting dynamic geoid model obtained accordingly to those studies, i.e. Rangelova (2007) and Rangelova and Sideris (2008), as a vertical datum for orthometric heights in Canada. Krynski et al. (2014) conducted research for analyzing variations of the Earth's gravity field over the whole area of Europe using release RL04 GRACE-based global geopotential models (GGMs) (cf., Watkins and Yuan 2007). The authors showed that amplitudes of geoid height variations for the area of Central Europe reach up to 7 mm. Godah et al. (2017) analyzed, modelled and predicted temporal variations of geoid heights determined from GRACE-based GGMs for four 3° × 5° subareas of Poland. Time series of geoid height variations obtained from GRACE-based GGMs from 7 years, with no gaps, were investigated. The authors revealed that seasonal geoid height variations reach to 1.1 cm. They recommended the seasonal decomposition method (cf. Makridakis et al. 1998) for modelling temporal variations of geoid heights over the area of Poland.

Besides temporal variations of geoid heights, the knowledge of temporal variations of the physical surface of the Earth is also needed for the realization of the vertical reference system. The GRACE mission brought very useful information related to the elastic ground loading deformation in response to the Earth mass variations (e.g. van Dam et al. 2007; Tan et al. 2016). For the area of Poland, Rajner and Liwosz (2011) indicated a good correlation between seasonal vertical displacements obtained, for the period between 1997 and 2007, from the hydrological loading, determined on the basis of the WGHM (WaterGAP (Water- a Global Assessment and Prognosis) Global Hydrological Model; Döll et al. 2003), and the corresponding ellipsoidal height variations determined from GNSS data from four permanent stations in Poland. A clear seasonal pattern of vertical displacements with maximum values in autumn and minimum values in spring has been shown. The authors also reveal that temporal vertical displacements at the Borowa Gora Observatory (BGO) can reach up to 1 cm. Jinwei (2014) analyzed seasonal displacements from GNSS stations data in the Tibetan plateau, around Great Lakes area, and around Danube basin including the BGO. The seasonal vertical displacements in the BGO, obtained by Rajner and Liwosz (2011) and Jinwei (2014) are very similar in terms of both phase and amplitude.

The objective of this contribution is to study temporal variations of geoid heights over the area of Poland using the full time series of GRACE mission data as well as to investigate the relation between temporal geoid height variations and temporal vertical displacements of the physical surface of the Earth and their role in the realization of the modern vertical reference system.

2 Data Used and Study Area

The area of Poland divided into four 3° × 5° subareas was chosen as a study area (Fig. 1; Godah et al. 2017). Temporal variations of geoid heights were determined for that area as well as at the BGO (Fig. 1) using the latest release RL05 GRACE-based GGMs developed by the GFZ (GeoForschungsZentrum) centre (Dahle et al. 2014) filtered with the use of the decorrelation (DDK) filter (Kusche 2007). In addition to those GFZ GRACE-based GGMs, CSR (Centre for Space Research) RL05 GRACE-based GGMs (Bettadpur 2012) filtered with the use of DDK filter, the Jet Propulsion Laboratory (JPL) mass concentration (mascon) solutions (Watkins et al. 2015), and the WGHM were used to estimate water mass variations at the BGO.

3 Temporal Geoid Height Variations

Geoid heights N at the centre point of each subarea have been determined from monthly GFZ RL05 GRACE-based GGMs for the period from 04/2002 to 03/2016 using the ICGEM calculation service (cf. http://icgem.gfz-potsdam.de/ICGEM/.html; Barthelmes 2016). The mathematical formulation applied to compute N values at point P on the ellipsoid, at the ICGEM can be written as follows (cf. Eq. (116) in Barthelmes 2013, p. 22)

Fig. 1 The study area and its four subareas; the *red circle* indicates the location of the BGO

$$N(\lambda,\varphi) = \frac{GM}{r_e \gamma(r_e,\varphi)} \sum_{\ell=0}^{\ell_{\max}=60} \left(\frac{R}{r_e}\right)^{\ell} \sum_{m=0}^{\ell} P_{\ell m}(\sin\varphi)\left(C_{\ell m}^{T}\cos m\lambda + S_{\ell m}^{T}\sin m\lambda\right) - \frac{2\pi G\rho}{\gamma(r_e,\varphi)}\left[R\sum_{\ell=0}^{\ell_{\max}=60}\sum_{m=0}^{\ell} P_{\ell m}(\sin\varphi)\left(C_{\ell m}^{topo}\cos m\lambda + S_{\ell m}^{topo}\sin m\lambda\right)\right]^2 \quad (1)$$

where φ and λ are the latitude and the longitude of P, respectively, GM is the product of the Newtonian gravitational constant G and the Earth's mass M, r_e is the radius of P, $\gamma(r_e, \varphi)$ presents the normal gravity of P, $C_{\ell m}^{T}$ and $S_{\ell m}^{T}$ are the differences between the Stokes' coefficients $\overline{C}_{lm}$ and $\overline{S}_{lm}$ and spherical harmonic coefficients $C_{\ell m}^{U}$ and $S_{\ell m}^{U}$ of the normal potential U, ρ presents a constant mass density, $C_{\ell m}^{topo}$ and $S_{\ell m}^{topo}$ are spherical harmonic coefficients of the topography, R is the Earth's mean radius and $P_{\ell m}$ are normalized Legendre functions of degree ℓ and order m, $\ell_{\max}$ is the applied maximum degree.

Temporal variations of geoid heights ΔN have been obtained by removing the mean geoid height for each subarea. For the whole area they were estimated as the average of ΔN for investigated subareas. There were thirteen gaps in time series of ΔN obtained from GFZ RL05 GRACE-based GGMs resulting from missing GRACE mission observations for some periods. In order to have continuous time series of ΔN for the analysis and modelling geoid height variation values at those gaps were interpolated using the 2nd degree polynomial.

Figure 2 illustrates temporal variations of geoid heights at four subareas investigated as well as at the whole area for the period from 04/2002 to 03/2016. It also depicts gaps in time series of ΔN. The obtained ΔN were analysed and modelled using the seasonal decomposition method (Makridakis et al. 1998; Chap. 3). The detailed description and the implementation steps of the seasonal decomposition method for analysing and modelling ΔN over Poland are given in Godah et al. (2017). According to the seasonal decomposition method, ΔN time series can be presented as follows

$$\Delta N_i = T_i^D + S_i^D + E_i \quad (2)$$

where S_i^D is a seasonal component, T_i^D is a trend-cycle component and E_i presents an unmodelled component.

The resulting components of ΔN and their models are shown in Fig. 3. The statistics of unmodelled components of geoid height variations are given in Table 1.

The results presented in Table 1 indicate that standard deviations of unmodelled components of geoid height variations, are at the level of 0.4–0.5 mm. Figures 2 and 3 illustrate a distinctive seasonal pattern of geoid height variations with maximum values at the beginning of spring and minimum values at the end of summer. They reveal that ΔN differences from epoch to epoch at the same subarea

Table 1 Statistics of unmodelled components (mm)

Statistics	Subarea 1	Subarea 2	Subarea 3	Subarea 4	Whole area
Min	−1.3	−1.1	−1.2	−1.1	−1.1
Max	1.1	1.1	1.4	1.4	1.2
Mean	0.0	0.0	0.0	0.0	0.0
Std.	0.5	0.5	0.4	0.5	0.4

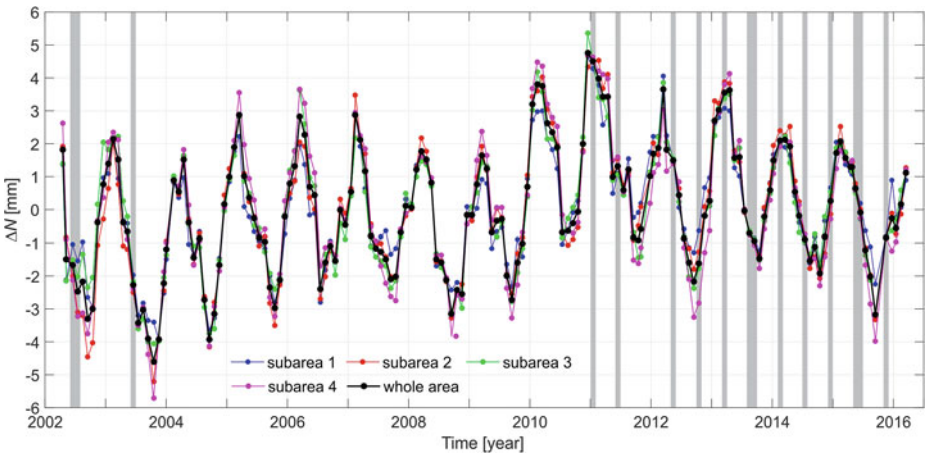

Fig. 2 Temporal variations of geoid heights; *grey columns* indicate gaps in time series of ΔN

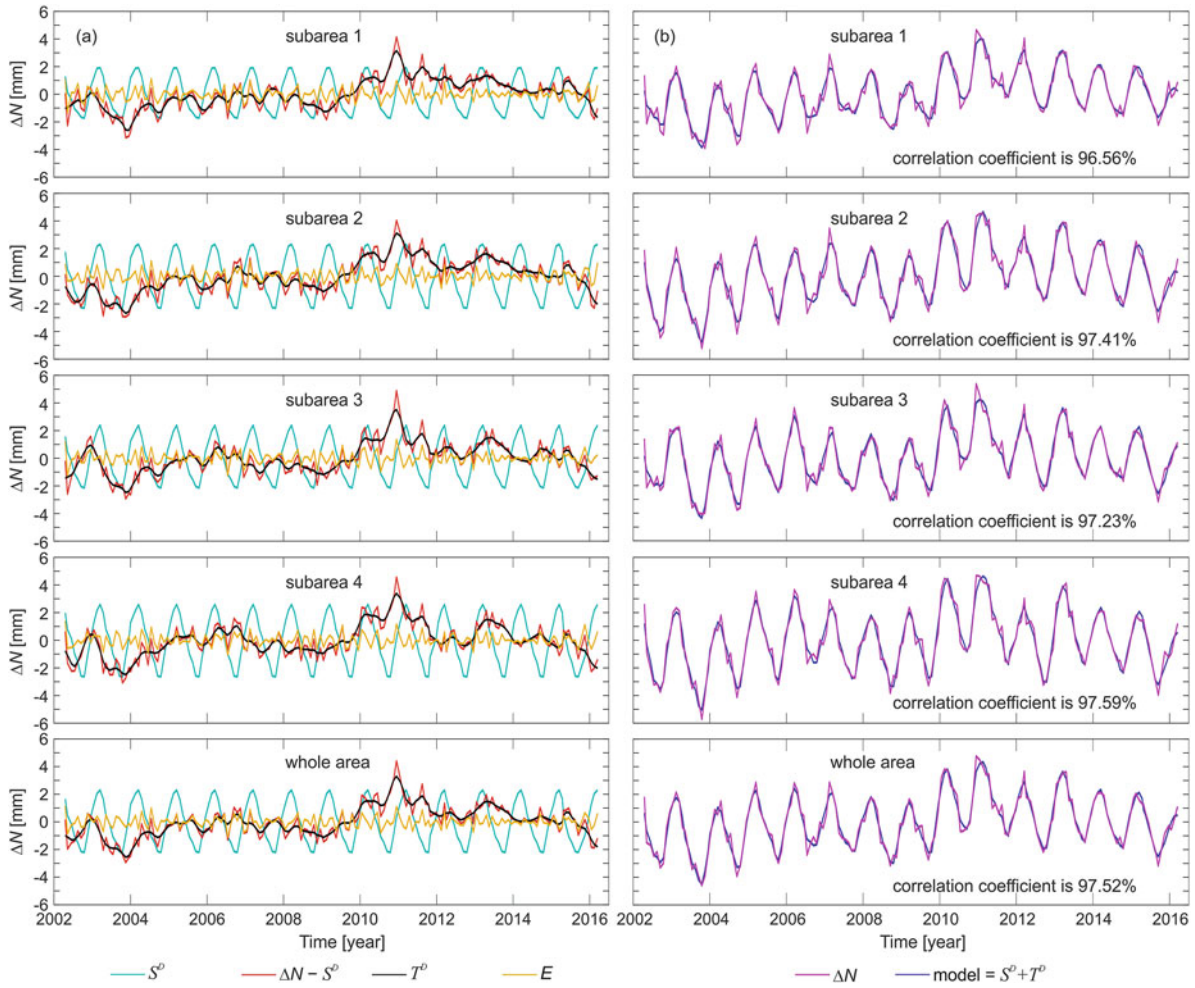

Fig. 3 (**a**) Components of geoid height variations ΔN: S^D presents a seasonal component, T^D is a trend-cycle component and E is an unmodelled component, obtained with the use of the seasonal decomposition method, and (**b**) ΔN and their models obtained by combining the seasonal S^D and trend-cycle T^D components of ΔN

can reach 1 cm. They also indicate that ΔN differences between two subareas can reach 2 mm at the same epoch and 11 mm at different epochs. The outcome models of ΔN obtained using the seasonal decomposition method are highly correlated with the monthly geoid height variations obtained from GFZ RL05 GRACE-based GGMs, i.e. correlation coefficients are ranging from 96.56% to 97.56%. Those results agree with the corresponding ones presented in Godah et al. (2017). This may indicate that filling gaps in time series of ΔN does not change the final results. It also indicates that the seasonal decomposition method is suitable for analysing and modelling ΔN over Poland using GRACE mission data from long time interval, i.e. 14 years that is twice longer than time interval considered in Godah et al. (2017).

4 Water Mass Variations and Vertical Displacements

The GRACE satellite mission detects temporal variations of the total water storage (*TWS*) that consists of soil moisture, snow and groundwater. The *TWS* produce significant geodynamic effects that are observed as displacements of the Earth surface in radial (vertical) and tangential (horizontal) directions. Those displacements are interpreted as elastic responses of the Earth to surface loads (e.g. van Dam et al. 2007; Tan et al. 2016).

In this contribution, an example of water mass variations and vertical displacements determined for the period between 01/2004 and 12/2006 at the BGO is discussed.

For that period both a continuous time series of GRACE mission data as well as vertical displacements from GNSS data obtained by Rajner and Liwosz (2011), which could be used for verification of the results obtained from GRACE mission data, are available. Temporal variations of *TWS* and temporal variations of equivalent water thickness (*EWT*) were obtained from the JPL mascon solutions using the Mascon Visualization Tool (http://ccar.colorado.edu/grace/). These JPL mascon solutions are represented by 4,551 equal areas of 166.9792 km radius (i.e. 3° on the equator) spherical cap mascons distributed globally. They were determined from SST (Satellite-to-Satellite Tracking) data acquired in GRACE mission (Watkins et al. 2015). In this investigation, *EWT* and *TWS* were obtained from the mascon number #:471 that covers the area of the BGO. Temporal variations of *EWT* were also computed from GFZ and CSR RL05 GRACE-based GGMs and the WGHM using the ICGEM calculation service. The resulting temporal variations of *TWS* and temporal variations of *EWT* are shown in Fig. 4a, b, respectively.

The results presented in Fig. 4a exhibit a clear seasonal pattern of *TWS* variations with maximum values observed in spring and minimum values in autumn. The variations of *TWS* range from −10.21 Gt to 9.11 Gt. Figure 4b shows that temporal variations of *EWT* obtained from GRACE mission data are in good agreement with the corresponding ones obtained from the WGHM. The seasonal patterns of *TWS* and *EWT* could be related to the melting of snow that was accumulated in the winter season, and water evaporation during dry months in the summer season (Godah et al. 2015). The phase of those seasonal patterns is consistent with the corresponding phase of seasonal variations of geoid heights over the area of Poland specified in Sect. 3 as well as in the literature (e.g. Krynski et al. 2014; Godah et al. 2017).

Vertical displacements (*dr*) at the BGO for the period from 01/2004 to 12/2006 were computed using CSR RL05 GRACE-based GGMs as follows (van Dam et al. 2007):

$$dr\,(\varphi,\lambda) = R \sum_{\ell=1}^{\ell_{\max}=60} \sum_{m=0}^{\ell} P_{\ell m}\,(\sin\varphi) \cdot \left(\overline{C}_{\ell m}\cos m\lambda + \overline{S}_{\ell m}\sin m\lambda\right) \frac{h'_l}{1+k'_l} \tag{3}$$

where h'_ℓ and k'_ℓ are load Love numbers calculated using the Gutenberg-Bullen Earth model. Their numerical values were obtained from (Farrell 1972). They can successfully be implemented for the estimation of the Earth's surface displacement, gravity variations and geocenter variations due to surface mass loads.

Assuming that temporal variations of ellipsoidal heights Δh are represented by those temporal vertical displacements, temporal variations of orthometric/normal heights ΔH can be estimated as follows:

$$\Delta H = \Delta h - \Delta N \tag{4}$$

Figure 5 shows temporal vertical displacements and temporal variations of geoid height as well as temporal variations of orthometric/normal height at the BGO.

The results presented in Fig. 5 indicate that temporal vertical displacements at the BGO for the period investigated range within ±4.2 mm. They reveal a seasonal pattern with minimum values in spring and maximum values in autumn.

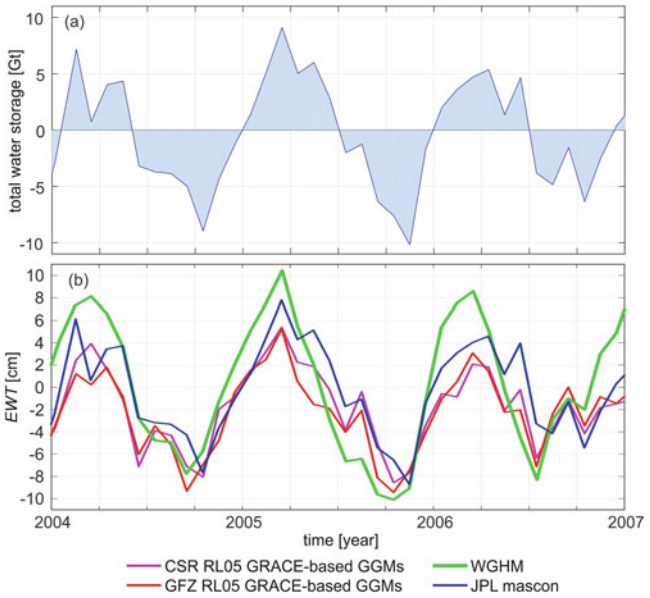

Fig. 4 Temporal variations of water mass at the Borowa Gora Observatory: (**a**) temporal variations of total water storage obtained from JPL mascon solutions, and (**b**) temporal variations of equivalent water thickness obtained from JPL mascon solutions, CSR and GFZ GRACE-based GGMs and the WGHM

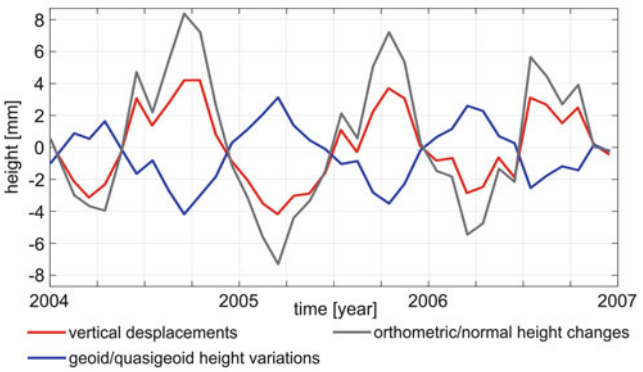

Fig. 5 Temporal vertical displacements, temporal variations of geoid height and temporal variations of the orthometric/normal height at the BGO

This seasonal pattern, in terms of phase and amplitude, agrees with those obtained from variations of ellipsoidal heights based on GNSS data (cf. Rajner and Liwosz 2011; Jinwei 2014). The results obtained indicate that temporal variations of geoid heights range from −4.2 mm to 3.1 mm. Figure 5 also illustrates that the seasonal pattern of vertical displacements is shifted in phase with respect to the seasonal pattern of geoid height variations by approximately 6 months. The annual variation of orthometric/normal height reach 1.6 cm.

5 Conclusions and Discussion

In this paper, temporal variations of geoid heights and temporal vertical displacements were discussed in the perspective of the realization of the modern vertical reference system. Temporal variations of geoid heights for the period from 04/2002 to 03/2016 over the area of Poland divided into four subareas of 3° × 5° were determined from GRACE mission data. The results reveal that temporal variations of geoid heights from epoch to epoch reach up to 1 cm at the same subarea and 1.1 cm between subareas. They also indicate that differences of temporal geoid height variations between two subareas can reach 2 mm at the same epoch. These results are consistent with the analysis and modelling of temporal geoid height variations over the same area for the period 01/2004–12/2009 (cf. Godah et al. 2017).

Water mass variations, vertical displacements and geoid height variations were estimated from GRACE mission data for the period between 01/2004 and 12/2006 at the Borowa Gora Observatory (BGO). The obtained temporal vertical displacements range within ±4.2 mm and temporal variations of geoid heights vary from −4.2 mm to 3.1 mm. They are clearly associated with the cycle of water mass variations in the BGO. They also reveal that temporal vertical displacements are shifted in phase with respect to the temporal variations of geoid heights by approximately 6 months. This might be explained as follows. The increase/decrease of water masses induces more/less loading that lead to a subsidence/uplift of the Earth surface, while the increase/decrease of water masses, consequently, changes the Earth's gravity potential and leads to an ascent/descent of the geoid surface.

The combination of temporal variations of geoid height and temporal vertical displacements may result in significant temporal variations of physical heights that are essential for the realization of the modern vertical reference system. The results obtained in the above example indicate that temporal variations of orthometric/normal height in the BGO for the period from 01/2004 to 12/2006 reach 1.6 cm. They also reveal that the dispersion (i.e. maximum – minimum) ratio between temporal variations of geoid height and temporal vertical displacement is 1:1.15. Taking into the consideration this dispersion ratio and the results presented in Sect. 3, temporal variations of orthometric/normal heights over the area of Poland may reach up to 2.4 cm from epoch to epoch. However, further intensive research focusing on the determination, analysis and modelling temporal vertical displacements in using GRACE mission data and GNSS data is recommended for the realization of a modern vertical reference system.

Acknowledgements This work was supported by the Polish National Science Centre (NCN) within the research grant No 2014/13/B/ST/10/02742. Dr. Marcin Rajner is greatly acknowledged for providing vertical displacements determined from GNSS data at the BGO to verify results obtained from GRACE mission data.

References

Barthelmes F (2013) Definition of functionals of the geopotential and their calculation from spherical harmonic models theory and formulas used by the calculation service of the International Centre for Global Earth Models (ICGEM), The GFZ series, Scientific Technical Report (STR), STR 09/02, Revised Edition Januray 2013, p 32

Barthelmes F (2016) International Centre for Global Earth Models (ICGEM). J Geod 90(10):1177–1180. In: Drewes H, Kuglitsch F, Adám J, Rózsa S (eds) The geodesists handbook 2016. J Geod 90(10):907–1205

Bettadpur S (2012) UTCSR Level-2 processing standards document for level-2 product release 0005. GRACE 327–742, CSR Publ. GR-12-xx, Rev. 4.0, University of Texas at Austin, p 16

Dahle C, Flechtner F, Gruber C, et al. (2014) GFZ RL05: an improved time-series of monthly GRACE gravity field solutions. Observation of the system earth from space – CHAMP, GRACE, GOCE and future missions. Adv Tech Earth Sci, 29–39

Döll P, Kaspar F, Lehner B (2003) A global hydrological model for deriving water availability indicators: model tuning and validation. J Hydrol 270(1–2):105–134

Farrell WE (1972) Deformation of the earth by surface loads. Rev Geophys 10:761–797

Godah W, Szelachowska M, Krynski J (2015) On the selection of GRACE-based GGMs and filtering method for estimating mass variations in the system earth over Poland. Geoinf Issues 7(1(7)):5–14

Godah W, Szelachowska M, Krynski J (2017) On the analysis of temporal geoid height variations obtained from GRACE-based GGMs over the area of Poland. Acta Geophys. doi:10.1007/s11600-017-0064-3

Huang J (2016) Regional geoid/quasi-geoid modelling – theoretical framework for the subcentimetre accuracy. J Geod 90(10):1067–1069. In: Drewes H, Kuglitsch F, Adám J, Rózsa S (eds) The geodesists handbook 2016. J Geod 90(10):907–1205

Jinwei Z (2014) Analysis of seasonal loading-induced displacements from GPS and GRACE. MSc thesis. University of Stuttgart, Germany. doi:10.18419/opus-3934

Krynski J (2007) Precise quasigeoid modelling in Poland–Results and accuracy estimation (in Polish), Monographic series of the Institute of Geodesy and Cartography, Nr 13, Warsaw, Poland, (266 pp)

Krynski J, Lyszkowicz A (2006) Centimetre quasigeoid modelling in Poland using heterogeneous data. In: IAG Proceedings 1st International Symposium of the Inter. Gravity Field Service (IGFS): Gravity Field of the Earth 28: 37–42

Krynski J, Kloch-Główka G, Szelachowska M (2014) Analysis of time variations of the gravity field over Europe obtained from GRACE

data in terms of geoid height and mass variations. IAG Symp 139:365–370

Kusche J (2007) Approximate decorrelation and non-isotropic smoothing of time variable GRACE-type gravity field models. J Geod 81(11):733–749

Makridakis S, Wheelwright SC, Hyndman RJ (1998) Forecasting: methods and applications, 3rd edn. Wiley, New York, p 656. ISBN: 978-0-471-53233-0

Rajner M, Liwosz T (2011) Studies of crustal deformation due to hydrological loading on GPS height estimates. Geod Cartogr 60:135–144

Rangelova E (2007) A dynamic geoid model for Canada. PhD thesis, University of Calgary, Department of Geomatics Engineering, Rep. No 20261

Rangelova E, Sideris MG (2008) Contributions of terrestrial and GRACE data to the study of the secular geoid changes in North America. J Geodyn 46(3):131–143

Rangelova E, Fotopoulos G, Sideris MG (2010) Implementing a dynamic geoid as a vertical datum for orthometric heights in Canada. IAG Symp 135:295–302

Szelachowska M, Krynski J (2014) GDQM-PL13 – the new gravimetric quasigeoid model for Poland. Geoinf Issues 6(1(6)):5–19

Tan W, Dong D, Chen J et al (2016) Analysis of systematic differences from GPS-measured and GRACE-modeled deformation in Central Valley California. Adv Space Res 57(1):19–29

Tscherning CC, Arabelos D, Strykowski G (2000) The 1-cm geoid after GOCE. IAG Symposia 123:267–270

van Dam T, Wahr J, Lavallée D (2007) A comparison of annual vertical crustal displacements from GPS and Gravity Recovery and Climate Experiment (GRACE) over Europe. J Geophys Res 112: B03404

Watkins MM, Yuan D (2007) GRACE JPL level-2 processing standards document for level-2 product release 04, GRACE 327–744 (Rev. 4.0)

Watkins MM, Wiese DN, Yuan DN et al (2015) Improved methods for observing Earth's time variable mass distribution with GRACE using spherical cap mascons. J Geophys Res Solid Earth 120(4):2648–2671

Analysis of GOCE Omission Error and Its Contribution to Vertical Datum Offsets in Greece and Its Islands

Martin Willberg, Thomas Gruber, and Georgios S. Vergos

Abstract

In this paper we evaluate three different geoid models (a pure and an extended satellite-only model and a local geoid solution) for the mainland of Greece and fourteen of its biggest islands in terms of signal content and applicability for height system unification. By comparing local geoid heights from GPS and spirit levelling with the three geoid models it is possible to make statements about the Earth's gravity signal that is omitted in these models (omission error). In a further step we try to quantify the contribution of the omission error to the height system unification between the investigated islands. It becomes obvious that a satellite-only gravity field model (GOCO05S) until degree and order 200 is not sufficient for the mountainous islands of Greece due to an omission error of up to 2 m. The same model with high frequency corrections from EGM08 as well as topography is able to reduce the omission error drastically and shows similar results as for the local geoid model. As an outcome, we can see homogenous omission errors for the smaller islands and in general a high correlation between the size of the island and the amplitudes of the omission error.

Keywords

GOCE • Height systems • Local vertical datum • Omission error

1 Introduction and Problem Definition

The connection and unification of height systems has been identified as one of the most important tasks in physical geodesy. The International Association of Geodesy (IAG) accommodated this and issued a resolution about the establishment of an International Height Reference System (IHRS) (Drewes et al. 2016). The basis of height system unification is a globally consistent Earth gravity field as it is observed by the Gravity field and steady-state Ocean Circulation Explorer mission (GOCE) satellite (Drinkwater et al. 2003) in combination with other satellite information as it is provided by the Gravity Recovery And Climate Experiment mission (GRACE) (Tapley et al. 2004). It has been proven that GRACE/GOCE based Earth gravity field models deliver the static part of the geoid with an accuracy of 1–2 cm at spatial scales of 100 km and larger (Brockmann et al. 2014). Still missing are geoid signals with smaller spatial resolution, which cannot be observed by satellites due to their distance from the Earth surface. This is the so-called omission error, which plays an important role in height system unification and is the major topic of this paper.

We investigate the possibility to account for the omission error (or in other words the omitted signal) in a satellite-only gravity field model depending on local characteristics at the evaluation points (e.g. availability of gravity observations, terrain roughness, land-ocean transition). We regard three possible approaches: (1) The omission error

M. Willberg (✉) • T. Gruber
Institute of Astronomical and Physical Geodesy, Technical University of Munich, Munich, Germany
e-mail: martin.willberg@tum.de; thomas.gruber@tum.de

G.S. Vergos
GravLab, Department of Geodesy and Surveying, Aristotle University of Thessaloniki, Thessaloniki, Greece
e-mail: vergos@topo.auth.gr

G. S. Vergos et al. (eds.), *International Symposium on Gravity, Geoid and Height Systems 2016*, International Association of Geodesy Symposia 148, DOI 10.1007/1345_2017_3

is neglected at all, assuming that no surface gravity data is available. (2) The omitted signal is estimated from a global high resolution gravity field model incorporating surface and altimetry-derived gravity data, e.g. the EGM2008 model (Pavlis et al. 2012, 2013), and topography-induced gravity field information (confer Hirt et al. 2010). (3) A regional geoid model (Grigoriadis 2009) based on a satellite model and terrestrial/altimetry gravity data is used, assuming that this model contains the full gravity signal. The results obtained from these three approaches are finally compared to independent geoid heights as they are derived from GPS and spirit levelling. This will allow us to gain accuracy estimates about the incorporated data sets and/or the estimation of the omission error at each individual point investigated. Finally, the impact of the omission error on offsets between different height systems can be quantified as well.

With its hundreds of islands Greece is an ideal test area for such analyses. The mainland of Greece and the islands have numerous different (orthometric) height systems, also known as locally realised vertical datums, which have never been connected through hydrostatic levelling. Most of the islands show large topographic effects and the omission error frequently lies far above the global average of about three decimetres as it is determined from standard degree variance models (Gruber et al. 2011, 2014). Furthermore, the islands in the Aegean and Ionian Sea have already been subject to several studies about the geopotential value W_0 and the height offsets (Kotsakis et al. 2012; Grigoriadis et al. 2014). These can be complemented with the different aspects of this analysis. The origin of the Hellenic Vertical Datum is defined by the tide gauge station in Piraeus harbour near Athens, but only the mainland of Greece is connected to this official vertical datum. All islands have their own vertical datum installed by the Hellenic Military Geographic Service between 1963 and 1986 according to the local mean sea level at one point respectively (Grigoriadis et al. 2014).

The situation between various islands is exemplified by two different vertical height systems and an ocean in between (Fig. 1). The following description is a summary of Gruber et al. (2012), but adapted to the situation in Greece. As orthometric heights are chosen as height coordinates in Greece we stick to these in the following analyses, but all conclusions are applicable to normal heights as well. For more details about height systems, geoid determination from spherical harmonics, or regional approaches we refer to Heiskanen and Moritz (1967).

Local height systems are defined by the local equipotential surface through the origin of the vertical system, which in most cases is set to the observed mean sea level at one point at the coast (e.g. tide gauge) (brown solid line). Orthometric heights (brown dotted lines) can then be transferred from the origin to every other point on the Earth surface by spirit levelling and gravimetry.

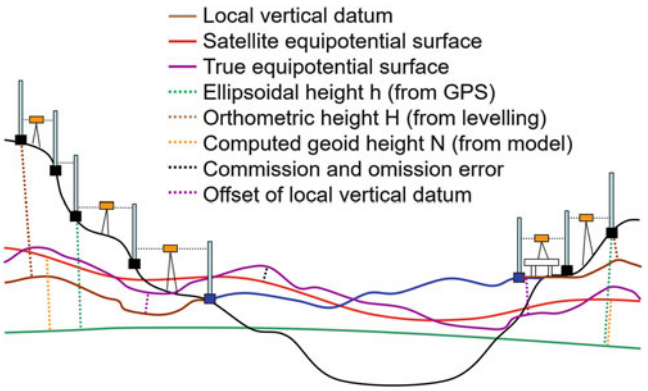

Fig. 1 Overview of different heights and reference surfaces as used in this paper. Adapted from Gruber et al. (2012)

With the combination of ellipsoidal heights determined from GPS (green dotted lines) and in case of error-free orthometric heights one can compute the height of the local equipotential surface above the reference ellipsoid, which is named local geoid throughout the paper. But neither the local geoid height nor the orthometric height can be compared between different height systems, because of different origins in the vertical datum (Fig. 1). Satellite based global gravity field models are able to deliver a globally consistent equipotential surface (red solid line), but as explained above this still differs from the true equipotential surface (purple solid line) due to the commission and omission error (black dotted line).

The paper is structured as follows: Sect. 2 describes the different data sets used in this study. After that, we present the procedures and their results for three different geoid models with a special emphasis on the accuracies of each model in Sect. 3 and the influence of these accuracies on height systems in Sect. 4. The final Sect. 5 summarizes the results and provides some conclusions.

2 Data Sets Used for the Study

For the evaluation we need geoid information from a Global Gravity Model (GGM) based on GOCE, a local geoid calculation based on terrestrial gravimetry information and GPS/levelling data, which we use to check our three approaches at selected stations. Of all the Greek islands we select only those with twelve or more GPS/levelling stations available for our study. In addition, we include data from the Greek mainland. The procedure itself is not limited to the chosen islands, but a minimum number of GPS/levelling stations helps to derive conclusive results. A map with the 14 selected islands (Andros, Chios, Corfu, Crete, Eyvoia, Karpathos, Kefalonia, Kos, Lesvos, Limnos, Naxos, Rhodes, Samos and Zakynthos) can be found in Sect. 4 (Fig. 3).

2.1 Geoid Solutions from Global Model

With GOCO05S we use a state-of-the-art satellite-only GGM based on all data from the GRACE and GOCE missions (Mayer-Gürr and GOCO Team 2015). Comparisons to other combined GGMs (EGM2008, GOCO05C) show that it has full signal content approximately up to degree 200–220. Therefore, using this model up to degree and order 200, assuming that no terrestrial data is available, is a good starting point for our initial analysis (confer case 1 in the introduction). For case 2 the omitted signal is approximated in two steps: first, by adding the EGM2008 model geoid from degree 201 to degree 2190, and second, by adding the geoid impact computed from a Residual Terrain Model (RTM) above the resolution of EGM2008. A more detailed description of the general approach of using a GGM in order to estimate the omission error can be found in Gruber et al. (2011).

2.2 Local Hellenic Geoid Model

The Hellenic Geoid Model 2009 (HGM2009) was derived from a thoroughly validated gravity database, which contains terrestrial data for land and sea areas as well as satellite altimetry derived gravity anomalies. The HGM2009 was estimated by employing the spherical Stokes kernel and the 1D spherical FFT approach (Haagmans et al. 1993). Regarding the necessary reductions, the EGM96 (Lemoine et al. 1998) was chosen as the geopotential reference model, while a Digital Terrain and Bathymetry Model, obtained from the combination of SRTM3 (Farr et al. 2007) and SRTM30-Plus (Becker et al. 2009), was used for computing the terrain corrections.

2.3 GPS-Levelling Data

The GPS measurements used in this paper originate from a nation-wide campaign carried out in 2007 and their resulting height accuracy is given as 2–5 cm (Vergos et al. 2014). The orthometric heights were measured by spirit and/or precise trigonometric levelling long before the GPS measurements were taken and their precision at that time was given as approximately 1–2 cm. Nevertheless, their true precision remains unknown, because the levelling was not accompanied by local gravimetric ground measurements; instead, interpolated values from free air anomaly maps were used (Kotsakis et al. 2012). This results in a hardly quantifiable error due to nonparallel equipotential fields. For this reason, the levelling data represent the most problematic data set used in our study.

3 Omission Error Analysis

For the omission error analysis, we compare the geoid solutions of the three mentioned cases with the local geoid height which we get from GPS-levelling by subtracting the orthometric height H from the ellipsoidal height h (compare Fig. 1). This is done for every point i with GPS/levelling observations by the difference

$$\Delta N_i = N_i - (h_i - H_i)\,, \tag{1}$$

where N_i is the selected geoid solution. As the geoid model N and the orthometric height H in general refer to different equipotential reference surfaces there is a height offset in ΔN. It is assumed that the GPS/levelling observations contain the full signal of the Earth gravity field, so the omission error of our geoid models N completely transfers to ΔN along with random and systematic errors in all three quantities involved. Systematic errors can occur due to geometrical distortions in the levelling network, long or medium wavelength effects in the geoid model, datum inconsistencies between geoid and ellipsoidal heights and unmodeled time-dependent variations (Kotsakis et al. 2012). For analyzing the omission error, we eliminate the constant offset and the systematic distortion from the observations by a planar fit to ΔN and by subtracting this plane from the differences.

$$\Delta N_i^{\text{corrected}} = N_i - (h_i - H_i) - \Delta N^{\text{correctionSurface}} \tag{2}$$

We do not apply a higher order correction surface as this could partially remove the omitted signal as well. Because there are outliers in the GPS/levelling data we also apply a simple 2σ criterion during the data processing, which eliminates about 5% of our observation points. Also, these outliers were not used for further analyses.

After removing the offset and the systematic distortions, the random errors as well as the omission errors remain in $\Delta N_i^{\text{corrected}}$ and can be interpreted for our three test cases. As we are not interested in single point differences we use the standard deviations over a target area (island or mainland Greece respectively) to evaluate geoid differences (Fig. 2). When we neglect the observation errors of GPS and levelling for a moment and assume that the estimation of the correction plane removes systematic distortions, then in cases 1 and 2 the remaining $\Delta N_i^{\text{corrected}}$ gives us the sum of omission and commission error of our geoid model N determined from spherical harmonics. In case 3, in contrast, $\Delta N_i^{\text{corrected}}$ shows mainly modelling errors in the local Hellenic Geoid. According to a variance-covariance propagation of the GOCO05S model, the commission error in Greece accounts for about 1.6 cm.

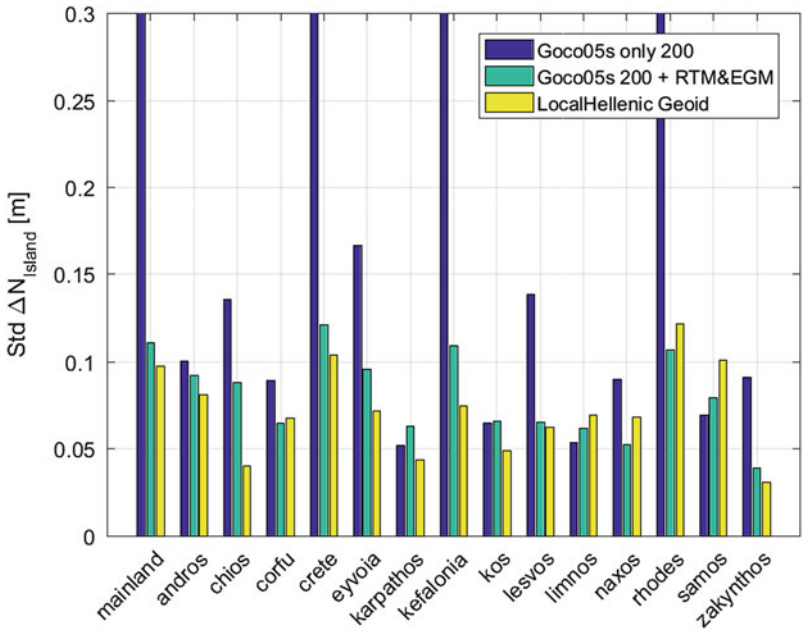

Fig. 2 Standard deviation of $\Delta N_i^{\text{corrected}}$ for the three different geoid models: case 1 (*blue*), case 2 (*green*) and case 3 (*yellow*). *All bars* are presented after parameter estimation of a plane and outlier removal by a 2σ criterion. *Cutted bars* show 48 cm for the mainland, 64 cm for Crete, 39 cm for Kefalonia and 33 cm for Rhodes

The standard deviations in case 1 range from 5 to 65 cm and are much higher than in the other cases (Fig. 2) because all gravity field signals above degree 200 are neglected. In both the second and the third case our extreme values account from 3 to 4 cm to about 12 cm; thereby the local Hellenic geoid in case 3 generally provides slightly better results.

As expected, case 1 shows by far the worst results, though there are islands (Karpathos, Limnos and Samos) where case 1 performs slightly better than case 2. In general, it can be seen that large islands, respectively islands with a higher number of measurement points, tend to show higher omission errors here.

Of course our simplification with error-free observations is not true and, in fact, we already know that our GPS/levelling observations were not optimally done. The visualized difference in Fig. 2 shows (in all 3 cases) random errors due to the observation accuracy of GPS and spirit levelling and therefore the omission error (cases 1 and 2) and the modelling errors (case 3) of the high frequency signal are even below the values presented in Fig. 2. As a conclusion, the approach in case 2, where we calculate the geoid heights N only by using a global satellite model, point positions, and EGM08 coefficients as input, shows almost the same performance as the far more complex local geoid calculation.

4 Height System Offsets Between Islands

In Sect. 3 we used the comparison of the selected geoid models to the local geoid from GPS/levelling to evaluate the accuracy of our models at selected islands. Now we take the geoid model differences ΔN again, but do not subtract the correction surface resulting in absolute geoid height offsets ΔN^{mean} for every island. This is done by calculating the mean value over Eq. (1), where n is the number of observation points per island:

$$\Delta N^{\text{mean}} = \Sigma \left(N_i - (h_i - H_i)\right) / n \tag{3}$$

These ΔN^{mean} values per island represent the mean offset of the Local Vertical Datum (LVD) to the geoid model N and enable the connection of different vertical datums. As in general, there are no well observed tide gauge stations on the Greek islands; it is considered to be more accurate to use mean values over the whole island instead of single reference points (e.g. tide gauges) for the offsets of the LVD. However, with this consideration it is not possible to compare heights between two individual points of different vertical datums as the offsets stay unknown.

In Fig. 3 the offsets of the LVD are visualized for every island and the mainland in case 1 (upper value) and case 2 (lower value). While in case 1 the offsets have a wide distribution from -243 to $+25$ cm, they range from -38 to $+13$ cm in case 2. Almost all of the offsets are negative which means that the LVD for that island is below the used geoid model.

In Sect. 3 we showed that the GOCO05S model performs much better when adding high frequency parts from EGM and RTM information. This allows us to calculate the omission error in case 1 by using the more accurate case 2 results as reference. The omission error of GOCO05S up to degree and order 200 is then a simple difference of the two values in Fig. 3. Regarding the islands, it varies from about 8 cm for

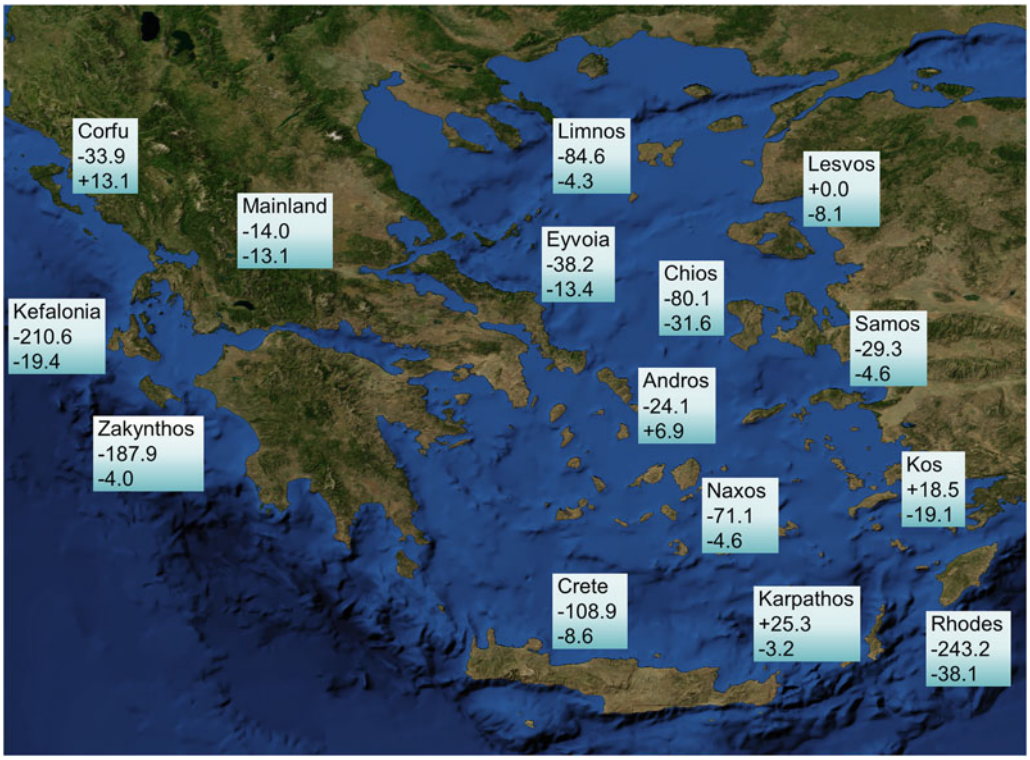

Fig. 3 Mean offset of GOCO05s and extended GOCO05s geoid models to point-wise GPS-levelling observations. The two values give the mean offset of the LVD when calculating the model with EGM and RTM above degree 200 (case 2, *bottom value*) and without them (case 1, *upper value*)

Lesvos to almost 2 m for Rhodes. Most of the islands show omission errors far above the average of 30 cm, while the impact for the mainland is much smaller (3 cm). The reason is the small size of the islands compared to the resolution of GOCE (about 100 km for degree 200). Even the biggest island, Crete, has only an extension of up to 55 km in the north-south direction. When a target area is smaller than the resolution of GOCE the satellite-only gravity field is not able to calculate a representative mean value (especially when there is variable topography) and this can result in increased omission errors (Fig. 3).

The bottom values in Fig. 3 are then used for the computation of height offsets between the data sets (islands and mainland) as shown in Fig. 4. The offsets of the LVD in case 2 are presented as absolute values of the pairwise differences which gives us a 15 × 15 matrix where the colour indicates the height system offset between two data sets. The result is a symmetric matrix with values up to 50 cm with the maximum being the result of the difference between the highest and the lowest offset (Corfu and Rhodes). Dark blue values show data sets with similar offsets of the vertical datum while brighter values (e.g. column or line of Rhodes) indicate that a LVD has a large discrepancy to the others. Pairwise differences provide an easy way for height system unification to visualize height systems offsets.

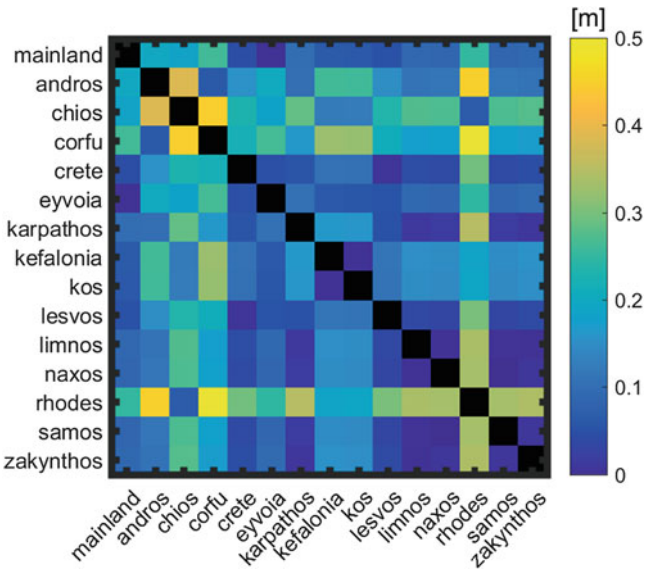

Fig. 4 Pairwise difference of the height offset between chosen islands/mainland. Calculation based on the GOCO05S model with EGM & RTM (case 2)

5 Summary and Conclusions

When combining the results from Sects. 3 and 4 it becomes clear that a satellite-only model (case 1) is not suitable to calculate geoid heights for the Greek islands. The small size of the islands leads to large omission errors because GOCE is not able to distinguish the island from the surrounding sea. However, the omission error for the smaller islands (all except Crete, Rhodes, Kefalonia) is homogenous and similar to all points on the island, which can be seen by the small standard deviations in Fig. 2.

Case 2 shows in both investigations large differences compared to case 1, which again demonstrates that the gravity field signal above degree 200 should not be neglected. The big differences between the smaller and the bigger islands in case 1 are reduced though not eliminated in case 2 when using the GOCO05S model with EGM and RTM information. And the geoid differences are quite similar between cases 2 and 3, which is a good indicator that a satellite-only model with corrections is able to adapt to local characteristics.

References

Becker JJ et al (2009) Global bathymetry and elevation data at 30 arc seconds resolution: SRTM30_PLUS. Mar Geodesy 32(4):355–371. doi:10.1080/01490410903297766

Brockmann JM, Zehentner N, Höck E, Pail R, Loth I, Mayer-Gürr T, Schuh W-D (2014) EGM TIM RL05: an independent geoid with centimeter accuracy purely based on the GOCE mission. Geophys Res Lett 41(22):8089–8099. doi:10.1002/2014GL061904

Drewes H, Kuglitsch F, Adám J, Rózsa S (2016) The Geodesist's handbook 2016. J Geodesy 90:907–1205. doi:10.1007/s00190-016-0948-z

Drinkwater MR, Floberghagen R, Haagmans R, Muzi D, Popescu A (2003) GOCE: ESA's first Earth explorer core mission. In: Earth gravity field from space-from sensors to Earth sciences. Space sciences series of ISSI, vol 17. Kluwer, Dordrecht, pp 419–432. ISBN: 1-4020-1408-2

Farr TG et al (2007) The shuttle radar topography mission. Rev Geophys 45(2):RG2004. doi:10.1029/2005RG000183

Grigoriadis VN (2009) Geodetic and geophysical approach of the Earth's gravity field and applications in the Hellenic area. Dissertation, Aristotle University of Thessaloniki (in Greek)

Grigoriadis VN, Kotsakis C, Tziavos IN, Vergos GS (2014) Estimation of the reference geopotential value for the local vertical datum of continental Greece using EGM08 and GPS/leveling data. In: International association of geodesy symposia, vol 141. Springer, Cham, pp 249–255. doi:10.1007/978-3-319-10837-7_32

Gruber T, Visser PNAM, Ackermann C, Hosse M (2011) Validation of GOCE gravity field models by means of orbit residuals and geoid comparisons. J Geodesy 85:845–860. doi:10.1007/s00190-011-0486-7

Gruber T, Gerlach C, Haagmans R (2012) Intercontinental height datum connection with GOCE and GPS-levelling data. J Geodetic Sci 2(4):240–280. doi:10.2478/v10156-012-0001-y

Gruber T, Rummel R, Ihde J, Liebsch G, Rülke A, Schäfer U, Sideris M, Rangelova E, Woodworth P, Hughes C, Gerlach C (2014) STSE - GOCE + height system unification with GOCE: summary and final report, Issue 1.0, 24 Feb 2014

Haagmans R, de Min E, van Gelderen M (1993) Fast evaluation of convolution integrals on the sphere using 1D FFT and a comparison with existing methods for Stokes' integral. Manuscr Geodaet 18:227–241

Heiskanen WA, Moritz H (1967) Physical geodesy. W.H. Freeman & Co Ltd, New York

Hirt C, Featherstone WE, Marti U (2010) Combining EGM2008 and SRTM/DTM2006.0 residual terrain model data to improve quasi-geoid computations in mountainous areas devoid of gravity data. J Geodesy 84(9):557–567. doi:10.1007/s00190-010-0395-1

Kotsakis C, Katsambalos K, Ampatzidis D (2012) Estimation of the zero-height geopotential level W_0^{LVD} in a local vertical datum from inversion of co-located GPS, leveling and geoid heights: a case study in the Hellenic islands. J Geodesy 84:423–439. doi:10.1007/s00190-011-0530-7

Lemoine FG et al (1998) The development of the joint NASA GSFC and National Imagery and Mapping Agency (NIMA) geopotential model EGM96. NASA Technical Paper, 1998-206861

Mayer-Gürr T, GOCO Team (2015) The combined satellite gravity field model GOCO05s. Presentation at EGU 2015, Vienna

Pavlis NK, Holmes SA, Kenyon SC, Factor JK (2012) The development and evaluation of the earth gravitational model 2008 (EGM2008). J Geophys Res 117:B04406. doi:10.1029/2011JB008916

Pavlis NK, Holmes SA, Kenyon SC, Factor JK (2013) Correction to the development and evaluation of the earth gravitational model 2008 (EGM2008). J Geophys Res 118:2633. doi:10.1002/jgrb.50167

Tapley BD, Bettadpur S, Watkins M, Reigber C (2004) The gravity recovery and climate experiment: mission overview and early results. Geophys Res Lett 31(9):L09607. doi:10.1029/2004GL019920

Vergos GS, Grigoriadis VN, Tziavos IN, Kotsakis C (2014) Evaluation of GOCE/GRACE global geopotential models over Greece with collocated GPS/levelling observations and local gravity data. In: International Association of Geodesy symposia, vol 141. Springer, Cham, pp 85–92. doi:10.1007/978-3-319-10837-7_11

Quality Control of Height Benchmarks in Attica, Greece, Combining GOCE/GRACE Satellite Data, Global Geopotential Models and Detailed Terrain Information

Vassilios D. Andritsanos, Orthodoxia Arabatzi, Vassilios Pagounis, and Maria Tsakiri

Abstract

The incorporation of the newly available satellite data of GOCE and GRACE missions into global geopotential model solutions provides valuable information on the low to medium frequency band of the gravity field spectrum, an important connection to height datum control and unification. The use of this enriched contribution to existing national height systems quality control will reveal the well known inconsistencies in previous vertical network establishment methods, as well as strengthen the connection solution between adjacent national networks.

The quality control of the vertical network in Attica region (Central Greece) is evaluated in the present study. Collocated GPS/levelling and gravity observation points are utilized with emphasis to trigonometric benchmarks and height reference sites. A spectral enhanced combination scheme is used for the network quality investigation based on the frequency content of pure satellite solutions (GOCE and GRACE) and combined satellite and ground global geopotential model solutions of high degree of expansion. Detailed DTM (Digital Terrain Model) information is incorporated in order to estimate Residual Terrain Model (RTM) effects, leading to an expansion degree of 648,000 (1 arcsec). Finally, detailed information about the quality of the height network in Attica is presented in conjunction to proposals towards the establishment of a new height network.

Keywords

GOCE/CHAMP satellites • GPS/levelling • Height network control • Spectral enhanced method

1 Introduction

The first-order vertical control network of Greece was established and measured by the Hellenic Military Geographical Service from 1963 to 1986 (Milona-Kotroyianni 1989). Approximately 11,000 km of traverses and 11,000 vertical control benchmarks comprise the Greek vertical network. The tide gauge in Piraeus harbor is the fundamental control point of the network. The establishment of the Hellenic Vertical Network was based on sea level changes observations at the reference tide gauge and no W_o estimation was performed. On the other hand, the first order Hellenic triangulation network has some height information, due to a limited number of trigonometric leveling lines. This vertical information has not been validated since its creation. The validation of the vertical reference network before the establishment of the European interconnection is thus essential. A first thorough validation of the Hellenic triangulation network using EGM2008 (Pavlis et al. 2008) was performed by

V.D. Andritsanos (✉) • V. Pagounis
Geospatial Technology Lab, Department of Civil Engineering and Surveying and Geoinformatics Engineering, Technological and Educational Institute of Athens, 12210 Athens, Greece
e-mail: vdandrit@teiath.gr

O. Arabatzi • M. Tsakiri
School of Rural and Surveying Engineering, National Technical University of Athens, 15780 Athens, Greece

G. S. Vergos et al. (eds.), *International Symposium on Gravity, Geoid and Height Systems 2016*, International Association of Geodesy Symposia 148, DOI 10.1007/1345_2017_7

Kotsakis et al. (2010) using GPS data from Hellenic Positioning System (HEPOS; Gianniou 2008) and the leveling information of selected pillars. Recent regional studies were also performed by Vergos et al. (2014), Andritsanos et al. (2015), Vergos et al. (2015) using combination solutions of recent Global Geopotential Models (GGMs) from GOCE mission.

In the present study, the validation of recent (2014–2016) GOCE/GRACE/CHAMP geopotential models at newly measured GPS/Leveling benchmarks of Central Greece is performed. Within this validation, the confirmation of low frequency spectrum improvement through the assimilation of low degree harmonics of satellite missions is proven. Detailed terrain information using Advanced Spaceborne Thermal Emission and Reflection Radiometer (ASTER) and Shuttle Radar Topography Mission (STRM) mission data for the Residual Terrain Model (RTM) effect computation is take into account. The paper comprises three sections. Section 2 presents the methodology followed and the data availability and Sect. 3 describes the results of the study. The conclusions are given in Sect. 4.

2 Methodology and Data

2.1 Data Availability and Test Area

2.1.1 GPS/Levelling Information

Newly available campaigns in Attica were carried out during the last 2 years with 59 GPS/Levelling benchmarks used as test control points. Trigonometric pillars of the Greek Triangulation Network as well as height reference sites of the Hellenic Vertical Network were utilized in this study. The orthometric height of the abovementioned sites were computed using classical spirit leveling (height reference sites) as well as trigonometric leveling (pillars) and are part of the Hellenic Vertical Network, measured and evaluated from 1960 to 1989 (Milona-Kotroyianni 1989). The accuracy of the orthometric heights used is largely unknown since there is not any scientific publication on the adjustment procedure available. Based on its documentation, the orthometric heights of the Hellenic Vertical Network refer to a mean-tide system (IERS Conventions 2010). The geometric heights on these sites were measured using GPS observations during the last 2 years with an estimated accuracy at the level of 2–5 cm and 1–2 cm in the horizontal position. The estimated benchmarks coordinates from GNSS observations refer to the ITRF2008 reference system (epoch 2011.0). The locations of the test points of this study are presented in Fig. 1.

2.1.2 Geopotential Model Availability

The geoid height information was obtained by the use of 12 newly available Global Geopotential Models (GGMs) published during the last 2 years (2014–2016). These models were used to their maximum degree and order (d/o). They incorporate satellite only or combined information (satellite and ground observations). The satellite models are divided to GOCE only models, GOCE, GRACE and CHAMP models and GRACE only or GRACE/GOCE models. EGM2008 (Pavlis et al. 2008) is used as reference model in the validation up to its maximum degree of expansion (2190). The detailed information of the 12 GGMs used in this study is presented in Table 1.

2.1.3 Detailed Terrain Information

The terrain effects on geoid height information were taken into account using satellite derived DTMs. Data from Advanced Spaceborne Thermal Emission and Reflection Radiometer (ASTER) mission and Shuttle Radar Topography Mission (SRTM) were utilized in terrain representation. The 1 arcsec resolution of the terrain information led to an increased accuracy on the computation of the masses effect on the geoid. It is the first time that this high terrain resolution is used in the area under study. The differences between the heights of the two DTMs are presented in Table 2 where a mean difference of -3.6 m and a std. of ± 8.2 m are noticed. These results are expected due to the different satellite measurement procedure of each mission. In addition, ASTER and SRTM mission internal accuracy reaches the level of ten of meters (namely, ± 20 m and ± 16 m).

2.2 Combination Scheme and Validation Procedure

2.2.1 Data Preprocessing and Datum Concept

The most important aspect in geodetic data combination techniques is the homogeneity of the reference systems used in the heterogeneous measurements. GPS observations for the horizontal positioning as well as for the ellipsoid height estimation, classical leveling techniques for the orthometric height estimation and GGM geoid heights must refer to a common system as accurately as possible. The horizontal positions refer to WGS84 global system. As far as the vertical position is concerned, the adopted tide system is also of great importance. WGS84/ITRF uses the tide-free system while geoid height from certain models refers to zero-tide system (ITU-GRACE16, ITU-GGC16, GOCO05C, GOCO05S, GGM05C and GGM05G). In this study, the "conventional tide-free system" (IERS Conventions 2010) is used. The zero-tide geoid heights were transformed to the tide-free system according to:

$$\delta C_{2,0}^{TF} = \delta C_{2,0}^{ZT} + 3.1108 \cdot 10^{-8} \frac{0.3}{\sqrt{0.5}} \quad (1)$$

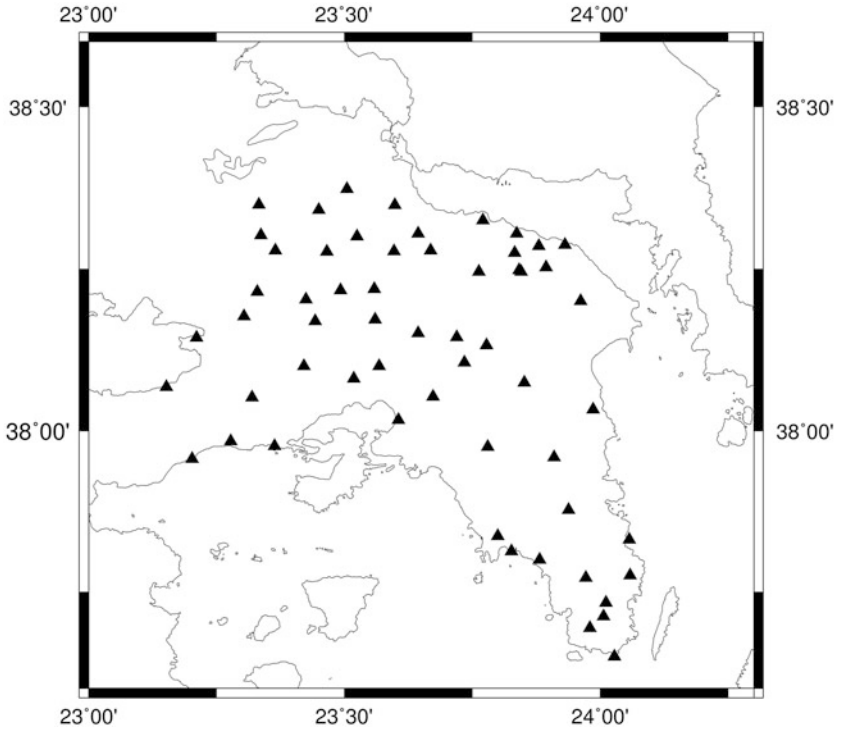

Fig. 1 The locations of the GPS/Levelling benchmarks in Attica

Table 1 The 12 GGMs used for the geoid height information

Satellite used	Model name	Max degree of expansion	Citation
GOCE only models	DIR ver. 4	260	Bruinsma et al. (2013)
	DIR ver. 5	300	Bruinsma et al. (2013)
	SPW ver. 4	280	Gatti et al. (2014)
	TIM ver. 4	250	Pail et al. (2010)
	TIM ver. 5	280	Brockmann et al. (2014)
GOCE, GRACE and CHAMP	EIGEN-6s4	300	Förste et al. (2016)
	GOCO05c	720	Pail et al. (2016)
	GOCO05s	280	Mayer-Gürr et al. (2015)
GRACE and GRACE/GOCE	GGM05c	360	Ries et al. (2016)
	GGM05g	240	Bettadpur et al. (2015)
	ITU-GGC16	280	Akyilmaz et al. (2016a)
	ITU-GRACE16	180	Akyilmaz et al. (2016b)

Table 2 Difference between ASTER and SRTM-1 1 arcsec DTMs

(m)	max	min	mean	rms	sd
ASTER–SRTM1	167	−302	−3.628	7.379	8.223

Units in m

where $\delta C_{2,0}^{TF}$ is the 2nd degree harmonic coefficient of the disturbing potential in the tide-free system and $\delta C_{2,0}^{ZT}$ is the respective coefficient in the zero-tide system. The residual part of the equation is derived from the ellipsoid model constants and the position and mean gravity of the computation point (IERS Conventions 2010).

The mean-tide orthometric heights (H_{MT}) of the Hellenic Vertical Datum were also transformed to the tide-free system (H_{TF}) according to Ekman (1989):

$$H_{TF} = H_{MT} + (1 + k)\left(9.9 - 29.6\sin^2\varphi\right) \quad [cm] \qquad (2)$$

where k is the Love number and φ is the geodetic latitude of the point. The final complete contribution of the GGM to a specific degree was computed using:

$$N_{GGM} = \zeta + N_o + \frac{\Delta g_B}{\overline{\gamma}} H \qquad (3)$$

where $N_o = -0.4376m$ is the zero–degree harmonic on geoid heights w.r.t. WGS84, and the $\frac{\Delta g_B}{\overline{\gamma}} H$ is the height anomaly to geoid height conversion term. The height anomaly ζ was computed from each model coefficients as:

$$\zeta(r,\vartheta,\lambda) = \frac{GM}{\gamma r}\sum_{n=2}^{n\,\max}\left(\frac{a}{r}\right)^n \sum_{m=0}^{n} \times \left(\delta\overline{C}_{nm}\cos m\lambda + \delta\overline{S}_{nm}\sin m\lambda\right)\overline{P}_{nm}(\cos\vartheta) \tag{4}$$

where r, ϑ, λ are the spherical coordinates of the point, γ is the normal gravity of the point and $\delta\overline{C}_{nm}$, $\delta\overline{S}_{nm}$, $\overline{P}_{nm}$ are the normalized spherical harmonic coefficients and Legendre functions of n degree and m order.

2.2.2 Combination Scheme and Heights Validation

The quality control of the GPS/Levelling benchmarks in Attica was achieved using a spectral enhancement approach (Vergos et al. 2014). In this method, EGM2008 is chosen as the reference GGM and the contribution of various GOCE/GRACE/CHAMP and surface gravity GGMs is taken into account in the low to medium frequency band. This enrichment of EGM2008 is calculated using an appropriate degree-step procedure. In this manner, the improvement of the newly available GGM can be considered w.r.t. the expansion degree of the tested model. In detail, the enhancement method can be divided into three steps:

Step a ➔ Geoid height of tested GGM i (N^i) is computed to a maximum degree of expansion n_1.

Step b ➔ Reference model EGM2008 ($N^{EGM2008}$) is used to fill-in medium and high frequency content (up to degree 2,190).

Step c ➔ Residual Terrain Modelling (N^{RTM}) effects complete the high and ultra high frequency information.

The residual geoid heights were computed using the following equation:

$$\Delta N = N^{GPS/Lev} - N^i\Big|_2^{n_1} - N^{EGM2008}\Big|_{n_1+1}^{2190} - N^{RTM} - N_o \tag{5}$$

A 10 degree step was used in the incorporation of the newly available test model information to the complete geoid spectrum. The signal of EGM2008 was substituted by the signal of the satellite-based model in successive different bands of the gravity spectrum from degree 2 to the maximum degree of the satellite model using the abovementioned degree step.

2.2.3 RTM Effects Consideration

The 1 arcsec detailed DTM information integrates the geoid signal to an expansion degree 648,000. The omission error in this combination procedure is below 1 mm based on the behavior of EGM2008 omission error model. The RTM effects computed from ASTER and SRTM1 DTMs are identical and the differences in the terrain effect to the geoid height are insignificant. The estimated RTM effects at the 59 GPS/Levelling benchmarks are presented in Fig. 2.

As seen from Fig. 2 the RTM effect to the geoid heights is below 3 mm, due to the small discrepancies of the terrain from the reference DTM used in the computations. This reference DTM is a mean surface used in RTM effects computations. A 5 arcmin resolution is chosen for this reference DTM according to the maximum degree of the geopotential model used.

3 Results and Discussion

The incorporation of the newly available models in EGM2008 signal resulted to improved statistics of the differences between GGM geoid heights and GPS/Levelling geoid heights at the tested benchmarks in Attica. Specifically, the assimilation of the frequency band 100–160 degree led to a significant improvement. The detailed model combination results are presented as follows.

3.1 GOCE Only Models

Both DIR, TIM and SPW GOCE solutions contributed significantly to the improvement of the EGM2008 geoid signal. In particular, when replacing the frequency content of EGM2008 at the low and medium band (maximum degree between 100 and 160) the improvement reached 1–2 cm in terms of the std. (standard deviation) of the differences at the benchmarks. In Fig. 3, the results of the assimilation of TIM-based solutions (version 4 and version 5) to the EGM2008 signal is presented.

The incorporation of GOCE TIM-R4 signal to the EGM2008 up to the maximum degree of 100–160 band led to improved statistics in terms of sd of the differences. For the frequency band 160–220, the results showed no difference with pure EGM2008 solution. In addition, the same improvement is noticed when the maximum degree of GOCE TIM-R4 model reached the 220–240 band. The 5th release of the model, although it incorporates more coefficients (maximum degree 280), showed that the assimilation of TIM-R5 signal above degree 240 led to worst

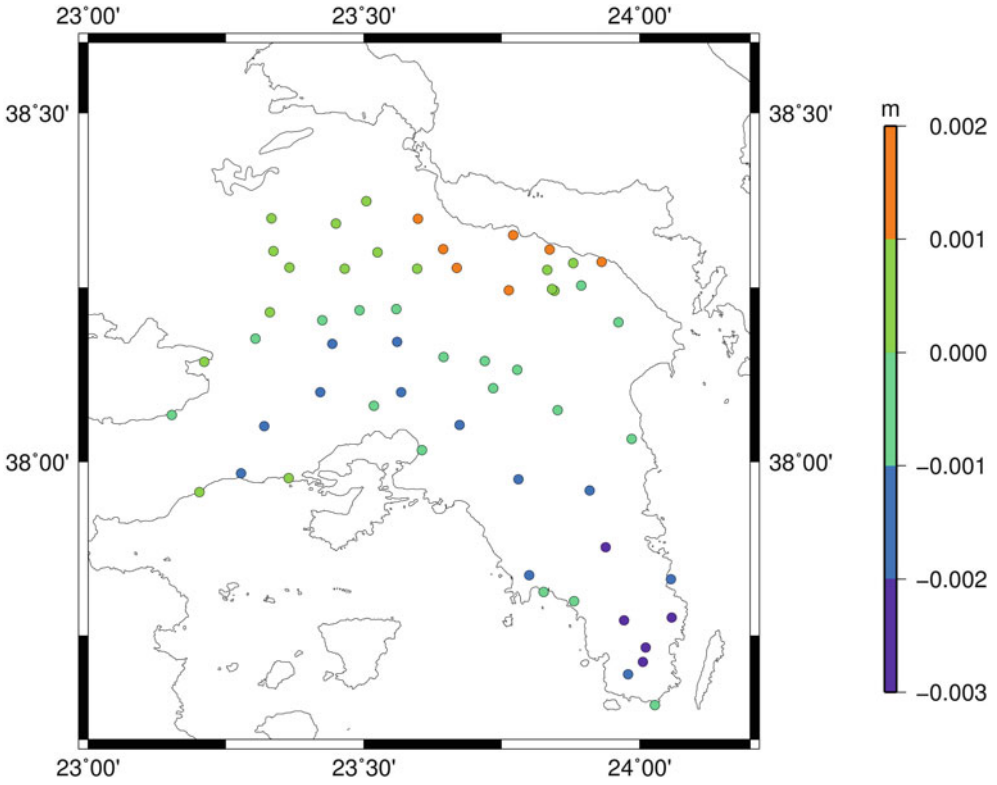

Fig. 2 The estimated RTM effects to the geoid height signal of the GPS/Levelling benchmarks using ASTER 1 arcsec DTM

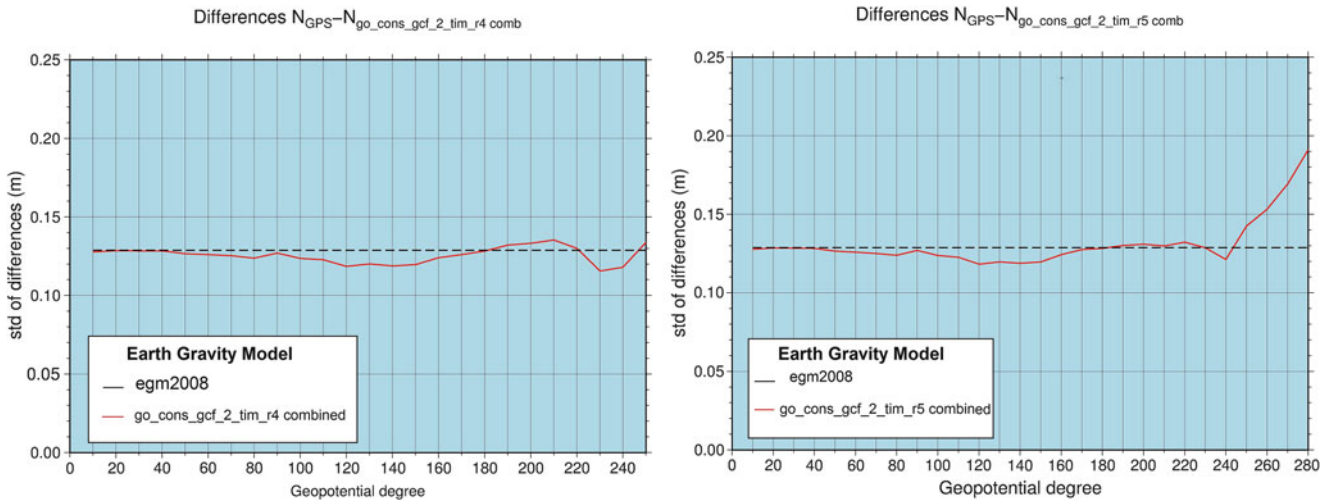

Fig. 3 The sd of the differences from the assimilation of GOCE TIM-R4 model (*left*) and GOCE TIM-R5 model (*right*) to the EGM2008 signal

results (see Fig. 3—right part). Similar results were noticed in all GOCE- only models. The incorporation of higher harmonics of the test models to the combination solution led to worst statistics. The differences at the 59 GPS/Leveling points are presented in Fig. 4. The maximum degree of the test model is 140 and 300, respectively (GOCE DIR ver. 5 model).

3.2 GOCE, GRACE and CHAMP Satellite and Combined Models

In this type of model, a constant improvement in the statistics of the differences at the GPS/Levelling benchmarks is noticed. The major improvement can be seen at the assimilation band of 100–160 degree. It is worth emphasiz-

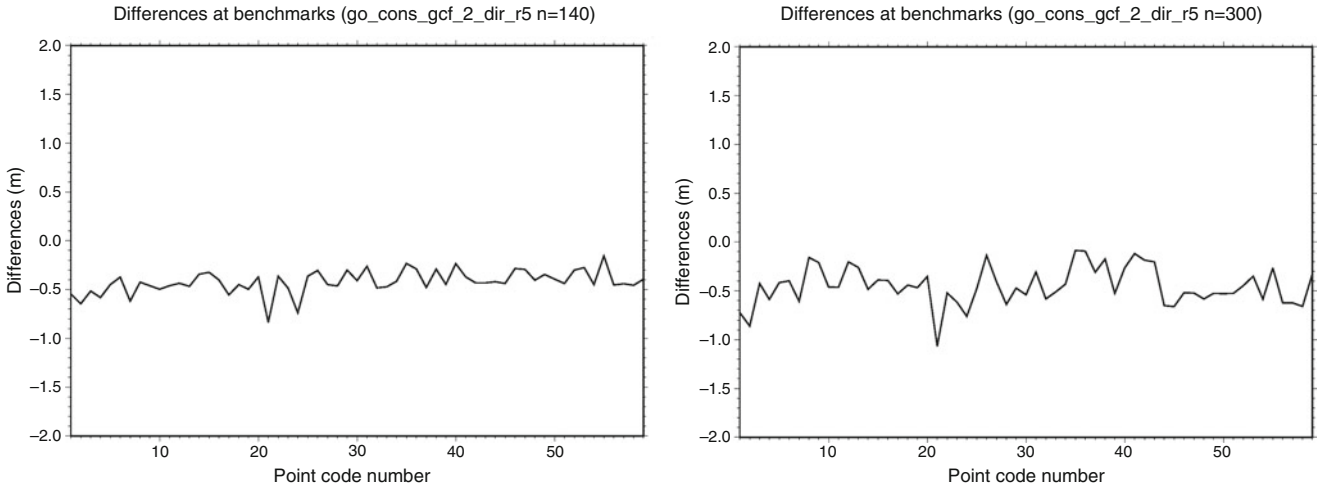

Fig. 4 Differences at the benchmarks using nmax = 140 (*left part*) and nmax = 300 (*right part*) in the assimilation of GOCE DIR-R5 model to EGM2008 signal

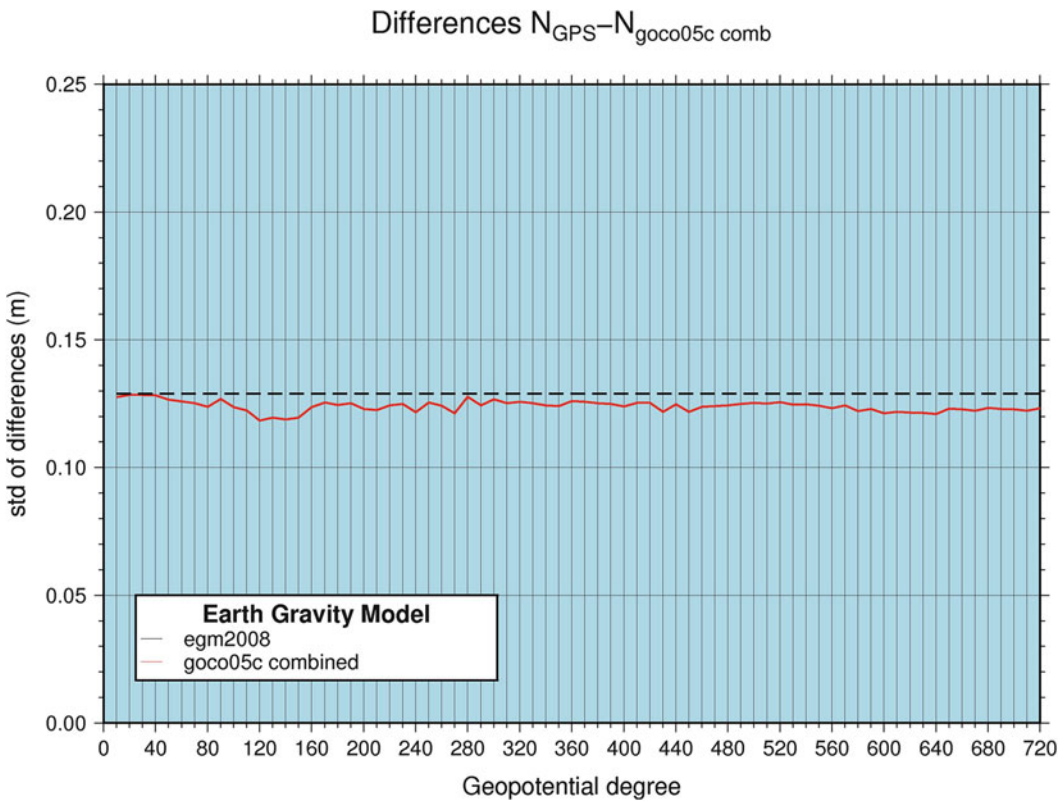

Fig. 5 The sd of the differences from the assimilation of GOCO05C model to the EGM2008 signal

ing the case of the GOCO05C model whereby the surface gravity data enriched the geoid signal in a manner that the assimilation of GOCO05C signal to EGM2008 heights led to statistical improvement regardless the maximum degree of expansion of the tested model. Figure 5 demonstrates the abovementioned statement.

3.3 GRACE: Only and GRACE/GOCE Combined Models

The same improvement in the assimilation band of degrees 100–160 is noticed in the results of GGM05C, GGM05G, ITU-GGC16 and ITU-GRACE16 models. The major differ-

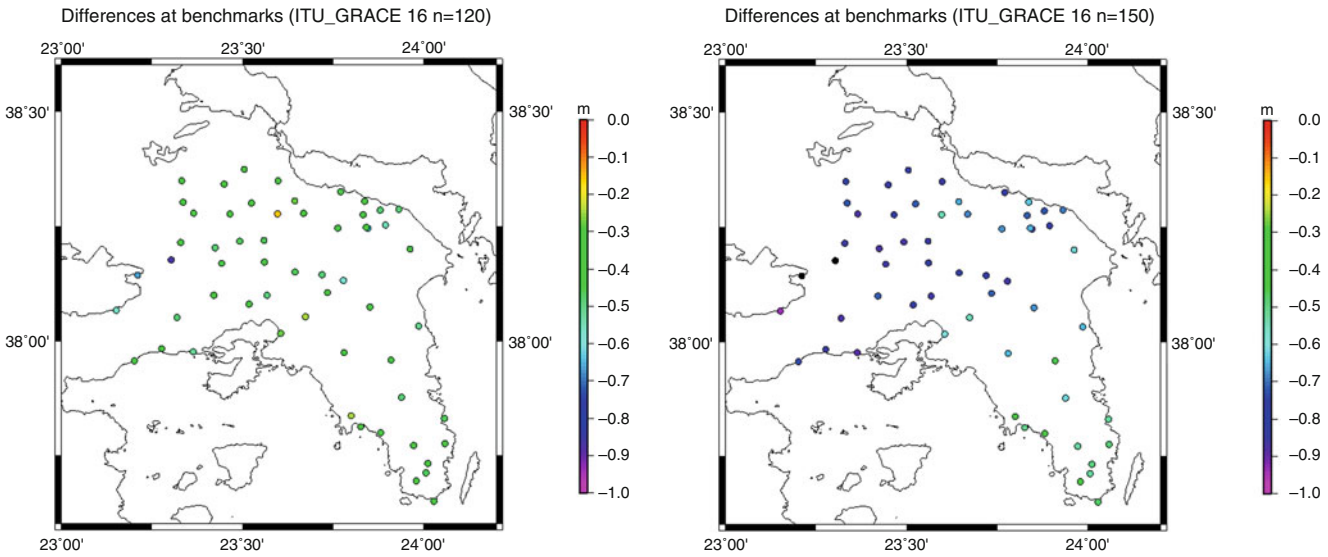

Fig. 6 The differences at the GPS/Levelling benchmarks when the assimilation degree of ITU-GRACE16 model reaches the maximum 120 (*left part*) and 150 (*right part*)

ence from all previous models is the case of GRACE – only model (ITU-GRACE16). This model performed well until the maximum degree of assimilation 120 but after the degree 150 it rapidly diverges. Figure 6 presents the differences at the GPS/Levelling benchmarks when the maximum degree of expansion of ITU-GRACE16 is 120 and 150.

3.4 Discussion on the Hellenic Vertical Network Quality

The enrichment of EGM2008 signal with the newly GGMs from GOCE, GRACE and CHAMP missions led to an improvement of 1–2 cm in terms of the sd of the differences at the benchmarks of the Hellenic Vertical Network. The estimated accuracy in the area of Attica from ±13 cm dropped to ±11 cm with the assimilation of the 100–160 frequency band of the new models (see also Andritsanos et al. 2014). The quality of this network can be validated accurately taking into account the estimated accuracy of GPS observations (various GPS solution strategies, e.g. Andritsanos et al. 2016a) and the computed geoid error through error propagation (Andritsanos et al. 2016b). The main drawback in this statistical procedure is the fact that the estimated accuracy of the orthometric heights of the Hellenic Vertical Network through an integrated adjustment is largely unknown and not scientifically documented. In this manner, only some assumptions can be made on the accuracy of the orthometric heights at the benchmarks (see, e.g., Vergos et al. 2014; Andritsanos et al. 2016b). A thorough study on the possible trends of the network (Andritsanos et al. 2016b) will reveal problematic areas and possible correlations with gravity based corrections. The W_o estimation for the Hellenic Vertical Network and its connection to the adopted value from IERS Conventions (2010) (Vergos et al. 2015) using recent satellite gravity dedicated missions is the contemporary alternative of tide gauge based network establishment. The local W_o estimation will provide an ideal solution to the numerous arbitrary height systems on the Greek islands.

4 Conclusions

The combination of newly available GOCE/GRACE global geopotential models with the reference model EGM2008 and adequate terrain information from RTM effects improved the statistics of geoid differences at GPS/Leveling benchmarks. The lower degree information from these models outperformed the satellite contribution of EGM2008. This improvement presented in the area of Attica can lead to the quality control of the Hellenic Vertical Datum. The sd of the differences at 59 newly measured GPS/Levelling benchmarks reaches ±11 cm after the enrichment of EGM2008 signal with GOCE, GRACE and CHAMP low to medium frequency information. The assimilation of the full signal of the tested models to the EGM2008 geoid heights led to worst results noticing that the absence of surface gravity data cannot be completely recovered by the attenuated satellite gravity signal. The case of GOCO05C, which incorporates surface data in its solution, corroborates the abovementioned statement.

References

Advanced Spaceborne Thermal Emission and Reflection Radiometer – ASTER Mission. Internet resources: https://asterweb.jpl.nasa.gov/index.asp

Andritsanos VD, Vergos GS, Grigoriadis VN, Pagounis V, Tziavos IN Spectral characteristics of the Hellenic vertical network – validation over Central and Northern Greece using GOCE/GRACE global geopotential models. Presented at the European Geosciences Union – General Assembly 2014, Vienna – Austria – April, 27th to May, 2nd 2014

Andritsanos VD, Grigoriadis VN, Vergos GS, Pagounis V, Tziavos IN (2015) GOCE/GRACE GGM evaluation over Attica and Thessaloniki, Greece and local geoid modelling in support of height unification. South-Eastern Eur J Earth Obs Geomatics 4

Andritsanos VD, Arabatzi O, Gianniou M, Pagounis V, Tziavos IN, Vergos GS, Zacharis E(2016a) Comparisons of various GPS processing solutions towards an efficient validation of the Hellenic vertical network: the ELEVATION project. J Surv Eng 142(1). http://dx.doi.org/10.1061/(ASCE)SU.1943-5428.0000164

Andritsanos VD, Grigoriadis VN, Natsiopoulos DA, Vergos GS, Gruber T, Fecher T (2016b) GOCE variance and covariance contribution to height unification. Presented at the GGHS 2016 Symposium, Thessaloniki 19–23 September

Akyilmaz O, Ustun A, Aydin C, Arslan N, Doganalp S, Guney C, Mercan H, Uygur SO, Uz M, Yagci O (2016a) ITU_GGC16 The combined global gravity field model including GRACE & GOCE data up to degree and order 280. http://doi.org/10.5880/icgem.2016.005

Akyilmaz O, Ustun A, Aydin C, Arslan N, Doganalp S, Guney C, Mercan H, Uygur SO, Uz M, Yagci O (2016b) ITU_GRACE16 The global gravity field model including GRACE data up to degree and order 180 of ITU and other collaborating institutions. http://doi.org/10.5880/icgem.2016.006

Bettadpur S, Ries J, Eanes R, Nagel P, Pie N, Poole S, Richter T, Save H (2015) Evaluation of the GGM05 Mean Earth Gravity models. In: Geophysical Research Abstracts, vol 17. EGU2015-4153

Brockmann JM, Zehentner N, Höck E, Pail R, Loth I, Mayer-Gürr T, Schuh W-D (2014) EGM_TIM_RL05: an independent geoid with centimeter accuracy purely based on the GOCE mission. Geophys Res Lett 41(22):8089–8099. doi:10.1002/2014GL061904

Bruinsma SL, Foerste C, Abrikosov O, Marty JC, Rio MH, Mulet S, Bonvalot S (2013) The new ESA satellite-only gravity field model via the direct approach. Geophys Res Lett 40:3607–3612. doi:10.1002/grl.50716

Förste C, Bruinsma S, Rudenko S, Abrikosov O, Lemoine J-M, Marty J-C, Neumayer KH, Biancale R (2016) EIGEN-6S4 A time-variable satellite-only gravity field model to d/o 300 based on LAGEOS, GRACE and GOCE data from the collaboration of GFZ Potsdam and GRGS Toulouse. GFZ Data Services. doi:10.5880/icgem.2016.004

Ekman M (1989) Impacts of geodynamic phenomena on systems for height and gravity. Bull Geod 63(3):281–296

Gatti A, Reguzzoni M, Migliaccio F, Sanso F Space-wise grids of gravity gradients from GOCE data at nominal satellite altitude. Presented at the 5th GOCE User Workshop, Paris, 25–28 November 2014

Gianniou M (2008) "HEPOS: designing and implementing an RTK-Network", geoinformatics magazine for surveying, mapping & GIS professionals, Jan./Feb. 2008 vol 11, pp 10–13

IERS Conventions (2010) In: Petit G, Luzum B (eds) IERS Conventions Center Technical Note No 36. Verlag des Bundesamts für Kartographie und Geodäsie, Frankfurt am Main

Kotsakis C, Katsambalos K, Ampatzidis D, Gianniou M (2010) Evaluation of EGM08 using GPS and leveling heights in Greece; IAG Symposia vol 135, "Gravity, Geoid and Earth Observation", pp 481–488, Springer eds., doi: 10.1007/978-3-642-10634-7_64

Mayer-Gürr T, et al The combined satellite gravity field model GOCO05s. Presented at EGU General Assembly, Vienna, April, 2015

Milona-Kotroyianni E (1989) The 1st order leveling network in the Hellenic territory. Hellenic Army Geographic Service Internal Report

Pail R, Goiginger H, Mayrhofer R, Schuh W, Brockmann JM, Krasbutter I, Hoeck E, Fecher T (2010) GOCE gravity field model derived from orbit and gradiometry data applying the time-wise method. Presented at the ESA Living Planet Symposium 2010, Bergen, June 27–July 2, Bergen, Norway

Pail R, Gruber T, Fecher T, GOCO Project Team (2016) The Combined Gravity Model GOCO05c. http://doi.org/10.5880/icgem.2016.003

Pavlis NK, Holmes SA, Kenyon SC, Factor JK (2008) An Earth gravitational model to degree 2160: EGM2008. Presented at the 2008 General Assembly of the European Geosciences Union, Vienna, Austria, April 13–18

Ries J, Bettadpur S, Eanes R, Kang Z, Ko U, McCullough C, Nagel P, Pie N, Poole S, Richter T, Save H, Tapley B (2016) The combined gravity model GGM05C. http://dx.doi.org/10.5880/icgem.2016.002

Shuttle Radar Topography Mission Internet resources: http://www2.jpl.nasa.gov/srtm

Vergos GS, Grigoriadis VN, Tziavos IN, Kotsakis C (2014) Evaluation of GOCE/GRACE global geopotential models over Greece with collocated GPS/levelling observations and local gravity data. In: IAG Symposia, vol 141, pp 85–92. doi: 10.1007/978-3-319-10837-7_11

Vergos, GS, Andritsanos VD, Grigoriadis VN, Pagounis V, Tziavos IN (2015) Evaluation of GOCE/GRACE GGMs Over Attica and Thessaloniki, Greece, and Wo Determination for Height System Unification; IAG Symposia Series, Springer eds., doi: 10.1007/1345_2015_53

GOCE Variance and Covariance Contribution to Height System Unification

V.D. Andritsanos, V.N. Grigoriadis, D.A. Natsiopoulos, G.S. Vergos, T. Gruber, and T. Fecher

Abstract

The definition and realization of vertical datum is a key concept in support of not only geodetic works but also for surveying and hydraulic studies to name a few. In the GOCE era, this is customarily done by estimating height and/or geopotential offsets with respect to a conventional reference geopotential value or to available GNSS/Leveling observations on trigonometric BMs and a GOCE-based geoid. This work investigates the influence of GOCE errors in the determination of the Hellenic Local Vertical Datum. This is facilitated through a least-squares adjustment of collocated GNSS/Leveling and GOCE geoid heights over a network of 1,542 BMs. TIM-R5, GOCO05s and GOCO05c Global Geopotential Models (GGMs) are used for representing the contribution of GOCE and GRACE to the Earth's gravity field. First, a weighted adjustment is carried out employing the GGMs commission error as indicative of the geoid height variance for all stations. Then, full variance-covariance matrices of the GGMs are employed for utilizing realistic GOCE error information and investigating their influence on the adjustment results. Using the available GNSS/Leveling formal errors, a Variance Component Estimation (VCE) is performed to evaluate height (*h, H, N*) error matrices and assess the stochastic model for the corresponding observational noise. VCE is used to address the impact of a simplified uniform variance assumption for all geoid height data on the final prediction variances in contrast to using the full covariance matrices. Finally, zero-level geopotential values are estimated for the Greek mainland following weighting schemes as the ones described above.

Keywords

Covariance • GOCE • GPS-levelling • Height system unification • LVD • Variance • VCE

1 Introduction

The use of heights is of main importance for a wide range of geodetic, surveying and engineering applications. In the case of orthometric heights, height differences are determined nationwide by conventional spirit leveling accompanied by gravity measurements along dedicated traverses. The orthometric heights of all established benchmarks (BMs) are then obtained, through a least-squares (LS) adjustment of the entire vertical network, as height differences w.r.t. a selected BM that serves as the origin point of the country's vertical reference system.

V.D. Andritsanos (✉)
Geospatial Technology Research Lab, Department of Civil Engineering and Surveying & Geoinformatics Engineering, Technological and Educational Institute of Athens, 12210 Athens, Greece
e-mail: vdandrit@teiath.gr

V.N. Grigoriadis • D.A. Natsiopoulos • G.S. Vergos
GravLab, Department of Geodesy and Surveying, Aristotle University of Thessaloniki, University Box 440, 54124 Thessaloniki, Greece

T. Gruber • T. Fecher
Institute for Astronomical and Physical Geodesy, Technical University of Munich, Arcisstrasse 21, 80333 Munich, Germany

G. S. Vergos et al. (eds.), *International Symposium on Gravity, Geoid and Height Systems 2016*, International Association of Geodesy Symposia 148, DOI 10.1007/1345_2017_12

With GOCE having completed its mission at the end of October 2013, there still exists a wide range of applications that GOCE-derived products can have a significant contribution to. It has been very recently concluded that GOCE, apart from a high-accuracy static gravity field (Brockmann et al. 2014; Bruinsma et al. 2013; Mayer-Gürr et al. 2015), can offer unique insights to oceanographic, engineering and geophysical applications (Albertella et al. 2012; Fuchs et al. 2013; Reguzzoni et al. 2013; Tziavos et al. 2013).

In the pure geodetic context, the contribution of GOCE is viewed in improving and assessing local gravity and geoid models also in combination with GPS/levelling measurements (Andritsanos et al. 2015; Tziavos et al. 2016; Vergos et al. 2014, 2015).

Height System Unification (HSU) over Greece is an issue of major importance since neither the mainland nor the islands use a common zero level geopotential value and/or common referend. The Hellenic Vertical Datum (HVD) was established by the Hellenic Geographic Military Service within the period 1963–1986. In principle, the physical heights in the HVD were modeled as Helmert orthometric heights in the mean-tide system. They refer to the TG station at the Piraeus harbor, where local MSL was computed from sea level measurements over the period 1933–1978 (Takos 1989). The true accuracy of the HVD's leveling network is largely unknown, while a common adjustment of the entire vertical network was never performed. Over the Greek islands, the corresponding vertical datums were established by the Hellenic Military Geographic Service through the fixed MSL at a single tide-gauge station in each island. In essence, each island has its own LVD, which is not connected to the mainland and to the origin of the HVD at Piraeus harbor.

Kotsakis et al. (2012) estimated the zero-level geopotential value for selected Greek Islands, while Grigoriadis et al. (2014) for the Greek mainland. In all previous studies, no additional information about the weighting of the geoid heights was taken into account. In this study, four different weighting scenarios were considered in order to perform efficient validation on the heights systems and draw some conclusions on the deformations present in the HVD.

2 Methodology and Data

2.1 Data and Preprocessing

For the present study, GPS/levelling data that refer to stations belonging to the Hellenic Triangulation Network were available along with geoid heights obtained from GOCE/GRACE-based GGMs, GOCO5C (Fecher et al. 2016), GOCO05S (Mayer-Gürr et al. 2015), DIR-R5 (Bruinsma et al. 2013) and TIM-R5 (Brockmann et al. 2014), and EGM2008 (Pavlis et al. 2012). Regarding the leveling data, these were measured by the Hellenic Military Geographic Service using spirit and trigonometric leveling. There is no scientific documentation available for the vertical datum of Greece and inconsistencies are known to exist between the mainland and the islands. On the other hand, the GPS data originate from measurements carried out using Geodetic GPS receivers in the frame of the HEPOS project (Gianniou 2008). For more information about the GPS/Leveling data and their distribution please consult Tziavos et al. (2016).

2.2 Adjustment Combination Schemes

The residual geoid heights ΔN have been evaluated first following a spectral enhancement approach (Vergos et al. 2015) as:

$$\Delta N = N^{GPS/Lev} - N^{GOCE}\Big|_{2}^{n_1} - N^{EGM2008}\Big|_{n_1+1}^{2190} - N^{RTM} - N_o, \quad (1)$$

where $N^{GPS/Lev}$ are the GPS/Leveling geoid heights, N^{GOCE} and $N^{EGM2008}$ the GOCE-based and EGM2008 GGM-derived geoid heights respectively and N_o the zero-degree geoid (see Heiskanen and Moritz, 1967 – Eq. 2.182) with GRS80 used as the reference ellipsoid. The Residual Terrain Model effects on geoid heights (N^{RTM}), was computed from an SRTM-based 3 arcsec digital terrain model (Tziavos et al. 2010) , so that the geoid spectrum represented is equivalent to d/o 216,000. Therefore, the geoid omission error is very small (mm-level), so it can be neglected in the formed differences. Finally, all computations have been performed in the Tide Free system, while the necessary conversions were performed according to Ekman (1989). The evaluation scheme has been carried out for d/o 175 of each GGM up to their n_{max}. The choice of the 175 d/o of expansion is made according to previous studies on the optimal combination synthesis, where the spectral range that the GOCE GGMs perform better than EGM2008 (Tziavos et al. 2016; Vergos et al. 2015). For a more elaborate discussion of the followed methodology and conventions Carrion et al. (2015), Tocho and Vergos (2015), Tziavos et al. (2016) and Vergos et al. (2015) should be consulted.

ΔN may be described by various parametric models following a least-squares adjustment procedure. For the validation of the GOCE/GRACE GGMs six models were selected. The well-known four- (MODEL A) and five-parameter (MODEL-B) similarity transformation models (Heiskanen and Moritz 1967), a model that corresponds to a height-dependent corrector surface with a simple bias and two scale terms (MODEL C), a bias and an orthometric height scale term (MODEL D) and a bias and a geoid height

scale term (MODEL E) (Kotsakis and Katsambalos 2010). Finally, a 3rd order polynomial (MODEL F) can be used as a corrector surface in the computations as outlined in Vergos and Sideris (2002).

2.3 Error Consideration

Crucial role in the height adjustment has the proper propagation of errors v, so that the final estimate will be reliable. The errors may be divided into an orthometric, ellipsoid and geoid height error component. Each unknown error component can be described by its second-order stochastic model of the form (Kotsakis and Sideris 1999):

$$E\left\{\mathbf{v}_h\mathbf{v}_h^T\right\} = \mathbf{C}_h,\quad E\left\{\mathbf{v}_H\mathbf{v}_H^T\right\} = \mathbf{C}_H,\quad E\left\{\mathbf{v}_N\mathbf{v}_N^T\right\} = \mathbf{C}_N \tag{2}$$

For the orthometric heights, the covariance (CV) matrix $\mathbf{C}_H$ is usually known from the adjustment of the leveling network, while $\mathbf{C}_h$ can be computed from the adjustment of the GPS surveys performed at the leveled benchmarks. Unfortunately, this is not the case in the present study. Since no reliable information about leveling and GPS error is available, only assumptions on their statistical information will be made. In the gravimetric geoid case, the covariance matrix $\mathbf{C}_N$ is computed using four different scenarios. These error scenarios that will be used in the weighting of the adjustment and the Variance Component Estimation (VCE) that follows can be summarized as:

Scenario 1. Equally Weighted Heights
The following stochastic model will be adopted for the random noise effects in the three height data sets:

$$\begin{aligned} E\left\{\mathbf{v}_h\mathbf{v}_h^T\right\} &= \sigma_h^2\mathbf{Q}_h,\ E\left\{\mathbf{v}_H\mathbf{v}_H^T\right\} = \sigma_H^2\mathbf{Q}_H, \\ E\left\{\mathbf{v}_N\mathbf{v}_N^T\right\} &= \sigma_N^2\mathbf{Q}_N \end{aligned} \tag{3}$$

where the cofactor matrices $\mathbf{Q}_h$, $\mathbf{Q}_H$, and $\mathbf{Q}_N$ are assumed equal to the identity matrix, and the three variance components are treated as unknown parameters controlling the validity of the a priori random error models. The assumption of the equally weighted height is not the case in real applications but we chose this scenario in order to investigate the adequacy of the tested parametric models (MODELS A to F) to the height fitting.

Scenario 2. Geoid Height Weights Based on Geoid Model Cumulative Errors
In this case, the stochastic model of the orthometric and ellipsoid heights is chosen to be a standard value based on some a-priori information about the accuracy of the respective observations. Weights of 1/0.01 and 1/0.04 are adopted for the ellipsoid heights and for the orthometric heights respectively. This accuracy ratio (1/4) is close to real world applications, where the ellipsoid heights are estimations with increased accuracy with respect to the orthometric heights of base trigonometric networks, derived from older measurement adjustments.

In this scenario, the geoid height stochastic model is derived using synthetic information of the cumulative geoid model error. The synthesis is based on the error degree variances of GOCE model till d/o 175 or $n_{\max}$ and the residual geoid error computed using error degree variances of EGM2008. The stochastic model of the current scenario is provided by the cofactor matrix of the geoid:

$$\mathbf{Q}_N = \varepsilon_{cml}^2 \cdot \mathbf{I} = \left(\varepsilon_{N_{GGM\_n\max}}^2 + \varepsilon_{N_{08\_n\max\_to\_2190}}^2\right)\cdot\mathbf{I} \tag{4}$$

where $\varepsilon_{N_{GGM}}$ is the cumulative error of the respective GOCE-based model and $\varepsilon_{N_{08}}$ is the contribution of the EGM2008 to the total error.

Scenario 3. Geoid Height Weights from Propagated Error Variances
The stochastic model of the geoid heights in this scenario is based on the propagated error variances of the GOCE geoid models. The stochastic model is constructed using the propagated error of the respective GOCE model ($\sigma^2_{prop_{N_{GGM\_n\max}}}$) till a specific degree (175 or n_{max}) and the residual of the cumulative error of EGM2008 geopotential model according to the equation:

$$\mathbf{Q}_N = \sigma_{prop}^2 \cdot \mathbf{I} = \left(\sigma^2_{prop_{N_{GGM\_n\max}}} + \varepsilon^2_{N_{08\_n\max\_to\_2190}}\right)\cdot\mathbf{I} \tag{5}$$

Scenario 4. Geoid Height Weights Using Full Geoid Variance-Covariance Matrix
In this final scenario, the full variance-covariance matrix of the GOCO05x models is used till a maximum degree of expansion ($n_{\max}$ = 175, 280 or 720) and the contribution of EGM2008 is taken into account from this degree and above. The cofactor matrix of the geoid heights is provided by:

$$\mathbf{Q}_N = \mathbf{C}^{full}_{prop_{N_{GGM\_n\max}}} + \varepsilon^2_{N_{08\_n\max\_to\_2190}}\cdot\mathbf{I} \tag{6}$$

where $\mathbf{C}^{full}_{prop_{N_{GGM\_n\max}}}$ is the full variance – covariance matrix of the geopotential model. The full covariance information is available only up to $n_{\max}$ and only for the GOCO05x models.

3 Results and Discussion

The differences ΔN at the 1,542 GPS/Levelling benchmarks using the spectral enhancement method are presented in Fig. 1. As it can be seen from Fig. 1, the standard devia-

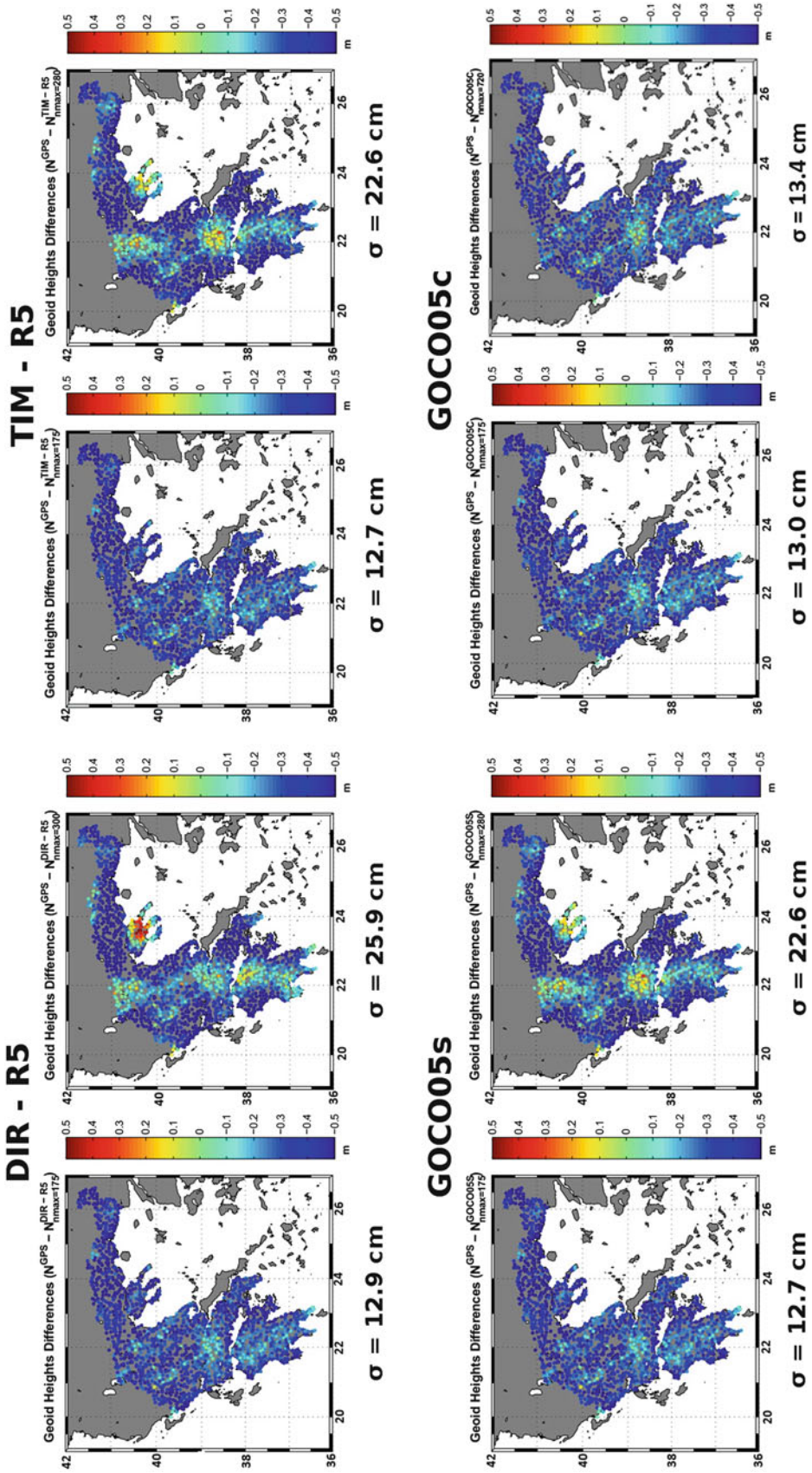

Fig. 1 The differences at GPS/levelling benchmarks. Below each model name are the differences using GOCE assimilation degree 175 (*left*) and the full degree of the model (*right*). The std of the differences in each case is also given

tion (std) of the differences between GPS/Levelling geoid heights and GGM geoid heights is at the level of ±12.7 to ±13.0 cm when the assimilation degree of the GOCE model reaches d/o 175 and decreases when the complete signal of the GOCE model is used. An interesting exception is the case of GOCO05C where the std of the differences stays at the level of ±13.4 cm probably due to the use of surface gravity data to the coefficients estimation. TIM-R5 performs slightly better, in terms of std of the differences, than the other models using an assimilation degree 175. Using the full spectra of TIM-R5 (expansion degree 280) some geographically correlated errors appeared before any parametric fitting. This fact confirms the weak character of the higher harmonics of GOCE models above degree 200. Still EGM2008 contribution performed better than GOCE models in the band between 200 and 280 degree. In addition, the geographically correlated errors remain smaller than the ones in the case of DIR-R5 to its full d/o 300, confirming the error augmentation as the assimilation degree grows.

3.1 Parametric Models Adjustment

The effect of the parametric model used in the adjustment of the differences is examined. Tables 1 and 2 present the statistics for TIM-R5 model which proved the best in the assimilation test of the previous section. In Table 1 MODEL C gave the best statistical results in terms of the std of the differences. An improvement of 1.6 cm is presented using this mixed bias, geoid and orthometric height factor model. Considering Fig. 2, major differences remain after the parametric adjustment at the mountainous areas of Greece, focusing on the problematic character of the orthometric heights in steep terrain.

The incorporation of the complete signal of GOCE models gave worst statistical results as seen in Table 2. An improvement of 1.4 cm in terms of the std of the differences is presented using a mixed bias and orthometric height scale factor model (MODEL D).

Table 1 The statistics of the parametric model adjustment of the GOCE TIM – R5 model when the assimilation reaches the degree 175 [m]

TIM – R5 (175)	Max	Min	Mean	Std
Before	0.081	−0.865	−0.393	0.127
After – MODEL A	0.468	−0.450	0.000	0.118
After – MODEL B	0.464	−0.451	0.000	0.118
After – MODEL C	0.403	−0.436	0.000	0.111
After – MODEL D	0.401	−0.424	0.000	0.119
After – MODEL E	0.480	−0.444	0.000	0.121
After – MODEL F	0.459	−0.462	0.000	0.117

Table 2 The statistics of the parametric model adjustment of the GOCE TIM – R5 model when the assimilation reaches the degree 280 [m]

TIM – R5 (280)	Max	Min	Mean	Std
Before	0.337	−1.114	−0.395	0.226
After – MODEL A	0.711	−0.700	0.000	0.224
After – MODEL B	0.708	−0.693	0.000	0.224
After – MODEL C	0.666	−0.717	0.000	0.214
After – MODEL D	0.644	−0.731	0.000	0.212
After – MODEL E	0.725	−0.692	0.000	0.224
After – MODEL F	0.648	−0.663	0.000	0.213

The statistics of the best performed parametric MODEL C using the tested GOCE GGMs are presented in Table 3. When the assimilation degree of each GOCE model reaches the degree 175 similar results are obtained. A std of ±11 cm is computed with the best results when TIM–R5 and GOCO05S are utilized. If the complete signal of GOCE GGMs is used, degradation in the statistics is noticed. This degradation is addressed to the erroneous effects of the higher coefficients of GOCE models w.r.t. the EGM2008 coefficients. It is to be noted that satellite-only GOCE models lack high frequency information found in GOCO05C since surface gravity data were not included in the computation of their coefficients. This is the main reason why the std of the differences remains at the order of ±11.5 cm. The values of the corrector surfaces computed from the parametric model adjustment reveal a South-to-North and East-to-West trend and a correlation with geoid and orthometric heights in the case of MODEL C and D.

3.2 Weighting Effect

The weighting effect on the adjustment results is studied using the four abovementioned scenarios. The statistics after the parametric adjustment remain exactly the same as in Scenario 1 showing minimal effect of the weighting in the final results. The major differences using Scenario 2–4 weighting procedure can be seen in the estimation of the parameters of each corrector surface as well as in the accuracy of this estimation and the a-posteriori variance of the adjustment (see Table 4). In Table 4 the degradation due to the higher coefficients of the GOCE models is also identified in the a-posteriori std estimation of the parametric adjustment. A 6 cm a-posteriori std is computed when equally weighting heights are used. Nevertheless, this is not the case in real applications. The introduction of more realistic information of the height error led to worst results. It is of great importance that with the incorporation of more realistic errors for the geoid heights (cumulative errors,

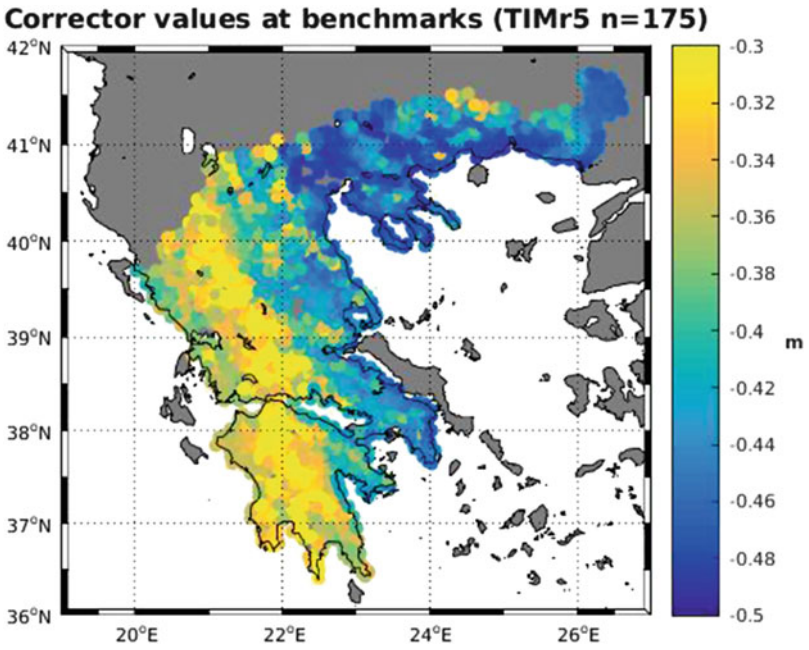

Fig. 2 Values of the corrector surface (MODEL C) for TIM-R5 (expansion degree 175)

Table 3 The statistics after the parametric adjustment (MODEL C) using GOCE GGMs till degree 175 and the maximum degree of expansion [m]

Geoid model	Max	Min	Std
DIR – R5 (175)	0.397	−0.429	0.113
DIR – R5 (300)	0.999	0.772	0.244
TIM – R5 (175)	0.403	−0.436	0.111
TIM – R5 (280)	0.666	−0.717	0.214
GOCO05S (175)	0.403	−0.435	0.111
GOCO05S (280)	0.664	−0.739	0.210
GOCO05C (175)	0.411	−0.422	0.112
GOCO05C (720)	0.393	−0.432	0.115

Table 4 Effect of the various weighting scenarios in the a-posteriori std of the parametric adjustment – parametric MODEL C [m]

Geoid model	E.W.	C.E.	P.E.	F.V.C.
DIR – R5 (175)	0.0652	0.5030	0.4786	–
DIR – R5 (300)	0.1412	1.0669	0.7985	–
TIM – R5 (175)	0.0644	0.4948	0.4335	–
TIM – R5 (280)	0.1213	0.8147	0.5851	–
GOCO05S (175)	0.0643	0.4953	0.4967	0.4938
GOCO05S (280)	0.1216	0.8086	0.7651	0.6100
GOCO05C (175)	0.0648	0.5001	0.5009	0.5002
GOCO05C (720)	0.0663	0.4466	0.5127	0.5074

E.W. equally weighted heights, *C.E.* cumulative errors weighting scenario, *P.E.* propagated errors weighting scenario, *F.V.C.* full variance/covariance weighting scenario

propagated errors and full variance/covariance matrix) the statistical results are improved in the case of the a-posteriori std.

3.3 Variance Component Estimation

The variance component estimation of the various heights used in the adjustment was performed using the MINQUE method (Rao 1971; Rao and Kleffe 1988). Two different cases of initial values were chosen, as seen in Table 5. The variance component estimation results presented in Table 5 and Fig. 3 confirm the statement that with the introduction of more realistic weighting scenario, the estimations of height variance components are smaller, signaling the importance of introducing real error information in such height adjustment schemes.

3.4 Estimation of the Zero-Level Geopotential Value

The estimation of the zero-level geopotential value W_o was carried out according to the methodology described in Grigoriadis et al. (2014) and Kotsakis et al. (2012) but with weighting schemes based on Scenarios 2–4. Table 6 provides the results of the computations carried out for determining W_o for the Greek mainland. From the given results, it may be noticed that no significant change in the results is observed with the substitution of the weight for geoid heights obtained from cumulative geoid errors with that from the error covariance matrix of the GOCO family of models. On the other hand, the computations with weights that are based on the full variance/covariance matrix of the GOCO models did not lead to a solution apart from the combination of the GOCO05s with EGM08. This is due to the fact that it was not possible to invert the computed covariance

Table 5 Variance component estimation results using various weighting scenarios and initial values for the calculation [m^2]

Initial values	E.W.	C.E.	P.E.	F.V.C.
$\sigma_h^2 = \sigma_H^2 = \sigma_N^2 = 1$	$\hat{\sigma}_h^2 = 0.00438$ $\hat{\sigma}_H^2 = 0.00438$ $\hat{\sigma}_N^2 = 0.00438$	$\hat{\sigma}_h^2 = 0.04119$ $\hat{\sigma}_H^2 = 0.21030$ $\hat{\sigma}_N^2 = 0.06968$	$\hat{\sigma}_h^2 = 0.03450$ $\hat{\sigma}_H^2 = 0.17642$ $\hat{\sigma}_N^2 = 0.09215$	$\hat{\sigma}_h^2 = 0.00146$ $\hat{\sigma}_H^2 = 0.02779$ $\hat{\sigma}_N^2 = 6.79 \cdot 10^{-8}$
$\sigma_h^2 = 0.01$ $\sigma_H^2 = 0.04$ $\sigma_N^2 = 1$		$\hat{\sigma}_h^2 = 0.06572$ $\hat{\sigma}_H^2 = 0.26653$ $\hat{\sigma}_N^2 = 0.10652$	$\hat{\sigma}_h^2 = 0.05627$ $\hat{\sigma}_H^2 = 0.22830$ $\hat{\sigma}_N^2 = 0.09155$	$\hat{\sigma}_h^2 = 0.04253$ $\hat{\sigma}_H^2 = 0.17217$ $\hat{\sigma}_N^2 = 0.01257$

E.W. equally weighting heights, *C.E.* cumulative errors based heights

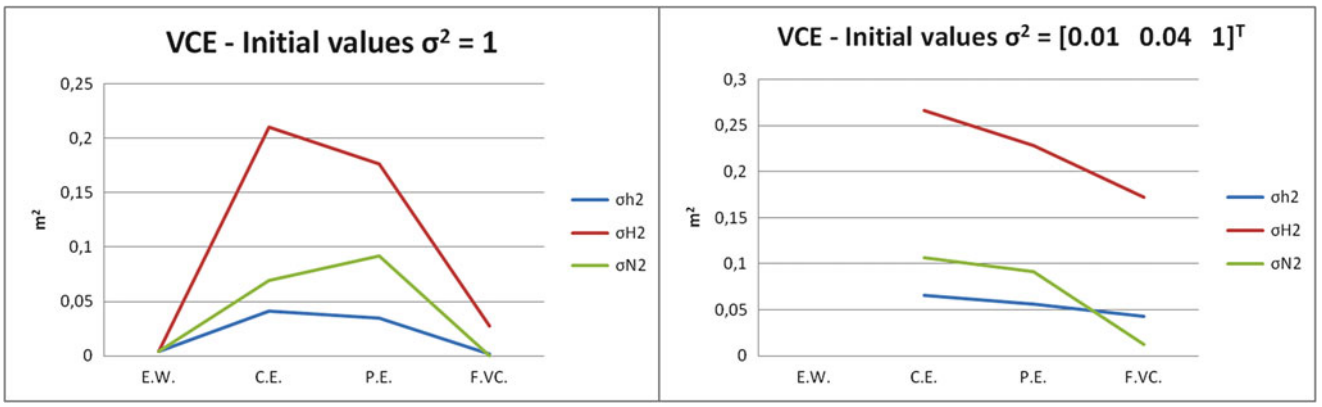

Fig. 3 Variance Component Estimation results for the different weighting schemes

Table 6 Zero-level geopotential values for different weighting scenarios [$m^2\ s^{-2}$]

		C.E.		P.E.	
GM	Max degree	W_o	σ	W_o	σ
EGM08	2,160	62,636,859.664	0.035	n/a	n/a
DIR-R5/EGM08	175/2,160	62,636,859.814	0.034	n/a	n/a
GOCO05c/EGM08	175/2,160	62,636,859.809	0.035	62,636,859.809	0.035
GOCO05s/EGM08	175/2,160	62,636,859.843	0.034	62,636,859.844	0.034
TIM-R5/EGM08	175/2,160	62,636,859.859	0.034	n/a	n/a
		F.V.C			
		W_o		σ	
GOCO05s/EGM08	175/2,160	62,636,859.801		0.039	

matrix and hence compute the corresponding weights. An explanation to this problem could be the size of the study area. It should be noted that this problem did not occur in the previous section, where heights were used in the adjustment procedure.

By further examining the results presented above, additional conclusions may be drawn with respect to the different models used and their degree of expansion. The combination of GOCE-based models with EGM08 (up to degree and order 2,160) leads to similar results. There is also an increase in the W_o of the order of 0.2 m^2/s^2 when comparing to the solution computed only with EGM08. Thus it is obvious that the GOCE-based models and the spectral patching applied have a significant impact on the computed results. The selection though of the best value to be adopted for the Greek mainland is currently not possible due to the accuracy of the source data used as well as to inhomogeneities present in the Greek vertical datum (see also Andritsanos et al. 2015).

4 Conclusions

Considering the parametric model adjustment, using the 175 degree GOCE data gave significantly better results than the use of the full signal of GOCE GGMs patched with EGM2008, in terms of the std and the range of the differences. The study of four different scenarios in the weighting of the parametric model adjustment showed minimal effect in the statistics of the differences. On the other hand, the estimation of the a-posteriori variance of the adjustment is

affected by the adopted stochastic model. With the incorporation of more realistic errors for the geoid heights, the statistical results are improved in the case of the a-posteriori std. This statement is also in line with the results of the VCE procedure, where the height variance component estimates obtain smaller values when a more realistic error value is introduced in the adjustment. Last, the GOCO-based models employed have a significant impact on the computation of the W_o but not the weighting schemes described in this study. The evaluation though of the W_o values obtained requires more accurate data.

Acknowledgments Funding provided for this work by the Greek State Scholarship Foundation (IKY) and Deutsche Akademischer Austausch Dienst (DAAD) (IKYDA2016) in the frame of the "GOCE for height system unification and dynamic ocean topography determination in the Mediterranean Sea (GOCEMed)" project is gratefully acknowledged.

References

Albertella A, Savcenko R, Janjić T, Rummel R, Bosch W, Schröter J (2012) High resolution dynamic ocean topography in the Southern Ocean from GOCE. Geophys J Int 190(2):922–930. doi:10.1111/j.1365-246X.2012.05531.x

Andritsanos VD, Arabatzi O, Gianniou M, Pagounis V, Tziavos IN, Vergos GS, Zachris E (2015) Comparison of various GPS processing solutions toward an efficient validation of the Hellenic Vertical Network: The ELEVATION Project. J Surv Eng, 142(1), doi: 10.1061/(ASCE)SU.1943-5428.0000164, 04015007.

Carrion D, Vergos GS, Albertella A, Barzaghi R, Tziavos IN, Grigoriadis VN (2015) Assessing the GOCE models accuracy in the Mediterranean area. Newton's Bull 5:63–82

Brockmann JM, Zehentner N, Höck E, Pail R, Loth I, Mayer-Gürr T, Schuh W-D (2014) EGM_TIM_RL05: an independent geoid with centimeter accuracy purely based on the GOCE mission. Geophys Res Lett 41(22):8089–8099. doi:10.1002/2014GL061904

Bruinsma S, Foerste C, Abrikosov O, Marty J-C, Rio M-H, Mulet S, Bonvalot S (2013) The new ESA satellite-only gravity field model via the direct approach. Geophys Res Lett 40(14):3607–3612. doi:10.1002/grl.50716

Ekman M (1989) Impacts of geodynamic phenomena on systems for height and gravity. Bull Geod 63(3):281–296

Fecher T, Pail R, Gruber T, the GOCO Project Team (2016) The combined gravity field model GOCO05C. EGU General Assembly, Geophys Res Abstr, vol 18, EGU2016-7696

Fuchs MJ, Bouman J, Broerse T, Visser P, Vermeersen B (2013) Observing coseismic gravity change from the Japan Tohoku-Oki 2011 earthquake with GOCE gravity gradiometry. J Geophys Res 118(10):5712–5721

Gianniou M (2008) HEPOS: designing and implementing an RTK network. GEOInformatics 11:10–13

Grigoriadis VN, Kotsakis C, Tziavos IN, Vergos GS (2014) Estimation of the geopotential value W_o for the local vertical datum of continental Greece using EGM08 and GPS/leveling data. In: Marti U (ed) Gravity,geoid and height systems, International Association of Geodesy Symposia, vol 141. Springer, Cham, pp 249–255. doi:10.1007/978-3-319-10837-7_32.

Heiskanen WA, Moritz H (1967) Physical geodesy. W.H. Freeman and Company, San Francisco

Kotsakis C, Katsambalos K, Ampatzidis D (2012) Estimation of the zero-height geopotential level in a local vertical datum from inversion of co-located GPS, leveling and geoid heights: a case study in the Hellenic islands. J Geod 86(6):423–439

Kotsakis C, Katsambalos K (2010) Quality analysis of global geopotential models at 1542 GPS/levelling benchmarks over the Hellenic mainland. Surv Rev 42(318):327–344

Kotsakis C, Sideris MG (1999) On the adjustment of combined GPS/levelling/geoid networks. J Geod 73(8):412–421

Mayer-Gürr T et al (2015) The combined satellite gravity field model GOCO05s. Presentation at EGU 2015, Vienna, April 2015

Pavlis N, Holmes S, Kenyon S, Factor J (2012) The development and evaluation of the Earth gravitational model 2008 (EGM2008). J Geophys Res 117(B04):406. doi:10.1029/2011JB008916

Rao CR (1971) Estimation of variance components – MINQUE theory. J Multivar Statist 1:257–275

Rao CR, Kleffe J (1988) Estimation of variance components and applications. North-Holland series in statistics and probability, vol 3

Reguzzoni M, Sampietro D, Sans F (2013) Global Moho from the combination of the CRUST 2.0 model and GOCE data. Geophys J Int 195(1):222–237

Takos I (1989) New adjustment of the national geodetic networks in Greece (in Greek). Bull Hellenic Mil Geogr Serv 49(136):19–93

Tocho C, Vergos GS (2015) Assessment of different-generation GOCE-only and GOCE/GRACE Earth global gravity models over Argentina using terrestrial gravity anomalies and GPS/levelling data. Newton's Bull 5:105–126

Tziavos IN, Vergos GS, Grigoriadis VN (2010) Investigation of topographic reductions and aliasing effects to gravity and the geoid over Greece based on various digital terrain models. Surv Geophys 31(3):23–67. doi:10.1007/s10712-009-9085-z

Tziavos IN, Vergos GS, Mertikas SP, Daskalakis A, Grigoriadis VN, Tripolitsiotis A (2013) The contribution of local gravimetric geoid models to the calibration of satellite altimetry data and an outlook of the latest GOCE GGM performance in GAVDOS. Adv Space Res 51(8):1502–1522. doi:10.1016/j.asr.2012.06.013

Tziavos IN, Vergos GS, Grigoriadis VN, Tzanou EA, Natsiopoulos DA (2016) Validation of GOCE/GRACE satellite only and combined global geopotential models over Greece, in the frame of the GOCESeaComb project. In: Rizos C, Willis P (eds) IAG 150 years, International Association of Geodesy Symposia, vol 143. Springer, Cham, pp 297–304. doi:10.1007/1345_2015_160

Vergos G, Grigoriadis V, Tziavos I, Kotsakis C (2014) Evaluation of GOCE/GRACE global geopotential models over Greece with collocated GPS/levelling observations and local gravity data. In: Marti U (ed) Gravity, geoid and height systems, International Association of Geodesy Symposia, vol 141. Springer, Switzerland, pp 85–92. doi:10.1007/978-3-319-10837-7_11.

Vergos GS, Andritsanos VD, Grigoriadis VN, Pagounis V, Tziavos IN (2015) Evaluation of GOCE/GRACE GGMs over Attika and Thessaloniki, Greece, and Wo determination for height system unification. In: International Association of Geodesy Symposia, vol 145. Springer, New York. doi:10.1007/1345_2015_53

Vergos GS, Sideris MG (2002) Evaluation of geoid models and validation of geoid and GPS/leveling undulations in Canada. IGeS Bull 12:3–17

The Use of GNSS/Levelling and Gravity Data for the Spanish Height System Unification

M. Reguzzoni, G. Venuti, M.C. de Lacy, D. Carrion, R. Barzaghi, M.J. Borque, A.J. Gil, and P.A. Vaquero

Abstract

From 2001 to 2008, the National Geographic Institute of Spain (IGN) carried out the REDNAP project to the establishment of a National High Precision Levelling Network in the whole Spanish territory. Within REDNAP, spirit levelling and gravity observations were complemented by GNSS data. The levelling network of the continental area and those of the main islands were referred to different tide gauges thus producing different height systems. In the paper, the GOCO-05S model from the GRACE and GOCE gravity missions is used to unify such systems. More precisely, it is used to estimate the normal heights of the mean sea level at the reference tide gauges, i.e. the height system biases. In the proposed solution such biases are determined through the least squares adjustment of the differences between height anomalies derived from GNSS/levelling and height anomalies derived from a proper combination of global gravity models. An accurate modelling of the observation error covariances is taken into account as well. The estimated accuracies of the resulting biases are in the order of few centimetres apart from that of continental Spain which is an order of magnitude better.

Keywords

Global gravity models • GNSS/leveling • GOCE • GRACE • Height datum problem • REDNAP • Spain

1 Introduction

Regional height systems derived from levelling and gravity measurements are referred to reference tide gauges. The height of a tide gauge is in turn set to a proper weighted average of its observed level differences with respect to the sea water surface. However, due to stationary currents, even a proper averaged sea surface does not lie on an equipotential surface and therefore different tide gauges do not refer to the same datum, as expected. Assume to indirectly define a global height datum by choosing a reference ellipsoid and its related normal potential U_0, such that $W_0 = U_0$. It is now possible to introduce for each region j an unknown bias δW^j equal to the difference between the reference potential W_0 and the actual potential at the point P_0^j on the mean sea surface corresponding to the considered tide gauge, i.e.

$$\delta W^j = W_0 - W(P_0^j)\,. \tag{1}$$

The bias in potential can be expressed in terms of normal height of the mean sea level at the tide gauge

$$\tilde{h}_j^*(P_0^j) = \frac{W_0 - W(P_0^j)}{\overline{\gamma}(Q_0^j)} = \frac{\delta W^j}{\overline{\gamma}(Q_0^j)} = b_j\,, \tag{2}$$

M. Reguzzoni • G. Venuti (✉) • D. Carrion • R. Barzaghi
DICA, Politecnico di Milano, P.zza Leonardo da Vinci 32, Milan, Italy
e-mail: giovanna.venuti@polimi.it

M.C. de Lacy • M.J. Borque • A.J. Gil
DICGF, Universidad de Jaén, Campus Las Lagunillas s/n, Jaén, Spain

P.A. Vaquero
IGN, General Ibáñez de Ibero 3, Madrid, Spain

G. S. Vergos et al. (eds.), *International Symposium on Gravity, Geoid and Height Systems 2016*,
International Association of Geodesy Symposia 148, DOI 10.1007/1345_2017_14

where Q_0^j is the telluroid point on the normal to the ellipsoid through P_0^j, such that $U(Q_0^j) = W(P_0^j)$, and $\overline{\gamma}(Q_0^j)$ is the average value of the normal gravity, along the same normal, between the ellipsoid and the telluroid. This bias is common to all normal heights of the benchmarks stemming from the considered tide gauge in the spirit levelling and gravity network adjustment.

The possibility to estimate height biases, thus solving regional height datum inconsistencies with respect to a common global datum, have been investigated and proven. Different solutions have been proposed by several authors, such as Rummel and Teunissen (1988), Rummel (2012), Kotsakis et al. (2012), Sideris et al. (2014). Furthermore, during the last IAG/IUGG Assembly in Prague, an official IAG resolution was voted for the establishment of the International Height Reference System (IHRS) and an ad-hoc group was set up with the objective of defining the requirements for the implementation of the IHRS (Idhe et al. 2015). One possible method for height systems unification was presented by some of the authors in Gatti et al. (2013) followed by a first application to the Italian case (Barzaghi et al. 2015), where three different regional height systems are present.

After shortly recalling such solution in Sect. 2, the dataset used in the Spanish case is illustrated in Sect. 3. In Sect. 4 the data pre-processing, needed to obtain the 'observations' and their covariance matrix for the least squares estimate of the height biases, is reported. The input data analysis and the solution obtained are discussed in Sect. 5, followed by conclusions in Sect. 6.

2 The Height Datum Problem and the Adopted Solution

Normal heights, as derived from the least squares adjustment of spirit levelling and gravity observations, are affected by the height bias of the tide gauge they refer to (Heiskanen and Moritz 1967; Betti et al. 2015). The difference between the unbiased, GNSS derived, ellipsoidal height $h(P)$ of any point P belonging to the region j, and its biased normal height $\tilde{h}_j^*(P)$ results in an observable biased height anomaly of the point (Barzaghi et al. 2015):

$$\tilde{\zeta}^j(P) = h(P) - \tilde{h}_j^*(P) = \zeta(P) + b_j \ . \tag{3}$$

The unbiased height anomaly ζ can be in turn modelled by using Bruns' formula:

$$\zeta(P) = \frac{T(P)}{\gamma(Q)} \ , \tag{4}$$

where Q is the point on the normal to the reference ellipsoid through P, whose height is implicitly defined by $U(Q) = W(P)$. Note that a large uncertainty, say 10 m, in the knowledge of the normal height of P has a quite negligible effect on the evaluation of the normal gravity $\gamma(Q)$.

Provided that an unbiased, sufficiently accurate value of the anomalous potential $T(P)$ is known, one can use the following equation in the estimation of the regional height datum biases:

$$\tilde{\zeta}^j(P) = \frac{T(P)}{\gamma(Q)} + b_j \ . \tag{5}$$

The satellite-only models, which are unbiased, do not contain the local feature of the anomalous field needed to accurately solve the height datum problem. On the contrary, high resolution global gravity models, mainly derived from locally determined gravity anomalies, also depending on levelling, are indirectly biased. Gatti et al. (2013) showed that the indirect effect of the height biases in the high degree coefficients can be disregarded on a global scale, namely in the estimate of the height biases of patches covering the whole Earth. Moreover, Gerlach and Rummel (2013) showed that the same conclusion can be drawn also on a 'local' scale, namely when determining the biases of few patches only. In Barzaghi et al. (2015) a local solution was attempted, which here is presented again by using the same error covariance modelling, but a larger and more suitable GNSS and gravity/levelling dataset (cf. Sect. 3) as well as more recent global gravity models.

By using Eqs. (3) and (4), the following observation equation can be written for a point P belonging to the region j:

$$\tilde{\zeta}^j(P) - \frac{T^L(P) + T^H(P)}{\gamma(Q)} = b_j + \nu \ , \tag{6}$$

where $T^L(P)$ is the prediction of the anomalous potential at the point P derived from the satellite-only gravity model up to degree L, $T^H(P)$ is the prediction derived from the high resolution global gravity models from degree $L+1$ up to degree H and ν is the error. For N_j points in J regions a linear system of $N = \sum_{j=1}^{J} N_j$ equations and J unknowns can be solved by a least squares adjustment, once the error covariance matrix C_ν is defined. This matrix has to account for the errors in the ellipsoidal heights derived from GNSS through the covariance matrix C_h, the errors in the normal heights derived from levelling and gravity measurements through $C_{\tilde{h}^*}$, the commission errors of the satellite-only gravity model up to the degree L through C_{T^L} and those in the high resolution model from degree $L+1$ up to degree H through C_{T^H}. No omission error is modelled above degree H. All the different error sources are assumed to be uncorrelated so that the covariance matrix of the total error can be written as follows:

$$C_\nu = \Gamma^{-1} \left(C_{T^L} + C_{T^H} \right) \Gamma^{-1} + C_h + C_{\tilde{h}^*} \ , \tag{7}$$

where Γ is a diagonal matrix containing the normal gravity values at points Q corresponding to points P. The covariance matrix used in the Spanish case will be defined in more details in the following.

3 The Used Dataset

3.1 The Spanish REDNAP Data

The Royal Decree 1071/2007 set the Spanish High Precision Levelling Network (REDNAP) as the legal frame for the realization of the Altimetric Reference System, taking as reference heights the records of the mean sea level in Alicante for the Peninsula, and those of local tide gauges for each of the main islands. These islands are Formentera, Ibiza, Mallorca, Menorca in the Balearic Archipelago and Tenerife, Gran Canaria, Fuerteventura, Lanzarote, La Palma, Gomera and El Hierro in the Canary Islands. Stemming from different tide gauges (see Table 1), the levelling networks of the peninsula area and those of the main islands are each referred to a different height datum. To estimate the biases between the different height systems and the reference geoid, data coming from the REDNAP network are here used. This high precision levelling network consists of about 25,000 benchmarks for an overall length of approximately 20,000 km. The network spirit levelling observations are complemented by GNSS and gravity ones.

The dataset used for this work, provided by the Spanish National Geographic Institute (IGN), is composed of orthometric heights, geopotential numbers and GNSS ellipsoidal heights. The accuracy of orthometric heights is at centimeter level, the accuracy of gravity observations is better than 100 μgal and that of ellipsoidal heights is better than 10 cm. GNSS heights are referred to ETRF96(1995.4) for the peninsula stations, to ETRF96(1998) for the Balearic Islands and to ITRF93(1994.9) for the Canary Islands (Quirós et al. 2011). The REDNAP dataset was already used by Rülke et al. (2015) for the estimation of the continental Spain bias only.

3.2 The Global Gravity Models

The observation equation (6) for the height datum biases requires the evaluation of the anomalous gravitational potential at points where GNSS/levelling observations are available. This evaluation is here performed by using global gravity models expressed as truncated series of spherical harmonics. As for the low degrees, the satellite-only GOCO-05S solution (Mayer-Gürr et al. 2015) is used up to degree and order 280. This model is basically a combination of the ITSG-GRACE2014S coefficients (Mayer-Gürr et al. 2014) and the last release of the GOCE time-wise solution computed from the analysis the whole mission dataset (Brockmann et al. 2014). The GOCO-05S coefficients were downloaded from the website of the International Center for Global Earth Models (ICGEM), while their error covariance matrix in a block-diagonal approximation was provided by J.M. Brockmann. It is important to underline that this approximation is sufficient for the purposes of this study (Gerlach and Fecher 2012).

As for the higher degrees, both the currently available EGM2008 (Pavlis et al. 2012) and EIGEN-6C4 (Förste et al. 2014) high resolution global gravity models are used to compare the corresponding results. From the ICGEM website, only error variances of the spherical harmonic coefficients are distributed. This modelling, producing an error covariance structure with a prevailing cylindrical symmetry, is not able to locally describe the geographical variability of the error, which is mainly due to the inhomogeneous spatial distribution and quality of the used ground gravity data. In the case of EGM2008, together with the error coefficient

Table 1 Spanish reference tide gauges

	Balearic Islands	
1	Formentera	Tide gauge of CEDEX at Puerto de La Savina
2	Ibiza	Tide gauge of Puertos del Estado at Puerto de Ibiza
3	Mallorca	Tide gauge of Instituto Español de Oceanografía at Puerto de Palma
4	Menorca	Tide gauge of Gobierno Balear at Puerto de Ciudadela
	Canary Islands	
5	Tenerife	Tide gauge of IGN at Puerto de Santa Cruz de Tenerife
6	Gran Canaria	Tide gauge of Instituto Español de Oceanografía at Puerto de la Luz
7	Fuerteventura	Tide gauge of IGN at Puerto del Rosario
8	Lanzarote	Tide gauge of Instituto Español de Oceanografía at Puerto de Arrecife
9	La Palma	Historical tide gauge of Instituto Español de Oceanografía at Santa Cruz de la Palma
10	La Gomera	Tide gauge of Instituto Hidrográfico de la Marina at Puerto de San Sebastián de la Gomera
11	El Hierro	Tide gauge of Puertos del Estado at Puerto de la Estaca
12	*Mainland*	Tide gauge of IGN in Alicante

variances, a global grid of local geoid error variances is also available from the website of the National Geospatial-Intelligence Agency (NGA) and this additional information is used to refine the error covariance modelling (Gilardoni et al. 2013, 2016). On the other hand, since this information is not available for EIGEN-6C4, its error covariance above degree 280 is modelled as the one of EGM2008.

A remark is due before concluding the section. The combination used between GOCO-05S and EGM2008 or EIGEN-6C4 consists in simply taking the satellite-only model up to its maximum degree and then complementing it with the chosen high-resolution model. This is not necessarily the best possible combination, e.g. when managing polar gaps, but it is the one here implemented according to the results of the previous Italian study (Barzaghi et al. 2015) with the aim of reducing the height datum indirect effects in EGM2008 or EIGEN-6C4. A deeper analysis on the role of different geoid combinations in the datum offset estimation can be found in Rülke et al. (2012).

4 Data Pre-processing

4.1 Reference Frame Transformations

The first step in the data pre-processing is a transformation of the REDNAP benchmark geodetic coordinates to make them consistent with the global gravity models in terms of reference ellipsoid. The procedure is the same described in Barzaghi et al. (2015) and basically consists in transforming the REDNAP data coordinates to ITRF2008 at epoch 2011. To perform this transformation the mean values of some Spanish station velocities are used, in particular, ALAC and CANT for the Peninsula, MALL for the Balearic Islands and LPAL for the Canary Islands. Also in the present case, like in the Italian one, the impact of this transformation on the prediction of the biased height anomalies is negligible. Statistics of the differences between original and transformed heights are reported in Table 2.

4.2 Computation of Normal Heights

From the available 'biased' geopotential numbers

$$\tilde{C}^j(P) = W(P_0^j) - W(P) = W_0 - \delta W^j - W(P)\,, \quad (8)$$

the normal heights, needed to derive the biased height anomalies in Eq. (3), are computed:

$$\tilde{h}^*_j(P) = \frac{\tilde{C}^j(P)}{\overline{\gamma}(Q)} = \frac{W_0 - \delta W^j - W(P)}{\overline{\gamma}(Q)} = h^*(P) - \frac{\delta W^j}{\overline{\gamma}(Q)}\,. \quad (9)$$

As it was already discussed in Barzaghi et al. (2015), when normal heights are derived from geopotential numbers, rather than from a direct adjustment of spirit levelling observations after applying proper normal corrections (Heiskanen and Moritz 1967; Betti et al. 2015), Eq. (6) has to be slightly modified as follows:

$$\tilde{\zeta}^j(P) - \frac{T^L(P) + T^H(P)}{\gamma(Q)} = \frac{\delta W^j}{\overline{\gamma}(Q)} + \nu\,, \quad (10)$$

the unknown parameter being the bias in potential δW^j. In practise, by recalling Eq. (2), one can write:

$$\frac{\delta W^j}{\overline{\gamma}(Q)} = b_j \frac{\overline{\gamma}(Q_0^j)}{\overline{\gamma}(Q)} \simeq b_j\,, \quad (11)$$

and then solve the originally stated problem in Eq. (6). It can be verified in fact that the ratio $\frac{\overline{\gamma}(Q_0^j)}{\overline{\gamma}(Q)}$, in the whole studied area, differs from 1 by at most one part per thousand.

Note that the normal gravity, $\gamma(Q)$, and the average normal gravity, $\overline{\gamma}(Q)$, are evaluated according to Heiskanen and Moritz (1967), by using the parameters of the GRS80 ellipsoid but disregarding its orientation in space, whose effects are negligible for our purposes. Normal heights to compute such gravity values are initially set equal to the REDNAP orthometric heights and they are iteratively computed once the normal heights are derived from geopotential numbers.

4.3 GNSS/Levelling Data Selection

A first data selection is performed by considering, among data labelled as 'observed', only those having an error standard deviation equal or smaller than 10 cm. After that, only 10% of the remaining data for continental Spain are considered, including all the levelling network nodal points.

Table 2 Statistics of the differences between REDNAP GNSS heights and the ones transformed into ITRF2008, epoch 2011

Region	Number of data	Mean (cm)	Std (cm)	Min (cm)	Max (cm)
Balearic Islands	440	0.1	0.2	−0.1	0.6
Canary Islands	1236	0.9	0.1	0.5	1.2
Mainland	11,990	1.0	0.6	−0.2	2.4

Table 3 Number of observations before and after outlier removal and estimated biases with their standard deviations using GOCO-05S in combination either with EGM2008 or EIGEN-64C, or using GOCO-05S only

	Number of data		Bias $\pm\sigma$ (cm)		
Region	Before	After	EGM2008	EIGEN-6C4	GOCO-05S only
Balearic Islands					
Formentera	13	13	-83.80 ± 6.07	-83.47 ± 6.07	-32.31 ± 17.02
Ibiza	67	67	-68.47 ± 5.45	-68.09 ± 5.45	16.64 ± 15.94
Mallorca	280	280	-77.46 ± 3.37	-77.63 ± 3.37	-30.01 ± 15.66
Menorca	75	75	-101.68 ± 6.47	-101.48 ± 6.48	-52.37 ± 19.90
Canary Islands					
Tenerife	397	239	-39.76 ± 5.39	-42.49 ± 5.39	81.11 ± 29.19
Gran Canaria	189	172	-44.66 ± 7.03	-33.19 ± 7.04	165.87 ± 27.74
Fuerteventura	122	122	-28.66 ± 6.97	-21.07 ± 6.97	156.63 ± 31.69
Lanzarote	110	110	-46.91 ± 6.65	-42.85 ± 6.65	117.01 ± 23.10
La Palma	274	241	-16.44 ± 7.17	-6.66 ± 7.17	188.64 ± 34.32
La Gomera	76	75	-13.37 ± 5.69	-19.51 ± 5.69	146.96 ± 15.75
El Hierro	66	59	-41.71 ± 8.35	-25.87 ± 8.35	275.80 ± 24.02
Mainland	1231	1231	-88.84 ± 0.28	-88.84 ± 0.28	-96.29 ± 1.43
Total	2900	2684			

This data under-sampling allows to reduce the dimension of the covariance matrix of the global model errors, and therefore the computational burden implied by its manipulation. Moreover, since the strong correlation between levelling-derived height values is not accounted for in the error stochastic model of Eq. (7), this data under-sampling prevents an unrealistic increase of the estimated bias accuracies.

4.4 Observation Equation Writing and Testing

The prediction of the anomalous potential is performed by using a combination of GOCO-05S and either EGM2008 or EIGEN-6C4 global models, as discussed in Sect. 3.2. The error covariance matrices (cf. Eq. 7) are then derived. The set of differences between GNSS and normal heights is assumed to have an uncorrelated noise with 10 cm standard deviation. The error covariance matrix for the set of potential values predicted from GOCO-05S is obtained by propagation from the order-wise block-diagonal error covariance matrix of the spherical harmonic coefficients; this is definitely the heaviest activity, in terms of computational burden, which is performed in this work. The error covariance matrix of the set of potential values predicted from EGM2008 is obtained by propagation from the error variances of the spherical harmonic coefficients above degree 280, rescaling the resulting variances of the potential values consistently with the available grid of geoid error estimates (Gilardoni et al. 2013). As for the set of potential values predicted from EIGEN-6C4, the same error covariance matrix of EGM2008 is used.

Before performing the estimate of the different biases, an assessment of the observation equation model is performed. By using the observations of one patch at time, a single bias parameter is determined by least squares adjustment, according to Eq. (6). A χ^2 test is therefore done at a significance level of 5%, to verify the null hypothesis $H_0 : \sigma_0^2 = 1$ (Koch 1987). The test is used within a data-snooping technique (Baarda 1968) to remove the observations in Eq. (6) showing the highest estimated residuals. The number of removed outliers in the different patches is reported in Table 3. Almost 200 observations are removed from the Canary Islands; this might be ascribed to the islands topography and to the omission error in the high resolution global model, which is here EGM2008.

5 Data Analysis and Results

Biases between the 12 regional height systems of Spain are estimated with an accuracy ranging from few millimetres to around 8 cm. The results are reported in Table 3. The number of observations per region, the size of the region with respect to the global model resolution and the approximations in the error covariance structure are the main limiting factor. In this respect, the availability of the covariance model for the levelling observations would impact on the result, correctly accounting for the high number of observations in small regions. A residual terrain correction in terms of height anomalies would further improve the result.

The residuals of the least squares adjustment are shown in Fig. 1. As one can see, they are well distributed without any systematical behaviour, differently from the result obtained for the Italian case (Barzaghi et al. 2015).

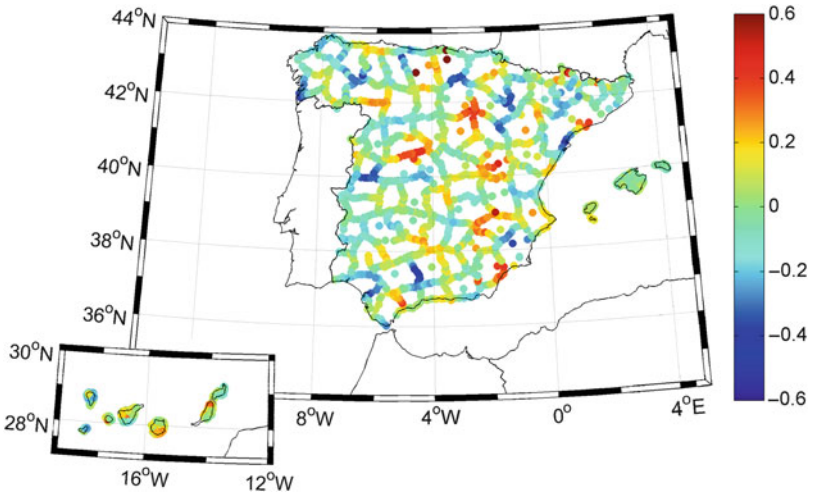

Fig. 1 Estimated residuals in meters of the least squares adjustment

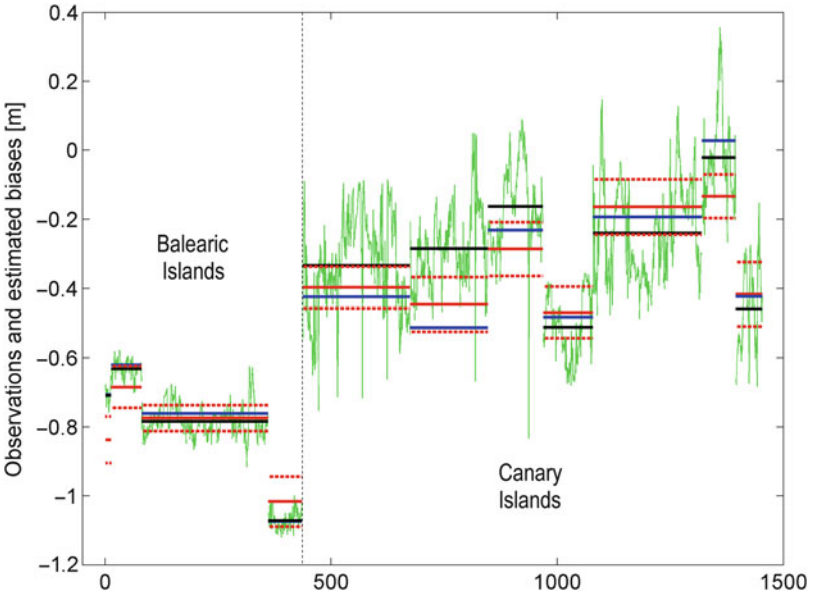

Fig. 2 Observations used for bias estimation in the Balearic and Canary Islands (*green*). Biases are estimated by observation arithmetic average (*black*), separate least squares adjustment per region (*blue*) and joint least squares adjustment (*red*). In the latter case the $\pm\sigma$ interval is shown (*red dashed lines*). As for the continental Spain the three estimates are statistically equivalent

By replacing EGM2008 with EIGEN-6C4, a statistically non significant variation in the biases estimation is found. The variation is anyway larger for the Canary than the Balearic Islands and completely negligible for the continental Spain (see Table 3). This result is mainly due to the high correlation between the two models in the spectral band above degree 280, as they are derived from almost the same datasets. On the other hand, the use of GOCO-05S only, by stochastically modelling the high frequency signal as omission error, proves to be too poor (see Table 3).

A final comment is worth about the importance of the covariance modelling. In Fig. 2 the observations as in Eq. (6) are plotted, grouped by regions. If they were considered as independent with the same error variance, each estimated bias would be independent from any other and would be equal to the arithmetic average of the corresponding observations. When introducing the error covariance of the used global models, one could decide to estimate each bias separately by a proper weighted average of the region observations or jointly by putting all the available observations into a unique system. Depending on this choice, the estimated biases are different (see Fig. 2). It is quite obvious that the better is the covariance modelling and the higher is the number of the considered regions, the more consistent and robust is the solution of the height datum problem. In other words, the availability of a large dataset in a certain region can be exploited to improve the bias estimate of another region thanks to the global model error correlation, which therefore plays an important role in the proposed solution.

6 Conclusions

The unification of the Spanish height system was performed by exploiting the REDNAP project data and a suitable combination of satellite-only and high resolution global

gravity models. The bias estimation was carried out by a least squares adjustment, caring about the modelling of the observation error covariance matrix. In general the obtained results prove the feasibility of the proposed approach and in particular they show the possibility of setting a unique Spanish height system with sub-decimeter accuracy.

Acknowledgements The authors would like to thank Dr. J. M. Brockmann for providing us the error covariance matrix of the GOCO-05S model in MATLAB format. This research has been funded by the University of Jaén by means of the project with reference UJA2016/08/14.

References

Baarda W (1968) A testing procedure for use in geodetic networks. Publications on Geodesy, vol 2, Issue 5. Netherlands Geodetic Commission, Delft, The Netherlands

Barzaghi R, Carrion D, Reguzzoni M, Venuti G (2015) A feasibility study on the unification of the Italian height systems using GNSS-leveling data and global satellite gravity models. In: International Association of Geodesy Symposia, vol 143, pp 281–288

Betti B, Carrion D, Sacerdote F, Venuti G (2015) The observation equation of spirit leveling in Molodensky's context. In: International Association of Geodesy Symposia, vol 142, pp 213–219

Brockmann JM, Zehentner N, Höck E, Pail R, Loth I, Mayer-Gürr T, Schuh W-D (2014) EGM_TIM_RL05: an independent geoid with centimeter accuracy purely based on the GOCE mission. Geophys Res Lett 41(22):pp 8089–8099

Förste C, Bruinsma SL, Abrikosov O, Lemoine JM, Schaller T, Götze HJ, Ebbing J, Marty JC, Flechtner F, Balmino G, Biancale R (2014) EIGEN-6C4: the latest combined global gravity field model including GOCE data up to degree and order 2190 of GFZ Potsdam and GRGS Toulouse. In: 5th GOCE User Workshop, Paris, 25–28 November 2014

Gatti A, Reguzzoni M, Sansò F, Venuti G (2013) The height datum problem and the role of satellite gravity models. J Geod 87(1): 15–22

Gerlach C, Fecher T (2012) Approximations of the GOCE error variance-covariance matrix for least-squares estimation of height datum offsets. J Geod Sci 2(4):247–256

Gerlach C, Rummel R (2013) Global height system unification with GOCE: a simulation study on the indirect bias term in the GBVP approach. J Geod 87(1):57–67

Gilardoni M, Reguzzoni M, Sampietro D, Sansò F (2013) Combining EGM2008 with GOCE gravity models. Boll Geofis Teor Appl 54(4):285–302

Gilardoni M, Reguzzoni M, Sampietro D (2016) GECO: a global gravity model by locally combining GOCE data and EGM2008. Stud Geophys Geod 60(2):228–247

Heiskanen WA, Moritz H (1967) Physical geodesy. W.H. Freeman, San Francisco

Ihde J, Barzaghi R, Marti U, Sánchez L, Sideris M, Drewes H, Förste C, Gruber T, Liebsch G, Pail R (2015) Report of the Ad-hoc Group on an International Height Reference System (IHRS). In: Drewes H, Hornik H (Eds.) Travaux de l'AIG 39, IAG Reports 2011–2015

Koch KR (1987) Parameter estimation and hypothesis testing in linear models. Springer, Berlin-Heidelberg.

Kotsakis C, Katsambalos K, Ampatzidis D (2012) Estimation of the zero-height geopotential level W_0^{LVD} in a local vertical datum from the inversion of co-located GPS, leveling and geoid heights: a case study in the Hellenic islands. J Geod 86(6):423–439

Mayer-Gürr T, Zehentner N, Klinger B, Kvas A (2014) ITSG-Grace2014: a new GRACE gravity field release computed in Graz. In: GRACE Science Team Meeting (GSTM), Potsdam, 29 September 2014

Mayer-Gürr T, Pail R, Gruber T, Fecher T, Rexer M, Schuh W-D, Kusche J, Brockmann JM, Rieser D, Zehentner N, Kvas A, Klinger B, Baur O, Höck E, Krauss S, Jäggi A (2015) The combined satellite gravity field model GOCO05s. Presentation at EGU 2015, Vienna, April 2015

Pavlis NA, Holmes SA, Kenyon SC, Factor JK (2012) The development and evaluation of the Earth Gravitational Model 2008 (EGM2008). J Geophys Res Solid Earth 117(B16):4406

Quirós R, Barbadillo A, Regidor J, Sanz M, Rodríguez E (2011) Regente Project. National Report of Spain. Euref 2011 Symposium, Dubrovnik, 15–20 May 2011

Rülke A, Liebsch G, Sacher M, Schäfer U, Schirmer U, Ihde J (2012) Unification of European height system realizations. J Geod Sci 2(4):343–354

Rülke A, Liebsch G, Sacher M, Schäfer U, Ihde J, Woodworth PL (2015) Practical aspects of the unification of height system realizations in Europe. In: International Association of Geodesy Symposia, vol 143, pp 367–373

Rummel R (2012) Height unification using GOCE. J Geod Sci 2(4):355–362

Rummel R, Teunissen P (1988) Height datum definition, height datum connection and the role of the geodetic boundary value problem. Bull Géod 62(4):477–498

Sideris MG, Rangelova E, Amjadiparvar B (2014) First results on height system unification in North America using GOCE. In: International Association of Geodesy Symposia, vol 141, pp 221–227

Comparison of Different Approaches to Gravity Determination and Their Utilization for Calculation of Geopotential Numbers in the Slovak National Levelling Network

Miroslava Majkráková, Juraj Papčo, Pavol Zahorec, Branislav Droščák, and Ján Mikuška

Abstract

Vertical reference system in the Slovak Republic is realized by the first and second order of the National levelling network with the normal heights according to Molodenski. The reference heights are still calculated by the traditional method using the components of gravity correction. Nowadays we are preparing a new realization of the height system which will be based on geopotential numbers. But there is a problem with the absence of the measured gravity values. Only at approximately 8% of levelling points we have the measured values of gravity. Therefore, we are trying to find the most reliable method for estimation of the gravity values and use them subsequently for determination of the geopotential numbers. The aim of this study is to analyze the different ways to the gravity determination and their application for calculation of the geopotential numbers on the points of the National levelling network. The first method is based on the reconstruction of the gravity on levelling points from the interpolated values of the complete Bouguer anomaly using the proprietary software. The second method is based on the modern global geopotential models improved by the residual terrain model approach. Calculated gravity was compared with directly measured gravity. The set of the points contained all geodetic control points within Slovakia where the gravity has been measured. Then, the calculated value of gravity was used to determine the geopotential numbers and normal heights according to Molodenski in the first order levelling lines of the National levelling network which connect the reference points determined within EVRF2007 adjustment for area of Slovakia.

Keywords

Geopotential numbers • Gravity prediction approaches • Slovak national levelling network

1 Introduction

Vertical reference system in the Slovak Republic is realized by points of the National levelling network (NLN) with the normal heights according to Molodenski in the system Baltic after adjustment. Currently, the basic frame of the NLN consists of the first order levelling lines which were

M. Majkráková (✉) • J. Papčo
Department of Theoretical Geodesy, Slovak University of Technology Bratislava, Bratislava, Slovakia
e-mail: miroslava.majkrakova@stuba.sk

P. Zahorec
Slovak Academy of Sciences, Earth Science Institute, Banská Bystrica, Slovakia
e-mail: pavol.zahorec@savbb.sk

B. Droščák
Geodetic Controls Division, Geodetic and Cartographic Institute Bratislava, Bratislava, Slovakia
e-mail: branislav.droscak@skgeodesy.sk

J. Mikuška
G-trend, Ltd., Bratislava, Slovakia
e-mail: jmikuska@gtrend.sk

G. S. Vergos et al. (eds.), *International Symposium on Gravity, Geoid and Height Systems 2016*, International Association of Geodesy Symposia 148, DOI 10.1007/1345_2017_20

designed as closed polygons with the length of approx. 280 km. It contains approximately 11,000 points and represents 3787 km of the levelling lines. There are levelling lines of the second order embedded into the first order areas with over 24,000 points which represents 9590 km of the levelling lines (Hudec and Ferianc 2007). The levelling lines of the NLN are located in the rugged terrain where the heights are in the range of 90 to 2700 m (Fig. 1).

The reference normal heights according to Molodenski theory in NLN are still calculated by the original historical method using the gravity correction. The calculation of the gravity correction is based on the historical development of the Czechoslovak levelling networks in accordance with Burša (1956) and Kruis (1957). Before that, the normal orthometric heights was the reference for Czechoslovakia, i.e. levelled differences between two benchmarks was corrected by so-called "the normal orthometric correction" O_γ (Burša 1956) which was modified for the territory of Czechoslovakia (mean latitude $\varphi_m = 49°23'$) with using parameters of previously ellipsoid ($\beta = 0.00265$):

$$O_\gamma = -2\beta H_m \sin 2\varphi_m \Delta\varphi \doteq -0.0000254 H_m \Delta\varphi'', \quad (1)$$

where H_m is the mean levelled height of the levelling line and $\Delta\varphi$ is the latitude difference between two benchmarks. For transformation to the system of the normal heights according to Molodenski it was derived so-called "the transfer correction" q:

$$q = \frac{1}{\overline{\gamma}} (g - \gamma)_m h, \quad (2)$$

where $\overline{\gamma}$ is the normal gravity for the mean latitude of the levelling line (according to Helmert), h is the levelled difference between two benchmarks and the term $(g - \gamma)_m$ is the mean free air anomaly between them computed by the interpolated value of the complete Bouguer anomaly. Then, the gravity correction is sum of the both terms (Burša 1956). The complete Bouguer anomaly value used for calculation of the gravity correction is interpolated from the original gravimetric map which is resulting of the gravity survey 1:25,000 in the Slovak realization of the Potsdam gravimetric system S-Gr64. The data are affected by the error of the reference level of the Potsdam gravity system i.e. 13.8 mGal and by the error of the data themselves. The value of the normal gravity was calculated by the Helmert formula. For these reasons the calculation of the normal heights according to Molodenski in the NLN needs some actualization (using the currently valid gravimetric system S-Gr95 and the ellipsoid GRS-80 for the normal gravity field). Moreover, the Slovak Republic has participated in the project EVRS (before UELN) and its realizations since 1994. The Slovak Republic contributed to the actual realization EVRF2007 with geopotential differences of the first order of the NLN, where the gravity data were interpolated from the mentioned original gravity maps. Nowadays we are preparing a new realization of the height system and it will be based on the geopotential numbers. There is a problem with the absence of the measured gravity values. We have the measured values of gravity only at approximately 8% of points in the NLN. Therefore, the aim of our study is to analyze the different ways to the gravity determination and their application for calculation of the geopotential numbers on the first order points of the NLN. The first method is based on the reconstruction of the gravity on levelling points from the interpolated values of the complete Bouguer anomaly using the CBA2G_SK software (Marušiak et al. 2015). The second method is based on the modern global geopotential models (GGM), e.g. EIGEN6C4 (Förste et al. 2015) and GOCO05c (Fecher et al. 2017), improved by the residual terrain model (RTM) approach (Fig. 1).

2 Comparison of Different Methods for the Gravity Calculation

In this article, following methods for the calculation of the gravity values were compared:

- using the interpolated value of the complete Bouguer anomaly, software CBA2G_SK
- using the available GGMs (EIGEN-6C4, GOCO05c)
- using the available GGMs with the effect of RTM

For this testing we selected all of the first order levelling points with measured gravity (964 points). Furthermore, it is necessary to say that the test points were not used in the computation of the complete Bouguer anomaly grid (Fig. 2).

2.1 Gravity Determination from the Interpolated Value of Complete Bouguer Anomaly

For this purpose we used the CBA2G_SK software which is designed for the gravity recalculation from the bilinear interpolated value of the complete Bouguer anomaly. The input data to the software CBA2G_SK contain coordinates and levelling heights in the system Baltic after adjustment, the grid of complete Bouguer anomaly and the digital elevation models (DEMs) for calculation of the terrain corrections. The output file contains the terrain corrections, interpolated value of the complete Bouguer anomaly and the calculated gravity value (Marušiak et al. 2015). For our experiment the new grid of complete Bouguer anomaly created on the basis of the gravity survey 1:25,000 (1956–1993) (Grand et al. 2001) was used. The old reprocessed data were supplemented by the detailed gravity measurements within the APVV-0194-10

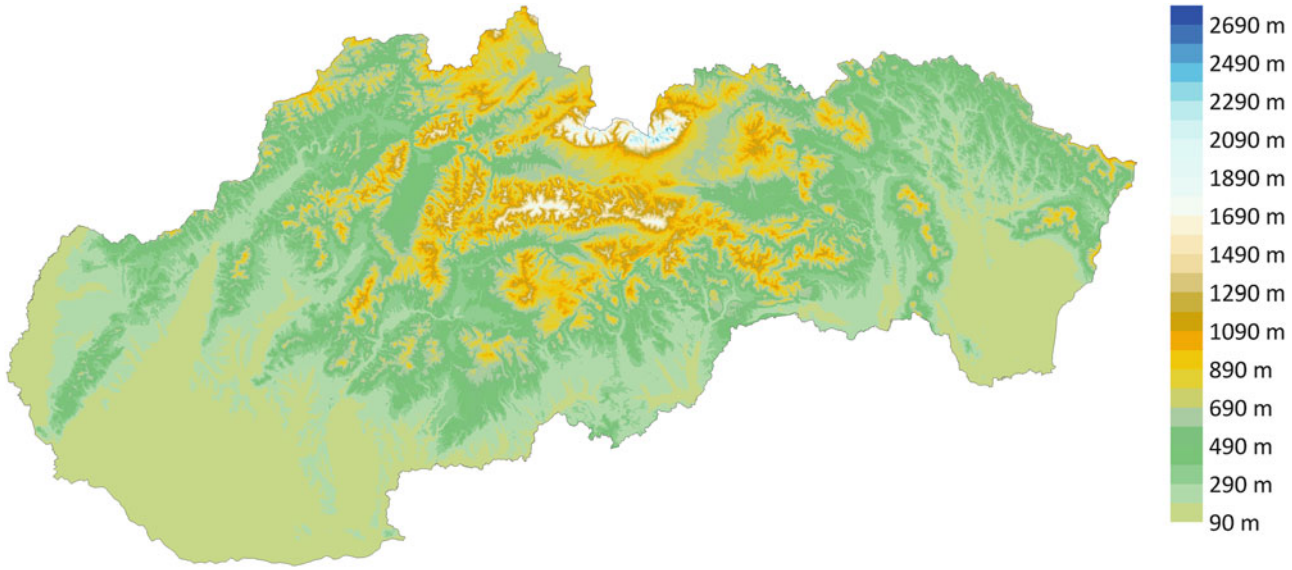

Fig. 1 Interpretation of the topography over the Slovak Republic based on the SRTM-3 (Reuter et al. 2007)

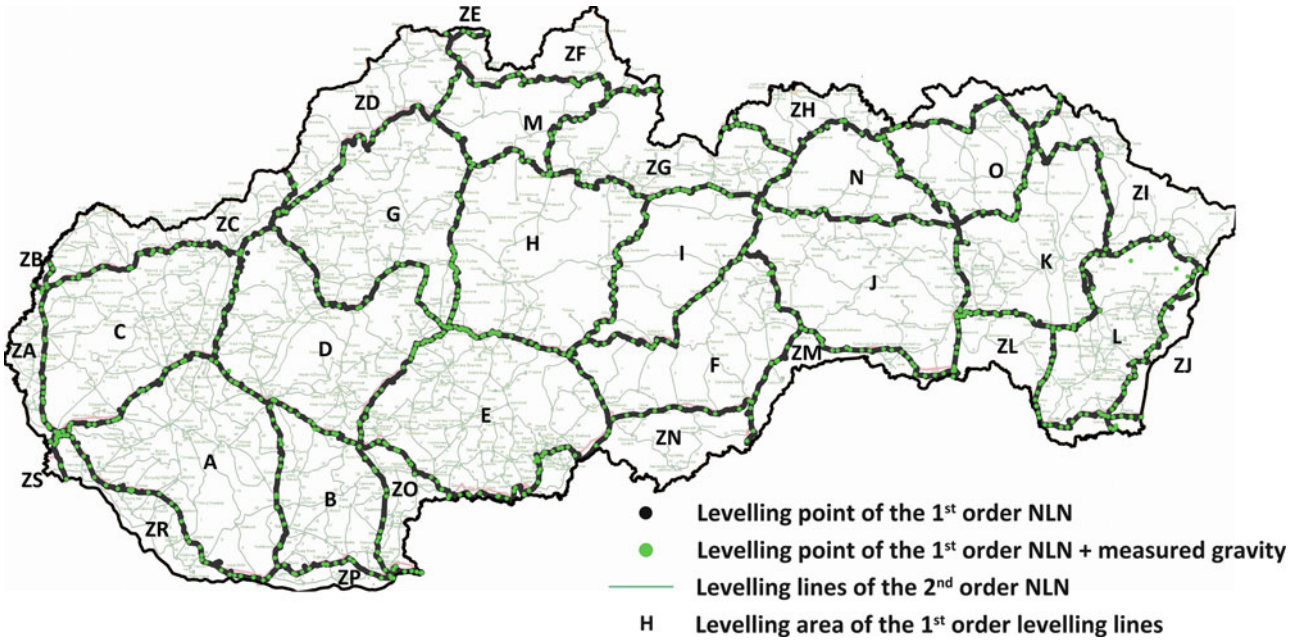

Fig. 2 Levelling lines of the Slovak national levelling network

project "Bouguer Anomalies of New Generation and Gravimetrical Model of Western Carpathians". The database now contains more than 319,000 gravimetric points in the territory of the Slovak Republic (Zahorec et al. 2017a). The terrain corrections were calculated using the software Toposk which was developed in order to recalculate the terrain corrections of the actual Slovak gravity database. The program primarily calculates the gravitational effect of the topographic masses using 3D polyhedral and/or segment method (Zahorec et al. 2017b). The terrain corrections was computed with the most recent DEMs in the calculation zones:

- zone T1: 0–250 m—DMR3 (Topographic Institute 2012)
- zone T2: 250–5240 m—DMR3-30 (Topographic Institute 2012)
- zone T31: 5240–28,800 m—SRTM-3 (Reuter et al. 2007)
- zone T32: 28,800–166,735 m—SRTM-30 (Reuter et al. 2007)

Finally, the complete Bouguer anomaly was defined by following formula:

$$CBA = g - \gamma_0 - \delta g_{faa} - \delta g_{sph.}^{0-166.7\,\mathrm{km}} + \delta g_{atm} + \delta g_{top.}^{0-166.7\,\mathrm{km}}, \quad (3)$$

where g is the measured gravity, γ_0 is the normal gravity on the reference ellipsoid GRS-80 calculated by the Somigliana formula (Moritz 1984), δg_{faa} is the free-air correction calculated using two degrees of the Taylor polynomial (Torge 1989), $\delta g_{sph.}^{0-166.7\text{km}}$ is the gravitational effect of truncated spherical layer up to the distance of 166.7 km with parameters of the GRS-80, δg_{atm} is the atmospheric correction which was modified for the territory of Slovakia including the allowing for topography (Mikuška et al. 2008). Resolution of the complete Bouguer anomaly grid is 100 m. The test on the independent set of the State gravimetric points show the small differences between the measured and calculated gravity (maximum about ±1 mGal). This result approves the very good quality of the new complete Bouguer anomaly grid and also the accuracy of the new software algorithm (Zahorec et al. 2017a).

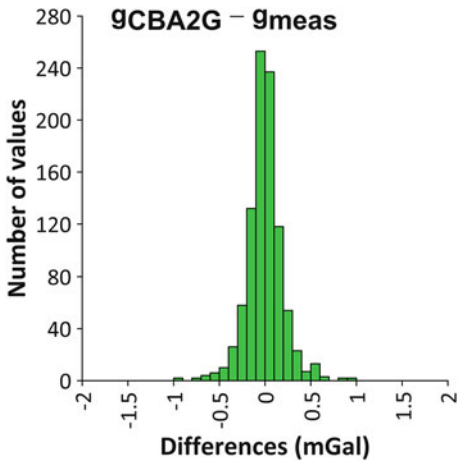

Fig. 3 Histogram of the differences between the directly measured gravity and the gravity calculated by the CBA2G_SK software

Calculated gravity in the our experiment was subsequently compared with the directly measured gravity. The differences are in the interval from −1.34 to 7.20 mGal. The most of the differences (99%) fall within to the interval ±1 mGal, see Figs. 3 and 4 and Table 1. The analysis indicates a good quality of the new complete Bouguer anomaly map. The standard deviation of the differences is 0.40 mGal.

Only nine points exceed the interval ±1 mGal. But, it is necessary to remind that the reliability of the gravity recalculated from complete Bouguer anomaly depends greatly on the accuracy of the point position. The position of the levelling points in the NLN is mostly interpolated from the original topographic maps with the accuracy of about 15–45 m (Bublavý and Droščák 2015). Nowadays, in the Geodetic and cartographic institute they are still working on the refinement of the levelling point locations, mostly by interpolation from the new vector cadaster map, completing by the original polygons measurements and also by direct measurements. Implementation of this levelling point positions, as expected, will improve the results from the comparison with the directly measured gravity.

Table 1 Statistic of the differences (mGal) between the directly measured gravity and the gravity calculated by the CBA2G_SK software

Number of values	964
Min	−1.342
Max	7.200
Mean	0.022
Stdev	0.402

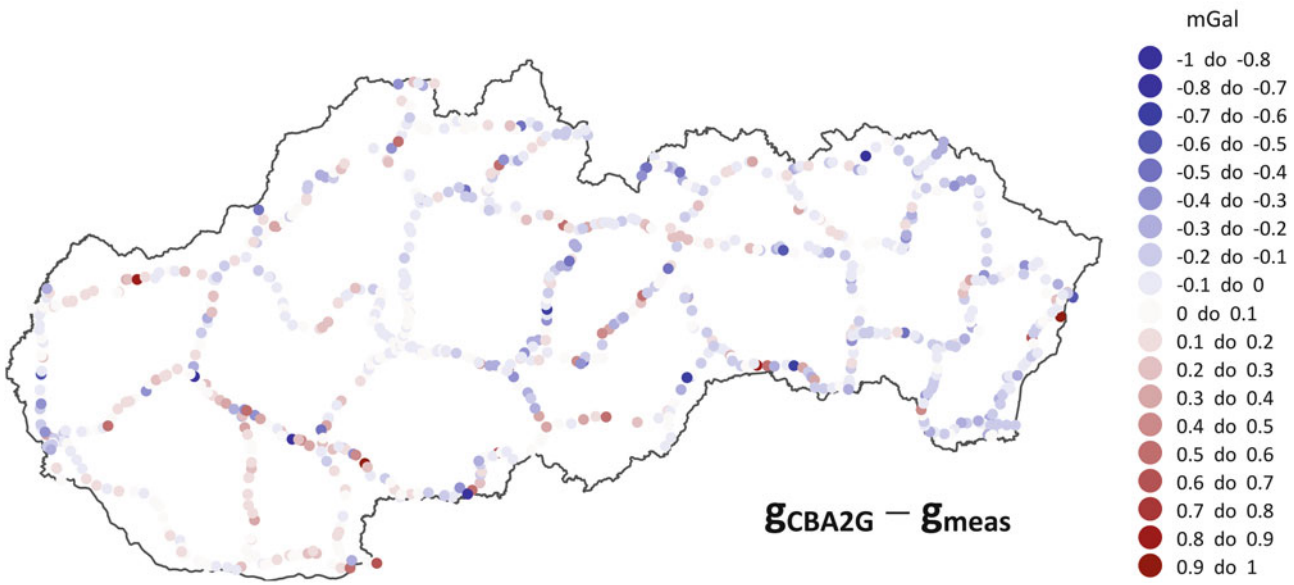

Fig. 4 Differences between the directly measured gravity and the gravity calculated by the CBA2G_SK software

2.2 Gravity Determination from GGM and GGM+RTM

For this purpose we used following GGMs:
- EIGEN 6C4 (up to d/o 2159)
- GOCO05c (up to d/o 720)
- GOCO05c (up to d/o 200)

For calculation of the gravity from mentioned GGMs we applied the GrafLab software which allows to compute various functionals of the geopotential up to ultra-high degree and orders of spherical harmonic expansion (Bucha and Janák 2013) and the gravitational effect of the RTM we calculated using the Toposk software. Output file includes the terrain corrections and the gravitational effect of the topographic masses (Near Topographic Effect—NTE) in the computing zones T1–T32. The gravity on the test points is finally determined by:

$$g_{GGM+RTM} = g_{GGM} - NTE^{DTM} + NTE^{DEM}, \qquad (4)$$

where NTE^{DTM} is a total gravitational effect of the topographic masses (0–166.7 km) calculated from the DTM2006.0 (Pavlis et al. 2012), NTE^{DEM} is a total gravitational effect of the topographic masses calculated from the detailed DEMs: zone T1: 0–250 m—DMR3, zone T2: 250–5240 m—DMR3-30; zone T31: 5240–28800 m—SRTM-3, zone T32: 28800–166735 m—SRTM-30.

The differences between the measured gravity and the gravity derived from different GGMs and GGMs with RTM are shown in Figs. 5 and 6. The method without using RTM (Fig. 5), especially for the GOCO05c, show the dependence on the terrain conditions, i.e. the greater differences are in

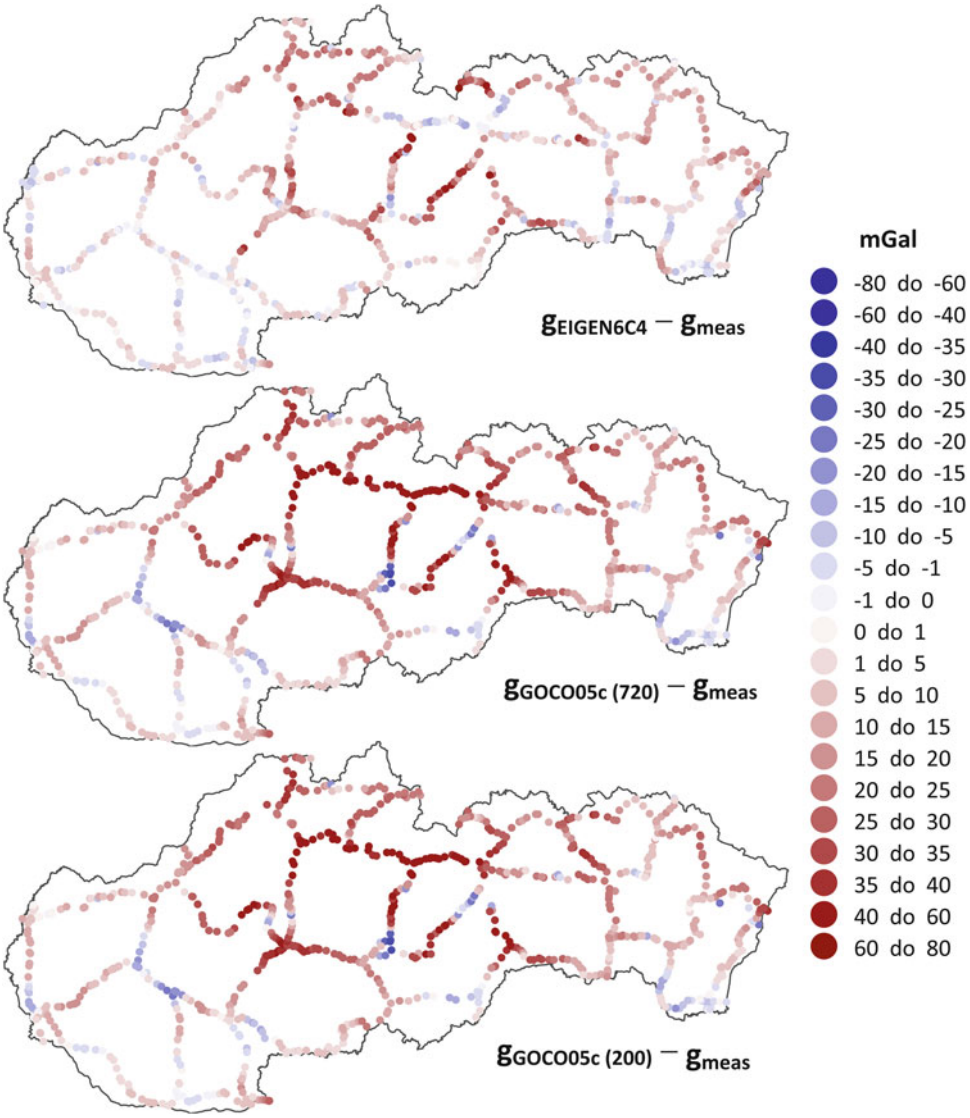

Fig. 5 Differences between the directly measured gravity and the gravity calculated from the different GGMs

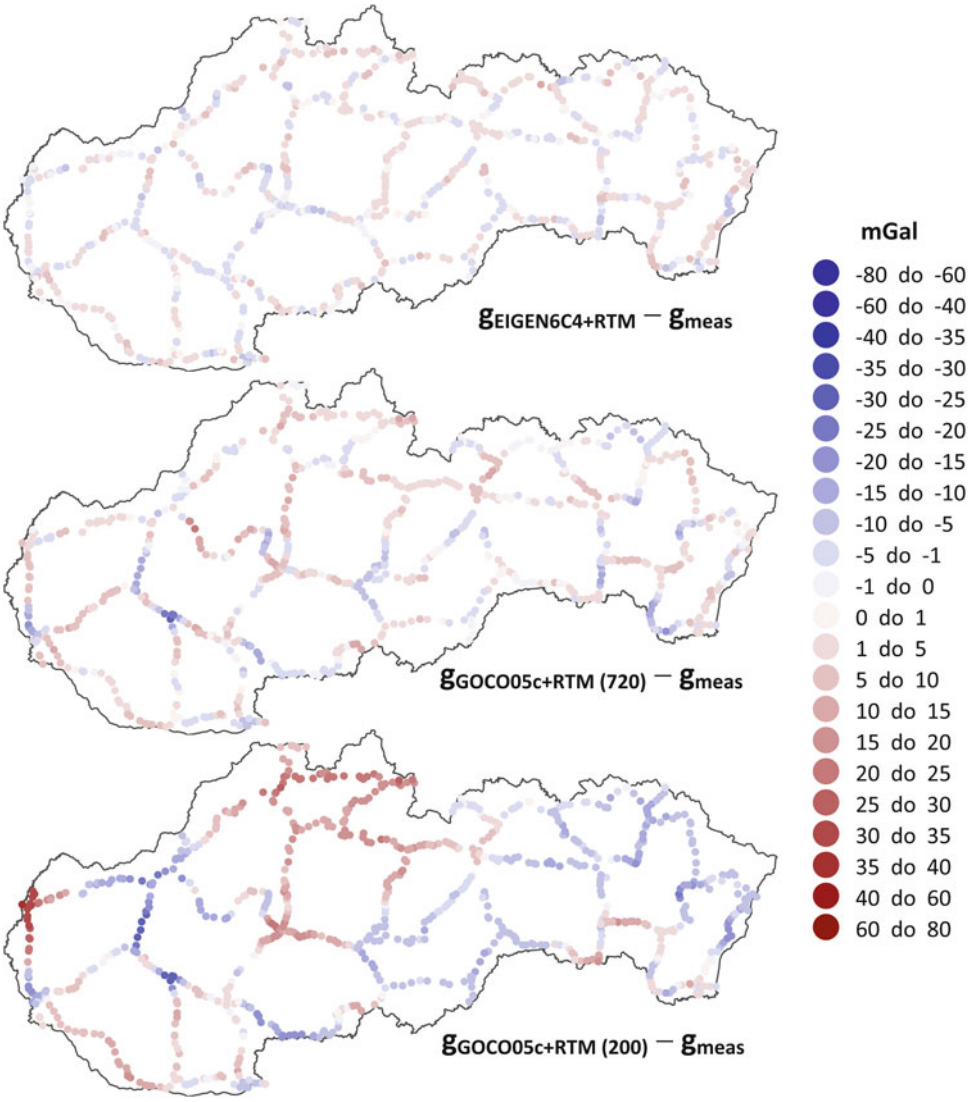

Fig. 6 Differences between the directly measured gravity and the gravity calculated from the different GGMs and RTM

the mountainous central part of Slovakia. Smaller differences are in the lowlands (the west and east part of Slovakia). The methods using GGMs and RTM (Fig. 6) lead to the smaller differences and the dependence is partially eliminated. Since the RTM effect is a function of the difference between the real height and specific DTM height at particular point, the distribution of the differences described in Table 2 and reproduces the mentioned height differences distribution within the territory. The elementary statistics of the gravity differences are shown in the next histograms. The histograms (g_{GGM} minus g_{meas}) show that most of the differences are in interval from −40 to 77 mGal (Fig. 7 and Table 2) and the best results were using EIGEN-6C4 (the standard deviation is 11.20 mGal). The histograms in Fig. 8 and the Table 3 present the differences $g_{GGM+RTM}$ minus g_{meas}. The minimum standard deviation was reached again using EIGEN-6C4 (3.45 mGal). Also, the mean value of the differences is close to zero. The good quality of the digital elevation models used for the RTM calculation contributes to the improvement of these results.

Table 2 Statistic of the gravity differences (mGal) between the directly measured gravity and the gravity calculated from the different GGMs

GGM	EIGEN-6C4	GOCO05c	GOCO05c
Maximal degree	2159	720	200
Number of values	964	964	964
Min	−15.306	−32.059	−39.894
Max	77.533	56.938	65.222
Mean	8.44	15.201	15.608
Stdev	11.204	16.008	19.157

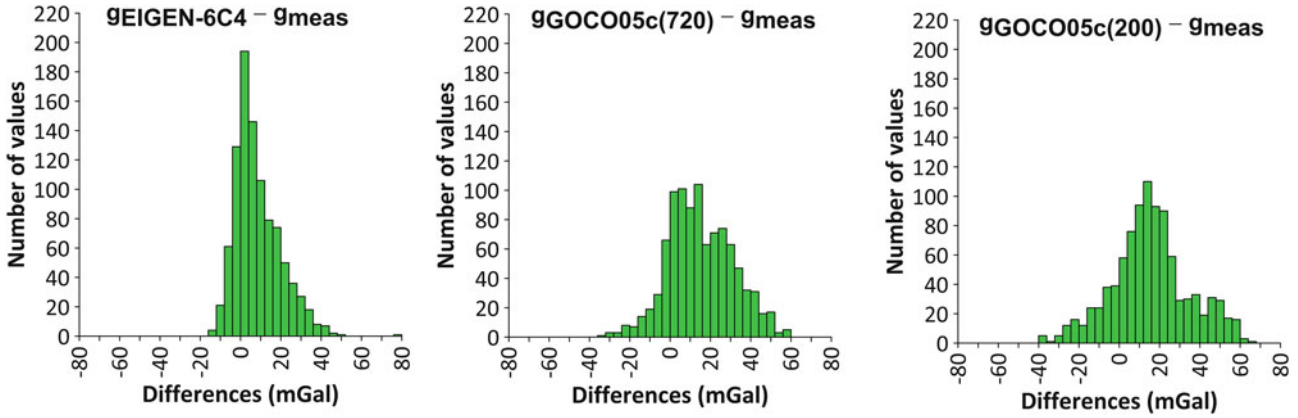

Fig. 7 Histograms of the gravity differences between the directly measured gravity and the gravity calculated from the different GGMs

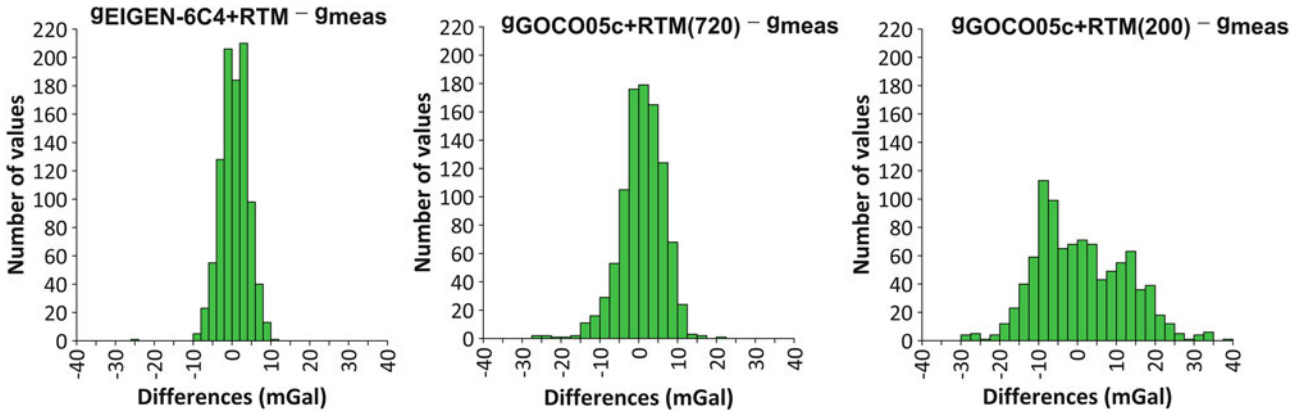

Fig. 8 Histograms of the gravity differences between the directly measured gravity and the gravity calculated from the different GGMs+RTM

Table 3 Statistic of the gravity differences (mGal) between the directly measured gravity and the gravity calculated from the different GGMs+RTM

GGM+RTM	EIGEN-6C4	GOCO05c	GOCO05c
Maximal degree	2159	720	200
Number of values	964	964	964
Min	−24.476	−25.684	−29.163
Max	10.035	21.894	38.787
Mean	0.633	0.922	0.962
Stdev	3.446	5.583	11.470

3 Determination of the Geopotential Numbers and Normal Heights According to Molodenski

The principle of the calculation of the geopotential numbers is based on the combination of the levelling and gravimetry along the levelling lines. The potential differences $W_B - W_A$ (or the geopotential differences ΔC_{AB}) can be calculated in accordance with (Hofmann-Wellenhof and Moritz 2005):

$$W_B - W_A = \Delta C_{AB} = -\int_A^B g dn \doteq \sum_A^B g\delta n, \qquad (5)$$

where g is gravity at the levelling station and δn is the levelling increment. It is assumed that the geopotential number of the reference point (the first point in the levelling line) is known. For this experiment we used all of the first order points NLN which belong also to the UELN. The geometric component of the geopotential numbers comes from very precise levelling measurement (Geodesy, Cartography and Cadastre Authority of The Slovak Republic 2006) which was realized from 1996 to 2002. As for the gravity (physical component) we used different values of the gravity calculated in the first part of the experiment. The process of calculation of the geopotential numbers and normal heights according to Molodenski is depicted step by step in the next scheme (Fig. 9).

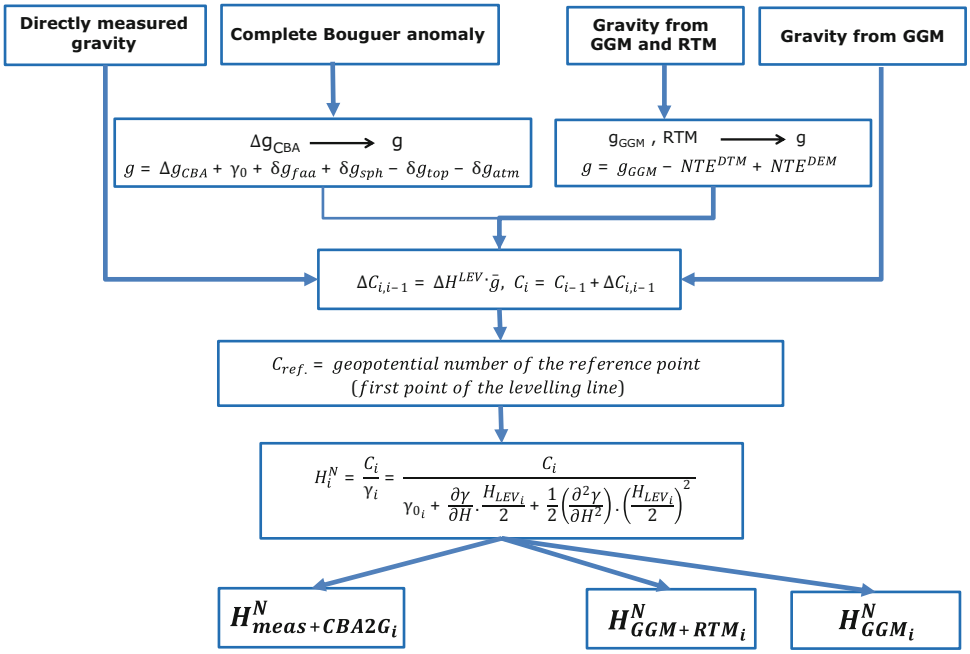

Fig. 9 Scheme of the normal Molodenski heights calculation

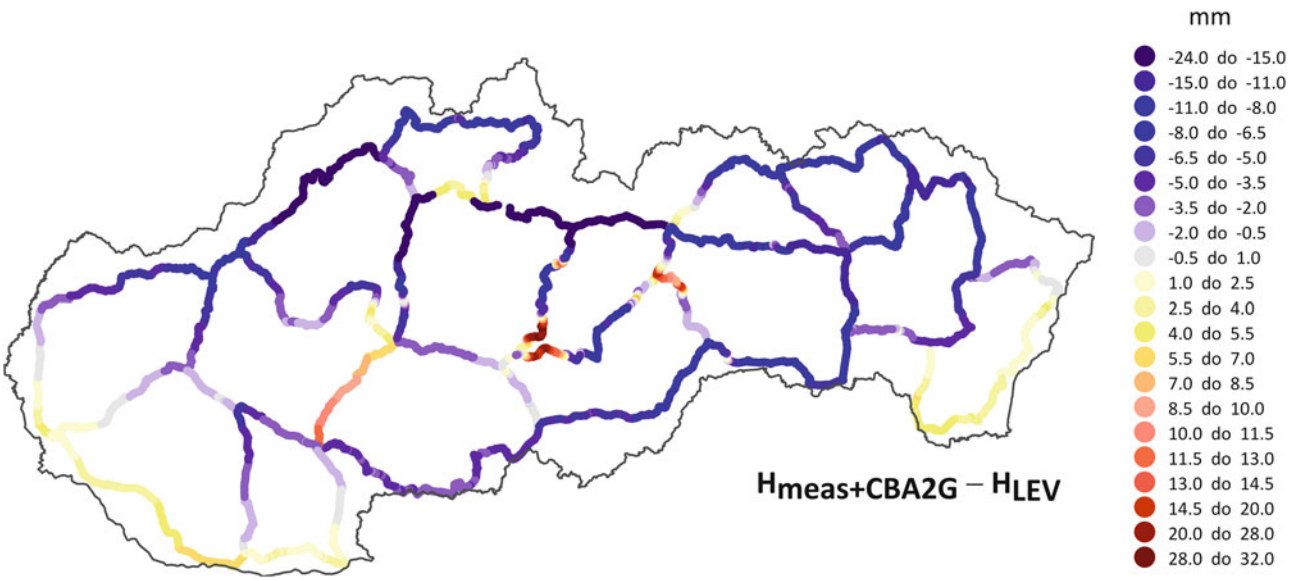

Fig. 10 Differences between the normal heights according to Molodenski $H_{meas+CBA2G}$ and the levelling heights H_{LEV}

Overall there are three types of heights which were based on precise levelling in combination with different ways of estimation of the gravity values:

- $H_{meas+CBA2G}$—directly measured gravity supplemented with the gravity estimated from the gravity map by the CBA2G_SK software
- H_{GGM}—gravity coming from the GGMs
  - $H_{EIGEN6C4}$, $H_{GOCO05c(720)}$, $H_{GOCO05c(200)}$
- $H_{GGM+RTM}$—gravity coming from the GGMs with the gravitational effect of the RTM
  - $H_{EIGEN6C4+RTM}$, $H_{GOCO05c+RTM(720)}$, $H_{GOCO05c+RTM(200)}$

The most reliable gravity value is, of course, the directly measured gravity. But, we do not have measured value on the all of the levelling points. Therefore we used the heights derived from the directly measured gravity and the gravity calculated by the best calculation method (g_{CBA2G}) as the comparison etalon. In the first map (Fig. 10) are shown the differences between heights $H_{meas+CBA2G}$ and the levelling heights H_{LEV}. The differences are in the range from −24

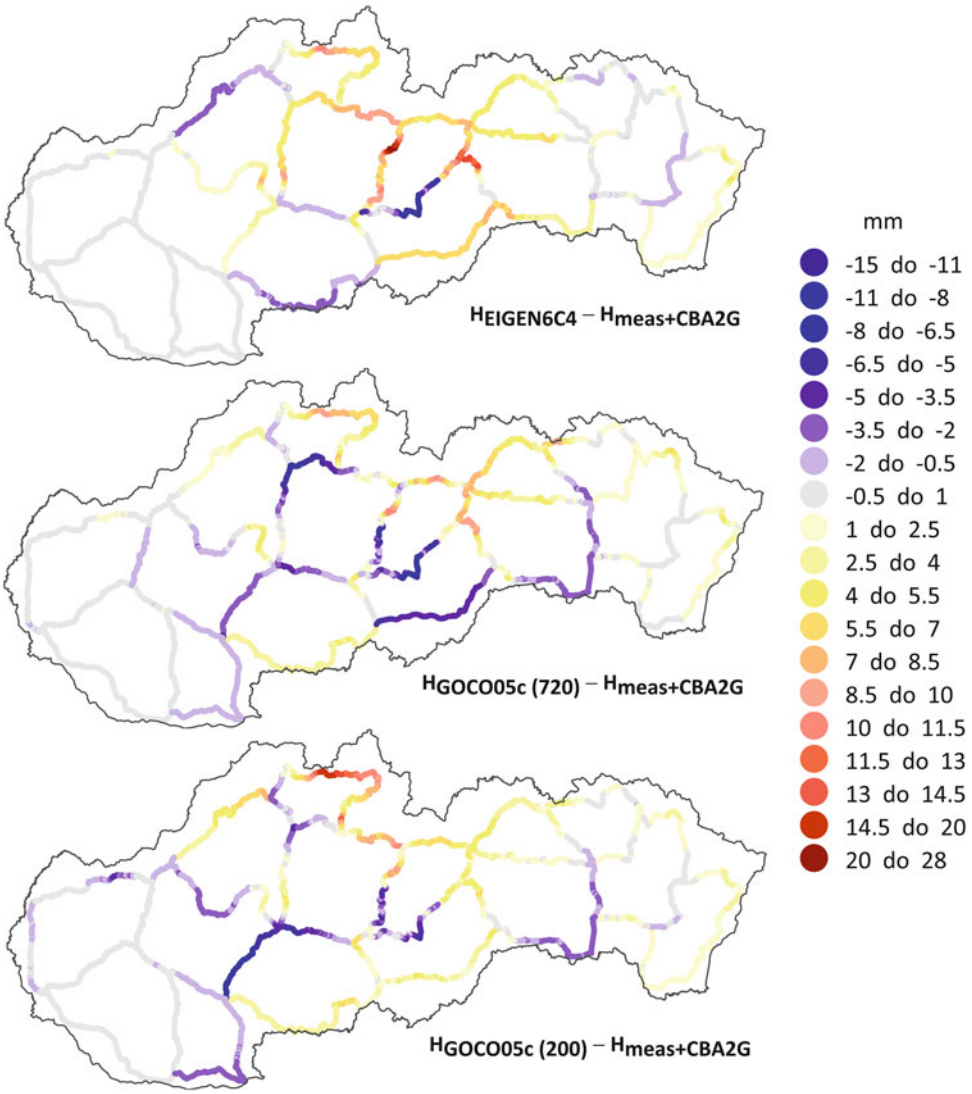

Fig. 11 Differences between the normal heights according to Molodenski H_{GGM} and $H_{meas+CBA2G}$

to 32 mm and they represent the contribution of the gravity field to the levelling heights. The differences between the normal Molodenski heights (H_{GGM}, $H_{GGM+RTM}$ minus $H_{meas+CBA2G}$) are in the range from −15 to 28 mm (Figs. 11 and 12). The smallest differences we reached using EIGEN-6C4 (d/o 2159) and these differences have reduced significantly after using RTM. The partial correlation with the topography conditions of the territory of Slovakia appear. The correlation is not evident with adding the RTM effect to the GGMs.

4 Conclusions

The aim of this study was to test alternative ways of determination of the gravity values and their application to the geopotential numbers and normal heights according to Molodenski calculation in the Slovak NLN on the points where the measured gravity is not available. The set of the testing points contains the first order points NLN with measured gravity, 964 levelling points. We have tested three independent approaches to the gravity estimation, namely the recalculation from the complete Bouguer anomaly using the CBA2G_SK software using the interpolated value of the complete Bouguer anomaly, the calculation using the GGMs (EIGEN6C4, GOCO05c to maximal degree 720 and 200, respectively) and GGMs corrected by the RTM.

– Directly measured gravity: the most reliable method to calculate the geopotential numbers, but this value is missing on the most of the Slovak levelling points. Only about 8% of all levelling points in the Slovak NLN have measured gravity.
– Gravity recalculated by the CBA2G_SK: minimum differences in comparison with the directly measured gravity. The most of these differences (99%) were in the interval ±1 mGal. This fact indicates good quality of the new

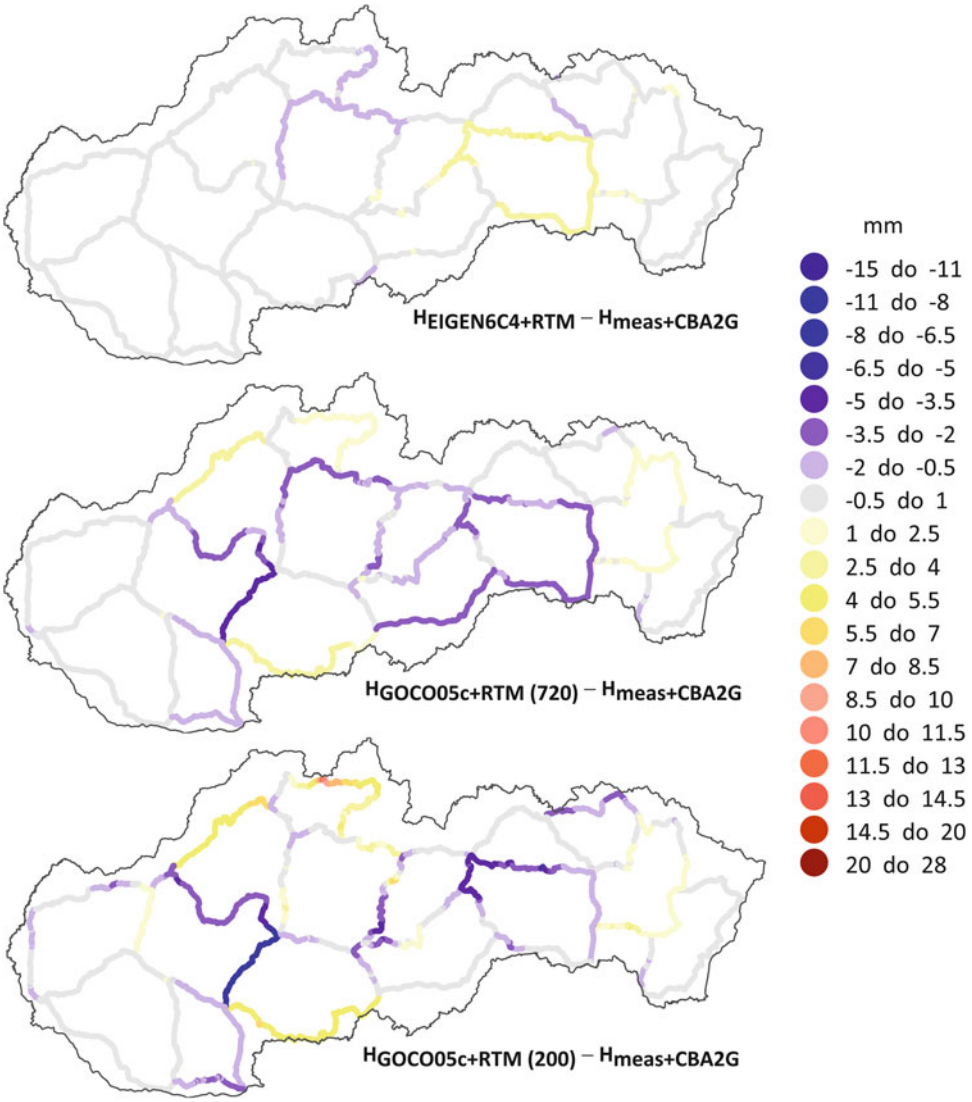

Fig. 12 Differences between the normal heights according to Molodenski $H_{GGM+RTM}$ and $H_{meas+CBA2G}$

Bouguer anomaly map. The accuracy depends also on the accuracy of the point location.

– Method with GGM and RTM: larger differences; the accuracy of the results depends on the accuracy of the using GGM model, on the quality of the point location and also on the quality of the used digital elevation model, i.e. DMR-3. These results clearly prove the improvement resulting from using the RTM. The smallest differences were achieved using EIGEN6C4 to maximal degree 2159.

The important factor for the gravity calculation is the accuracy of the levelling point location. The position of the levelling points in the Slovak national levelling network is mostly interpolated from the topographic maps with the accuracy at the level of ten of meters (Bublavý and Droščák 2015). Subsequently, we can use the estimated gravity values to the calculation of the geopotential numbers and normal heights according to Molodenski in the Slovak National levelling network, which will be used for the adjustment in the new realization of the NLN.

Acknowledgements This work was supported by the Slovak research and development agency APVV (grants No. APVV-0827-12 and APVV-0194-10) and the Slovak Grant Agency VEGA (grants No. 1/0714/15, 1/0954/15 and 1/0462/16).

References

Bublavý J, Droščák B (2015) First steps to the new realization of the height system in the Slovak Republic and the status of the quasi-geoids. Geodetic Control and Geodynamics Kočovce (in Slovak), Oct 6–7, 2015

Bucha B, Janák J (2013) A MATLAB-based graphical user interface program for computing functionals of the geopotential up to ultra-high degrees and orders. Comput Geosci 56:186–196. http://dx.doi.org/10.1016/j.cageo.2013.03.012

Burša M (1956) The transformation theory of the Czechoslovak levelling control to the system of the normal heights. Research report No. 37, VÚGTK, Praha (in Czech)

Fecher T, Pail R, Gruber T (2017) The GOCO consortium: GOCO05c: a new combined gravity field model based on full normal equations and regionally varying weighting. Surv Geophys 38:571. doi:10.1007/s10712-016-9406-y

Förste C, Bruinsma SL, Abrikosov O, Lemoine J-M, Schaller T, Götze H-J, Ebbing J, Marty JC, Flechtner F, Balmino G, Biancale R (2015) EIGEN-6C4. The latest combined global gravity field model including GOCE data up to degree and order 2190 of GFZ Potsdam and GRGS Toulouse. http://dx.doi.org/10.5880/icgem.2015.1

Geodesy, Cartography and Cadastre Authority of the Slovak Republic (2006) Guideline for Management of the Geodetic Control. Standard, Bratislava (in Slovak)

Grand T, Šefara J, Pašteka R, Bielik M, Daniel S (2001) Atlas of geophysical maps and profiles. Part D1: gravimetry. Final report. State Geological Institute, Bratislava, MS Geofond (in Slovak)

Hofmann-Wellenhof B, Moritz H (2005) Physical geodesy. Springer, New York

Hudec M, Ferianc D (2007) The Slovak national levelling network. In: Geodetic networks and spatial information, Podbanské (in Slovak)

Kruis B (1957) Conversion of the 1st and 2nd order of the Czechoslovak united levelling network from the Adriatic height system to the system Baltic after adjustment. Research report No. 45, VÚGTK, Praha (in Czech)

Marušiak I, Mikuška J, Papčo J, Zahorec P, Pašteka R (2015) CBA2G_SK (Complete Bouguer Anomaly To Gravity), program for calculation of the gravity from complete Bouguer anomaly, program guide. Manuscript, G-trend Ltd. (in Slovak)

Mikuška J, Marušiak I, Pašteka R, Karcol R, Beňo J (2008) The effect of topography in calculating the atmospheric correction in gravimetry. SEG Las Vegas 2008 annual meeting, expanded abstract, 84–788

Moritz H (1984) Geodetic reference system 1980. Bull Géod 58:388–398. doi:10.1007/BF02519014

Pavlis NK, Factor JK, Holmes SA (2012) Terrain-related gravimetric quantities computed for the next EGM. In: Kilioglu A, Forsberg R (eds) Gravity field of the Earth: Proceedings of the 1st international symposium of the international gravity field service (IGFS), Special Issue 18. Gen. Command of Mapp. Ankara, pp 318–323 (2012)

Reuter HI, Nelson A, Jarvis A (2007) An evaluation of void filling interpolation methods for SRTM data. Int J Geogr Inform Sci 21(9):983–1008. http://dx.doi.org/10.1080/13658810601169899

Topographic Institute: Digital terrain model version 3 (DMR-3). [Online] http://www.topu.mil.sk/14971/digitalny-model-reliefu-urovne-3-%28dmr-3%29.php.2012

Torge W (1989) Gravimetry. De Gruyter, Berlin/New York

Zahorec P, Pašteka R, Mikuška J, Szalaiová V, Papčo J, Kušnirák D, Pánisová J, Krajňák M, Vajda P, Bielik M, Marušiak I (2017a) National gravimetric database of the Slovak republic. In: Pašteka R, Mikuška J, Meurers B (eds) Understanding the Bouguer anomaly: a gravimetry puzzle. Elsevier, Amsterdam, pp 113–125. ISBN 978-0-12-812913-5

Zahorec P, Marušiak I, Mikuška J, Pašteka R, Papčo J (2017b) Numerical calculation of terrain correction within the Bouguer anomaly evaluation (program toposk). In: Pašteka R, Mikuška J, Meurers B (eds) Understanding the Bouguer anomaly: a gravimetry puzzle. Elsevier, Amsterdam, pp 79–92. ISBN 978-0-12-812913-5

Assessment of the Greek Vertical Datum: A Case Study in Central Greece

V.N. Grigoriadis, E. Lambrou, G.S. Vergos, and I.N. Tziavos

Abstract

In this study, the consistency of the Greek Vertical Datum (GVD) is examined, focusing on an area in central Greece and following similar efforts made in previous researches for the establishment of an International Height Reference System (IHRS). High precision GNSS measurements are available at trigonometric benchmarks located along the Gulf of Corinth, with benchmarks residing on both coasts along. First, the zero-level geopotential value (W_o^{LVD}) for the two areas, north and south coast, is determined, based on the classical Helmert theory using GNSS/leveling data and surface geopotential values derived from GOCE-based global geopotential models (GO-DIR-R5, GO-TIM-R5, GOCO05s and GECO) and EGM08. Then, the relative offset between the two areas is estimated while subsets of the computed benchmark values are also examined. Significant inconsistencies are detected that depend on the choice of benchmarks used in the computations. Moreover, a per benchmark analysis showed that the inconsistencies present a random spatial distribution and are attributed mainly to the orthometric height values of the benchmarks. Furthermore, the local W_o^{LVD} estimates are compared with previous results related to the GVD and the VD of the Greek islands and the corresponding value adopted by the IHRS. Finally, some remarks are drawn on the feasibility of the unification of the GVD with a global one.

Keywords

Greek Vertical Datum • Local Vertical Datum • World Height System • Zero-height geopotential level

1 Introduction

The establishment of a consistent and unified National Vertical Datum is a fundamental prerequisite for using reliable heights and their associated accuracy in a wide list of applications and studies including infrastructure development, public works and monitoring of natural risks and disasters. This is not though the case for the Greek Vertical Datum (GVD). The GVD is a tidal-based datum with different points of origin for the Greek mainland and the Greek islands. The point of origin of the mainland datum is located at the tide gauge station at the Piraeus harbor, while each island has its own point of origin set at the tide gauge station located on it. Additionally, there is not available a consistent connection between the mainland and the islands. The GVD currently includes a set of leveling BenchMarks (BMs) that form the first order national leveling network, as well as a set of trigonometric BMs, which belong also to the Horizontal Greek Datum. The trigonometric BMs are the ones that are

V.N. Grigoriadis (✉) • G.S. Vergos • I.N. Tziavos
GravLab, Department of Geodesy and Surveying, Faculty of Rural and Surveying Engineering, Aristotle University of Thessaloniki, Box 440, 54124 Thessaloniki, Greece
e-mail: nezos@topo.auth.gr

E. Lambrou
Laboratory of General Geodesy, School of Rural and Surveying Engineering, National Technical University of Athens, Zografou, Greece

G. S. Vergos et al. (eds.), *International Symposium on Gravity, Geoid and Height Systems 2016*, International Association of Geodesy Symposia 148, DOI 10.1007/1345_2017_1

most commonly used in current studies, applications and engineering projects.

The orthometric heights of the 1st order national leveling network were derived by performing two separate adjustments for the mainland (Peloponnese was adjusted separately from the rest of the mainland) and one for the island of Crete. These adjustments were carried out in 1986 and they were based on spirit leveling measurements carried out between 1963 and 1986 (Mylona-Kotrogianni 1990). Moreover, in 1989 the orthometric heights of the trigonometric BMs were derived from several adjustments carried out in different parts of the country based on its division in map-sheets of the Greek Geographical Military Service. The data employed within the adjustment processes did not take into account the adjusted heights of the 1st order leveling network, although the unadjusted heights of the trigonometric BMs were measured by spirit or trigonometric leveling with reference to the BMs of the leveling network. The estimated adjustment accuracy of the orthometric heights of the trigonometric network is of the order of 1–2 cm (Takos 1989) and the final accuracy has a mean value of approximately 2 cm although for some BMs it exceeds 10 cm.

Based on the above discussion, it is evident that there are inherent inconsistencies and shortcomings in the GVD that need to be further investigated. It should be noticed that these inconsistencies are further strengthened by the fact that there is no practical long-term monitoring of the VD variation with time, although Greece is an area of high seismicity with strong geodynamic features and peculiarities. These inconsistencies were detected also in previous researches, which were mainly conducted for the determination of zero-level geopotential values (W_o) and/or in the frame of a global effort for establishing an International Height Reference System (IHRS). In this frame, it should be noticed that Andritsanos et al. (2016) detected these inconsistencies in their study for two regions, one in northern Greece (wider area of Thessaloniki) and one in southern Greece (area of Attica). Grigoriadis et al. (2014) determined the W_o for the entire Greek mainland and an attempt was made to model height-correlated errors towards the improvement of the results achieved in this study. On the other hand, Kotsakis et al. (2012) and Vergos et al. (2016) focused on the determination of W_o for the Greek islands, where, as mentioned before, tide-gauge station at each island defines its own local VD. The present paper aims to highlight and examine more thoroughly the aforementioned inconsistencies referred to the Greek mainland in combination with those found in a restricted test area. The latter is an area in Central Greece that covers part of Peloponnese and part of the rest of the Greek mainland (see Fig. 1), where the available GNSS/leveling data at trigonometric BMs are contained in different map-sheets. Moreover, the specific area is characterized by sizeable earthquake phenomena and significant geological irregularities. The assessment is made after first determining the W_o based on the classical Helmert theory using GOCE-based Global Geopotential Models (GGMs) (Bruinsma et al. 2013; Brockmann et al. 2014; Mayer-Gürr et al. 2015; Gilardoni et al. 2016) and EGM08 (Pavlis et al. 2012).

2 Available Data and Models

The test area of the present study is located along the Gulf of Corinth in Central Greece (see Fig. 1). The selected area lies about 70 km west from the point of origin of the GVD, i.e., the tide gauge at Piraeus Harbor. For the datum

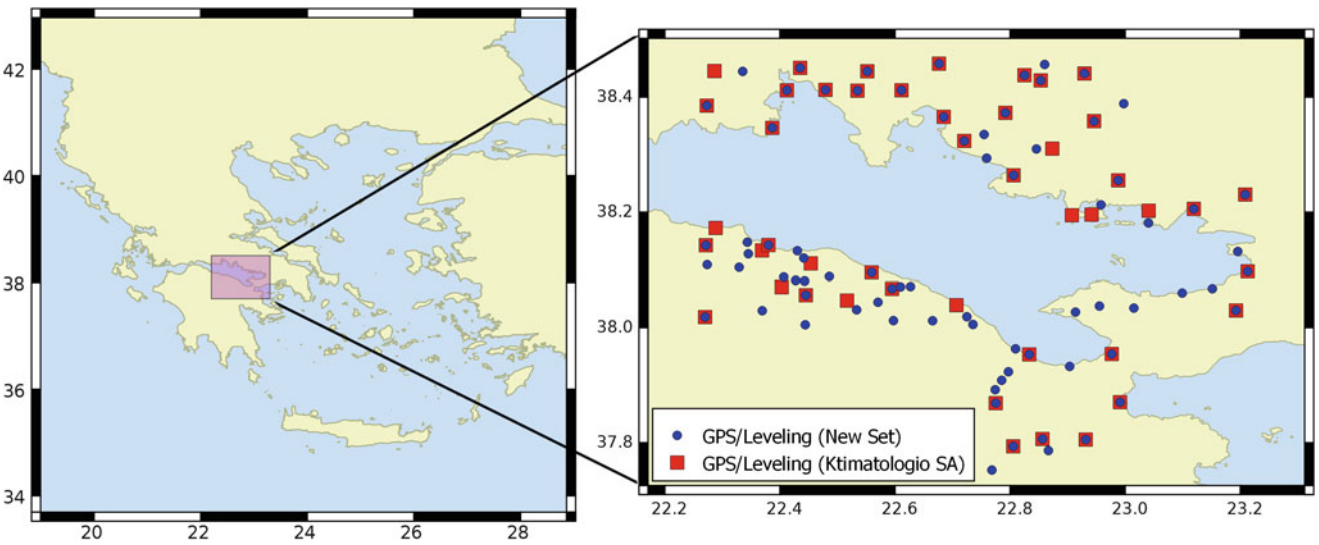

Fig. 1 Distribution of the GPS/leveling data for the two available datasets. Over-lapping points refer to the same BM station

assessment, two independent sets of GPS measurements on BMs of the Greek Trigonometric Network were available (see Fig. 1) that reside on both coasts along. The first set of GPS measurements (46 BMs) originates from Ktimatologio SA (Gianniou 2008), i.e., the organization responsible for the Greek Cadastre, while the second set was conducted by the second of the authors and her scientific group in 2009 in the frame of three field campaigns. The BMs from Ktimatologio SA belong to a wider set that was used in the transformation procedure between the Hellenic Terrestrial Reference Frame 07 (HTRS07) and the Hellenic Geodetic Datum 1987 (EGSA87). In the measurements of the second set (76 BMs) Trimble 5800 geodetic receivers (observation time at each BM 45–60 min) were used and the solution of baselines ranging from 8 to 40 km were carried out. The orthometric height of each BM is known and both datasets refer to the HTRS07. A number of 35 BMs belong to both data sets.

Regarding the GGMs used in the assessment procedure, four GOCE-based models were selected along with EGM08 that are reported in Table 1. It should be noticed that EGM08 and GECO were used up to a maximum degree and order (d/o) of 2,160. The rest of the models were used up to d/o 175 spectrally enhanced with EGM08 up to 2,160 d/o. The choice of d/o 175 was made after considering the results of the spectral evaluation carried out by Tziavos et al. (2016) for the geoid error spectrum of different GOCE-based GGMs and selecting a value where the error spectrum is below that of EGM2008 for all models.

3 Methodology

The W_o of the Local Vertical Datum (W_o^{LVD}) was computed using the following equation (Kotsakis et al. 2012; Grigoriadis et al. 2014):

$$W_o^{LVD} = W_o^{ref} - \frac{\sum_1^m (h_i - H_i - N_i)\ g_i}{m} \qquad (1)$$

where W_o^{ref} is set equal to 62,636,853.4 $m^2\ s^{-2}$ (IAG Resolution No. 1/2015; Sanchez et al. 2016), h_i is the geometric height of each BM derived by GPS measurements, H_i is the known orthometric height of each BM, N_i is the geoid height derived from the GGMs used, g_i is the gravity at each BM computed from GGMs and m is the total number of the available stations.

Each BM of the Greek network belongs to one of the 387 map-sheets that cover the wider area of Greece. As this map-sheet distribution is commonly used in practice and engineering applications, computations were carried out for both datasets as a whole and in parts based on the map-sheet the BMs belong to. Moreover, the BMs were also split into two subsets, the BMs that lie north of the Gulf of Corinth and those that lie south of the Gulf (see Fig. 1). In all cases, the same methodology was applied for the computation of W_o^{LVD} and all calculations were carried out in a tide-free system.

4 Results and Discussion

The first step of the assessment was the comparison of the W_o^{LVD} estimates computed from the new GPS dataset with those derived from the Ktimatologio one. Five different W_o^{LVD} values were estimated per dataset corresponding to the GGM used in the computational procedure (four GOCE-based GGMs and EGM08). The results of the W_o^{LVD} estimates are summarized in Table 2. It is seen that the two datasets are compatible in terms of the standard deviation, but a small offset is detected at the level of 0.28 $m^2\ s^{-2}$, which corresponds to 2.7 cm approximately in terms of height difference. Additionally, the range of height value differences varies between 4 and 5 $m^2\ s^{-2}$. Since the latter cannot be attributed to errors or blunders in the measurements, further investigation was carried out as it is described below. Moreover, several remarks are pointed out concerning the results contained in Table 2. The first one is that the new dataset contains more BMs for the study area than the one by Ktimatologio. The second remark is that the new dataset derived from measurements with an observation time of up to 1 h per BM, while the Ktimatologio (Ktima) dataset from several hours of measurements at each trigonometric point. It should also be noticed that the calculations with GOCO05s combined model show the lowest standard deviation equal to about 1.2 $m^2\ s^{-2}$ (marked in bold). The latter value corresponds to approximately 12 cm in terms of height

Table 1 The GGMs used in the assessment procedure

Model	Year	n_{max}	Data	Reference
GECO	2015	2,190	S(GOCE), EGM08	Gilardoni et al. (2016)
GOCO05s	2015	280	S(GOCE, GRACE, other)	Mayer-Gürr et al. (2015)
DIR-R5	2014	300	S(GOCE, GRACE, LAGEOS)	Bruinsma et al. (2013)
TIM-R5	2014	280	S(GOCE)	Brockmann et al. (2014)
EGM08	2008	2,190	S(GRACE), G, A	Pavlis et al. (2012)

Data: *S* satellite tracking, *G* gravity, *A* altimetry

Table 2 Statistics of W_o^{LVD} for the study area with respect to the IAG adopted W_o value ($m^2\ s^{-2}$)

	New dataset				Ktima dataset			
GGM	Mean	Std	Min	Max	Mean	Std	Min	Max
GOCO05s (d/o 175 + EGM08)	6.472	**1.174**	3.871	9.282	6.762	**1.168**	4.398	8.862
DIR-R5 (d/o 175 + EGM08)	6.479	1.201	3.812	9.262	6.760	1.194	4.388	8.940
TIM-R5 (d/o 175 + EGM08)	6.489	1.183	3.861	9.291	6.778	1.176	4.408	8.901
EGM08 (d/o 2,160)	6.396	1.253	3.763	9.066	6.653	1.240	4.330	8.989
GECO (d/o 2,160)	6.417	1.252	3.744	9.223	6.694	1.252	4.271	8.960

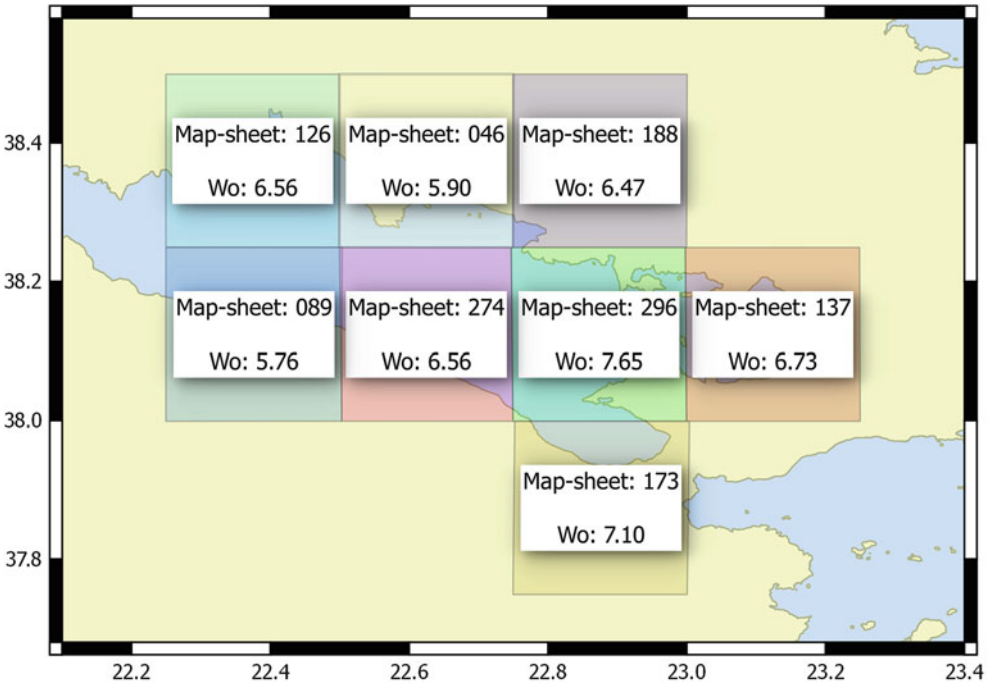

Fig. 2 Map-sheet distribution in the study area with the corresponding W_o^{LVD} estimates computed per map sheet with respect to the IAG W_o value ($m^2\ s^{-2}$)

Table 3 W_o^{LVD} estimates computed separately for the northern (W_o^N) and southern coast (W_o^S) of the study area with respect to the IAG W_o value and their corresponding differences ($m^2\ s^{-2}$)

	GOCO05s		DIR-R5		TIM-R5		EGM08		GECO	
	New	Ktima	New	Ktima	New	Ktima	New	Ktima	New	Ktima
W_o^N	6.50	6.92	6.49	6.90	6.51	6.93	6.32	6.72	6.42	6.82
W_o^S	6.44	6.53	6.47	6.56	6.47	6.56	6.47	6.56	6.42	6.51
$\lvert W_o^N - W_o^S \rvert$	0.06	0.39	0.02	0.34	0.04	0.37	0.15	0.16	0.00	0.31

difference which may be considered as significant like, for example, in geodetic applications.

Additional numerical tests were carried out in order to investigate an eventual offset between the BMs that lie in the northern (map-sheets 46, 126, 137, 188 and 296) and southern coast (map-sheets 89, 173 and 274) of the study area (see Fig. 2 for the map-sheet distribution). Table 3 presents the mean W_o^{LVD} values for the northern coast (W_o^N) and the southern coast (W_o^S) with respect to the IAG W_o value for all GGMs and GNSS datasets used in the present study. For the northern part of the test area 35 BMs from the new dataset and 27 BMs from the Ktimatologio database were used. It should be noticed that 22 BMs belong to both data sets. For the southern values, 32 and 19 BMs were used from the new and the Ktimatologio dataset, respectively, with 13 BMs contained in both data sets. Although the differences found with respect to the new dataset may be considered as negligible, as their values are lower than the accuracy of the available data, this is not the case for the Ktimatologio dataset (see Table 3). The Ktimatologio dataset presents five times larger differences than those of the new dataset. An unexpected exception for both datasets is the case of EGM08,

Table 4 W_o^{LVD} estimates computed per map-sheet with respect to the IAG W_o value ($m^2\ s^{-2}$)

	GOCO05s		DIR-R5		TIM-R5		EGM08		GECO	
Map-sheet	New	Ktima	New	Ktima	New	Ktima	New	Ktima	New	Ktima
46	5.90	6.30	5.83	6.23	5.90	6.30	5.51	5.91	5.59	5.99
89	**5.76**	**5.62**	**5.73**	**5.58**	**5.76**	**5.62**	**5.67**	**5.52**	**5.63**	**5.49**
126	6.56	6.95	6.44	6.58	6.54	6.83	6.11	6.93	6.18	6.51
137	6.73	6.92	6.84	7.21	6.77	7.03	6.97	6.97	7.02	7.15
173	7.10	7.33	7.20	7.44	7.15	7.43	7.29	7.38	7.20	7.53
188	6.47	7.13	6.46	7.09	6.48	7.12	6.26	7.15	6.41	6.94
274	6.56	6.97	6.58	6.93	6.58	6.99	6.52	6.99	6.51	6.92
296	**7.65**	**7.87**	**7.73**	**8.02**	**7.69**	**7.92**	**7.73**	**7.90**	**7.83**	**7.87**

Lowest and highest values are indicated by bold font

Table 5 Orthometric heights (rounded to nearest integer) (m) and zero-geopotential values ($m^2\ s^{-2}$) computed with respect to the IAG W_o value for map-sheet 188 based on GOCO05 spectrally patched with EGM08

	Map-sheet codes												
	01	03	17	27	29	39	59	67	76	98	101	103	111
H	225	441	243	1,244	1,452	698	553	998	169	396	300	201	308
W_o (new)	7.36	7.82	9.28	4.60	–	6.45	6.40	5.82	5.20	6.53	6.58	5.53	6.09
W_o (Ktima)	8.00	8.37	–	–	5.13	–	7.09	6.74	–	7.62	7.72	6.36	–

where the differences are almost equal. Since the above mentioned results depend on the choice of the BMs, it was decided in a next step to focus on each map-sheet separately.

In the frame of this specific numerical analysis the computation of W_o^{LVD} for each map-sheet (scale 1:50,000) was made following the cartographic breadboard of the Greek Geographical Military Service. In Table 4 the new W_o^{LVD} estimates are reported, which are based on the new dataset and that of Ktimatologio, while Fig. 2 depicts each map-sheet and its estimated W_o^{LVD} using the new dataset and the GOCO05s model. From the results of Table 4 a significant difference larger than 1 $m^2\ s^{-2}$ is observed between the different map-sheets, where the largest difference for the GOCO05s-based solution reaches 1.89 $m^2\ s^{-2}$. These results indicate inconsistencies, which may be attributed on the one hand partly to the GGM used (2.3 cm cumulative geoid error for the GOCO05s combination), especially in the medium to high frequencies band of the gravity spectrum, and on the other hand mainly to the orthometric heights of the BMs. This conclusion is in line with the conclusions reported in Tziavos et al. (2012), who indicated incompatibilities in the orthometric heights of BMs belonging to adjacent map-sheets. Therefore, further examination of the results was then carried out for each map-sheet on a per BM basis.

The examination of each map-sheet separately revealed that even the BMs that belong to a specific map-sheet are not consistent. Additionally, no correlation between the orthometric height and the W_o of each BM was found. Table 5 presents the orthometric heights and the estimated W_o for the BMs of map-sheet number 188, as these were obtained from both GNSS datasets and GOCO05s. W_o ranges between 4.60 and 9.28 for the new dataset while for the dataset obtained from Ktimatologio, where less BMs are used, the values are between 5.13 and 8.37 $m^2\ s^{-2}$. It is interesting to notice that for the new dataset the minimum and maximum values occur on BMs that were not included in the Ktimatologio dataset. These BMs though are currently used in everyday engineering projects, while the accuracy of their orthometric height is claimed to be approximately 1 cm. From the presented results it may be deduced that the accuracies provided for the orthometric heights are overly optimistic.

A last step of our assessment methodology was to compare our W_o^{LVD} estimates with those derived by previous studies for the Greek mainland and four Greek Islands towards the unification of the GVD with a global one. The W_o^{LVD} values are tabulated in Table 6. Two of these previous studies (Kotsakis et al. 2012; Vergos et al. 2016) were based on the Ktimatologio dataset, while Andritsanos et al. (2016) used an independently measured dataset. The values given in the present study are practically equal to those provided by Andritsanos et al. (2016) while there is a difference of 0.47 $m^2\ s^{-2}$ with that given by Grigoriadis et al. (2014) for the Greek mainland. Regarding the islands, apart from Evia, which is directly accessible from the mainland, we notice that there are significant differences in the estimated values. As all studies are affected by the inconsistencies associated with the orthometric heights of the trigonometric BMs, any chosen value for the W_o^{LVD} would face severe difficulties in practice.

Table 6 Comparison of W_o^{LVD} estimates for the study area, mainland of Greece and Greek islands with respect to the IAG W_o value from the current and previous studies ($m^2\ s^{-2}$)

	GOCO05s	DIR-R5	TIM-R5	EGM08	GECO
Test area of the current study	6.47	6.48	6.49	6.40	6.42
Mainland					
Grigoriadis et al. (2014)	–	–	–	6.87	–
Andritsanos et al. (2016)	6.41	6.41	6.46	6.26	–
Island of Crete					
Kotsakis et al. (2012)[a]	–	–	–	7.55	–
Vergos et al. (2016)	–	–	7.78	–	–
Island of Evia					
Kotsakis et al. (2012)[a]	–	–	–	6.79	–
Vergos et al. (2016)	–	–	6.47	–	–
Island of Corfu					
Kotsakis et al. (2012)[a]	–	–	–	9.34	–
Vergos et al. (2016)	–	–	7.90	–	–
Island of Lesvos					
Kotsakis et al. (2012)[a]	–	–	–	8.37	–
Vergos et al. (2016)	–	–	7.73	–	–

[a]Computations were carried out in a zero-tide system

5 Conclusions and Recommendations

In this study, two independent GPS datasets, GGMs and orthometric heights were used for carrying out an assessment of the Greek LVD in the wider area of the Gulf of Corinth in Central Greece. Different W_o^{LVD} values were computed from each GPS dataset and GGM. First, all BMs were used in order to estimate the mean W_o^{LVD} for the study area for all dataset combinations. Although the mean values of all estimates, considering all BMs each time, were consistent, the values estimated at the BMs had a range from 4 and 5 $m^2\ s^{-2}$ and a standard deviation larger than 1 $m^2\ s^{-2}$. In the next assessment step, the W_o^{LVD} values were computed for two areas, the northern and southern coast of the Gulf of Corinth. The comparison of the results based on the two different GPS datasets showed that the choice of BMs used in the computations affects significantly the computed W_o^{LVD} values. Then, W_o^{LVD} was computed for each map-sheet of the test area. Adjacent map-sheets were found to have differences from 0.5 up to 1.2 $m^2\ s^{-2}$ when using GOCO05s in the computations. Further examination of the BM values for each map-sheet revealed inconsistencies in terms of the determined zero geopotential-values. It should be noticed that no systematic errors were detected in the data used in the computations nor correlation between the estimated zero geopotential-values with height or the geographic location of the BM stations.

The discrepancies found between the different W_o^{LVD} values following a per BM investigation are mainly attributed to the orthometric height values of BMs and present a random spatial distribution. Since it is not possible with the available data to identify which BMs are problematic, additional GPS/GNSS measurements should be carried out and, most importantly, leveling measurements, in order to further extend our research and draw more safe conclusions. Thus, modern techniques as accurate trigonometric heighting (Lambrou 2007; Lambrou and Pantazis 2007), astrogeodetic leveling by means of modern automated instrumentation and procedures (Lambrou 2015) followed by gravimetry measurements can also be applied in the future field work. A higher accuracy and resolution gravimetric geoid model would also be of benefit in the proposed procedure. It should be finally noticed that before the connection of the Greek LVD with a global one, it is mandatory to: (a) resolve the inconsistencies detected by the present and previous studies for the Greek mainland and islands and (b) introduce monitoring of the existing VD with time.

References

Andritsanos VD, Grigoriadis VN, Natsiopoulos DA, Vergos GS, Gruber T, Fecher T (2016) GOCE variance and covariance contribution to height system unification. Presented at the 1st Joint Commission 2 and IGFS Meeting (GGHS 2016), 19–23 September 2016, Thessaloniki

Brockmann JM, Zehentner N, Höck E, Pail R, Loth I, Mayer-Gürr T, Schuh WD (2014) EGM-TIM-RL05: an independent geoid with centimeter accuracy purely based on the GOCE mission. Geophys Res Lett 41:8089–8099

Bruinsma SL, Förste C, Abrikosov O, Marty J-C, Rio M-H, Mulet S, Bonvalot S (2013) The new ESA satellite-only gravity field model via the direct approach. Geophys Res Lett 40:3607–3612

Gianniou M (2008) HEPOS: designing and implementing an RTK network. Geoinformatics 11(1):10–13

Gilardoni M, Reguzzoni M, Sampietro D (2016) GECO: a global gravity model by locally combining GOCE data and EGM2008. Stud Geophys Geod 60:228

Grigoriadis VN, Kotsakis C, Tziavos IN, Vergos GS (2014) Estimation of the geopotential value Wo for the local vertical datum of continental Greece using EGM08 and GPS/leveling data. In: Marti U (ed) Gravity, geoid and height systems, IAG symposia, vol 141. Springer, Switzerland, pp 249–255

Kotsakis C, Katsambalos K, Ampatzidis D (2012) Estimation of the zero-height geopotential level in a local vertical datum from inversion of co-located GPS, leveling and geoid heights: a case study in the Hellenic islands. J Geodesy 86(6):423–439

Lambrou E (2007) Accurate height difference determination using reflectorless total stations (in Greek). Technika Chronika Sci J Tech Chamber Greece 1–2:37–46

Lambrou E (2015) Accurate geoid height differences computation from GNSS data and modern astrogeodetic observations. In: Marti U (ed) Gravity, geoid and height systems, IAG symposia, vol 141. Springer, Cham, pp 163–170

Lambrou E, Pantazis G (2007) A convenient method for accurate height differences determination. In: Proceedings of the 17th International Symposium on Modern technologies, education and professional practice in Geodesy and related fields, Sofia, pp 45–53

Mayer-Gürr T et al (2015) The combined satellite gravity field model GOCO05s. Presented at the EGU 2015, April 2015, Vienna

Mylona-Kotrogianni H (1990) The 1st order leveling net of Greece (in Greek). Bull Hellenic Mil Geogr Serv 50(138):1–26

Pavlis NK, Holmes SA, Kenyon SC, Factor JK (2012) The development and evaluation of the earth gravitational model 2008 (EGM2008). J Geophys Res 117(B4):B04406

Sanchez L, Čunderlík R, Dayoub N, Mikula K, Minarechová Z, Šíma Z, Vatrt V, Vojtíšková M (2016) A conventional value for the geoid reference potential W_0. J Geodesy 90:815–835. doi:10.1007/s00190-016-0913-x

Takos I (1989) New adjustment of the national geodetic networks in Greece (in Greek). Bull Hellenic Mil Geogr Serv 49(136):19–93

Tziavos IN, Vergos GS, Grigoriadis VN, Andritsanos VD (2012) Adjustment of collocated GPS, geoid and orthometric height observations in Greece. Geoid or orthometric height improvement? In: Kenyon S, Pacino C, Marti U (eds) Geodesy for planet earth, International Association of Geodesy Symposia, vol 136. Springer, Heidelberg, pp 481–488. doi:10.1007/978-3-642-20338-1_58

Tziavos IN, Vergos GS, Grigoriadis VN, Tzanou EA, Natsiopoulos DA (2016) Validation of GOCE/GRACE satellite only and combined global geopotential models over Greece, in the frame of the GOCESeaComb Project. In: Rizos C, Willis P (eds) IAG 150 Years, International Association of Geodesy Symposia, vol 143. Springer, Cham, pp 297–304. doi:10.1007/1345_2015_160

Vergos GS, Erol B, Natsiopoulos DA, Grigoriadis VN, Isik MS, Tziavos IN (2016) GOCE-based height system unification between Greece and Turkey. Presented at the 2016 EGU General Assembly, Session G4.2 "Satellite Gravimetry: Data Analysis, Results and Future Concepts", April 17th–April 22nd, Vienna

Evaluation of NRTK-Based Heighting Techniques from Different Continuously Operating GNSS Reference Networks in Greece

N. Aslanidis and C. Kotsakis

Abstract

GNSS positioning using network-based real-time kinematic (NRTK) techniques, such as the virtual reference station (VRS) and the master auxiliary concept (MAC), is widely used in surveying and geomatics applications. The accuracy of the estimated height component by those techniques is known to be at the centimeter level although several factors, like the deployment of reference stations, the correction message transmission delay, the satellite signal availability and the employed software package, could limit the vertical accuracy obtained in practice. The scope of this paper is to present preliminary results from several field tests that were conducted by the Department of Geodesy and Surveying of the Aristotle University of Thessaloniki for the purpose of evaluating the heighting accuracy from different commercial providers of NRTK positioning services in Greece. Our aim is to investigate the actual positional quality of the vertical component from an end-user's point of view by considering how different factors, such as the number of in-view satellites and their geometry, the duration of station occupancy, the distance to the reference stations and the choice of the applied correction method (VRS or MAC) might affect the final accuracy of the estimated heights. The validation of our results is based on high-quality height information that was independently obtained by precise spirit leveling over all considered test points.

Keywords

GNSS positioning • Height estimation • NRTK • Spirit leveling • Vertical accuracy

1 Introduction

GNSS positioning using network-based real-time kinematic (NRTK) techniques, such as the virtual reference station (VRS) and the master auxiliary concept (MAC) is widely used in surveying and geomatics applications (Hoffmann-Wellenhof et al. 2008; Meng et al. 2007; Wang et al. 2010; Janssen 2009). The accuracy of height information that is obtained by those techniques is known to be at the centimeter level, although several factors like the deployment of reference stations, the correction message transmission delay, satellite signal availability and multipath effects, and the employed software package, could limit in practice the actual accuracy level of the estimated heights (e.g. Featherstone and Stewart 2001; El-Mowafy et al. 2006). Numerous case studies have been performed over the last years for the quality assessment of GNSS/NRTK-based heighting (see, for instance, Bae et al. 2015; Paar et al. 2011, 2014; Saghravani et al. 2009; Dawidowicz 2013) yet the particular topic still signifies an active area of ongoing research that has not been fully investigated in all related aspects.

The scope of this paper is to present some preliminary results from several field tests that were conducted by the Department of Geodesy and Surveying of the Aristotle

N. Aslanidis • C. Kotsakis (✉)
Department of Geodesy and Surveying, Aristotle University of Thessaloniki, Thessaloniki, Greece
e-mail: kotsaki@topo.auth.gr

G. S. Vergos et al. (eds.), *International Symposium on Gravity, Geoid and Height Systems 2016*, International Association of Geodesy Symposia 148, DOI 10.1007/1345_2017_21

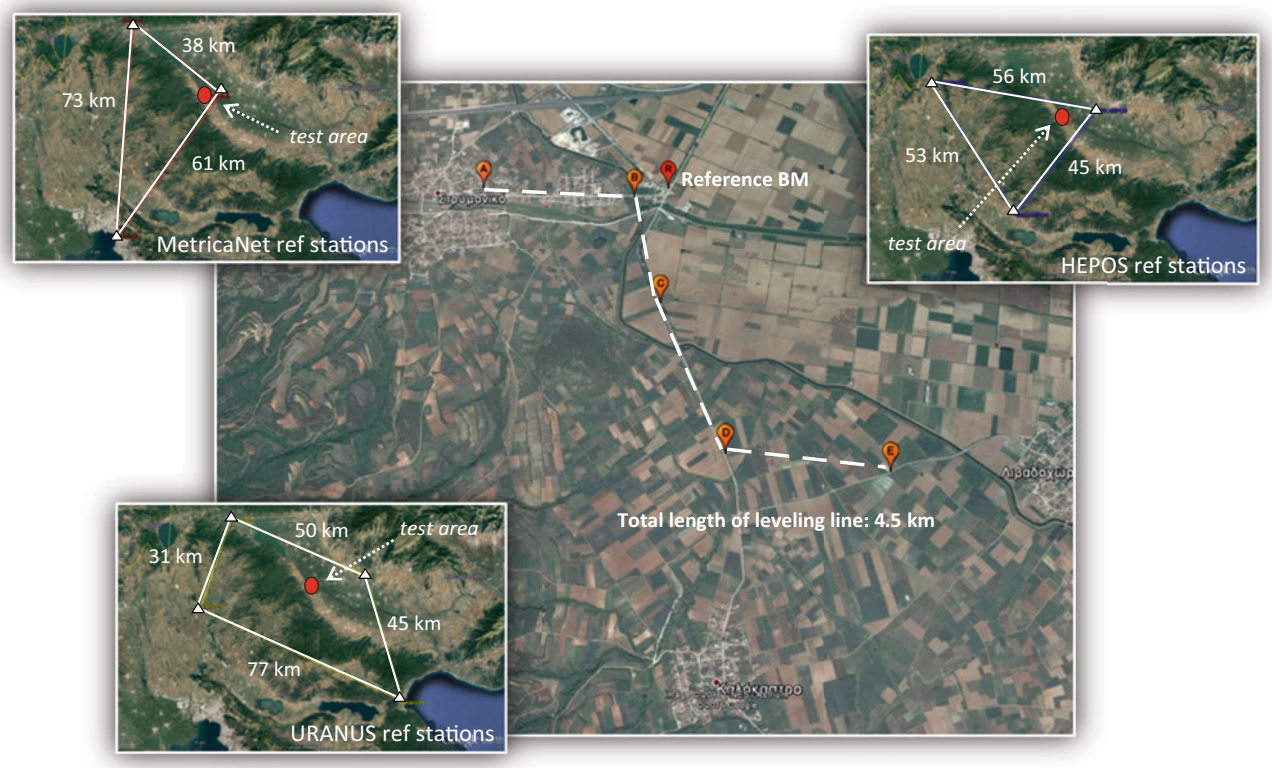

Fig. 1 Maps showing the location of the test points (A–E), the reference benchmark of the national vertical datum, and the nearby permanent stations of the three GNSS/NRTK positioning networks

University of Thessaloniki to evaluate the heighting accuracy from different commercial providers of NRTK-based positioning services in Greece. Our aim is to investigate the positional quality of the vertical component from an end-user's point of view in relation to:

- the choice of the applied correction method (VRS or MAC),
- the number of in-view satellites and their geometry (PDOP), and
- the duration of station occupancy.

The validation of our results relies on high-quality height information which was independently obtained by precise spirit leveling, in double-traverse mode, over the test network shown in Fig. 1.

2 Data: Methodology

To evaluate the NRTK operational performance in height determination, a test network of five points (A–E) was established in the area of Strymoniko near the city of Serres in northern Greece (see Fig. 1). The test points were placed along the main road network at successive distances of about 1 km, using typical stainless-steel urban survey markers which were installed on existing concrete surface with epoxy reinforcing. Their spatial positions with respect to the Hellenic Terrestrial Reference System 2007 (Katsambalos et al. 2010) were determined via three nationwide commercial GNSS positioning services, namely MetricaNet (GPS/GLONASS), Uranus (GPS/GLONASS) and HEPOS (GPS only), using both types of NRTK correction methods (Brown et al. 2006; Retscher 2002). The measurements were collected with 1 Hz sampling rate at each test point, and they were processed with the Leica Geo Office software according to different scenarios for various duration levels of station occupancy (see Table 1). In all cases the elevation cut-off angle was set to 10°. Three different Leica Viva dual-frequency GPS/GLONASS receivers were used for the observation campaigns as follows: GS08plus (MetricaNet), GS08 (Uranus) and GS14 (HEPOS). The data collection was performed in different days but at the same time each day, in order to ensure similar GNSS constellations and uniform multipath effect in the estimated results.

The GNSS-based orthometric heights of the test points were derived with the help of respective geoid models which are "internally" used by the three NRTK positioning services. Unfortunately, no actual information is readily available regarding the type, accuracy or spatial resolution for these auxiliary geoid models. The derived orthometric heights from each GNSS/NRTK method and provider were

Table 1 Details of the NRTK heighting tests that were performed in this study

Test point	GNSS permanent network	NRTK method	Duration of station occupancy (s)
A	MetricaNet, Uranus, HEPOS	VRS/MAC	50/100/200
B	MetricaNet, Uranus, HEPOS	VRS/MAC	50/100/200
C	MetricaNet, Uranus, HEPOS	VRS/MAC	50/100/200
D	MetricaNet, Uranus, HEPOS	VRS/MAC	50/100/200
E	MetricaNet, Uranus, HEPOS	VRS/MAC	50/100/200

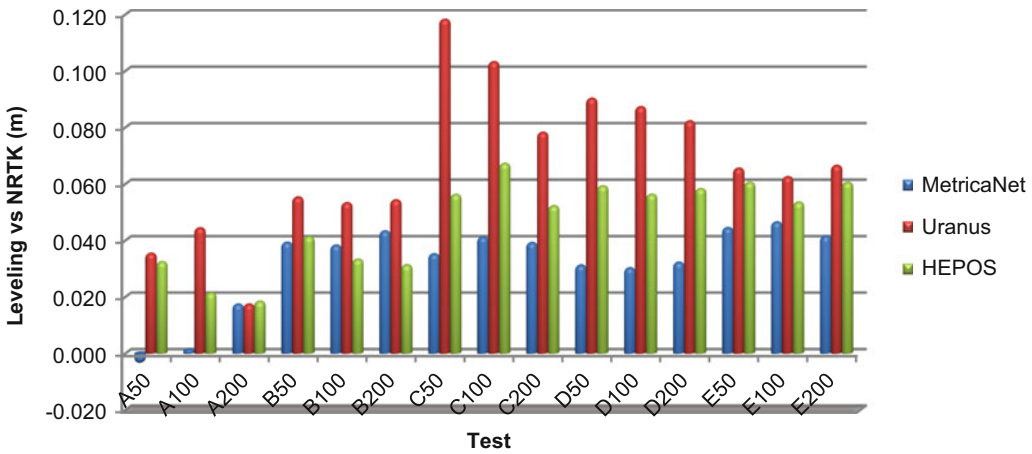

Fig. 2 Differences between the NRTK/MAC-derived orthometric heights (for station occupancy time of 50/100/200 s) and the spirit-leveled heights

compared against the precise spirit-leveled heights of the test points which were transferred from a nearby reference benchmark of the Hellenic vertical datum (see Fig. 1). All leveling measurements were performed by a Leica Sprinter 150 digital level and the achieved (relative) height accuracy lied in the range of 0.5–2 mm.

3 Test Results

The vertical coordinate of each test point (A–E) was determined via the VRS and MAC correction methods, both of which are offered by the positioning services considered in this study. Three ensembles of GNSS measurements, each containing different number of observations (50, 100, 200) collected at a uniform sampling rate of 1 Hz, were analyzed by both correction methods. Hence, a total of 18 estimates were finally obtained for the GNSS-based orthometric height of each test point. These estimates are compared with the leveling-based orthometric heights of the respective points, and the derived results are shown in Figs. 1 and 2.

In general, the three NRTK positioning services exhibit similar accuracy level for orthometric height determination, regardless of the applied correction method (MAC or VRS). The duration of station occupancy does not seem to have a sizeable influence on the vertical positioning performance, either for the MAC or the VRS method (see Figs. 2 and 3). Both methods appear to behave in the same way within each GNSS reference network, and they lead to comparable statistics for the differences with respect to the spirit-leveled heights; see Table 2.

The results obtained via the Uranus reference network are a bit worse compared to the other two GNSS reference networks, probably due to the fact that the test area is located much closer to MetricaNet and HEPOS permanent stations, as indicated in the map of Fig. 1. This is crucial for the actual performance of the NRTK interpolation engine (VRS and MAC) and it is likely the cause of the worse behavior shown in the Uranus results. Overall, the maximum height differences among the NRTK positioning services reach a few cm, which can be considered significant for a number of precise surveying applications.

3.1 Absolute Height Bias

As seen in Figs. 2 and 3, the GNSS-based orthometric heights in all testing scenarios appear to be biased by several cm with respect to the spirit-leveled heights which were transferred from the national leveling benchmark R. This is also evident in Table 2 where the mean offset between the aforementioned height types at the test points ranges from 3 to 6 cm, depending on the data processing scheme. Such an effect is probably caused by an (unknown) systematic offset

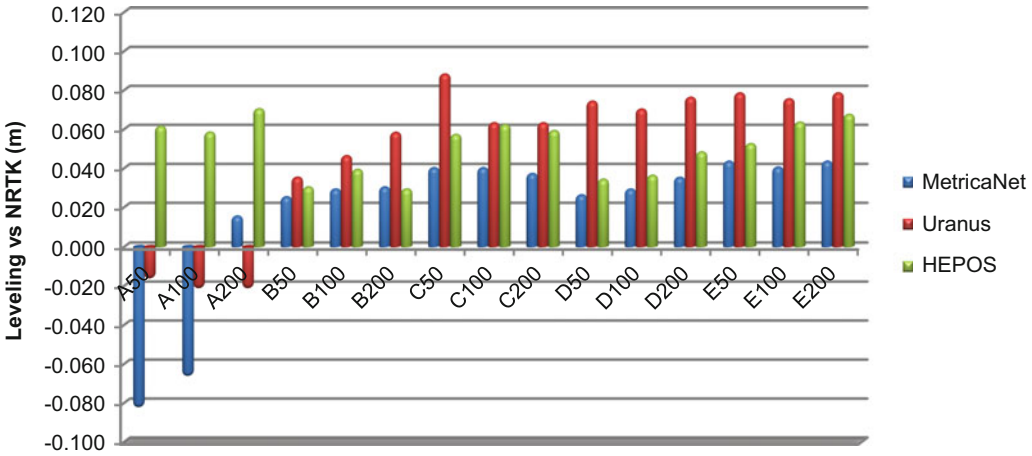

Fig. 3 Differences between the NRTK/VRS-derived orthometric heights (for station occupancy time of 50/100/200 s) and the spirit-leveled heights

Table 2 Statistics of the differences between the NRTK-derived orthometric heights and the spirit-leveled heights

	MetricaNet		Uranus		HEPOS	
	MAC	VRS	MAC	VRS	MAC	VRS
Min	1.7	1.5	1.7	−2.2	1.8	2.9
Max	4.3	4.4	8.2	7.9	6.1	7.0
Mean	3.5	3.2	6.0	5.1	4.4	5.5
Std	1.1	1.1	2.6	4.1	1.8	1.7

The results refer to station occupancy of 200 s. All values in centimeters

Table 3 Statistics of the discrepancies between the NRTK-derived height differences and the spirit-leveled height differences over all possible baselines in the test network

	MetricaNet		Uranus		HEPOS	
	MAC	VRS	MAC	VRS	MAC	VRS
Min	−0.7	−0.2	−1.6	0.2	0.2	−4.3
Max	2.4	1.3	3.5	7.8	2.1	3.0
Mean	0.6	0.7	1.2	2.5	1.0	−0.1
Std	1.4	0.6	2.2	3.6	0.8	3.3

The results refer to station occupancy of 200 s. All values in centimeters

between the geoidal surfaces that are utilized by the NRTK positioning services and the Hellenic vertical datum over the test area. Considering the magnitude of the average height biases listed in Table 2, it is likely that the NRTK positioning services do not use the exact same model to perform the ellipsoidal-to-orthometric height conversion.

3.2 Assessment of Relative Orthometric Heights

In most practical cases, relative instead of absolute height information is more critical for a large number of surveying applications. The evaluation of the NRTK positioning services in terms of relative height determination is given in Table 3. It is seen that the maximum discrepancies between the GNSS-based and the leveling-based orthometric height differences over all formed baselines in our test network reach up to several centimeters. Interestingly enough, the average value of the aforementioned discrepancies seems to be significantly different from zero, especially in the results by the Uranus (MAC/VRS) and HEPOS (MAC only) reference networks. This indicates the presence of a "scaling" bias between the spirit leveling and the GNSS heighting techniques, which in our case can reach up to 2.5 cm.

3.3 PDOP

It is generally assumed that the PDOP index (position dilution of precision) is closely associated with the errors in the GNSS measurements and the resulting accuracy of the NRTK-derived spatial coordinates of the underlying station (Hoffmann-Wellenhof et al. 2008). Figure 4 illustrates the PDOP-dependency of the differences between the spirit-leveled heights and the GNNS-based orthometric heights for all positioning services considered in this study. The results do not reveal any particular correlation between the satellite geometry and the vertical positioning performance of the NRTK heighting techniques in our test network. Note that a high PDOP value does not necessarily imply a poor height estimate, neither does a low PDOP value guarantee a truly accurate result (e.g. Featherstone and Stewart 2001). In our case, the largest PDOP value reached 2.8 for the HEPOS-related analysis at the test point C – the difference between the GNSS-based and the spirit-leveled orthometric height in this case was 5.6 cm. It should be mentioned that the HEPOS reference network supports GPS-only satellite tracking, a fact which is reflected in Fig. 4 by the larger PDOP values compared to the cases of MetricaNet and Uranus networks.

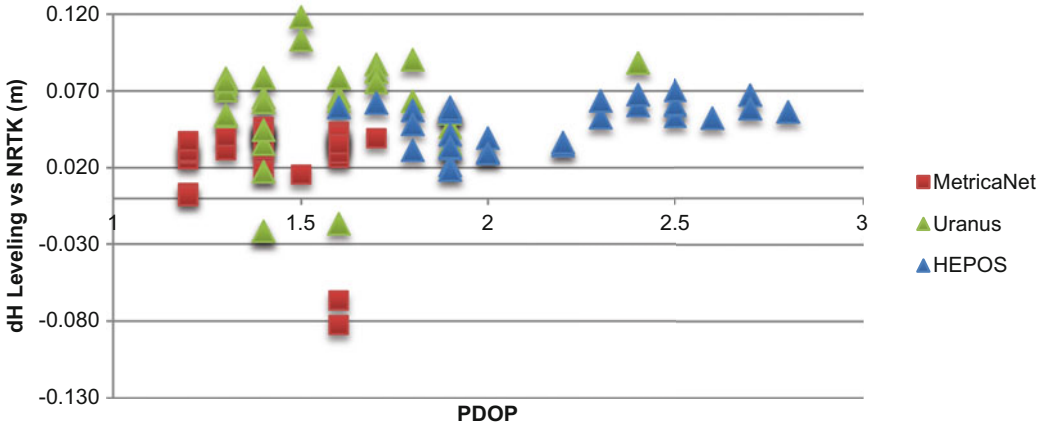

Fig. 4 PDOD dependency of the differences between the NRTK-derived orthometric heights and the spirit-leveled heights. The results shown in this graph refer to both MAC and VRS datasets at each test point for different durations of station occupancy (50, 100, 200 s)

4 Conclusions

This study presented some first results on the vertical accuracy assessment for three NRTK positioning services in Greece. Based on comparisons with precise spirit-leveled orthometric heights over a small test area in northern Greece, it has been shown that an average accuracy level of a few cm is feasible, in both absolute and relative sense, regardless of the used correction method (VRS or MAC) and the chosen GNSS reference network. This can be considered sufficient for several types of surveying and cadastral-related applications, but it cannot ensure the realization of GNSS-derived orthometric heights with 1–2 cm (or better) consistency level in relation to the Hellenic vertical datum. In fact, a sizeable systematic bias (>3 cm) between the GNSS-derived and the spirit-leveled heights has been identified in all testing scenarios, which is probably caused by the used external geoid model(s). Additional tests over larger distances in different parts of the country are certainly needed to reach safer conclusions regarding the achievable vertical accuracy of NRTK positioning services in Greece.

References

Bae T-S, Grejner-Brzezinska D, Mader G, Dennis M (2015) Robust analysis of network-based real-time kinematic for GNSS-derived heights. Sensors 15:27215–27229

Brown N, Geisler I, Troyer L (2006) RTK rover performance using the master-auxiliary concept (MAC). J Glob Position Syst 5(2): 135–144

Dawidowicz K (2013) Analysis of height determination using the ASG-EUPOS NAWGEO service. Tech Sci 16(1):19–39

El-Mowafy A, Fashir H, Al Habbai A, Al Marzooqi Y, Babiker T (2006) Real-time determination of orthometric heights accurate to the centimeter level using a single GPS receiver: case study. J Surv Eng 132(1):1–6

Featherstone WE, Stewart MP (2001) Combined analysis of real-time kinematic GPS equipment and its users for height determination. J Surv Eng 127(2):31–51

Hoffmann-Wellenhof B, Lightenegger H, Walse E (2008) GNSS – global navigation satellite systems. Springer, New York, pp 262–266

Janssen VA (2009) A comparison of the VRS and MAC principles for network RTK. In: Proceedings of the international global navigation satellite systems society, surfers paradise, Australia, Dec 1–3, 2009

Katsambalos K, Kotsakis C, Gianniou M (2010) Hellenic terrestrial reference system 2007 (HTRS07): a regional realization of ETRS89 over Greece in support of HEPOS. Bull Geod Geomat LXIX(2–3):329–348

Meng X, Dodson A, Liu C, Moore T, Hill C (2007) Quality assurance of network RTK GNSS positioning: an end-user perspective. In: Proceedings of XXIV IUGG general assembly, Perugia, July 2–13, 2007

Paar R, Novakovic G, Kolovrat D (2014) Vertical component quality comparison of GPS RTK method in combination with laser system vs. conventional methods for height determination. In: Proceedings of INGEO 2014, 6th international conference of engineering surveying, Prague, Apr 3–4, 2014

Paar R, Zrinjski M, Marendic A (2011) Quality check of vertical component using GPS RTK method and laser system. Geodetski vestnik 55(4):689–700

Retscher G (2002) Accuracy performance of virtual reference station (VRS) networks. J Glob Position Syst 1(1):12–20

Saghravani SR, Mustapha S, Saghravani SF (2009) Accuracy comparison of RTK-GPS and automatic level for height determination in land surveying. MASAUM J Surv 1(1):10–13

Wang C, Feng Y, Higgins M, Cowie B (2010) Assessment of commercial network RTK user positioning performance over long inter-station distances. J Glob Position Syst 9(1):78–89

SLA Determination in Coastal Areas Using Least-Squares Collocation and Cryosat-2 Data

O.N. Altiparmaki, D.A. Natsiopoulos, and G.S. Vergos

Abstract

Satellite altimetry has provided during the last 30 years an unprecedented amount of high-resolution and high-accuracy data for the state of the oceans. With the latest altimetric satellites utilizing the SAR and SAR-in modes, reliable sea surface heights close to the coastline can be determined more efficiently. The main purpose of this paper is to estimate Sea Level Anomalies (SLAs) close to the coastline and to areas where data are absent, while Least Squares Collocation (LSC) has been used to carry out the prediction. The selected study area is the entire Mediterranean Sea and the estimation of SLA values was carried out using raw Cryosat-2 observations. For LSC to be applied, empirical and analytical covariance function models are defined and evaluated for estimating SLAs within 10° block windows. In order to investigate the accuracy of the analytical covariance functions that provide the most accurate results, prediction has been carried out at a single point, randomly selected in the Greek region being close to the coastline. From the analysis carried out, three types of analytical covariance functions were deemed as the optimal ones, providing a mean prediction accuracy at the 3.7 cm level. These models were then used for the SLA estimation at the 10° windows, specifying local empirical and analytical covariance function models. The prediction accuracies achieved range between 3.7 cm and 12.5 cm depending on the presence of islands.

Keywords

Coastal areas • Cryosat-2 • Least-squares collocation • Prediction • Sea level anomalies

1 Introduction

Over the last few decades, climate induced ocean variations have been one of the most important environmental problems worldwide. Taking into consideration and studying these changes, the scientific community has tried to gather even more information about their triggering factors and their consequences. This has been largely achieved through dedicated satellite missions aiming to monitor the marine environment and the mass loss in the Polar Regions, which is caused by ice melting. One of the main consequences are increasing levels of the Earth's oceans with foreseen impact on the anthropogenic and natural environment. To that respect, and in order for satellite data to be incorporated in forecasting and assimilation models, their inherent high-accuracy over marine regions should be extended to coastal ones and to areas where data are absent. Additionally, improved representation and estimation of sea surface heights close to the coastline will have a direct, positive, impact on height system unification (HSU) in remote areas and regions where GPS-derived ellipsoidal heights cannot be acquired (Gruber et al. 2012). For the altimetric records to be extended close to the coastline an interpolation, extrapolation in reality, needs

O.N. Altiparmaki (✉) • D.A. Natsiopoulos • G.S. Vergos
GravLab, Department of Geodesy and Surveying, Aristotle University of Thessaloniki, Thessaloniki, 54124 Greece
e-mail: raltiparmaki@hotmail.com; dnatsio@topo.auth.gr; vergos@topo.auth.gr

G. S. Vergos et al. (eds.), *International Symposium on Gravity, Geoid and Height Systems 2016*, International Association of Geodesy Symposia 148, DOI 10.1007/1345_2017_11

to be carried out. In that way, the continuous along-track measurements in pure sea areas will be brought closer to coastal areas and within a small distance (close to 1 km) from the coasts, where a Tide Gauge (TG) station is situated. For this prediction to be carried out accurately, a rigorous method should be employed. In physical geodesy, Least Squares Collocation (LSC) has been used for long as an optimal estimator (Barzaghi et al. 2009; Moritz 1980), in the sense that it provides highly accurate prediction results, given the data accuracy and the statistical characteristics of the input field. LSC requires knowledge of both input data and error variance-covariance matrices, the latter being defined by the analytical covariance functions of the input signals. The mission of Cryosat-2 offers dense cross-track spacing as a result of the Synthetic Aperture Radar (SAR) and SAR-in drifting modes leading to high spatial resolution (Francis 2007; Wingham et al. 2006). Due to the fact that the Mediterranean Sea is a semi-enclosed marine region with many islands and isles disrupting the pure marine observations, Cryosat-2 was chosen as the most appropriate for the specific nature of this particular study area (Andersen and Piccioni 2016). Through Cryosat-2 data, analytical covariance functions were estimated based on exponential, polynomial and Gauss-Markov models, and prediction of Sea Level Anomaly (SLA) values has been carried out to conclude on the most proper ones in order to derive SLAs in coastal areas. The analytical models providing the highest prediction accuracy are then used to extend the SLA information in areas with little or no data, especially close to the coastline. To that respect, the entire Mediterranean basin was split in individual windows of 10 × 10 degrees, and separate empirical covariance functions have been estimated, in order to derive representative analytical models for each sub-area. Finally, the absolute accuracies offered by the various covariance models were assessed by comparing them as to the results they provide in a specific prediction case.

2 Satellite Altimetry Data Availability and Methodology

The used raw data refer to SLAs for one cycle (cycle 13 – 12,127 SLA values) of the Cryosat-2 satellite mission from 14.03.2011 to 12.04.2011 within the entire Mediterranean Sea ($30° \leq \varphi \leq 50°$ and $-10° \leq \lambda \leq 40°$). The Cryosat-2 data were acquired from the RADS system (RADS 2016; Scharroo et al. 2013), which has a collection of data from past and current satellite altimetry missions. All geophysical and instrumental corrections have been applied, using the default models proposed by the RADS system, so that corrected SLAs would be available. During this pre-processing step, the derived SLAs have been referred to the EGM2008 Zero-Tide (ZT) geoid (Pavlis et al. 2012) and the Jason ellipsoid (Dumont et al. 2016). Figure 1 depicts the distribution of the Cryosat-2 data over the entire Mediterranean basin as well as the SLA variations, while Table 1 presents the respective statistics.

To evaluate the performance of SLA prediction close to the coastline, LSC has been employed using various covariance functions. Initially, in order to evaluate their performance the available data have been separated in two equal halves, one acting as the input dataset and the other as

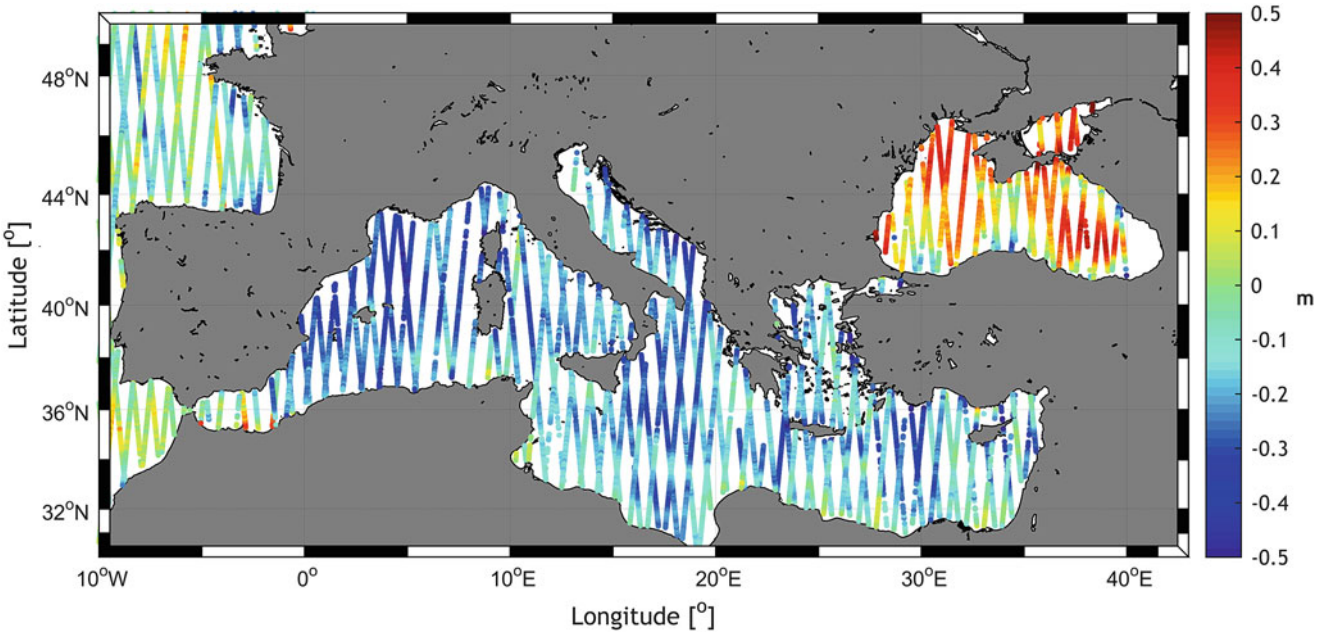

Fig. 1 Cryosat-2 cycle 13 data distribution over the entire Mediterranean Sea

Table 1 Statistics of the original SLAs and differences with the predictions based on the various covariance function models

	Initial	Model A	Model B	Model C	Model D	Model E	Model F	Model G
Min	−100.0	−42.4	−44.0	−3, 345.1	−42.0	−42.1	−224.3	−146.8
Max	67.9	50.2	50.6	1, 740.0	50.2	50.2	218.2	135.4
Mean	−11.8	0.0	−0.1	0.1	0.0	0.0	0.1	0.1
Std	17.1	*3.7*	3.8	60.6	*3.7*	*3.7*	8.4	5.4
RMS	20.8	3.7	3.8	60.6	3.7	3.7	8.4	5.4

Units: [cm]

the prediction one. A bin size of 20 km was chosen for the analytical covariance functions, while points up to distances of 300 km from the prediction point have been used. Initially, the empirical covariance function model was calculated in order to represent the local statistical characteristics. If each observation y_i represents a small area A_i and y_j represents an area A_j then the empirical covariance is (Tscherning and Rapp 1974):

$$Ck = \frac{\sum AiAjyiyj}{\sum AiAjk}. \tag{1}$$

If the area is subdivided into small cells holding one observation each and Ai and Aj are assumed to be equal then Eq. (1) reduces to:

$$Ck = \frac{\sum yiyj}{\sum Nk}, \tag{2}$$

where N_k is the number of products y_i y_j in the k^{th} interval (Knudsen 1987). In our case the empirical covariances of SLA (h^{SLA}) for a given spherical distance ψ is:

$$Ck = \left(h_i^{SLA}, h_j^{SLA}, \psi\right) = M\left\{h_i^{SLA}, h_j^{SLA}\right\}_{\psi}. \tag{3}$$

where $M\left\{h_i^{SLA}, h_j^{SLA}\right\}_{\psi}$ is the mean value of products between h_i^{SLA} and h_j^{SLA} which are included in the bin size of 20 km.

The analytical covariance function models employed have been based on four exponential, one polynomial and two Gauss-Markov models (Natsiopoulos et al. 2016; Vergos et al. 2013), as:

$$C_{h^{SLA}h^{SLA}}(\psi) = a\mathrm{e}^{(b\psi)} + c\mathrm{e}^{(d\psi)}, \tag{4}$$

$$C_{h^{SLA}h^{SLA}}(\psi) = a\mathrm{e}^{(-b\psi^2 - c\psi)}, \tag{5}$$

$$C_{h^{SLA}h^{SLA}}(\psi) = a\mathrm{e}^{(-(\psi/b)^2)} + c\mathrm{e}^{(-((\psi-d)/u)^2)}, \tag{6}$$

$$C_{h^{SLA}h^{SLA}}(\psi) = a\mathrm{e}^{(-b\psi)}\cos(c\psi), \tag{7}$$

$$C_{h^{SLA}h^{SLA}}(\psi) = a\psi^3 + b\psi^2 + c\psi + d. \tag{8}$$

In Eqs. (4)–(8), a, b, c and d denote parameters to be determined, so that the analytical covariance model will fit the empirical one, ψ is the spherical distance and $\psi k - 1 < \psi ij < \psi k$. The 2nd and 3nd order Gauss-Markov models are outlined in Eqs. (9) and (10) respectively, where D is the characteristic distance, r is the planar distance and $\sigma^2_{h^{SLA}}$ the SLA variance (Jordan 1972; Knudsen and Tscherning 2007):

$$C_{h^{SLA}h^{SLA}}(r) = \sigma^2_{h^{SLA}}\left(1 + \frac{r}{D}\right)e^{(-\frac{r}{D})}, \tag{9}$$

$$C_{h^{SLA}h^{SLA}}(r) = \sigma^2_{h^{SLA}}\left(1 + \frac{r}{D} + \frac{r^2}{3D^2}\right)e^{(-\frac{r}{D})}. \tag{10}$$

The above models are represented as model A, B, ..., G in the following tables, in order to make it easier to read. The estimation is carried out as (Knudsen and Tscherning 2007; Tscherning and Rapp 1974):

$$\hat{\boldsymbol{h}}^{SLA}(P) = \boldsymbol{C}_{\hat{h}^{SLA}h^{SLA}}(P,\cdot)\,\boldsymbol{C}^{-1}_{h^{SLA}h^{SLA}}\boldsymbol{h}^{SLA} \tag{11}$$

In Eq. (11), $\hat{\boldsymbol{h}}^{SLA}(P)$ denotes the SLA to be predicted at point P, $\boldsymbol{h}^{SLA}$ is the vector of observations, $\boldsymbol{C}_{\hat{h}^{SLA}h^{SLA}}(P,\cdot)$ is the cross-covariance matrix between the SLA to be predicted and the input signals and $\boldsymbol{C}^{-1}_{h^{SLA}h^{SLA}}$ is the full variance-covariance matrix of the input SLA determined from the used analytical covariance function model.

3 Numerical Results for Mediterranean Sea

In the sequel, the results from the evaluation of alternative analytical covariance function models are presented. Table 1 presents the statistics of the initial SLA dataset and its

differences with the predicted ones using the aforementioned analytical covariance function models. From Table 1 it can be seen that the accuracy of SLA values is improved using LSC method, as indicators precision are taken into account at original ones. All models present a mean value close to zero, whereas simultaneously the exponential models A and D and the polynomial model E provide the optimum results with a std at the 3.70 cm, 3.72 cm and 3.69 cm respectively. The exponential model B provides a std at the 3.76 cm, which can also be accepted for a subsequent prediction. In this paper were chosen the three optimum models for further investigation. The 2nd and 3rd order Gauss Markov models provide a std at the 8.38 cm and 5.44 cm respectively, which can be considered as larger compared to that of the exponential and polynomial models. The exponential model C presents the worst fitting at initial data with a std at the 60.60 cm, both in open sea and close to coastline.

Models A, D and E were then chosen to carry-out SLA estimation close to the coastline. In order to predict those SLA values with high prediction accuracy, the input data were separated in 10 windows each spanning 10° (see Fig. 2). The concept is that locally estimated analytical covariance functions will depict the SLA variability better compared to a global Mediterranean-wide one. The estimation was carried-out to specific points up to a radius of 100 km from the coastline. From this set of points, those within a distance of 15 km from the coastline were the prediction ones, whereas those between 16 km and 100 km were the ones acting as the input since they are located in the open water. This scenario resembles the case where altimetry data are available in purely marine areas and they need to be interpolated and/or extended close to the coastline. Table 2, presents the statistics of the differences between the original SLAs and those predicted with the chosen analytical covariance function models A, D and E.

From above table, it can be seen that using LSC SLA prediction is carried out with reasonable accuracy in all windows except windows 8 and 10. In window 8 an initial std at the 11.20 cm was calculated, whereas for the exponential model A the accuracy is at the 5.13 m, which indicates that this model does not fit well to the dataset. Model E in the same window provides also a worse std compared to the initial values at the 15.30 cm, whereas the exponential model D provides a std at the 7.70 cm, which can be considered as acceptable, despite the fact that it is at the almost equal to the input std. In window 10 the SLA has a std of 22.32 cm, while model E provides a prediction accuracy of 26.66 cm. Model A and Model D provide a better std than that of the initial one at the 8.65 cm and 8.64 cm respectively. The optimum prediction accuracy is achieved for window 3 and specifically for the polynomial model E at the 3.63 cm, which is smaller by 63% compared to the error of the input data, if one considers the std as an indication of the variability of the input field. Models A and D in the same window present also high prediction accuracy at the 4.47 cm and 3.71 cm respectively. The same behavior is also see for window 2 with a std at the 3.98 cm, 3.97 cm and 3.88 cm for Models A, D and E, respectively. In window 4 the SLA has a std of 12.71 cm and the prediction accuracy reaches 7.05 cm, 6.66 cm and 7.09 for model A, D and E respectively. Window 5 presents slightly worse prediction accuracy at the 8.80 cm, 7.29 cm and 7.89 cm. For window 1, polynomial model E presents the best results at the 7.76 cm compared to the others optimum models A and D in the same window which provide a std at the 11.81 cm and 12.09 cm respectively. This worst performance

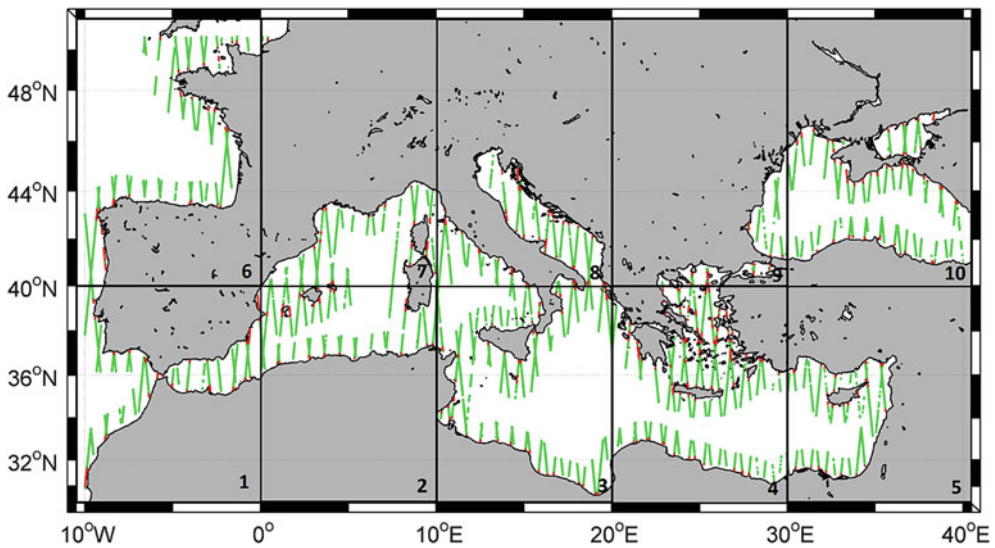

Fig. 2 Satellite altimetry data availability at a radius of 15 km (*red*) and 85 km (*green*) from the coastline within the 10° × 10° windows

Table 2 Statistics of initial SLAs and differences with the estimated ones for all 10 windows (pts: points)

1 [87 pts]	Initial	Model A	Model D	Model E	6 [70 pts]	Initial	Model A	Model D	Model E
Min	−47.6	−33.4	−35.1	−24.0	Min	−90.1	−27.1	−66.4	−64.9
Max	35.5	37.8	37.7	37.8	Max	29.4	26.8	22.9	23.1
Mean	−8.3	−4.3	−4.4	−1.1	Mean	−5.4	−1.8	1.0	1.2
Std	19.4	11.8	12.1	7.8	Std	18.9	8.8	12.2	12.1
RMS	21.1	12.6	12.9	7.8	RMS	19.6	9.0	12.2	12.2
2 [53 pts]	Initial	Model A	Model D	Model E	7 [41 pts]	Initial	Model A	Model D	Model E
Min	−38.6	−9.0	−9.2	−9.1	Min	−101.6	−68.9	−68.9	−64.9
Max	−3.1	10.2	10.8	10.8	Max	−7.5	14.9	17.5	23.1
Mean	−24.4	1.5	1.4	1.4	Mean	−34.6	−3.9	−3.7	1.2
Std	8.5	4.0	4.0	3.9	Std	15.2	12.4	12.5	12.1
RMS	25.8	4.3	4.2	4.1	RMS	37.8	13.0	13.0	12.2
3 [70 pts]	Initial	Model A	Model D	Model E	8 [80 pts]	Initial	Model A	Model D	Model E
Min	−38.6	−10.5	−11.8	−11.3	Min	−49.8	−3, 593.5	−34.6	−93.1
Max	9.1	8.1	9.0	7.6	Max	7.9	9.2	11.3	13.8
Mean	−16.2	0.6	0.3	0.2	Mean	−24.5	−129.4	−3.6	−6.2
Std	10.2	4.5	3.7	3.6	Std	11.2	513.1	7.7	15.3
RMS	19.1	4.5	3.7	3.6	RMS	27.0	529.2	8.5	16.5
4 [172 pts]	Initial	Model A	Model D	Model E	9 [29 pts]	Initial	Model A	Model D	Model E
Min	−73.1	−40.3	−22.9	−26.1	Min	−100.0	−11.3	−9.0	−93.1
Max	6.9	22.7	34.9	32.3	Max	67.8	45.6	47.6	13.8
Mean	−20.8	−2.1	−0.8	−0.9	Mean	−5.6	2.2	2.3	−6.2
Std	12.7	7.1	6.7	7.1	Std	31.5	11.9	11.9	15.3
RMS	24.3	7.4	6.7	7.1	RMS	32.0	12.1	12.1	16.5
5 [41 pts]	Initial	Model A	Model D	Model E	10 [91 pts]	Initial	Model A	Model D	Model E
Min	−49.2	−27.1	−17.1	−17.8	Min	−42.6	−41.0	−40.9	−122.1
Max	23.2	26.8	20.0	19.5	Max	70.7	24.1	24.0	41.0
Mean	−17.7	−1.8	−0.2	0.4	Mean	19.8	2.1	2.1	−1.7
Std	14.6	8.8	7.3	7.9	Std	22.3	8.7	8.6	26.7
RMS	22.9	9.0	7.3	7.9	RMS	29.8	8.9	8.9	26.7

Units: [cm]

by almost 4 cm is seen for window 6 as well, in which the exponential model A provides a std at the 8.80 cm, whereas exponential model D and polynomial model E give 12.18 cm and 12.10 cm respectively. Windows 7 and 9 provide results with a std more than 10 cm, but simultaneously better than that of initial ones. Specifically, window 7 presents a std at the 12.38 cm, 12.45 cm and 12.10 cm and window 9 provides a std at the 11.90 cm, 11.88 cm and 15.28 cm for the three optimum models A, D and E respectively. From the above results it can be concluded that the highest std is provided by the prediction windows with good distribution of points, that act as the input data for the calculation of analytical covariance functions, around the prediction points. For example, window 5 presents for the exponential model A a std smaller by 40% compared to the corresponding model in window 9, for exponential model D a std smaller by 44% and for polynomial model E a std smaller by 54%.

In order to evaluate the three optimum analytical covariance function model and different scenarios for the distribution of the input data, a point was randomly selected for a Greek area close to coastline (see Fig. 3). The above prediction strategy was carried out once more, utilizing three different approaches concerning the distribution of points which act as the input data for the calculation of the analytical covariance functions and the prediction. Table 3, presents the differences between the original SLAs and those predicted from the three alternative scenarios. For the first test, all points within window 4, where the estimation point is located, were chosen. For the second test a window of 2° (∼220 km) around the estimation point was chosen and for the third test all points within the entire Mediterranean basin were taken into account.

From Table 3 it can be seen that model D provides the smallest differences for all three scenarios. Specifically, for

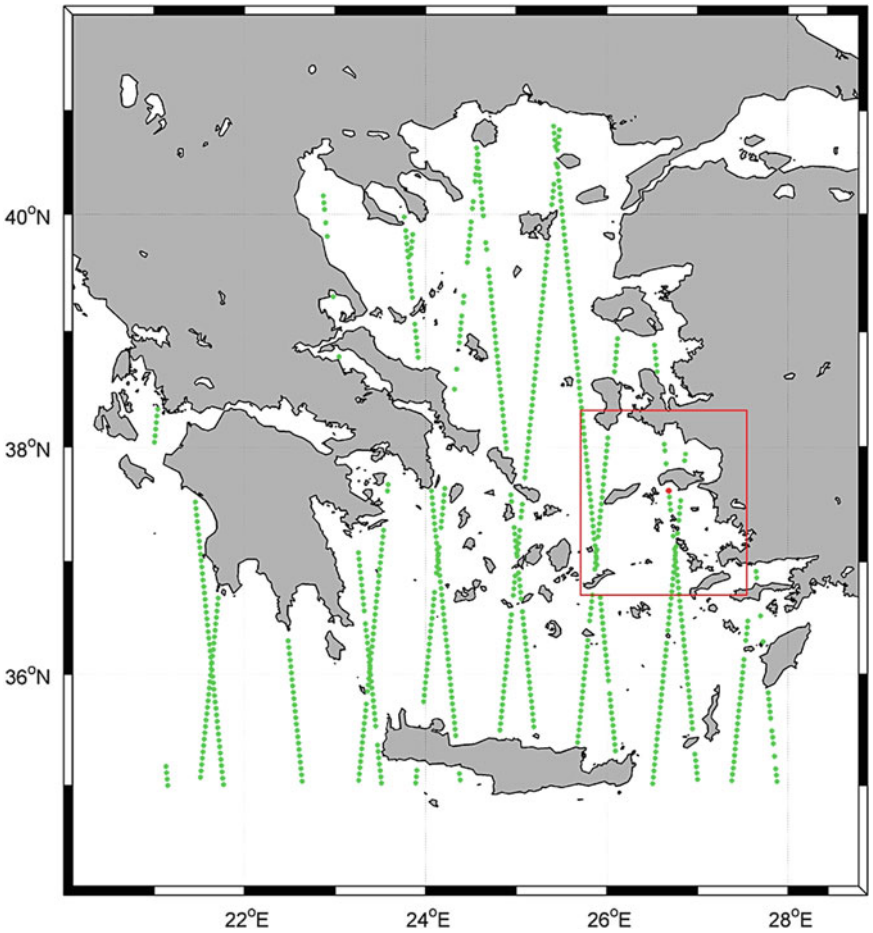

Fig. 3 Cryosat-2 data availability around the prediction point

Table 3 Differences between the original altimetry SLA value and the estimated ones for three alternative scenarios

Point code	Latitude (°)		Longitude (°)		Initial SLA value (cm)	
	37.569032		26.689857		−26.80	
7287	SLA estimation	Difference (1)	SLA estimation	Difference (2)	SLA estimation	Difference (3)
Model A	−24.0	−2.8	−27.0	−0.2	−23.6	−3.2
Model D	−26.8	0.0	−26.8	0.0	−26.9	−0.1
Model E	−26.7	−0.1	−26.9	−0.1	−26.5	−0.4

Units: [cm]

Model A the best results are given from scenario 2 with a difference at 0.15 cm. Scenario 1 and 3 provide a difference at the 2.8 cm and 3.23 cm respectively. Exponential model D presents differences less at the 0.03, 0.04 and 0.09 cm level with the optimal results being achieved when the points located in the immediate vicinity of the prediction point are considered. Polynomial Model E gives also good results at the 0.14, 0.09 and 0.35 cm. From the above we can conclude that scenario 2 gives the best results for this test case. This is due to the fact that only points around a small region of the prediction point were taken into account for the calculation of the analytical covariance functions, so that only the local variability of the LSA around the prediction point is considered, therefore within a radius of ∼220 km. In general, it will differ depending on the area extent around the prediction point and the amount of data within it, as well as on the quality of the sea level anomalies given proximity to land. Further statistical tests are needed for the bounds of the data used in the analytical function computation, as this case is based on the prediction of only one point.

4 Conclusions

A preliminary estimation of SLA values in the entire Mediterranean Sea was carried out using LSC and Cryosat-2 data, with the aim to investigate prediction errors in coast areas. Seven analytical covariance functions were

evaluated and the three best of these, i.e., Models A, D and E, were then used for the re-estimation of SLA values at points within a distance of 15 km from the coastline. The study area was separated at 10 windows each spanning 10° and locally estimated analytical covariance functions were calculated with the purpose to depict better the SLA variability compared to a global Mediterranean-wide covariance function. The higher prediction accuracy was achieved at the windows in which there are many data with good spatial distribution. In order to further investigate the performance of the optimum models, a point was randomly selected in the Aegean Sea close to the coastline. Then, three different scenarios of input data availability and distribution were evaluated. It was concluded that LSC provides high accuracy for the prediction of SLA values in areas with little or no data, especially close to the coastline, with an optimal selection radius of 220 km around the prediction point. The selection radius is based on the results of the present scenario set-up and can vary in other areas given sea/land setup and data availability. In that case, a sub-cm prediction accuracy can be achieved, with obvious applications in extending the sea level altimetry records from open sea to coastal areas.

References

Andersen OB, Piccioni G (2016) Recent Arctic Sea level variations from satellites. Front Mar Sci 3:76. doi:10.3389/fmars.2016.00076

Barzaghi R, Tselfes N, Tziavos IN, Vergos GS (2009) Geoid and high resolution sea surface topography modelling in the Mediterranean from gravimetry, altimetry and GOCE data: evaluation by simulation. J Geod 83(8):751–772. doi:10.1007/s00190-008-0292-z

Dumont JP, Rosmorduc V, Carrere L, Picot N, Bronner E, Couhert A, Guillot A, Desai, S, Bonekamp, H, Figa J, Scharroo R, Lillibridge J (2016) Jason-3 products handbook, SALP-MU-M-OP-16118-CN

Francis CR (2007) CryoSat mission and data description. CS-RP-ESA-SY-0059. ESTEC, Noordwijk

Gruber T, Gerlach C, Haagmans R (2012) Intercontinental height datum connection with GOCE and GPS-levelling data. J Geod Sci 2(4):270–280. doi:10.2478/v10156-012-0001-y

Jordan SK (1972) Self-consistent statistical models for the gravity anomaly, vertical deflections, and undulation of the geoid. J Geophys Res 77(20):3660–3670

Knudsen P (1987) Estimation and modelling of the local empirical covariance function using gravity and satellite altimeter data. Bull Geod 61:45–160

Knudsen P, Tscherning CC (2007) Error characteristics of dynamic topography models derived from altimetry and GOCE Gravimetry. In: Tregoning P, Rizos C (eds) IAG symposia "dynamic planet 2005 – monitoring and understanding a dynamic planet with geodetic and oceanographic tools", vol 130. Springer, Heidelberg, pp 11–16. doi:10.1007/978-3-540-49350-1_2

Moritz H (1980) Advanced physical geodesy, 2nd edn. Wichmann, Karlsruhe

Natsiopoulos DA, Vergos GS, Tziavos IN, Grigoriadis VN (2016) Sea level variability in the Mediterranean Sea through satellite altimetry analytical covariance functions. In: Rossikopoulos D, Fotiou A, Paraschakis I (eds) Special issue dedicated to the Emeritus Professor Christogeorgis Kaltsikis. Ziti Editions, Thessaloniki, pp 327–347

Pavlis NK, Holmes SA, Kenyon SC, Factor JK (2012) The development and evaluation of the earth gravitational model 2008 (EGM2008). J Geophys Res 117(B04):406. doi:10.1029/2011JB008916

RADS (2016) Available from: http://rads.tudelft.nl (Radar Altimeter Database System). Accessed May 2016

Scharroo R, Leuliette EW, Lillibridge JL, Byrne D, Naeije MC, Mitchum GT (2013) RADS: Consistent multi-mission products. European Space Agency "20 Years of progress in radar altimetry", ESA Publications SP-710

Tscherning CC, Rapp RH (1974) Closed covariance expressions for gravity anomalies, geoid undulations, and deflections of the vertical implied by anomaly degreevariance models. In: Reports of the Department of Geodetic Science, 208. The Ohio State University, Columbus

Vergos GS, Natsiopoulos DA, Tziavos IN (2013) Sea level anomaly and dynamic ocean topography analytical covariance functions in the Mediterranean Sea from ENVISAT data. European Space Agency "20 Years of progress in radar altimetry", ESA Publications SP-710

Wingham D, Francis C, Baker S, Bouzinac C, Brockley D, Cullen R, de Chateau-Thierry P, Laxon S, Mallow U, Mavrocordatos U, Phalippou L, Ratier G, Rey L, Rostan F, Viau P, Wallis D (2006) CryoSat: a mission to determine the fluctuations in earths land and marine ice fields. Adv Space Res 37:841–871. doi:10.1016/j.asr.2005.07.027

Spectral Analysis and Validation of Multiple Input/Multiple Output DOT Estimation in the Eastern Mediterranean Sea

Vassilios D. Andritsanos and Ilias N. Tziavos

Abstract

Fifteen years (2000–2015) of altimetric data from ERS2, ENVISAT, SARAL and GEOSAT-FOLLOW-ON satellites are optimally combined with in situ marine gravity observations employing the spectral Multiple Input/Multiple Output System Theory (MIMOST) for Dynamic Ocean Topography (DOT) estimation. The spectral behavior of the method is investigated by assimilating low frequency information from GOCE-derived geopotential models in a test area of the Eastern Mediterranean Sea. The frequency content of the reference field used in the reductions of the original observations and its effect to the DOT approximation is studied. The evolution of the annual DOT is validated against oceanographic information of recently available circulation models in the area under study. The effect of the reference field used in data reductions to the geostrophic circulation of the Eastern Mediterranean Sea is analyzed and remarks on the combination of gravity, altimetry and pure oceanographic data are outlined.

Keywords

DOT • Geostrophic circulation • GOCE geopotential models • Marine gravity • Satellite altimetry

1 Introduction

The separation between the geoid surface and the sea surface represents the well-known Dynamic Ocean Topography (DOT) in the open seas. This separation can reach the level of ±2 m in global scale (Mather 1975) and drops to some decimetres at closed seas. The knowledge of DOT is of main importance towards the definition of a consistent vertical system, since the height reference surface (geoid) can be connected with the sea surface by implementing in-situ or satellite measurements. This fact is essential for height systems unification procedures (e.g., Fotopoulos et al. 2005). The deviation of the Mean Sea Surface (MSS) from an equipotential surface is one of the major problems in the establishment of a unified height system based on classical sea surface observations at tide-gauges. The key to the connection of the sea surface observations with the equipotential surface of the geoid is the DOT. The latter can be divided into a quasi-stationary part which can be estimated over an averaged sea surface and a time-dependent part mainly due to wind and currents. The existence of the quasi-stationary part in the DOT signal was first analysed by Stommel (1965) using pure oceanographic data (temperature and salinity).

In this paper, the basic principles of the input/output system theory (IOST) (Bendat and Piersol 1986) and its spectral approximation, first introduced by Sideris (1996) and Sansò and Sideris (1997) for geodetic applications, are employed for the estimation of the stationary part of DOT.

V.D. Andritsanos (✉)
Geospatial Technology Lab, Department of Civil Engineering and Surveying & Geoinformatics Engineering, Technological Educational Institute of Athens, 12210 Athens, Greece
e-mail: vdandrit@teiath.gr

I.N. Tziavos
GravLab, Department of Geodesy and Surveying, Aristotle University of Thessaloniki, 54124 Thessaloniki, Greece

G. S. Vergos et al. (eds.), *International Symposium on Gravity, Geoid and Height Systems 2016*, International Association of Geodesy Symposia 148, DOI 10.1007/1345_2017_10

A generalized form of IOST, i.e. the Multiple Input/Multiple Output System Theory (MIMOST), mainly focused on the combination of heterogeneous data sets (see Andritsanos and Tziavos 2000; Andritsanos et al. 2000, 2001) is used in order to determine and validate a high resolution DOT model over the geodynamically active area of the Eastern Mediterranean Sea. Surface gravity data as well as altimetry observations are optimally combined in order to estimate the DOT signal and its approximation error over a 15 year (2000–2015) period. In addition, a combination scheme of the newly available GOCE-DIR5 geopotential model (Bruinsma et al. 2014) with EGM2008 (Pavlis et al. 2012) is investigated for the reduction of the observation signal within the available data sets. The evolution of the annual DOT is validated against oceanographic information of recently available circulation models for the area under study. The effect of the reference field used in data reductions to the geostrophic circulation of the Eastern Mediterranean Sea is analysed and some remarks on the combination of gravity, altimetry and pure oceanographic data are outlined.

2 Mathematical Background

A model of MIMOST can be used for the estimation of the DOT for a specific time period. The stationary character of the final estimate is preserved while the time-varying part is incorporated into the observation noise. A specific noise treatment must be applied to observations. Figure 1 depicts a MIMOST model for DOT estimation.

In Fig. 1, S_1 to S_n stand for the spectra of the input Sea Surface Heights (SSHs) signal, DG is the spectra of the shipborne gravity anomalies and T is the output spectra of DOT. H_{xoyo} is the optimal transfer function which connects the input signals with the output ones through an output noise minimization criterion (E_i; "i" stands for the error of each output signal). Detailed information about the structure of the aforementioned MIMOST system, the minimization criterion used and the final solution can be found in Andritsanos and Tziavos (2000), Andritsanos et al. (2000, 2001). The exact algorithm used in the DOT estimation is analyzed in Andritsanos and Tziavos (2000). The main drawback of MIMOST is that the input noise Power Spectral Density (PSD) must be known. In common geodetic practice, only the measurement noise variances are known and not the errors themselves in order to compute directly the respective error PSDs. Two different ways to manage the noise of MIMOST can be followed: (a) A simulated noise field of normal as well as uniform distribution and the direct computation of the error PSD using Fast Fourier Transform (FFT) and (b) PSD models of white or colored noise. In the specific case of altimetric data the repeated tracks of each satellite provide a PSD estimation procedure through a new variable definition (Sailor 1994). This new variable contains the statistical information of the observation noise as well as the assumed random time-varying part of DOT. It should be noticed that this assumption is not exactly valid in the case of slow-moving oceanographic features (Sailor 1994; Andritsanos et al. 2001). The deviations from a MSS are eliminated due to the import of the time-varying part into the error, the use of mean observations, and the average signal PSD. Therefore, the average PSD and data information, when introduced to a MIMOST, yields an estimation of DOT.

Given the DOT, the components of the geostrophic circulation velocity v and u can be estimated for the specific time period using the following equations in spherical approximation (e.g., Knudsen 1992):

$$u_s = -\frac{g}{fR}\frac{\partial QSST}{\partial \varphi}$$
$$v_s = \frac{g}{fR\cos\varphi}\frac{\partial QSST}{\partial \lambda} \quad (1)$$

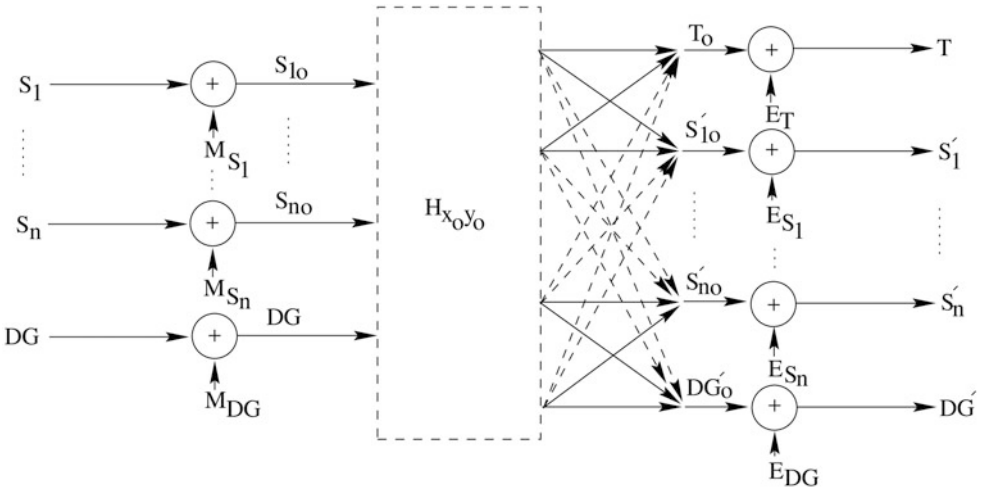

Fig. 1 A MIMOST model for DOT estimation in the eastern Mediterranean Sea using surface gravity and satellite altimetry data with reference to an assimilated GOCE geopotential model

where g is the gravity at the specific point, R a mean Earth radius and

$$f = 2\Omega \sin\varphi \tag{2}$$

is the Coriolis force component. Ω stands for the angular velocity of the Earth.

3 Results and Discussion

3.1 Test Area and Data Combination Scheme

A combination scheme is applied for the estimation of yearly DOT in the Eastern Mediterranean Sea. This test area was selected due to its main geophysical and geodynamic features, i.e. the dominated extension of the Hellenic Trench, the boundary between the Eurasian and the African tectonic plates, the Mediterranean Ridge, the Eratosthenes Basin, the Herodotus Seamount and the Levantine Basin. These geophysical and geodynamic characteristics produce some special circulation features named Mid Mediterranean Jet, Cretan Cyclone, Ierapetra and Mersa-Matruh Anticyclone and Rhodes gyre (see also Fig. 2). The bounds of the area under study are $32° \leq \varphi \leq 35°$ and $22° \leq \lambda \leq 34°$ and a representation is depicted in Fig. 2.

For the efficient yearly DOT estimation and the associated geostrophic flow marine gravity data from various campaigns (BGI 2012) were combined optimally using MIMOST with altimetry derived SSHs collected by four satellites (ERS2, ENVISAT, Geosat-Follow-On, SARAL/Altika) in the last 15 years. The satellites used in the annual consideration of DOT and the geostrophic circulation are shown in Table 1.

47,241 shipborne marine gravity anomalies, collected in the frame of various campaigns during a temporal interval of 50 years (1934–1988) with a spatial resolution varying between 5 and 10 km, were used in conjunction with EGM2008 global geopotential model. The accuracy information of the gravity anomaly database is not available (BGI 2012). In addition, information regarding low and medium frequency of the gravity anomaly signal from GOCE satellite mission was assimilated to the contribution of EGM2008. This enrichment was achieved following a spectral enhancement method for the validation of the GOCE contribution to the data reductions. This spectral enhancement technique is based on a step–by–step assimilation of GOCE signal to the EGM2008 gravity anomaly spectrum using a 20 degree rate according to equation:

$$\Delta g_{red} = \Delta g_{obs} - \left(\Delta g_{GOCE}^{n\,\max} + \Delta g_{EGM2008}^{n\,\max \to 2190}\right) \tag{3}$$

The combination solution is used towards the investigation of the effect of the low frequency information of the newly available GOCE geopotential models to the DOT estimation and geostrophic flow calculation. Previous studies indicate the increased accuracy in the low-band gravity field spectrum with the incorporation of GOCE satellite data (Vergos et al. 2014, 2015).

Table 1 The satellite used in the annual consideration of the DOT and the geostrophic flow

Year	Satellite(s)	Year	Satellite(s)
2000	E2	2008	EN, GFO
2001	E2, GFO	2009	EN
2002	E2, GFO	2010	EN
2003	EN, GFO	2011	EN
2004	EN, GFO	2012	EN
2005	EN, GFO	2013	AL
2006	EN, GFO	2014	AL
2007	EN, GFO	2015	AL

E2 ERS-2, *GFO* Geosat Follow-On, *EN* Envisat, *AL* Saral/Altika

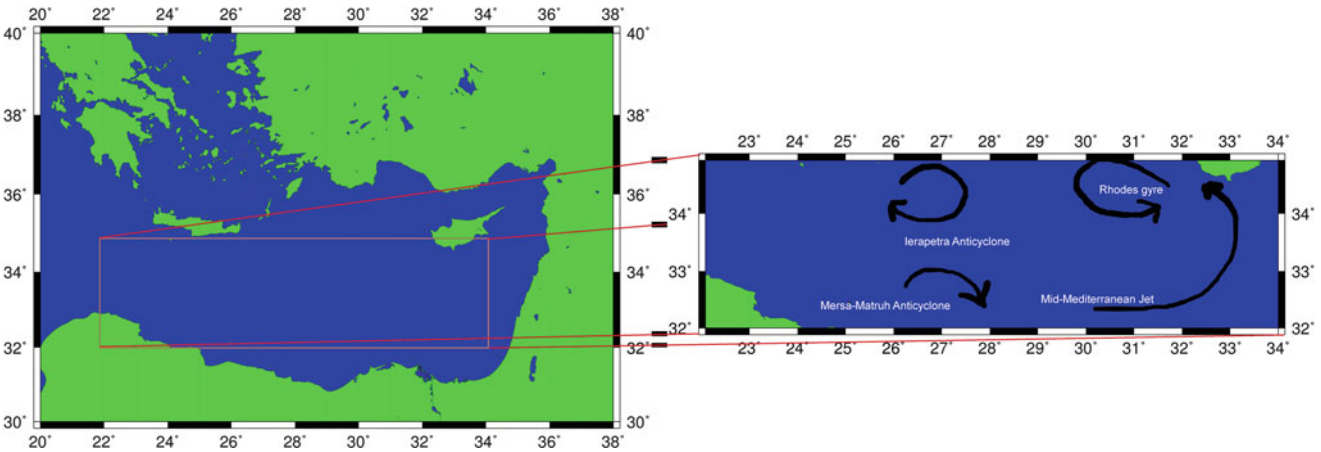

Fig. 2 The test area and the major oceanographic features in the *right* panel

An issue associated with the combination of altimetry data with seaborne gravity anomalies towards the DOT estimation is the different reference and tide systems used (Albertella and Rummel 2014). Seaborne gravity anomalies usually refer to GRS80 ellipsoid. Recent campaigns due to the use of GNSS positioning utilize WGS84 ellipsoid for gravity anomaly computations. On the other hand, Corrected SSHs (CORSSH), as well as corresponding satellite altimetry data are computed based on the so-called Topex/Poseidon ellipsoid (AVISO 2014). In addition, oceanographic data sets are defined in the mean-tide system (Albertella and Rummel 2014) while GNSS positioning refers to a tide-free system. A common tide-system must be maintained in all gravity and altimetry observations. Since the geodetic applications of the MSS include height system definition and unification and should be in line with geodetic positioning, a "conventional" tide-free system is chosen according to IERS (2010). Atlimetric observations h_{TPell} are transformed to WGS84 ellipsoid (h_{WGS84}) following (Heiskanen and Moritz 1967)

$$h_{WGS84} = h_{TPell.} - (a_{TPell.} - a_{WGS84}) + a_{TPell.}\sin^2\varphi\,(f_{TPell.} - f_{WGS84}) \quad (4)$$

and the transition from mean-tide (MT) to tide-free (TF) system for the altimetric data can be calculated by Albertella and Rummel (2014)

$$h_{MT} - h_{TF} = (1+k)\left(9.9 - 29.6\sin^2\varphi\right) \quad [cm] \quad (5)$$

where $k = 0.3$ is the conventional value of the Love number.

MIMOST is based on the spectral properties of the data used. Appropriate pre-processing is needed in order to minimize aliasing and spectral leakage effects due to the inherent problems of the discrete Fourier transform. In this study EGM2008 (Pavlis et al. 2012) global geopotential model complete to degree and order 2190 is used for gravity anomaly and CORSSH reductions.

3.2 GOCE Assimilation Effect to Data Reduction

The contribution of the recent available global geopotential models based on GOCE satellite is carried out by the spectral combination approach presented in the previous section. The last version of GOCE models computed by the Direct Method (GOCE-DIR5; Bruinsma et al. 2014) is combined with EGM2008 in order to calculate the data reductions. The maximum degree of GOCE DIR5 model was set to 100, 120, 140, 160 and 300 for an efficient examination of the assimilation effect to data reductions. Table 2 summarizes the effect of the different enhancement degree to the data reduction statistics.

Table 2 The statistics of data reduction using different assimilation degrees for GOCE – DIR5 model

	Max	Min	Mean	Std
Δg_{obs}	140.000	−260.900	−69.147	±64.336
$\Delta g_{red(GOCE100)}$	29.997	−29.999	−3.140	±7.852
$\Delta g_{red(GOCE120)}$	**29.836**	**−29.975**	**−3.109**	**±7.821**
$\Delta g_{red(GOCE140)}$	29.920	−29.965	−2.996	±7.853
$\Delta g_{red(GOCE160)}$	29.989	−29.995	−3.318	±7.917
$\Delta g_{red(GOCE300)}$	35.996	−35.999	−3.593	±10.889
$\Delta g_{redEGM2008}$	**29.985**	**−29.993**	**−3.162**	**±7.841**

Units in mGal

As seen from the statistics of Table 2, the combination of GOCE – DIR5 model coefficients with EGM2008 performed slightly better in terms of gravity data reduction, especially around nmax = 120. The incorporation of low and medium frequency information from GOCE models resulted in smoother gravity anomaly field. A requirement for MIMOST application is the proper reduction of the input field. GOCE low and medium frequency assimilation led to smoother reduced data than the use of the pure EGM2008 signal.

3.3 MIMOST DOT Estimation

The complete methodology for the yearly DOT estimation is presented in Andritsanos et al. (2001). In the present paper DOT estimation using MIMOST is achieved by the combination of CORSSH (AVISO 2014) and seaborne gravity anomalies. Both input data sets are reduced to EGM2008 model (2190 degree of expansion) and to the combined GOCE – DIR5 and EGM2008 models using maximum degree of expansion for GOCE – DIR5 100, 120, 140, 160 and 300, respectively, and the remaining contribution derived from EGM2008 up to degree 2190.

The statistics of the estimated yearly DOT as well as the estimated error standard deviation (std) of the MIMOST solution with reference to EGM2008 are presented in Table 3.

The respective DOT estimation for the year 2000 is depicted in Fig. 3.

Some basic features indicating the geostrophic circulation in the area under study can be identified in Fig. 3. The same hydrographical features are presented in other studies using different data sources (both geodetic and oceanographic) as well as different estimation methods, e.g., Limpach et al. (2006), Rio et al. (2007), Hainbucher et al. (2014) and Rio et al. (2014). In Fig. 3 features of the Cretan Cyclone can be observed at south, southwest of the island of Crete, the Ierapetra Anticyclone is depicted in the area $34° \le \varphi \le 35°$ and $25° \le \lambda \le 29°$, and, finally, the Mid-Mediterranean Jet

and the Mersa-Matruh Anticyclone are identified in the south part of the map.

A remarkable effect is observed over the 2009–2010 time period. Figure 4 represents the estimated DOT for year 2009, which shows an increase at the level of 50.5 cm on average as compared with the corresponding estimation of the year 2000 (see Fig. 3). This significant difference for this period is also identified in other studies, see, e.g., Figs. 7 and 8 in Fenoglio-Marc et al. (2014), Fig. 4e, f in Bonaduce et al. (2016) and Natsiopoulos et al. (2015).

After 2010, DOT is restored gradually to its previous state. Finally, 2015 estimation is approximately the same as that of the 2000 solution, as can be seen in the statistics of Table 3.

Table 3 Statistics of the estimated yearly DOT and the error std. of MIMOST method (EGM2008 reference field)

Year	Max (m)	Min (m)	Mean (m)	Std (m)	Error std (cm)
2000	**0.888**	**−0.650**	**−0.013**	**±0.212**	**±4.92**
2001	0.708	−0.776	−0.109	±0.212	±4.22
2002	0.883	−0.635	0.013	±0.208	±3.43
2003	1.124	−0.509	0.159	±0.209	±3.31
2004	0.980	−0.428	0.134	±0.210	±3.20
2005	1.084	−0.486	0.159	±0.214	±2.82
2006	0.942	−0.576	0.100	±0.219	±3.13
2007	0.964	−0.506	0.116	±0.204	±3.08
2008	1.073	−0.398	0.230	±0.206	±3.38
2009	**1.366**	**−0.166**	**0.492**	**±0.211**	**±4.86**
2010	**1.334**	**−0.180**	**0.450**	**±0.219**	**±5.02**
2011	**1.285**	**−0.366**	**0.331**	**±0.223**	**±5.02**
2012	1.083	−0.399	0.239	±0.209	±4.07
2013	0.809	−0.715	−0.085	±0.210	±3.80
2014	0.734	−0.786	−0.151	±0.207	±3.99
2015	**0.808**	**−0.676**	**−0.046**	**±0.216**	**±3.83**

3.3.1 Geopotential Model Effect

The effect of the geopotential model employed in data reduction prior to their input into MIMOS is also studied in this research. The differences between the yearly DOT estimates are computed using EGM2008 and combined EGM2008/GOCE – DIR5 models as reference fields. Maximum degree of GOCE – DIR5 contribution is set to 100, 120, 140, 160 and 300 degree, respectively, in the combination schemes. The yearly DOT estimates are affected by the choice of the geopotential model. As the degree of the assimilation of GOCE – DIR5 coefficients increases, more effects on the DOT estimation are noticed. It is worth mentioning that the large differences revealed along the land/sea boundary indicate the satellite altimetry ineffectiveness close to seashore. This geopotential model effect shows the same behavior even over the period 2009–2011. At that time, a significant difference in the estimation of DOT is reported in several studies (see, e.g., Fenoglio-Marc et al. 2014; Natsiopoulos et al. 2015).

3.3.2 DOT by MIMOST and Synthetic Models

The major oceanographic features of the Eastern Mediterranean Sea detected by the MIMOST-based DOT can be also identified in synthetic models, where data from oceanographic campaigns and satellite altimetry missions were used. Two models of DOT are discussed in our study, which were developed by Rio et al. (2007) and Rio et al. (2014), respectively. In both models in situ oceanographic measurements with altimetric data and global geopotential solutions were combined.

Apart from the fact that the dominant oceanographic features of the test area are detected by the three DOT models, a direct and more detailed comparison between them cannot be carried out, since the resolution of the MIMOST DOT model and that of the two synthetic models

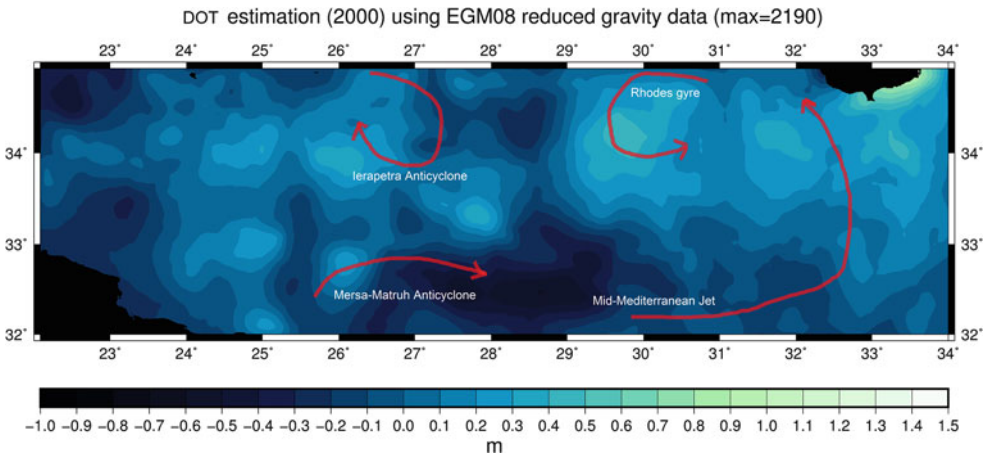

Fig. 3 DOT estimation by MIMOST for year 2000 along with the dominant oceanographic features of the test area

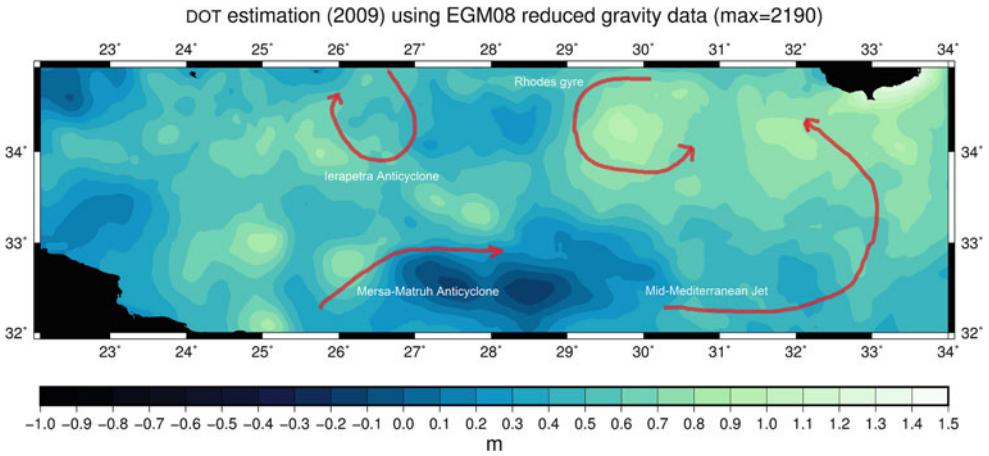

Fig. 4 DOT estimation by MIMOST for year 2009 along with the dominant oceanographic features of the test area and the increased MSS as compared with that of the year 2000

Table 4 The statistics of the v-component of the geostrophic flow estimation using EGM2008 only and combined GOCE DIR v5/EGM2008 reference geopotential model

v-comp (m/s)	Max	Min	Mean	Std
EGM08 based	2.854	−2.341	−0.026	±0.515
GOCE DIR v. 5 to 100 + EGM08	**1.146**	**−0.913**	**0.002**	**±0.129**
GOCE DIR v. 5 to 120 + EGM08	**1.254**	**−0.823**	**0.000**	**±0.138**
GOCE DIR v. 5 to 140 + EGM08	**1.130**	**−0.913**	**0.000**	**±0.135**
GOCE DIR v. 5 to 160 + EGM08	1.285	−0.790	−0.001	±0.136
GOCE DIR v. 5 to 300 + EGM08	2.562	−2.289	−0.009	±0.333

Table 5 The statistics of the u-component of the geostrophic flow estimation using EGM2008 only and combined GOCE DIR v5/EGM2008 reference geopotential model

u-comp (m/s)	Max	Min	Mean	Std
EGM08 based	2.148	−2.657	−0.042	±0.545
GOCE DIR v. 5 to 100 + EGM08	**1.623**	**−2.092**	**−0.006**	**±0.126**
GOCE DIR v. 5 to 120 + EGM08	**1.408**	**−2.156**	**−0.006**	**±0.136**
GOCE DIR v. 5 to 140 + EGM08	**1.636**	**−2.093**	**−0.001**	**±0.129**
GOCE DIR v. 5 to 160 + EGM08	1.382	−2.131	0.010	±0.140
GOCE DIR v. 5 to 300 + EGM08	2.486	−3.192	−0.006	±0.274

is different. This is due to the marine gravity data sets used in the development of the MIMOST model, the different period of analysis (yearly in MIMOST against multi-annual analysis in synthetic models) and the level of reference hypothesis adopted in the oceanographic solution. An appropriate filtering of the MIMOST solution is needed in order to produce a comparable solution to that derived by the synthetic data. The filtering methodology of the MIMOST solution is under preparation and will appear in a forthcoming paper.

3.4 Estimation of Geostrophic Circulation by MIMOST

The surface current velocities are estimated on the basis of the assumption of geostrophic flow. The effect of GOCE assimilation to the reduction of gravity data towards the approximation of geostrophic circulation is investigated as well. Tables 4 and 5 present the effect of GOCE assimilation to the estimation of the v- and u-component of the geostrophic circulation in the area under study.

It can be seen that the incorporation of GOCE low frequency information led to more realistic estimates of the geostrophic velocities, especially at the 100–140 degree band. The main drawback of the geostrophic assumption, due to the presence of land, results in extreme velocity values near the seashore in the south-west and north-east regions of the test area. This fact can also be seen in the synthetic solutions which are based on pure oceanographic information (see Fig. 5). A visual inspection of the DOT models represented in Fig. 5 shows that identical hydrographic features were revealed by the three solutions.

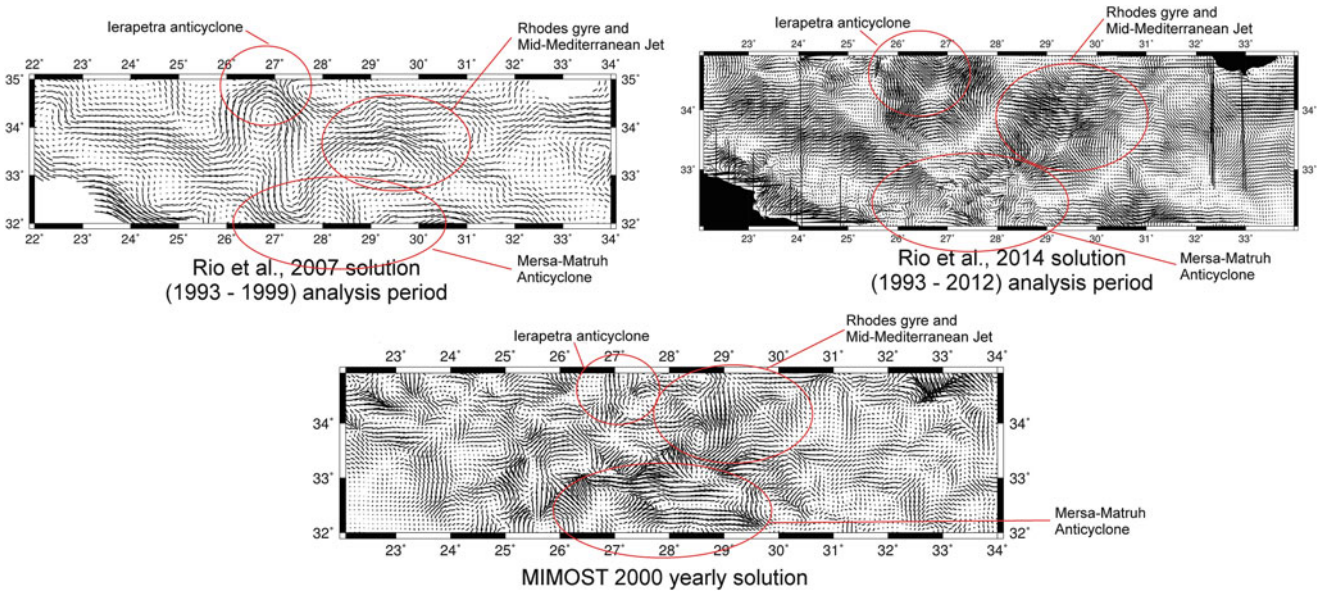

Fig. 5 The geostrophic circulation estimation using different solutions (synthetic and MIMOST models) and the geophysical features revealed in the test area

4 Conclusions

The assimilated GOCE global geopotential model contributed to data pre-processing and led to a smoother gravity anomaly field than that derived by the contribution of EGM2008. A slight improvement in terms of std. and mean value of the reduced data is noticed, especially when using GOCE harmonic coefficients up to degree 120.

The yearly DOT estimated field by the MIMOST method revealed some interesting features, associated with the hydrographic characteristics of eastern Mediterranean. These features are also observed when comparing MIMOST solution with the synthetic models for the same test area, which were primarily based on in-situ oceanographic information.

More realistic estimates of the geostrophic circulation of the sea surface are computed with the incorporation of GOCE low band frequency information to MIMOST solution. Especially, the assimilation of GOCE information up to degree 120 led to reasonable velocity values at the central part of the test area, far from land masses. An appropriate filtering of the final DOT solution will produce comparable results between the MIMOST gravity-based solution and the synthetic models. This topic will be further discussed and presented in a future research paper.

References

Albertella A, Rummel R (2014) GOCE geoid, mean dynamic topography and geostrophic velocities. Centre of Geodetic Earth System Research Report no 6, Munich, Germany

Andritsanos VD, Tziavos IN (2000) Estimation of gravity field parameters by a multiple input/output system. Phys Chem Earth A 25(1): 39–46

Andritsanos VD, Sideris MG, Tziavos IN (2000) A survey of gravity field modelling applications of the Input-Output System Theory (IOST). IGeS Bull 10:1–17

Andritsanos VD, Sideris MG, Tziavos IN (2001) Quasi-stationary sea surface topography estimation by the multiple input/output method. J Geod 75:216–226

AVISO (2014) DT CorSSH product handbook. CLS-DOS-NT-14.077, Aviso Altimetry, CNES, France

Bendat JS, Piersol AG (1986) Random data: analysis and measurement procedures. Wiley, New York

Bonaduce A, Pinardi N, Oddo P, Spada G, Larnicol G (2016) Sea-level variability in the Mediterranean Sea from altimetry. Clim Dyn. doi:10.1007/s00382-016-3001-2

Bruinsma SL, Förste C, Abrikosov O, Lemoine J-M, Marty J-C, Mulet S, Rio M-H, Bonvalot S (2014) ESA's satellite-only gravity field model via the direct approach based on all GOCE data. Geophys Res Lett 41. doi:10.1002/2014GL062045

Bureau Gravimétrique International – BGI (2012) The EOL/EOS format. Internet resources. http://bgi.omp.obs-mip.fr/content/download/720/4949/file/BGI_EOL_EOS_Data_format.pdf

Fenoglio-Marc L, Dangendorf S, Becker M, Jensen J, Wahl T, Sannino G (2014) Regional sea level rise in the North Sea and Mediterranean basins. Presented at OSTST meeting "new frontiers of altimetry", Lake Constance, Germany, 27–31 Oct

Fotopoulos G, Tziavos IN, Sideris MG (2005) On the incorporation of sea surface topography in establishing vertical control. In: International Association of Geodesy symposia "gravity, geoid and space missions", Springer ed, vol 129, pp 185–190

Hainbucher D, Rubino A, Cardin V, Tanhua T, Schroeder K, Bensi M (2014) Hydrographic situation during cruise M84/3 and P414 (spring 2011) in the Mediterranean Sea. Ocean Sci 10: 669–692

Heiskanen WA, Moritz H (1967) Physical geodesy. W.H. Freeman, San Francisco

IERS (2010) In: Petit G, Luzum B (eds) IERS Conventions 2010. Technical Note no 36. Verlag des Bundesamts für Kartographie und Geodäsie, Frankfurt am Main. ISBN 3-89888-989-6

Knudsen P (1992) Altimetry for geodesy and oceanography. In: Kakkuri J (ed) Geodesy and geophysics. Finnish Geodetic Institute, Kirkkonummi, pp 87–129

Limpach P, Geiger A, Kahle H-G (2006) Sea surface topography by airborne laser altimetry and offshore GPS Buoys in the Eastern Mediterranean: comparison with JASON-1 altimeter data and GRACE gravity field. Presented at geodetic week 2006, 10–12 Oct, Munich, Germany

Mather RS (1975) On the evaluation of stationary sea surface topography using geodetic techniques. Bull Géod 115:65–82

Natsiopoulos DA, Vergos GS, Tziavos IN, Grigoriadis VN (2015) Sea level variability in the Mediterranean Sea through satellite altimetry analytical covariance functions. In: Measuring and mapping the earth. Special volume for Prof. Emer. C. Kaltsikis, Aristotle University of Thessaloniki

Pavlis NK, Holmes SA, Kenyon SC, Factor JK (2012) The development and evaluation of the Earth Gravitational Model 2008 (EGM2008). J Geophys Res 117(B4):2156–2202. doi:10.1029/2011JB008916

Rio M-H, Poulain P-M et al (2007) A mean dynamic topography of the Mediterranean Sea computed from altimetric data, in-situ measurements and a general circulation model. J Mar Syst 65: 484–508

Rio M-H, Pascual A, Poulain P-M, Menna M, Barceló B, Tintoré J (2014) Computation of a new mean dynamic topography for the Mediterranean Sea from model outputs, altimeter measurements and oceanographic in situ data. Ocean Sci 10:731–744

Sailor RV (1994) Signal processing techniques. In: Vanicek P, Christou NT (eds) Geoid and its geophysical interpretations. CRC Press, Boca Raton, pp 147–185

Sansò F, Sideris MG (1997) On the similarities and differences between systems theory and least-squares collocation in physical geodesy. Boll Geod Sci Aff 2:174–206

Sideris MG (1996) On the use of heterogeneous noisy data in spectral gravity field modelling methods. J Geod 70:470–479

Stommel H (1965) The Gulf stream: a physical and dynamical description. University of California Press, Berkeley

Vergos G, Grigoriadis V, Tziavos IN, Kotsakis C (2014) Evaluation of GOCE/GRACE global geopotential models over Greece with collocated GPS/levelling observations and local gravity data. In: Marti U (ed) Gravity, geoid and height systems. International Association of Geodesy symposia, vol 141. Springer International Publishing Switzerland, Cham, pp 85–92. doi:10.1007/978-3-319-10837-7_11

Vergos GS, Andritsanos VD, Grigoriadis VN, Pagounis V, Tziavos IN (2015) Evaluation of GOCE/GRACE GGMs over Attika and Thessaloniki, Greece, and Wo determination for height system unification. International Association of Geodesy symposia, vol 145. Springer International Publishing Switzerland, New York. doi:10.1007/1345_2015_53

Preliminary Results on the Estimation of Ground Water in Africa Using GRACE and Hydrological Models

Hussein A. Abd-Elmotaal, Atef Makhloof, Ayman A. Hassan, and Hussein Mohasseb

Abstract

Groundwater is a main source of fresh water in many parts of the world. Monitoring the global and regional groundwater resources is challenging nowadays because of the very scare and high cost in situ measurement networks, especially in Africa. Satellite gravimetry can be used in combination with land surface hydrological models (e.g., Global Land Data Assimilation System (GLDAS) and WaterGAP Global Hydrology Model (WGHM)) to infer groundwater storage behavior. Since 2002, the Gravity Recovery and Climate Experiment (GRACE) satellite mission provides estimation of the Earth's dynamic gravity field with unprecedented accuracy. Differences between monthly GRACE gravity field solutions give an estimation of the Terrestrial Water Storage (TWS) changes. The groundwater storage can be obtained using the available hydrological models by subtracting the surface water, soil moisture, snow, ice and canopy water from the TWS. GRACE data are available in terms of spherical harmonics expansion. However, GLDAS and WGHM hydrological models are available in the space domain as grids of 1° and 0.5°, respectively. For consistency, both GLDAS and WGHM are approximated in terms of spherical harmonic expansions to be comparable with the used GRACE data. In this paper, the groundwater storage in Africa is studied using GRCAE data (2003–2016) as well as GLDAS and WGHM models for the same time period. Inter annual variations is investigated from monthly groundwater time series.

Keywords

GLDAS · GRACE · Groundwater storage estimation · Terrestrial Water Storage (TWS) · WGHM

1 Introduction

Groundwater is an important part of the water cycle. In Africa, groundwater is considered as one of the major resources of fresh water. The total groundwater storage in Africa is estimated to be approximately 0.66 million km^3 (MacDonald et al. 2012). Not all of this groundwater storage is available for discharge, but it is estimated to be more than 100 times that of annual renewable freshwater resources in Africa. Groundwater resources are unequal distributed, while the largest found in the large aquifers in the North African countries like Libya, Algeria, Egypt and Sudan (MacDonald et al. 2012). Groundwater was normally monitored by traditional instruments, e.g. Ground Penetrating Radar (GPR), and nets of wireless sensors. However, global groundwater storage and its variability are difficultly monitored due to the lack of comprehensive global monitoring network with high cost and strong labor intensity (Jin and Feng 2013).

H. A. Abd-Elmotaal (✉) · A. Makhloof · A. A. Hassan
Civil Engineering Department, Faculty of Engineering, Minia University, Minia, Egypt
e-mail: abdelmotaal@lycos.com

H. Mohasseb
Water and Wastewater Company, Minia, Egypt

G. S. Vergos et al. (eds.), *International Symposium on Gravity, Geoid and Height Systems 2016*, International Association of Geodesy Symposia 148, https://doi.org/10.1007/1345_2018_32

The Gravity Recovery and Climate Experiment (GRACE) mission, provides an unprecedented opportunity to detect continental water-storage variations with a spatial resolution of about 300 km (half wavelength) and monthly temporal resolution. Tapley et al. (2004) and Wahr et al. (2004) provided early results on the application of the GRACE products for detecting hydrological signals in different major river basins (e.g., Amazon basin and Mississippi River). Although it has relatively low spatial and temporal resolutions, GRACE has the ability to sense the changes in total water storage in all levels; including groundwater, as well as surface water (Rodell et al. 2009).

GRACE has been widely used in numerous studies to retrieve water storage variations, both globally and regionally. For instance, Ramillien et al. (2004, 2005) investigated the continental water storage variations using the first 2 years data GRACE, and compared these changes with the output from four global hydrological models in different drainage basins of the world. It was possible to correlate large scale hydrological events with the estimated change in the gravity field for certain areas of the world at an accuracy of 9 mm equivalent water thickness.

Few GRACE applications have been carried out to study water storage variations over Africa. Crowley et al. (2006) estimated the TWS within the Congo Basin in Africa for the period from April 2002 up to May 2006. A total loss of about 280 km^3 of water was found over the period of study with a seasonal signal of 30 ± 6 mm of equivalent water thickness. Klees et al. (2007) compared monthly mean water storage variations inferred from GRACE in the upper Zambezi River (southern Africa) with the outputs of the LEW (Lumped Elementary Watershed) regional hydrological model. Rodell et al. (2009) studied groundwater depletion in India during the period from August 2002 to October 2008. They used the TWS change observed from GRACE as well as the simulated soil-water variations from GLDAS (Global Land Data Assimilation System). Their results showed that the groundwater depleted at a mean rate of 4.0 ± 1.0 cm/year equivalent water height. In this work, GRACE observations are used with the outputs from GLDAS hydrological model to study the groundwater storage variations in Africa during the period from January 2003 to December 2016. Comparison with the groundwater estimates from WGHM (WaterGAP Global Hydrology Model) is carried out.

2 Data Sources

2.1 Gravity Recovery and Climate Experiment (GRACE)

Since 2002, the Gravity Recovery and Climate Experiment (GRACE) satellite mission, sponsored by NASA and its German counterpart DLR, has been collecting gravimetric observations. One of the main products of the GRACE mission are the level-2 time-variable gravity fields (Flechtner 2007) which are monthly geopotential solutions released in terms of spherical harmonic coefficients. The latest Level-2 Release05 (RL05) monthly spherical harmonics coefficients provided by the Centre of Space Research (CSR) of the University of Texas at Austin (CSR, Bettadpur 2012) up to degree and order 60 are used for this study during the period from January 2003 up to December 2016 (except unavailable months, e.g., June 2015).

2.2 GLDAS Hydrological Model

The Global Land Data Assimilation System (GLDAS) project is led by scientists of the National Aeronautics and Space Administration (NASA) and the National Oceanic and Atmospheric Administration (NOAA). GLDAS is a land surface simulation system which aims to ingest satellite- and ground-based observational data products in order to generate optimal fields of land surface state (e.g., soil moisture, snow, and surface temperature) and flux (e.g., evapotranspiration, sensible heat flux) products (Rodell et al. 2004). In this paper, GLDAS version-1 NOAH model with 1° resolution is used during the period from January 2003 to December 2016.

2.3 WaterGAP Global Hydrological Model (WGHM)

The WaterGAP Global Hydrology Model (WGHM) provides time series of monthly runoff (surface/subsurface runoff and groundwater recharge) and river discharge by using 724 globally distributed stations. All computations are done at a spatial resolution of $0.5° \times 0.5°$ covering all land areas with the exception of Antarctica and Greenland. The model has basically been developed to simulate variations of water storage components within the framework of water availability and water use assessment at the global scale over river basins (Döll et al. 2003; Güntner et al. 2007). In this paper we used the total groundwater storage from the WGHM model at $0.5° \times 0.5°$ spatial resolution for January 2003–December 2013 (no data are available after 2013) for comparison purposes.

3 Methodology

The Terrestrial water storage variations (Δ_{TWS}) observed by GRACE include a combined contribution of the modeled changes in soil moisture (Δ_{SM}), groundwater (Δ_{GW}),

snow/ice water equivalent (Δ_{SWE}), and biomass ($\Delta_{biomass}$), i.e.,

$$\Delta_{TWS} = \Delta_{SM} + \Delta_{\mathrm{GW}} + \Delta_{\mathrm{SWE}} + \Delta_{biomass}. \quad (1)$$

Because of the common warm weather in Africa, snow is uncommon (i.e., Δ_{SWE} nearly vanishes in Africa). Biomass water variation ($\Delta_{biomass}$) is negligible in most cases (Cazenave and Chen 2010). Accordingly, the non-negligible sources of the Terrestrial Water Storage variability (Δ_{TWS}) in Africa were assumed herein to be the soil moisture (Δ_{SM}) and the groundwater (Δ_{GW}) variations. Accordingly, the groundwater variation is computed as:

$$\Delta_{GW} = \Delta_{TWS} - \Delta_{\mathrm{SM}}. \quad (2)$$

4 Estimation of TWS from GRACE

The terrestrial water storage (TWS) anomalies over the land can be related to changes in the Stokes coefficients, $\triangle C_{lm}$ and $\triangle S_{lm}$, for each month as (Wahr et al. 1998):

$$\Delta\sigma(\theta,\lambda) = \frac{a\,\rho_{av}}{3\,\rho_w}\sum_{l=0}^{\infty}\sum_{m=0}^{l}\frac{2l+1}{1+k_l}W_l \times\left[\bar{P}_{lm}(\cos\theta)\left(\Delta C_{lm}\cos m\lambda+\Delta S_{lm}\sin m\lambda\right)\right], \quad (3)$$

where $\Delta\sigma$ is the surface mass variability (which reflects the change in water storage), a is the earth's semi-major axis, ρ_{av} is the average density of the earth (5,517 kg/m^3), ρ_w is the density of the fresh water (1,000 kg/m^3), $\bar{P}_{lm}$ is the normalized associated Legendre functions with degree l and order m, k_l is the elastic love number of degree l, W_l corresponds to the Gaussian smoothing operator, θ is the co-latitude, λ is the eastward longitude, $\triangle C_{lm}$ and $\triangle S_{lm}$ are the monthly Stokes coefficient anomalies (Han and Wahr 1995). GRACE level-2 spherical harmonics solutions are provided by a number of institutes. In this work, GRACE CSR-RL05 solutions up to degree/order 60 are processed to infer TWS variations in Africa. The study area extends from 40.5°S latitude to 40.5°N and from 20.5°W longitude to 60.5°E.

GRACE CSR-RL05 solutions are also available up to degree/order 96. In order to study the effect of using a higher upper degree than 60, the TWS monthly anomaly in Africa during 2007 is computed from GRACE-CSR coefficients taking $\mathrm{N_{max}} = 60$ and $\mathrm{N_{max}} = 96$; Fig. 1. Figure 1 shows practically no differences. Thus, it can be concluded that using upper degree greater than 60 has *insignificant* influence on the geophysical signals.

The temporal mean, computed over the period of the study, has been removed from the monthly estimated GRACE fields. After removing the temporal mean, GRACE data are corrected for correlated errors by post-processing GRACE monthly solutions by applying a moving window filtering method according to Swenson and Wahr (2006). However, the window width used by Swenson and Wahr (2006) is not provided in the original paper, Duan et al. (2009) cited Swenson and Wahr's unpublished result of window width. Decorrelation filter is done for the spherical harmonics of order $m = 5$ and above, and the window width w depends on m in the following form:

$$w = \max\left(Ae^{-\frac{m}{k}} + 1, 5\right), \quad (4)$$

where the function $max(x_1,x_2)$ selects the larger argument. Swenson and Wahr (2006) have empirically chosen $A = 30$ and $K = 10$ for the CSR RL02 data they used at the time, evidently based on a trial-and-error procedure. Here the same values of A and K are used.

Additionally, GRACE does not provide degree 1 coefficient changes C_{10}, C_{11}, and S_{11}, which represent variation of the earth's center of mass relative to the crust-fixed terrestrial reference frame (geocenter motion) (Chen et al. 1999; Chambers et al. 2004). The monthly degree 1 coefficients are used from (Swenson et al. 2008). The monthly C_{20} coefficients are replaced with the solutions from Satellite Laser Ranging (SLR) (Chen et al. 2004), because the native GRACE-C20 values have a larger uncertainty than the SLR-values.

The gravity field produced by GRACE satellite mission requires a smoothing operator to reduce the effects of the errors present in the short wavelength components. As the smoothing radius decreases, these errors manifest themselves in maps of surface mass variability as long, linear features generally oriented north to south (i.e., stripes). Then the spherical harmonic coefficients are smoothed with a Gaussian averaging kernel of 500 km radius, using the formula represented by Chambers (2006):

$$W_l = \left[-\frac{(lr/a)^2}{4\ln(2)}\right], \quad (5)$$

where W_l is the smoothed value, and r is the smoothing radius.

Figure 2 shows the GRACE-derived TWS monthly mean difference and trend in Africa using a 500 km Gaussian smoothing. It shows that the maximum positive trend in Zambezi river basin in southern Africa. The maximum negative trend happened in Congo River basin in middle Africa. A negative trend happened in northern Africa.

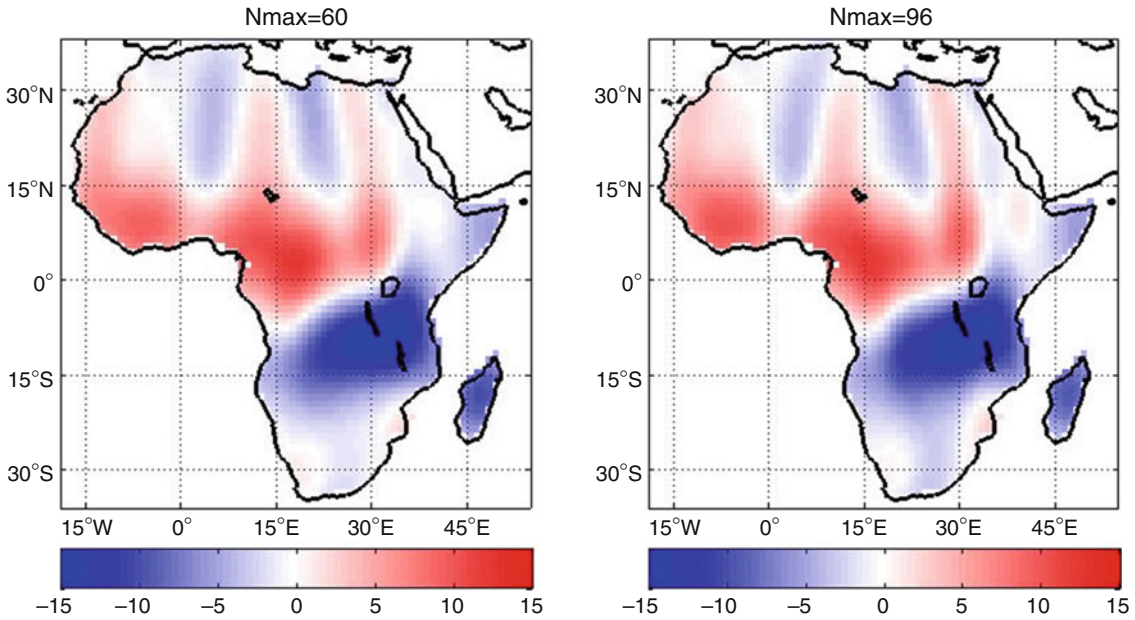

Fig. 1 The GRACE TWS monthly anomaly for 2007 using $N_{max} = 60$ and $N_{max} = 96$. Units in [mm]

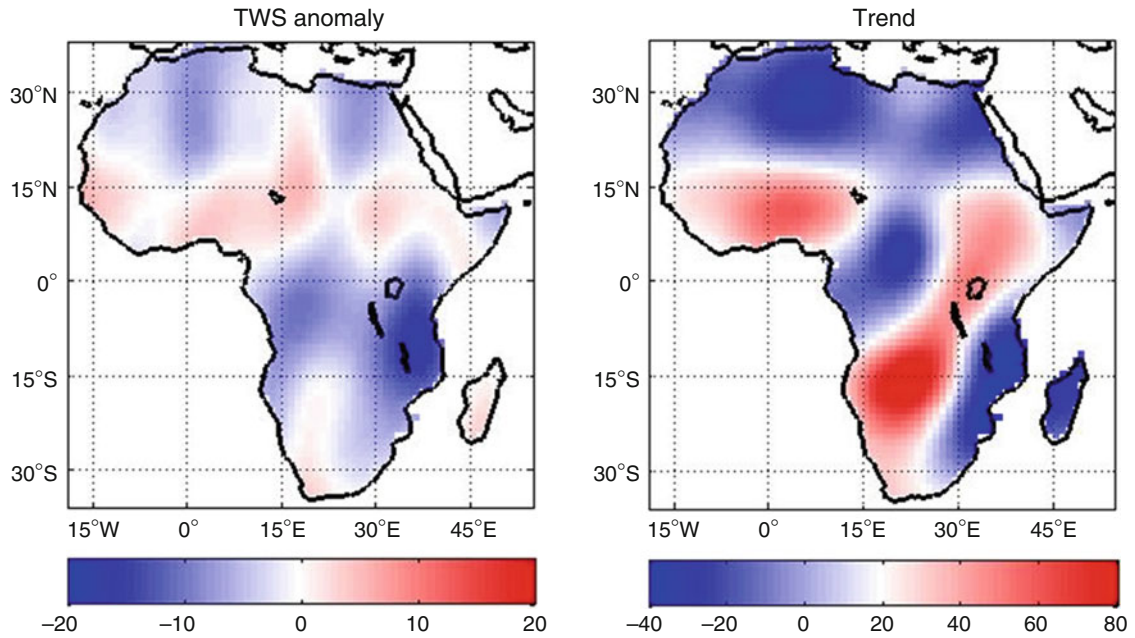

Fig. 2 The GRACE average monthly difference of TWS (*left panel*) and trend of TWS (*right panel*) from Jan. 2003 to Dec. 2016. Units in [mm]

5 Spherical Harmonic Analysis of the Hydrological Models

GRACE data are available in terms of spherical harmonics expansion. However, GLDAS and WGHM hydrological models are available in the space domain as grids of 1° and 0.5°, respectively. Accordingly, for fair comparisons, both GLDAS and WGHM are approximated in terms of spherical harmonic expansions to the same degree (i.e., 60) as the used GRACE data. Then, the same filtering process has been applied to the transformed GLDAS and WGHM (i.e., 500 km Gaussian smoothing filter and the decorrelation filter).

The estimation of the harmonic coefficients for both GLDAS and WGHM models is done using the Gauss-Legendre numerical integration harmonic analysis technique within an iterative approach (Abd-Elmotaal et al. 2014). In order to evaluate the performed spherical harmonics analysis, the estimated fields of GLDAS and WGHM, computed from their spherical harmonic expansions on a global grid of $1° \times 1°$, are compared to their original fields.

Figure 3 shows the original GLDAS field for January 2003, while Fig. 4 shows the approximated GLDAS filed for the same month computed from the spherical harmonic expansion. Figure 5 illustrates the difference between the original and the approximated GLDAS fields. Figure 5 demonstrates good approximation.

The soil moisture storage variation is estimated using the GLDAS NOAH (1° resolution) model by summing the four layers of soil moisture. Figure 6 shows the GLDAS soil moisture (monthly anomaly and trend) for Africa computed from the spherical harmonic analysis mentioned above. Figure 6 shows that the maximum signal occurs at Congo basin in middle Africa. The minimum signal happened in northern Africa.

6 Groundwater Estimation Using GRACE and GLDAS and Its Evaluation Using WGHM

We used GLDAS time series of soil moisture storage to isolate groundwater storage variations from the GRACE TWS anomalies (using Eq. (2)) by subtracting the GLDAS soil moisture storage (Δ_{SM}) from GRACE-TWS (Δ_{TWS}). Figure 7 represents the mean monthly variation of groundwater in Africa (*left panel*) as well as the trend over the time period (*right panel*). The maximum positive trend happened in Zambezi river basin in southern Africa. An increase in groundwater storage occurred in western Africa in Volta River basins while a negative variation happened in middle Africa in Congo River basin.

Figure 8 represents the time series of the averaged total (vertically-integrated) TWS over Zambezi river basin and estimates from the GRACE, GLDAS hydrological model and Groundwater (GRACE – GLDAS). It shows a small depletion at 2005 followed by a significant increasing trend from 2006 to 2010. The overall trend value of 16.60 + 1.1 mm/year is observed during the period of study.

In the view of the lack of in situ measurements, groundwater estimated directly from WGHM model is used to evaluate the GRACE-based groundwater variations. The disadvantage of the WGHM model is that it is only available up to December 2013. Figure 9 shows the WGHM groundwater monthly anomaly in Africa (*left panel*) and the trend over the time period (*right panel*) computed from the spherical harmonic expansion performed in Sect. 5. Comparing Figs. 7 and 9 illustrates the same positive trend in Volta River basin in western Africa. In addition, same strong negative signal appears in the western part of middle Africa, while almost zero signal appears in northern Africa. This proves that the used approach in the current paper to estimate the groundwater using GRACE and GLDAS is successful to a good extent.

7 Conclusion

In this paper, the groundwater variations in Africa are estimated and investigated from GRACE–GLDAS in the period of January 2003 to December 2016.

Figure 2 represents the mean monthly variation of TWS which comes from GRACE spherical harmonics, with the maximum signal occurs at Congo basin and zero signal in northern Africa. Figure 6 shows the mean monthly variation of soil moisture content which comes from GLDAS-NOAH model computed by its spherical harmonic expansion estimated by the Gauss-Legendre numerical integration harmonic analysis technique. Subtracting the soil moisture variation from total water storage variation gives the variation of the groundwater. Figure 7 represents the mean monthly variation of groundwater in Africa. An increase in groundwater storage occurred in western Africa in Niger and Volta River basins while a negative variation happened in middle Africa in Congo River basin. The results are then compared with the groundwater storage variation estimated from WGHM model. It shows similar results, which proved the success of the proposed developed approach. The proposed approach of using GRACE and GLDAS having the advantage of continuous data availability up to date. In contrast, WGHM is only available until December 2013.

Acknowledgements The authors would like to thank the editor of the current paper and two anonymous reviewers for their useful comments.

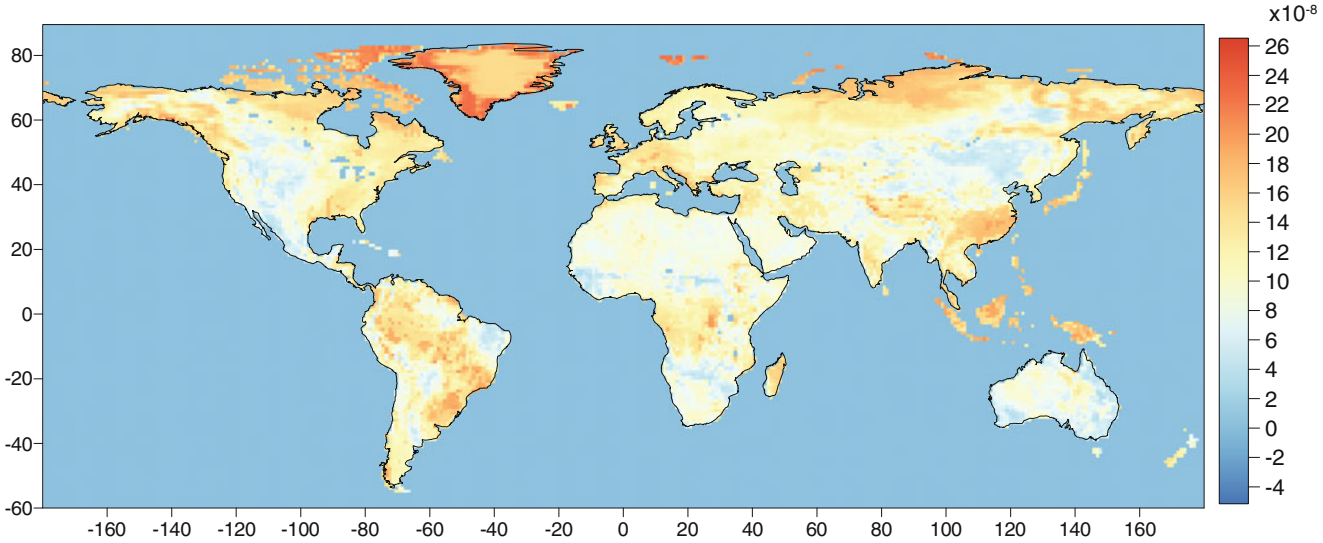

Fig. 3 The January 2003 original GLDAS. Units in [kg/m^2]

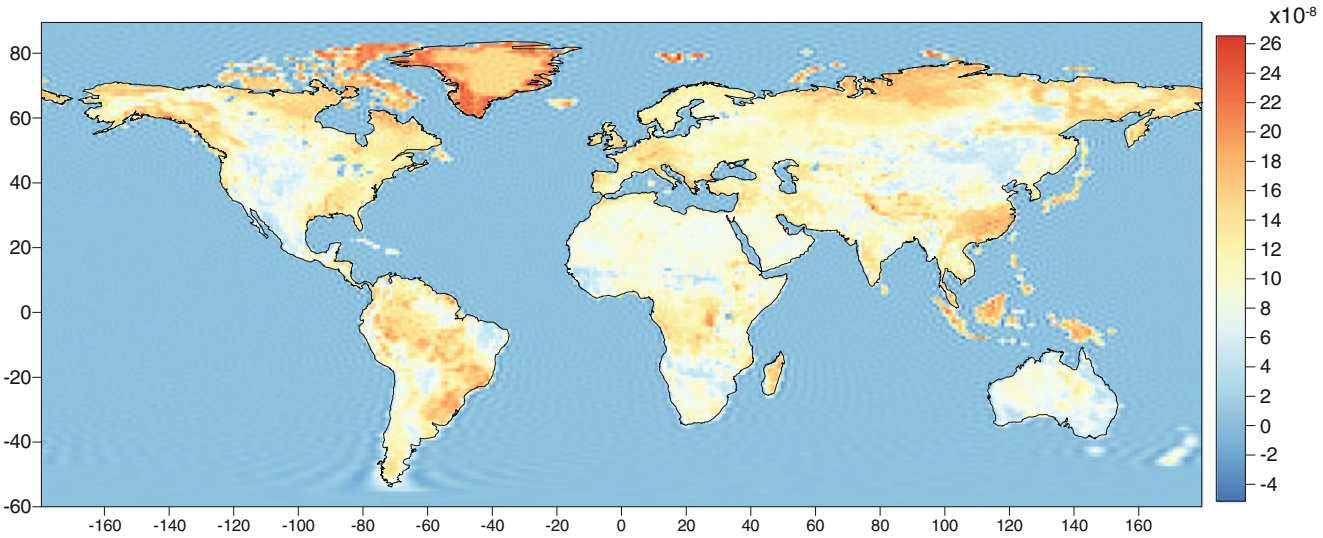

Fig. 4 The January 2003 approximated GLDAS computed from spherical harmonic expansion. Units in [kg/m^2]

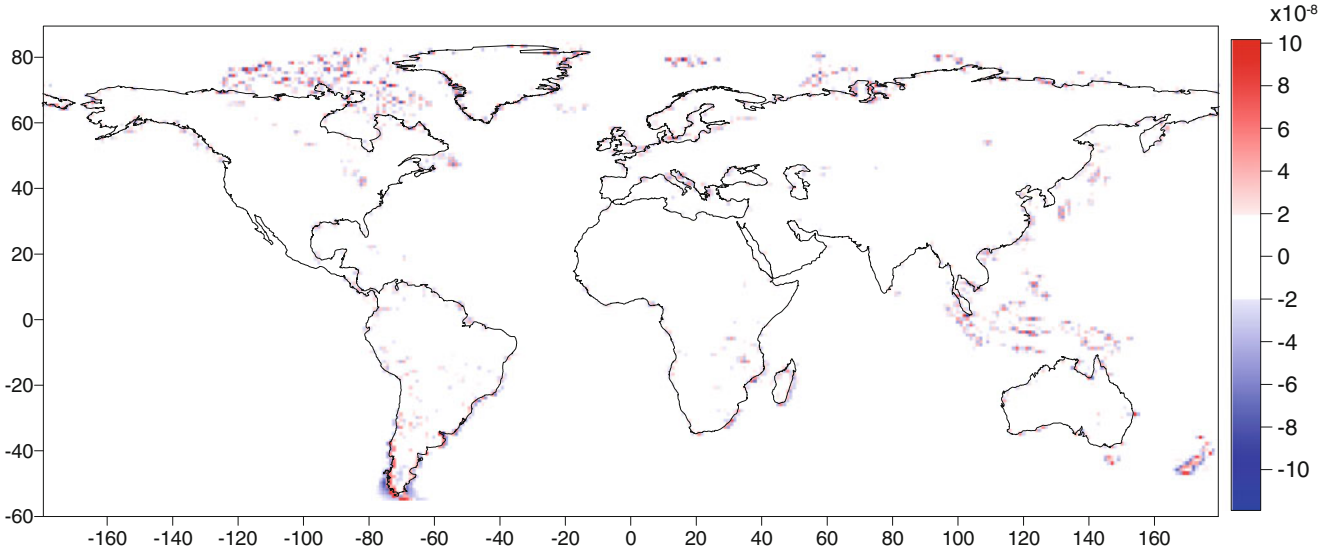

Fig. 5 The Difference between original GLDAS and approximated GLDAS by spherical harmonic expansion. Units in [kg/m^2]

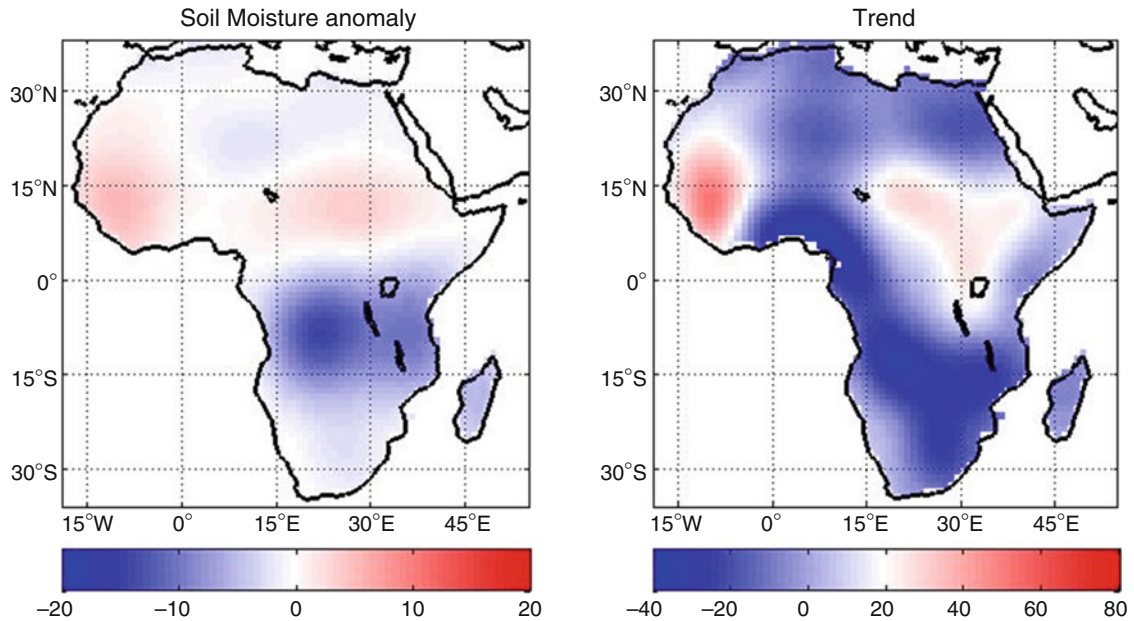

Fig. 6 The GLDAS average monthly difference of soil moisture (*left panel*) and trend of soil moisture (*right panel*) (both are computed from the spherical harmonic expansion) from Jan. 2003 to Dec. 2016. Units in [cm]

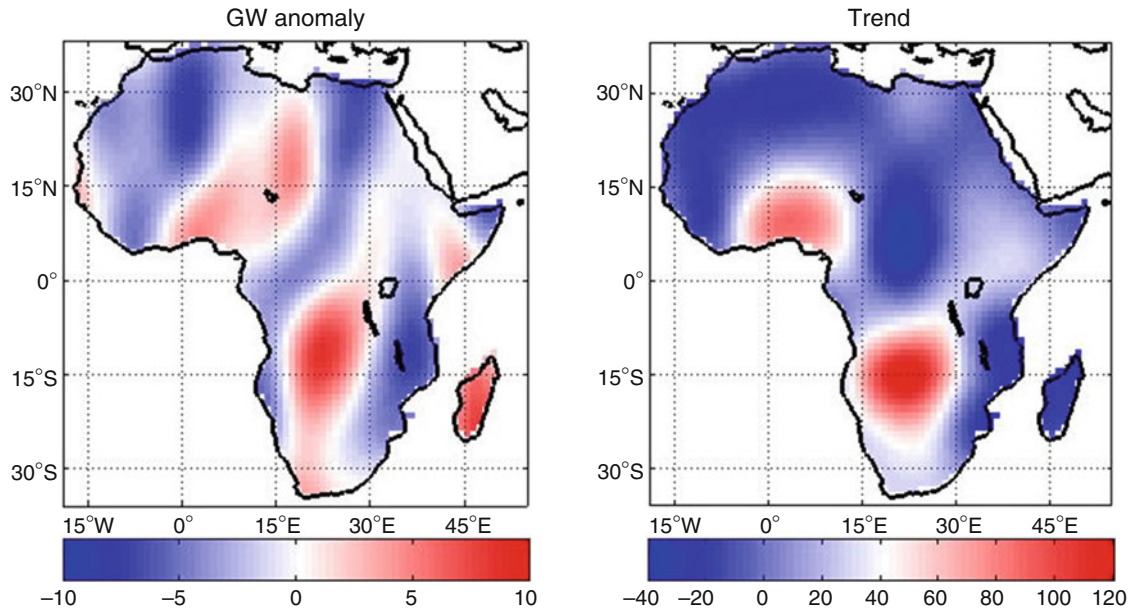

Fig. 7 The average monthly difference of groundwater (GW) (*left panel*) and trend (*right panel*) from Jan. 2003 to Dec. 2016 estimated using GRACE and GLDAS. Units in [cm]

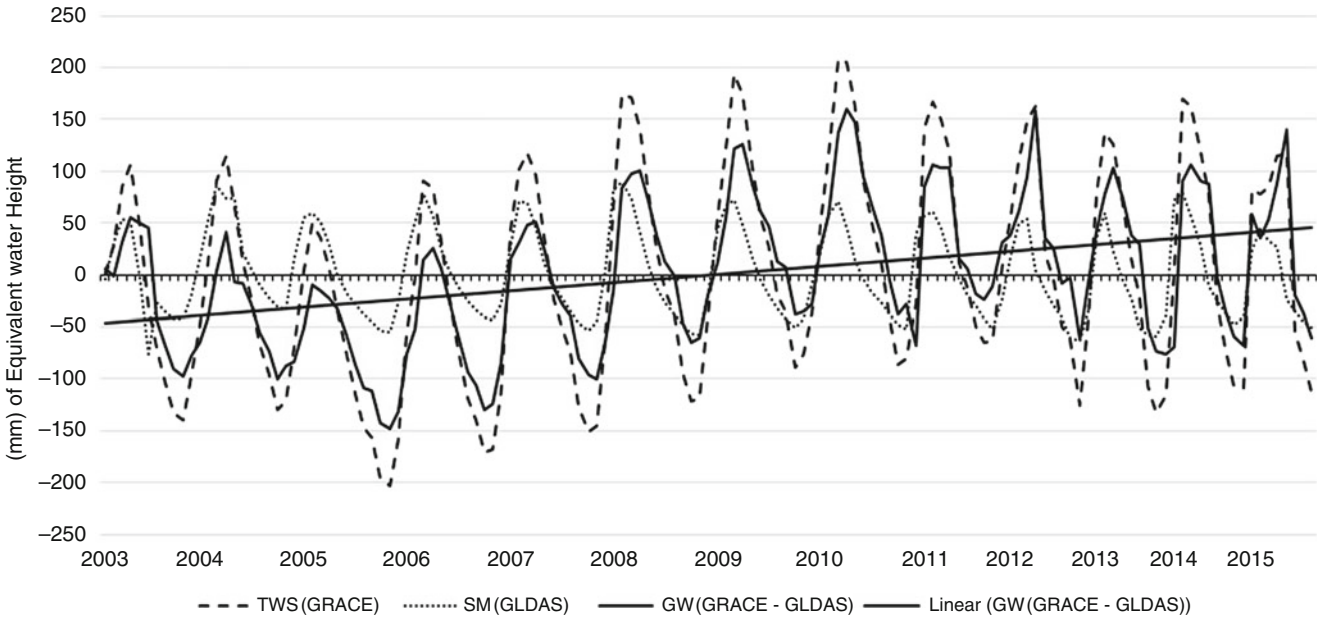

Fig. 8 The averaged TWS from GRACE, GW storage (GRACE - GLDAS), and GW trend for Zambezi river basin for the period from Jan 2003 to Sep 2015. Units in [cm]

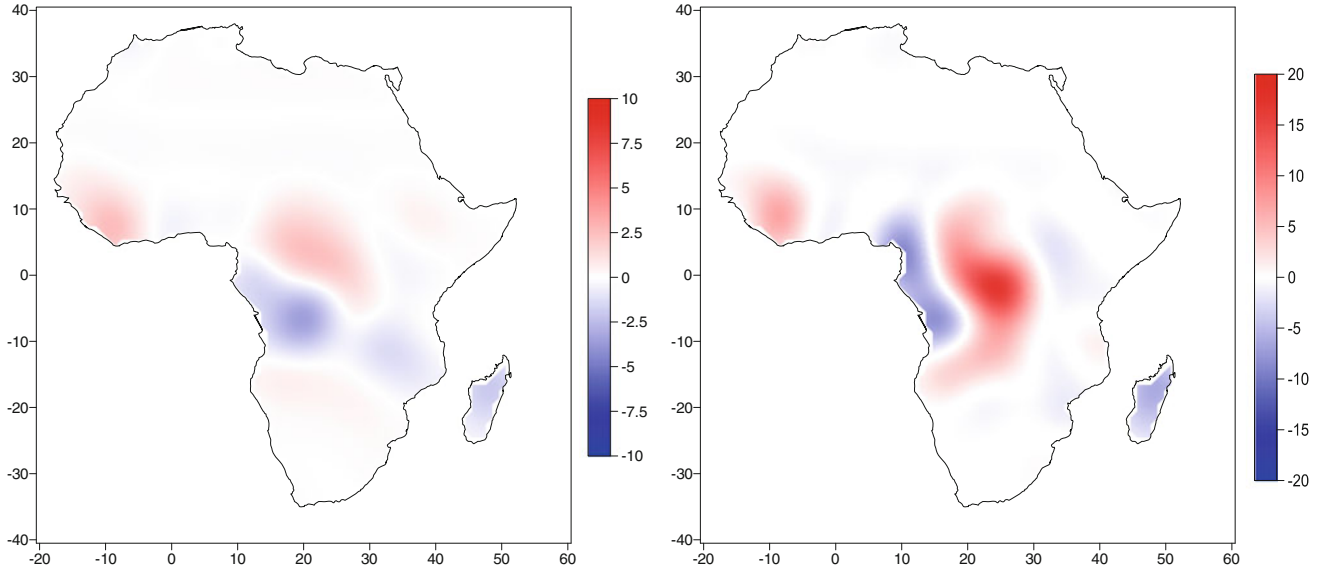

Fig. 9 The average monthly difference of groundwater from WGHM model (*left panel*) and trend (*right panel*) computed from spherical harmonic expansion from Jan. 2003 to Dec. 2013. Units in [cm]

References

Abd-Elmotaal HA, Seitz K, Abd-Elbaky M, Heck B (2014) Comparison among three harmonic analysis techniques on the sphere and the ellipsoid. J Appl Geod 8(1):1–20. https://doi.org/10.1515/jag-2013-0008

Bettadpur S (2012) UTCSR Level-2 processing standards document for level-2 product release 0005, GRACE 327-742, CSR Publ. GR-12-xx, Rev, 4, 16

Cazenave A, Chen J (2010) Time-variable gravity from space and present-day mass redistribution in the Earth system. Earth Planet Sci Lett 298(3):263–274. https://doi.org/10.1016/j.epsl.2010.07.035

Chambers DP (2006) Observing seasonal steric sea level variations with GRACE and satellite altimetry. J Geophys Res Oceans 111(C3). https://doi.org/10.1029/2005JC002914

Chambers DP, Wahr J, Nerem RS (2004) Preliminary observations of global ocean mass variations with GRACE. Geophys Res Lett 31(13). https://doi.org/10.1029/2004GL020461

Chen JL, Wilson CR, Eanes RJ, Nerem RS (1999) Geophysical interpretation of observed geocenter variations. J Geophys Res Solid Earth 104(B2):2683–2690

Chen JL, Wilson CR, Tapley BD, Ries JC (2004) Low degree gravitational changes from GRACE: validation and interpretation. Geophys Res Lett 31(22). https://doi.org/10.1029/2004GL021670

Crowley JW, Mitrovica JX, Bailey RC, Tamisiea ME, Davis JL (2006) Land water storage within the Congo Basin inferred from GRACE satellite gravity data. Geophys Res Lett 33(19). https://doi.org/10.1029/2006GL027070

Duan XJ, Guo JY, Shum CK, Van Der Wal W (2009) On the post-processing removal of correlated errors in GRACE temporal gravity field solutions. J Geod 83(11):1095–1106. https://doi.org/10.1007/s00190-009-0327-0

Döll P, Kaspar F, Lehner B (2003) A global hydrological model for deriving water availability indicators: model tuning and validation. J Hydrol 270(1):105–134. https://doi.org/10.1016/S0022-1694(02)00283-4

Flechtner F GFZ level-2 processing standards document for level-2 product release 0004 (Rev. 1.0, February 19, 2007)

Güntner A, Stuck J, Werth S, Döll P, Verzano K, Merz B (2007) A global analysis of temporal and spatial variations in continental water storage. Water Resour Res 43:W05416. https://doi.org/10.1029/2006WR005247

Han D, Wahr J (1995) The viscoelastic relaxation of a realistically stratified Earth and a further analysis of postglacial rebound. Geophys J Int 120(2):287–311. https://doi.org/10.1111/j.1365-246X.1995.tb01819.x

Jin S, Feng G (2013) Large-scale variations of global groundwater from satellite gravimetry and hydrological models, 2002–2012. Glob Planet Chang 106:20–30. https://doi.org/10.1016/j.gloplacha.2013.02.008

Klees R, Zapreeva EA, Winsemius HC, Savenije HHG (2007) Monthly mean water storage variations by the combination of GRACE and a regional hydrological model: application to the Zambezi River. In: Dynamic planet. Springer, Berlin, pp 488–495

MacDonald AM, Bonsor HC, Dochartaigh BÉÓ, Taylor RG (2012) Quantitative maps of groundwater resources in Africa. Environ Res Lett 7(2):024009. https://doi.org/10.1088/1748-9326/7/2/024009

Ramillien G, Cazenave A, Brunau O (2004) Global time variations of hydrological signals from GRACE satellite gravimetry. Geophys J Int 158(3):813–826. https://doi.org/10.1111/j.1365-246X.2004.02328.x

Ramillien G, Frappart F, Cazenave A, Güntner A (2005) Time variations of land water storage from an inversion of 2 years of GRACE geoids. Earth Planet Sci Lett 235(1):283–301. https://doi.org/10.1016/j.epsl.2005.04.005

Rodell M, Houser PR, Jambor UEA, Gottschalck J, Mitchell K, Meng CJ, Entin JK, Walker JP, Lohmann D, Toll D (2004) The global land data assimilation system. Bull Am Meteorol Soc 85(3):381–394. https://doi.org/10.1175/BAMS-85-3-381

Rodell M, Velicogna I, Famiglietti JS (2009) Satellite-based estimates of groundwater depletion in India. Nature 460(7258):999–1002. https://doi.org/10.1038/nature08238

Swenson S, Wahr J (2006) Post-processing removal of correlated errors in GRACE data. Geophys Res Lett 33(8). https://doi.org/10.1029/2005GL025285

Swenson S, Chambers DP, Wahr J (2008) Estimating geocenter variations from a combination of GRACE and ocean model output. J Geophys Res Solid Earth 113(B8). https://doi.org/10.1029/2007JB005338

Tapley BD, Bettadpur S, Watkins M, Reigber C (2004) The gravity recovery and climate experiment: mission overview and early results. Geophys Res Lett 31(9). https://doi.org/10.1029/2004GL019920

Wahr J, Molenaar M, Bryan F (1998) Time variability of the Earth's gravity field: hydrological and oceanic effects and their possible detection using GRACE. J Geophys Res Solid Earth 103(B12):30205–30229. https://doi.org/10.1029/98JB02844

Wahr J, Swenson S, Zlotnicki V, Velicogna I (2004) Time-variable gravity from GRACE: first results. Geophys Res Lett 31(11). https://doi.org/10.1029/2004GL019779

List of Reviewers

Alberta Albertella
Bruno Meurers
Christian Ullrich
Daniela Carrión
Derek VanWestrum
Elena Rangelova
Hussein A. Abd-Elmotaal
Jan Krynski
Laura Sánchez
Marco Pierozzi
Mirko Reguzzoni
Przemysław Dykowski
Shuanggen Jin
Tomislav Bašić
Vassilios Grigoriadis
Yoichi Fukuda
Artu Ellmann
C. Hwang
Christopher Kotsakis
David Becker
Dimitrios Natsiopoulos
Federica Migliaccio
Ilias Tziavos
Jianliang Huang
Lucia Seoane
Maria Clara de Lacy
Nikolaos Konstantinos Pavlis
Richard Taylor
Silvio R.C. de Freitas
Urs Marti
WenBin Shen
Gabriel do Nascimento Guimaraes
Bernhard Heck
Christian Gerlach
Daniel R. Roman
David Zuliani
Dimitrios Tsoulis
Gyula Toth
Ismael Foroughi
Jonas Ågren
Luisa M. C. Bastos
Michal Sprlak
Oliver Francis
Rossen Grebenitcharsky
Sten Claessens
Vassilios D. Andritsanos
Wolf-Dieter Schuh

G. S. Vergos et al. (eds.), *International Symposium on Gravity, Geoid and Height Systems 2016*,
International Association of Geodesy Symposia 148, https://doi.org/10.1007/978-3-319-95318-2

Author Index

G. S. Vergos et al. (eds.), *International Symposium on Gravity, Geoid and Height Systems 2016*,
International Association of Geodesy Symposia 148, https://doi.org/10.1007/978-3-319-95318-2